

Physicochemical Problems of Mineral Processing

Index No. 32213X

ISSN 1643-1049

Volume 52, Issue 1

January 1, 2016

**Physicochemical
Problems
of Mineral Processing
52(1), January 1, 2016**

Instructions for preparation of manuscripts

It is recommended that the following guidelines be followed by the authors of the manuscripts:

- original papers dealing with principles of mineral processing and papers on technological aspects of mineral processing will be published in the journal which appears twice a year (January 1 and June 1)
- the manuscript should be sent to the journal via manuscript management system available at <http://www.editorialsystem.com/ppmp>
- only manuscripts written in English are accepted
- contributors whose native language is not English are urged to have their manuscript competently edited prior to submission
- the manuscript should not exceed 10 pages
- there is a 150 EUR fee for publishing and printing the paper
- additional correspondence regarding the journal should be sent to either jan.drzymala@pwr.edu.pl or przemyslaw.kowalcuk@pwr.edu.pl.

Submission of papers is tantamount to a transfer of copyrights by the author(s) to Faculty of Geoengineering, Mining and Geology of Wroclaw University of Technology Publisher covering publication in printed forms as well as electronic media (CD-ROM or Internet) of the articles and any modifications of it.

Wroclaw University of Technology
Wybrzeze Wyspianskiego 27
50-370 Wroclaw, Poland

www.minproc.pwr.edu.pl/journal
jan.drzymala@pwr.edu.pl
przemyslaw.kowalcuk@pwr.edu.pl

Physicochemical Problems of Mineral Processing

Volume 52, Issue 1, January 1, 2016

www.minproc.pwr.edu.pl/journal
wwwdbc.wroc.pl/dlibra/publication/11251

Faculty of Geoengineering, Mining and Geology
Wroclaw University of Technology

Wroclaw 2016

Editor-in-Chief

Jan DRZYMALA, Wroclaw University of Technology

Editors

Emre Naci ALTUN, Middle East Technical University, Turkey

Jari AROMAA, Aalto University, Finland

Teofil JESIONOWSKI, Poznan University of Technology, Poland

Christian JUNGNICKEL, Gdansk University of Technology, Poland

Przemyslaw B. KOWALCZUK, Wroclaw University of Technology, Poland

Marcin LUTYNSKI, Silesian University of Technology, Poland

Katarzyna OCHROMOWICZ, Wroclaw University of Technology, Poland

Orhan OZDEMIR, Istanbul University, Turkey

Editorial Advisory Board

El-Sayed Ali ABDEL-AAI, Central Metallurgical R&D Institute

Witold PAWŁOS, KGHM Polska Miedź S.A.

Marian BROZEK, AGH University of Science and Technology

Andrzej POMIANOWSKI, Polish Academy of Science

Stanisław CHIBOWSKI, Maria Skłodowska-Curie University

PRADIP, Tata R&D Design Centre

Tomasz CHMIELEWSKI, Wroclaw University of Technology

Fereshteh RASHIDII, University of Tehran

Hylke J. GLASS, University of Exeter

Zygmunt SADOWSKI, Wroclaw University of Technology

Jan HUPKA, Gdansk University of Technology

Oktay SAHBAZ, Dumluçinar University

Andrzej KONIECZNY, KGHM Polska Miedź S.A.

Stanisława SANAK-RYDLEWSKA, AGH University of Science and

Janusz LASKOWSKI, University of British Columbia

Technology

Andrzej LUSZCZKIEWICZ, Wroclaw University of Technology

Adem TASDEMIR, Eskisehir Osmangazi University

Kazimierz MALYSA, Polish Academy of Science

Barbara TORA, AGH University of Science and Technology

Jan D. MILLER, University of Utah

Production Editor

Marek J. BATTEK, Wroclaw University of Technology, Poland

The papers published in the Physicochemical Problems of Mineral Processing journal are abstracted in BazTech, Chemical Abstracts, Coal Abstracts, EBSCO, Google Scholar, Scopus, Thomson Reuters (Science Citation Index Expanded, Materials Science Citation Index, Journal Citation Reports) and other sources

© Copyright by Faculty of Geoengineering, Mining and Geology Wroclaw University of Technology

ISSN 1643-1049 (print)

previously 0137-1282

ISSN 2084-4735 (online)

Faculty of Geoengineering, Mining and Geology Wroclaw University of Technology

Wybrzeze Wyspianskiego 27, 50-370 Wroclaw, Poland

CONTENTS

M.S. Trumic, M.M. Antonijevic, <i>Toner recovery from suspensions with fiber and comparative analysis of two kinetic models</i>	5
F. Karakas, B. Vaziri Hassas, <i>Effect of surface roughness on interaction of particles in flotation</i>	18
Y. Erdogan, E. Yasar, P. Gamage Ranjith, <i>Obtaining lightweight concrete using colemanite waste and acidic pumice</i>	35
Z. Ren, J. Guan, H. Gao, J. Tian, Y. Wen, R. Zheng, <i>Characteristics of cationic Red X-GRL adsorption by raw diatomite and diatomite concentrate</i>	44
S. Ali, Y. Iqbal, U. Farooq, S. Ahmad, <i>Leaching of manganese ores using corncob as reductant in H_2SO_4 solution</i>	56
A.G. Celik, G.O. Cakal, <i>Characterization of Espey colemanite and variation of its physical properties with temperature</i>	66
G. Leon, G. Martinez, L. Leon, M. A. Guzman, <i>Separation of cobalt from nickel using novel ultrasound-prepared supported liquid membranes containing Caynex 272 as carrier</i>	77
P. Religa, J. Rajewski, P. Lobodzin, <i>Kinetics of chromium(III) transport through the double-carrier supported liquid membrane</i>	87
D. Foszcz, M. Duchnowska, T. Niedoba, T. Tumidajski, <i>Accuracy of separation parameters resulting from errors of chemical analysis, experimental results and data approximation</i>	98
H. Basturkcu, N. Acarkan, <i>Leaching behaviour of a Turkish lateritic ore in the presence of additives</i>	112
E. S. Abdel-Aal, E. Abdel Rahman, A. H. Kandil, <i>Enhancing filtration rate of New Valley oxidized phosphate concentrate with additives</i>	124
B. Tufan, T. Batar, <i>Electro-deposition parameters of boron carbonitride (BCN) from borax pentahydrate ($Na_2B_4O_7 \cdot 5H_2O$)</i>	136
P.B. Kowalcuk, J. Drzymala, <i>Some remarks on attachment of a gas bubble to another phase both immersed in water</i>	147
J. Yu, Y. Ge, J. Hou, <i>Behavior and mechanism of colophane and dolomite separation using alkyl hydroxamic acid as a flotation collector</i>	155
B. Feng, P. Wang, Y. Lu, Q. Feng, <i>Role of sodium hexametaphosphate in flotation of a nickel ore</i> ..	170
D. Saramak, D. Foszcz, T. Gawenda, A. Konieczny, W. Pawlos, <i>Influence of type of lining in high-pressure grinding rolls on effectiveness of copper ore comminution</i>	182
I. Pyka, K. Wierzchowski, <i>Split of mercury between products of coal cleaning versus mercury emissions reduction</i>	193
M. Kademli, O. Y. Gulsoy, <i>Influence of particle size and feed rate on coal cleaning in a dry separator</i>	204
H. Xu, G. Huagn, X. Li, L. Gao, Y. Wang, <i>Removal of quinoline from aqueous solutions by lignite, coking coal and anthracite. Adsorption isotherms and thermodynamics</i>	214
A. Surowiak, M. Brozek, <i>A physical model of separation process by means of jigs</i>	228
R. Ahtiainen, M. Lundstrom, <i>Preg-robbing of gold in chloride-bromide solution</i>	244
F. Nakhaci, M. Irannajad, A. Sam, A. Jamalzadeh, <i>Application of D-optimal design for optimizing copper-molybdenum sulphides flotation</i>	252

K. Barani, H. Balochi, <i>First-order and second-order breakage rate of coarse particles in ball mill grinding</i>	268
X. Gui, J. Liu, Y. Cao, Y. Xing, Y. Deng, S. Li, <i>Effect of intergrown particle liberation on difficult-to-separate coking coal flotation</i>	279
M. Kiviluoma, M. Aaltonen, J. Aromaa, M. Lundstrom, O. Forsen, <i>Development of characterization methods for adherent anode slimes in copper electrorefining</i>	295
L. Shen, H. Wang, <i>Properties of fatty acid/dodecylamine mixtures and their application in steam coal reverse flotation</i>	303
Ch. Ni, G. Xie, Z. Li, X. Bu, Y. Peng, J. Sha, <i>Flotation of long flame coal pretreated by polyoxyethylene sorbitan monostearate</i>	317
H. Li, Y. Chen, X. Zhang, Y. Zhao, Y. Tao, Ch. Li, X. He, <i>Experimental study on triboelectrostatic beneficiation of wet fly ash using microwave heating</i>	328
H. H. Gharehgheshlagh, <i>Kinetic grinding test approach to estimate the ball mill work index</i>	342
B. Pospiech, <i>Synergistic solvent extraction of Co(II) and Li(I) from aqueous chloride solutions with mixture of Cyanex 272 and TBP</i>	353
J. Li, S. Li, F. Zhou, <i>Effect of moisture content in coal dust on filtration and cleaning performance of filters</i>	365
B. Bozecka, P. Bozecki, S. Sanak-Rydlewska, <i>Removal of Pb(II) and Cd(II) ions from aqueous solutions with selected organic wastes</i>	380
H. Xu, Y. Wang, G. Huagn, G. Fan, L. Gao, X. Li, <i>Removal of quinoline from aqueous solutions by lignite, coking coal and anthracite. Adsorption kinetics</i>	397
M. D. Dimitrijevic, D. M. Urosevic, Z. D. Jankovic, S. M. Milic, <i>Recovery of copper from smelting slag by sulphation roasting and water leaching</i>	409
L. Gao, S. Li, Y. Wang, X. Gui, H. Xu, <i>Pretreatment of coking wastewater by an adsorption process using fine coking coal</i>	422
B. Zeytuncu, <i>Dissolution of alkaline batteries in reductive acidic media</i>	437
M.J. Janicki, J. Drzymala, P.B. Kowalcuk, <i>Structure and surface energy of both fluorite halves after cleaning along selected crystallographic planes</i>	451
L. Klapiszewski, T. J. Szalaty, J. Zdarta, T. Jesionowski, <i>Activated lignin and aminosilane-grafted silica as precursors in hybrid material production</i>	459
E. Guler, <i>Pressure acid leaching of sphalerite concentrate. Modeling and optimization by response surface methodology</i>	479
N.E. Altun, <i>Reactivity of marble wastes for potential utilization in wet flue gas desulphurization</i>	497
Professor Janusz Kazimierz Girczys, Ph.D., D.Sc., a tribute on his 80 th birthday	365

Received February 15, reviewed; accepted April 8, 2015

TONER RECOVERY FROM SUSPENSIONS WITH FIBER AND COMPARATIVE ANALYSIS OF TWO KINETIC MODELS

Maja S. TRUMIC, Milan M. ANTONIJEVIC

University of Belgrade, Technical Faculty, Bor, Serbia, majatrumic@tf.bor.ac.rs

Abstract: This paper studies kinetic aspects of toner flotation in a mechanical cell with methyl isobutyl carbinol (MIBC) as a frother by using a synthetic toner sample 212+0 μm in a size at variable pH. The effect of the MIBC dosage and pH value on the flotation behavior of the toner has been investigated in terms of toner recovery and fiber recovery. Two kinetic models, the classical first order model and a modified first order model, have been tested and compared. It was established that the achieved optimal parameters of flotation were MIBC 1.5 mg/dm³ and pH from 7 to 12. The obtained results indicate that the toner floats rapidly and that flotation kinetics fits well the modified first order model with a very good correlation coefficient compared to the correlation coefficient for the classical first order model.

Keywords: toner, flotation rate, toner recovery, fiber recovery, kinetic model

Introduction

For the first time flotation was applied to the separation of mineral ores at the end of 19th century the beginning of 20th century. It became the primary method of recovery for a large variety of minerals (Schmidt, 1996). Today, it is used for recovering different types of metallic and nonmetallic minerals and it has a wide range of applications in a number of areas other than mineral processing. These include technologies such as oil recovery (Ramaswa et al., 2007), waste water treatment (Rubio et al., 2002; Bogdanovic et al., 2013), soil remediation (Dermont et al., 2010), plastic separation (Hui et al., 2012) and deinking - flotation of ink (Jameson, 1998; Trumic et al., 2007; Vashisth et al., 2011).

Flotation is a dynamic process caused by an interaction of forces acting in the bubble-particle-water system (Kowalcuk et al., 2011). In the ink flotation, the air is blown into the fiber suspension creating air bubbles to which the hydrophobic ink particles are attached. The attached particles are carried to the top of the flotation

vessel, where they are removed as deinking froth (Pan et al., 1996; Rutland and Pugh, 1997). The purpose of the ink flotation process is to separate the hydrophobic ink particles from the hydrophilic fibre by using the differences in their chemical properties (Labidi et al., 2007).

To improve the hydrophobicity of floated particles, it is very common to apply flotation reagents. The laser and photocopy toner particles are hydrophobic and do not need the use of any collector, but a frother must be used in order to obtain a stable foam layer to remove the toner particles (Schmidt, 1996; Zhao et al., 2004). It is shown that the froth stability and the recovery of ink particles are closely related as the ink recovery increases with the increase of froth stability (Bajpai, 2014). Nonionic surfactants are widely applied as frothers in the flotation of ink due to their excellent foamability and they are not sensitive to water hardness (Zhao et al., 2004). The research has shown that the concentration of the nonionic frother should be between 0.1 and 5 mg/dm³ in order to avoid the decrease in the hydrophobicity of the toner particles, as well as to minimize the loss of fibers and fillers in froth (Doriss and Sayegh, 1994).

The recovery of ink particles can be affected by many factors. Generally, all significant factors can be classified in three groups: chemistry (collectors, frothers, activators, depressants, pH), equipment (cell design, agitation, gas flow rate) and operation parameters (feed rate, mineralogy, particle size, pulp density, temperature) (Theander and Pugh, 2004). The way these factors affect recovery is measured in terms of the toner flotation kinetics.

Kinetics is a very important aspect of flotation, and its main purpose is to study the role of the flotation rate constant. The flotation rate is measured by the recovery change of the floating material in the product per unit time and is characterized by the rate constant and the kinetics order (Li et al., 2013). Different functions can be used for delineation of kinetics of flotation. The most widely used is the first order model (Pan et al., 1996; Pelach Serra, 1997; Presta Maso, 2006; Labidi et al., 2007; Shemi, 2008, Allix et al., 2010; Doriss et al., 2011).

Pan et al. (1996) in his research described the flotation kinetics of ink particles under laboratory conditions by the classical model of the first order kinetics using the expressions

$$\ln \frac{1}{1-I} = kt \quad (1)$$

$$I = \frac{C_0 - C}{C_0} \quad (2)$$

where

I- flotation recovery of ink particles in froth product

t- flotation time

k- kinetic constant of flotation

c_o - concentration of particles at $t=0$ in sink product

c - concentration of particles at time t in sink product.

According to Pan et al. (1996) for a constant bubble flow through the stationary suspension of homogeneous particles and for a short flotation time, the particle flotation process follows the first order kinetics. However, for a longer flotation time, for all particle sizes, a sharp break is observed in the plots (no straight line for a given particle size at the plot of $\ln \frac{1}{1-I}$ vs. t). This implies that no single value of the constant k suffices to express the data. According to Pan the break between the two linear portions of each curve implies that for any given particle size two flotation mechanisms operate: one is a short-time mechanism and the other is a longer-time mechanism.

Generally, many scientists agree that the value of k can be determined from the expression (1) as long as the flotation time is short and the diameter of the ink particles is constant (Pan et al., 1996; Pelach Serra, 1997; Labidi et al, 2007). In this work, the flotation rate data were subjected to the curve fitting procedure in order to compare two models: the classical first order model and a modified first order model. This was done to determine which model better describes the kinetics of the toner flotation.

Material and methods

Toner

According to the material safety data sheet (MSDS), the toner inside the cartridge CB435A is mainly composed of a styrene/acrylate copolymer (<55 wt %) with ferrite (<45 wt %) and wax (<10 wt %). Its solubility in water is negligible, and it is partially soluble in toluene and xylene. The material should soften between 100 and 150°C. The density of the toner is 1.5 g/cm³. The average particle size of toner inside the cartridge is about 10 µm and particles have a spherical shape (Fig.1a). The polymerization of toners during the printing process results in the formation of larger particles (Fig.1b). This process might lead to the chemical bonding between the cellulose fiber and the new large toner particle and/or the physical entrapment of the cellulose fiber within the large toner particle. The toner can be separated from paper fiber in a disintegration process, but particles shapes will be flat or cubic (Nie et al., 1998). The surface roughness and shape of the toner particle have been changed after the printing process, as it can be seen in Fig.1b. In order to obtain a realistic synthetic sample, the toner from the cartridge has been thermally treated in an oven at 90 degrees for 60 minutes, and then it has been ground and screened to obtain three different fractions of different particle sizes. Screens used had 212, 150, 106 micrometers openings. The used toner fractions were -212+150 µm, -50+106 µm - 106+0 µm, and their masses were 0.25, 0.25 g, and 0.5 g, respectively. The particle shape is given in Fig.1c.

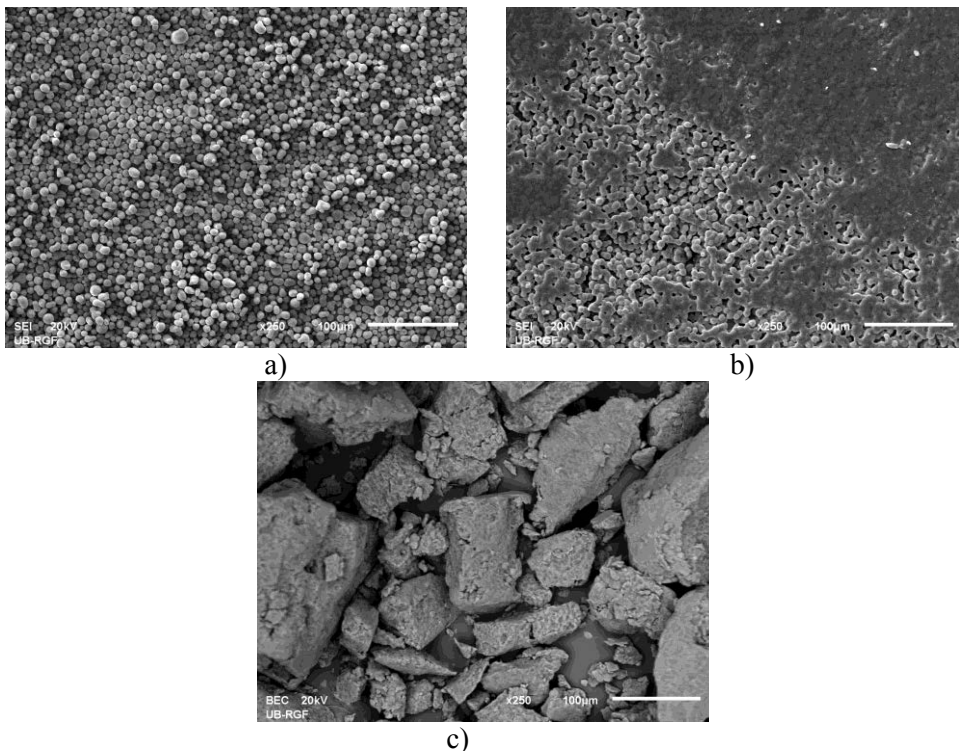


Fig. 1. Scanning electron microscopy (SEM) photographs of toner from:
 a) cartridge, b) laser printed sample and c) synthetic sample; (20 kV, 250x). Samples were coated with gold

Paper fiber

The paper fiber was prepared by soaking the alkaline copy paper (MAESTRO standard, A4, 80 g/m², the total filler content 28.8 wt. %) in distilled water for 16 hours and then disintegrated in an overhead stirrer. The operating conditions, during the disintegration stage, were held constant for all experiments (5% consistency, 45 °C, 400-900 rpm agitation speed, 120 min, pH 8).

Flotation

After the disintegration, toner was added to the paper fiber to obtain the suspension for flotation experiments. Flotation was carried out in a 2.2 dm³ laboratory flotation cell (Denver D12). The operating conditions of the flotation stage were held constant for all experiments (1100 rpm agitation speed, 270 dm³/h air flow rate). The frother MIBC (methyl isobutyl carbinol) was added during the conditioning stage. The condition time was 10 min, and the MIBC dosage varied from 0.5, 1.5, 3 to 6 mg/dm³ to find the optimum concentration. The pH value of the suspension was varied from highly acidic (pH 3) to highly alkaline (pH 12). The pH was maintained by sodium hydroxide and hydrochloric acid during the flotation. Deionized water was used in flotation. The

samples were extracted from the froth at 1, 2, 4, 6 and 10 min to study the kinetics during the flotation process. Subsequently, the float (toner particles in froth) and nonfloat (cellulose fiber in suspension) products were carefully filtered through a Buchner funnel, then dried at the room temperature and weighed to determine the fiber recovery.

The dried froth filter pads were then heated at 550 °C in a muffle furnace to determine the ash content. At this temperature, the calcination of calcium carbonate present in the alkaline paper was negligible. The ash was analyzed for iron by x-ray fluorescence (XRF). With toners of high iron oxide content, the percentage of iron in the froth allowed a reasonably good assessment of the toner content in the froth (Dorris and Sayegh, 1994; Li et al., 2011).

Results and discussion

It is apparent that a high recovery of toner (I) in the froth and a high recovery of fiber (Y) in the sink product are two important requirements (Huber et al., 2011). From economic and environmental points of view, the flotation process has to be optimized in terms of both high ink recovery and high fiber recovery and for the analysis of such results it is convenient to use the Fuerstenau plot (Bakalarz and Drzymala, 2013). The values of the ink and fiber recoveries, being also efficiency indicators, should be around 90 % (Suss et al., 1994). Many factors have an influence on these indicator value. The stability of the foam is one of the most important factor. The stable foam layer must be obtained for a high toner removal, but on the other hand, it causes high fiber losses, so it is necessary to determine the optimal frother concentration (Dorris and Sayegh, 1994; Deng and Abazeri, 1998).

Table 1 shows the values of the fiber and toner flotation recovery values obtained experimentally in the laboratory flotation tests.

Table 1. Results of fiber and toner flotation recovery values for the flotation time of 10 min

pH	MIBC Dosage, mg/dm ³							
	0.5		1.5		3		6	
	I , %	Y , %	I , %	Y , %	I , %	Y , %	I , %	Y , %
3	60.10	95.45	79.31	90.64	81.35	92.18	84.80	87.64
5	76.70	93.86	84.51	92.23	87.68	92.73	85.99	90.59
7	82.69	92.36	92.09	91.23	89.91	93.32	95.13	71.23
9	85.38	93.55	96.33	93.77	95.34	92.27	92.93	76.32
12	84.41	92.77	94.27	88.27	90.73	92.18	92.51	72.50

It can be seen from Table 1 that a high recovery of fiber of over 90 % was achieved at MIBC dosages of 0.5, 1.5 and 3 mg/dm³, under all pH conditions. Under neutral and highly alkaline conditions (pH 7, 9 and 12), with increasing dosages of MIBC from 3

to 6 mg/dm³, there was a fiber loss, i.e. fiber recovery reduction of about 22, 16, 20%, respectively. During the experiments, by the visual analysis of froth, it was observed that there was a physical entrapment of fiber in the bubble network of the foam due to the formation of a high stable foam layer (Fig.2). Many authors have postulated that the fiber loss in toner flotation depends not only on the fiber surface chemistry, but also strongly depends on the froth stability, froth structure and fiber geometry. Experimental results suggest that both true flotation and physical entrainment contribute to the total fiber loss, but the physical entrainment is the dominating factor. Thus, the fiber loss in flotation can be controlled by varying the froth height (Ajersch, 1997; Deng and Abazeri, 1998; Luo et al., 2003; Huber et al., 2011). An effective surfactant for toner particles flotation should be used, and the foam should be controlled in a way that does not affect the toner removal but in can reduce the fiber entrapment. It is an imperative to control toner hydrophobicity, toner removal efficiency and fiber entrapment in the froth.

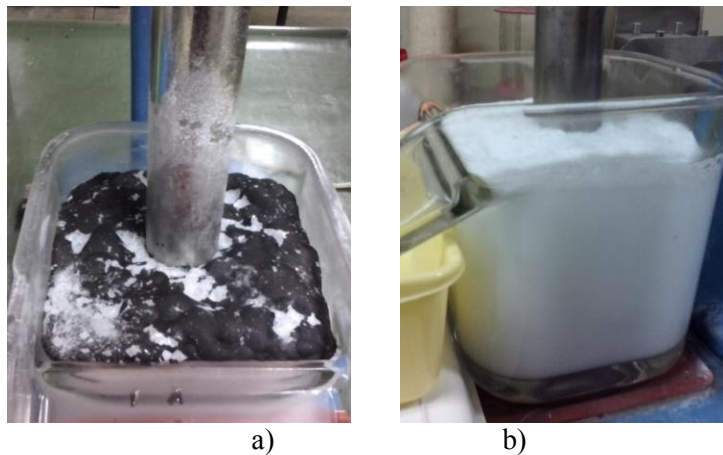


Fig. 2. Stable foam layer during toner flotation with MIBC,
a) top view b) side view

The pH factor plays an insignificant role in the recovery of fiber, but the toner recovery response is strongly affected by pH of flotation. It was shown that the removal of the toner is significantly improved under the neutral to alkaline pH conditions in comparison to the results of flotation under acidic conditions. The high value of the flotation recovery of about 90% was achieved for 1.5, 3 and 6 mg/dm³, at pH 7, 9 and 12, as it can be seen from Table 1. Generally, a pH between 8 to 10 is reported to be optimum for the toner flotation (Samasundaran et al., 1999; Theander and Pugh, 2004; Bajpai, 2014). However, Alzevedo et al. (1999) reported that the acidic flotation conditions increase the removal of the toner and the maximum removal about 90% is achieved between pH 5 and 7. Taking into consideration the fact that the author used a collector based on oleic acid for the toner flotation, which also

has good foaming properties, more studies are needed to determine the optimal pH conditions, because the influence of a surfactant type is obvious and is not negligible.

The effect of frother dosages on flotation recovery of toner in froth product and recovery of fiber in the sink product is shown in Fig. 3.

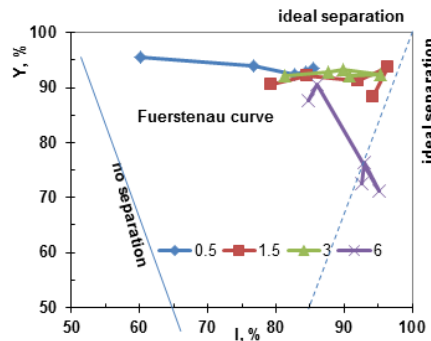


Fig. 3. The Fuerstenau plot: relationship between flotation recovery of toner (I) in the froth product and recovery of fiber (Y) in the sink product

It can be observed in Fig. 3 that a very good selectivity of toner separation from the fiber suspension was achieved at the MIBC dosage in the range of 1.5 to 3 mg/dm³. The best separation selectivity ($I=96.33$, $Y=93.77\%$) was obtained at MIBC dose of 1.5 mg/dm³ and pH 9 (Table 1, Fig. 3).

Kinetic flotation tests

Flotation recoveries of the toner are shown in Fig. 4 as a function of time. Figure 4 indicates recoveries between 90.57% and 95.56% within 6 min, depending on the pH. These results were obtained using a fixed MIBC dosage of 1.5 mg/dm³ to provide a good and stable foam to allow high recovery of the toner.

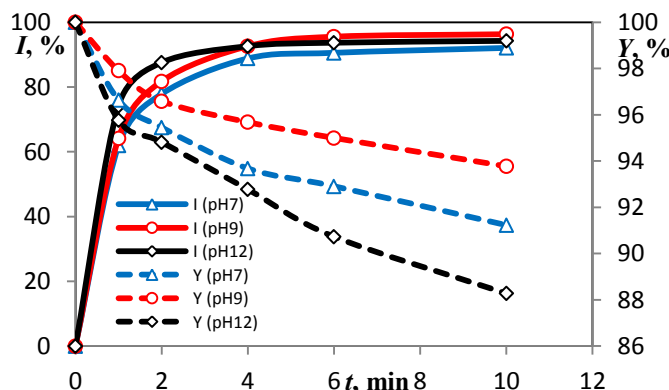


Fig. 4. The flotation recovery of toner (I) in froth product and recovery of fiber (Y) in the sink product as a function of time at different pH values and MIBC dosage of 1.5 mg/dm³

The recoveries of fiber are also given in Fig. 4. In general, such a low fiber recovery loss, less than 5 %, is due to a low and stable foam layer with a fine texture. Comparing the values of the flotation recovery of toner and the recovery of fiber at pH 7 and 9 for a short flotation time (2 min) and a longer flotation time (6 min), it can be noticed that the flotation recovery of toner has increased by about 13% and fiber recovery decreased by about 2% in both cases. Analyzing the flotation efficiency indicators at pH 12, it can be seen that there is a flotation recovery increase of toner and recovery of fiber decreases about 5%. Basing on the all presented results, it can be concluded that the pH value between 7 to 9 is the optimum value in flotation.

The flotation data plotted in Fig. 4 have been utilized from the kinetic point of view for comparison of the two kinetic models: the classical first order and the modified first order model proposed by Trumic and Magdalinovic (2011). The kinetics models for the toner flotation will be tested for a MIBC dosage of 1.5 mg/dm³ at pH 7, 9 and 12.

Classical first order model

The extent of fitting the kinetic responses to Eq. (1) can be seen in Fig. 5, which shows a high flotation rate observed in this study.

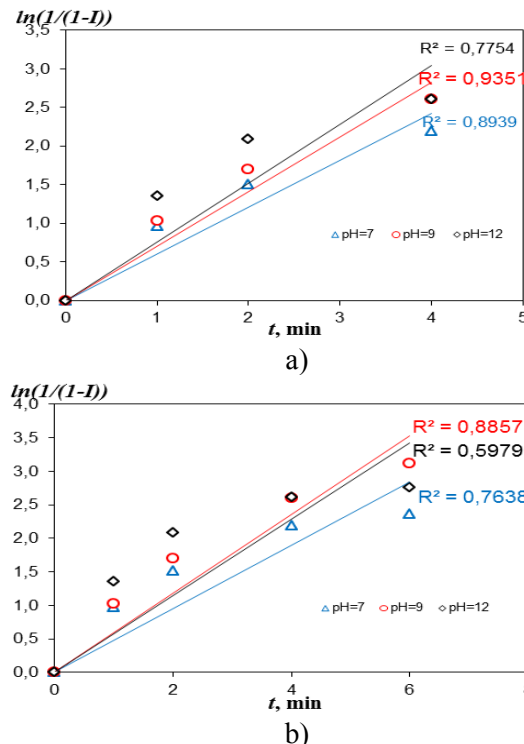


Fig. 5. The classical first order fitting of flotation responses under various pH. Fitting for the total flotation time: a) 4 min, b) 6 min

The data presented in Figure 5 indicate that with the prolonged flotation time, the value of correlation coefficient, R^2 , depending on the pH, is reduced from about 0.12 to 0.16, for the total flotation time experiment of 4 min and for all pH values and R^2 is between 0.775 and 0.935, which indicate a weak correlation (Fig. 5a). For a longer flotation time of 6 min (Fig. 4b), the correlation is even weaker with $R^2 < 0.885$. According to Volk (1965) the minimum R^2 value for a correlation to exists for 3 data point (4 min) is 0.994, while for 4 points (6 min) is 0.903. These data confirm the Pan et al. (1996) observation that only for short flotation time the particle flotation process follows the first order kinetics with a very good correlation.

Modified first order model

Trumic and Magdalinovic (Trumic, 1999; Trumic and Magdalinovic, 2011) have suggested a model which represents a modification of the first order kinetic model. Milosevic (2004) applied successfully this model for delineating the kinetics of oiled water by using equation

$$\frac{dc}{dt} = -kck_f \quad (3)$$

where k is a kinetic constant of flotation, while k_f is a coefficient of changing the probability of floating (the formation of particle-bubble aggregate and levitation into the foam).

Taking into consideration the fact that the decrease of the floating probability, during a certain period of time, occurs because the easily floating particles are floated first at the beginning and then the poorly floating particles, the authors assumed that the coefficient of changing probability k_f can be defined by the relation:

$$k_f = \frac{c}{c_0} \quad (4)$$

When the expression for k_f from Eq. 4 is included in the differential Eq. 3, after the integration within the limits from c_0 to c , and 0 to t we get:

$$\frac{I}{1-I} = kt \quad (5)$$

where flotation recovery I is as in Eq. (2).

Equation 5 represents the first order kinetic model modified by Trumic and Magdalinovic. It provides straight lines for $\frac{I}{1-I}$ vs. t plots for a given particle size with k as the slope of the straight line. The fit of the kinetic responses to Eq. 5 can be seen in Fig. 6.

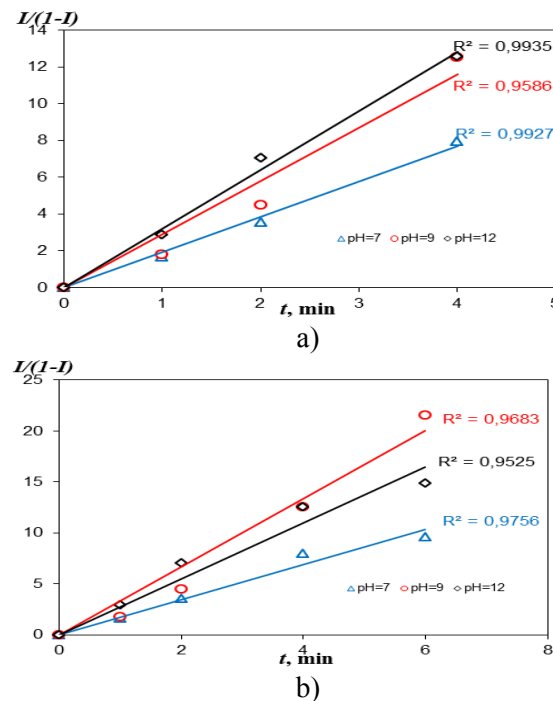


Fig. 6. Modified first order fitting of flotation responses under various pH for the total flotation time of a) 4 min, b) 6 min

Comparing the correlation coefficients for both models for shorter flotation time (4 min), it may be argued that for the neutral and highly alkaline flotation conditions, a modified model considerably better describes the kinetics with the R^2 of 0.993 for pH 7 and 0.994 for pH 12, with respect to the R^2 values obtained by the classical model of first order, 0.894 and 0.775 respectively (Fig. 5a and Fig. 6a). The values of R^2 for the modified model are in the range of minimum R^2 for a correlation to exists.

The longer flotation time (6 min) resulted in reduced R^2 from 0.01 to 0.03, depending on the pH value (Fig. 6b), referring to the shorter flotation time. By comparing these values with the coefficient values, obtained by the classical model of first order, it can noticed that the modified model gives much better correlation with R^2 between 0.953 and 0.976 when compared to the classical model of the first order, where the value of R^2 ranged between 0.598 and 0.886. The values of R^2 for the modified model are above minimum R^2 for a correlation to exists.

Based on the data discussed above, it can be concluded that the modified model gives a better correlation for obtained flotation results.

Table 2 lists the correlation coefficients, R^2 and rate constants, k which were obtained under various pH conditions. The rate constants were estimated from the plots for all experiments.

Table 2. Kinetics of flotation of investigated samples with obtained R^2 . Note: minimum R^2 for a correlation to exist for 3 data points is 0.994 while for 4 points is 0.902 (Volk, 1965)

		pH=7		pH=9		pH=12	
		4 min	6 min	4 min	6 min	4 min	6 min
classical first order model	k	0.607	0.472	0.707	0.588	0.759	0.570
	R^2	0.893	0.763	0.935	0.885	0.775	0.597
modified model	k	1.925	1.720	2.896	3.331	3.200	2.744
	R^2	0.992	0.975	0.958	0.968	0.993	0.952

When the kinetic behavior of toner flotation was analyzed, it was observed that the flotation rate constant k , depended on pH. With the increase alkalinity, there is an increase in the value of the flotation rate constant for the flotation time of 4 min. So, the maximum value was achieved at pH 12, while for a longer flotation time, the maximum value of k was obtained for pH 9. Obtaining and interpreting kinetic constant k must be done with the same caution, since there are many parameters that affect this constant. For the toner flotation for flotation time of 6 min, the constant increases when the pH increases until it reaches a maximum value. From this maximum value, any increase in the pH causes a small decrease of the kinetic constant.

In order to optimize the flotation process, it is not only necessary that the constant should have the greatest value, but also the influence of the parameters on the final product quality must be taken into account. For example, in addition to the flotation recovery, the influence of pH values should be considered from the standpoint of brightness, a parameter which defines the quality of fiber. With this viewpoint, pH 12 causes yellowing of fibers which leads to the reduction of brightness, so the toner flotation is carried out in the alkaline range of pH up to 10 (Ferguson, 1992; Bajpai, 2014).

Conclusions

The best selectivity of separation of ink from fiber was obtained at the MIBC dose of 1.5 mg/dm³ and pH 9.

In general, the flotation efficiency is considered to follow the first order kinetics. In the comparative study on the flotation kinetics of toner, involving two models, i.e., the classical first order and the first order modified by Trumic and Magdalinovic, the modified model was proved to represent the data better than the classical first order model, both for short and long flotation time.

In literature, there are several studies that report the first order kinetics for the toner flotation with the smallest particle sizes in a short flotation time. So, there are no experimental data to be compared with the results obtained in this paper.

The contribution of this work is in demonstrating that there is a good model to describe the kinetics of flotation toner with the largest particle sizes for short and long flotation time, with a very good correlation coefficient.

Further research should focus on testing the modified model by changing different flotation parameters.

Acknowledgments

The authors wish to thank the Ministry of Science and Environmental Protection of Republic of Serbia for the financial support (Project No. 172031).

References

AJERSCH M., 1997, *Mechanisms of pulp loss in flotation deinking*, Dissertation, McMaster University, Hamilton, USA, Paper 304.

ALLIX J., BENEVENTI D., ZENO E., NORTIER P., 2010, *Flotation de-inking of 50% ONP/ 50% OMG recovered papers mixtures using nonionic surfactant, soap and surfactant/soap blends*, BioResources 5 (4), 2702-2719.

AZEVEDO D., ELICH J., MILLER, J.D , 1999, *The effect of ph on pulping and flotation of mixed office wastepaper*, Journal of Pulp and Paper Science, 25(9), 317- 320.

BAJPAI P., 2014, *Recycling and Deinking of Recovered Paper*, 1st Edition, 240.

BAKALARZ A., DRZYMALA J., *Interrelation of the Fuerstenau upgrading curve parameters with kinetics of separation*, Physicochemical Problems of Mineral Processing, 49(1), 443–451.

BOGDANOVIC G., TRUMIC Z. M., STANKOVIC V., ANTIC D., TRUMIC S. M., MILANOVIC Z., 2013, *Mine waters from mining and smelting basin Bor - a resource for the recovery of copper or polluter of the environment*, Recycling and Sustainable Development 6, 41-50. (in Serbian).

DENG Y AND ABAZERI M., 1998, *True flotation and physical entrainment: the mechanism of fiber loss in flotation deinking*, Nordic Pulp and Paper Research Journal 13(1), 4-9.

DERMONT G., BERGERON M., RICHER-LAFLÈCHE M., MERCIER G., 2010, *Remediation of metal-contaminated urban soil using flotation technique*, Science of the Total Environment, 408 (5), 1199–1211.

DORRIS G.M., SAYEGH N.N., *The role of print layer thickness and cohesiveness on deinking of toner printed papers*, Pulping Conference Proceedings, TAPPI PRESS, (1994) 1273-1289.

DORRIS G., BEN Y., RICHARD M., 2011, *Overview of flotation Deinking*, Progress in paper recycling, 20 (1), 3-43.

FERGUSON L. D., 1992, *Deinking chemistry: part 1*, Tappi Journal, 75-83.

HUBER P., ROUSSET X., ZENO E., VAZHURE T., 2011, *Parameters of deinking efficiency in an industrial flotation bank*, Industrial & Engineering Chemistry Research, 50, 4021–4028.

HUI W., XIAO-LEI C., YANG B., CHAO G., LI Z., 2012, *Application of dissolved air flotation on separation of waste plastics ABS and PS*, Waste Management, 32, 1297–1305.

JAMESON, G. J., 1998, *New technology and science in flotation separations*, Current Opinion in Colloid & Interface Science, 3, 351-359.

KOWALCZUK, P.B., SAHBAZ O., DRZYMALA, J., 2011, *Maximum size of floating particles in different flotation cells*, Minerals Engineering 24, 766–771.

LABIDI J., PE'LACH M.A', TURON X., MUTJE 'P., 2007, *Predicting flotation efficiency using neural networks*, Chemical Engineering and Processing, 46, 314–322.

LI, B., WANG, G., CHEN, K., VAHEY, D. W, ZHU, J. Y., 2011, *On Quantification of Residual Ink Content and Deinking Efficiency in Recycling of Mixed Office Waste Paper*, Ind. Eng. Chem. Res. 50, 6965–6971.

LI Y., ZHAO W., GUI X., ZHANG X., 2013, *Flotation kinetics and separation selectivity of coal size fractions*, Physicochemical Problems of Mineral Processing, 49(2), 387–395.

LUO Q., DENG Y., ZHU J., SHIN W. T., 2003, *Foam control using a foaming agent spray: a novel concept for flotation deinking of waste paper*, Ind. Eng. Chem. Res., 15(42), 3578-3583.

MILOSEVIC V., 2004, *Kinetic model of oil electro flotation from waste water*, Dissertation, University of Belgrade, Serbia, 93, (in Serbian)

NIE X., MILLER J. D., YEBOAH Y. D., 1998, *The effect of ink types and printing processes on flotation deinking efficiency of wastepaper recycling*, Environ Engg and Policy, 1, 47–58.

PAN, R., PAULSEN F. G., JOHNSON D. A., BOUSFIELD D. W., THOMPSON E. V., 1996, *A global model for predicting flotation efficiency: Part 1. Model results and experimental studies*, Tappi Journal 79 (4), 177-185.

PELACH SERRA, M. A., 1997, *Proces de destintatge del paper per flotacio. Avaluacio de l'eficacia d'eliminacio de tinta*, Dissertation, Universitat de Girona, Girona, 278.

PRESTA MASO, S., 2002, *Estudi fonamental i aplicat de l'etapa d'elimanacio de tinta per flotacio*, Dissertation, Universitat de Girona, Girona, 325.

RAMASWAMY B., KAR D.D., DE S., 2007, *A study on recovery of oil from sludge containing oil using froth flotation*, Journal of Environmental Management, 85, 150–154.

RUBIO J., SOUZA M.L., SMITH R.W., 2002, *Overview of flotation as a wastewater treatment technique*, Minerals Engineering, 15, 139–155.

RUTLAND M., PUGH R.J., 1997, *Calcium soaps in flotation deinking; fundamental studies using surface force and coagulation techniques*, Colloids and Surfaces A: Physicochemical and Engineering Aspects, 125, 33-46.

SCHMIDT D. C., 1996, *Flotation deinking of toner-printed papers*, Dissertation, University of Washington, USA, 137.

SHEMI A., 2008, *Flexographic deinking with electric field technology by destabilization and flotation*, Dissertation, Georgia Institute of Technology, 183.

SOMASUNDARAN P., ZHANG L., KRISHNAKUMAR S., SLEPETYS R., 1999, *Flotation deinking-A review of the principles and techniques*, Progress in Paper Recycling, 22-37.

SUSS H., KRONIS J., NIMMERFROH N., HOPF B., 1994, *Yield of fillers and fibers in froth flotation*, Tappi Pulping Conference, 1-9.

THEANDER K., PUGH R. J., 2004, *Surface chemicals concepts of flotation de-inking*, Colloids and Surfaces A: Physicochem. Eng. Aspects, 240, 111–130.

TRUMIC M., 1999, *Screening kinetic model*, Dissertation, University of Belgrade, Serbia, 100. (in Serbian).

TRUMIC Z. M., TRUMIC S. M., MARKOVIC Z., 2007, *Separation of ink particles from waste newspaper by deinking flotation*, Journal of Mining and Metallurgy, 43 A, 33 – 41.

TRUMIC M., MAGDALINOVIC N., 2011, *New model of screening kinetics*, Minerals Engineering, 1(24), 42-49.

VASHISTH S., BENNINGTON C.P.J., GRACE J. R., KEREKES R. J., 2011, *Column Flotation Deinking: State-of-the-art and opportunities*, Resources, Conversation and Recycling, 55, 1154-1177.

VOLK W., 1965, *Statystyka stosowana dla inżynierów*, Wydawnictwa Naukowo – Techniczne, Warszawa.

ZHAO Y., DENG Y., ZHU J.Y., 2004, *Roles of surfactants in flotation deinking*, Progress in Paper Recycling, 1 (14), 41-45.

Received January 6, 2015; reviewed; accepted April 5, 2015

EFFECT OF SURFACE ROUGHNESS ON INTERACTION OF PARTICLES IN FLOTATION

Firat KARAKAS, Behzad VAZIRI HASSAS

Istanbul Technical University, Faculty of Mines, Mineral Processing Engineering Department, 34469, Maslak, Istanbul, TURKEY, karakasf@itu.edu.tr

Abstract: In this study, the effect of roughness of particles on flotation efficiency along with surface forces among interacting particles was investigated. Glass beads representing smooth spherical particles with a size fraction of $-150+90\text{ }\mu\text{m}$ were used. The etching technique was used to produce roughness of different degrees. Microflotation of round+smooth, and its corresponding etched samples were used to evaluate the efficiency of flotation in the case of smooth and rough systems. Atomic Force Microscope (AFM) was used to reveal the interaction forces between the smooth and rough surfaces. According to the results, roughness of particles increased the flotation efficiency. Although the roughness of particles increased with the etching, excess etching time caused a decrease on the roughness and in turn in the flotation recoveries. The interaction forces between the glass beads changed from repulsion to attraction with the increasing hexadecyltrimethylammonium bromide (HTAB) concentration. Further, the increase in HTAB concentration caused a change in the reversal of interaction forces from attraction to repulsion for both smooth and rough surfaces. This change started at low HTAB concentrations for rough surfaces compared to smooth ones though the magnitude of interacting forces decreased for the rough surfaces. The extent and kinetics of HTAB adsorption was dramatically influenced by the roughness of particles that affected the interaction forces as revealed by AFM measurements, and governs the flotation efficiency of particles. These results showed that roughness of particles causes significant improvement in flotation recoveries.

Keywords: *glass beads, roughness, flotation, AFM*

Introduction

Morphological features of particles significantly affect their interactions with bubbles in the flotation pulp. Effect of shape factor and roughness on wettability and flotation recoveries has been shown in a number of studies (Ahmed, 2010; Hicyilmaz, 2004; Ulusoy and Yekeler, 2005; Ulusoy, 2004). Verelli et al. (2014) measured the induction time of borosilicate glass particles using milli timer apparatus, and found that angular particles have smaller induction time than spherical ones. Guven et al. (2015)

proposed a new concept consisting of sand blasting of quartz particles to produce particles of different shape factors and roughness of particles, and correlated them with flotation results. There is a general consensus in that angular particles have more affinity to the bubble than spherical particles. However, the exact effect of roughness and shape factor on flotation recoveries is still controversial.

Interaction forces among particles in flotation are governed by surface properties of the particles, ionic strength, pH, flotation aids including surfactants or polymers as well as hydrodynamic conditions. Among these, surfactants are crucial because they modify particle hydrophobicity and froth stability. Particle shape and roughness also control the particle-particle and particle-bubble interactions. There are some efforts to reveal these interaction forces between the particle and bubble especially using the AFM (Albijanic et al., 2011; Nguyen, 2003; Wang, 2005). Development of AFM (Binnig, 1986) and introducing the colloidal probe in AFM (Ducker, 1992) have made the direct measurements of surface forces and quantify the interaction among particles for a variety of areas including mineral processing, paint production, ceramics, adhesive industry etc.

Attachment time including induction time, forming time of three-phase contact nucleus and three-phase contact line are important and more reliable parameters compared to the contact angle that shows the attraction of a particle to the bubble (Albijanic et al., 2010). Interaction forces between a particle and a bubble considering the attachment time are currently and intensively studied by different groups (Verrelli, 2011; Wang et al., 2005). However, there is not enough concern about the effect of particle shape and especially that of roughness on flotation efficiency. These two physical variables should be both considered in particle-particle and particle-bubble interactions for improving the behavior of particles in flotation.

In this study, the effect of roughness of glass bead particles on flotation was investigated by micro-flotation experiments and AFM measurements. Interaction forces between particles were correlated with micro-flotation data.

Experimental

Materials and methods

Glass beads particles of -150+90 μm size fraction were used for the micro-flotation and AFM experiments whereas -38 μm particles for making colloidal probe. The particles were cleaned by washing in acid and base in three consecutive cycles and rinsed by de-ionized water to ensure that the particles were free of any contamination and their surface were hydrophilic. They were then left to dry in clean room environment. HTAB of analytical grade was purchased from Sigma-Aldrich. Solutions of HTAB were prepared in a concentration range of $1 \cdot 10^{-6}$ mol/dm 3 to $1 \cdot 10^{-3}$ mol/dm 3 in distilled water. All the solutions were free of turbidity indicative of the above the Krafft temperature of the surfactant. Zeta potential measurements of the glass bead

particles was carried out at 0.1 wt.% by Zeta meter 3.0+ equipped with a microprocessor unit that automatically calculates the electrophoretic mobility of the particles and converting it to the zeta potential by using the Smoluchowski equation.

Micro-flotation experiments

Etching method was first used in order to produce the desired roughness on the surface of particles. An etching solution of 10% hydrofluoric (HF) acid was prepared using 40% HF acid and de-ionized water. The particles were washed by de-ionized water for 5 cycles after the acid etching. Different roughness on the surfaces was achieved by varying etching time from 5 to 300 s. Scanning Electron Microscopy (SEM) micrographs of the samples are given in Fig. 1. Etched sample was selected from the sample after 120 s of etching as it showed maximum flotation recoveries.

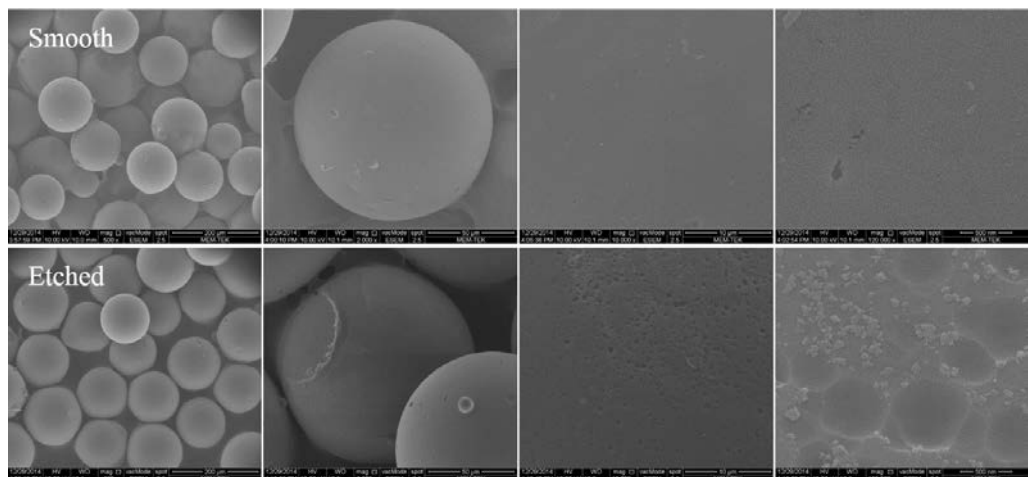


Fig. 1. SEM micrographs of smooth and etched glass beads

The micro-flotation tests were carried out with -150+90 μm glass bead particles using a 150 cm^3 micro-flotation column cell (25×220 mm) with a ceramic frit (pore size of 15 μm) which was mounted on a magnetic stirrer and a magnetic bar used for the agitation. HTAB was used as collector surfactant in various concentrations. It has been reported that the adsorption of cationic surfactants on smooth silica surfaces reaches its maximum in less than 10 min (Howard and Craig, 2009), and adsorption kinetics is even higher for rougher surfaces than smooth ones (Wu et al., 2011). Exactly 1.0 g of sample was stirred for 10 min in desired concentration of HTAB according to the conditions and was subjected to flotation for 1 min in a micro-flotation cell. The pH of the medium was around 6.2. Both floated and unfloated parts were collected and filtered. The samples were dried in an oven at 105 °C for 2 h and weighed to determine the flotation recovery.

Colloidal probe atomic force microscopic studies

For the force measurements, a spherical smooth glass bead with an average particle size of 10 μm was attached to the end of the tipless cantilever using micromanipulator and camera system. UV curable glue with the viscosity of 100 cP was used for attachment of the particle. The measurements performed with one pair of glass bead of which one of them was attached to the cantilever and the other one onto the smooth mica surface as a substrate under the cantilever of the AFM. Both the glass beads used as a colloidal probe and as the surface were cleaned before the experiments to remove the possible contaminants. Acid (2.5% v/v H_2SO_4) and alkali (2.5% w/v NaOH) and de-ionized water were used for cleaning as described elsewhere (Koh et al., 2009) followed by rinsing by ethanol and de-ionized water just before the experiments. Cleaning process may affect the measured force. Bowen et al. (1999) investigated the effect of different cleaning processes of the silica sphere and silica surfaces on the measured force. They used ethanol washing and plasma treatment and showed that higher repulsion force when plasma treatment is applied probably because of increasing the density of silicic acid groups on the surface.

The same colloidal probe was used for both the smooth and rough particles in order to compare the force measurements. The velocity of the approach and retraction was 300 nm/s.

Rectangular cantilever was used to measure the interaction forces. Cantilever deflection was converted to the force using spring constant. Cantilever manufacturers give only the average spring constant for a batch of cantilever; typically 10 of them. Therefore, accurate spring constant is necessary for getting reliable force measurements. There are a number of methods for measuring the spring constant of the cantilevers. We used one of the simplest and reliable technique based on the Sader method to identify individual spring constant of each cantilever (Sader et al., 1999). Width (b), length (L), resonant frequency (ω_f), and Q factor (quality factor) (Q_f) of the cantilever are measured at density (ρ_f) and viscosity (μ_f) of surrounding fluid (air). The spring constant was calculated using Eq. 1:

$$K_n = 0.1906 \rho_f b^2 L Q_f \omega_f \Gamma_i^j (\omega_a) \quad (1)$$

where Γ_i^j is the imaginary component of the hydrodynamic function which is a function of Reynolds R_e number given by Eq. 2:

$$Re = \frac{\rho_f \omega_f b^2}{4\mu_f}. \quad (2)$$

The spring constant of the cantilever was calculated as 0.055 N/m which is close to the manufacturers' value of 0.080 N/m.

For the attachment of the particle to the end of the cantilever, a required amount of epoxy resin was picked up by the tungsten wire controlled by a micromanipulator and the cantilever was placed for microscopic observation. After that glass bead particle was picked up with another tungsten wire electrostatically and put on the glued cantilever. The cantilever was then allowed to dry for about 30 min under the UV. The cantilever with attached particle is shown in Fig. 2.

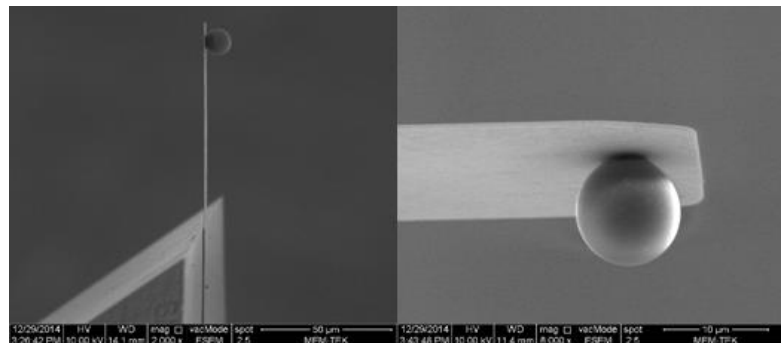


Fig. 2. AFM cantilever with glass bead sphere used in force spectroscopy experiments

Results and discussion

Micro-flotation experiments

In order to probe the effect of roughness of particles, all other parameters were determined through a series of tests and kept constant at optimum experimental conditions. The results of various concentrations of HTAB on the flotation recovery are shown in Fig. 3.

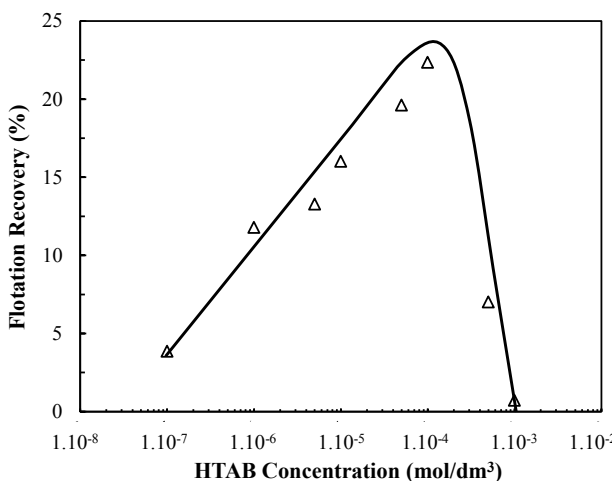


Fig. 3. Micro-flotation recovery of glass beads vs. HTAB concentration

It is found that the flotation recovery of glass spheres increased with the increasing HTAB concentration up to a certain point after which it decreased dramatically. This turning point for HTAB was found to be $1 \cdot 10^{-4}$ mol/dm³ which is in good agreement with the previous works and the atomic force measurements described in this study. Using a tensiometer, critical micelle concentration (CMC) of HTAB was found to be $1 \cdot 10^{-3}$ mol/dm³ by measuring surface tension of water as a function of HTAB concentration. It is clear that the turning point in the flotation recovery curve (Fig. 3) is just below CMC.

One possible explanation for this turning point is bilayer formation of surfactant on the particles. Surface active agents are added to the systems in different processes i.e. flotation and dewatering in order to render the surface of the particles hydrophobic as they adsorb on the surface with their hydrophobic tails toward medium (water in these cases). Since there are also strong hydrophobic attraction forces between tails of the surfactant molecules, bilayer formations are expected as reported and described excessively in previous works (Asmatulu, 2001; Eraydin, 2009; Vaziri Hassas et al, 2014). Bilayer formation decreases the hydrophobicity of the particles rendering them hydrophilic and results in a fall in flotation recovery. Vidyadhar et al. (2001) reported that flotation of quartz using amine surfactants of various carbon chain lengths, for each surfactant depending on its hydrophobicity, there is a specific and characteristic point after which recovery of quartz flotation decreases. This point for C₁₆ amine surfactant (CTAB) was reported as $1 \cdot 10^{-4}$ mol/dm³. In order to probe the details of any change in flotation recovery for different experimental conditions, surfactant concentration for flotation experiments was chosen to be $1 \cdot 10^{-6}$ mol/dm³. Gas velocity in flotation runs was kept at a lower rate of 60 cm³/min to overcome any possibility of hydrodynamic effect of gas on rising and entrainment of particles. This rate was determined through a series of flotation experiments with varying gas velocity.

The samples were etched as described in detail previously in materials and methods section. As a results of this method a series of combination of round samples with varying etching durations to obtain various roughness values were prepared and subjected to flotation runs, the results of which are given in Fig. 4.

Roughness of particles was seen to increase the flotation recovery according to Fig. 4. Similarly, about 30% increase in the flotation recovery resulted from surface roughness was reported by Ahmed (2010). Feng and Aldrich (2000) also reported large differences in the particles prepared by wet and dry milling with the dry-ground samples exhibiting faster dissolution, faster reagent adsorption, more stable and higher-loaded froths, and faster flotation kinetics based on the difference of their surface features. Chau et al. (2009) also reported that both elongation and smoothness increased the contact angle of talc while roundness and roughness of particles decreased. It has been reported that the contact angle of the surfaces changes by varying the surface roughness, however, there is not any specific trend that can summaries the behavior of wide variety of materials. Buscher et al. (1984) used the polishing and abrasion method to produce different degrees of roughness on more than

10 different polymers. They measured the roughness using profilometry. They concluded that the roughness of less than 100 nm has no effect on the wettability of the surface. Later on other works validated these results explaining that for the surfaces with roughness of less than 100 nm, chemical heterogeneity and the composition is dominant for surface behaviors (Exstrand et al. 1997; Eske and Kumagai, 1999). In another work Exstrand (2004) explained that the contact angle in rough surfaces is higher due to presence of valleys and gutters. Exstrand emphasized that the edges of the water droplet get stuck at these gutters and water cannot penetrate through valleys. Veeramasuneni et al. (1997) also validated that the increase in surface roughness increases the contact angle in hydrophobic surfaces. They investigated the roughness of 6-13 nm on polytetrafluoroethylene which is inherently hydrophobic surface. Chau et al. (2009) concluded that although wetting behavior of liquid-solids interface can be calculated by contact angle measurements, obtaining exact and reproducible values is quite difficult. They argued that this value is very sensitive to other parameters, namely particle shape factor, its surface roughness, heterogeneity, and particle size.

Flotation recovery highly depends on the parameters that affect the bubble-particle attachments. Attachment between particle-bubble is commonly described as a “critical” time to occur, which means the minimum time required for attachment. This time is denoted as (τ) and known as induction time. Since the induction time was described based on particle-bubble interactions conventionally, it was assumed that this time should be constant for a given particle-bubble pair (Nguyen and Schulze, 2004). It is however expected that this interaction should depend on other variables such as particle’s size, shape, surface groups, velocity and other factors. Verelli et al. (2012) indicated that τ actually changes upon the particle’s approach trajectory towards bubble surface. Here Davis (1992) findings on particle settling should be taken into account. Davis (1992) described that horizontal position of a falling body with respect to another one (a background sphere) in a dilute suspension is affected by surface roughness of the particles as there is a higher interaction between them. Considering the findings of Davis (1992) and Verelli et al. (2012) one can expect that roughness of particles can have considerable effect on induction time in flotation. The effect of roughness of particles on flotation recovery has been investigated individually and reported that longer detachment force is required to separate the rougher particles from the attached bubbles than that of smoother one. This in turns indicates a stronger adhesion force for bubble-particle pair in rougher surfaces and lower induction time as well (Ahmed, 1999; Ahmed et al. 1999). Furthermore, the effect of surface roughness on contact angle of particles has been investigated and found that rougher glass beads have higher penetration in contact angle measurements using capillary rise method (Dang-Vu, 2006) which means surface roughness has a significant effect on surface properties of particles. Adsorption behavior of HTAB on both smooth and roughened surfaces was investigated by Wu et al. (2011). They reported that adsorption behavior strongly depends on concentration of surfactant with

regards to its CMC and there are three regions with different characteristics i.e. below, close to, and above CMC regions. Considering the CMC point of $1 \cdot 10^{-3}$ mol/dm³ for HTAB used in this study which has been determined by surface tension method, concentration range of this study is below the CMC point. Wu et al. (2011) suggested that roughness of particles affects not only the amount of surfactant adsorbed, but also the morphology of the adsorbed surfactants aggregates. Furthermore, at this region (below CMC) increasing roughness may lower the surface to be covered with surfactant aggregates i.e. patchy adsorption (some areas of surface are covered by surfactants at higher density, other by lower density of surfactants due to uneven distribution of surfactant molecules). Even more increasing specific surface area may cause much more spreading of surfactant molecules on surface than forming semi micelles which is favorable in flotation. In such a situation the force measured by AFM between these two particles can increase while the flotation rate does not. It is also emphasized that the surfactant aggregates formed on rougher surfaces are less compact and consequently more flexible than those formed on smoother surfaces (Wu et al., 2011).

As shown in Fig. 4, flotation recoveries for glass beads increase with increasing roughness of particles. This increment in flotation yield is 12%. It was also found that the roughness of particles increases at prolonged etching time of up to 120-150 s of etching period after which roughness of particles was found to decrease upon further etching time.

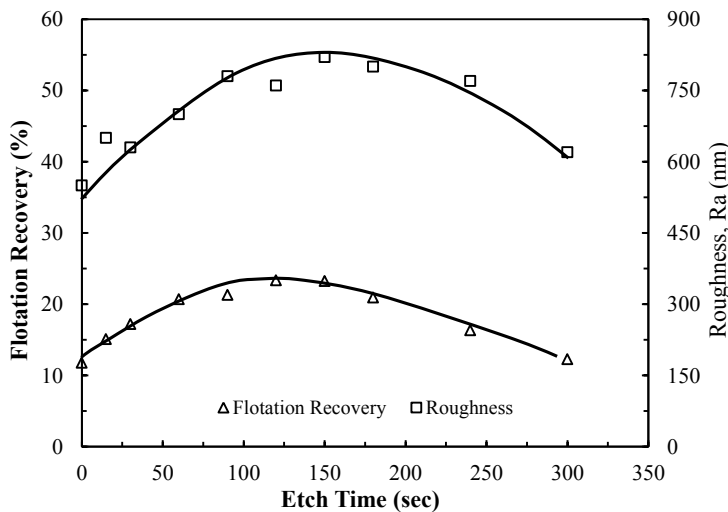


Fig. 4. Micro-flotation recovery (at $1 \cdot 10^{-6}$ HTAB concentration) and roughness of round glass beads measured by AFM against different etching time. Flotation time was 1 min

Rough particles can attach on bubbles more easily on their notches as they protrude into the bubble decreasing the possibility of bubble-particle detachment. Topological

features on the rough surfaces then expand this three-phase contact line causing dewetting on the surface (Oliver and Mason, 1977; Verelli et al. 2012). Another, maybe the most important feature of rough surfaces, is confining air bubbles to the surface of particles both in micro and nano scale. These air bubbles increase the attachment mechanism due to different phenomena such as “hydrophobic forces” known as long range interactions (Krasowska et al., 2007).

Krasowska and Malysa (2007) reported a difference in attachment time for a bubble on a teflon surface with different roughness. They categorized roughness in two groups of asperity, e.g. 1 μm and above 50 μm . Here in this study we can take the former group as roughened surface and the latter as shape factor. They recorded four to five “approach-bounce” cycles at the moment bubble collides with the surface with roughness (below 1 μm) before the attachment. In the case of shape factor (roughness above 50 μm), however, bubble particle attachment always occurred within the first collision without any bouncing at that time.

Roughness of particles and thereby flotation recovery increases up to a point after which both start to decrease (Fig. 4). One possible explanation that can be speculated about this phenomenon is that much smoother features forms in longer etching. In bubble-particle attachment the first film rupture is known to be done by sharp and severe parts of particles and roughness of particles is accepted to strengthen the bubble particle attachment. Shape factor is the dominant variable to get the better efficiency followed by the roughness in flotation (Krasowska et al., 2007; Krasowska and Malysa, 2007; Chau et al., 2009). In the former part of etching the roughness of surface increases and causes a boost in flotation recovery. Upon further increase in etching the roughened features becomes smoother and as a result flotation recovery decreases.

Colloidal probe atomic force microscope studies

Interaction forces between glass beads were measured by averaging 16 of the most representative force curves for each HTAB concentration using mapping property of the instrument. The force was normalized to the radius of the particle attached to the top of the AFM tip.

There is an electrostatic repulsion between glass beads without HTAB. Repulsion is also present at low HTAB concentrations; $1 \cdot 10^{-6} \text{ mol/dm}^3$ and $5 \cdot 10^{-6} \text{ mol/dm}^3$. Addition of $1 \cdot 10^{-5} \text{ mol/dm}^3$ HTAB decreased the repulsive forces with further increase caused a snap in and hydrophobic attraction forces were dominant at $1 \cdot 10^{-4} \text{ mol/dm}^3$ HTAB concentration with a rapid snap in, as shown in approaching force curve of smooth particle in Fig. 5a. On the other hand, repulsive force appeared once more with the excess amount of HTAB. It is clearly seen that repulsive forces dramatically increased with HTAB concentration of $5 \cdot 10^{-4} \text{ mol/dm}^3$ and $1 \cdot 10^{-3} \text{ mol/dm}^3$.

The possible mechanism for this behavior originates from the adsorption form of HTAB onto the glass bead surfaces both at colloidal probe and the surface. At lower concentration ($0 \cdot 5 \cdot 10^{-6} \text{ mol/dm}^3$), the surface of the glass beads is partly covered by

the surfactant and concentration of HTAB is not enough for providing hydrophobic attraction to overcome the electrostatic repulsion forces caused by double-layer potential. Adsorption form is also dominant in this concentration range. Although perpendicular arrangement of the surfactant with the hydrophobic tails facing towards water at low concentration was also reported in literature (Tyrode, 2008), surfactant molecules may arrange parallel to the surface rather than perpendicular and hydration forces, which overcome the hydrophobic force, coming from dehydration of the ammonium head groups result in repulsion (Luderitz and Klitzing, 2013). Importance of hydration force was also reported by Jinming (2009). He showed that even at very low ion concentration hydration forces exist and these forces hinder the attraction of two silica surface even at close contact. At 1.10^{-5} mol/dm³ repulsion considerably decreased and attraction was observed at 5.10^{-5} mol/dm³ HTAB. Monolayer coverage was reached and strong attraction force was observed at 1.10^{-4} mol/dm³ HTAB concentration.

Electrostatic interaction between particle surface and oppositely charged surfactant head group governs this attraction. The zeta potential of the smooth glass bead particles at natural pH (6.2) was measured as -23 mV. The zeta potential of the glass beads particles in the presence of 1.10^{-5} mol/dm³ HTAB reversed from -9 mV to +19 mV with 5.10^{-5} mol/dm³ HTAB that supports the interaction from repulsive to attractive. The zeta potential values of the particles were obtained as +19 mV and +31 mV for 5.10^{-5} mol/dm³ and 1.10^{-4} mol/dm³ HTAB, respectively. An increase of zeta potential value with an increasing surfactant concentration—indicates an increase in adsorbed amount of surfactant (Luderitz and Klitzing, 2013). Further increase in HTAB concentration made a change on the adsorption form of the surfactant, and bilayer was possibly formed. Positive head group of the HTAB started to retract each other and electrostatic retraction was again dominant at this condition. This mechanism is also shown in the retrace of the force curves. Strong adhesion forces with jump in points were obtained with 5.10^{-5} mol/dm³ and 1.10^{-4} mol/dm³ HTAB concentration as shown in Fig. 5b.

Donose et al. (2007) observed only repulsion between pure silica spheres as a colloidal probe and polished silicon wafers as a surface in solutions of aluminum sulfate. Repulsion still exists with flushing of de-ionized water into the system while after flushing of de-ionized water attraction was occurred for borosilicate glass beads as a colloidal probe and polished silicon wafers as a surface.

Luderitz and Klitzing (2013) used the same concentration range of HTAB from 5.10^{-6} mol/dm³ to 1.2 mol/dm³ for two different systems: a pair of silica particles and silica particle-silica wafer. They observed repulsive interaction in water for all distance. For the pair of silica particles repulsion was observed from 0 to 5.10^{-5} mol/dm³ HTAB. There is no repulsion and only attraction was observed at 5.10^{-5} mol/dm³ HTAB concentration. Further increase of concentration caused repulsion again. This trend is also true for the silica particle-silica wafer system but HTAB concentrations for reversing the interaction forces from repulsion to attraction and

attraction to repulsion are different. They explained this difference as different hydrophobicity between silica sphere and silica wafer that may be caused by different cleaning processes. Additionally they showed that different surface charges originating by different adsorption form of HTAB onto silica sphere and silica wafer are responsible for different interaction forces with the same HTAB concentration for these systems.

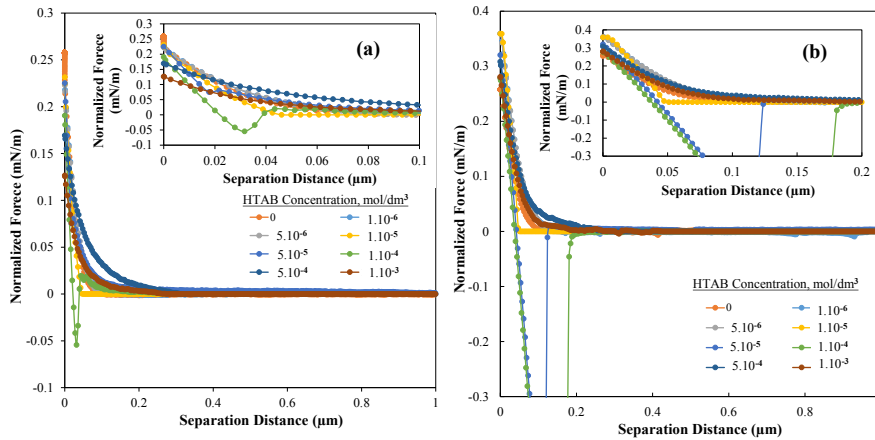


Fig. 5. Normalized interaction force curves measured for smooth surface in various HTAB concentrations
(a) approach (b) retraction

Repulsion at lower concentration range of HTAB, attraction at moderate concentration and repulsion at higher concentration range of HTAB was also observed for the rough glass bead surface, however, attraction force, snap in and jump in started at lower concentration compared to the smooth glass bead surface. As shown in Fig. 6a, monolayer coverage was completed at $5 \cdot 10^{-5}$ mol/dm 3 HTAB, and net attraction force was observed with a strong snap in at this concentration. The increasing HTAB concentration started to change the monolayer coverage to bilayer even if there was still a small snap in at $1 \cdot 10^{-4}$ mol/dm 3 HTAB. This, in contrast, is the optimum concentration for monolayer coverage and highest attraction force for the smooth glass bead surface. Further increase in HTAB caused electrostatic repulsion but not as much as the one obtained with the smooth glass bead. This is again because of the adsorption form of the HTAB. Monolayer and bilayer formed at lower concentration for rough than smooth glass bead surface because of the stronger attraction for adsorption of HTAB on rough surface. Even at $5 \cdot 10^{-6}$ mol/dm 3 and $1 \cdot 10^{-5}$ mol/dm 3 of HTAB concentration there is an adhesion force shown in Fig. 6b that did not exist for smooth surface. Beyond the formation of bilayer, more HTAB was adsorbed on the rough surface and electrostatic repulsion became weaker compared to smooth surface, as shown in Fig. 6a in the case of $5 \cdot 10^{-4}$ mol/dm 3 and $1 \cdot 10^{-3}$ mol/dm 3 of HTAB. This mechanism was clearly shown and supported by the force curves of the rough and

smooth particle systems and the micro-flotation experiments explained in previous section.

Stronger adsorption affinity of HTAB on the rough glass bead surface than the smooth one is also shown at retrace force curve of the rough glass beads in Fig. 6b. Adhesion and jump in started at even $5 \cdot 10^{-6}$ mol/dm³. Adhesion energy increased up to $5 \cdot 10^{-5}$ mol/dm³ HTAB addition. Adhesion energy decreased but still exists at $1 \cdot 10^{-4}$ mol/dm³ and ceased at further HTAB levels of $5 \cdot 10^{-4}$ mol/dm³ and $1 \cdot 10^{-3}$ mol/dm³.

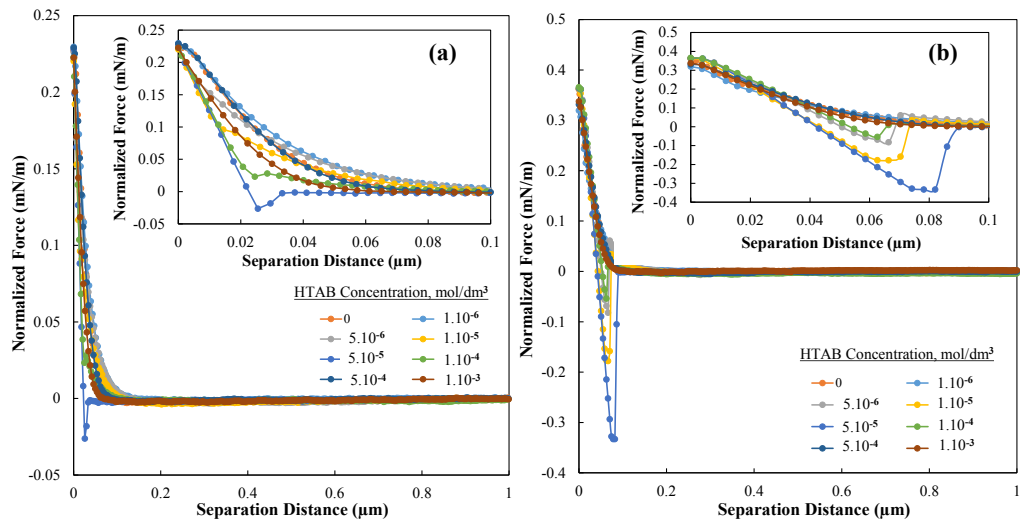


Fig. 6. Normalized interaction force curves measured for rough surface in various HTAB concentrations
(a) approach (b) retraction

It is known that roughness of particles significantly affects adhesion force. Dry and capillary adhesion decreases with nanoscale roughness (Rabinovich et al., 2002). The same finding is also available in our study that shows the dramatic effect of roughness on interaction forces among the particles.

Hydrophobic attraction force is long range attraction force in aqueous solutions and there are many studies that identify this long range interaction force starting from the early 1970s. The first direct measurement of this force is reported by Israelachvili and Pashley (1982). There are different sources which can result in long range hydrophobic interactions such as adsorbed surfactant molecules on the surface which render it more hydrophobic. Another possible reason for such interaction can be presence of nanobubbles on the surfaces which results in capillary interaction between particles. Tyrrell and Attard (2002) showed that coverage of the surface by nanobubbles is close to 100%. They observed a long range attraction between two silica spheres. Addition of ethanol removed the nanobubbles that were responsible for long range attraction (Tyrrell and Attard, 2002). In another study, forces between two colloidal silica particles in the presence of HTAB at concentrations between $5 \cdot 10^{-6}$ mol/dm³ and

$1.2 \cdot 10^{-3}$ mol/dm³ were measured and nanobubbles were formed at concentrations up to $5 \cdot 10^{-4}$ mol/dm³ surfactant concentration. Above this concentration they were flat and less prominent at force measurements of two silica spheres (Luderitz, 2012).

Nguyen et al. (2003) argued that solid particles are in contact with air before contact with water and air is trapped in solid surface. Preexisting air at the particle surface is hard to be removed by the liquid and causes the bridging action when particle-bubble interaction in flotation especially for hydrophobic particles. They used glass sphere as a colloidal probe and glass microscope slide as the surface to show the effect of nanobubbles on long range hydrophobic attraction force. They made both the probe and the surface hydrophobic by silanation process using trimethylchlorosilane. They observed a long range attractive hydrophobic force in pure water. The magnitude of this force and jump in distance decreases with increasing of ethanol as a medium. Hydrophobic attraction force disappeared in pure ethanol which shows that the origin of hydrophobic attraction is preexisting nanobubbles on the hydrophobic particles (Nguyen et al., 2003).

In our study, on the other hand, we could not observed the effect of nanobubbles on hydrophobic force since there was no long range attraction for both smooth and rough surface without HTAB and hydrophobic attraction started with the addition of HTAB. This indicates that hydrophobicity of the particle is the crucial parameter for preexisting nanobubbles on the surface. We used hydrophilic glass beads and hydrophobicity of the particles increased gradually with the addition of HTAB. Therefore, HTAB is the only parameter that governs the hydrophobic attraction in our system.

The mechanism for the long range hydrophobic attraction is still controversial for the particulate systems. Nanobubbles, long range electrostatic attraction or steric force with existing surfactant or a polymer may cause the long range attraction force. Kekicheff and Spalla (1995) reported that long range attraction between hydrophobic surfaces may have electrostatic origin for silica particles in CTAB solutions.

Conclusions

Effect of roughness on flotation recovery and extent of interaction forces between smooth and rough glass bead particles were investigated. Roughness of particles is found to improve the flotation recovery. The highest recovery was obtained with an optimum etching level to induce roughness. Interaction forces for the smooth particles were somewhat higher than that of rough particles as measured by AFM. Interaction forces between glass beads changed from repulsive to attractive with increasing HTAB adsorption. Further increase reversed the interaction from attraction to repulsion again. This change was in accord with the zeta potential measurements and showed the effectiveness of the electrostatic force on interaction potential between glass bead particles in the presence of HTAB. This trend is true for both smooth and rough surfaces. However, the extent of HTAB concentration in breakthrough points

(from attraction to repulsion and vice versa) is less in the case of rough particles. This behavior arises probably because of the difference in adsorption form of HTAB on smooth and rough glass beads which reveal the affinity of HTAB towards rough particles.

In this investigation, the importance of roughness of particles was shown by direct micro-flotation experiments. Effect of roughness of particles was also elaborated by particle-particle interactions using AFM measurements. These findings can be further improved by AFM and induction time measurements to understand the nature of particle-bubble interactions.

Acknowledgements

Authors are grateful to Prof. Dr. Mehmet Sabri Celik for his comments and advices on the study.

References

AHMED, M. M., 2010, *Effect of comminution on particle shape and surface roughness and their relation to flotation process*, International Journal of Mineral Processing, 94, 180-191.

AHMED, M.M., 1999, *Fractal surfaces of particles and their floatability*, Ph.D. Thesis, Assiut University, Assiut, Egypt.

AHMED, M.M., STECHEMESSER, H., MABROUK, S.A., IBRAHIM, G.A., TARSHAN, M.M., 1999, *Image analysis technique for determination of the size, structure and texture of fine particle profile*, The 6th International Conference on Mining, Petroleum and Metallurgy, Vol. I-B, Mineral Processing, Fac. of Eng., Cairo University, Cairo, Egypt, Feb. 20-24, pp. 40-56, 1999.

ALBIJANIC, B., AMINI, E., WIGHTMAN, E., OZDEMIR, O., NGUYEN, A.V., BRADSHAW, D., 2011, *A relationship between the bubble-particle attachment time and the mineralogy of a copper-sulphide ore*, Minerals Engineering, 24, 1335-1339.

ALBIJANIC, B., OZDEMIR, O., NGUYEN, A.V., BRADSHAW, D., 2010, *A review of induction and attachment times of wetting thin films between air bubbles and particles and its relevance in the separation of particles by flotation*, Advances in Colloid and Interface Science, 159(1), 1-21.

NGUYEN, A.V., NALASKOWSKI, J., MILLER, J.D., BUTT, HANS-JURGEN, 2003, *Attraction between hydrophobic surfaces studied by atomic force microscopy*, International Journal of Mineral Processing, 72, 215-225.

ASMATULU, R., 2001, *Advanced chemical-mechanical dewatering of fine particles*, Ph.D. Thesis, Virginia Polytechnic Institute and State University.

ASTON, D.E., BERG, J.C., 2000, *Long-range attraction between silanated silica materials studied by an electrolyte titration with atomic force microscopy*, Colloids and Surfaces A: Physicochemical and Engineering Aspects, 163, 247-263.

BINNIG G., QUATE C., GREBER G., 1986, *Atomic force microscope*, Physical Review Letters, 56(9), 930-933.

BOWEN W.R., HILAL N., LOVITT R.W., WRIGHT C.J., 1999, *An atomic force microscopy study of the adhesion of a silica sphere to a silica surface effects of surface cleaning*, Colloids and Surfaces A: Physicochemical and Engineering Aspects, 157, 117-125.

BUSSCHER, H.J., VAN PELT, A.W.J., DE BOER, P., DE JONG, H.P., ARENDTS, J., 1984, *The effect of surface roughening of polymers on measured contact angles of liquids*, Colloids and Surfaces, 9, 319-31.

CHAU, T.T., BRUCKARD, W.J., KOH, P.T.L., NGUYEN, A.V., 2009, *A review of factors that affect contact angle and implications for flotation practice*, Advances in Colloid and Interface Science, 150, 106-115.

DANG-VU, T., HUPKA, J., DRZYMALA, J., 2006, *Impact of roughness on hydrophobicity of articles measured by the Washburn method*, Physicochemical Problems of Mineral Processing, 40, 45-52.

DAVIS, R.H., 1992, *Effects of surface roughness on a sphere sedimenting through a dilute suspension of neutrally buoyant spheres*, Physics of Fluids A: Fluid Dynamics (1989-1993), 4, 2607-2619.

DONOSE, B., NGUYEN, A.V., EVANS, G.M., YAN, Y., 2007, *Effect of aluminium sulphate on interactions between silica surfaces studied by atomic force microscopy*, Water Research, 41(15), 3449-3457.

DUCKER, W.A., SENDEN, T.J., PASHLEY, R.M., 1991, *Direct measurement of colloidal forces using an atomic force microscope*, Nature, 353, 6341, 239-241.

DUCKER, W.A., SENDEN, T.J., PASHLEY, R.M., 1992, *Measurement of forces in liquids using a force microscope*, Langmuir, 8(7), 1831-1836.

ERAYDIN, M.K., 2009, *Scale-up of using novel dewatering aids*, Ph.D. Thesis, Virginia Polytechnic Institute and State University.

ESKE, L.D., GALIPEAU, D.W., 1999, *Characterization of SiO_2 surface treatments using AFM, contact angles and a novel dewpoint technique*, Colloids and Surfaces A: Physicochemical and Engineering Aspects, 154, 33-51.

EXTRAND, C.W., 2004, *Criteria for ultrahydrophobic surfaces*, Langmuir, 20, 5013-18.

EXTRAND, C.W., KUMAGAI, Y., 1997, *An experimental study of contact angle hysteresis*, Journal of Colloid Interface Science, 191, 378-83.

FENG, D., ALDRICH, C., 2000, *A comparison of the flotation of ore from the Merensky Reef after wet and dry grinding*, International Journal of Mineral Processing, 60(2), 115-129.

GUVEN, O., OZDEMIR, O., KARAAGACIOGLU, I.E., CELIK, M.S., 2015, *Surface morphologies and floatability of sand blasted 1 quartz particles*, Minerals Engineering, 70, 1-7.

HICYILMAZ, C., ULUSOY, U., YEKELER, M., 2004, *Effects of the shape properties of talc and quartz particles on the wettability based separation processes*, Applied Surface Science, 233, 204-212.

HOWARD, S.C. and CRAIG, V.S.J., 2009, *Adsorption of the cationic surfactant cetyltrimethylammonium bromide to silica in the presence of sodium salicylate: Surface excess and kinetics*, Langmuir, 25(22), 13015-13024.

ISRAELACHVILI, J., PASHLEY, R., 1982, *The long-range hydrophobic interaction decaying exponentially with distance*, Nature, 300, 5890, 341.

JINMING D., 2009, *Interfacial forces between silica surfaces measured by atomic force microscopy*, Journal of Environmental Sciences, 21, 30-34.

KEKICHEFF P., SPALLA O., 1995, *Long-range electrostatic attraction between similar, charge-neutral walls*, Physical Review Letters, 75, 1851-1854.

KOH, P.T.L., HAO, F.P., SMITH, L.K., CHAU, T.T., BRUCKARD, W.J., 2009, *The effect of particle shape and hydrophobicity in flotation*, International Journal of Mineral Processing, 93, 128-134.

KRASOWSKA, M., KRASTEV, R., ROGALSKI, M., MALYSA, K., 2007, *Air-facilitated three-phase contact formation at hydrophobic solid surfaces under dynamic conditions*, Langmuir, 23(2), 549-557.

KRASOWSKA, M., MALYSA, K., 2007, *Kinetics of bubble collision and attachment to hydrophobic solids: I. Effect of surface roughness*, International Journal of Mineral Processing, 81(4), 205-216.

LIU, J., XU, Z., MASLIYAH, J., 2003, *Studies on bitumen-silica interaction in aqueous solutions by Atomic Force Microscopy*, Langmuir, 19, 3911-3920.

LUDERITZ, L.A.C., 2012, *An AFM study of the interactions between colloidal particles*, Ph.D. thesis, Technische Universität Berlin.

LUDERITZ, L.A.C., KLITZING, R.V., 2013, *Interaction forces between silica surfaces in cationic surfactant solutions: An atomic force microscopy study*, Journal of Colloid and Interface Science, 402, 19-26.

NGUYEN, A.V., NALASKOWSKI, J., MILLER, J.D., 2003, *A study of bubble-particle interaction using atomic force microscopy*, Minerals Engineering 16, 1173-1181.

NGUYEN, A.V., SCHULZE, H.J., 2004, *Colloidal Science of Flotation*, Marcel Dekker: New York, U.S.A.

OLIVER, J.F., MASON, S.G., 1977, *Microspreading studies on rough surfaces by scanning electron microscopy*, Journal of Colloid and Interface Science, 60(3), 480-487.

RABINOVICH Y.I., ADLER J.J., ESAYANUR M.S., ATA A., SINGH R.J., MOUDGIL B.M., 2002, *Capillary forces between surfaces with nanoscale roughness*, Advances in Colloid and Interface Science, 96, 213-230.

RALSTON, J., FORNASIERO, D., HAYES, R., 1999, *Bubble-particle attachment and detachment in flotation*, International Journal of Mineral Processing, 56(1-4), 133-164.

SADER, J.E., CHON, J.W.M., MULVANEY, P., 1999, *Calibration of rectangular atomic force microscope cantilevers*, Review of Scientific Instruments, 70(10), 3967-3969.

TYRODE, E.C., RUTLAND, M.W., BAIN, C.D., 2008, *Adsorption of CTAB on hydrophilic silica studied by linear and nonlinear optical spectroscopy*, Journal of American Chemical Society, 130, 17434-17445.

TYRRELL, J.W.G., ATTARD, P., 2002, *Atomic force microscope images of nanobubbles on a hydrophobic surface and corresponding force-separation data*, Langmuir, 18, 160-167.

ULUSOY, U., YEKELER, M., 2005, *Correlation of the surface roughness of some industrial minerals with their wettability parameters*, Chemical Engineering and Processing, 44, 557-565.

VEERAMASUNENI, S., DRELICH, J., MILLER, J.D., YAMAUCHI, G., 1997, *Hydrophobicity of ion-plated PTFE coatings*, Progress in Organic Coatings, 31, 265-70.

VERRELLI, D.I., BRUCKARD, W.J., KOH, P.T.L., SCHWARZ, M.P., FOLLINK, B., 2014, *Particle shape effects in flotation. Part 1: Microscale experimental observations*, Minerals Engineering, 58, 80-89.

VERRELLI, D.I., BRUCKARD, W.J., KOH, P.T.L., Schwarz, M.P., Follink, B., 2012, *Influence of Particle Shape and Roughness on the Induction Period for Particle-Bubble Attachment*, 26th International Mineral Processing Congress (IMPC-XXVI), New Delhi, India, 24 - 28 September.

VERRELLI, D.I., KOH P.T.L., NGUYEN, A.V., 2011, *Particle-bubble interaction and attachment in flotation*, Chemical Engineering Science, 66, 5910-5921.

VIDYADHAR, A., HANUMANTHA RAO, K., CHERNYSHOVA, I. V., PRADIP, FORSSBERG, K. S. E. 2001, *Mechanisms of amine-quartz interaction in the absence and presence of alcohols studied by spectroscopic methods*, Journal of Colloid and Interface Science, 256, 59-72.

VAZIRI HASSAS, B., KARAKAS, F., CELIK, M.S., 2014, *Ultrafine coal dewatering: Relationship between hydrophilic lipophilic balance (HLB) of surfactants and coal rank*, International Journal of Mineral Processing, 133, 97-104.

WANG, W., ZHOU, Z., NANDAKUMAR, K., MASLIYAH, J.H., XU, Z., 2005, *An induction time model for the attachment of an air bubble to a hydrophobic sphere in aqueous solutions*, International Journal of Mineral Processing, 75, 69-82.

WANG, Y., WANG, L., HAMPTON, M.A., NGUYEN, A.V., 2013, *Atomic force microscopy study of forces between a silica sphere and an oxidized silicon wafer in aqueous solutions of NaCl, KCl, and CsCl at concentrations up to saturation*, The Journal of Physical Chemistry, 117, 2113-2120.

WU, S., SHI, L., GARFIELD, L.B., TABOR, R.F., STRIOLO, A., GRADY, B.P., 2011, *Influence of surface roughness on cetyltrimethylammonium bromide adsorption from aqueous solution*, Langmuir, 27, 6091-6098.

YEKELER, M., ULUSOY, U., HICYILMAZ, C., 2004, *Effect of particle shape and roughness of talc mineral ground by different mills on the wettability and floatability*, Powder Technology, 140(1-2), 68-78.

Received September 5, 2014; reviewed; accepted September 8, 2014

OBTAINING LIGHTWEIGHT CONCRETE USING COLEMANITE WASTE AND ACIDIC PUMICE

Yasin ERDOGAN*, Ergul YASAR*, Pathegama GAMAGE RANJITH**

*Mustafa Kemal University, Faculty of Engineering, Department of Petroleum and Natural Gas Engineering, 31200 Iskenderun, Hatay-Turkey, erdogan@mku.edu.tr (Yasin Erdogan)

** Monash University, Faculty of Engineering, Department of Civil Engineering, Melbourne-Victoria-Australia

Abstract: This paper presents some results of ongoing laboratory work to design a lightweight concrete using colemanite waste and pumice. Hisarcik and Espey colemanite wastes, acidic pumice aggregate as well as normal Portland cement were used to produce lightweight concrete with economic and environmental advantages. Two different groups and twenty different prescriptions were tried to produce lightweight concrete. The effect of colemanite waste on workability and strength of lightweight concrete were analysed by fresh and hardened concrete tests. The properties of materials examined include slump, air content, density and uniaxial compressive strength of the mortar. The results obtained were compared with control concrete properties and Turkish standard values. The examined tests results showed that lightweight concrete can be produced by the use of acidic pumice aggregate and colemanite waste. Furthermore, the colemanite waste can be used as cement additives and can reduce the cost and environmental pollution with using natural stone aggregate.

Keywords: *lightweight concrete, colemanite waste, acidic pumice, density, uniaxial compressive strength*

Introduction

In recent years boron waste materials have been used in a number of construction materials as a partial cement replacement and as an aggregate in concrete. The presence of boron oxide (B_2O_3) in colemanite ore waste has remarkable effects on the mechanical properties of cement (Kula et al., 2001) and the increased replacement of colemanite waste with Portland cement results in higher setting time and specific surface (Olgun et al., 2007). Waste containing boron improves concrete properties, lowers the costs of cement production, and is ecologically beneficial. Furthermore, as colemanite waste and pumice have low density, they can be used to reduce dead load to minimise earthquake risk. For these reasons, colemanite waste and pumice materials can be used to produce lightweight concrete.

Turkey has 851 teragrams (Tg) of boron reserves which comprise 73% of the total world reserves. The most important boron ores in Turkey are tincal, colemanite and ulexite. These minerals contain different amounts of B_2O_3 . The average boron ore production of Turkey is about 1.3 Tg per year (Tbar, 2008; Tspo, 1996; Figen et al., 2010; Bocukoglu et al., 2002).

Turkey's boron operations are under the control of Eti Holding A.S, formerly Etibank, through its subsidiary Eti Boron Inc. Boron production is managed by five operations, four of which are integrated mine and plant facilities and one is a plant facility. The Eti Holding Emet Boron Plant has been operational since 1958 in Emet county, Kütahya. In the facilities, open pit mines of Hisarcık and Espey colemanite produce 28-30% B_2O_3 and boric acid (H_3BO_3) grade to a total of 1 Tg/year (Tbar, 2008). Annually, 0.08 Tg of clay and colemanite waste (CW), known as Hisarcık colemanite waste (HCW) and Espey colemanite waste (ECW) are produced in the concentrated colemanite and boric acid units during production. These wastes are stored in tailing dams. Colemanite wastes of the Hisarcık and Espey areas containing about 8-28% B_2O_3 are discharged to the plant area. As the wastes contain boron oxide in quite high concentrations, this represents an environmental pollution problem as well as an economic loss (Kavas, 2006; Ozdemir and Ozturk, 2003).

Pumice is a natural rock of volcanic origin produced by the release of gases during the solidification of lava. Acidic pumice aggregate (APA) obtained from the Nevşehir area and has been used as aggregate with colemanite waste in the production of lightweight colemanite waste. Satisfactory concrete which has approximately three times lighter than normal concrete and good insulating characteristics with high absorption and shrinkage can be manufactured using acidic pumice (Nevile, 1995; Hossain, 2004).

The use of lightweight aggregate (LWA) in concrete has a number of advantages (Mays and Barnes, 1991; Fragoulis et al., 2004; Yasar et al., 2003; Erdogan, 2007). These advantages include the reduction of dead load that may result in reduced footing sizes and lighter and smaller upper structures, reductions in the sizes of columns and slab and beam dimensions that result in larger space availability, lighter and smaller pre-cast elements needing smaller and less expensive handling and transportation equipment, high insulation rating and enhanced fire resistance (Kayali, 2008).

The aim of this study is to investigate the use of colemanite waste containing boron and pumice for the production of lightweight concrete, to find the best combination of these mixtures and evaluate acidic pumice aggregate, colemanite waste and Portland cement. Therefore, various combinations of concrete containing acidic pumice aggregate, Hisarcık colemanite waste, Espey colemanite waste and Portland cement were prepared. The properties of the prepared concrete and materials examined include slump, air content, density and uniaxial compressive strength (UCS) of the mortar.

Materials and methods

Cement

The cement used was ASTM Type I normal Portland cement (NPC) with a 28-day compressive strength of 42.5 N/mm². The specific gravity of the cement was 3.15 g/cm³, and the initial and final setting times of the cement were 4 and 5 h, respectively. Its Blaine specific surface area was 3140 cm²/g and its chemical and physical compositions are given in Table 1.

Table 1. Chemical and physical characteristics of used materials

Component	Clinker	HCW	ECW	APA
Boron oxide (B ₂ O ₃)	-	27.20	25.77	-
Calcium oxide (CaO)	61.87	17.42	15.90	0.75
Silica (SiO ₂)	20.65	20.59	22.46	71.10
Iron oxide (Fe ₂ O ₃)	4.13	0.95	1.51	1.74
Alumina (Al ₂ O ₃)	5.60	2.40	5.83	16.3
Magnesia (MgO)	2.60	5.76	5.02	0.14
Sodium oxide (Na ₂ O)	0.14	-	-	0.52
Potassium oxide (K ₂ O)	0.83	-	-	0.60
Titanium oxide (TiO ₂)	-	5.25	4.84	-
Loss on ignition	1.39			
Physical Properties				
Fineness, (wt.%)				
+32 µm sieve	26.4	26.9	26.7	-
+90 µm sieve	3.05	10.6	10.4	-
+200 µm sieve	0.3	0.2	0.2	-
Specific surface (cm ² /g)	2390	3594	3542	
Specific gravity (g/cm ³)	3.21	2.42	2.48	0.85

Aggregate and its grading

The chemical and physical compositions of the colemanite waste and pumice which were used as an aggregate in the production of the LWC were determined. Acidic pumice aggregates were obtained from Nevsehir and the ARBIMS Brick Factory in Osmaniye, Turkey. Colemanite waste was provided from Eti Holding, Emet Boron in Kutahya, Turkey. The chemical and physical properties of the Portland cement, the Hisarcık colemanite waste, the Espey colemanite waste and the acidic pumice aggregate are given in Table 1.

The dry density and compressive strength of pumice were 850 kg/m³, and 8.7 MPa, respectively. Colemanite waste and pumice were separated according to their size. They were sieved using standard sieves and separated into seven groups (0/0.15, 0.15/0.3, 0.3/0.6, 0.6/1.18, 1.18/2.36, 2.36/4.75, 4.75/9.5) as shown in Table 2. A combination of separated aggregates was obtained with a grading that complied with the requirements of ASTM C136-01.

Table 2. Grain size distribution of aggregates

Sieve size, mm	% Passing		
	APA	HCW	ECW
9.5	100.0	100.0	100.0
4.75	87.5	100.0	100.0
2.36	69.0	90.5	91.0
1.18	54.0	68.0	69.5
0.6	37.5	43.0	44.0
0.3	21.5	24.0	24.5
0.15	9.0	10.5	11.0

Concrete mixture composition and sample preparation for tests

Three series of mixtures noted as Hisarcik (H: APA + PC + HCW), Espey (E: APA + PC + ECW) and the reference mix (R), were prepared according to ASTM C330-00 and TS 699. The grading of Acidic Pumice Aggregate (APA) met the requirement of lightweight aggregate for concrete as per ASTM C330-00. A laboratory ball-mill was used for the grading process, and particle size analysis was carried out according to ASTMC136-01. Specimen preparation for the tests was performed at room temperature. The mix proportion of the reference mix specimens corresponded to 400 g of cement content, 1600 g of APA and 0.55 water-to-binder (W/B) ratio. LWC mixtures were made using 2, 4, 6, 8, 10 % CW as NPC replacement. The W/B ratio of the LWC was kept constant at 0.55.

The slump values of fresh LWC were determined as per ASTM C143-00 while the air contents were determined by pressure meter as per ASTM C231-97. Superplasticizer (SP) content was adjusted in order to achieve a slump ranging between 65 and 80 mm SP content (based on solid mass) in percentage by weight of binder. No air entraining admixtures were used. The details of the mixtures are given Table 3.

The cement-water mixture were stirred at low speed for 30 s, and following the addition of CW and APA, the mixtures were stirred for 5 min. Twenty-one batches were prepared and cast into 100 x 100 x 200 mm moulds for density and compressive strength tests. After 24 h of curing at 20°C with 95 % humidity, the samples were demolded and immersed in tap water and cured for up to 7, 14, 28 and 90 days. All the specimens were compacted by external vibration using a table vibrator.

The density and strength values were the average of six specimens. Some of the prismatic specimens were not perfectly regular due to difficulties encountered in demolding (H10, E10), hence the compressive strength values of these samples were tested on two or three samples.

After the density and compressive strength tests, the results for the LWC were tabulated and are given in Figs. 1-4.

Table 3. Admixture ratios in LWC mixture (%)

Symbol	PC	AP	HCW	ECW	Slump (mm)	Air Content (%)	SP (%)
R _H	20	80	-	-	68	2.3	1.6
H1	10	80	10	-	70	2.6	1.6
H2	10	82	8	-	68	2.8	1.6
H3	10	84	6	-	70	2.8	1.6
H4	10	86	4	-	72	2.9	1.6
H5	10	88	2	-	76	3.0	1.6
H6	5	85	10	-	72	3.1	1.6
H7	5	87	8	-	76	3.1	1.6
H8	5	89	6	-	76	3.3	1.6
H9	5	91	4	-	80	3.4	1.6
H10	5	93	2	-	76	3.4	1.6
E1	10	80	-	10	72	2.7	1.6
E2	10	82	-	8	70	2.8	1.6
E3	10	84	-	6	70	2.9	1.6
E4	10	86	-	4	74	2.9	1.6
E5	0	88	-	2	74	3.1	1.6
E6	5	85	-	10	70	3.1	1.6
E7	5	87	-	8	78	3.2	1.6
E8	5	89	-	6	76	3.2	1.6
E9	5	91	-	4	78	3.3	1.6
E10	5	93	-	2	80	3.3	1.6

Results and Discussion

The air content and slump values of non-air entrained LWCs are presented in Table 3. The air content ranges between 2.3% and 3.4% and generally increases with increased APA content. All the mixtures produced a slump ranging between 65 and 80 mm.

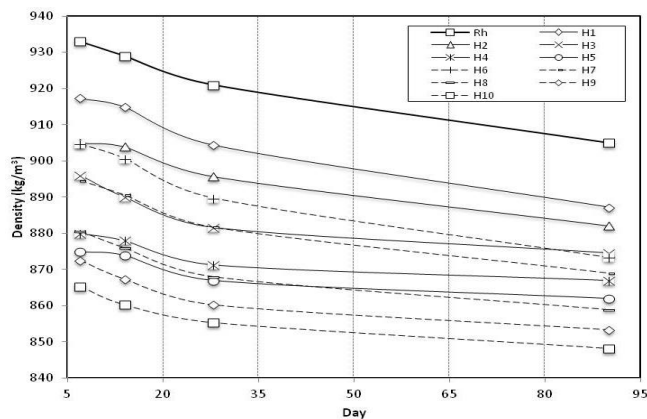


Fig. 1. Changing with time density of LWC containing HCW

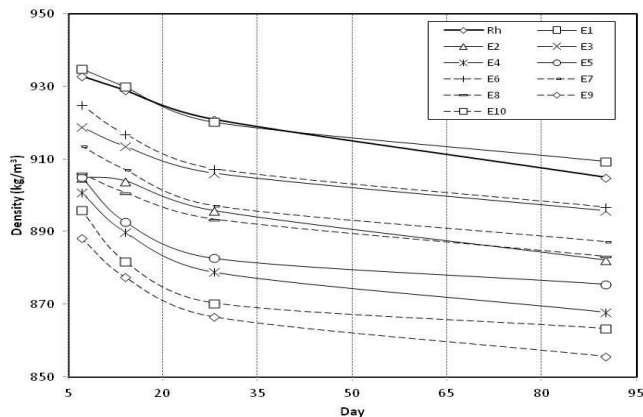


Fig. 2. Changing with time density of LWC containing ECW

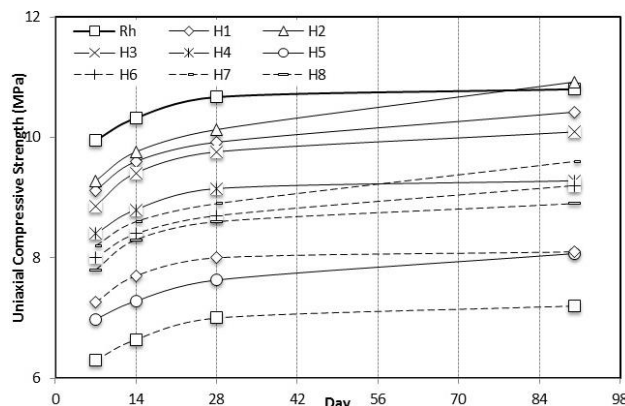


Fig. 3. Changing with time UCS of LWC containing HCW

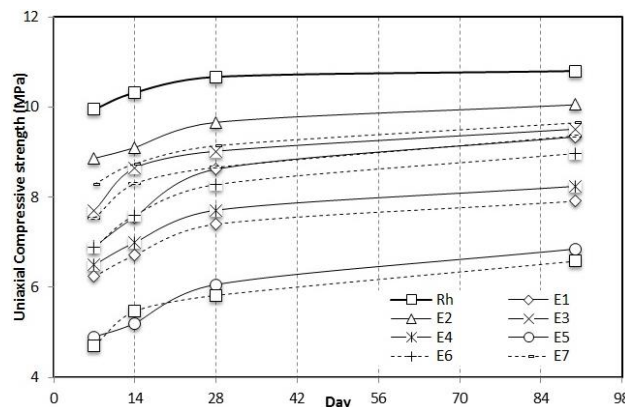


Fig. 4. Changing with time UCS of LWC containing ECW

The chemical and mineralogical composition of HCW were examined. HCW was added in different proportions as cement additive in concrete. The effect of CW on workability and strength of concrete were analysed by fresh and hardened concrete tests. The results obtained were compared with control concrete properties and Turkish standard values. The results showed that the addition of CW had a small effect upon the workability of the concrete but an important effect on the reduction of its strength. As a result of the studies, the ideal lightweight concrete mixture was found to be better by the use of Hisarcik colemanite ores and wastes and also the test results of Espey waste is lower than those of Hisarcik. The good results were found due to both the high percentage of boron and less percentage of the secondary minerals (especially such as Fe_2O_3 and Al_2O_3) in Hisarcik colemanite ores and wastes.

As Figs 1 and 2 show, the density of LWC samples ranged from 850 to 935 kg/m³. Low density materials are preferred in lightweight construction sector and the earthquake countries. In addition, the density results of concrete with prepared HCW are lower than those for the Espey colemanite concrete.

The mixture of H10 (5 % PC + 93% AP + 2 HCW) has the lowest density value. After 7, 14, 28 and 90 days, the density of the H10 mixture, 865.4, 860.3, 855.4 and 848.3 kg/m³ were found respectively (Fig. 1).

As seen in Figs 3 and 4, the UCS of LWC samples range from 4.5 to 5.5 MPa. The UCS values of the concrete made with HCW mixtures gave better results than those made with ECW mixtures. As the HCW mixture has been shown to increase the strength, the chemical analysis of HCW in Table 1 was examined due to the high amount of B_2O_3 in the HCW mixture.

The H2 mixture (10 % PC + 82% AP + 8 HCW) has the highest UCS value. After 7, 14, 28 and 90 days, H2 mixture densities of 9.28, 9.76, 10.13 and 10.92 MPa were found, respectively (Fig. 3).

Another purpose of this study was to use colemanite waste instead of cement in concrete. For this purpose, in the mixture with H6, H7, H8, H9, H10 between E6, E7, E8, E9, E10 codes, the amount of cement was reduced by 5%, and the amount of the APA was increased. The results of the CW concrete samples were examined and the test values were not found much difference from the normal concrete samples.

The H7 mixture (5% PC + 87% AP + 8 HCW) is shown to have a much higher strength than the H5 mixture (10% PC + 88% AP + 2 HCW) in Fig. 3.

The E7 mixture (5% PC + 87% AP + 8 ECW) is shown to have a much higher strength than mixture E5 (10% PC + 88% AP + 2 ECW) in Fig. 4.

Although there is a high amount of cement in mixtures H5 and E5, the mixtures H7 and E7 have higher strength. The amounts of CW in mixtures H7 and E7 are shown to increase the UCS.

Conclusions

In this study, the usability of Hisarcik and Espey colemanite wastes as aggregate and a replacement for Portland cement has been determined. Due to their low density and

high strength, the Hisarcik and Espey colemanite wastes and acidic pumice are suitable for the production of lightweight concrete and enable the reduction of dead load to lessen earthquake risk. The colemanite waste improves concrete properties, reduces the cost of concrete production and is ecologically beneficial. The density and UCS test results of concrete made with Espey colemanite and pumice aggregate were found to be between 850 and 935 g/cm³, and 4.5 and 5.5 MPa, respectively. The density test results of concrete made with Hisarcik colemanite and pumice aggregate were found to be between 848.3 and 917.4 g/cm³, and 6.3 and 10.92 MPa, respectively. According to the test results, the density and UCS of concrete with prepared HCW are preferable to those of Espey colemanite concrete. The difference in the test results depends upon the amount of B₂O₃ in the waste mixture. The examined tests results showed that lightweight concrete can be produced by the use of acidic pumice aggregate and colemanite waste. Furthermore, colemanite waste can be used as cement additives and can reduce the cost and environmental pollution with using natural stone aggregate.

Acknowledgements

The authors thank the National Boron Research Institute (BOREN) for its support of this project (Project No: 2006-31-C30-21). The authors are grateful for the contributions of Dr. Mehmet Savaş, the director of Eti Mine Works General Management and Dr. Atila Gurhan Celik who is engineering of BOREN company.

References

ASTM C136-01, 2003, *Standard test method for sieve analysis of fine and coarse aggregate*, Annual Book of ASTM Standards, Philadelphia, USA.

ASTM C143-00, 2003, *Standard test method for slump of hydraulic cement concrete*, Annual Book of ASTM Standards, Philadelphia, USA.

ASTM C231-97 2003, *Test method for air content for freshly mixed concrete by pressure method*, Annual Book of ASTM Standards, Philadelphia, USA.

ASTM C330-00. 2003, *Specification for lightweight aggregates for structural concrete*, Annual Book of ASTM Standards, Philadelphia, USA.

BONCUKOGLU, R., YILMAZ, M.T., KOCAKERIM, M.M., TOSUNOGLU, V., 2002, *Utilization of trammel sieve waste as an additive in Portland cement production*, Cement and Concrete Research, (32), 35–9.

ERDOGAN, Y., 2007, *Investigation of engineering properties of building materials made with acidic and alkaline pumice*. Dept. of Mining Eng. Inst. of Natural and Applied Sci. University of Çukurova, PhD Thesis, 300 p. Adana, Turkey.

FIGEN, A.K., YILMAZ M.S., PISKIN, S., 2010, *Structural characterization and dehydration kinetics of Kirka inderite mineral: Application of non-isothermal models*, Materials Characterization, (61), 640–64.

FRAGOULIS, D., STAMATAKIS, M. G., CHANIOTAKIS, E., COLUMBUS, G., 2004, *Characterization of lightweight aggregates produced with clayey diatomite rocks originating from Greece*, Materials Characterization, (53), 307–316.

HOSSAIN, K. M. A., 2004, *Properties of volcanic pumice based cement and lightweight concrete*, Cement and Concrete Research, (34), 283–291.

KAVAS, T., 2006, Use of boron waste as a fluxing agent in production of red mud brick, Building and Environment, (41), 1779-1783.

KAYALI, O., 2008, *Fly ash lightweight aggregates in high performance concrete*, Construction and Building Materials, (22), 2293-2399.

KULA, I., OLGUN, A., ERDOGAN, Y., SEVINC, V., 2001, *Effects of colemanite waste, coal bottom ash and fly ash on the properties of cement*, Cement and Concrete Research, (31), 491–494.

MAYS, G. C., BARNES, R. A., 1991, *Performance of lightweight aggregate concrete structures in service*, Structural Engineering (20), 351–61.

NEVILE, A. M., 1995, *Properties of Concrete*, 4th ed., Longman, Harlow, England.

OLGUN, A., KAVAS, T., ERDOGAN, Y., ONCE, G., 2007, *Physico-chemical characteristics of chemically activated cement containing boron*, Building and Environment, (42), 2384-2395.

OZDEMIR, M., OZTURK, N. U., 2003, *Utilization of clay wastes containing boron as cement additives*, Cement and Concrete Research, (33):1659–1661.

TBAR, 2008, *The boron annual report*, Eti mine works general management, p.83.

TS 699, 2009, *Natural building stones - Methods of inspection and laboratory testing*. Ankara

TSPO, 1996, *The State Planning Organization*. DPT, Report, No. 2427, Ankara, Turkey.

YASAR, E., ATIS, C. D., KILIC, A., GULSEN, H., 2003, *Strength properties of lightweight concrete made with basaltic pumice and fly ash*, Material Letters, (57), 2267-2270.

Received October 15, 2014; reviewed; accepted February 24, 2015

CHARACTERISTICS OF CATIONIC RED X-GRL ADSORPTION BY RAW DIATOMITE AND DIATOMITE CONCENTRATE

**Zjie REN, Junfang GUAN, Huimin GAO, Jingjing TIAN, Yafei WEN,
Renji ZHENG**

School of Resources and Environment Engineering, Wuhan University of Technology, Wuhan 430070, China,
guanjfang@163.com

Abstract: Raw diatomite (RD) and diatomite concentrate (DC) were used for the adsorption of cationic Red X-GRL from aqueous solutions. Mono-factor experiments were carried out to investigate the effects of the operation factor, and adsorption kinetics, isotherms, thermodynamics and mechanisms were explored. Similar trend for X-GRL adsorption onto RD and DC was observed. The adsorption capacity of dyes increased slightly with temperature, and the neutral pH was the optimum level. The adsorption processes occurred in accordance with the pseudo second-order model and were well fitted by the Langmuir isotherm model. The main driving forces of the physical adsorption on the diatomite were electrostatic attraction and van der Waals force. The RD could uptake more X-GRL than DC due to its higher content of fine particle and therefore, due to higher surface area available for adsorption. Raw diatomite as a cheap absorbent for X-GRL removal can be suggested as a promising supplement to activated carbon.

Keywords: diatomite, dye, adsorption, fine particles

Introduction

Dyes, which form a class of colored chemicals, have been used in textile, leather, paper, plastic, and other industries for a long time (Yu and Fugetsu, 2010). If discharged without any treatment, the dyes are not only toxic to aquatic life, but are also potentially carcinogenic that can cause severe damage to human beings (Bea and Freeman, 2007; Lei et al., 2007; Amin, 2009). More than 60% of the global commercial dyes are Azo dyes (Isil and Sponza, 2005). The cationic Red X-GRL (X-GRL) is a very popular azo dye and widely used in dyeing acrylic and blended fabric (Qiu et al., 2012). Physical adsorption, because of its low cost, high efficiency, easy handling, wide variety of adsorbents, and high stabilities towards the adsorbents, has become the mostly widely used method for eliminating dyes (Yu and Fugetsu, 2010; Wu et al., 2008; Lin et al.,

2007). The active carbon is the most common and effective absorbent, but its use is limited due to a costly regeneration process (Lim and Okada, 2005).

Diatomite is a non-metallic mineral raw material, which is composed of skeletal remains of single-cell water plants (algae). Diatomite is approximately 500 times cheaper than commercial activated carbon (Erdem et al., 2005). Because of its complex structure with abundant fine microscopic pores, cavities and channels, diatomite has long been applied as a filter aid, filler, insulator, and catalyst support (Ediz et al., 2010; Wang et al., 2011; Bahramian et al., 2008). The diatomite also can eliminate water-soluble organic dyes, especially cationic dyes, because of the silanol groups available on the surface of diatomite particles (Khraisheh et al., 2005A). Diatomite or modified diatomite has shown its effectiveness for the removal of methylene blue, reactive black, reactive yellow (Khraisheh et al., 2005A,B; Tsai et al., 2004), telon red A2R and ramazol golden yellow RGB (Lin et al., 2007), but its use for the removal of X-GRL has not been mentioned previously.

China has substantial diatomite resources, most of which are of moderate quality, having a SiO_2 content of about 60%-80% (Sun et al., 2013). The impurities in the raw diatomite may block the pores in the diatom skeletons, and thereby decrease the adsorption ability. A comparative study of the adsorption of X-GRL onto low grade diatomite (RD) and diatomite concentrate (DC) obtained by purifying low grade diatomite has not been conducted before.

Objective of this study is to investigate the effects of main operational parameters aiming X-GRL removal by raw diatomite (RD) and diatomite concentrate (DC). Kinetic model, equilibrium isotherm and some thermodynamic parameters were estimated from experimental results. Further, the mechanism of adsorption was explored.

Materials and methods

Materials

The low grade diatomite (RD) was obtained from the Linjiang region of China. The diatomite concentrate (DC) used for the adsorption tests was obtained by scrubbing technique and centrifugation of RD using the previously described procedures (Sun et al., 2013). The chemical and phase compositions of RD and DC were determined by an X-ray Fluorescence (XRF, Axios advanced, PAN Alytical B.V., Netherlands) and X-ray Diffractometer (XRD, D/Max-IIIa, RIGAKU, Japan) with monochromatic $\text{Cu K}\alpha$ radiation in $5-70^\circ$ at a rate of $0.02^\circ/\text{s}$. The results of XRF and XRD are shown in Table 1 and Fig. 1, respectively.

DC had higher SiO_2 content and lower extents of Al_2O_3 , Fe_2O_3 , K_2O than the RD. The phase analysis showed that the amorphous opal was the main component, and small amount of illite, quartz and plagioclase existed in both the RD and DC (Ren et al., 2014). However, the extent of impurities in DC was lower than those in RD. The chemical structure of cationic Red X-GRL, the azo-dye used for the adsorption tests with DC and RD, is presented in Fig. 2 (Lei et al., 2007; He et al., 2009; Li et al., 2010).

Table 1. Chemical composition of RD and DC

Component	SiO ₂	Al ₂ O ₃	Fe ₂ O ₃	CaO	K ₂ O	Na ₂ O	L.O.I. ^a
RD (wt. %)	78.37	7.15	4.45	0.46	1.00	0.40	6.46
DC (wt. %)	85.54	3.78	1.81	0.40	0.76	0.47	6.41

^a Loss on ignition

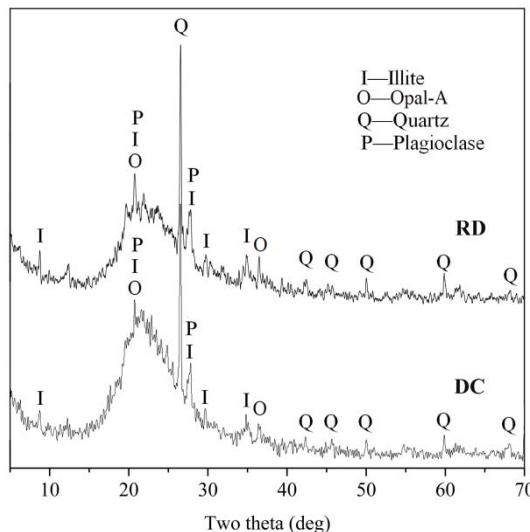


Fig. 1. XRD patterns of RD and DC

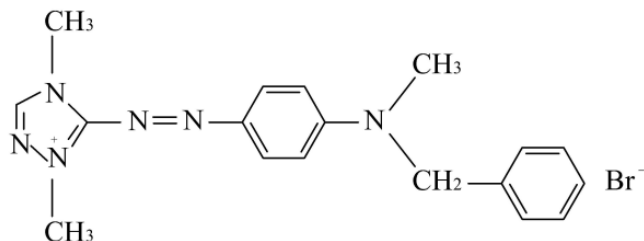


Fig. 2. Chemical structure of cationic Red X-GRL

Adsorption tests

The diatomite sample was added into 50 cm³ X-GRL aqueous solution with particular concentration. The solution was agitated at 150 rpm in a thermostat shaker (85-2, Wenhua, Jintan, China) prior to centrifuging at 4000 rpm for 5min. The supernatant was used to determine the concentration of the residual X-GRL using a MAPADA, V-1100D spectrophotometer at 535nm. The conditions of adsorption experiments are given in Table 2. The final concentrations were calculated with the absorbance

standards curve. The X-GRL removal data was calculated using the method described by Lei et al. (2007).

Table 2. Conditions of adsorption experiments

	Adsorption temp. (°C)	pH	Initial Con. of X-GRL (mg/dm ³)	Adsorbent Con. (g/dm ³)	Contact time (min)
Effect of adsorption temp.	20–40	7	20	0.8	0.5–15
Effect of adsorbent con.	20	7	20	0.6–2.4	5
Effect of initial pH	20	3–11	20	0.8	9
Effect of initial con. of X-GRL	20	7	4–28	0.8	5

Analytical methods

The morphology of the diatomite skeletons in RD and DC was identified by scanning electron microscopy (SEM, JSM-5610LV, JEOL Ltd., Japan) with an accelerating voltage of 20 kV. Adsorbent samples were removed from the X-GRL solution after equilibrium is achieved and drying at 70 °C for preparation for the analysis. FT-IR spectra of the samples were obtained using a Nicolet spectrophotometer (IS-10, US).

Results and discussion

Effect of operation parameters

The mono-factor experiment method was adopted to investigate the effect of individual operational parameters including temperature, adsorbent concentration, initial pH, and initial concentration of X-GRL. Figure 3 shows the influence of these parameters on X-GRL removal.

Effect of adsorption temperature

As shown in Fig. 3a, the adsorption of X-GRL onto RD increased rapidly with increasing contact time from 0 to 1 min. The fast adsorption at the initial stage may be due to the higher driving force along with the availability of both the uncovered surface area and the active silanol groups on the RD. Subsequently, the adsorption rate slowed down with further increase in contact time. This could be attributed to the reduction of both the extent of the uncovered surface area and remaining active silanol groups. It took around 11 minutes to reach adsorption equilibrium for X-GRL on to RD.

The adsorption of X-GRL onto DC also increased with an increase in contact time, but at a comparatively slower rate as compared to adsorption onto RD (Fig. 3b). It also took around 11 minutes to reach adsorption equilibrium for X-GRL onto DC, while the X-GRL removal rate by DC was much lower. An increase in the X-GRL uptake onto both the RD and DC was observed with an increase in temperature from 20 to 40 °C. This indicates that X-GRL adsorption on both the RD and DC was an endothermic process.

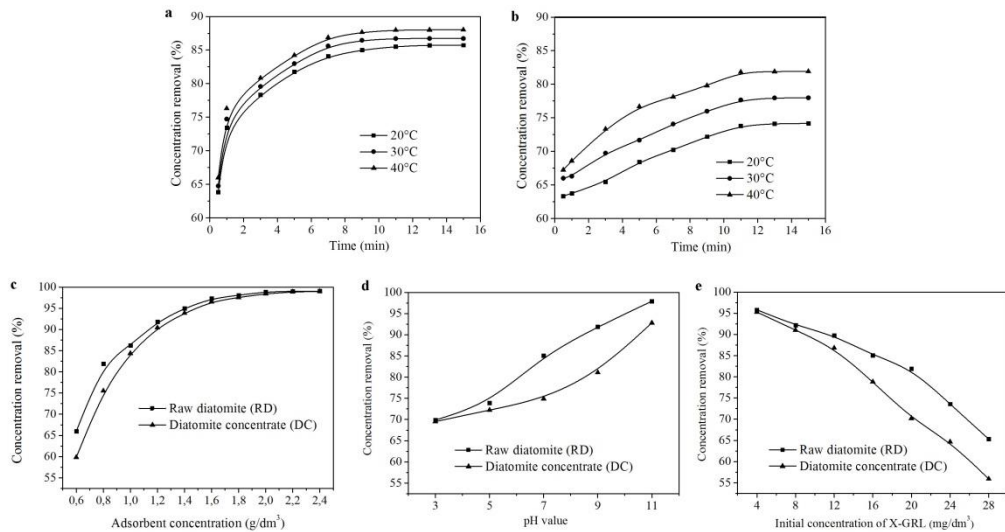


Fig. 3. X-GRL removal with respect to; (a) temperature for RD, (b) temperature for DC, (c) adsorbent concentration, (d) initial pH, (e) initial X-GRL concentration

Effect of adsorbent concentration

The influence of adsorbent concentration on X-GRL removal is shown in Fig. 3c. As the RD and/or DC concentration increased from 0.6 to 2.4 g/dm³, the X-GRL removal rate increased from around 60% up to 100%. When the adsorbent concentration was lower than 1.4 g/dm³, the X-GRL removal rates by RD were higher than those by DC. However, the difference in removal rate decreased gradually after 1.4 g/dm³, and the X-GRL removal rate reached 99% at 2.4 g/dm³. Obviously, the higher the amount of diatomite disposed into the aqueous solution, the higher was the X-GRL absorption.

Effect of initial pH

Figure 3d shows notable increases in the X-GRL adsorption by RD and DC in a pH range of 3–11. However, the degradation of X-GRL by OH⁻ was very obvious. Before adding any adsorbent, the X-GRL removal rate reached to over 80% in the pH of 9–11. In a previous work it has been proved that the auxochrome of some kinds of dyes may be affected from the absence of OH⁻ in alkaline conditions (Hao et al., 2000). The reason for the low removal rates in acid conditions is the fact that excess H⁺ ions compete with the dye cation to adsorb onto available sites on the adsorbent surface. In this regard, the neutral pH is the optimum condition for the X-GRL removal onto RD and DC.

Effect of initial concentration of X-GRL

As shown in Fig. 3e, with the increase of initial concentration of X-GRL from 4 to 28 mg/dm³, the rate of adsorption of X-GRL on both RD and DC significantly decreased. This can be attributed to the fact that higher initial concentration of X-GRL corresponds

to a higher extent of X-GRL molecules, and the removal rate will therefore be lower as the amount of adsorbent remains unchanged.

Adsorption kinetics, isotherms and thermodynamics

Adsorption kinetics

Two kinetic models, namely, pseudo-first-order and pseudo-second-order are analyzed according to the method reported by Ho and McKay (1999) and Ho et al. (2000). From the slope and intercept of straight portion of the linear plots obtained by plotting $\ln(q_e - q_t)$ vs. t (Fig. 4a), the values of the pseudo-first-order rate constants k_1 and q_e were calculated and listed in Table 3. Figure 4b shows the plot of t/q_t against t . The values of the pseudo-second-order rate constants k_2 and q_e (Table 3) were determined from the slope and intercept of the plot.

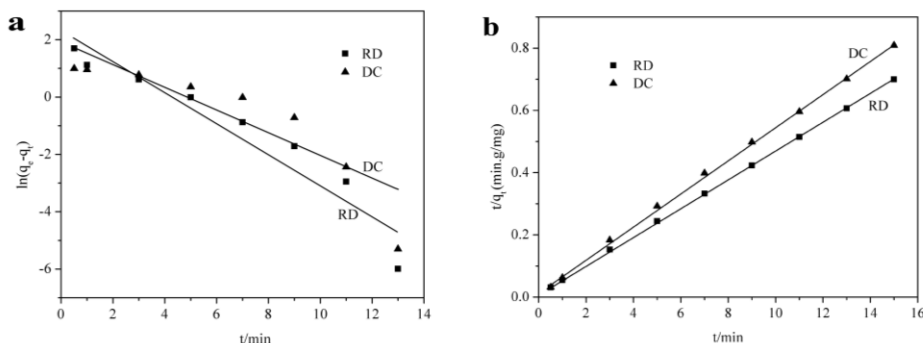


Fig. 4. Comparison of kinetics of X-GRL adsorption onto RD and DC according to
(a) pseudo-first-order, (b) pseudo-second-order

Table 3. Kinetic parameters for X-GRL adsorption by RD and DC

	equation	sample	model	parameters		
Pseudo 1 st order model	$\ln(q_e - q_t) = \ln q_e - k_1 t$	RD	$\ln(q_e - q_t) = -0.523t + 2.225$	k_1	q_e	R^2
		DC	$\ln(q_e - q_t) = -0.425t + 1.960$	0.523	9.25	0.915
Pseudo 2 nd order model	$\frac{t}{q_t} = \frac{1}{k_2 q_e^2} + \frac{1}{q_e} t$	RD	$t/q_t = 0.046t + 0.011$	k_2	q_e	R^2
		DC	$t/q_t = 0.053t + 0.017$	0.192	21.74	0.999

The results show that both of the correlation coefficients of the pseudo-second-order model for RD and DC are 0.999, and these values are larger than those obtained according to the pseudo-first-order model (0.915 and 0.803). This implied that the adsorption of X-GRL onto RD and DC was better represented the pseudo-second-order model.

Equilibrium isotherms

The equilibrium data were analyzed according to two isotherm equilibrium models, namely, Langmuir and Freundlich. Parameters were obtained using the method described previously (He et al., 2009; Li et al., 2011). From the slope and intercept of straight portion of the linear plots of C_e/q_e vs. C_e (Fig. 5a), the parameters of the Langmuir equations were calculated and listed in Table 4. Figure 5b shows the plot of $\ln q_e$ against $\ln C_e$. The parameters of the Freundlich equations (Table 4) were determined from the slope and intercept of the plot.

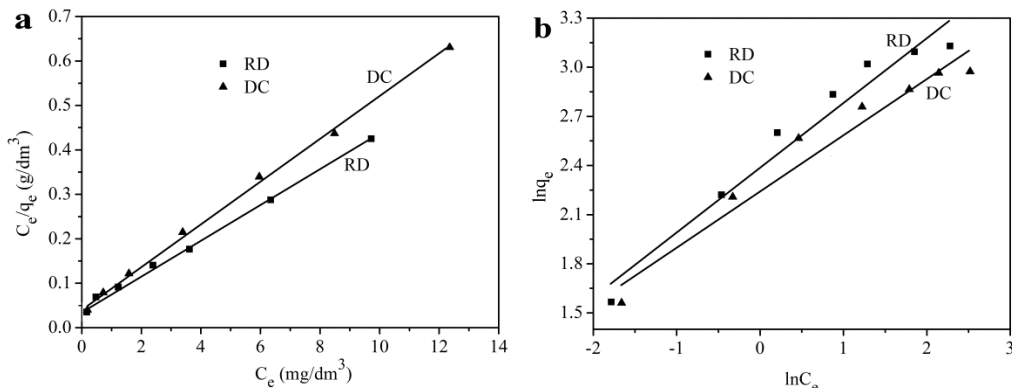


Fig. 5. Isotherm equilibrium models of X-GRL adsorption onto RD and DC according to Langmuir (a), Freundlich (b)

The Langmuir isotherms represented the X-GRL adsorption onto RD and DC in a better way as has been indicated by the comparatively higher R^2 . This corresponds to monolayer adsorption behavior of X-GRL onto RD and DC. According to the fitting results, the corresponding monolayer saturated adsorption capacity for RD and DC reaches 25.19 mg/g and 20.96 mg/g, respectively.

Table 4. Parameters of Langmuir and Freundlich equations

Sample	Langmuir			Freundlich		
	q_m (mg/g)	K_L (dm ³ /mg)	R^2	K_F (dm ³ /mg)	$1/n$	R^2
RD	25.19	1.04	0.998	11.00	0.40	0.959
DC	20.96	1.09	0.998	9.60	0.34	0.955

Thermodynamic study

Due to a better representation of X-GRL adsorption onto RD and DC by the Langmuir isotherms, the thermodynamic data could be calculated using Van't Hoff equations. From the slope and intercept of straight portion of the linear plots of $\ln K_d$ vs. $1/T$ (Fig. 6), the values of the standard enthalpy change (ΔH) and standard entropy change (ΔS) were

calculated. The calculated thermodynamic parameters (standard free energy changes (ΔG), standard enthalpy change (ΔH), standard entropy change (ΔS)) at each temperature and equilibrium adsorption amount for RD and DC are presented in Table 5 and Table 6, respectively.

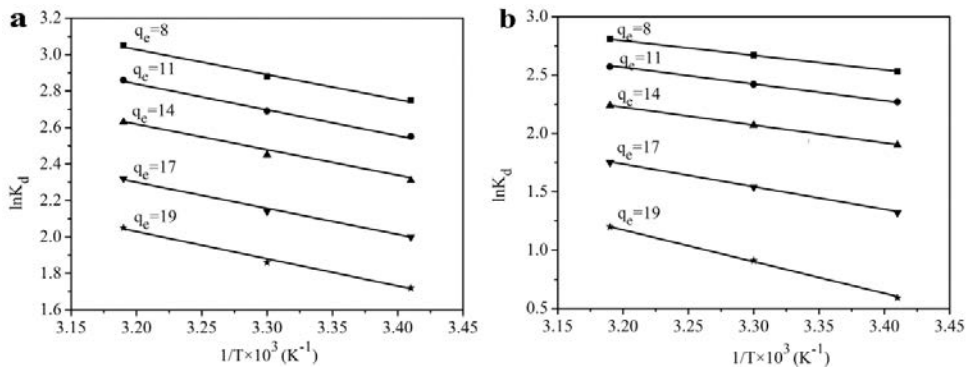


Fig. 6. Fitted curves of changes of standard enthalpy and standard entropy of X-GRL adsorption on RD (a) and DC (b)

Table 5. Values of thermodynamic parameters for absorption of X-GRL onto RD with respect to temperature and equilibrium adsorption amount

q_e (mg/g)	ΔH (kJ/mol)	ΔS J/(mol K)	ΔG /(kJ/mol)		
			293K	303K	313K
8.0	11.76	62.91	-6.69	-7.26	-7.95
11.0	11.88	61.71	-6.22	-6.78	-7.45
14.0	12.06	60.34	-5.64	-6.18	-6.85
17.0	12.37	58.79	-4.87	-5.39	-6.05
19.0	12.75	57.71	-4.18	-4.69	-5.34

Table 6. Values of various thermodynamic parameters for absorption of X-GRL onto DC with respect to temperature and equilibrium adsorption amount

q_e (mg/g)	ΔH (kJ/mol)	ΔS J/(mol K)	ΔG /(kJ/mol)		
			293K	303K	313K
8.0	10.67	57.45	-6.17	-6.74	-7.32
11.0	11.42	57.83	-5.52	-6.09	-6.68
14.0	12.81	59.54	-4.63	-5.22	-5.82
17.0	16.15	66.15	-3.22	-3.88	-4.55
19.0	23.39	84.72	-1.43	-2.30	-3.12

These results show that there is a similar trend in terms of thermodynamic parameters for RD and DC. The negative values of ΔG at all studied conditions indicate

that the adsorption of X-GRL onto RD and DC followed a spontaneous trend. Besides, physical adsorption could be accepted to have played an important role in the X-GRL uptake by both adsorbents, as confirmed by the ΔG values ranging between -20 to 0 kJ/mol. The positive values of ΔH at all studied conditions revealed that the adsorption was an endothermic process and this was supported by the increasing removal rate with rising temperature. The positive values of ΔS reflected the affinity of X-GRL towards RD and DC, and also indicated increased randomness at the adsorbent/solution interface during adsorption (Li et al., 2011).

Adsorption mechanisms

The FT-IR spectra of X-GRL, RD, DC and the diatomite samples after adsorption are presented in Fig. 7. The band at around 3440 cm^{-1} is due to the stretching vibrations of adsorbed water, and the band at 1635 cm^{-1} reflects H-O-H bending vibration of water. For RD and DC, the bands at around 1097 , 797 and 469 cm^{-1} represent the asymmetric stretching, symmetric stretching and bending vibrations of Si-O-Si bonds, respectively (Saidi et al., 2012; Xiao et al., 2004). Compared with RD, the SiO_2 content of DC was higher as shown by the relatively higher intensity of the peak at 1097 cm^{-1} , which complies with the results of the XRF and XRD analysis. Moreover, the intensity of the bands at 3435 and 1097 cm^{-1} increased when the dye was adsorbed onto RD and DC. These two bands also tended to occur at higher wavenumbers after adsorption under the influence of the 3447 and 1147 cm^{-1} bands of the azo-dye, X-GRL.

Figure 8 shows the morphology of RD and DC obtained by SEM. It is known that the fine particles rejected by concentration consisted of little extents of diatomite skeletons and clay particles. The specific surface area decreased from 27.3 to $13.0\text{ m}^2/\text{g}$ after concentration of diatomite. The decrease of specific surface area was attributed to the removal of these fine impurities with relatively higher specific surface areas (Ediz et al., 2010; Sun et al., 2013). It was previously shown that clay minerals like illite with high surface area could have a remarkable ability of dye adsorption (Kahr and Madsen, 1995). In this respect, it could be claimed that RD with a higher content of fine particles and thus, higher surface area could uptake more X-GRL as compared to DC.

It is known that the zero point of charge (ZPC) of diatomite is around pH 5.4. Diatomite surface is degenerated by -OH groups and oxygen bridges, which act as adsorption sites. The reason for the poor removal of X-GRL at lower pH's than the ZPC condition is that the electrostatic repulsion between positively charged X-GRL molecules and the diatomite surface was increased. With a pH higher than the ZPC value, negative charges on the biomass surface starts to accumulate, and cationic X-GRL becomes attractive to the diatomite surface (Khraisheh et al., 2005A; Vijayaraghavan et al., 2008). These findings comply with the findings about the effects of initial pH in this study.

There is an electrostatic attraction between the X-GRL molecules and the negatively charged diatomite surface. The X-GRL is hydrophilic in nature due to the hydration of polar groups and charged groups in the molecular structure of X-GRL (He et al., 2009),

and hence, the X-GRL molecules adsorb onto diatomite surface through van der Waals force. In this respect it could be deduced that the main driving forces of the physical adsorption of the azo-dye, X-GRL on diatomite were electrostatic attraction and Van der Waals force.

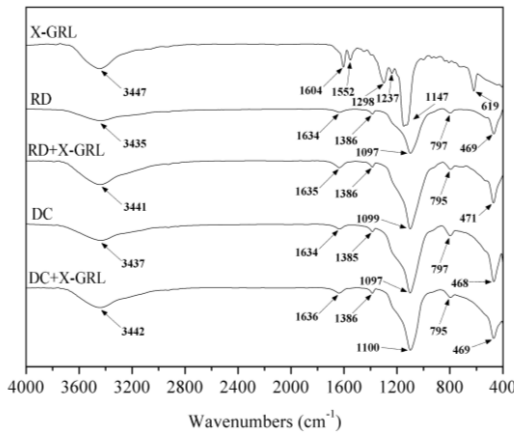


Fig. 7. FT-IR spectra of the samples

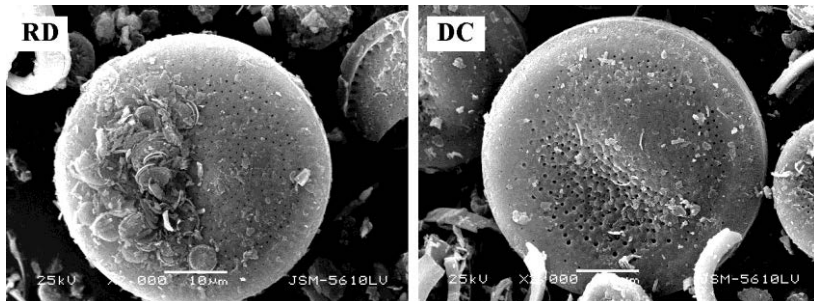


Fig. 8. SEM images of RD and DC

Conclusions

Similar mechanisms were found responsible for X-GRL adsorption onto raw diatomite (RD) and diatomite concentrate (DC). The equilibrium adsorption capacity of RD and DC increased slightly with temperature, and the neutral pH condition was found to favour the adsorption process. Adsorption processes was best represented by the pseudo-second-order model, the Langmuir adsorption isotherms. Adsorption was endothermic under all conditions. The adsorptions followed a spontaneous trend, and physical adsorption could have played an important role. The main driving forces of the physical adsorption of X-GRL on the diatomite were electrostatic attraction and Van der

Waals forces. Also, it was seen that RD could uptake more X-GRL than DC owing to higher content of fine particles with higher surface area. In view of the findings of this study, raw diatomite can be suggested as a cost-effective absorbent alternative to active carbon for the removal of azo-dye, X-GRL.

Acknowledgements

This work was financially supported by the Key Science and Technology Support Programs (2011BAB03B07) of the Ministry of Science and Technology of China.

References

AMIN N.K., 2009, *Removal of direct blue-106 dye from aqueous solution using new activated carbons developed from pomegranate peel: adsorption equilibrium and kinetics*, J. Hazard. Mater. 165, 52–62.

BAE J. S., FREEMAN H. S., 2007, *Aquatic toxicity evaluation of new direct dyes to the daphnia magna*, Dyes Pigments, 73, 81–85.

BAHRAMIAN B., ARDEJANI F.D., MIRKHANI V., BADII K., 2008, *Diatomite-supported manganese Schiff base: An efficient catalyst for oxidation of hydrocarbons*, Appl. Catal. A: Gen. 345, 97–103.

EDIZ N., BENTLI I., TATAR I., 2010, *Improvement in filtration characteristics of diatomite by calcination*, Int. J. Miner. Process. 94, 129–134.

ERDEM E., COLGESEN G., DONAT R., 2005, *The removal of textile dyes by diatomite earth*, J. Colloid Interface Sci. 282, 314–319.

HAO O.J., KIM H., CHIANG P.C., 2000, *Decolorization of wastewater*, Crit. Rev. Environ. Sci. Technol. 30, 449–505.

HE S.H., ZHOU Y., GU Z.P., XIE S.B., DU X., 2009, *Adsorption of two cationic dyes from aqueous solution onto natural attapulgite*, Int. Conf. Bioinformatics Biomed. Eng., iCBBE. 1–5.

HO Y. S., MCKAY G., 1999, *Pseudo-second order model for sorption processes*, Process. Biochem. 34, 451–465.

HO Y. S., NG J. C. Y., MCKAY G., 2000, *Kinetics of pollutant sorption by biosorbents: Review*, Sep. Purif. Methods. 29, 189–232.

ISIL M., SPONZA D.T., 2005, *Effects of alkalinity and co-substrate on the performance of an upflow anaerobic sludge blanket (UASB) reactor through decolorization of Congo Red azo dye*, Bioresour. Technol. 96, 633–643.

KAHR G., MADSEN F.T., 1995, *Determination of the cation exchange capacity and the surface area of bentonite, illite and kaolinite by methylene blue adsorption*, Appl. Clay Sci. 9, 327–336.

KHRAISHEH M.A.M. , AL-GHOUTI M.A., ALLEN S.J., AHMAD M.N., 2005A, *Effect of OH and silanol groups in the removal of dyes from aqueous solution using diatomite*, Water Res. 39, 922–932.

KHRAISHEH M.A.M., AL-GHOUTI M.S., 2005B, *Enhanced dye adsorption by microemulsion-modified calcined diatomite (μ E-CD)*, Adsorpt. 11, 547–559.

LEI L.C., DAI Q.Z., ZHOU M.H., ZHANG X.W., 2007, *Decolorization of cationic red X-GRL by wet air oxidation: Performace optimization and degradation mechanism*, Chemosphere. 68, 1135–1142.

LI H.L., LEI H.Y., YU Q., LI Z., FENG X., YANG B.J., 2010, *Effect of low frequency ultrasonic irradiation on the sonoelectro-Fenton degradation of cationic red X-GRL*, Chem. Eng. J. 160, 417–422.

LI Y.H., DU Q.J., LIU T.H., QI Y., ZHANG P., WANG Z.H., XIA Y.Z., 2011, *Preparation of activated carbon from Enteromorpha prolifera and its use on cationic red X-GRL removal*, Appl. Surf. Sci. 257, 10621–10627.

LIM J.L., OKADA M., 2005, *Regeneration of granular activated carbon using ultrasound*, Ultrason. Sonochem. 12, 277–282.

LIN J.X., ZHAN S.L., FANG M.H., QIAN X.Q., 2007, *The adsorption of dyes from aqueous solution using diatomite*, J. Porous Mater. 14, 449–455.

QIU B., CHENG X., SUN D.Z., 2012, *Characteristics of cationic Red X-GRL biosorption by anaerobic activated sludge*, Bioresour. Technol. 113, 102–105.

REN Z.J., GAO H.M., ZHANG H.Q., LIU X., 2014, *Effects of fluxes on the structure and filtration properties of diatomite filter aids*, Int. J. Miner. Process. 130, 28–33.

SAIDI R., TLILI A., FOURATI A., AMMAR N., OUNIS A., JAMOUSSI F., 2012, *Granulometric distribution of natural and flux calcined chert from Ypresian phosphatic series of Gafsa Metlaoui basin compared to diatomite filter aid*, IOP Conf. Ser. Mater. Sci. Eng. 28, 1–8.

SUN Z.M., YANG X.P., ZHANG G.X., ZHENG S.L., FROST R.L., 2013, *A novel method for purification of low grade diatomite powders in centrifugal fields*, Int. J. Miner. Process. 125, 18–26.

TSAI W.T., HSIEN K.J., YANG, J.M., 2004, *Silica adsorbent prepared from spent diatomaceous earth and its application to removal of dye from aqueous solution*, J. Colloid Interface Sci. 275, 428–433.

VIJAYARAGHAVAN K., MAO J., YUN Y.S., 2008, *Biosorption of methylene blue from aqueous solution using free and polysulfone-immobilized Corynebacterium glutamicum: batch and column studies*, Bioresour. Technol. 99, 2864–2871.

WANG H., ZHU M.F., LI Y.G., ZHANG Q.H., WANG H.Z., 2011, *Mechanical properties of dental resin composites by co-filling diatomite and nanosized silica particles*, Mater. Sci. Eng.: C. 31, 600–605.

WU J.S., LIU C.H., CHUB K.H., SUEN S.Y., 2008, *Removal of cationic dye methyl violet 2B from water by cation exchange membranes*, J. Membrane Sci. 309, 239–245.

XIAO W.S., LI Y.C., LIU J., WEN K.N., CHEN J.Y., 2004, *High-pressure and high-temperature phase transformation of cristobalite at a pressure of up to 63 GPa*, Nucl. Technol. 27, 926–930. (in Chinese).

YU H.W., FUGETSU B., 2010, *A novel adsorbent obtained by inserting carbon nanotubes into cavities of diatomite and applications for organic dye elimination from contaminated water*, J. Hazard. Mater. 177, 138–145.

Received December 12, 2014; reviewed; accepted March 30, 2015

LEACHING OF MANGANESE ORES USING CORNCOB AS REDUCTANT IN H_2SO_4 SOLUTION

Sajad ALI, Yaseen IQBAL, Umar FAROOQ, Sajjad AHMAD

Materials Research Laboratory, Department of Physics, University of Peshawar, Pakistan, Post code 25120
Pakistan, sajjad2485@yahoo.com

Abstract: In this study, corncob was used as reductant for sulfuric acid leaching of manganese ore from Daweezi, Upper Mohmand Agency, Pakistan. X-ray diffraction of representative powdered samples revealed the presence of manganese silicate $MnSiO(SiO_4)$, calcite ($CaCO_3$), and α -quartz (SiO_2). X-ray diffraction and energy dispersive spectroscopy analyses indicated that the examined manganese ore was siliceous in nature. Three process parameters were investigated in the present study including the particle size of the ore, leaching temperature, and amount of corncob. Manganese extraction of 92.48 wt% was achieved for a leaching time of 60 min at 90 °C using 1.9 mol/dm³ H_2SO_4 concentration and 4 g of corncob. The present results demonstrated that corncob is a low cost, renewable, and non-hazardous reducing agent for manganese leaching under mild acid conditions in comparison to the other available reagents.

Keywords: siliceous manganese ore, characterization, leaching, corncob, H_2SO_4

Introduction

Manganese is an important element with several industrial applications such as steel, non-ferrous alloys, and paints production. Its non-metallurgical uses include fertilizers, animal feeds, colorants for bricks, textile dyes, and medicine (Pagnanelli et al., 2004). With increasing demand for manganese and gradual depletion of high grade manganese ore, various routes have been tried to develop an economical and efficient process to recover manganese from low-grade manganese dioxide ores (Haifeng et al., 2010). Low and medium-grade ores of manganese usually contain phosphorous, iron, and silica, rendering these ores unsuitable for usual industrial applications (Pagnanelli et al., 2004). Manganese occurs in nature mostly as pyrolusite (MnO_2) which is stable in acidic and alkaline media. Therefore, extraction of manganese from such a source has to be carried out under reducing conditions (Hariprasad et al., 2007). Low-grade of manganese dioxide ore can be treated by reductive acid leaching using different kinds

of reducing agents and acids (Pagnanelli et al., 2004). Coal is used as a reductant in traditional technology in order to convert manganese dioxide to manganese oxide which can be leached by sulfuric acid. This method produces smoke, dust, oxysulfide, and nitrogen oxides which greatly pollute the environment. Additionally, this method requires reaction temperature over 800 °C, which is too high for most of the reactors (Cheng et al., 2009).

Several other reducing agents have also been used traditionally under different acidic media e.g. pyrite, ferrous sulfate, aqueous sulfur dioxide, and hydrogen peroxide. Some of the reducing agents used as SO_2 , may be harmful for the environment. Therefore, many investigators focused on reductive leaching of manganese dioxide ores using organic reductants mainly carbohydrates like glucose, sucrose, lactose, and oxalic acid. The use of organic reductant to leach manganese dioxide ores has been reported to be simple and efficient under mild temperature conditions (<90 °C) (Hariprasad et al., 2009), however the cost of reductant and high consumption rate limit the commercial applications of this technique (Tian et al., 2010).

Biomass can be used as a cheap and effective reductant to reduce manganese oxide ore at temperatures below 450 °C with a degree of reduction more than 95%. Moreover, as the amount of CO_2 released during the roasting process is equal to the amount absorbed during biomass growth, and this is a zero emission process for biomass fuel (Zhang et al., 2013). Adopting a zero-waste approach, carbohydrates from agriculture wastes are low-cost, renewable, and non-hazardous reducing agents that can be used for manganese leaching under mild acidic conditions (Lasheen et al., 2009). Among the biomass wastes, sawdust, cane molasses, corncob, cornstalks, rice husk, wheat stalks, bagass, bamboo, and shredded papers have been considered as environment-friendly and low-cost reducing agents for roasting reduction and leaching of manganese dioxide ore (Zhang et al., 2013). In order to extract manganese efficiently and economically by using waste materials, the hydrometallurgical treatment of low-grade manganese ore has attracted much attention in recent years (Chao et al., 2013).

In the present work, corncob was used as a reducing agent in a dilute sulfuric acid medium to extract manganese from siliceous manganese ores. In this process, corncob was hydrolyzed to release glucose under the acidic condition so that manganese dioxide could be reduced at a low temperature. The use of corncob for reduction of manganese dioxide is a simple, low cost, and economical method in comparison to the other available raw reductants. Using this method, manganese could be extracted up to about 90% (Tian et al., 2010).

Materials and methods

Manganese ore was obtained from Daweezi (34°35'60" N and 71°30'25" E), Upper Mohmand Agency, Khyber Pukhtunkhwa (KP), Pakistan. Semi-quantitative EDS

detected 60.7 wt% Mn, 15.8 wt% Ca, and 23.5 wt% Si in as-mined ore sieved through at 74 μm sieve. The ore was crushed, ground and passed through 149 and 74 μm sieves.

The leaching experiments were carried out in a 400 cm^3 glass beaker kept over a ceramic hot plate with magnetic stirring system in a fume hood. Initially 100 cm^3 concentrated H_2SO_4 (1.9 mol/dm³) was mixed thoroughly with weighed amount of corncob (2, 3, and 4 g) to release the glucose into the acid. After 15 min, the weighed amount of ore (10 g) powder was transferred to the pulp. The leaching experiments were carried out for different sets of parameters i.e. different amounts of corncob, particles size, and temperatures.

Room temperature X-rays diffraction (XRD) data were recorded using a JEOL JDX-3532 X-ray diffractometer, operating at 40 kV and 30 mA, with $\text{Cu K}\alpha$ radiation ($\lambda \sim 0.154$ nm) at the Centralized Resource Laboratory (CRL), University of Peshawar, Pakistan. The samples were scanned from 10°-70° (2θ) with a count time/step of 1.25 s and 0.02° step size. Secondary electron scanning electron microscope (SEM) images of chemically etched samples were recorded using a JEOL JSM5910 SEM, operating at 30 keV. Semi-quantitative energy dispersive X-ray electron (EDS) data were collected using an INCA200 EDS detector (Oxford instruments, UK) with analysis range from Boron to Uranium, connected with a JEOL-JSM5910 SEM. A PMG-3 microscope coupled with a DP-12 CCD camera, Olympus (Japan) was used for recording optical images in the present study at CRL.

Results and discussion

Characterization of as-mined samples

Figure 1a is a reflected light micrograph of chemically etched, finely polished manganese ore sample, showing the presence of three distinct micro-regions with different texture and morphology. The micro-regions with brownish golden contrast comprised anhedral grains (granular mineral with no definite morphology), marked as "A" (Fig. 1a), were manganese-rich (confirmed by SEM EDS). The jet-dark and cracked micro-regions, labeled as "B" (Fig. 1a), may also be rich in manganese as reported previously by Miah et al. (2009). These micro-regions appeared as druses (crystals grown in a cavity, resulting in numerous crystal-tipped surfaces) and irregular in shape with no sharp boundaries/edges. The irregular cracks and slight alteration along the cracks are the characteristic features of manganese mineral. The apparently swelled grey regions marked as "C" (Fig. 1a) may be due to the effect of etching which could be seen in all the images of the chemically etched samples. The narrow black veins on the borders of the brownish gold color are also rich in manganese (Miah et al., 2009). There were long zigzag cracks and veins in most of the micro-regions. However, some short and curved cracks were also seen.

Thin section study of the same sample showed two different textures that is one with dark and the other with bright contrast when viewed under the plane-polarized

light (Fig. 1b). Quartz appeared with bright contrast under plane polarized light and bright or grey when viewed under cross polarized light (MacKenzie et al., 1980). Iron was detected in veins and cracks as shown in Fig. 1b. The interlocked gangue mineral containing calcite or quartz was surrounded by manganese mineral with dark contrast. The micro-regions with bright contrast may be quartz or calcite as these minerals appear bright in plane polarized light (MacKenzie et al., 1980). Under plane polarized light the calcite shows granular texture and can be recognized by its good cleavage and twin lamellae.

The micro-regions with grey contrast in the cross polarized light photomicrograph (Fig. 1c) may be calcite with silica grains embedded in it (MacKenzie et al., 1980). The dark matrix may be the manganese-rich region. Mehdilo et al. (2013) reported the presence of bright and dark micro-regions in manganese ore under transmitted light microscope. The dark contrast was associated with the presence of manganese while the bright texture with calcite or quartz.

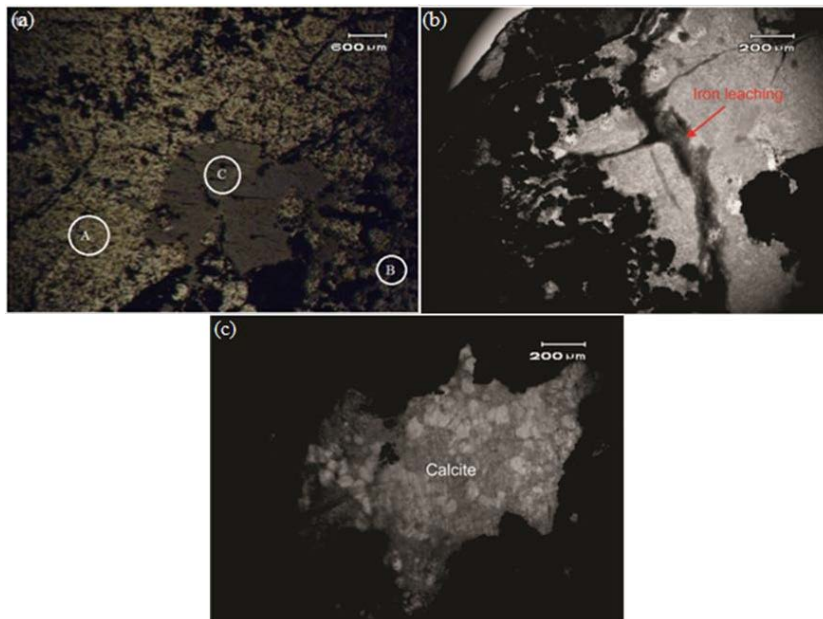


Fig. 1. a) Reflected light micrograph of as-mined Mn ore sample b) thin section view of Mn ore under plane polarized light c) thin section of the same sample under cross polarizer, showing various grains and micro-regions of varying contrast

Figure 2 shows room temperature XRD pattern recorded for as-mined manganese ore powder. The inter-planer spacings (d-values) and relative intensities corresponding to the major XRD peaks (labeled as \blacktriangledown) matched PDF# 88-1232 for manganese silicate $MnSiO(SiO_4)$ indicating it to be the major phase in the examined sample. Additionally, some minor peaks matched PDF# 5-586 for calcite and PDF# 2-

458 for quartz showing these to be gangue minerals. A previous XRD study of manganese ore (Cheng et al., 2009) show the presence of pyrolusite (MnO_2) as the major phase along with small quantities of MgO , quartz (SiO_2), hematite (Fe_2O_3) and Al_2O_3 . Another XRD study (Su et al., 2008) of low-grade manganese ore from Bayi manganese mine, Guangxi, China reported the presence of todorokite ($\text{Mn}_6\text{O}_{12} \cdot 4.16\text{H}_2\text{O}$) and hematite (Fe_2O_3) as the major phases and quartz (SiO_2) and kaolinite ($\text{Al}_2\text{Si}_2\text{O}_5(\text{OH})_4$) as gangue minerals. Tian et al. (2010) also used XRD to investigate Hunan manganese ore, and reported the presence of a variety of metallic minerals including pyrolusite (MnO_2), todorokite ($\text{Mn}_6\text{O}_{12} \cdot 4.16\text{H}_2\text{O}$), goethite ($\text{Fe}_2\text{O}_3 \cdot \text{H}_2\text{O}$), and gangue minerals consisting primarily of quartz (SiO_2), and kaolinite ($\text{Al}_2\text{Si}_2\text{O}_5(\text{OH})_4$).

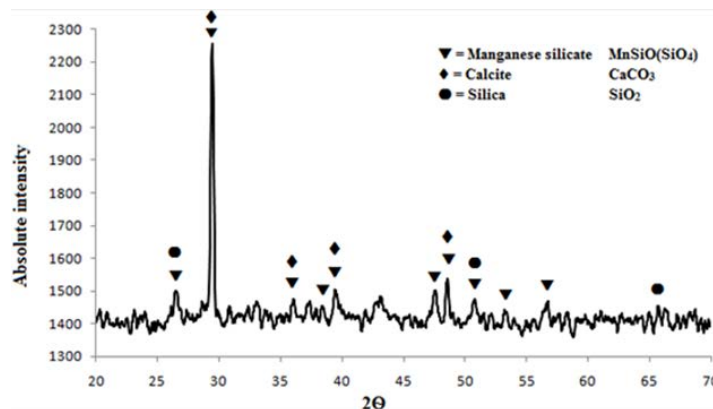


Fig. 2. XRD pattern of as-mined manganese ore showing peaks matching manganese silicate, calcite, and quartz

Figure 3 shows the secondary electron SEM images (SEIs) of as-mined manganese ore sample. EDS revealed that the irregular-shaped grains with light grey contrast marked as “A” were rich in manganese. The large grains with bright contrast and foggy surfaces “B” in Fig. 3 were calcium rich. EDS detected only Si in the relatively smaller grains with smooth surfaces marked as “C” which may be quartz. The gross elemental composition of the micro-regions shown in Fig. 3 is given in Table 1.

Table 1. Gross, white and light grey micro-regions composition of Fig. 3

Gross Composition		Bright Micro-region (B)		Light-grey Micro-region (A)	
Element	wt %	Element	wt %	Element	wt%
Mn	60.7	Mn	62.2	Mn	65.5
Ca	15.8	Ca	24.1	Ca	19.6
Si	23.5	Si	13.7	Si	14.9

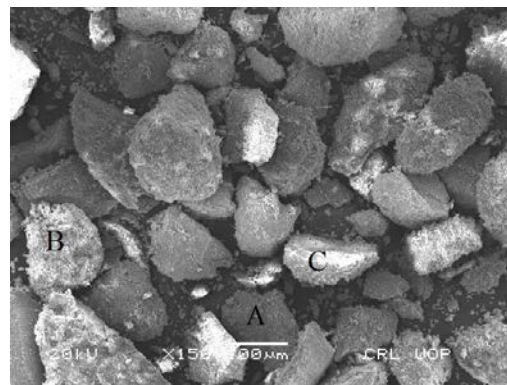


Fig. 3. SEI of as-mined manganese ore powdered sample sieved through 74 μ m screen A and B show manganese-rich grains, and C shows silica-rich grain

Characterization of leached samples

Effect of particle size

EDS of the grains shown in Fig.4 (a-b) revealed an increase in manganese content from 51.8 wt.% to 76.4 wt.% by increasing particle size from 149 μ m to 74 μ m. The variation in elemental composition for 149 μ m to 74 μ m sizes is given in Table 2, and shown in Fig. 5.

The presence of sulfur observed in the leached manganese samples may be due to H_2SO_4 treatment of ore. Due to high density of manganese (7.35 g/cm³), it settles down and calcium, silicon and sulfur cover the upper surface as evident from Fig. 4. EDS detected calcium and sulfur in the crushed grass-like features on the surface of the large grains of manganese with dark contrast. Table 3 shows the manganese extraction with different particle size.

Table 2. Elemental composition of 149 μ m to 74 μ m size sample

Size Fraction (μ m)	Element Concentration (wt %)			
	Mn	Si	Ca	S
-149	51.8	21.5	2.1	---
-74	76.4	21.8	14.2	12.2

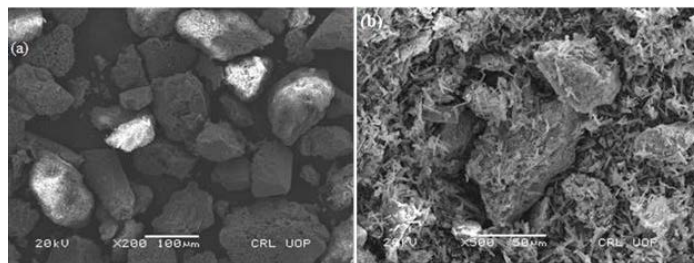


Fig. 4. SEI of processed sample through a) -149 μ m particle size b) -74 μ m particle size

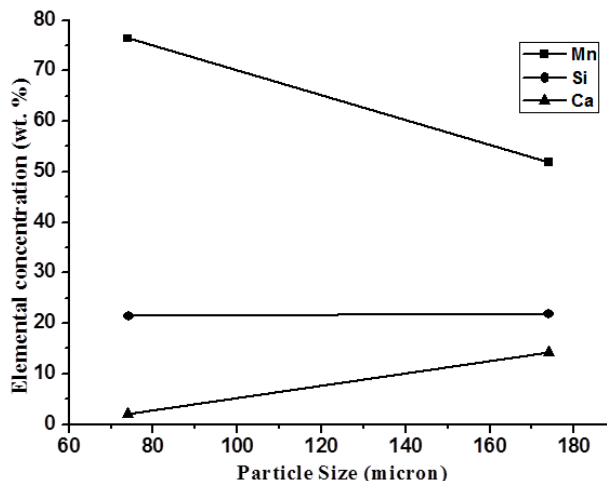


Fig. 5. Variation of elemental concentration with particle size

Table 3. Leaching results for 10 g of manganese ore treated with 3g of corncob for 60 min in 1.9 mol/dm³ of H₂SO₄ concentration at 90 °C for various particle sizes

Particle Size (μm)	Manganese Extraction (wt%)
-149	76.4
-74	51.80

Effect of corncob amount

Keeping the same concentration of sulfuric acid (i.e. 1.9 mol/dm³), leaching time of 60 min for 10 g of ore at 90 °C and particle size of 74 μm, the influence of corncob amount on leaching efficiency was investigated in detail. The variation in leaching efficiency of manganese ore and other elements with the amount of corncob are shown in Fig. 6. This experiment demonstrated that the leaching efficiency of manganese increased with the increase in the amount of corncob. The leaching efficiency of manganese increased up to ~92.5% when the amount of corncob was increased to ~4 g (Table 4). This was the highest leaching efficiency of manganese achieved in the present study. Therefore, 4 g of corncob was taken as the optimal parameter.

Table 4. Manganese extractions from its ore (-74 μm particle size) at 90 °C for a leaching time of 60 min in H₂SO₄ concentration of 1.9 mol/dm³ for various corncob amounts

Corncob Amount (g)	Manganese Extraction (wt%)
2	64.8
3	81.3
4	92.5

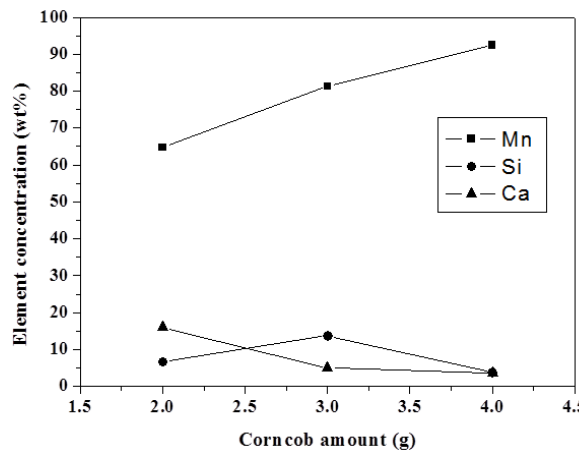


Fig. 6. Variation of chemical elements concentration with corn cob amount

Effect of temperature

Table 5. Manganese extractions from its ore treated with 3 g corn cob, 60 min of leaching time, H_2SO_4 concentration of 1.9 mol/dm³, particle size of 74 μm for various temperatures

Temperature (°C)	Manganese Extraction (wt%)
70	58.39
100	81.20

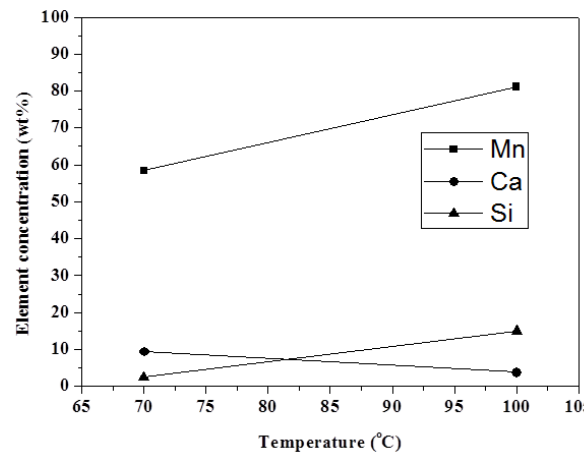


Fig. 7. Variation of chemical elements concentration with temperature

Keeping the corn cob amount fixed at 4 g, sulfuric acid concentration at 1.9 mol/dm³, leaching time of 60 min, ore amount of 10 g and particle size of 74 μm , the influence of temperature on leaching efficiency was investigated. Two leaching experiments were carried out at 70 °C and 100 °C. The result obtained is given in Fig.

7 showing variation of elemental concentration with temperature. It is observed that by increasing the temperature from 70 °C to 100 °C, manganese recovery after 60 min leaching increased from 58.39% to 81.20%. In this study, the most favorable leaching temperature was 100 °C (Table 5).

Conclusion

In this study, a manganese ore from Daweezi (Mohmand Agency, Pakistan) was characterized using optical microscopy, XRD, SEM and EDS techniques. The Daweezi manganese ore is a high-grade siliceous manganese ore. The mineralogical constituents of the ore are manganese silicate [MnSiO(SiO₄)], calcite (CaCO₃) and α -quartz (SiO₂). Manganese ore was upgraded by acid reductive leaching using predetermined concentration of H₂SO₄ in the presence of corncob as reductant. The investigated factors were temperature, particle size and corncob amount. The best operating conditions giving the highest manganese content were 90 °C, 74 μ m size, leaching time of 60 min, H₂SO₄ concentration of 1.9 mol/dm³ and 4 g corncob. The present results indicated that with the variation of temperature the rate of leaching efficiency increased. Manganese extraction from manganese ore strongly depends on the reaction temperature. With the decrease of ore particle size, the manganese recovery increased. With the increase of corncob amount the manganese extraction increased while the silica concentration decreased. Considering that the process productively use corncob from the environment, the technology should be beneficial from both economic and environmental perspective.

Acknowledgment

The authors acknowledge the financial support of the Higher Education Commission (HEC) for Pakistan, the US National Academy of Science under the Pak-US S&T Cooperation Program, Materials Research Laboratory (MRL) and Centralized Resource Laboratory (CRL) University of Peshawar, Pakistan.

References

- CHENG, Z., ZHU, G., ZHAO, Y., 2009, *Study in reduction-roast leaching manganese from low-grade manganese dioxide ores using cornstalk as reductant*, Hydrometallurgy, 96, 176-179.
- CHAO, X., LONGJUN, X., TIEFENG, P., KUN, C., JING, Z., 2013, *Leaching process and kinetics of manganese in low-grade manganese ore*, Chinese Journal of Geochemistry, 32, 222-226.
- HARIPRASAD, D., DASH, B., GHOSH, M.K., ANAND, S., 2007, *Leaching of manganese ores using sawdust as a reductant*, Minerals Engineering, 20, 1293-1295.
- HARIPRASAD, D., DASH, B., GHOSH, M.K., ANAND, S., 2009, *Mn recovery from medium grade ore using a waste cellulosic reductant*, Indian Journal of Chemical Technology, 16, 322-327.
- HAIFENG, S., HUAIKUN, L., FAN, W., XIAOYAN, L., YANXUAN, W., 2010, *Kinetics of reductive leaching of low-grade pyrolusite with molasses alcohol wastewater in H₂SO₄*, Chinese Journal of Chemical engineering, 18(5), 730-735.

LASHEEN, T.A., EL-HAZEK, M.N., HELAL, A.S., EL-NAGAR, W., 2009, *Recovery of manganese using molasses as reductant in nitric acid solution*, International Journal of Mineral Processing, 92, 109-114.

MACKENZAI, W.S., GUILFORD, C., 1980, *Atlas of Rock-forming Minerals in Thin Sections*, Longman Scientific & Technical, 89-90.

MIAHA, P.P., MOHAPATARA, B.K., MAHANTA, K., 2009, *Upgradation of low-grade siliceous manganese ore from Bonai-Keonjhar belt, Orissa*, Indian Journal. Minerals and Materials Characterization and Engineering, 8(1), 47-56.

MEHDILLO, A., IRANNAJAD, M., HOJJATI-RAD, M.R., 2013, *Characterization and beneficiation of Iranian low grade manganese ore*, Physicochemical Problems of Mineral Processing, 49(2), 725-741.

PAGNANELLI, F., FURLANI, G., VALENTINI, P., VEGLIO, F., TORO, L., 2004, *Leaching of low-grade manganese ores by using nitric acid and glucose: optimization of the operating conditions*, Hydrometallurgy, 75, 157-167.

SU, H., WEN, Y., WANG, F., SUN, Y., TONG, Z., 2008, *Reductive leaching of manganese from low-grade manganese ore in H_2SO_4 using cane molasses as reductant*, Hydrometallurgy, 93, 136-139.

TIAN, X., WEN, X., YANG, C., LIANG, Y., PI, Z., WANG, Y., 2010, *Reductive leaching of manganese from low-grade manganese dioxide ores using corncob as reductant in sulfuric acid solution*, Hydrometallurgy, 100, 157-160.

ZHANG, H., ZHU, G., YAN, H., LI, T., ZHAO, Y., 2013, *The mechanism on biomass reduction of low-grade manganese dioxide ore*, The Minerals, Metals and Materials Society and ASM International.

ZHANG, H., ZHU, G., YAN, H., ZHAO, Y., LI, T., FENG, X., 2013, *Reduction of low-grade manganese dioxide ore pellets by biomass wheat stalk*, Acta Metallurgica Sinica, 26 (2), 167-172.

Received July 3, 2014; reviewed; accepted December 13, 2014

CHARACTERIZATION OF ESPEY COLEMANITE AND VARIATION OF ITS PHYSICAL PROPERTIES WITH TEMPERATURE

Atila G. CELIK*, Gaye O. CAKAL**

* National Boron Research Institute, Dumlupinar Bulvari, 166-10, 06520 Ankara, Turkey

** Ankara University, Institute of Nuclear Sciences, 06100 Tandoğan, Ankara, Turkey,
gayecakal@hotmail.com, +90 3122128577-2736

Abstract: It is important to characterize boron containing minerals because of their uses in a wide range of applications. The purpose of this study is to characterize Espey colemanite by mineralogical, petrographical and thermal means and to investigate the variation of its physical properties with temperature (up to 600 °C). Colemanite, having a non-porous crystalline structure, was found to consist of 35.8% B₂O₃ and 30.5% SiO₂. The thermal decomposition of colemanite occurred within the temperature range of 300–600 °C. It was found that calcination, a thermal treatment method, influenced the physical properties of colemanite. The highest surface area, 131.9 m²/g, was obtained at 500 °C. The physical properties were found to have high statistical relation.

Keywords: colemanite, boron mineral, characteristic property, physical property, temperature

Introduction

Turkey is the largest producer of natural borates worldwide. Boron reserves are highly concentrated in Turkey, which accounts for around 70% of the world total (Roskill, 2010). The Turkish borate deposits occur in western Anatolia in five main districts; Bigadic, Kestelek, Sultancayiri, Emet, and Kirka (Palmer and Helvaci, 1995). The borates in Turkey are tincal, colemanite and ulexite. Colemanite reserves have the largest share (73.9%) compared to tincal (24.5%) and ulexite (1.6%) (Eti Mine, 2008). Colemanite (calcium borate, Ca₂B₆O₁₁·5H₂O) and tincal (sodium borate, Na₂B₄O₇·10H₂O) are the most widely-used boron minerals. B₂O₃ wt. percentages of the minerals are 50.8% and 36.5%, respectively. Nearly 10% of the natural borates are consumed as it is; whereas the rest is used to produce refined products. Turkey is the world's major source of colemanite, although USA is also a significant source (Roskill, 2010).

Boron compounds and minerals find applications in many products in a variety of industries. The main consumption areas of borates are glass, ceramics, soap and detergents, and agriculture. Borates are used in industrial applications primarily because they are safe to handle and their natural functions impart a wide range of performance, cost, and environmental health and safety advantageous in various products (Freedonia, 2010).

Colemanite is an industrially important mineral, which is mostly used in textile type fiberglass, glass and ceramic industries and metallurgy. Colemanite is also used in detergent and cosmetic industries and for production of boric acid by reacting with sulfuric acid. When used in textile type fiberglass industry, colemanite drops the melting temperature of the mixture, provides low viscosity at the melting temperature, prevents crystallization and positively affects the chemical and physical properties of final glass product. Colemanite reduces the melting point in glass industry and it is resistant to thermal shocks. In formulation of ceramic and enamel glazes, it provides a stable structure, homogeneous melting and low segregation. Since it is a solvent for almost all metal oxides, it is used as a fluxing agent in the metallurgy industry (Eti Mine, 2014). As seen, the most important factor that determines the potential application of colemanite is that it decreases the melting point during production.

In literature, there are studies that characterize colemanite. The location and geological map of the Emet Borate Mine is presented by Colak et al., (2000), together with the mineralogical composition of Hisarcik and Espey Colemanites. Christ et al., (1958) studied the crystalline structure of colemanite. It was reported that colemanite contains infinite chains linked together laterally by ionic bonds through Ca^{2+} ions to form sheets parallel to [010]. The sheets, in turn, are linked together through a system of hydrogen bonds involving the hydroxyl groups of the chains and water molecules. Burns and Hawthorn (1993) investigated the hydrogen bonds of colemanite as these bonds control many of the physical and chemical properties of the mineral. Frost et al., (2013) studied the infrared and Raman spectroscopic characterization of colemanite. It was stated that the basic structure of colemanite contains endless chains of interlocking $\text{BO}_2(\text{OH})$ triangles and $\text{BO}_3(\text{OH})$ tetrahedrons with the calcium, water and extra hydroxide units interspersed between these chains. Thermal analysis of hydrated borates, including colemanite, was studied by Waclawska (1998). It was stated that the thermal decomposition of hydrated borates comprises two stages: formation of free water molecules and removal of these towards the outside of the solid matrix. Other studies investigate the use of colemanite as a raw material mainly during boric acid production (Cakal, 2004; Cakal et al., 2006) or additive (Celik, 2010; Celik et al., 2014).

The main aim of this work is to evaluate the influence of temperature on the physical properties of the Espey Colemanite, Emet, Kutahya, Turkey. The characteristic properties of this mineral are also determined.

Materials and methods

Colemanite was supplied by the Espey Mine, Eti Mine Works, Emet, Turkey. Colemanite, having 1-3 mm particle size, was used in this study after being pulverized to 0.5 mm. The characteristic properties of the colemanite were determined by performing petrographic analysis, X-ray fluorescence (XRF), X-ray diffraction (XRD), scanning electron microscopy (SEM) analysis, energy dispersive X-ray spectroscopy (EDS) analysis, thermo-gravimetric/differential thermal (TG-DTA) analysis and loss on ignition measurements.

The colemanite samples having 35.4% B_2O_3 were calcinated according to the Turkish patent TR-2007/03372, describing the calcination of tincal, sodium borate mineral. The colemanite samples were calcinated in closed vessels in a laboratory furnace at temperatures 100–600 °C. The calcination process duration was 2 hours. The vessels only have an outlet for water vapor. After the calcination process at 600 °C, colemanite mineral having 45% B_2O_3 was obtained. To find out some of the important physical properties of colemanite at ambient temperature and temperatures up to 600 °C, surface area, specific gravity, bulk density, porosity, water absorption and compactness ratio analyses were carried out on five different samples. Calcination is known to affect these parameters significantly. Analyses were performed at Mining Technical Research Institute (MTA), Ankara, Turkey, Middle East Technical University (METU) Chemical Engineering and Mining Engineering Departments, Ankara, Turkey and Cukurova University Mining Engineering Department, Adana, Turkey.

Petrographic analysis was done by an Olympus BH-2 microscope. For the petrographic investigation, 0.02 mm thick slices of colemanite were prepared. Chemical analysis of the 105 °C dried samples was performed by using Siemens SRS 300 X-ray Fluorescence Spectrometer (XRF) instrument. XRD of the powdered samples was carried by using Rigaku XRD Geigerflex equipped with Cu X-ray tube. XRD patterns were recorded from $20^\circ < 2\theta < 60^\circ$ with step of 0.02°. Images and elemental composition of the samples were obtained by SEM instrument using FEI Quanta 400 MK2 equipped with EDAX Genesis XM 4i detector. Proportional elemental distribution was found by EDS analyzer. The amount of weight loss of the colemanite samples were determined by TG-DTA using TG/DTA 6300 S11 EXSTAR 6000. The measurements were performed up to 1000 °C under air flow using uniform heating rate of 20 °C/min. The sample holder was cylindrical-shaped platinum crucible having a diameter of 6 mm and height of 10 mm.

BET (Brunauer, Emmett and Teller) surface area measurements were performed using Nova Instruments Quantochrome 2200. To determine the bulk densities, the samples were ground, sieved through 16 mesh sieves (1 mm sieve opening) and impurities were removed. The bulk density analyses were done according to the TS 3529 (1980) and ASTM C127-42 (2003) standards. Specific gravities were determined by means of a pycnometer in accordance with TS 1114 EN 13055-1 (2004) standards.

Porosity measurements were performed using a Autopore IV 9220 mercury porosimeter. Before the mentioned analyses, the samples were put into the furnace at the preset temperature for two hours.

Water absorption properties of the particles were found according to the TS 1114 EN 13055-1 and ASTM C 127-42 standards. The compactness ratio was determined in accordance with the ASTM C127-42 and ASTM C128-57 (2003) standards while the loss on ignition analysis of colemanite according to the TS 1114 EN 13055-1 standards.

Results and discussion

Mineralogical and petrographical analysis of Espey colemanite

The chemical analysis performed by XRF and mass loss on ignition analyses are given in Table 1. It can be seen there, that colemanite consisted of 35.8% B_2O_3 and 30.5% SiO_2 . The values in Table 1 are the average of 5 different samples.

Table 1. Chemical analysis of colemanite samples (%)

Element	Content (%)
B_2O_3	35.8±1.2
SiO_2	30.5±2.1
Al_2O_3	12.2±0.8
CaO	8.6±1.2
Fe_2O_3	1.2±0.2
$MgO + SrO$	3.1±0.2
Other	8.3±2.1
Loss on ignition	4.95±0.2

As a result of the XRD analysis, Fig. 1, the major component of the boron samples (80–85%) were found to be colemanite. The other components were smectite and illite (10%). There were also trace amounts of chlorite and mica. Colak et al. (2000) investigated the mineralogical composition of Espey colemanite by XRD and found out that Espey colemanite has calcite, quartz, K-rich feldspar, cahnite, plagioclase, smectite, illite, chlorite, kaolinite and clay. As known, the composition of the colemanite mineral may differ from sample to sample as it is a heterogeneous mineral. The samples were subjected to the XRD analysis. Colak et al. (2000) also studied colemanite obtained from the upper limestones, to the bottom of the open pit mines. When the XRD peaks of the samples in Colak et al., (2000)'s study were examined, it was seen that samples had a high clay (saponite) content. In this study, before the colemanite samples were supplied by the Eti Mine Works, they were subjected to a standard processing and milling including screening and washing. That is why the samples had a low clay content. Thus, the peak intensity of the colemanite in the XRD analysis was higher. Besides, Yildiz (2004), obtained a similar XRD result for Emet

colemanite having about 83 wt% purity, which was also subjected to a standard processing and milling.

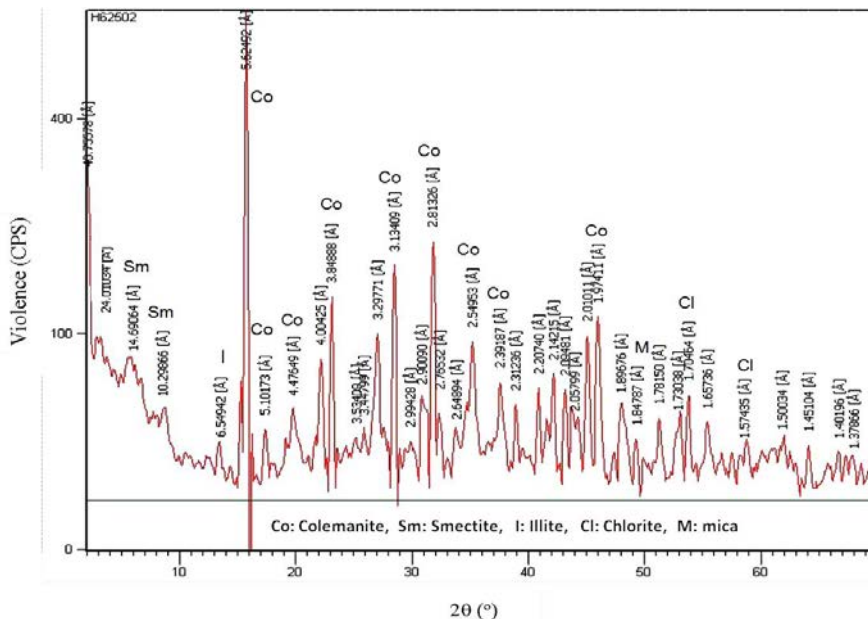


Fig. 1. XRD analysis of Espey colemanite

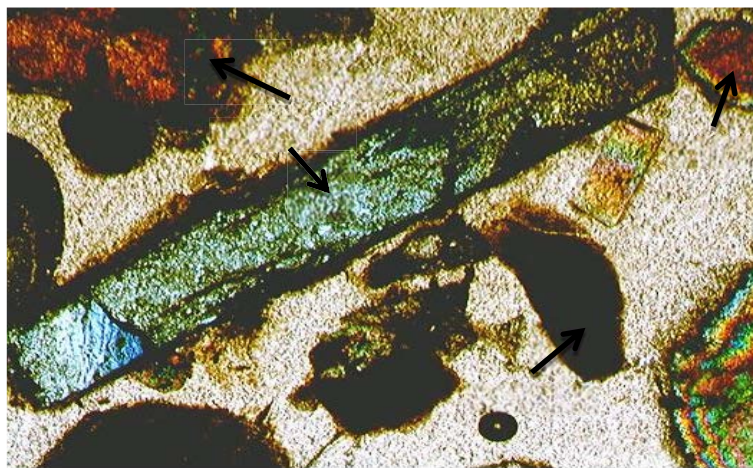


Fig. 2. Microphotograph of Espey colemanite

In general, sodium and calcium borates are formed under near-surface conditions as a result of volcanic activity and are associated with continental sediments and volcanic rocks (Roskill, 2010). Palmer and Helvaci (1995) reported that although there are differences between the different districts, borates are all generally enclosed within

limestones and clays and are interbedded with layers of volcanic ash, limestone, marl, and clays. From the petrographic investigation (Fig. 2) it was observed that the boron samples were colemanite. There was also iron together with quartz, chlorite, feldspar, mica and illite minerals.

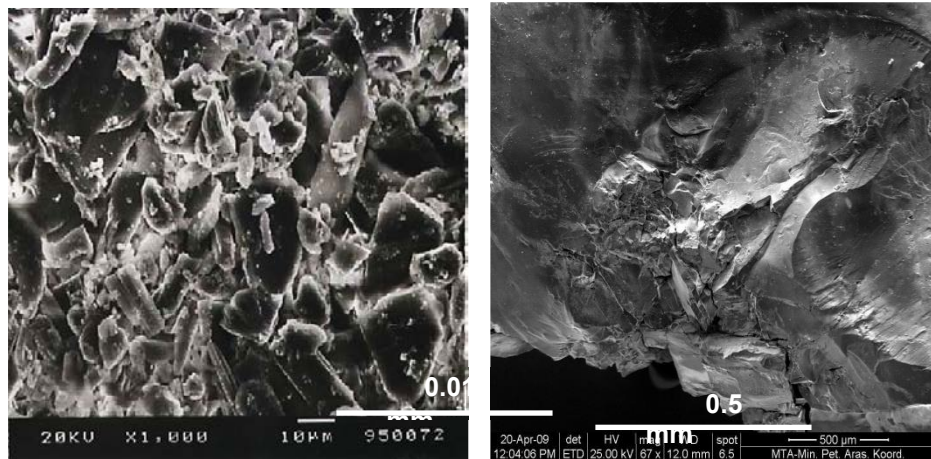


Fig. 3. SEM images of Espey colemanite

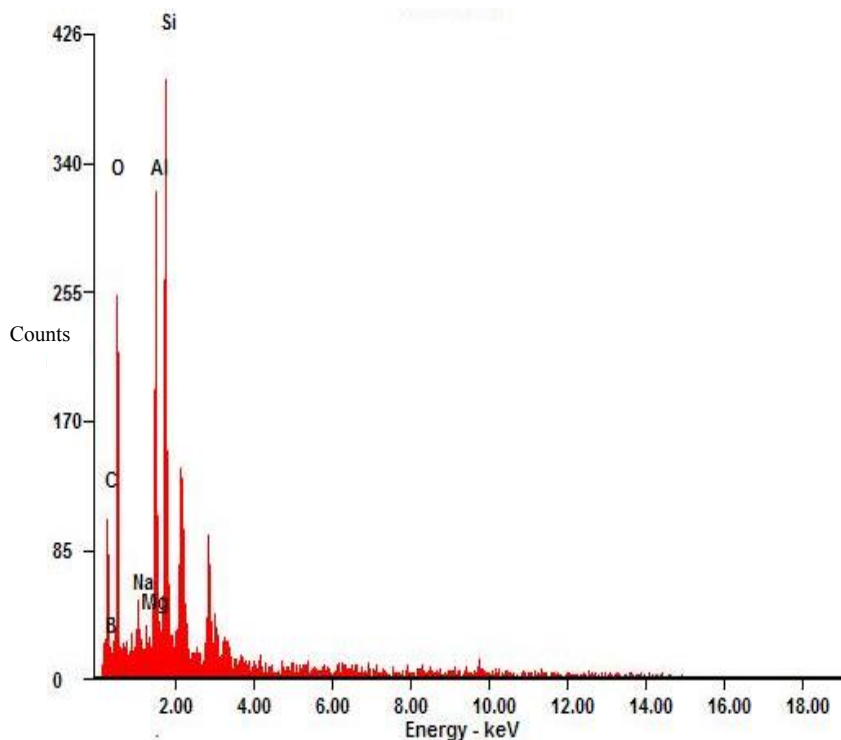


Fig. 4. EDS analysis of Espey colemanite

As seen from the SEM images (Fig. 3) colemanite has a non-porous crystalline structure and the accompanying clays are smectite and illite. A proportional distribution of the elements, determined by the EDS analysis (Fig. 4) showed that there are 35.4% boron and 27.6% silicon within the colemanite samples. Besides a high content of Si, B, O, C and Al, the colemanite samples also have trace amounts of Mg, Ca, Fe and Na.

Thermal analysis of Espey colemanite

From the TGA analysis (Fig. 5) it was seen that the decomposition of colemanite begins with the removal of water molecules. First, colemanite loses 1.8% of its weight up to 350 °C. The thermal decomposition of colemanite occurs within 300-450 °C as examined from DTA curve. A distinct inflection is seen at 307 °C. It means that the thermal dissociation of colemanite begins with the removal of the OH groups, which form water molecules. Next, the bonds of molecular water with borate rings become broken. This can be judged from the endothermic peak at 389 °C. Next, the removal of water proceeds rapidly as observed from the TG curve. The remaining water escapes slowly up to 600 °C. At temperatures between 350 and 600 °C, colemanite loses 35.7% of its weight. At 600 °C, the completion of the reaction occurs. A similar TG/DTA curve was also obtained by Waclawska (1998).

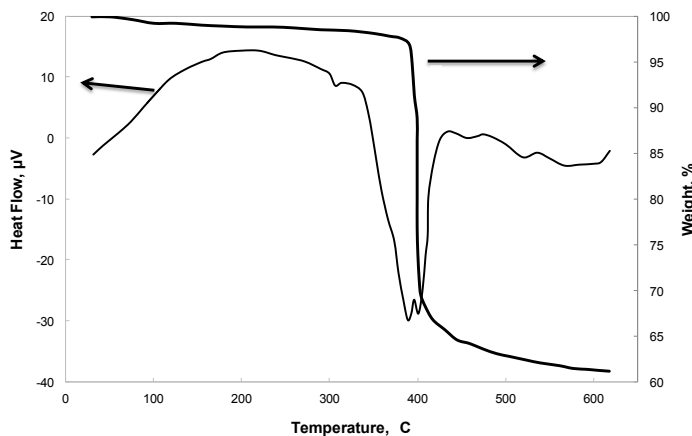


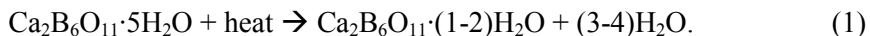
Fig. 5. TG-DTA curves of Espey colemanite (heating rate 20 °C /min)

Variation of physical properties of Espey colemanite with temperature

Surface area, bulk density, specific gravity, porosity, water absorption and compactness ratio values of colemanite were determined at different temperatures and are given in Table 2.

As seen from Table 2, the surface area and porosity of colemanite increases with temperature. The highest surface area ($131.9 \text{ m}^2/\text{g}$) is at 500 °C and porosity (52%) at

400 °C. The surface area and porosity do not change considerably above that temperature. Bulk density, specific gravity compactness ratio and water absorption values decrease depends on the temperature. Colemanite has a density of 2.37 g/cm³ and bulk density of 1150 kg/m³ at 100 °C. These values decreased to 2.25 and 690 kg/m³ at 500 °C, respectively. The water absorption and compactness ratio of colemanite decreased from 27.85% to 15.45% and 0.49% to 0.31% at 500 °C, respectively. With the increase of temperature, the water content in the colemanite structure decreases, leading to increased surface area and porosity of the colemanite sample. The release of water can be explained with Eq.1:



As the mass of colemanite was decreased with temperature, the bulk density, which is mass per volume, also decreased together with density. The compactness ratio, which is 1-void ratio, also decreased with the increase of void ratio.

The thermal treatment of other borate minerals, namely tincal (Yilmaz, 2014) and ulexite (Sener et al., 2000) was also studied. It was also found that porosity of the borate minerals increased with calcination process up to 600 °C. The increase of porosity was attributed to the formation of microcracks throughout the structure during the removal of water.

Table 2. Physical properties of Espey colemanite at different temperatures

Temperature (°C)	Surface area (m ² /g)	Bulk density (kg/m ³)	Specific gravity	Porosity (%)	Water absorption (%)	Compactness ratio
Ambient	27.6±1.9	1170±110	2.38±0.05	18±1	27.85±0.05	0.49±0.09
100	29.3±1.5	1150±80	2.37±0.09	21±2	26.15±0.04	0.48±0.08
200	34.2±5.1	1130±10	2.37±0.03	28±1	25.28±0.07	0.48±0.11
300	77.0±8.2	1020±60	2.34±0.15	49±2	24.33±0.12	0.44±0.07
400	117.4±5.4	870±50	2.28±0.08	52±4	19.62±0.07	0.38±0.10
500	131.9±13.5	690±40	2.25±0.14	50±2	15.45±0.05	0.31±0.05
600	128.7±15.8	550±40	2.21±0.09	48±3	12.55±0.04	0.27±0.08

Comparison of characteristic properties of Espey colemanite

When the characteristic properties of colemanite were examined, it was observed that chemical, petrographic, XRD, SEM and EDS analyses results support each other. Besides, significant statistical relations exist between the physical properties of the colemanite; especially between specific gravity and bulk density ($R^2 = 0.9921$) (Fig. 6(a)), specific gravity and water absorption ($R^2 = 0.988$) (Fig. 6(b)), specific gravity and compactness ratio ($R^2 = 0.9917$) (Fig. 6(c)) and specific gravity and surface area ($R^2 = 0.9076$) (Fig. 6(d)). It can also be seen that although there exists sets of relationships between the physical properties of the colemanite, they also decrease with temperature, except surface area and porosity.

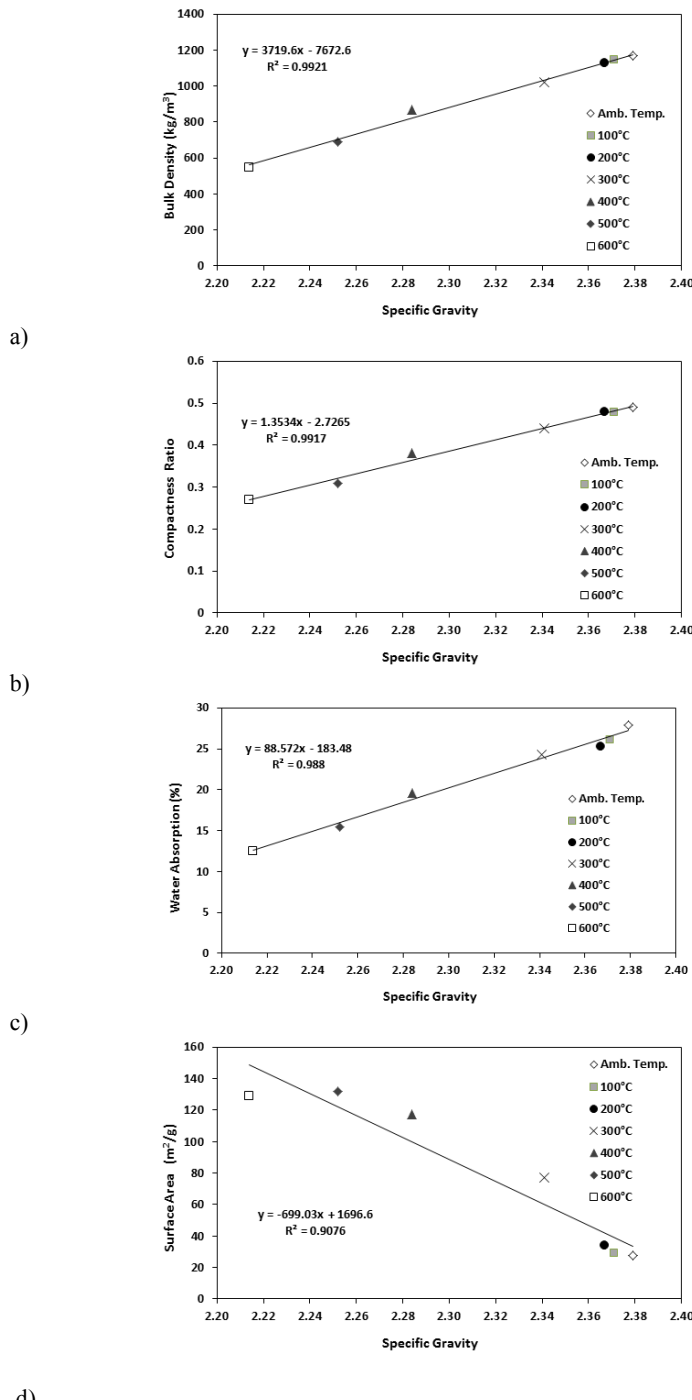


Fig. 6. Relationship between specific gravity and (a) bulk density, (b) water absorption, (c) compactness ratio, (d) surface area. R^2 min for a core

Conclusions

In this study, the thermal and physical properties of colemanite were determined. Colemanite consists of 35.8% B_2O_3 and 30.5% SiO_2 . The petrographic observations confirmed that the boron sample was colemanite. There was also some iron minerals together with quartz, chlorite, feldspar, mica and illite minerals. SEM images of colemanite showed a non-porous crystalline structure and the clays that accompany it are smectite and illite. The EDS analysis showed the presence of 35.4% boron and 27.6% silicon within the colemanite samples. A weight loss of 1.8% at 350 °C, and 35.7% between 350 and 600 °C was found from the TG-DTA analysis. There existed a sharp endothermic peak at 389 °C. Although specific gravity, bulk density, water absorption, compactness ratio and surface area of colemanite differ at different temperatures, they were found to have high statistical relation. In addition, the surface area and porosity values increased up to 500 °C and 400 °C, respectively and then, decreased slightly.

Acknowledgements

This work is supported by National Boron Research Institute (BOREN) via project number BOREN-2008-B0201. We are grateful to Eti Mine Emet Works for the supply of colemanite, Mining Technical Research Institute (MTA), Middle East Technical University (METU) Chemical Engineering and Mining Engineering Departments and Cukurova University Mining Engineering Department for the analyses.

References

- ASTM C127-42., 2003, *Standard test method for specific gravity and absorption of coarse aggregates*, Annual Book of ASTM Standards, Philadelphia, USA.
- ASTM C128-57., 2003, *Standard test method for specific gravity and absorption of fine aggregates*, Annual Book of ASTM Standards, Philadelphia, USA.
- BURNS P.C., HAWTHORNE F.C., 1993, *Hydrogen bonding in colemanite: an X-ray and structure-energy study*, Canadian Minerologist, 31, 297–304.
- CAKAL G.O., 2004, *Dynamic behavior of continuous flow stirred slurry reactors in boric acid production*, PhD Dissertation, Middle East Technical University, Ankara,
- CAKAL G.O., EROGLU I., OZKAR S., 2006, *Gypsum crystal size distribution in four continuous flow stirred slurry boric acid reactors in series compared with the batch*. J. Crys. Grow., 290, 197–202.
- CELIK A.G., 2010, *Production of lightweight bricks from boron added perlite mixtures and determination of technological properties*, PhD Dissertation, Cukurova University, Department of Mining Engineering, Adana.
- CELIK A.G., DEPCI T., KILIÇ A.M., 2014, *New lightweight colemanite-added perlite brick and comparison of its physicomechanical properties with other commercial lightweight materials*, Con. Build. Mat., 62, 59–66.
- CHRIST C.L., CLARK J.R., EVANS H.T., 1958., *Studies of borate minerals (III): the crystal structure of colemanite, $CaB_3O_4(OH)_3H_2O$* , Acta Cryst. 11, 761–770.
- COLAK M., HELVACI C., MAGGETTI M., 2000, *Saponite from the Emet Colemanite Mines, Kütahya, Turkey*, Clays and Clay Minerals, 484, 409–423.

ETI MINE, 2008, *Eti Mine Works General Management Annual Report*, Ankara.

ETI MINE, 2014, *Espey Colemanite, Product Data Sheet*, Ankara.

The Freedonia Group Inc., 2010, *Freedonia Focus on Boron*, Cleveland.

FROST R.L., XI Y., SCHOLZ R., BELOTTI F.M., FILHO M.C., 2013, *Infrared and Raman spectroscopic characterization of the borate mineral colemanite – $\text{CaB}_3\text{O}_4(\text{OH})_3\text{xH}_2\text{O}$ – implications for the molecular structure*, *J. Mol. Struc.*, 1037, 23–28.

PALMER M.R., HELVACI C., 1995, *The boron isotope geochemistry of the Kirka borate deposit, western Turkey*, *Geochimica et Cosmochimica Acta*, 59, 3599–3605.

Roskill Information Services Ltd., 2010, *The Economics of Boron*, 12th edition, London.

SENER S., OZBAYOGLU G., DEMIRCI S., 2000, *Changes in the structure of ulexite on heating*. *Thermochim. Acta*, 362, 107–112.

YILMAZ O., YALÇINOĞLU Y., ERGÜL T., DEMİRBAĞ C., ŞENTÜRK B., AKÇİN H., KAYANDAN İ., ULUDAĞ T., 2007, TR-2007/03372. *Calcinated tincal production with single-stage calcination-autogeneous grinding and separation method (cgs)*.

TS 1114 EN 13055-1, 2004, *Lightweight aggregates - Part 1: For use in concrete, Mortar and the juice*.

TS 3529, 1980, *Determination of specific gravity and water absorption ratio in concrete aggregates*.

WACLAWSKA I., 1998, *Controlled rate thermal analysis of hydrated borates*, *J. Therm. Anal.*, 53, 519–532.

YILDI, O., 2004, *The effect of heat treatment on colemanite processing: a ceramics application*, *Powder Technol.*, 142, 7–12.

YILMAZ O., 2014, *Production of calcined tincal from run-of-mine tincal*, *Journal of the Faculty of Engineering and Architecture of Gazi University*, 29, 401–406.

Received: December 15, 2014; reviewed; accepted: March 12, 2015

SEPARATION OF COBALT FROM NICKEL USING NOVEL ULTRASOUND-PREPARED SUPPORTED LIQUID MEMBRANES CONTAINING CYANEX 272 AS CARRIER

Gerardo LEON^{*}, Guillermo MARTINEZ^{*}, Loreto LEON^{},
María Amelia GUZMAN^{*}**

^{*} Departamento de Ingeniería Química y Ambiental, Universidad Politécnica de Cartagena, 30203 Cartagena, Spain, gerardo.leon@upct.es

^{**} Departamento de Ciencias Politécnicas, UCAM, Campus de los Jerónimos, Guadalupe, 30107 Murcia, Spain

Abstract: The demand for cobalt has increased significantly in recent years due to its use in a wide variety of products and processes. Cobalt and nickel often accompany each other in nature and close physicochemical properties of both metals make their separation a complicated practical problem. Organophosphorous extractants have been widely used to separate cobalt from nickel. This paper presents the preliminary results obtained for separation of cobalt from nickel using Cyanex 272 containing supported liquid membranes prepared by a novel ultrasound-assisted method. The results show that this novel supported liquid membrane preparation method leads to higher separation factors than those described in the literature under similar separation conditions.

Keywords: cobalt, nickel, separation, supported liquid membranes, ultrasound, facilitated counter-transport, Cyanex 272

Introduction

Cobalt is a metal of high economic value and strategic importance due its potential application in both scientific and technological fields. Cobalt is widely used in a variety of products and processes including alloys, hard materials (carbines), magnets, batteries, catalysts, glass, ceramics, pigments and lacquers (Cote, 2000). Its production has grown steadily over the last two decades, from a total production of 23.2 gigagrams (Gg) in 1995 to 56.6 Gg in 2005 (Kapusca, 2007) and to 77.2 Gg in 2012 (Cobalt Development Institute, 2013). Cobalt and nickel often accompany each other in nature and their separation is a complicated practical problem. As they have very close physicochemical properties, classical separations methods are not applicable and search for a new separation technologies has led to many achievements in solvent

extraction (Flett, 2005; Reddy et al., 2009; Sun et al., 2010), ion exchange (Mendes and Martins, 2004; Li et al., 2012) and liquid membrane (Gega et al., 2001; Kumbasar, 2012) techniques.

Liquid membranes have shown great potential as a separation method, especially in cases where solute concentrations are relatively low and other techniques cannot be applied efficiently. They offer a potentially attractive alternative in that they combine the processes of extraction and stripping (removal and recovery) into a single unit operation (Sastre et al., 1998).

As cobalt is usually recovered from nickel, to improve the selectivity of the liquid membrane separation process, a carrier reagent is incorporated in the membrane phase to preferentially transfer Co(II), rather than Ni(II), from the feed to the receiving phase across the membrane. Widely used carriers are organophosphorus compounds (Juang, 1993; Youn et al., 1997; Gega et al., 2001; Ribeiro et al., 2004; Kumbasar, 2009a; Kumbasar, 2009b), though, other extractants such as Alamine 300, (Kumbasar and Tutkun, 2008; Surucu et al., 2012) and 8 hydroxyquinoline (Kumbasar, 2012) have also been used. Though Cyanex 272 has been widely used in separation of Co(II) from Ni(II) by extraction (Gandhi et al., 1993; Lindell et al., 2000; Evans et al., 2012), its use in the liquid membrane processes is not so common.

Three kinds of liquid membranes have been described: bulk, supported and emulsion liquid membranes (Sastre et al., 1998). Supported liquid membranes are obtained when a rigid porous substrate is filled with the organic solution of the carrier. Most of the studies on Co(II)/Ni(II) separation by liquid membranes has been the carried out using emulsion liquid membranes (Longquan et al., 1997; Ribeiro et al., 2004; Kumbasar, 2009a; Kumbasar, 2009b; Kumbasar, 2012). Only a few studies have used supported liquid membranes (Juang, 1993; Youn et al., 1997; Gega et al., 2001; Surucu et al. 2012) and only one of them have used Cyanex 272 as the carrier (Gega et al., 2001).

The object of this paper is to present the preliminary results obtained for separation of cobalt from nickel using supported liquid membranes prepared by a novel ultrasound-assisted method (León et al., 2013). This novel method enables higher values of transport efficiency, flux and permeability than other classical preparation methods (León et al., 2013). This is due to the modifications introduced in the structure of the polymeric support (increasing its pore radius and its pore density (Masselin et al., 2001; León et al. 2013)), and to increase in pore filling on the part of the organic solution of the carrier (León et al. 2013). These effects result from acoustical streaming and cavitation, generated when ultrasound passes through the organic solution (León et al., 2013), which decrease the viscosity of solution. It is due to higher temperature (Masselin et al., 2001), and high speed liquid jets directed at the support surface, which appear when cavitation occurs near the surface of the polymeric support used to prepare the supported liquid membrane (Kyllonen et al., 2005).

A carrier mediated counter-transport mechanism of Co(II) and Ni(II) ions through the supported liquid membrane, using Cyanex 272 as the carrier and H⁺ as counter

ions, is presented in Fig.1. The carrier diffuses from the bulk membrane phase to the feed membrane interface, where metal(II) ions are exchanged for protons. Due to the high interfacial reactivity of Cyanex 272 (Vandergrift and Horowitz, 1980), a dimerized molecule undergoes acid dissociation and reacts with metal(II). During the process each metal(II) ion is exchanged for two protons (Reddy, Priya, 2006). The metal(II) carrier complexes formed diffuse through the membrane to the membrane receiving phase interface, where, by reversing the above reaction, protons are exchanged for metal(II) ions, which are released into the product phase; the carrier is regenerated, thus beginning a new separation cycle. The metal(II) transport mechanism is a coupled counter ion transport mechanism, with metal(II) and H^+ travelling in opposite directions.

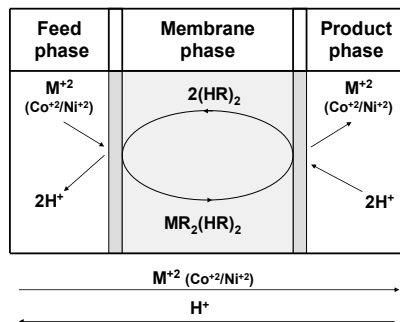


Fig. 1. Schematic representation of carrier-mediated counter-transport mechanism of Co(II) and Ni(II) through supported liquid membrane

Experimental

Experimental studies were carried out using two compartment permeation cells, which consisted of a feed phase (250 cm^3) separated from a receiving phase chamber (250 cm^3) by a supported liquid membrane with an effective area of 15 cm^2 . A schematic illustration of the experimental cell is shown in Fig. 2a.

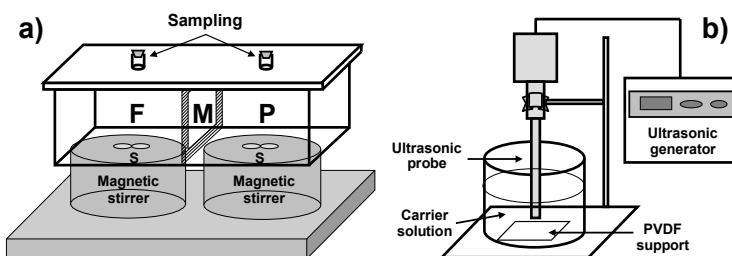


Fig. 2. Schematic representations of experimental transport cell (a) and sonication system (b)

Mixtures of cobalt(II) and nickel(II) at different concentrations ($8.5 \cdot 10^{-4}$ – $8.5 \cdot 10^{-3}$ M) in acetate buffer at different values of pH (3–6) were used as a feed phase. Aqueous sulphuric acid solutions (0.05–0.5 M) were used as a receiving phase. Both feed and receiving phases were mechanically stirred (50–300 rpm) at room temperature. A microporous hydrophobic PVDF GVHP film (20 cm^2 geometrical area) from Millipore Durapore (porosity 75%; pore dimension $0.22 \mu\text{m}$; thickness $125 \mu\text{m}$) was used as a solid porous support. The liquid membrane phase was formed of Cyanex 272 solutions of different concentrations (0.0689–0.6890 M) in commercial paraffin. The typical experimental conditions were: initial metal ion concentrations in the feed phase $3.4 \cdot 10^{-3}$ M, feed pH 5.5, carrier concentration in the membrane phase 0.344 M, sulphuric acid concentration in the receiving phase 0.2 M, and stirring speed in both feed and receiving phases 200 rpm.

The pores of micro porous support were filled with the organic solution of Cyanex 272 by soaking the polymeric support in the organic solution, at atmospheric pressure, assisted by ultrasound, using a Labsonic M (Sartorius) ultrasound equipment (titanium probe 10 mm diameter, sound rating density 130W/cm^2), at 30 KHz, $150 \mu\text{m}$, for 30 minutes (three times, 10 minutes each time at 5 minute intervals). The active layer of polymeric support was positioned perpendicularly to the direction of ultrasound and at a distance of 16 mm from the ultrasound probe (Fig. 2b).

Samples from the receiving phase compartment were taken at given time intervals and Co(II) and Ni(II) concentrations were measured by flame atomic absorption spectrophotometry using a Shimadzu AA-2600 equipment. Significant separation factor values were obtained after times of 120 minutes, which was selected as the end time. The experiments were carried out in duplicate and the results obtained showed less than 3% deviation.

Membrane fluxes (J) were determined by monitoring cobalt(II) and nickel(II) concentrations in the receiving phase as the function of time, based on the following equation (Hor et al., 2010):

$$J = \frac{V}{A} \frac{dC}{dt} \quad (1)$$

where V is volume of the product phase, A effective surface area of the membrane (geometrical area multiplied by porosity (Parhi, Sarangi, 2008)), C metal(II) concentration in the receiving phase, and t time elapsed. The metal(II) fluxes were calculated from the slope of straight line obtained, when plotting the metal concentration in the product phase as a function of time.

The Co/Ni separation factor (α), under different experimental conditions, was calculated by the following equation (Youn et al., 1997).

$$\alpha = \frac{\frac{J_{Co}}{[Co]_{f,0}}}{\frac{J_{Ni}}{[Ni]_{f,0}}} \quad (2)$$

where $[Co]_{f,0}$ and $[Ni]_{f,0}$ are the initial concentrations of Co(II) and Ni(II) in the feed phase, and J_{Co} and J_{Ni} are the initial fluxes of Co(II) and Ni(II), respectively.

Results and discussion

Cobalt-nickel separation by Cyanex 272 containing supported liquid membranes prepared by an ultrasound-assisted method leads to Co(II) fluxes that are about one hundred-folds higher than the fluxes of Ni(II) under all the experimental conditions assayed and to cobalt/nickel separation factors ranging from 20 to 200 (Figs. 3-7).

The effect of initial feed phase pH on the initial fluxes of Co(II) and Ni(II) and on their separation factor is shown in Figs. 3a and 3b. The Co(II) initial flux increases from pH 3 to 5.5 and then remains constant. The Ni(II) initial flux increases over the studied range of pH, although the increase between pH 3 and 5.5 is slightly lower than that observed for Co(II). The result of these flux variations with feed pH is an increase in the separation factor above pH 3, which reaches a maximum at pH 5.5.

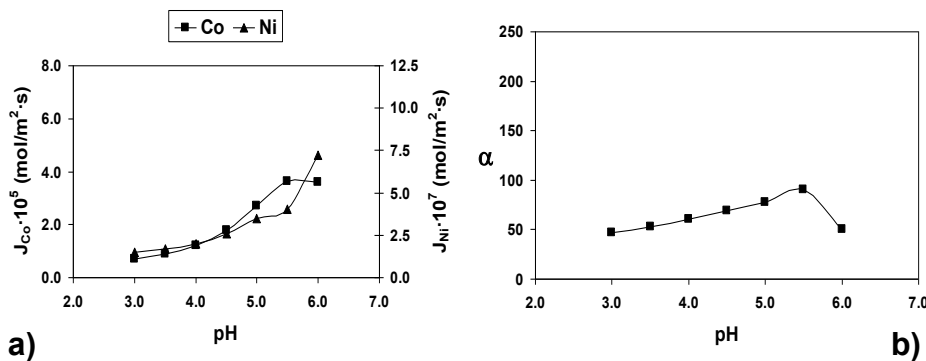


Fig. 3. Variation of initial fluxes of Co(II) and Ni(II) (a) and separation factor (b) with initial feed pH

The effect of carrier concentration in the membrane phase on the initial fluxes of Co(II) and Ni(II), and on their separation factor is shown in Figs. 4a and 4b. It can be seen that two metals behave differently. While the Co(II) initial flux increases with carrier concentration between 0.0689 and 0.344 mol/dm³ and then remains constant, the Ni(II) flux increases over the whole range of studied Cyanex 272 concentration. It leads to a continuous decrease in the separation factor as the Cyanex 272 concentration increases.

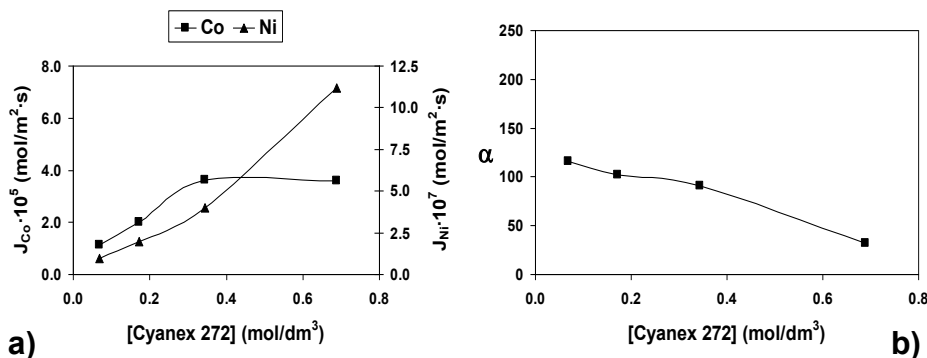


Fig. 4. Variation of initial fluxes of Co(II) and Ni(II) (a) and separation factor (b) with Cyanex 272 concentration in membrane phase

The effect of sulphuric acid concentration in the receiving phase on the initial fluxes of Co(II) and Ni(II), and on their separation factor is shown in Figs. 5a and 5b. Both metals behave similarly, their initial flux increasing as the sulphuric acid concentration increases from 0.05 to 0.20 M, while the initial fluxes of both metals remain constant above this concentration (a slight increase of Ni(II) initial flux is observed). It leads to gentle decrease in the Co/Ni separation factor, as the sulphuric acid concentration increases.

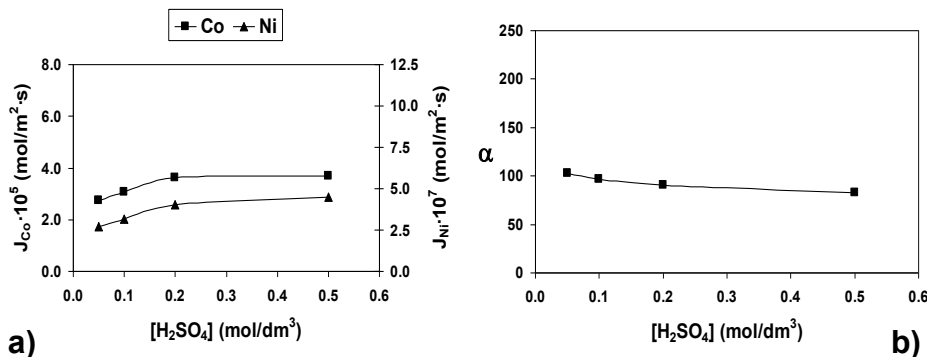


Fig. 5. Variation of initial fluxes of Co(II) and Ni(II) (a) and separation factor (b) with H₂SO₄ concentration in receiving phase

The effect of stirring rate on the initial fluxes of Co(II) and Ni(II), and on their separation factor is shown in Figs. 6a and 6b. For both metals, the initial flux increases when the stirring rate increases from 50 to 200 rpm (the increase is higher for the Ni(II) flux), and remains constant at higher stirring rates. It leads to decrease in the separation factor between 50 and 200 rpm and to a constant value above this stirring rate value.

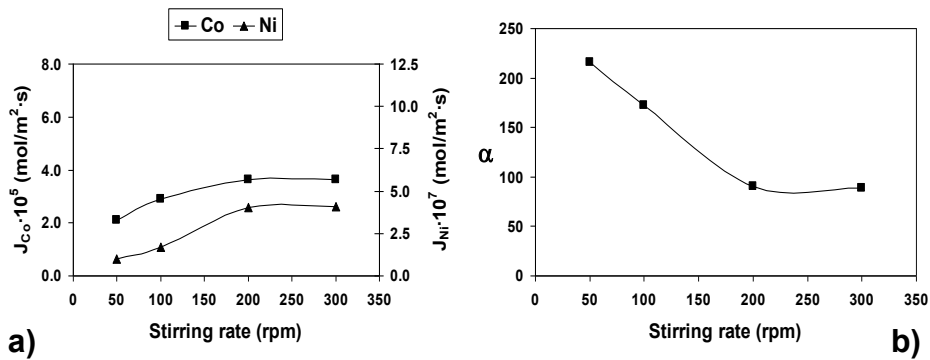


Fig. 6. Variation of initial fluxes of Co(II) and Ni(II) (a) and separation factor (b) with stirring rate

The effect of feed concentration on initial fluxes of Co(II) and Ni(II) and on their separation factor is shown in Figs. 7a and 7b. The flux of both metals increases with the metal concentration in the feed phase, although the increase in the Ni(II) flux is greater. It leads to decrease in the separation factor as the metal concentration in the feed phase increases (this decrease is four-fold when the metal concentration decreases ten-fold).

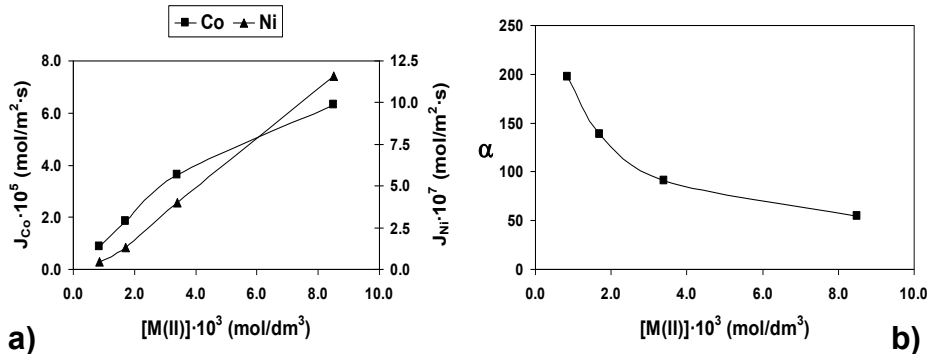


Fig. 7. Variation of initial fluxes of Co(II) and Ni(II) (a) and separation factor (b) with Co(II), Ni(II) concentrations in feed phase

According to these results, higher Co(II)/Ni(II) separation factors were obtained with a feed pH of 5.5, Cyanex 272 concentration in the membrane phase of 0.0689 M, sulphuric acid concentration in the receiving phase of 0.05 M, 50 rpm stirring rate and $8.5 \cdot 10^{-4}$ M metallic ion concentration in the feed phase. Comparison of the results obtained in this work with those related with separation of cobalt(II) and nickel(II) by liquid membranes mentioned in the literature is difficult due to different experimental conditions used, that is different type of liquid membrane, carrier nature, receiving

phase nature, polymeric support, etc. Only Gega et al. (2001) used the same carrier and receiving phase (but different polymeric support), and a classical liquid membrane preparation method (soaking the polymeric support in the organic solution during 12 hours) can be compared. The separation factors obtained using our ultrasound-assisted method are about twenty-fold higher than those obtained by Gega et al. (2001). A possible explanation is that the supported liquid membrane prepared by the ultrasound-assisted method increases the preferential transport of Co(II) over Ni(II), due to higher pore size and porosity of the polymeric support, and to the greater degree of pore filling by the Cyanex 272 organic solution derived from the ultrasound-assisted preparation method.

Conclusions

In this work we present the preliminary results obtained for separation of cobalt from nickel through supported liquid membranes prepared by a novel ultrasound-assisted method. Separation was carried out through a carrier mediated counter-transport mechanism by using Cyanex 272 as the carrier and protons (H_2SO_4) as the counter-ions, under different experimental conditions. The supported liquid membrane was prepared by filling the pores of the microporous support with the organic solution of Cyanex 272 through soaking the polymeric support in the organic solution, at atmospheric pressure, assisted by ultrasound. The supported liquid membranes prepared by the ultrasound-assisted method led to fluxes of Co(II) that they are about one hundred-folds higher than the fluxes of Ni(II) under any of the experimental conditions assayed, and the cobalt-nickel separation factors ranging from 20 to 200. The highest Co(II)/Ni(II) separation factors were obtained at pH 5.5, at Cyanex 272 concentration in the membrane phase of 0.0869 M, 0.051 M sulphuric acid concentration in the receiving phase, 50 rpm stirring rate and $8.5 \cdot 10^{-4}$ M metallic ion concentration in the feed phase. The Co(II)/Ni(II) separation factors obtained in this work are about twenty-fold higher than those described in the literature (Gega et al., 2001) using the same carrier and receiving phase. This is due to increase in the preferential transport of Co(II) over Ni(II) through the supported liquid membrane prepared by the ultrasound-assisted method, derived from the higher pore size and porosity of the polymeric support and from the greater degree of pore filling by the Cyanex 272 organic solution.

References

COBALT DEVELOPMENT INSTITUTE, 2013. *First Half Production Statistics*. Cobalt News. 13, 3-4.

COTE G., 2000. *Hydrometallurgy of strategic materials*, Solv. Extr. Ion Exch. 18, 703-727.

EVANS H.A., VU L., BAHRI P.A., BARNARD K.R., 2012. *Development of an integrated model for cobalt solvent extraction using Cyanex 272*. Comput. Aid. Chem. Eng. 31, 550-554.

FLETT D.S., 2005. *Solvent extraction in hydrometallurgy: The role of organophosphorus extractants*. J. Organometallic Chem. 690, 2426-2438.

GANDHI M.N. DEORKAR N.V., KHOPKAR S.M., 1993. *Solvent extraction separation of cobalt(II) from nickel and other metals with cyanex 272*. *Talanta* 40, 1535-1539.

GEGA J., WALKOWIAK W., GAJDA B., 2001. *Separation of Co(II) and Ni(II) ions by supported and hybrid liquid membranes*. *Sep. Purif. Technol.* 22-23, 551-558.

HOR M., RIAD A., BENIJJAR A., LEBRUM L., HLAÏBI M., 2010. *Technique of supported liquid membranes (SLMs) for the facilitated transport of vanadium ions (VO₂⁺)*. *Parameters and mechanism on the transport*. *Desalination* 255, 188-195.

JUANG R.S., 1993. *Modelling of the competitive permeation of cobalt and nickel in a di(2-ethylhexyl)phosphoric acid supported liquid membrane process*. *J. Membr. Sci.* 85, 157-166.

KAPUSCA J.P.T., 2007; *Cobalt production and markets: A brief overview*. *Cobalt News* 7, 9-12.

KUMBASAR R.A., 2009a. *Selective extraction and concentration of cobalt from acidic leach solution containing cobalt and nickel through emulsion liquid membrane using PC-88A as extractant*. *Sep. Purif. Technol.* 64, 273-279.

KUMBASAR R.A., 2009b. *Cobalt–nickel separation from acidic thiocyanate leach solutions by emulsion liquid membranes (ELMs) using TOPO as carrier*. *Sep. Purif. Technol.* 68, 208-215.

KUMBASAR R.A., 2012. *Selective transport of cobalt (II) from ammoniacal solutions containing cobalt and nickel by emulsion liquid membranes using 8-hydroxyquinoline*. *J. Ind. Eng. Chem.* 18, 145-151.

KUMBASAR R.A., TUTKUN O. 2008. *Separation of cobalt and nickel from acidic leach solutions by emulsion liquid membranes using Alamine 300 (TOA) as a mobile carrier*. *Desalination* 224, 201-208.

KYLLONEN, H.M., PIRKONEN, P., NYSTROM, M., 2005. *Membrane filtration enhanced by ultrasound: a review*. *Desalination* 181, 319-335.

LEÓN G., MARTÍNEZ G., GUZMÁN M.A., MORENO J.I., MIGUEL B., FERNÁNDEZ-LÓPEZ J.A., 2013. *Increasing stability and transport efficiency of supported liquid membranes through a novel ultrasound-assisted preparation method: Its application to cobalt(II) removal*. *Ultrason. Sonochem.* 20, 650-654.

LI B., LIU F., WANG J., LING C., LI L., HOU P., LI A., BAI Z., 2012. *Efficient separation and high selectivity for nickel from cobalt-solution by a novel chelating resin: Batch, column and competition investigation*. *Chem. Eng. J.* 195-196, 31-39.

LINDELL E., JÄÄSKELÄINEN E., PAATERO E., NYMAN B., 2000. *Effect of reversed micelles on Co/Ni separation by Cyanex 272*. *Hydrometallurgy* 56, 337-357.

LONGQUAN L., CHENG W., YADONG L. 1997. *Separation of cobalt and nickel by emulsion liquid membrane with the use of EDTA as masking reagent*. *J. Membr. Sci.* 135, 173-177.

MASSELIN I., CHASSERAY X., DURAND-BOURLIER L., LAINE J.M., SYZARET P.Y., LEMORDANT D., 2001. *Effect of sonication on polymeric membranes*. *J. Membr. Sci.* 181, 213-220.

MENDES F.D., MARTINS A.H., 2004. *Selective sorption of nickel and cobalt from sulphate solutions using chelating resins*. *Int. J. Min. Proc.* 74, 359-371.

PARHI P.K., SARANGI K., 2008. *Separation of copper, zinc, cobalt and nickel ions by supported liquid membrane technique using LIX 84I, TOPS-99 and CYANEX 272*. *Sep. Purif. Technol.* 59, 169-174.

REDDY B.R., PRIYA D.N., 2006. *Chloride leaching and solvent extraction of cadmium, cobalt and nickel from spent nickel-cadmium batteries using Cyanex 923 and 272*. *J. Power Sources* 161, 1428-1434.

REDDY B.R., RAO S.V., PARK K.H., 2009. *Solvent extraction separation and recovery of cobalt and nickel from sulphate medium using mixtures of TOPS 99 and TIBPS extractants*. *Min. Eng.* 22, 500-505.

RIBEIRO C.P., COSTA A.O.S., LOPES I.P.B., CAMPOS F.F., FERREIRA A.A., SALUD A., 2004. *Cobalt extraction and cobalt–nickel separation from a simulated industrial leaching liquor by liquid surfactant membranes using Cyanex 302 as carrier*. J. Membr. Sci. 241, 45-54.

ASTRE A.M., KUMAR A., SHUKLA J.P., SINGH R.K., 1998. *Improved techniques in liquid membrane separations: An overview*. Sep. Purif. Meth. 27, 213-298.

SUN X., JI Y., ZHANG L., CHEN J., LI D., 2010. *Separation of cobalt and nickel using inner synergistic extraction from bifunctional ionic liquid extractant (Bif-ILE)*. J. Hazard. Mater. 182, 447-452.

SURUCU A., EYUPOGLU V., TUTKUN O., 2012. *Selective separation of cobalt and nickel by flat sheet supported liquid membrane using Alamine 300 as carrier*. J. Ind. Eng. Chem. 18, 629-634.

VANDERGRIFT C.F., HOROWITZ E.P., 1980. *Interfacial activity of liquid-liquid extraction reagents-I: Dialkyl phosphorous based acids*. J. Inorg. Nucl. Chem. 42, 119-125.

YOUN I.J., LEE Y., JEONG J., LEE W.H., 1997. *Analysis of Co-Ni separation by a supported liquid membrane containing HEH(EHP)*. J. Membr. Sci. 125, 231-236.

Received August 14, 2014; reviewed; accepted November 26, 2014

KINETICS OF CHROMIUM(III) TRANSPORT THROUGH THE DOUBLE-CARRIER SUPPORTED LIQUID MEMBRANE

Pawel RELIGA^{*}, Jakub RAJEWSKI^{}, Paulina LOBODZIN^{***}**

^{*} Department of Environmental Protection, Kazimierz Pulaski University of Technology and Humanities in Radom, Chrobrego 27, Radom, Poland, j.rajewski@ichip.pw.edu.pl

^{**} Faculty of Chemical and Process Engineering, Warsaw University of Technology, Waryńskiego 1, Warsaw, Poland

^{***} Institute of Sustainable Technology – National Research Institute in Radom, Pulaskiego 6/10, Radom, Poland

Abstract: The kinetics of chromium(III) transport through a supported liquid membrane containing both a di-(2-ethylhexyl) phosphoric acid (D2EHPA) and bis-(2,4,4-trimethylpentyl) phosphinic acid (Cyanex272) as an ions carrier was investigated. It was found that under a characteristic concentration of the carriers into the organic phase membrane provides much higher efficiency than the membrane containing only one of the extractants. In the studied system the optimal carrier concentration in the membrane is 0.16 mol/dm³ and 0.9 mol/dm³ for Cyanex272 and D2EHPA, respectively. Moreover, the authors indicate that only D2EHPA can act as an individual carrier in the membrane. In the case of Cyanex272 the stable structures with chromium(III) ions are formed in the membrane, which prevents effective re-extraction. Additionally, intensive stirring of an aqueous phase in another factor that has a positive influence on the transport kinetics in the double-carrier membrane. Increasing a stirring rate up to 1200 rpm shortens the process time and allows total re-extraction of chromium.

Keywords: SLM, chromium, D2EHPA, Cyanex27, separation, membrane

Introduction

Chromium belongs to metals commonly used in many industries, mainly in metallurgy, electroplating, tanning, paper industry, and pigment production. The partial consumption of chromium in the process (Jian-Hong et al., 2013) results in its presence in wastewaters. Due to the toxic properties of chromium, its separation from wastewater prior to its discharge to the environment is an important concern. Moreover, due to growing prices of chromium ores, the possibility to separate chromium from wastewater and recirculating it to the process is also economically

viable. Research results (Ochromowicz and Apostoluk, 2010; Religa et al., 2009) show that the process of simultaneous extraction and re-extraction (pertraction) carried out in the system with a liquid membrane (LM) may be a very effective solution with regard to the separation of metals from aqueous solutions. The reason for this is that the mass exchange in the LM system is done through facilitated transport. This type of transport is related to the presence of a carrier in the membrane – a substance which, by reversible reaction, forms chemical compound with a specific component, easily diffusible through the membrane. A popular group of substances applied as carriers/extractants of ions are alkyl derivatives of phosphoric acids (Azzoug et al., 2014). The most vital in this group are di-(2-ethylhexyl) phosphoric acid (D2EHPA) and bis-(2,4,4-trimethylpentyl) phosphinic acid (Cyanex272). The review of literature (Konczyk et al., 2010; Azzoug et al., 2014) on the transport of metal ions through the LM proves that, regardless the type of the transported ion, its effectiveness and selectivity are mostly affected by the type and concentration of the applied carrier. Unfortunately, even for optimal composition of the membrane, the LM systems are characterized by relatively low streams of transported ions, which significantly extends the process time, and adversely affects the system stability. Researchers (Darvishi et al., 2005; Iberhan and Wisniewski, 2002; Sarangi et al., 1999) examining extraction systems for the separation of metal ions from aqueous solutions, suggest an extraction with two extractants in order to increase the effectiveness of the process. They observe that a synergistic effect may be achieved with an adequate concentration ratio of extractants characterized by an increased rate of process and selectivity. Results of a few published references (Wojciechowski et al., 2008; Biswas, 2012) reveal a positive impact of the addition of the second carrier/extractants also to the liquid membrane. Similarly to extraction systems, a synergistic effect is observed for the specific ratio of carriers in the membrane. The works deal with tests on the possibility of using liquid membranes with two extractants for the separation of cobalt(II), copper(II) and nickel(II) ions. However, no results of tests on the possibility of applying immobilized liquid membranes with two extractants for the separation of chromium ions can be found in the literature. From the practical point of view, the SLM is the system with the membrane immobilized in the pores of the polymer that ensures the most effective level of separation of metal ions, including the separation of chromium(III) from aqueous solutions (Religa et al. 2009).

The aim of the work is to determine the impact of the presence of two extractants/carriers in the immobilized liquid membrane, i.e. di(2-ethylhexyl) phosphoric acid (D2EHPA) and bis-(2,4,4-trimethylpentyl) phosphinic acid (Cyanex272) on the transport kinetics of chromium(III) ions.

Experimental

Test system and process parameters

Transport experiments were carried out in a tank consisting of two cylindrical chambers (Fig. 1). The volume of both chambers was 130 cm³. The solutions: feed with Cr(III) concentration equal 0.002 mol/dm³ (aqueous chromium(III) chloride solution, CrCl₃·6H₂O) and stripping (6M HCl) were separated by SLM. The active membrane area covered 15.2 cm². The initial pH of the feed phase was 5. The whole process was thermostated to ambient temperature ($T = 25 \pm 0.5$ °C). The solutions were mixed in both chambers with mechanical stirrers (IKA, OST20 digital). The study was carried out for a stirring rate of 300, 600 and 1200 rpm.

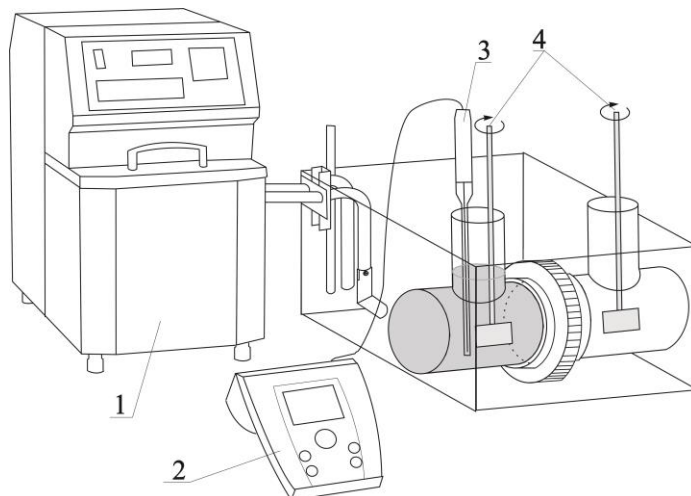


Fig. 1. Apparatus for transport experiment. 1 – circulator (thermostat) with temperature and water-level control system, 2 – pH-meter, 3 – microelectrode, 4 – stirrers

Preparation of a membrane

The immobilized liquid membrane was a PTFE porous polymer film (Sartorius) with a pore size of 0.45 mm and porosity of 64%. The membrane was soaked for 24 hours in a mixture of an organic phase consisting of kerosene (Dragon), o-xylene (Fluka) and carriers.

Di-(2-ethylhexyl) phosphoric acid (D2EHPA, Fluka) and bis-(2,4,4-trimethyl pentyl) phosphinic acid (Cyanex272, Cytec) were used as the ion carriers. The structure of the carriers shown in Fig. 2.

The Cyanex272 was selected based on the literature review (Langan and Ibana, 2002; Biswas and Singh, 2006), which concerned high activity of the Cyanex272 in the process of extraction of chromium(III). There are no works about the transport of chromium(III) through a liquid membrane with Cyanex272 as a carrier.

D2EHPA was selected on the basis of literature data (Ochromowicz and Apostoluk, 2010; Konczyk et al., 2010) and our own experience (Religa et al., 2014), that shows that D2EHPA has very good transporting properties for chromium(III) in a liquid membrane system.

The concentration of the carriers in the membrane was changed in the range of 0-1.2 M. The volume ratio of the concentrations of the other ingredients (kerosene/o-xylene) was constant and equal to 2:1.

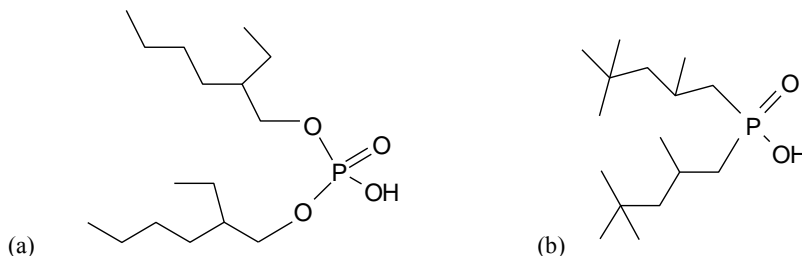


Fig. 2. The structure of the compounds used as carriers: (a) di-(2-ethylhexyl) phosphoric acid (D2EHPA), (b) bis-(2,4,4-trimethylpentyl) phosphinic acid (Cyanex272)

Characteristics of measurement methods

To determinate chromium concentration, we regularly collected samples from the feed and the receiving phase, and then, using a Nanocolor UV/Vis NUV480 spectrophotometer and employing a 1,5-difenylokarbazyde method with the wave length $\lambda = 540$ nm, we analyzed concentration of Cr(III) ions after the mineralization of samples. Each measurement was repeated three times. The standard deviation of the measured value determined with statistical methods was ± 0.0003 . Based on the results, the flux of Cr(III) (J_0) and the penetration coefficient (k) were determined in the way described by Religa et al. (2014).

Results and discussion

SLM with Cyanex272 as a carrier

Literature data (Langan and Ibana, 2003) show that Cyanex272 is an excellent extractant of chromium(III), and that the effectiveness of the extraction process is clearly fostered by a high level of hydrolyzation of chromium(III) ions, which is ensured by pH 4.5-6.5 of the solution (Gawronski and Religa, 2007). The aim of the first stage of the tests was to investigate whether Cyanex272 can be the sole carrier of chromium(III) in the liquid membrane. To ensure good conditions of pertraction, the process was carried out at the initial pH of the feed phase equal to 5. The authors conducted experiments for various concentrations of Cyanex272 in the membrane, but they did not obtain the expected results. However, the experiments did help the authors to observe that effectiveness of the chromium(III) extraction was maintained

at the level of 20-30 %, regardless of the concentration of Cyanex272 in the membrane (Fig. 3). The process was extremely intensive in the first phase that lasted about 1 hour. In the later phase, the process came to a stop. It is also significant, that a considerable sudden decrease (from 5 to about 2) in the pH in the feed solution was observed in the first phase of pertraction. The rapid decrease in the pH determines the forms of chromium(III) to be found in the solution. They will be hydrolyzed to a slight extent at low pH. It is probably the reason for the fast decrease of the rate of extraction in the system.

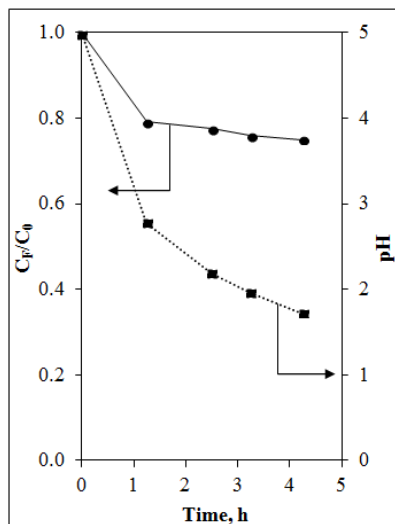


Fig. 3. Variation of chromium(III) concentration and the pH in the feed phase vs. time for SLM with $0.16 \text{ mol}/\text{dm}^3$ Cyanex272 as a carrier. Initial chromium(III) concentration in the feed phase $\text{C}_0 = 0.002 \text{ mol}/\text{dm}^3$; initial pH = 5. Receiving phase $6 \text{ mol}/\text{dm}^3$ HCl.
 C_F – actual concentration of Cr(III) in feed phase

Additionally, no presence of chromium(III) ions was reported in the receiving phase, which may suggest the formation of stable, polymeric structures between chromium(III)-Cyanex272 molecules in the membrane. The movement of these expanded structures in the membrane phase is significantly hampered. Moreover, high stability of the structure prevents effective re-extraction of chromium(III). In studies on chromium(III) extraction by Cyanex272, Lanagan and Ibana, (2003) indicate that Cyanex272 can easily create stable forms with chromium(III). In the case of the structures formed, even when $8 \text{ mol}/\text{dm}^3$ HNO_3 is applied, the re-extraction of chromium was partial and possible only directly after the extraction process. Therefore, the achieved results show that the ions of Cr(III) cannot be effectively transported by SLM containing only Cyanex272 as a carrier.

The double-carrier SLM

Various concentrations of Cyanex272 in the double-carrier SLM

In the next phase of the study, the authors applied, for the transport of chromium(III), a membrane with a constant concentration of D2EHPA that has proven capacity to transport chromium(III) in LM (Ochromowicz and Apostoluk, 2010; Konczyk et al., 2010), and used various concentrations of Cyanex272. The aim of the investigations was to determine the type of the effect caused by the presence of two strong extractants of chromium(III) in the membrane. According to Azzoug et al. (2014), Biswas et al. (2012), Konczyk et al. (2010) and Gawronski and Religa (2007), in the liquid membrane for a specific concentration of the transported substance the optimal concentration of a carrier can be found at which the transport of ions runs most effectively. For the initial concentration of chromium(III) ions equal to 0.002 mol/dm^3 , the most effective concentration of D2EHPA in the membrane is 0.45 mol/dm^3 (Religa et al., 2014). Therefore, the concentration of D2EHPA was adopted in further tests. The impact that the addition of various amounts of Cyanex272 has on the transport of Cr(III) ions, while maintaining constant, and optimal concentration of D2EHPA in the membrane is shown in Fig. 4. As presented, the system with a certain concentration of Cyanex272 in the membrane containing 0.45 mol/dm^3 of D2EHPA achieves significantly higher effectiveness compared to the membrane containing only D2EHPA. As to the analyzed system, this optimal concentration of Cyanex272 equals 0.16 mol/dm^3 and is almost 3 times lower than the concentration of D2EHPA. Moreover, in the case of a membrane with two carriers with concentration of 0.45 mol/dm^3 D2EHPA/ 0.16 mol/dm^3 CYANEX272 respectively, faster release of Cr(III) ions from the membrane was observed. Owing to this, the process time was shortened, and it lasted less than 3 hours for the applied conditions in the analyzed system. Therefore, for a defined ratio of concentration of carriers in the membrane, a clear synergistic effect may be observed that is reflected in the improvement of kinetic properties of the examined transport system.

Darvishi et al. (2005) who carried out the extraction of nickel(II) and cobalt(II) with a simultaneous application of D2EHPA and Cyanex272 as extractants, proved a synergistic effect, however in the case of the system they analyzed, this effect occurred with an increased content of Cyanex272 and with a simultaneous decrease in D2EHPA concentration. Therefore, the concentration proportions of carrier mixtures in the membrane have to be selected individually, depending on the type of ions transported.

Both, for lower and higher concentrations of Cyanex272 in the system, a decrease in effectiveness of pertraction compared to the membrane containing only D2EHPA, was observed. This phenomenon was accompanied by a decrease in chromium(III) concentration in the membrane, and an extension of the time needed for chromium to achieve the maximum concentration in the membrane (Fig. 5).

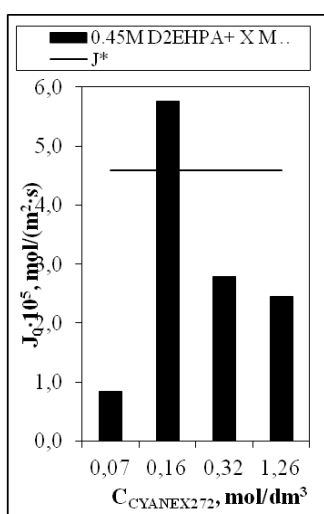


Fig. 4. Effect of addition of Cyanex272 to the membrane containing $0.45 \text{ mol}/\text{dm}^3$ D2EHPA on Cr(III) ions flux (J_o) penetrating to the membrane. J^* - flux of chromium(III) ions penetrating the membrane containing only $0.45 \text{ mol}/\text{dm}^3$ D2EHPA

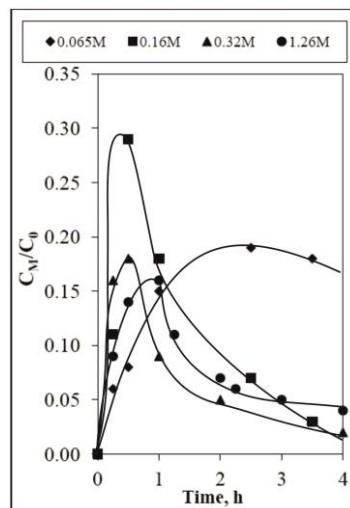


Fig. 5. Variation of chromium(III) concentration in the membrane phase containing $0.45 \text{ mol}/\text{dm}^3$ D2EHPA and different concentrations of Cyanex272. Initial chromium(III) concentration in the feed phase $C_0 = 0.002 \text{ mol}/\text{dm}^3$; pH = 5. Receiving phase $6 \text{ mol}/\text{dm}^3$ HCl

The pertraction process is a multiple stage process, therefore the course of once stage depends on the adequate accumulation of the transported substance in the previous stage. The lower the concentration and the longer the time needed for reaching it, the slower and less effective the subsequent stage, i.e. re-extraction. This explains the obtained results of experiments. The decrease in the chromium(III) concentration in the membrane and the extension of the time needed for its procurement, are probably caused by the lack of a stable transporting structure in the membrane with two carriers in concentrations different than the optimal ones. The achieved results and their analysis indicate that Cyanex272 is responsible for the stabilization of the transporting structure in the membrane.

Variable concentrations of D2EHPA in the double-carrier SLM

Based on the obtained results, the concentration of Cyanex272 of $0.16 \text{ mol}/\text{dm}^3$, considered to be the most favorable for the speed of the process, was selected for further analyses. At this stage of the research various amounts of D2EHPA were put to the membrane at a constant concentration of Cyanex272. Upon analyzing the results (Fig. 6) the authors discovered that the presence of two carriers in the membrane in the amounts, respectively $0.9 \text{ mol}/\text{dm}^3$ D2EHPA and $0.16 \text{ mol}/\text{dm}^3$ Cyanex272, reduces the time of pertraction 3-fold when compared to the process carried out only with D2EHPA and by more than one hour compared to the process carried out with the membrane having $0.45 \text{ mol}/\text{dm}^3$ D2EHPA/ $0.16 \text{ mol}/\text{dm}^3$ Cyanex272. A significantly

smaller share of Cyanex272 in the membrane, compared to D2EHPA, confirms the earlier conclusion claiming that the role of Cyanex272 in the membrane is probably to join and stabilize the transporting structure formed by D2EHPA. Based on the analysis of the structure of both carriers (Fig 1), and their concentration range in the membrane, as well as the review of reports by Xu, (2009) or Kundu and Bidyut, (2013), it can be concluded that spherical aggregation of carriers molecules occurs in the membrane, combined with the formation of stable, complex micellar structures in which the polar ends of the carrier molecules together with the connected, often hydrolyzed ion of the transported substance are inside, while its non-polar elements are outside the micelles. However, the thorough analysis of chromium(III) transport mechanism requires more experiments and it will be the subject of future research.

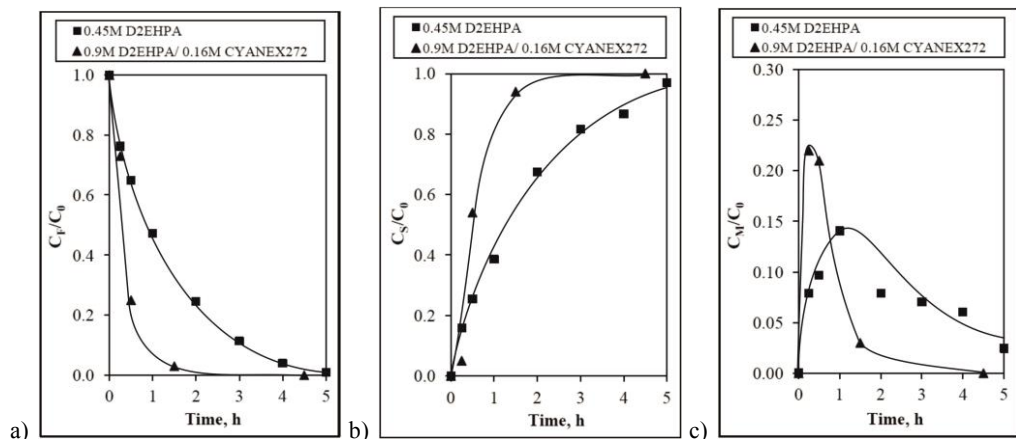


Fig. 6. Variation of chromium(III) concentration vs. time in a) feed phase, b) receiving phase and c) membrane phase, for membrane with D2EHPA and the double-carrier membrane with D2EHPA and Cyanex272 under their most effective concentration. Initial chromium(III) concentration in the feed phase $C_0 = 0.002\text{M}$; pH = 5. Receiving phase 6 M HCl

Intensity of the stirring rate of aqueous phases

It was stated that in the two-carrier membrane Cyanex272/D2EHPA the structure enabling the effective transport of chromium(III) is formed at the defined mutual ratio of the carriers. In this situation the stage limiting the rate and effectiveness of the process may be the formation of laminar layers on interphase surfaces, which slows down the stage of penetration of chromium(III) ions into and out of the membrane. A properly intensive stirring of aqueous phases may limit the thickness of these layers. Therefore, the next stage of the research was to determine the impact of the stirring rate, both of the feed phase and the receiving phase, on changes in the transport of chromium(III) ions through a liquid membrane with two carriers. The membrane with the selected optimal composition, i.e. $0.16\text{ mol}/\text{dm}^3$ of Cyanex272; $0.90\text{ mol}/\text{dm}^3$ of

D2EHPA was subjected to testing. The tests were carried out for the stirring rate of 300, 600 and 1200 rpm. The results are presented in Fig. 7.

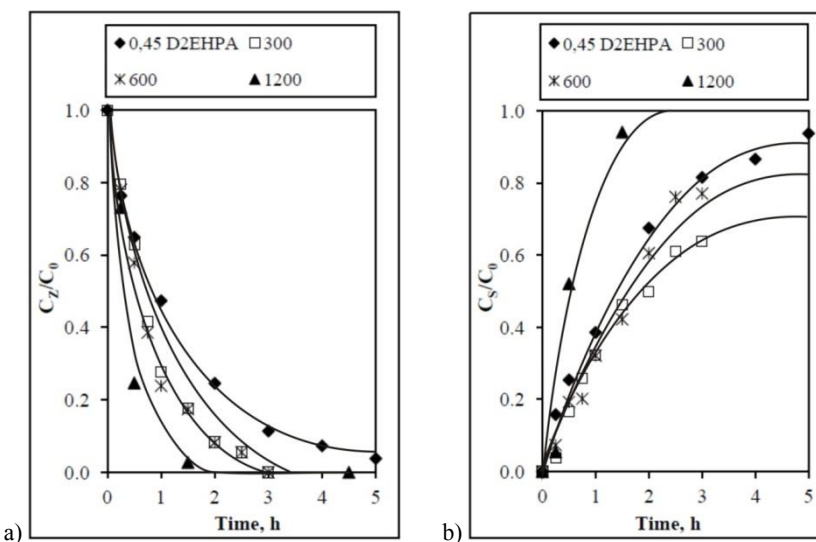


Fig. 7. Influence of the stirring rate on changes in the concentration of Cr(III) vs. time in the feed phase (a) and in the receiving phase (b) for the membrane with D2EHPA and the double-carrier membrane with 0.9M D2EHPA and 0.16M Cyanex272. Initial chromium(III) concentration in the feed phase $C_0 = 0.002M$; pH = 5. Stripping phase 6 M HCl

Increasing stirring rate up to 1200 rpm significantly improved the kinetics of the process of separation of chromium(III) ions. The time of the process was shortened, which allowed in the case of re-extraction, a complete extraction of chromium. Moreover, the thickness of the laminar boundary layers on the boundary of phases was significantly reduced as well, enabling a faster transport of chromium(III), and increased efficiency of the process.

Conclusions

Literature review helped to indicate D2EHPA and Cyanex272 as effective extractants of chromium(III), while our own experiments confirmed high efficiency of D2EHPA as a carrier of Cr(III) in the SLM system. However, for the pertraction of chromium(III) by the SLM with Cyanex272 as a carrier, there was no presence of the Cr(III) ions in the receiving phase. This result may indicate a formation of a polymeric structure in the membrane between molecules of the chromium(III) and Cyanex272, which is not able to effectively move in a membrane phase. The results indicate that the ions of Cr(III) cannot be transported through the SLM that only contains Cyanex272 as a carrier.

Transport properties of the membrane containing both the di-(2-ethylhexyl) phosphoric acid (D2EHPA) and the bis-(2,4,4-trimethylpentyl) phosphinic acid

(Cyanex272) were investigated. It was found that for certain optimum carriers ratio concentrations in the membrane, the SLM system achieves significantly higher efficiency over the membrane containing only D2EHPA as a carrier. For the investigated system, the optimal concentration of Cyanex272 is 0.16 mol/dm³, when the concentration of D2EHPA is 0.9 mol/dm³. As a result of a synergistic effect, the processing time was reduced 3-fold and took 2 hours less than the conditions set in the system investigated.

The obtained results suggest that in the double-carrier membrane there is a spherical carriers particle aggregation coupled with the formation of a stable micellar structures. Cyanex272 is responsible for stabilizing the transport structure. However, a detailed explanation of the transport mechanism of Cr(III) ions requires additional experiments. It will be the subject of a future work.

An additional factor that has a positive influence on the transport kinetics in the double-carrier membrane is intensive stirring of aqueous phases. The increase in the mixing speed to 1200 rpm improved the kinetics of separation of chromium(III) ions in the double-carrier membrane system. The process time was reduced. Moreover, in the case of re-extraction, chromium was fully recovered.

References

AZZOUG S., AROUS O., KERDJOUDJ H., 2014, *Metallic ions extraction and transport in supported liquid membrane using organo-phosphoric compounds as mobile*, J. Environ. Chem. Eng., 2, 154–162.

BISWAS R.K., SINGHA H.P., 2006, *Purified Cyanex 272: its interfacial adsorption and extraction characteristics towards iron(III)*, Hydromet., 82, 63–74.

BISWAS S., PATHAK, P. N., ROY S. B., 2012, *Carrier facilitated transport of uranium across supported liquid membrane using dinonyl-phenyl phosphoric acid and its mixture with neutral donors*, Desal., 290, 74–82.

DARVISHI D., HAGHSHENAS D.F., KESHAVARZ A.E., SADRNEZHAAD S.K., HALALI M., 2005, *Synergistic effect of Cyanex 272 and Cyanex 302 on separation of cobalt and nickel by D2EHPA*, Hydromet., 77, 227–238.

GAWRONSKI R., RELIGA P., 2007, *Transport mechanism of chromium(III) through the unmixed bulk liquid membrane containing dinonylnaphthalenesulfonic acid as a carrier*, J. Memb. Sci., 289, 187–190.

IBERHAN L., WISNIEWSKI M., 2002, *Extraction of arsenic(III) and arsenic(V) with Cyanex 925, Cyanex 301 and their mixtures*, Hydromet., 63, 23–30.

JIAN-HONG L., JUN L., ZHAO-PENG Y., XUE-FENG L., 2013, *Removal of chromium(III) from aqueous waste solution by predispersed solvent extraction*, Transact. Nonferr. Met. Soc. China, 23, 524–529.

KONCZYK J., KOZLOWSKI C., WALKOWIAK W., 2010, *Removal of chromium(III) from acidic aqueous solution by polymer inclusion membranes with D2EHPA and Aliquat 336*, Desal., 263, 211–216.

KUNDU K., BIDYUT K.P., 2013, *Physicochemical investigation of mixed surfactant reverse micelles: Water solubilization and conductometric studies*, Colloids Surf. A, 433, 154–165.

LANAGAN M.D., IBANA D.C., 2003, *The solvent extraction and stripping of chromium with Cyanex 272*, Miner. Eng., 16, 237–245.

OCHROMOWICZ K., APOSTOLUK W., 2010, *Modelling of carrier mediated transport of Cr(III) in the SLM system with D2EHPA*, Sep. Pur. Technol., 72, 112–117.

RELIGA P., GAWRONSKI R., GIERYCZ P., 2009, *Kinetics of chromium(III) transport through a liquid membrane containing DNNSA as a carrier*, Int. J. Mol. Sci., 10, 964–975.

RELIGA P., RAJEWSKI J., GIERYCZ P., ŚWIETLIK R., 2014, *Supported liquid membrane system for Cr(III) separation from Cr(III)/Cr(VI) mixtures*, J. Water Sci. Technol., 69, 2476–2481.

SARANGI K., REDDY B.R., DAS R.P., 1999, *Extraction studies of cobalt(II) and nickel(II) from chloride solutions using Na-Cyanex 272. Separation of Co(II)/Ni(II) by the sodium salts of D2EHPA, PC88A and Cyanex 272 and their mixtures*, Hydromet., 52, 253–265.

WOJCIECHOWSKI K., KUCHAREK M., BUFFLE M., 2008, *Mechanism of Cu(II) transport through permeation liquid membranes using azacrown ether and fatty acid as carrier*, J. Membr. Sci., 314, 152–162.

XU Z., 2009, *Microcalorimetric study on the critical micelle concentration and thermodynamic functions of di(2-ethyl-hexyl) phosphate salts in organic solvent + sec-octyl alcohol systems at 298.15 K*, J. Chem. Eng. Data, 54, 2827–2830.

Received October 7, 2014; reviewed; accepted: March 31, 2015

ACCURACY OF SEPARATION PARAMETERS RESULTING FROM ERRORS OF CHEMICAL ANALYSIS, EXPERIMENTAL RESULTS AND DATA APPROXIMATION

Dariusz FOSZCZ^{*}, Magdalena DUCHNOWSKA^{}, Tomasz NIEDOBA^{*},
Tadeusz TUMIDAJSKI^{*}**

^{*} AGH University of Science and Technology, Al. Adama Mickiewicza 30, 30-059 Krakow

^{**} Wroclaw University of Technology, Wybrzeze Wyspianskiego 27, 50-370 Wroclaw,
magdalena.duchnowska@pwr.edu.pl

Abstract: Accuracy of determination of different separation parameters and selectivity indicators depends on the error of chemical analysis of feed and separation products as well as experimental and approximation errors. In this paper different selectivity parameters were considered which formulae was based on the content of useful component in the feed, concentrate and tailing. It was shown that the impact of chemical analysis on the selectivity parameters was small and the error determined by means of partial derivative approach for a copper ore upgraded by flotation was negligible. Also experimental errors were found to be insignificant. The largest errors occurred for approximation of the upgrading data with inadequately selected selectivity indicators.

Keywords: upgrading curve, approximation, copper ore, flotation, selectivity

Introduction

Evaluation and approximation of upgrading results are very important elements in mineral processing. They help to find parameters which provide the best separation results for a given way of upgrading and to search for optimal conditions of processes. A knowledge of separation technological optimal points is crucial for a proper utilization of ores and it enables to minimize inevitable losses of useful components in tailings.

The principal parameters useful for evaluation of separation results are feed (α), concentrate (β) and tailing (θ) grades. They can be used either directly or as a combination of grades providing numerous separation parameters including recovery, yield, upgrading ratio and different selectivity parameters. For instance, the

recovery of a component in concentrate (ε) can be calculated from equation (1) (Drzymala, Ahmed, 2005):

$$\varepsilon = \frac{\alpha - \vartheta}{\beta - \vartheta} \cdot \frac{\beta}{\alpha} \cdot 100, \quad (1)$$

while the recovery of others-than-considered component in the tailing (ε_r) is:

$$\varepsilon_r = \left(100 - \frac{\alpha - \vartheta}{\beta - \vartheta} \cdot 100 \right) \cdot \frac{100 - \vartheta}{100 - \alpha}. \quad (2)$$

The selectively parameters of separation are usually determined by using different upgrading plots relating such parameters as grades, recoveries, yield and other parameters (Vera et al., 1999). For instance the Henry curve relates grade and yield (Neethling and Cilliers, 2008), while the Halbich curve represent grade vs. recovery (Drzymala, 2005). An especially useful upgrading curve is the Fuerstenau plot, which relates to recovery of a useful component in concentrate ε and recovery of gangue in tailing ε_r (Drzymala, 2005-2008, Drzymala et al., 2010; Brozek and Surowiak, 2010; Duchnowska and Drzymala, 2011, 2012; Foszcz, 2006; Foszcz et al., 2009; 2010; Nowak and Surowiak, 2011, 2013; Jamroz and Niedoba, 2014; Niedoba, 2013). The Fuerstenau curve provides different selectivity factors (Drzymala and Ahmed, 2005). One of them is defined as:

$$a = \frac{\varepsilon \varepsilon_r}{\varepsilon + \varepsilon_r + 100} \quad (3)$$

and its formula, expressed by means of grades of feed (α), concentrate (β), and tailing (ϑ), is:

$$a = \frac{100(\alpha - \vartheta)\beta(100\beta - 100\vartheta - \alpha + \vartheta)(100 - \vartheta)}{(\beta - \vartheta)[(\alpha - \vartheta)\beta 100(100 - \alpha) - 100(\beta - \vartheta)(100 - \alpha) + \alpha(100\beta - 100\vartheta + \vartheta - \alpha)(100 - \vartheta)]}. \quad (4)$$

The separation parameters consist of a real value and error resulting from inaccuracy of the chemical analysis and experimental procedure as well as errors of data approximation. Therefore, the goal of this paper is to evaluate these errors using flotation results of a copper ore.

Accuracy of separation selectivity parameter a resulting from error of chemical analysis of products grades

According to the error analysis, the formula for the mean square error is:

$$error = \sqrt{\sum_{p=1}^l s_p^2 f_p^2(\bar{x}_1, \bar{x}_2, \dots, \bar{x}_l)}, \quad (5)$$

where $f_p^2(\bar{x}_1, \bar{x}_2, \dots, \bar{x}_l)$ is partial derivative of function $f_p^2(x_1, x_2, \dots, x_l)$ with respect to x_p , s_p^2 is standard deviation of parameter and p is from 1 to l and stands for number of variables (Wackerly and Scheaffer, 2008, Fuller, 2006). In the case of selectivity indicator a given by Eq. 4, which depends on α , β and ϑ , the error is

$$error a = \sqrt{\left(\frac{\partial a}{\partial \alpha}\right)^2 \cdot s_\alpha^2 + \left(\frac{\partial a}{\partial \beta}\right)^2 \cdot s_\beta^2 + \left(\frac{\partial a}{\partial \vartheta}\right)^2 \cdot s_\vartheta^2}, \quad (6)$$

where s_α , s_β and s_ϑ are the errors of chemical analysis of the useful component in products, that is in the feed, concentrate and tailing, respectively, while $\frac{\partial a}{\partial \alpha}$, $\frac{\partial a}{\partial \beta}$, $\frac{\partial a}{\partial \vartheta}$ are partial derivatives of selectivity indicator a with respect to the grade. The formulas for $\frac{\partial a}{\partial \alpha}$, $\frac{\partial a}{\partial \beta}$ and $\frac{\partial a}{\partial \vartheta}$ and their calculations are given in Appendix A.

To calculate the error of selectivity indicator a determination, which results from the chemical analysis errors of α , β and ϑ , one needs to know a , α , β , ϑ , $\frac{\partial a}{\partial \alpha}$, $\frac{\partial a}{\partial \beta}$, $\frac{\partial a}{\partial \vartheta}$, s_α , s_β , and s_ϑ . In the case of the Kupferschiefer stratiform copper ore, typical results of separation performed on a laboratory scale is $\alpha = 2.0\%$, $\beta = 25.0\%$ and $\vartheta = 0.2\%$. For these data the selectivity indicator a , calculated by using Eq. 3, is equal to 100.60. Numerous chemical analyses of feeds and separation products showed that s values are: feed $s_\alpha = 0.06\%$, concentrate $s_\beta = 0.30\%$ and tailing $s_\vartheta = 0.03\%$. It means that the values and errors of the considered here separation results are $\alpha = 2.0 \pm 0.06\%$,

$\beta = 25.0 \pm 0.30\%$ and $\vartheta = 0.2 \pm 0.03\%$. The partial derivatives of the selectivity indicator a , determined by using Eqs. 28–30 (see Appendix A) are $\frac{\partial a}{\partial \alpha} = 0.02$, $\frac{\partial a}{\partial \beta} = -0.09$, $\frac{\partial a}{\partial \vartheta} = 2.21$. After substituting these values into Eq. 6, the error of selectivity indicator a is 0.07 meaning that its value is 100.60 ± 0.07 . Thus, the accuracy of a , assuming that the experiments were conducted ideally and the errors were caused only by the chemical analysis of the separation products and feed, is 100.60 ± 0.07 . The error, as shown in Fig. 1, is small and should not influence interpretation and evaluation of separation data of the considered in this paper copper ore.

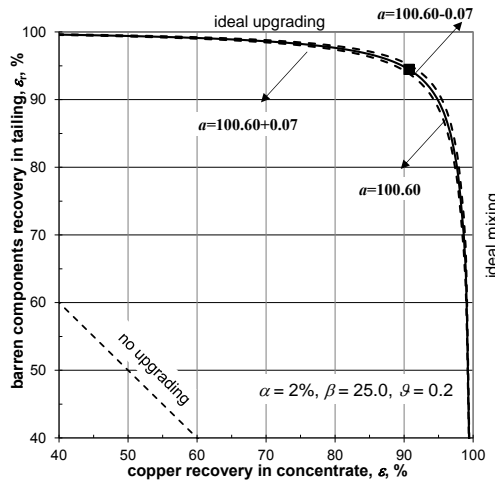


Fig. 1. Accuracy of selectivity indicator a resulting from feed and separation products chemical analysis error for a single separation providing
 $\alpha = 2.0\%$, $\beta = 25.0\%$, $\theta = 0.2\%$ for $s_\alpha = 0.06\%$, $s_\beta = 0.30\%$, $s_\theta = 0.03\%$

Accuracy of separation selectivity parameter a based on experimental errors of products grades

To find the error of a resulting from the experimental inaccuracy of α , β , θ , the data for the same experiment conducted many times are needed. It is assumed that for a given experiment, the error of the chemical analysis of feed α , concentrate β and tailing θ grades determination is small. To find the error of a resulting from the experimental error, it is convenient to use the equation based on a general formula given in Eq. 3:

$$\text{error } a = \sqrt{\left(\frac{\partial a}{\partial \varepsilon}\right)^2 \cdot s_\varepsilon^2 + \left(\frac{\partial a}{\partial \varepsilon_r}\right)^2 s_{\varepsilon_r}^2}. \quad (7)$$

where $\frac{\partial a}{\partial \varepsilon}$, $\frac{\partial a}{\partial \varepsilon_r}$, s_ε^2 and $s_{\varepsilon_r}^2$ are partial derivatives and standard deviation for ε and ε_r , respectively. The values of ε and ε_r can be calculated from α , β , θ using Eq. 4. The partial derivatives $\frac{\partial a}{\partial \varepsilon}$ and $\frac{\partial a}{\partial \varepsilon_r}$ can be calculated as shown in Appendix A. The partial derivatives are:

$$\frac{\partial a}{\partial \varepsilon} = \frac{\varepsilon_r^2 - 100 \cdot \varepsilon_r}{(\varepsilon_r - 100 + \varepsilon)^2}, \quad (8a)$$

$$\frac{\partial a}{\partial \varepsilon_r} = \frac{100 \cdot \varepsilon + \varepsilon^2}{(\varepsilon_r - 100 + \varepsilon)^2}. \quad (8b)$$

To determine the experimental error of selectivity indicator a , the considered here copper ore was subjected to separation into concentrate and tailing by flotation. The feed was a run-of-mine ore from the Polkowice Divisions of Concentrators. It was crushed and milled and subjected to organic carbon separation by flotation. The tailing was subjected to xanthate flotation of sulfides. The results of flotation, conducted four times for identical but separate samples, taking into account only the xanthate flotation process, are given in Table 1.

Table 1. Upgrading parameters for the investigated copper ore

Product	1st flotation			2nd flotation			3rd flotation			4th flotation		
	$\beta, \%$	$\Sigma \varepsilon, \%$	$\Sigma \varepsilon_t, \%$	$\beta, \%$	$\Sigma \varepsilon, \%$	$\Sigma \varepsilon_t, \%$	$\beta, \%$	$\Sigma \varepsilon, \%$	$\Sigma \varepsilon_t, \%$	$\beta, \%$	$\Sigma \varepsilon, \%$	$\Sigma \varepsilon_t, \%$
C1	40.70	62.03	98.41	46.14	63.28	98.80	46.27	55.51	98.95	42.34	60.64	98.61
C2	29.74	77.08	96.80	31.81	78.42	97.27	33.19	73.39	97.59	29.39	76.37	96.92
C3	16.75	87.44	92.35	18.06	87.10	93.58	17.00	84.77	93.25	15.28	86.20	91.97
C4	13.22	89.38	89.68	14.04	89.08	91.14	12.67	87.36	90.18	11.79	88.27	88.91
C5	8.99	90.89	83.81	8.99	90.65	85.09	8.29	89.55	83.85	8.74	89.84	84.24
C6	4.43	93.77	64.37	4.24	93.52	65.72	4.07	93.31	64.14	4.00	94.08	62.03
T	1.73	100.00	0.00	1.60	100.00	0.00	1.61	100.00	0.00	1.65	100.00	0.00
feed	$\alpha = 1.73$			$\alpha = 1.60$			$\alpha = 1.61$			$\alpha = 1.65$		

The flotation results were plotted as the upgrading Halbich curve (Fig. 2.), and next the copper recovery was read from the graph at $\beta=30.0\%$. Then, the grades of the remaining components in the tailing were calculated using Eq. 1 (Table 2).

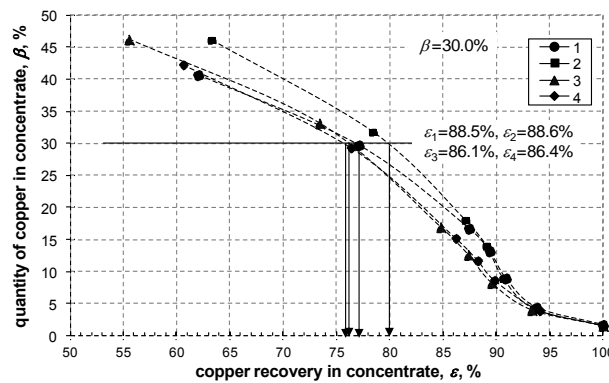


Fig. 2. The Halbich (grade – recovery) upgrading curve plotted for determination of recoveries at $\beta=30\%$ for four flotation tests run under the same conditions

Table 2 shows the calculated values of the derivatives and s . The calculated error of the selectivity indicator a is equal to 0.27, meaning that $a = 100.93 \pm 0.27$. Figure 3 shows graphically the results of the upgrading process and experimental error. The

experimental error for other concentrate grades can be calculated by the same procedure, also for different equations describing the Fuerstenau curve.

Since there are other equations evaluating upgrading curves based on ε and ε_r (Drzymala and Ahmed, 2005), the approximation was performed also by means of these formulae. Table 3 shows additional equations used for calculation of selectivity indicators b and c . They were determined on the basis of equations (35) and (36) presented in Appendix A. Figure 4 shows the errors resulting from the use of these indicators. Appendix A includes formulas for estimating the error of selectivity indicators b and c . Figures 3 and 4 show that the best fit, with the smallest error, is obtained for selectivity indicator b .

Table 2. Analysis of error of selectivity indicator a for a constant grade of concentrate

Flotation	$\beta, \%$	$\varepsilon, \%$	$\varepsilon_r, \%$
1		76.4	96.86
2		79.8	96.97
3	30.0	75.9	97.10
4		76.1	97.02
Average		77.1	96.99
standard deviation s		1.8	0.10
average selectivity indicator a for set of all flotation ($\beta = 30.0\%$)		100.93	
$\frac{\partial a}{\partial \varepsilon}$ (Eq. 22) for $\varepsilon = 87.4\%$ and $\varepsilon_r = 91.7\%$		-0.05	
$\frac{\partial a}{\partial \varepsilon_r}$ (Eq. 23) for $\varepsilon = 87.4\%$ and $\varepsilon_r = 91.7\%$		2.49	
error a (Eq. 24)		0.27 $\rightarrow a = 100.93 \pm 0.27$	

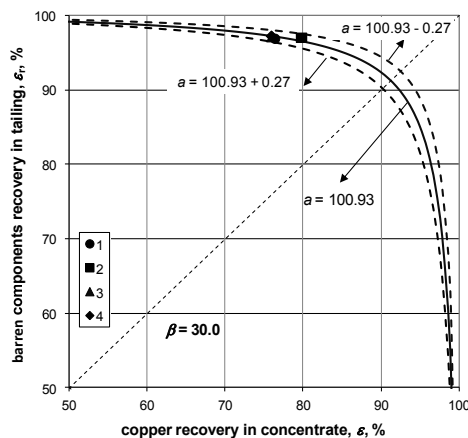
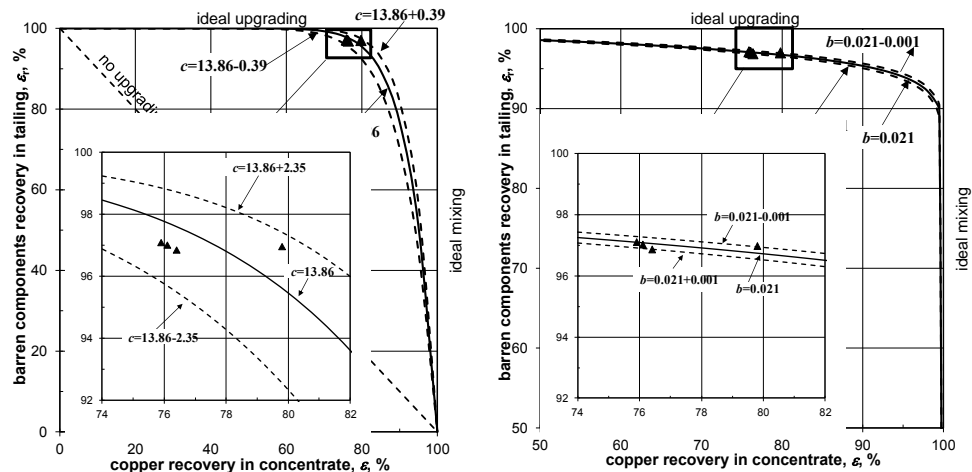


Fig. 3. Experimental (four identical experiments) error of selectivity indicator a determination at copper content in the concentrate equal to 30%

Table 3. Selectivity indicators determined based on the Fuerstenau curve

selectivity indicator	<i>a</i>	<i>b</i>	<i>c</i>
equation	$\varepsilon_r = a(100 - \varepsilon)/(a - \varepsilon)$	$\varepsilon_r = ((100 - \varepsilon)^b)/100^{(b-1)}$	$\varepsilon_r = (100^c - \varepsilon^c)/100^{(c-1)}$
ideal upgrading	100	0, ∞	0, ∞
no upgrading	∞	1	1

Fig. 4. Experimental (four identical experiments) error of selectivity indicators *b* and *c* determination at copper content in the concentrate equal to 30%

Approximation accuracy

The experimental data can be also used to determine the error of approximation. Since the separation data can be approximated by using with different selectivity indices, the most useful are given in Table 4. The error of their approximation in the form of standard error of estimation (SEE) was calculated from the equation (Hair et al., 1995):

$$SEE = \sqrt{\frac{\sum_{i=1}^n (\varepsilon_r - \varepsilon_{rt})^2}{n-2}} \quad (9)$$

where ε_r is barren components recovery in tailing (as-received), ε_{rt} barren components recovery in tailing (calculated) and n stands for number of experimental points. The calculated SEE values are given in Table 4. It can be seen that the best approximation was obtained for selectivity parameter *c* (the smallest standard error of estimate).

Table 4. Approximation of the flotation tests with different selectivity indicators for Fuerstenau curve

Equation	Fitting parameter	R^2	SEE*	Fitting parameter	R^2	SEE*
	1st flotation	2nd flotation				
$\varepsilon_r = a(100 - \varepsilon) / (a - \varepsilon)$	$a = 101.0634$	0.9939	2.5322	$a = 100.8004$	0.9896	3.2932
$\varepsilon_r = ((100 - \varepsilon)^b) / 100^{(b-1)} *$	$b = 0.0756$	0.9446	7.9083	$b = 0.0695$	0.9437	8.0088
$\varepsilon_r = (100^c - \varepsilon^c) / 100^{(c-1)} *$	$c = 17.9810$	0.9951	2.3509	$c = 18.1697$	0.9945	2.4948
	3rd flotation	4th flotation				
$\varepsilon_r = a(100 - \varepsilon) / (a - \varepsilon)$	$a = 100.9717$	0.9863	3.8038	$a = 101.0446$	0.9892	3.3633
$\varepsilon_r = ((100 - \varepsilon)^b) / 100^{(b-1)} *$	$b = 0.0805$	0.9454	7.8969	$b = 0.0820$	0.9403	8.2372
$\varepsilon_r = (100^c - \varepsilon^c) / 100^{(c-1)} *$	$c = 15.8415$	0.9980	1.4988	$c = 16.6582$	0.9985	1.3132
for date points of all flotation tests						
$\varepsilon_r = a(100 - \varepsilon) / (a - \varepsilon)$	100,9612	0,9649	3,7582			
$\varepsilon_r = ((100 - \varepsilon)^b) / 100^{(b-1)} *$	0,0767	0,8335	8,5213			
$\varepsilon_r = (100^c - \varepsilon^c) / 100^{(c-1)} *$	17,2063	0,9860	2,4729			

* Standard Error of Estimate, $b = \log_{100-\varepsilon} \frac{\varepsilon_r}{100}$, $c = \log_{\varepsilon/100} \left(1 - \frac{\varepsilon_r}{100} \right)$

The difference in errors of selectivity indicator c was determined for the entire set of points. The value of selectivity indicator c is 17.21 and its value is from 22.34 to 13.52 (errors taken into consideration). The value of the standard estimation error (SEE) is 2.47, with the value of R^2 equal to 0.99.

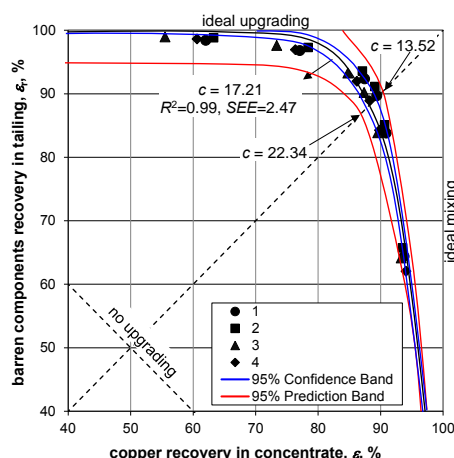


Fig. 5. Approximation of four sets of experimental data with selectivity indicator c and its accuracy of determination

The difference in errors of selectivity indicator c was determined for the maximum position of the prediction band $[(1 - \alpha)100\%]$ determined according to a general equation for random variable y (Johnson and Wichern, 2007):

$$\hat{y} \pm t_{\alpha/2} (\text{estimated standard error of prediction}), \quad (10)$$

where \hat{y} is dependent variable (predicted), α established prediction band and t value of the t -Student statistics. The location of the confidence and prediction bands, relative to the obtained upgrading curve, was determined using SigmaPlot 11.0, while STATISTICA 9 was used to determine the confidence and prediction band at 95%. It means that the best fit line is within 95% confidence ranges (Härdle et al., 2004). The points of intersection of the prediction interval with the diagonal line joining points on the Fuerstenau graph (0,0;100,100) were also determined. Then, substituting these points to the equation for selectivity indicator c :

$$c = \log_{e/100} \left(1 - \frac{\varepsilon_r}{100} \right) \quad (11)$$

for ε and ε_r ((86.0,87.0); (90.0, 91.5)) (values seen in Figure 5), the range of the selectivity indicator error was obtained. Thus, value selectivity indicator c is from 13.52 to 22.34 (values calculated from Fig. 5).

To find the error of approximation of experimental data with the selectivity indicator a , similar calculations were performed and the results are presented in Fig. 6.

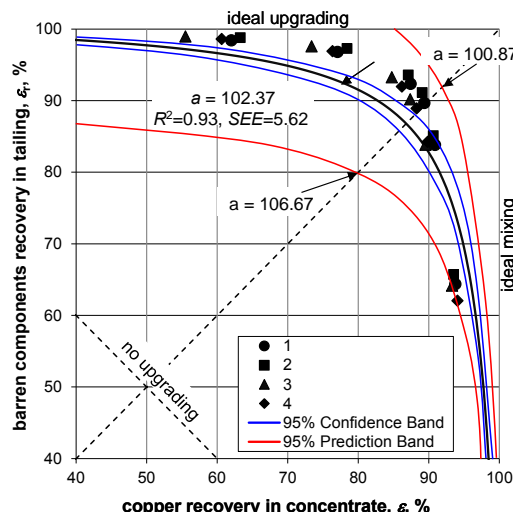


Fig. 6. Approximation of four sets of experimental data with selectivity indicator a and its accuracy of determination

For the entire set of points the value of selectivity indicator a is 102.37, and by taking into account the standard error equal of estimate its value is from 106.67 to 100.87 (with errors taken into consideration). The value of the standard error of estimation (SEE) is 5.62, with the value of R^2 equal to 0.93. As in the case of selectivity indicator c , the difference in errors of selectivity indicator a value was determined by the maximum opening of the significance interval. For values ε and ε_r taken from Fig. 6 [(92.0, 91.0); (80.0; 80.0] the value of selectivity indicator a was determined basing on Eq. 3. The value of a is then from 100.87 to 106.67.

Conclusions

Determination of selectivity indicators error depends on accuracy of chemical analysis of the separation feed and process products as well as on experimental and approximation errors. For the Kupferschiefer stratiform copper ore mined by KGHM Polska Miedz S.A. the analytical errors are small and are equal to: concentrate $\pm 0.3\%$, tailing $\pm 0.03\%$ and feed $\pm 0.06\%$. The experimental errors made during laboratory flotation tests using the same ore sample and methodology are also insignificant. In the case of selectivity indicator a equal to 100.93 the error is ± 0.27 .

The largest errors can be made during approximation of the upgrading curves with an inappropriate selectivity indicator. Therefore, a correct determination of the selectivity indicator in the first stage of work must be based on the analysis of alignment degree of equation for the chosen selectivity indicator to the real results. The analysis shows that although the experimental error is not significant, the experiment should be conducted at least twice using the same methodology, so that the upgrading curves are of similar shape and their prediction intervals are the biggest and they overlap. Due to the fact that estimation, experimental and chemical analysis errors may sum up, a full analysis of accuracy of determination of selectivity indicator should not be simplified as in this paper, but should take into consideration the influence of all three factors simultaneously.

Acknowledgements

Financial support by the Polish Statutory Research Grant (B30029 and S30103) is greatly acknowledged.

References

BROZEK M., SUROWIAK A., 2010. *Argument of separation at upgrading in the JIG*, Archives of Mining Sciences, vol. 55(1), pp. 21-40.

DRZYMALA J., 2005. *Evaluation and comparison of separation performance for varying feed composition and scattered separation results*, International Journal of Mineral Processing, vol. 75, pp. 189-196.

DRZYMALA J., 2005-2008. *Atlas of upgrading curves used in separation and mineral science and technology*, Part I, Physicochemical Problems of Mineral Processing.

DRZYMALA J., AHMED H.A.M., 2005. *Mathematical equations for approximation of separation results using the Fuerstenau upgrading curves*, International Journal of Mineral Processing, Vol. 76, Issue: 1-2, pp. 55-65.

DRZYMALA J., LUSCZKIEWICZ A., FOSZCZ D., 2010. *Application of upgrading curves for evaluation of past, present and future performance of a separation plant*, Mineral Processing and Extractive Metallurgy Review, vol. 31(3), pp. 165–175.

DUCHNOWSKA M., DRZYMALA J., 2011. *Transformation of equation $y = a(100 - x)/(a - x)$ for approximation of separation results plotted as Fuerstenau's upgrading curve for application in other upgrading curves*, Physicochemical Problems of Mineral Processing, vol. 47, pp. 123–130.

DUCHNOWSKA M., DRZYMALA J., 2012. *Self-similarity of upgrading parameters used for evaluation of separation results*, International Journal of Mineral Processing, vol. 106–109, pp. 50–57.

FOSZCZ D., 2006. *Estimation of parameters of regressive functions by means of classical method and bootstrap method*, AGH Journal of Mining and Geoengineering, vol. 3(1), Uczelniane Wydawnictwa Naukowo-Dydaktyczne AGH, 67-78. [in Polish]

FOSZCZ D., NIEDOBA T., TUMIDAJSKI T., 2009. *Chosen problems of balancing of copper ores beneficiation products*, AGH Journal of Mining and Geoengineering, vol. 4, 71–80. [in Polish]

FOSZCZ D., NIEDOBA T., TUMIDAJSKI T., 2010. *Analysis of possibilities of forecasting the results of Polish copper ores beneficiation with applied technology taken into account*. AGH Journal of Mining and Geoengineering, vol. 4/1, 25-36. [in Polish]

FULLER W.A., 2006. *Measurement Error Models*, Wiley.

HAIR J.F., ANDERSON R.E., TATHAM R.L., BLACK W.C., 1995. *Multivariate Data Analysis with Readings*. Prentice Hall International, London.

HÄRDLE W., MÜLLER M., SPERLICH S., WERWATZ A., 2004. *Nonparametric and Semiparametric Models*, Springer.

JAMROZ D., NIEDOBA T., 2014. *Application of Observational Tunnels Method to Select Set of Features Sufficient to Identify a Type of Coal*, Physicochemical Problems of Mineral Processing, vol. 50(1), pp. 185-202.

JOHNSON R.A., WICHERN D.W., 2007. *Applied multivariate statistical analysis*. Prentice Hall, New York.

NEETHLING S.J., CILLIERS J.J., 2008. *Predicting and correcting grade recovery curves. Theoretical aspects*, Int. J. Miner. Process., 89, 17-22.

NIEDOBA T., 2013. *Statistical analysis of the relationship between particle size and particle density of raw coal*, Physicochemical Problems of Mineral Processing, vol. 49(1), 175-188.

NOWAK A., SUROWIAK A., 2013. *Methodology of the efficiency factors of fine grained clayish suspensions separation in multileveled hydrocyclone systems*, Archives of Mining Sciences, vol. 58(4), pp. 1209-1220.

VERA M.A., FRANZIDIS J_P., MANLAPIG E. V. 1999. *An empirical equation for recovery - enrichment ratio curve (AREV model)*, Copper 99-Cobre 99 International Environment Conference, Volume II - Mineral Processing/Environment, Health and Safety, B.A. Hancock and M.R.L. Pon Eds, The Minerals, Metals & Materials Society, 69-82.

WACKERLY D., SCHEAFFER W., 2008. *Mathematical Statistics with Applications* (7 ed.). Belmont, CA, USA: Thomson Higher Education.

Appendix A

It is convenient to calculate the derivative of a^{-1} instead of a because there is a sum in the numerator, which can be split into a sum of terms

$$a^{-1} = \frac{(\beta-\vartheta)[(\alpha-\vartheta)100\beta(100-\alpha)-100\alpha(\beta-\vartheta)(100-\alpha)+\alpha(100\beta-100\vartheta-\alpha+\vartheta)(100-\vartheta)]}{100(\alpha-\vartheta)\beta(100\beta-100\vartheta-\alpha+\vartheta)(100-\vartheta)} \quad (12)$$

or

$$a^{-1} = \frac{(\beta-\vartheta)(100-\alpha)}{(100\beta-100\vartheta-\alpha+\vartheta)(100-\vartheta)} - \frac{\alpha(\beta-\vartheta)^2(100-\alpha)}{(\alpha-\vartheta)\beta(100\beta-100\vartheta-\alpha+\vartheta)(100-\vartheta)} + \frac{\alpha(\beta-\vartheta)}{100(\alpha-\vartheta)\beta} \quad (13)$$

and briefly

$$a^{-1} = b_1 - b_2 + b_3 \quad (14)$$

For further calculations it is convenient to use logarithmic forms of term b :

$$\ln b_1 = \ln(\beta - \vartheta) + \ln(100 - \alpha) - \ln(100\beta - 100\vartheta - \alpha + \vartheta) - \ln(100 - \vartheta) \quad (15)$$

$$\ln b_2 = \ln \alpha + 2 \ln(\beta - \vartheta) + \ln(100 - \alpha) - \ln(\alpha - \vartheta) - \ln \beta - \ln(100\beta - 100\vartheta - \alpha + \vartheta) - \ln(100 - \vartheta) \quad (16)$$

$$\ln b_3 = \ln \alpha - \ln 100 - \ln(\alpha - \vartheta) - \ln \beta + \ln(\beta - \vartheta). \quad (17)$$

Since

$$[\ln(f(x))]' = \frac{1}{f(x)} \cdot f'(x) \quad \text{thus} \quad f'(x) = f(x)[\ln(f(x))]' \quad (18)$$

we get

$$\frac{\partial b_1}{\partial \alpha} = b_1 \left(\frac{-1}{100-\alpha} + \frac{1}{100\beta-100\vartheta-\alpha+\vartheta} \right) \quad (19)$$

$$\frac{\partial b_2}{\partial \alpha} = b_2 \left(\frac{1}{\alpha} - \frac{1}{100-\alpha} - \frac{1}{\alpha-\vartheta} + \frac{1}{100\beta+100\vartheta-\alpha+\vartheta} \right) \quad (20)$$

$$\frac{\partial b_3}{\partial \alpha} = b_3 \left(\frac{1}{\alpha} - \frac{1}{\alpha-\vartheta} \right) \quad (21)$$

$$\frac{\partial b_1}{\partial \beta} = b_1 \left(\frac{1}{\beta-\vartheta} - \frac{100}{100\beta-100\vartheta-\alpha+\vartheta} \right) \quad (22)$$

$$\frac{\partial b_2}{\partial \beta} = b_2 \left(\frac{2}{\beta-\vartheta} - \frac{1}{\beta} - \frac{100}{100\beta-100\vartheta-\alpha+\vartheta} \right) \quad (23)$$

$$\frac{\partial b_3}{\partial \beta} = b_3 \left(-\frac{1}{\beta} + \frac{1}{\beta-\vartheta} \right) \quad (24)$$

$$\frac{\partial b_1}{\partial \vartheta} = b_1 \left(-\frac{1}{\beta-\vartheta} + \frac{100-1}{100\beta-100\vartheta-\alpha+\vartheta} + \frac{1}{100-\vartheta} \right) \quad (25)$$

$$\frac{\partial b_2}{\partial \vartheta} = b_2 \left(-\frac{2}{\beta-\vartheta} + \frac{1}{\alpha-\vartheta} + \frac{100-1}{100\beta-100\vartheta-\alpha+\vartheta} + \frac{1}{100-\vartheta} \right) \quad (26)$$

$$\frac{\partial b_3}{\partial \vartheta} = b_3 \left(\frac{1}{\alpha-\vartheta} - \frac{1}{\beta-\vartheta} \right) \quad (27)$$

Based on equations 4-16, the partial derivatives are:

$$\frac{\partial a}{\partial \alpha} = -a^2 \left(\frac{\partial b_1}{\partial \alpha} - \frac{\partial b_2}{\partial \alpha} + \frac{\partial b_3}{\partial \alpha} \right) \quad (28)$$

$$\frac{\partial a}{\partial \beta} = -a^2 \left(\frac{\partial b_1}{\partial \beta} - \frac{\partial b_2}{\partial \beta} + \frac{\partial b_3}{\partial \beta} \right) \quad (29)$$

$$\frac{\partial a}{\partial \vartheta} = -a^2 \left(\frac{\partial b_1}{\partial \vartheta} - \frac{\partial b_2}{\partial \vartheta} + \frac{\partial b_3}{\partial \vartheta} \right). \quad (30)$$

Similar calculations can be performed using another formula for a (from the Eq. 1):

$$a = \frac{\varepsilon \varepsilon_r}{\varepsilon + \varepsilon_r - 100} \quad (31)$$

for which the partial derivatives are

$$\frac{\partial a}{\partial \varepsilon} = \frac{\varepsilon_r^2 - 100 \cdot \varepsilon_r}{(\varepsilon_r - 100 + \varepsilon)^2} \quad (32)$$

$$\frac{\partial a}{\partial \varepsilon_r} = \frac{100 \cdot \varepsilon + \varepsilon^2}{(\varepsilon_r - 100 + \varepsilon)^2}. \quad (33)$$

The final equation is

$$\text{error } a = \sqrt{\left(\frac{\partial a}{\partial \varepsilon} \right)^2 \cdot s_{\varepsilon}^2 + \left(\frac{\partial a}{\partial \varepsilon_r} \right)^2 s_{\varepsilon_r}^2}. \quad (34)$$

where s_{ε}^2 standard deviation for ε and $s_{\varepsilon_r}^2$ standard deviation for ε_r .

Similar calculations can be performed using another formulas for b and c :

$$b = \log_{\frac{100-\varepsilon}{100}} \frac{\varepsilon_r}{100} \quad (35)$$

$$c = \log_{\varepsilon/100} \left(1 - \frac{\varepsilon_r}{100} \right) \quad (36)$$

for which the partial derivatives are

$$\frac{\partial b}{\partial \varepsilon} = \frac{\ln\left(\frac{\varepsilon_r}{100}\right)}{(100 - \varepsilon) \left[\ln\left(\frac{100 - \varepsilon}{100}\right) \right]^2} \quad (37)$$

$$\frac{\partial b}{\partial \varepsilon_r} = \frac{1}{\varepsilon_r \ln\left(\frac{100 - \varepsilon}{100}\right)} \quad (38)$$

$$\frac{\partial c}{\partial \varepsilon} = -\frac{\ln\left(1 - \frac{\varepsilon_r}{100}\right)}{\varepsilon \left[\ln\left(\frac{\varepsilon}{100}\right) \right]^2} \quad (39)$$

$$\frac{\partial c}{\partial \varepsilon_r} = \frac{-1}{(100 - \varepsilon_r) \ln\left(\frac{\varepsilon}{100}\right)} \quad (40)$$

Received October 31, 2014; reviewed; accepted April 17, 2015

LEACHING BEHAVIOUR OF A TURKISH LATERITIC ORE IN THE PRESENCE OF ADDITIVES

Huseyin BASTURKCU, Nese ACARKAN

Istanbul Technical University, Mining Faculty, Mineral Processing Engineering Department, Istanbul, Turkey,
basturkcu@itu.edu.tr

Abstract: This paper investigates the dissolution mechanism of a lateritic nickel ore from the Caldag Region of Manisa in Turkey. The ore sample contained 1.2% Ni, 24.8% Fe, and 0.062% Co. The optimum leaching conditions were found to be temperature 80 °C, particle size -74 µm, H₂SO₄ concentration 200 g/dm³, solids ratio (by weight) 10% and leaching duration 8 h. The extractions of 98.2% Ni, 98.6% Fe and Co 98.9% were obtained under these conditions. Additionally, the effects of additional substances such as NaCl, Na₂S₂O₅, Na₂SO₄, and KCl were investigated in order to decrease the leaching duration. The results showed that the additives accelerated the leaching kinetics and achieved nearly the same nickel and cobalt extractions at the end of 4 h compared to the results obtained after 8 h without the additives. If the additives containing chlorine were used, it was determined that the iron extraction showed no increase, although both the nickel and cobalt extractions increased.

Keywords: laterite, nickel, agitation leaching, dissolution

Introduction

There is a growing interest in improving the processing technology of lateritic nickel from huge reserves representing nearly 70% of the world nickel resources due to the declining nickel sulphide reserves (McDonald and Whittington, 2008). Although it is possible to process nickel sulphide ores using several methods such as flotation, the extraction of nickel from lateritic ores requires either pyrometallurgical or hydrometallurgical methods where high energy and reagent costs exist. While the cobalt content in the lateritic ores provides an economic advantage, the processing costs strongly depend on the mineralogy of the ore in which nickel can be hosted in a variety of different minerals.

Goethite is a major nickel-bearing mineral in many laterites, and nickel occurs in three modes: associated with amorphous or poorly crystalline goethite, weakly adsorbed by the crystalline goethite surface, and as a substituent in the goethite structure (Chang et al., 2010; Schwertmann et al., 1982). According to Dalvi et al. (2004), there are four different regions of the laterite profile: limonite, nontronite,

serpentine, and garnierite. Since the nickel content of all these regions varies, the extraction methods also change.

Today, basically two processing methods are used in the industry: pyrometallurgical and hydrometallurgical methods. Pyrometallurgical processes include energy intensive techniques such as drying, calcination, and smelting. On the other hand, atmospheric leaching (AL), high pressure acid leaching (HPAL), and the Caron process are classified as hydrometallurgical processes. While the Caron process requires drying, calcination, and ammoniacal leaching, high pressure and temperature within autoclaves are necessary for HPAL. In comparison, AL is undertaken using the agitation or heap leaching methods. When hydrometallurgical methods are compared to each other, AL has considerable advantages over HPAL such as lower CAPEX and energy consumption, simpler process control, and lower maintenance costs. However, higher acid consumptions, more voluminous residue in tank leaching, slower extraction kinetics, ensuring heap permeability in heap leaching and lower nickel/iron ratios are disadvantages of AL (McDonald and Whittington, 2008; Neudorf, 2007; Chander, 1982).

Various methods have been tried to improve nickel extraction kinetics for AL and selectivity over iron to reduce acid consumption. These comprise increasing temperature or leaching time, controlling redox potential, adding various chemicals and pre-treatment. However, all the tests performed gave similar results: high acid consumption, high dissolved iron content in pregnant leach solution, and high residual acid concentration (McDonald and Whittington, 2008; Buyukakinci and Topkaya, 2009).

Researchers have found that the addition of sodium salts showed a positive effect on the dissolution mechanism of nickel (Krause et al., 1997; Johnson et al., 2002; Whittington et al., 2003; Johnson et al., 2005). Adsorption of Ni^{2+} cations onto negative surface charged silica can be inhibited by increasing free acid amount in solution. When Na^+ ions are added to the leaching solution, competition between Ni^{2+} and Na^+ was proposed to hinder Ni^{2+} adsorption (Whittington et al., 2003). Furthermore, Johnson and Whittington (2004) used sulphate salts of Na^+ , NH_4^+ , and K^+ to accelerate the leaching kinetics. Although Kaya and Topkaya (2011) investigated the additions of FeSO_4 , Cu^+ , and S , the results were unsatisfactory in terms of the increasing nickel and cobalt extractions to the target levels. The addition of an oxidant, MnO_2 , was tested by Loveday (2008), and provided higher nickel extraction and reduction of acid consumption.

All the additives described above were tested in the pressure leaching studies, and there were no studies carried out under AL conditions. In this study, the dissolution mechanism of a lateritic nickel ore from Caldag-Manisa (Turkey) using an atmospheric leaching method with various additives was investigated.

Materials and methods

Material characterization

A lateritic ore sample obtained from Caldag-Manisa (Turkey) was used in the tests. The chemical analyses of lateritic ore sample were performed out using Inductively Coupled Plasma (ICP) and X-Ray Fluorescence (XRF) methods, and the results are presented in Table 1. To characterize the mineralogy of the sample, polished sections were prepared, and the analyses were performed by using a JEOL – JSM 6010LV model Scanning Electron Microscope (SEM) coupled with SEM, Energy-dispersive X-ray spectroscopy (EDS). According to the results, the main source of nickel mineral was found to be goethite $[(\text{Fe},\text{Ni})\text{O}(\text{OH})]$ occurring in particle sizes up to 500 μm , which contained Fe-Mn-Ni-Co. In addition, chromite and hematite were determined as gangue minerals. The X-ray elemental maps of the sample are shown in Figs. 1 and 2. Likewise, the X-ray diffraction (XRD) analysis showed that the lateritic ore sample consisted of mainly quartz and goethite minerals while serpentine minerals were also indicated. The XRD result of the sample is given in Fig. 3.

Table 1. Chemical analyses of a representative ore sample

Component	Content	Component	Content (%)
	(%)		
Al_2O_3	4.00	MnO	0.383
CaO	0.660	Na_2O	0.080
Co	0.062	Ni	1.20
Cr_2O_3	1.13	P_2O_5	0.028
Cu	0.001	SiO_2	40.9
Fe	24.8	TiO_2	0.130
K_2O	0.250	Zn	0.026
MgO	5.88	LOI	9.26

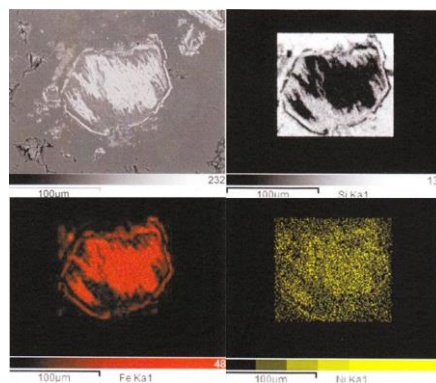


Fig. 1. X-ray elemental map of the nickeliferous limonite sample

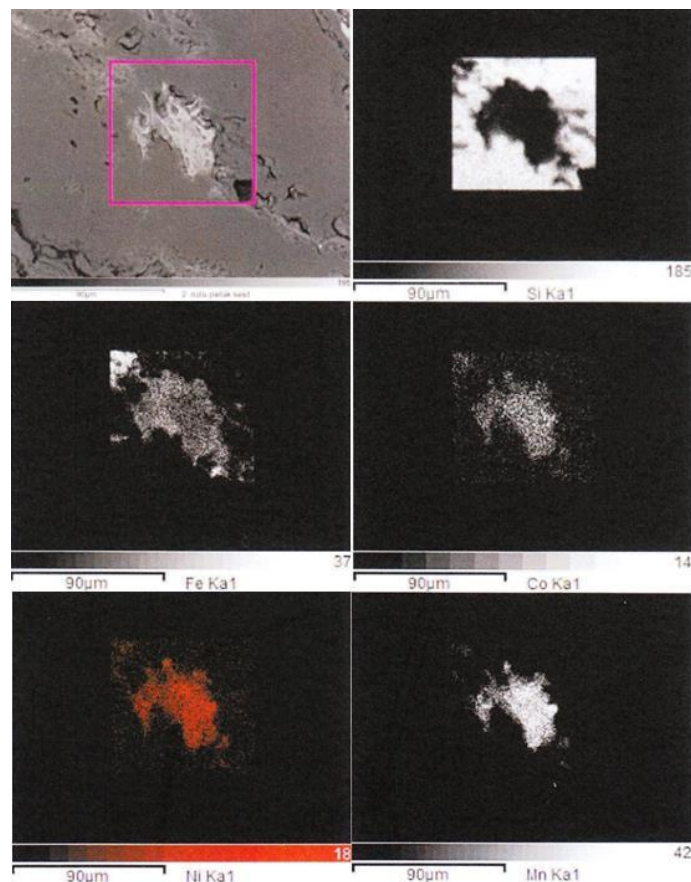


Fig. 2. X-ray elemental map of nickeliferous sample showing Fe-Mn-Ni-Co enriched zone

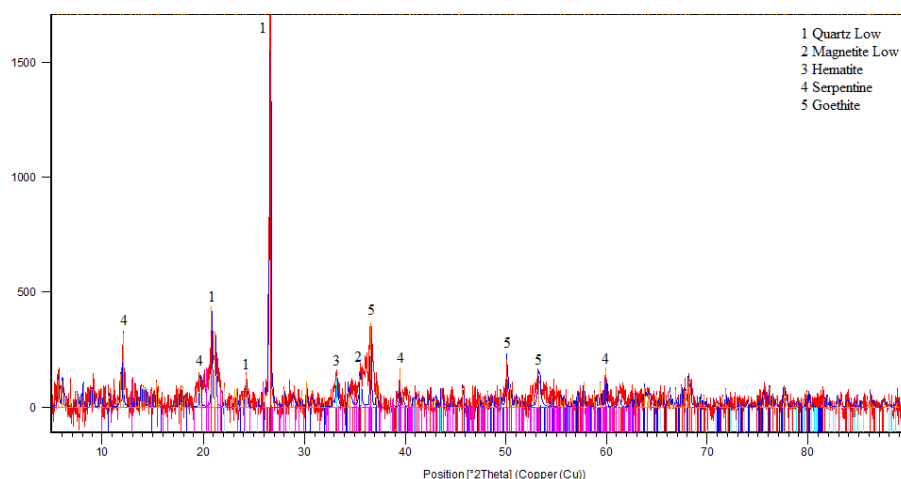


Fig. 3. XRD pattern of the nickeliferous laterite sample

Experimental

The representative sample for the agitation leaching tests was prepared using a ring mill. The leaching tests were conducted in a heated reaction vessel with Teflon® coated impeller at the speed of 500 rpm. The leaching temperature was controlled by an IKA temperature controller. The analytic grade of H_2SO_4 was used in the leaching tests. An acid resistant material was used to cover the top of the baker to prevent volatilization and help maintain the temperature during the leaching. At the end of the leaching, the leached residue was filtered and washed with water using a Buchner funnel. The dried leach cakes were analyzed. In order to determine the acid consumption, the titration was carried out with 0.1 N NaOH solution and methyl orange as an indicator.

In the agitation leaching tests, the parameters such as temperature, particle size, solid ratio (solid weight/total weight), various acid concentrations, leaching duration, and added substances were tested in detail. The added substances were included NaCl, $\text{Na}_2\text{S}_2\text{O}_5$, Na_2SO_4 , and KCl. The metal extraction values were evaluated at the end of the leaching tests.

Results and discussion

Effect of temperature

In this part of the study, the leaching temperatures of 40, 50, 60, 70, 80, and 90 °C were tested to obtain higher metal extractions. The parameters of 150 g/dm³ H_2SO_4 concentration, -100 µm particle size, 20% solids ratio were kept constant for a leaching duration of 2 h. As seen from Fig. 4, the nickel and cobalt extractions increased 44% and 37%, respectively between 40 °C and 90 °C of the leaching temperatures. On the other hand, Fe extraction increased to 55% between these temperatures. The reason for the 1.7% nickel extraction increase from 80 °C to 90 °C was attributed to the increase in the iron extraction since nickel and iron minerals were associated in the same minerals. Since the nickel extraction increased marginally at 80 °C, compared with iron extraction, 80 °C was seen to be an optimum.

Effect of particle size

In these leaching tests, the effect of particle size on the metal extractions was investigated with -300, -150, -106, -74, and -38 µm size fractions. The d_{50} and d_{90} sizes of the samples can be seen in Table 2. The experiments were carried out with 150 g/dm³ acid concentration and 20% solids ratio at 80 °C for 2 h. According to the results shown in Fig. 5, the highest extractions were obtained with the -74 and -38 µm size fractions. This implies good mineral liberation in these fine fractions although the particle size showed no significant effect on the metal extractions. While the metal extractions were close to each other within the finer particle size fractions, based upon

the higher milling costs, it was decided to continue to use the -74 μm size fraction for further tests.

Table 2. d_{50} and d_{90} sizes of the samples

Sample (μm)	d_{50} size (μm)	d_{90} size (μm)
-300	183	260
-150	62	130
-106	54	87
-74	47	68
-38	23	31

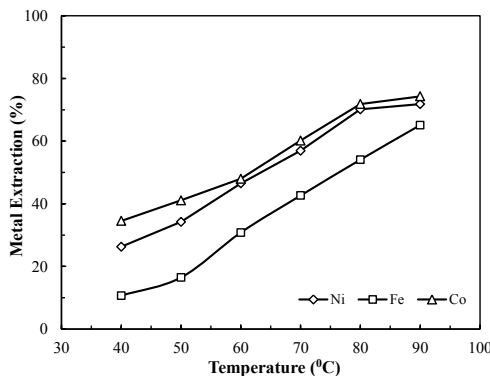


Fig. 4. Effect of temperature on metal extractions during AL of a nickeliferous laterite ore (2 h leaching duration, 150 g/dm³ H₂SO₄, 20% solids ratio, -100 μm particle size)

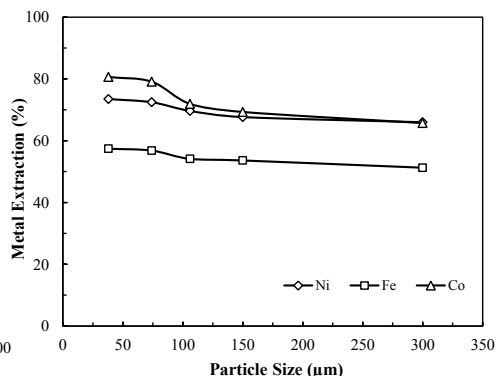


Fig. 5. Effect of particle size on metal extractions during AL of a nickeliferous laterite ore (2 h leaching duration, 150 g/dm³ H₂SO₄, 20% solids ratio)

Effect of acid concentration on solid ratio

Up to this part of this study, all conditions were optimized at 20% solids ratio, where only Ni 72.3% and Co 79.1% extractions could be achieved. Although higher solids ratios are preferred in industrial applications to optimize plant capacity, solids ratio might be reduced in order to improve metal extractions. Therefore, the acid concentrations of 150, 200, and 250 g/dm³ of H₂SO₄ were tested at solids ratios of 10, 20, 30, and 40%. These solids ratios were chosen to cover potential industrial application of the agitation leaching. The results shown in Fig. 6 clearly indicated that the increase in the solids ratio negatively affected nickel, cobalt, and iron extractions even with high acid concentration. In particular, the amount of the acidic solution was insufficient, especially at 40% solids ratio. As the solids ratio decreased, better results were obtained, and nearly 88% of nickel extraction could be achieved at 10% solids ratio. The results obtained with 200 and 250 g/dm³ were similar, and therefore, 200 g/dm³ was employed as the optimum acid concentration at 10% solids ratio.

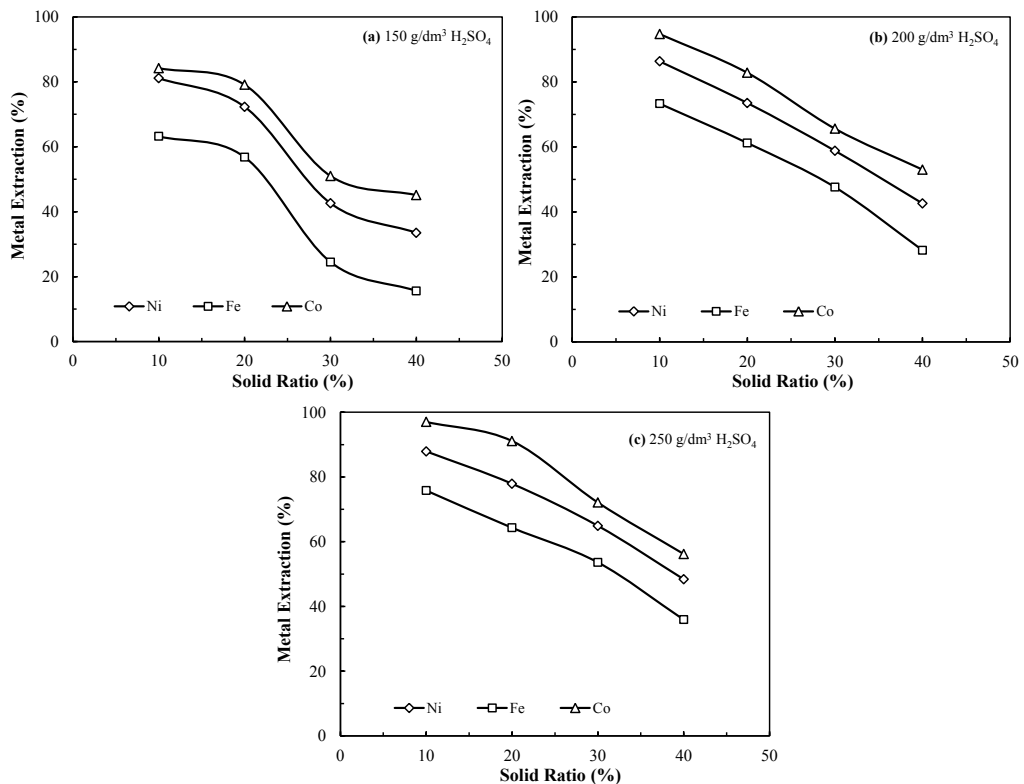


Fig. 6. Effect of solids ratio on metal extractions during AL of a nickeliferous laterite ore for an acid concentration of (a) 150 g/dm³ (b) 200 g/dm³ (c) 250 g/dm³ (2 h leaching duration, -74 µm)

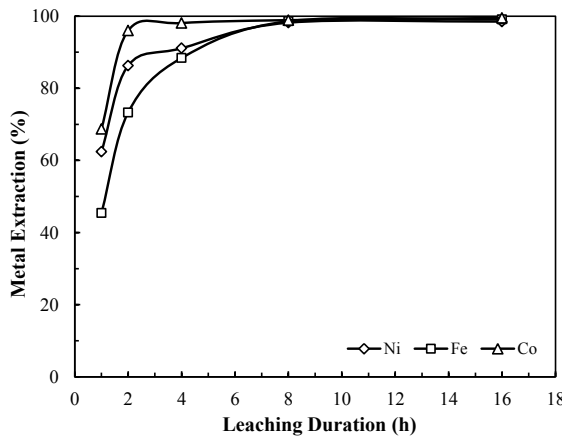


Fig. 7. Effect of leaching time on metal extractions during AL of a nickeliferous laterite ore (2 h leaching duration, 200 g/dm³ H₂SO₄, 10 % solids ratio, -74 µm)

Effect of leaching time

The experiments were performed at various leaching times of 1, 2, 4, 8, and 16 h in order to investigate the effect of leaching time on the metal extractions. All experiments were carried out with 200 g/dm³ of H₂SO₄ concentration, -74 µm particle size at 10% solids ratio and 80 °C temperature. The results of the experiments given in Fig. 7 showed that the increase of the leaching time had a positive effect on the nickel, cobalt, and iron extractions. After 8 h of the leaching time, almost all the metals were extracted. With longer leaching duration more than 8 h, a linear trend was observed.

Ultimately, Ni 98.2%, Fe 98.6%, and Co 98.9% extractions were obtained with 200 g/dm³ of H₂SO₄ concentration at 10% solids ratio, 500 rpm agitation speed, and 80 °C for 8 h leaching duration. To provide these extractions under the optimum conditions determined, 928 kg/Mg of H₂SO₄ was consumed. Also, the theoretical acid consumption was calculated as 922 kg/Mg, which supported the experimental findings. In comparison with the literature, the acid consumption appeared to be very high, where Buyukakinci and Topkaya (2009) indicated that the acid consumptions were 669 kg of H₂SO₄/Mg and 714 kg H₂SO₄/Mg for dry ore nontronite and limonite, respectively. It can be concluded that the iron content in the laterite samples affects the acid consumption while limonitic ores have higher acid requirement under the atmospheric conditions. Furthermore, the pregnant leach solution contained Ni 1.31 g/dm³, Fe 27.14 g/dm³, and Co 0.07 g/dm³. The extraction values obtained as a function of time indicated that nickel and iron were leached congruently.

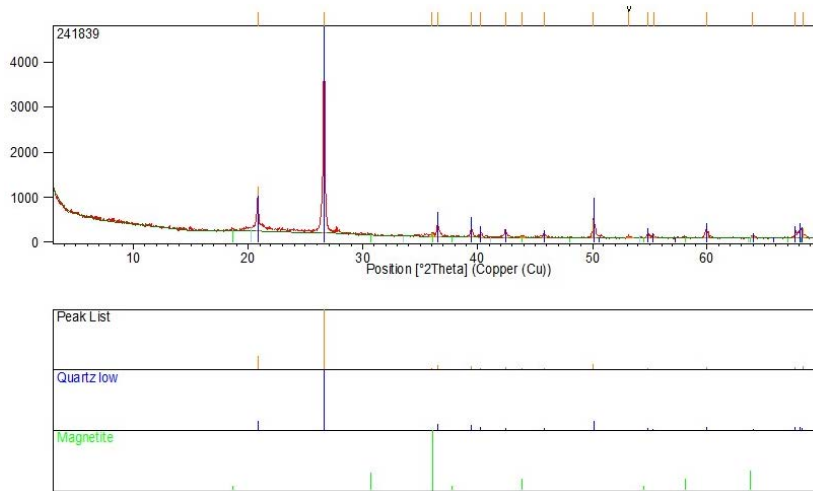


Fig. 8. XRD pattern of nickeliferous laterite leach residue

The XRD analysis was performed for the dried leach cakes, as seen in Fig. 8. In comparison to the raw ore sample, the peaks for goethite disappeared during the leaching. Furthermore, quartz and weaker magnetite peaks existed as expected since these minerals are leached poorly in the acidic medium. Additionally, the leaching of

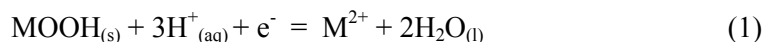
silicate minerals resulted in amorphous silica formation which was noted in the leach cake.

Effect of additives

In a series of tests, an alternative ways to increase the extraction values and/or decrease the leaching duration were investigated. The examination of the literature indicated that the addition of sodium salts in HPAL had a positive effect on the dissolution of nickel. Whittington et al. (2003) indicated that cations such as Ni^{2+} adsorbs on silica surface which has a strongly negative surface charge. This adsorption can be inhibited by an increase in the free acidity. When silica-hydroxyl sites are associated with nickel, the competition between Ni^{2+} and cations such as Na^+ can also prevent the adsorption of Ni^{2+} . On the other hand, although the association mechanism for nickel with amorphous silica is currently unknown, Whittington and Johnson (2005) reported that the reduction in nickel presenting in the hematite and silica was mostly responsible for the increase in nickel extraction. They proposed a mechanism that involves the competition between cations for adsorption on silica-hydroxyl sites.

The possibility of accelerating the dissolution during AL was investigated with various additions. Here 5, 10, 20, and 40 g/dm³ of NaCl, $\text{Na}_2\text{S}_2\text{O}_5$, Na_2SO_4 , and KCl were tested under the optimum leaching conditions except for a shorter leaching duration of 2 h. The results obtained were compared with the reference metal extractions of Ni 86.3%, Fe 73.3%, and Co 97.7% (the results of 2 h leaching without additives).

It can be concluded from the results with the use of the various additives that sodium (and potassium) salts had a positive effect on the metal extractions. With the additions, 91.4% of Ni extraction was achieved, which corresponds to a 5.1% of Ni extraction increase. The highest extractions were obtained with 10 g/dm³ of NaCl, 20 g/dm³ of Na_2SO_4 , 5 g/dm³ of $\text{Na}_2\text{S}_2\text{O}_5$, and 20 g/dm³ of KCl additions (Table 3). These optimum dosages of the additives were then tested for various leaching durations. As seen from Table 4, higher nickel extractions could be obtained after 4 h in the presence of additives in comparison with the extraction values obtained without the additives. However, the iron concentrations in the pregnant solutions increased with Na_2SO_4 and $\text{Na}_2\text{S}_2\text{O}_5$ additions. In the presence of $\text{Na}_2\text{S}_2\text{O}_5$ (sodium metabisulphite), known as a reducing agent, iron was leached as Fe^{2+} rather than Fe^{3+} . Therefore, the higher overall iron extraction might be attributed to high ferrous iron content in solution. Chong et al. (2013) indicated the reduction reaction as follows:



Mwema et al. (2002) reported the practices of using ferrous ion, copper powder, and $\text{Na}_2\text{S}_2\text{O}_5$ as the reducing agents for the leaching of trivalent cobalt oxide at Shituru plant (Congo). Also, the addition of sulphur dioxide (SO_2) as a reducing agent

facilitates the acid dissolution of laterite ore resulting in high nickel and cobalt extractions (Das et al., 1997; Das and de Lange, 2011).

Table 3. Effect of various additives on metal extractions on metal extractions during AL (2 h leaching duration, 200 g/dm³ H₂SO₄, 10% solids ratio, -74 µm particle size)

Additive	Amount (g/dm ³)	Metal Extractions (%)		
		Ni	Fe	Co
NaCl	5	89.1	76.6	98.2
	10	91.4	80.1	99.8
	20	88.4	76.1	99.5
	40	88.1	74.2	99.4
	5	83.5	72.2	97.1
Na ₂ SO ₄	10	86.0	82.4	97.6
	20	91.4	91.9	99.8
	40	86.9	88.2	97.2
	5	89.4	87.0	98.9
	10	86.4	81.3	99.9
Na ₂ O ₅ S ₂	20	84.5	80.5	99.5
	40	82.3	78.6	98.4
	5	85.4	78.4	99.4
	10	87.5	81.7	99.5
	20	91.2	83.3	99.7
KCl	40	87.1	81.0	99.4
	Without additive	2 h	86.3	73.3
			97.7	

Table 4. Effect of additives on metal extractions during AL for various leaching durations (200 g/g/dm³ H₂SO₄, 10% solids ratio, -74 µm particle size)

Additive	Duration (h)	Metal Extractions (%)		
		Ni	Fe	Co
NaCl	2	91.4	80.1	99.8
	4	96.3	80.8	99.9
	8	97.5	81.1	99.9
Na ₂ SO ₄	2	91.4	91.9	99.8
	4	95.7	93.1	99.9
	8	97.3	94.5	99.9
Na ₂ O ₅ S ₂	2	89.4	87.0	98.9
	4	92.6	92.1	99.9
	8	97.5	93.6	99.9
KCl	2	91.2	83.3	99.7
	4	96.4	82.7	99.8
	8	98.2	82.2	99.9
Without additive	4	91.1	88.4	98.1
	8	98.2	98.6	98.9

Conspicuously, NaCl and KCl provided higher nickel extractions with lower iron extractions when compared to the leaching tests performed without the additives. Here the presence of the chloride also appeared to suppress the extraction of iron though the reason for this is unclear.

As a result of these tests, it was shown that it is possible to perform the leaching tests for 4 h with NaCl or KCl additions instead of leaching at 8 h without the additives in order to achieve the similar nickel extractions.

Conclusion

In this study, agitated atmospheric leaching tests were conducted on a lateritic nickel ore sample, which contained Ni 1.2%, Fe 24.8%, and Co 0.062%. This process resulted in 98.2% of Ni, 98.6% of Fe, and 98.9% of Co extractions at 10% solid ratio, 500 rpm agitation speed, and 80 °C for 8 h leaching duration with 928 kg/Mg of H₂SO₄ consumption. As expected, the association of nickel and cobalt with iron in goethite was confirmed. Additional substances – NaCl, Na₂S₂O₅, Na₂SO₄, and KCl – were tested in order to decrease the leaching duration. Overall, the results from this study indicated that it was possible to obtain the same nickel and cobalt extractions with 16% lower iron extraction after 4 h leaching with NaCl or KCl addition in comparison with 8 h leaching without additives.

References

BUYUKAKINCI E., TOPKAYA Y.A., 2009, *Extraction of nickel from lateritic ores at atmospheric pressure with agitation leaching*, Hydrometallurgy, 97, 33-38.

CHANDER S., 1982, *Atmospheric pressure leaching of nickeliferous laterites in acidic media*, Transactions of the Indian Institute of Metals, 35, 366-371.

CHANG Y.F., ZHAI X.J., LI B.C., FU Y., 2010, *Removal of iron from acidic leach liquor of lateritic nickel ore by goethite precipitate*, Hydrometallurgy, 101, 84-87.

CHONG S., HAWKER W., VAUGHAN J., 2013, *Selective reductive leaching of oxidised cobalt containing residue*, Minerals Engineering, 54, 82-87.

DALVI A., BACON G., OSBORNE R.C., 2004, *The Past and the Future of Nickel Laterites*, PDAC International Convention, Trade Show & Investors Exchange.

DAS G.K., ANAND S., DAS R.P., MUIR D.M., SENANAYAKE G., SINGH P., HEFTER G., 1997, *Acid leaching of nickel laterites in the presence of sulphur dioxide at atmospheric pressure*, In: Cooper, W.C., Mihaylov, I. (Eds.), Proceedings of the Nickel–Cobalt 97 International Symposium: Hydrometallurgy and Refining of Nickel and Cobalt, Vol. 1. Canadian Institute of Mining Metallurgy and Petroleum, pp. 471-488.

DAS G.K., DE LANGE J.A.B., 2011, *Reductive atmospheric acid leaching of West Australian smectitic nickel laterite in the presence of sulphur dioxide and copper (II)*, Hydrometallurgy, 105, 264-269.

JOHNSON J.A., MCDONALD R.G., WHITTINGTON B.I., QUAN L.P., MUIR D.M., 2002, *Process water salinity effects in the pressure acid leaching of Cawse nickel laterite ore*, In: Peek E., Van Weert G. (Eds.), Chloride Metallurgy 2002, 1. Canadian Institute of Mining, Metallurgy and Petroleum, Montreal, pp. 339-354.

JOHNSON J.A., WHITTINGTON B.I., 2004, *Effect of ammonium, sodium and potassium sulphates and chlorides in the pressure acid leaching of Western Australian nickel laterite ores*, In: Collins M.J., Papangelakis V.G. (Eds.), Pressure Hydrometallurgy 2004. Canadian Institute of Mining, Metallurgy and Petroleum, Montreal, pp. 199-214.

JOHNSON J.A., CASHMORE B.C., HOCKRIDGE R.J., 2005, *Optimization of nickel extraction from laterite ores by high pressure acid leaching with addition of sodium sulphate*, Minerals Engineering, 18, 1297-1303.

KAYA S., TOPKAYA Y.A., 2011, *High pressure acid leaching of a refractory lateritic nickel ore*, Minerals Engineering, 24, 1188-1197.

KRAUSE E., SINGHAL A., BLAKELY B.C., PAPANGELAKIS V.G., GEORGIOU D., 1997, *Sulphuric acid leaching of nickeliferous laterites*, In: Cooper, W.C., Mihaylov, I. (Eds.), Proc. Nickel-Cobalt 97 International Symposium, 1. Canadian Institute of Mining, Metallurgy and Petroleum, Montreal, pp. 441-458.

LOVEDAY B.K., 2008, *The use of oxygen in high pressure acid leaching of nickel laterites*, Minerals Engineering, 21, 533-538.

MCDONALD R.G., WHITTINGTON B.I., 2008, Atmospheric acid leaching of nickel laterites review Part I. Sulphuric acid technologies, Hydrometallurgy, 91, 35-55.

MWEMA M.D., MPOYO M., KAFUMBILA K., 2002, *Use of sulfur dioxide as reducing agent in cobalt leaching at Shituru hydrometallurgical plant*, Journal of the South African Institute of Mining and Metallurgy, (January/February), 1-4.

NEUDORF D., 2007, *Atmospheric Leaching Forum*, ALTA 2007 Nickel/Cobalt 12. ALTA Metallurgical Services, Melbourne. pp.5.

SCHWERTMANN U., 1991, *Solubility and dissolution of iron oxides*, Plant and Soil 130, 1-25.

WHITTINGTON B.I., MCDONALD R.G., JOHNSON J.A., MUIR D.M., 2003, *Pressure acid leaching of arid region nickel laterite ore Part I. Effect of water quality*, Hydrometallurgy, 70, 31-46.

WHITTINGTON B.I., JOHNSON J.A., 2005, *Pressure acid leaching of arid-region nickel laterite ore. Part III: Effect of process water on nickel losses in the residue*, Hydrometallurgy, 78, 256-263.

Received September 28, 2014; reviewed; accepted May 19, 2015

ENHANCING FILTRATION RATE OF NEW VALLEY OXIDIZED PHOSPHATE CONCENTRATE WITH ADDITIVES

El-Sayed ABDEL-AAL*, Emad ABDEL RAHMAN**, Abdel-Hakim KANDIL***

* Central Metallurgical R&D Institute, P.O. Box 87 Helwan, Cairo, Egypt; eabde2@gmail.com

** Egypt Phosphate Company, New Valley, El-Kharga Oasis, Abu-Tartur, Egypt

***Chemistry Department, Faculty of Science, Helwan University, Cairo, Egypt

Abstract: Phosphoric acid is utilized for production of fertilizers. It is mainly produced by wet processes, in which phosphate concentrate, produce by several operations including crushing, scrubbing, classification, attritioning, and desliming, is leached with sulfuric acid with coproduction of calcium sulfate dihydrate (phosphogypsum). The New Valley oxidized phosphate concentrate was processed for phosphoric acid production by addition of certain additives to improve gypsum filtration through modifying its morphology and particle size distribution. The additives used were cetylpyridinium chloride (CPC) as a cationic surfactant, sodium dodecyl sulfate (SDS) as an anionic surfactant and sulfonic acid (SA). The applied dosages ranged from 0.25 to 2.5 kg additive/Mg P₂O₅ in the phosphate concentrate. The filtration rate of the New Valley oxidized phosphate concentrate is 3.6 Mg P₂O₅ /m²·day without additives. The filtration rate was increased by 33% and 31% with 1 and 0.8 kg/Mg P₂O₅ doses of CPC surfactant and sulfonic acid (SA), respectively. On the other hand, the filtration rate was decreased by 33% with addition of 1 kg/Mg P₂O₅ dose of SDS. The aspect ratios of gypsum crystals were 6:1, 3:1, 3:1 and 12:1 without additive, with CPC, SA and SDS surfactant, respectively. Reaction efficiencies without and with 0.8 kg/Mg P₂O₅ of CPC, SA and SDS dose of additives were 95.0%, 97.9%, 97.9% and 94.7%, respectively. The P₂O₅ recoveries without and with 0.8 kg/Mg P₂O₅ of CPC, SA and SDS dose of additives were 92.6%, 95.5%, 95.8% and 90.8%, respectively.

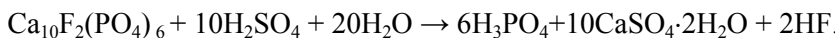
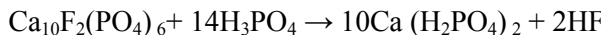
Keywords: New Valley phosphate concentrate, surfactant, filtration rate, gypsum morphology, crystal size distribution

Introduction

The necessity of securing food for the rapidly increasing human population requires increasing the cultivated area as well as its quality by the application of fertilizers. Phosphatic fertilizers are produced from phosphate rocks which are abundant all over Egypt (New Valley, Nile Valley and Red Sea).

Phosphoric acid (H₃PO₄) is an important intermediate product for production of phosphatic fertilizers and also it used in other areas of chemical industries. In fertilizer

production it serves as an intermediate material between phosphate ore and major end products such as ammonium phosphates, triple superphosphate, liquid fertilizers and some types of nitric phosphates. Phosphoric acid is mainly produced by a dihydrate process in which phosphate ore concentrates are leached with sulfuric acid (H_2SO_4) and recycled weak phosphoric acid to produce phosphoric acid and gypsum. Each year, more than 25 teragrams (Tg) of P_2O_5 equivalent phosphoric acid is produced by this method in the world (Becker, 1989). The reactions of this process are as follows (El-Shall et. al, 1999):



The total reaction is fast. It takes from 2 to 10 minutes, depending on phosphate reactivity and process conditions. However, the crystallization of gypsum extends for a long time (2-8 hours) (Becker, 1989). Productivity of phosphoric acid depends mainly on the gypsum filtration. A high production capacity with low operating costs can be achieved if the filtration rate is increased. It is known that the filtration rate depends on the characteristics of the filter cake such as crystal size, size distribution and morphology of the crystals. Therefore, enhancing the formation of large and uniform gypsum crystals is desired in achieving better filtration rate in the phosphoric acid manufacture (Abdel-Aal, 1984, 1989, 2004).

The basic objective of the phosphoric acid manufacture is to obtain the highest concentration of phosphoric acid possible with the maximum yield (Becker, 1989; Slack, 1968). The yield is dependent on the completeness of the reaction of phosphate concentrate with sulfuric acid, the efficiency of separation of phosphoric acid from calcium sulfate and the quantity of wash water required to remove essentially all P_2O_5 from the calcium sulfate during the filtration (Becker, 1989; Slack, 1968).

Many materials are tested for enhancing crystallization of calcium sulfate dihydrate including aluminum sulfate, clay, calcined clay (Abdel-Aal, 1989), aluminum hydroxide, perlite, active silica, active charcoal, manganese dioxide (Ismail, 1997; Abdel-Aal et al., 2004), polymers (Amjad and Hooley, 1986; Kerr et al., 1991; Zhu, 1996), surfactants (El-Shall et al., 1999, 2000, 2005; Mahmoud et al., 2004; Abdel-Aal et al. 2007), phosphonate (El-Shall et al., 2002; Tadros and Mayes, 1997), foreign ions (Rashad et al., 2004; De Vreugd et al., 1994), carboxylic acids (Tadros and Mayes, 1997; Badens et al., 1999; Rashad et al., 2005), and other organic additives such as EDTA and gelatin (Liu and Nacollas, 1973). In addition, studies about crystallization of other calcium salts such as calcium oxalate and calcium phosphate with and without additives at different levels of supersaturation are reported (El-Shall

et al., 2004a; 2004b; Abdel-Aal et al., 2008; 2009). The mechanism for enhancing filtration rate by organic additives is discussed elsewhere (El-Shall et al., 1999).

Phosphoric acid production from the New Valley phosphate concentrate suffers from poor gypsum filtration. This problem affects feasibility study for production of phosphoric acid from the New Valley phosphate concentrate of 1 petagram (Pg) estimated potential reserves. The New Valley phosphate rock has a good potential of rare earths metals source (Ismail and Abdel-Aal, 1990; Abdel-Aal and Amer, 1995; Abdel-Aal et al., 1998).

A low filtration rate requires large filter areas which means high capital and operation costs. It is worth mentioning that, generally in phosphoric acid plants, the capital cost of filtration unit is about 50% of the total cost of the plant. So, enhancing the filtration rate of phosphoric acid produced from the New Valley phosphate concentrate is very important for the project to be economically feasible.

The main objective of this paper is to enhance filtration rate of phosphoric acid produced from the New Valley phosphate by addition of different organic additives.

Experimental

Materials and reagents

The chemical analysis of the New Valley phosphate concentrate is given in Table 1.

Table 1. Chemical analysis of New Valley phosphate concentrate

Constituent, %	Phosphate concentrate
P ₂ O ₅	31.6
CaO	44.5
SiO ₂	3.2
Fe ₂ O ₃	3.7
Al ₂ O ₃	0.6
MgO	0.1
Na ₂ O	0.9
K ₂ O	0.2

The run of mine phosphate ore is concentrated by crushing followed by scrubbing to reject +2 mm oversize, and then by classification at 0.149 mm. Attritioning of the classifier undersize -2.0 +0.149 mm is performed followed by desliming to get primary concentrate. The concentration and density of the used sulfuric acid were 97.99% and 1.825 g/cm³ while the phosphoric acid concentration and density were 85% (61.58% P₂O₅) and 1.689 g/cm³, respectively. The phosphoric acid was used to prepare solution containing 20% P₂O₅. Organic additives used in enhancing or retarding the growth rate of gypsum were cetylpyridinium chloride (CPC)

$C_{21}H_{38}ClN \cdot H_2O$ (cationic surfactants), sodium dodecyl sulfate (SDS) $C_{12}H_{25}NaO_4S$ (anionic surfactants) and sulfonic acid (carboxylic acid).

Experimental procedure

The reaction between phosphate concentrate and sulfuric acid was performed in a 1 dm³ covered reactor. The solution was heated to 80 °C using a water bath. The electric mechanical stirrer speed was 450 rpm. The calculated amount of recycle acid (~20 % P_2O_5) was put in the reaction vessel. The calculated amount of phosphate concentrate was added continuously for 1 hour using a vibrating rock feeder. Sulfuric acid was added continuously for 1 hour using a peristaltic dosing pump. The calculated amount of additive solution was added continuously for 1 hour using a peristaltic dosing pump. The slurry was stirred using an electrical mechanical stirrer with propelling shaft mounted through an opening of the beaker cover to avoid losses of solution by evaporation. The reaction system and the experimental procedures were given in our previous work (El-Shall et al., 1999). The filtration process was performed using a Buchner type filter funnel. The slurry was poured on an 8.5 cm diameter filter funnel with a polypropylene filter cloth. The suction was induced by a vacuum pump. The applied pressure difference was 0.67 Bar. The filtration system was described in our previous work (El-Shall et al., 1999). The filtration time was recorded when the surface of the cake was no longer wetted. The gypsum cake was then washed three times using heated solutions. The times of washing stages were recorded. Chemical analyses of filter acid as well as gypsum were performed according to the standard methods of analysis using a Shimadu UV-VIS recording spectrophotometer UV-160 with a double beam. The produced acid after filtration contained about 28 % P_2O_5 and 2.5 % sulfate. The most important are the P_2O_5 and sulfate contents. The range of P_2O_5 content in the filter acid was from 27 to 29% while sulfate range is from 2.0 to 3.0%. The P_2O_5 content was analyzed using the colorimetric method (Vogel, 1978). This method is applied for the P_2O_5 of filter acid and phosphate concentrate. Different methods for the chemical analysis of phosphates, phosphoric acid and gypsum were reported (Young, 1971).

Calculations of filtration rate, reaction efficiency and P_2O_5 recovery

The total filtration time is defined as a sum of the filtration time of product acid and washing time of gypsum. Reaction efficiency (digestion or process efficiency, in percent of extraction or conversion) is defined as the percent of P_2O_5 removed from the phosphate concentrate into solution, because some of P_2O_5 is lost with incompletely washed gypsum. The reaction efficiency is calculated from the following equation (El-Shall et al., 1999):

$$\text{Reaction efficiency} = 100 - 94 \cdot (A - B) \cdot C / (D \cdot E)$$

where A is the total P_2O_5 in gypsum cake, B water-soluble P_2O_5 in gypsum cake, C CaO in phosphate concentrate used to make the acid, D P_2O_5 in phosphate concentrate used to make the acid and E CaO in gypsum cake. Parameters from A to E are given in percent. Also P_2O_5 recovery (either overall or plant efficiency, or yield) is defined as the percent of P_2O_5 passing from the phosphate concentrate into the produced phosphoric acid. It can be calculated as follows (El-Shall et al., 1999):

$$P_2O_5 \text{ recovery} = 100 - (94 - A \cdot C) / (D \cdot E).$$

The filtration rate (FR) is calculated as follows:

$$F.R. = \frac{X \cdot P_2O_5 \% \cdot K_{re} \cdot 10^4 \cdot 86400}{100 \cdot 100 \cdot 10^6 \cdot A \cdot T}$$

where FR is filtration rate, $Mg\ P_2O_5/m^2 \cdot day$, X weight of concentrate used, $g\ P_2O_5$ in phosphate concentrate, K_{re} P_2O_5 recovery, 10^4 conversion factor from cm^2 to m^2 , 86400 conversion factor from seconds to day, 10^6 conversion factor from g to Mg , A active filter area, cm^2 and T total time of filtration and washing, in seconds.

Results and discussion

Chemical processing without additives

Leaching and filtration data

Tests were carried out under the optimum leaching and filtration conditions (El-Shall, 1999). The obtained results are given in Table 2. The average filtration rate, reaction efficiency and P_2O_5 recovery, are $3.6\ Mg\ P_2O_5/m^2 \cdot day$, $95.0\ %$ and $92.6\ %$, respectively.

Table 2. Results of leaching and filtration of New Valley phosphate concentrate without additives (Ismail, 1997)

Experiment Number	Filtration Rate, $MgP_2O_5/m^2 \cdot day$	Reaction Efficiency, %	P_2O_5 Recovery, %
1	3.6	95.7	93.2
2	3.5	94.7	92.4
3	3.8	96.7	94.3
4	3.5	94.2	92.0
5	3.5	93.7	91.0
Average	3.6	95.0	92.6

Gypsum quality and morphology

The chemical composition and density of co-produced gypsum is given in Table 3. This table shows that the quality of gypsum is good as it contains low levels of impurities. A scanning electron microscope picture of gypsum crystals in the absence

of additives is given in Fig. 1 which indicates that the shape of obtained crystals are needle type crystals with average aspect (length to width) ratio about 6:1. These crystals are difficult to filter and wash during phosphoric acid production (Rashad et al., 2003).

Table 3. Chemical analysis and physical properties of New Valley gypsum cake

Constituent	Gypsum cake, wt. %, dry basis
Total P ₂ O ₅	0.83
Water-Soluble P ₂ O ₅	0.38
Citrate-Soluble P ₂ O ₅	0.40
CaO	31.7
SO ₄ ²⁻	49.6
SiO ₂	1.60
Fe ₂ O ₃	1.01
Al ₂ O ₃	0.16
MgO	0.04
Na ₂ O	0.22
K ₂ O	0.015
Density, g/ml	2.29

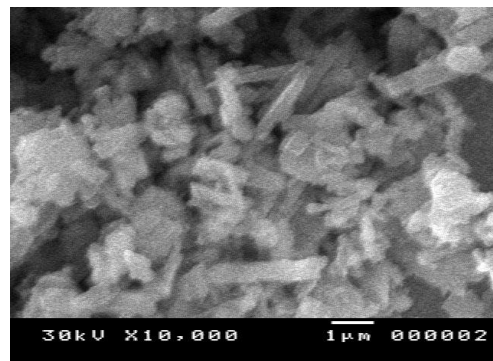


Fig. 1. SEM of gypsum crystals in absence of additives

Chemical processing with cetylpyridinium chloride (CPC)

The effect of different dosages of cetylpyridinium chloride (CPC) from 0.25 kg/Mg P₂O₅ to 2.5 kg/Mg P₂O₅ on filtration rate, reaction efficiency and P₂O₅ recovery were studied as shown in Table 4. The obtained results revealed that with increasing dose of CPC, the filtration rate increased from 3.6 Mg P₂O₅/m²·day to 4.8 Mg P₂O₅/m²·day. Also, it was found that with increasing dose of CPC, the reaction efficiency increased from 95.0% to 97.6% and the P₂O₅ recovery was increased from 92.6% to 95.9. The

optimum CPC dose is 1 kg/Mg P₂O₅, which gives the highest filtration rate of 4.8 Mg P₂O₅/m²·day.

The SEM of the gypsum crystals in the presence 1 kg/Mg P₂O₅ of CPC is given in Fig. 2. The majority of these crystals are tabular and are not uniform crystals. The average aspect ratio decreased to about 3:1, compared to the ratio of 6:1 without additives. This means that relatively thicker and larger crystals were formed. CPC increases both the mean diameter, nucleation rate and the crystal growth rate of gypsum (El-Shall et al., 2005). CPC may be adsorb on 101 plane of gypsum crystals enhancing filtration rate as Al ions do (Abdel-Aal, 1989).

Table 4. Results of leaching and filtration of New Valley phosphate concentrate with cetylpyridinium chloride (CPC) surfactant

Experiment Number	Dose of CPC surfactant, kg/Mg P ₂ O ₅	Filtration rate, MgP ₂ O ₅ /m ² ·day	Reaction efficiency, %	P ₂ O ₅ recovery, %
1	0	3.6	95.0	92.6
2	0.25	4.3	97.4	95.5
3	0.5	4.5	97.6	95.5
4	0.8	4.6	97.9	95.5
5	1.0	4.8	97.6	95.9
6	1.25	4.4	97.7	95.8
7	1.5	4.2	97.9	95.6
8	2.5	3.7	97.9	96.0

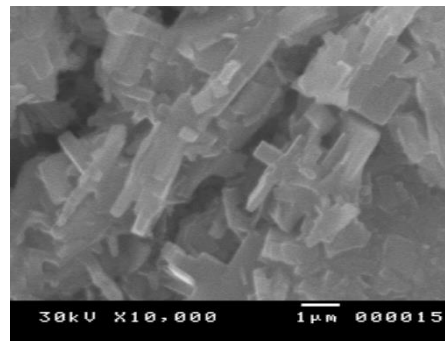


Fig. 2. SEM of gypsum crystals with 1 kg/Mg P₂O₅ of cetylpyridinium chloride

Chemical processing with sulfonic acid (SA)

The effect of different dosages of sulfonic acid from 0.25 kg/Mg P₂O₅ to 2.5 kg/Mg P₂O₅ on filtration rate, reaction efficiency and P₂O₅ recovery were studied as shown in Table 5. The results revealed that with addition of 0.8 kg/Mg P₂O₅ SA the filtration rate was increased from 3.6 to 4.7 Mg P₂O₅/m²·day. At this dose of SA the reaction efficiency was increased from 95.0% to 96.5% and the P₂O₅ recovery was increased

from 92.6% to 95.8%. A further increase of sulfonic acid leads to a decrease of the filtration rate.

Table 5. Results of leaching and filtration of New Valley phosphate concentrate with sulfonic acid

Experiment number	Dose of sulfonic acid, kg/Mg P ₂ O ₅	Filtration rate, Mg P ₂ O ₅ /m ² ·day	Reaction efficiency %	P ₂ O ₅ recovery %
1	0	3.6	95.0	92.6
2	0.25	4.0	97.8	95.7
3	0.5	4.4	97.8	96.2
4	0.8	4.7	97.9	95.8
5	1.0	3.7	98.1	96.0
6	1.25	3.4	98.1	96.3
7	1.5	3.1	98.2	96.6
8	2.5	3.0	98.2	96.6

The SEM of the gypsum crystals with 0.8 kg/Mg P₂O₅ of sulfonic acid is given in Fig. 3. The majority of these crystals are tabular and their shapes are mostly uniform. The average aspect ratio decreased to about 3:1 compared to the ratio of 6:1 without additives. This means that relatively thicker and larger crystals are formed. It appears that SA has a similar mechanism as CPC. This is apparent from the average particle size of baseline (without surfactant), with CPC and with SA as 5.9, 8.9 and 8.2 micrometer, respectively. So, sulfonic acid increases both the mean diameter, nucleation rate and crystal growth rate of gypsum crystals. Also, SA may be adsorbed on 101 gypsum plane enhancing filtration rate as Al ions do (Abdel-Aal, 1989).

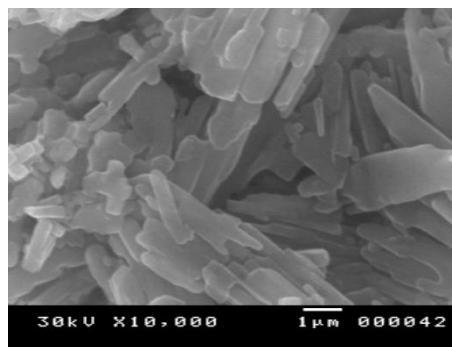


Fig. 3. SEM of gypsum crystals with 0.8 kg/Mg P₂O₅ of sulfonic acid

Chemical processing with sodium dodecyl sulfate (SDS)

The effect of different dosages of SDS from 0.25 kg/Mg P₂O₅ to 2.5 Kg/Mg P₂O₅ on filtration rate, reaction efficiency and P₂O₅ recovery were studied as shown in Table 6. The obtained results reveal that with increasing the dose of SDS, the filtration rate decreased. Also, it was found that with increasing the dose of SDS, the reaction efficiency and the P₂O₅ recovery decreased.

Table 6. Results of leaching and filtration of New Valley open-cast phosphate concentrate with sodium dodecyl sulfate (SDS) surfactant

Experiment number	Dose of (SDS) surfactant, kg/Mg P ₂ O ₅	Filtration rate, Mg P ₂ O ₅ /m ² .day	Reaction efficiency %	P ₂ O ₅ recovery %
1	0	3.6	95.0	92.6
2	0.25	3.3	95.3	90.9
3	0.5	2.7	95.1	90.6
4	0.8	2.7	94.7	90.8
5	1.0	2.4	93.9	90.0
6	1.25	2.4	94.0	90.7
7	1.5	2.3	93.8	89.3
8	2.5	2.2	93.7	89.7

The SEM of the gypsum crystals with 1 kg/Mg P₂O₅ of SDS is given in Fig. 4. It is apparent that SDS surfactant helps to form needle-type and some plate-like crystals. The nonuniform mixture of crystals gives relatively low filtration rate. The average length to width ratio was decreased to about 12:1 compared to the ratio of 6:1 without additives.

It appears that SDS works by an opposite mechanism as the CPC surfactant. The average particle size without surfactant, with CPC and with SDS were 5.9, 8.9 and 4.8 μ m, respectively. So, SDS decreases the mean diameter, nucleation rate and the crystal growth rate of gypsum crystals.

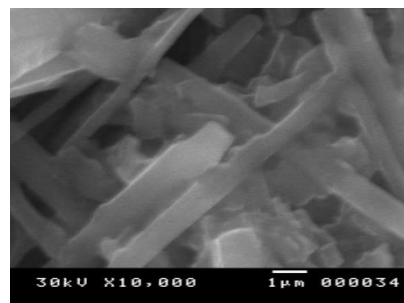


Fig. 4. SEM of gypsum crystals with 1 kg/Mg P₂O₅ of sodium dodecyl sulfate

Conclusion

The filtration rate of the New Valley oxidized phosphate concentrate is low (about 3.6 Mg P₂O₅/m²·day). The filtration rates were calculated without and with different dosages ranging from 0.25 to 2.5 kg additive/Mg P₂O₅ in phosphate concentrate from cetylpyridinium chloride surfactant (CPC), sodium dodecyl sulfate surfactant (SDS) and sulfonic acid (SA). The filtration rate was increased by 33% and 31% with 1.0 and 0.8 kg/Mg P₂O₅ doses of CPC and SA, respectively. On the other hand, the filtration rate decreased by 33% with addition of 1 kg/Mg P₂O₅ of SDS.

The aspect ratios of gypsum crystals were 6:1, 3:1, 3:1 and 12:1 without additive, with CPC, with SA and with SDS, respectively. Reaction efficiencies and P₂O₅ recoveries increased with CPC and SA in comparison without the additives. Addition of SDS decreased the reaction efficiencies and P₂O₅ recoveries.

References

ABDEL-AAL E.A., 1984, *Comparative Study on Phosphoric Acid Production from Egyptian Phosphate Ore Concentrates by the Wet Process*, M. Sc. Thesis, Chemistry Department, Faculty of Science, Cairo University, Cairo, Egypt.

ABDEL-AAL E.A., 1989, *Industrial Simulation for Wet Process Phosphoric Acid Production*, Ph.D. Thesis, Chemistry Department, Faculty of Science, Cairo University, Cairo, Egypt.

ABDEL-AAL E.A., 2004, *Crystallization of phosphogypsum in continuous phosphoric acid industrial plant*, Cryst. Res. Technol. 39, No. 2, 121 – 128.

ABDEL-AAL E.A., IBRAHIM I.A., MAHMOUD M.H.H., EL-SHALL H., ISMAIL A.K., 2002, *Improvement of phosphoric acid production parameters from Egyptian phosphor-concentrate through inorganic and organic additives*, Proc. Mineral Processing Technology Conference, Bangalore. Regional Research Laboratory, India, 85-93.

ABDEL-AAL E.A., RASHAD M.M., EL-SHALL H., 2004, *Crystallization of calcium sulfate dihydrate at different supersaturation ratios and different free sulfate concentrations*, Cryst. Res. Technol. 39, No. 4, 313 – 321.

ABDEL-AAL E.A., MAHMOUD M.H.H., EL-SHALL H., ISMAIL A.K., 2007, *Increasing the filtration rate of phospho-gypsum using surfactant*, Hydrometallurgy 85, 53-58.

ABDEL-AAL E.A., AMER A.M., 1995, *Evaluation of Sebaya-West Phosphate Concentrate For Nitrophosphate Fertilizer Production*, Minerals Engineering Journal 8, No. 10, 1995, 1221-1230.

ABDEL-AAL E.A., IBRAHIM I.A., MAHMOUD M.H.H., ISMAIL A.K., 1998, *Industrial Simulation of Continuous Leaching and Filtration Processes; Case Study of Phosphoric Acid Production*, Acta Metallurgica Slovaca 4, Special Issue 1, 25-32.

ABDEL-AAL E.A., EL-MIDANY A.A., EL-SHALL H., 2008, *Mechanochemical-Hydrothermal Preparation of Nano-crystallite Hydroxyapatite Using Statistical Design*, Materials Chemistry and Physics 112, 202-207.

ABDEL-AAL E.A., DAOSUKHO S., EL-SHALL H., 2009, *Effect of supersaturation ratio and Khella extract on nucleation and morphology of kidney stones*, J. Cryst. Growth 311, 2673-2681.

EL-SHALL H., JIN-HWAN J., ABDEL-AAL E.A., KHAN S., GOWER L., RABINOVICH Y., 2004 A, *A study of primary nucleation of calcium oxalate monohydrate: I-Effect of supersaturation*, Cryst. Res. Technol. 39, No. 3, 214 – 221.

EL-SHALL H., JIN-HWAN J., ABDEL-AAL E.A., KHAN S., GOWER L., RABINOVICH Y., 2004 B, *A study of primary nucleation of calcium oxalate monohydrate: II-Effect of urinary species*, Cryst. Res. Technol. 39, No. 3, 222-229.

AMJAD Z., HOOLEY J., 1986, *Influence of Polyelectrolytes on the Crystal Growth of Calcium Sulfate Dihydrate*, J. Colloid Interface Sci. 111, 2, 496-503.

BADENS E., VEESLER S., BOISTELLE R., 1999, *Crystallization of Gypsum From Hemihydrate in Presence of Additives*, J. Cryst. Growth 198/199, 704-709.

BECKER P., 1989, *Phosphates and Phosphoric Acid: Raw Materials, Technology and Economics of the Wet Processes*, Marcel Dekker, Inc., New York, USA.

DE VREUGD C.H., WITKAMP G.J., ROSMALEN G.M.V., 1994, *Growth of gypsum III. Influence and incorporation of lanthanide and chromium ions*, J. Cryst. Growth 144, 70-78.

EL-SAYED A., ABDEL-AAL, 2000, *Recovery of Phosphoric Acid From Egyptian Nile Valley Phosphate Tailings*, Minerals Engineering Journal 13, No. 2, 223-226.

EL-SHALL H., ABDEL-AAL E.A., MOUDGIL B., 1999, *Cost-Effective Reagents as Defoamers and Crystal Modifiers to Enhance the Filtration of Phosphogypsum*, Serial No. 01-141-162, Florida Institute of Phosphate Research (FIPR), FL, USA.

EL-SHALL H., MOUDGIL B., ABDEL-AAL E.A., 2000, *Effect of surfactants on phospho-gypsum crystallization and filtration during wet-process phosphoric acid production*, Separation Science and Technology 35, No. 3, 395-410.

EL-SHALL H., RASHAD M.M., ABDEL-AAL E.A., 2002, *Effect of phosphonate additive on crystallization of gypsum in phosphoric and sulfuric acid medium*, Cryst. Res. Technol. 37, 12, 1264-1273.

EL-SHALL H., RASHAD M.M., ABDEL-AAL E.A., 2005, *Effect of Cetyl Pyridinium Additive on Crystallization of Gypsum in Phosphoric and Sulfuric Acids Medium*, Cryst. Res. Technol. 40, No. 9, 860 - 866.

ISMAIL A.K., August 1997, *Chemical processing of Abu-Tartur Phosphate Concentrate for Phosphoric Acid Production*, Internal Report, Abu-Tartur Phosphate Project, Ministry of Industry and Mineral Wealth, Cairo, Egypt.

ISMAIL A.K., ABDEL-AAL E.A., *Evaluation of Abu-Tartur Phosphate as a potential Resource for Rare Earth Metals*, Rare Metals'90 37-41.

KERR E.M., CONNELLY L.J., ROE W.J., VALLOWE R.M., 1991, *Crystal Modification in Wet Process Phosphoric Acid*, U.S. Patent 5,009, 873.

LIU S.T., NANCOLLAS G.H., 1973, *The Crystal Growth of Calcium Sulfate Dihydrate in the Presence of Additives*, J. Colloid Interface Sci. 44, 3, 422-429.

MAHMOUD M.H.H., RASHAD M.M., IBRAHIM I.A., ABDEL-AAL E.A., 2004, *Crystal Modification of Calcium Sulfate Dihydrate in the Presence of Some Surface-Active Agents*, J. Colloid Interface Sci. 270, 99-105.

RASHAD M.M., BAIOMY H.M., ABDEL-AAL E. A., 2003, *Structural and spectral studies on gypsum crystals under simulated conditions of phosphoric acid production with and without organic and inorganic additives*, Cryst. Res. Technol. 38, 6, 433-439.

RASHAD M.M., MAHMOUD M.H.H., IBRAHIM I.A., ABDEL-AAL E.A., 2004, *Crystallization of Calcium Sulfate Dihydrate under Simulated Conditions of Phosphoric Acid Production in the Presence of Aluminum and Magnesium Ions*, J. Cryst. Growth 267, 372-379.

RASHAD M.M., MAHMOUD M.H.H., IBRAHIM I.A., ABDEL-AAL E.A., 2005, *Effect of Citric Acid and 1,2- Dihydroxybenzene 3,5-disulfonic Acid on Crystallization of Calcium Sulfate Dihydrate Under Simulated Conditions of Phosphoric Acid Production*, Cryst. Res. Technol. 40, No. 8, 741-747.

SLACK A.V., 1968, *Phosphoric Acid*, Marcel Dekker, Inc., New York, USA.

TADROS M.E., MAYES I., 1997, *Linear growth rates of calcium sulfate dihydrate crystals in the presence of additives*, J. Colloid Interface Sci. 72, 245–254.

VOGEL A.I., 1978, *A Textbook of Quantitative Inorganic Analysis including Elementary Instrumental Analysis*, fourth ed., Longman Inc., New York, USA.

YOUNG R.S., 1971, *Chemical Analysis in Extractive Metallurgy*, Canada.

ZHU S., 1996, *Modification of Crystal Size Distribution for Enhanced Filtration of Phosphogypsum Using Poly (Ethylene Oxide)*, Ph.D. Thesis, University of Florida, U.S.A.

Received December 14, 2014; reviewed; accepted May 18, 2015

ELECTRO-DEPOSITION PARAMETERS OF BORON CARBONITRIDE (BCN) FROM BORAX PENTAHYDRATE ($\text{Na}_2\text{B}_4\text{O}_7 \cdot 5\text{H}_2\text{O}$)

Baran TUFAN*, **Turan BATAR****

* Dokuz Eylul University, Department of Mining Engineering, 35390, Buca, Izmir, baran.tufan@deu.edu.tr

** Gediz University, Department of Mechanical Engineering, Seyrek, Izmir

Abstract: The primary objective of this research is the fabrication of boron end products from boron derivatives by electro-deposition as powder or coating. The production of boron carbonitride is achieved by electro-deposition at low temperatures without carbon dioxide emission, regardless of sintering and thermal treatment. The extensive usage of boron is aimed and should be accomplished by application of electro-deposition method for boron carbonitride fabrication.

Keywords: *electro-deposition, boron carbonitride, borax pentahydrate, low temperature*

Introduction

Turkey has the most abundant boron reserves in the world, however the boron end products to be used in advanced technology are not available since the existing production plants in Turkey do not fit the requirements and technology to produce high-end and sophisticated boron products. The production of boron end products such as boron carbide (B_4C , BC_5 and B_{13}C_2), boron nitride (BN) and boron carbonitride (BCN) are possible in industrial scale (Tufan and Batar, 2014). However such procedures require great energy consumption and also result in environmental problems such as CO_2 emission.

A technology for obtaining material based boron nitride and boron carbide powders, called boron carbonitride (BCN), was developed more than three decades ago. Since then, boron carbonitride has been used in various areas of high temperature technology. However, its structure has not been conclusively studied so far. It has been hypothesized that in addition to the starting components (BN, B_4C), a third phase of the B-N-C compound type was present in the material (Ulrich et al, 2005). Evidence for this finding arises from the properties of boron carbonitride, which differ

from the properties of a mechanical mixture of the starting components, and specifically, from the substantial increase in the crystal lattice parameter c of BN and a decrease in the B_4C content during reactive sintering. The sinterability of the material was also explained by the formation of a ternary B-N-C compound, since the components BN and B_4C themselves were not sintered under the synthesis conditions (Grigorev et al, 2005).

BCN can be synthesized through different routes, including thermolysis of organic, inorganic and polymeric precursors. Arc-methods and laser ablation may additionally be used for direct synthesis of BCN, utilizing solid state sources of B, C and a N compound. The BCN synthesis method, utilizing a substitution reaction where the high temperature reaction (2000 K) of carbon nanotubes performed, can be managed within a stream of gaseous nitrogen or NH_3 or in the presence of B_2O_3 powder, CuO and Au_2O_3 (Blank et al, 2009; Zhi et al, 2002; Zhuge and Yamanaka, 2008).

There has been much effort to synthesize the new BCN phase by various techniques such as nitriding of solid phase precursors at relatively high temperatures, gas phase reactions using CVD techniques and solid phase's pyrolysis (Watanabe et al, 1996). However, few reports consider solvothermal synthesis of boron carbonitride phase. Recently, the solvothermal technique has attracted much attention and has been used to synthesis some important semiconductors (Mannan et al, 2008). In a study by Huang et al. (2004), a solvothermal reaction of $CH_3CN \cdot BCl_3$ and lithium nitride (Li_3N) using benzene as the solvent has been successfully applied to prepare boron carbonitride at 300 °C and less than about 7 MPa. X-ray photoelectron spectroscopy and Fourier transform infrared spectroscopy were used to confirm their chemical composition and atomic-level hybrid. X-ray diffraction and transmission electron diffraction analysis indicated that the powders had hexagonal network structures.

BCN films were deposited by plasma-assisted chemical vapor deposition (PACVD) at 390°C by Aoki et al. (2008). A Si wafer, used as a substrate, was placed in a quartz reactor and source gases were introduced into the reactor. Boron trichloride (BCl_3), methane (CH_4), and nitrogen (N_2) were used as source gases. A radio frequency (RF) power of 80W was supplied to produce N_2 remote plasma by induction coupling. BCl_3 was transported with hydrogen (H_2) gas near the substrate. The substrate temperature was maintained at 390 °C using an infrared lamp. The deposition time was 30 min. BCN films with thicknesses of 150–250 nm were prepared in this experiment.

Transparent and hard BCN films were deposited on polycarbonate and silicon wafer by means of different radio frequency plasma-assisted chemical vapor deposition conditions with two liquid organic compounds as precursors by Ahn et al. (2003). The mechanical and optical properties of BCN films deposited were characterized by nano-indentation. The chemical composition of BCN films was determined by Rutherford backscattering spectroscopy and elastic recoil detection analysis. The influence of the plasma parameters on the mechanical and optical

properties of films was described. Hard and transparent BCN films with low refractive index were deposited through low-energy and high-density ion.

Wohle et al. (1999) have given an overview of the plasma-assisted techniques for coating ceramics on polymer substrates at low temperature. Deposition of boron carbon nitride was carried out on polycarbonate substrates by a radio-frequency plasma-assisted chemical vapor deposition process using different metallo-organics as precursors. The films deposited were found to be stable and adherent under ambient conditions. The chemical composition of the layers varied in a wide range. Nearly stoichiometric BCN layers, as well as films with high carbon content, were obtained. The chemical bonding of boron, carbon and nitrogen was analyzed by X-ray photoelectron spectroscopy.

In a study by Torres et al. (2007), ternary boron-carbon-nitrogen (BCN) compounds have been prepared as nano-metric powders by low-energy ball milling, using as precursors h-BN, graphite and polypropylene micrometric powders. Different proportions of the reactants were used aiming at the synthesis of BCN, BC₂N, BC₄N and BCNH₂ compositions. Ball milling induced chemical reaction between the precursors resulting in ternary BCN materials in the form of nanoparticles with an average diameter of 60 nm, as revealed by Scanning Electron Microscopy. Infrared spectroscopy confirmed the dominant hexagonal bonding structure, although with new spectral features.

The primary objective of this study was to reveal the possibility of production of a boron end product by a low cost and low energy consuming method, namely electro-deposition. Faraday's first law of electrolysis and Faraday's second law of electrolysis state that the amount of a material deposited on an electrode is proportional to the amount of electricity used. The amount of different substances liberated by a given quantity of electricity is proportional to their electrochemical equivalent (Lou and Huang, 2006). An electrolytic cell essentially consists of two or more electrodes dipping into an electrolyte. These electrodes are connected to an external electric power source (Gupta, 2003). When a direct electric current passes through an electrolyte, chemical reactions take place at the contacts between the circuit and the solution. By this the electrolysis or electroplating takes place.

During electrolysis the cations or the positively charged ions move towards the cathode and the anions or the negatively charged ions migrate towards the anode. Various reactions take place at the electrodes during electrolysis. In general, reduction takes place at the cathode, and oxidation takes place at the anode (Bossio and Gaseca, 1971; Lou and Huang, 2006). Many different studies have been conducted by using electro-deposition method such as Chen et al. (2011); Ebrahimi et al. (1999) and Naik et al. (2002). Boron was electro-extracted from boron carbide and deposited on a mild steel cathode as boron related electro-deposition study by Jain et al. (2013). Boron nitride was successfully deposited on copper electrodes by Tufan and Batar (2014).

There exist many different studies in the literature on the application of many different methods. However, electro-deposition, a classical method to be utilized mainly

in electro-plating, has not been employed for the production of BCN. The production of boron carbonitride (BCN) was achieved at low temperatures, regardless of sintering and thermal treatment. Unlike the conventional production methods relying on high energy consumption and high temperatures reported in literature, electro-deposition method is anticipated to provide an opportunity for environmentally justifiable boron carbonitride production at relatively lower energy consumption levels.

Materials and methods

The commercially available borax pentahydrate samples used were obtained from the borax pentahydrate (BPH) production plant of Eskisehir, Kirka Boron Works. Borax pentahydrate is the refined form of natural sodium borate and has the chemical formula $\text{Na}_2\text{B}_4\text{O}_7 \cdot 5\text{H}_2\text{O}$. Composed of boron oxide (B_2O_3), sodium oxide, and water, it is a mild, white and crystalline alkaline salt, with excellent buffering and fluxing properties. It is available in crystalline (granular) form and is an important multifunctional source of B_2O_3 , particularly for processes for which the simultaneous presence of sodium is beneficial. Borax pentahydrate used at the correct equivalent rate gives solution or melts identical in composition with those of borax decahydrate. It may, therefore, be substituted in all applications where borax is used. Among the applications of borax pentahydrate are the production of wire drawing baths, corrosion inhibitor solutions, starches, adhesives and the manufacture of other boron compounds (Eti Mine, 2003). The physical and chemical characterization and particle size distribution of commercially available BPH is listed in Table 1. The solubility of borax pentahydrate in distilled water with respect to electro-deposition bath temperature was also determined (Fig. 1).

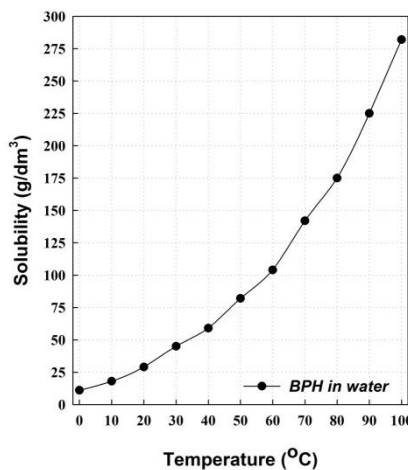


Fig. 1. Solubility of borax pentahydrate (BPH) in distilled water

Table 1. Features of borax pentahydrate (BPH) (Eti Mine, 2012)

Physical and chemical properties	
Physical State	White crystals
Melting Point	741 °C
Boiling Point	1575 °C
Specific Gravity	1.81 g/cm ³ at 20 °C
Molecular Weight	291.35 g/mole
pH	9.3 (3% solution)
Physical State	White crystals
Melting Point	741 °C
Boiling Point	1575 °C
Chemical specifications	
B ₂ O ₃	47.76 % (min.)
Purity	99.90% (min.)
Na ₂ O	21.25% (min.)
SO ₄	135 ppm (max.)
Cl	70 ppm (max.)
Fe	5 ppm (max.)
Insolubles in Water	150 ppm (max.)
Particle size distribution	
+1.000 µm	6% (max.)
-1.000 +0.063 µm	90% (min.)
-0.063 µm	4% (max.)

Electro-deposition tests

Electro-deposition tests were performed to determine the optimum parameters for production of boron carbonitride from borax pentahydrate. Copper, iron and graphite electrodes with dimensions of 100×20×0.2 mm were used during electro-deposition tests. The dissolved B₂O₃ amounts were investigated for borax pentahydrate with respect to bath temperature to achieve the most stable and saturated solution. The bath temperature was set at 80 °C and the initial concentrations of solutes were determined with respect to their solubilities at this temperature. The laboratory experimental setup involved a polypropylene bath, a thermo-couple, a magnetic stirrer with a heating feature and an Alpha-Tech brand redressor which can operate at 0–200 amperes and 0–600 volts (Fig. 2).

The design of electro-deposition tests using Na₂B₄O₇·5H₂O as the solute is listed in Table 2. The table lists the experimental conditions for the tests conducted. Several different electrode types were used for the electro-deposition tests. The combinations of copper, graphite and iron were determinant in the formation of BCN with several additives. The chemical, surface and phase characterizations of electrolytes and deposited electrode bars were performed using Thermo Scientific, Cu-K α type X-ray diffractometer (XRD); Coxem, EM-30 type scanning electron microscope (SEM) and Varian, 710-ES type inductively coupled plasma optical emission spectroscopy (ICP-OES).



Fig. 2. Setup for electro-deposition tests: From left to right: the redressor, touch screen control panel and electro-deposition bath

Table 2. Experimental conditions for electro-deposition tests

Code	Anode	Cathode	pH	Addition	V	A	Duration (min.)
BPH01	Cu	Cu	9–10	–	6	3	10
BPH02	Cu	Cu	9–10	–	8	3	10
BPH03	Cu	Cu	9–10	–	10	3	10
BPH04	Cu	Cu	9–10	–	12	3	10
BPH05	Cu	Cu	9–10	–	14	3	10
BPH06	Cu	Cu	9–10	–	16	4	10
BPH07	Cu	Cu	9–10	–	18	5	10
BPH08	Cu	Cu	9–10	–	20	5	10
BPH09	Cu	Cu	9–10	–	22	5	10
BPH10	Cu	Cu	9–10	–	24	7	10
BPH11	Cu	Cu	9–10	–	26	7	10
BPH12	Cu	Cu	9–10	–	28	8	10
BPH13	Cu	Cu	9–10	–	30	7	10
BPH14	Cu	Cu	9–10	–	14	3	10
BPH15	Cu	Cu	9–10	–	14	5	10
BPH16	Cu	Cu	9–10	–	14	7	10
BPH17	Cu	Cu	9–10	–	14	9	10
BPH18	Cu	Cu	9–10	–	14	11	10
BPH19	Cu	Cu	9–10	–	18	13	10
BPH20	Cu	Cu	9–10	–	20	15	10
BPH21	Graphite	Fe	9–10	–	4	1	10
BPH22	Graphite	Fe	9–10	–	6	1	10
BPH23	Graphite	Fe	9–10	–	8	1	10
BPH24	Graphite	Fe	9–10	–	18	4	10
BPH25	Graphite	Fe	9–10	–	20	5	10
BPH26	Graphite	Cu	9–10	–	12	3	10
BPH27	Graphite	Cu	4.5	C ₆ H ₈ O ₇	24	9	10
BPH28	Cu	Cu	9–10	Active C	24	7	10
BPH29	Cu	Cu	9–10	NaSCN	24	7	10
BPH30	Graphite	Cu	4	CH ₃ COOH	24	10	10

For the tests listed in Table 2 initial concentration of borax pentahydrate was set at 175 g/dm³ which corresponds to its maximum solubility value for its saturated solution at 80°C. The bath temperature was varied between 60 and 100°C to achieve rapid crystallization and precipitation of borax pentahydrate at low temperatures and to avoid possible safety issues at high temperatures. The bath volume, and thus, the electrode surface area changed with tests, resulting in variations in the current densities.

Results and discussion

In several experiments conducted, formation of BCN was observed. The objective was determining the optimum parameters for such formations. For instance, in the test BPH21 with parameters listed in Table 3, a small amount of deposition on Fe cathode was observed and the coated substrate was analyzed by XRD to determine the phases formed (Fig. 3). This impurity detected in XRD analysis was due to a non-uniform coating, causing the substrate (Fe) identification in XRD.

Table 3. Experimental conditions of BPH21 test

Anode	Cathode	pH	Addition	V	A	Duration (min)
Graphite	Fe	9–10	–	4	1	30

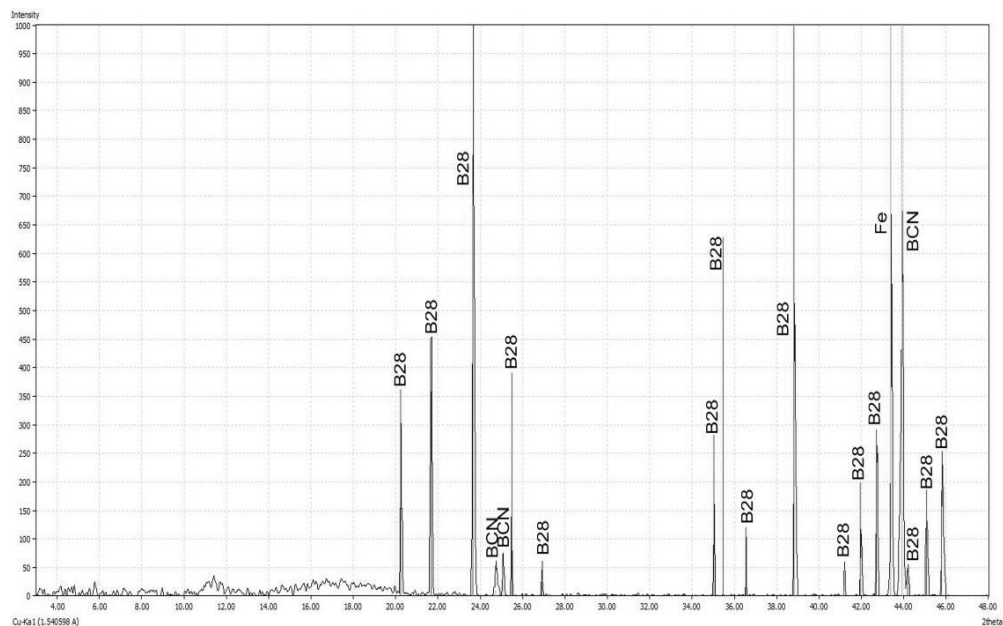


Fig. 3. XRD spectrum of deposited Fe cathode of BPH21

The formation of BCN, B_{28} and Fe phases were determined as a result of XRD analysis. The formation of B_{28} and BCN peaks were proven, however the B_2O_3 removal from the electrolyte during the experiment remained low. It was found that a sufficient amount of B_2O_3 should be bound and removed from solution to form boron carbide. Otherwise, elemental boron or other boron products could be deposited.

As a result of the BPH29 test (Table 4), a successful deposition on Cu cathode was achieved and the coated substrate was analyzed by XRD (Fig. 4). The XRD spectrum showed that addition of NaSCN not only enhanced the formation of nitrogen and carbon based boron products, such as BC_5 and BCN, but also caused some impurities such as oxides of copper and free carbon peaks due to the undesired reactions amongst the substrate (Cu) and remaining dissolved carbon. NaSCN, as a source of nitrogen and carbon dissolved in distilled water (solvent) provided sufficient amounts liable to react with boron, showing the highest electron affinities with N and C.

Table 4. Experimental conditions of BPH29 test

Code	Anode	Cathode	pH	Addition	V	A	Duration (min.)
BPH29	Cu	Cu	9-10	NaSCN	24	7	10

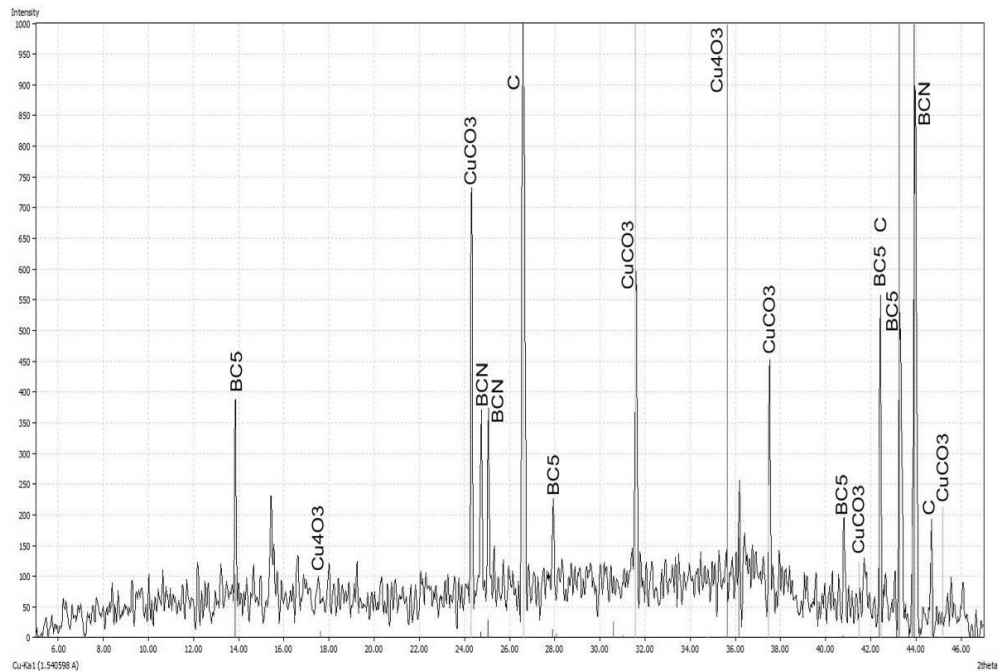


Fig. 4. XRD analysis of deposited Fe cathode of BPH29

The experimental studies conducted with borax pentahydrate as solute were finalized by the determination of optimum intervals for production of boron

carbonitride. The maximum optimum deposition time was determined as 8 to 10 minutes as a result of observations and B_2O_3 removal amount from the electrolyte. Addition of sodium cyanide in equal molar ratios as solute enhanced the formation of boron carbonitride. The optimum experimental conditions as intervals and the resultant phases detected by XRD analysis are listed in Table 5.

Table 5. Optimum experimental conditions and resultant products

Borax pentahydrate as solute (saturated, 175 g/dm ³)					
Fixed Parameters					
Solvent	pH		Temperature	Duration	
Distilled Water	9.0–10.0 (natural)		75–85°C	8–10 min.	
Variables					
Anode	Cathode	Potential (volt)	Current (amper)	Additive	Deposited Products
Cu	Cu	18–30	5–7	NaSCN	BC ₅ , BCN
Gr	Fe	4–20	1–5	–	BCN, B ₂₈

Conclusions

This study shows the possibility of boron carbonitride production using an environmental friendly, low energy consuming alternative methodology at significantly lower temperature levels (80 °C) as compared to the conventional procedures. Among many different variables, emphasis were given on the intervals of pH, bath temperature, solute concentration, voltage set, current acquired and duration of the tests. Different phase formations with different anode and cathode electrodes and different chemical compound additions were achieved. Successful depositions of BCN were obtained after a deep parameter screening process. The addition of sodium cyanide had positive affects in formation of carbon and nitrogen based phases. BCN, BC₅ and elemental boron formations were achieved in low voltage (max. 30 V) and current (max. 7 A) levels.

The optimum parameter intervals to form BCN were determined and the opportunity of purifying the product was revealed. The necessity in purification of final coatings was revealed, in addition to further characterization of purified coatings by different methods. For future work, studies to produce BCN in pilot or industrial scale should be performed. In addition, the mechanical properties of the product should be compared to the commercially available alternatives and market value of the laboratory scale product should be determined prior to further studies.

References

AHN H., KLIMEK K.S., RIE K.T., 2003, *BCN coatings by RF PACVD at low temperature*, Surface and Coatings Technology, 174-175, 1225-1228.

AOKI H., TOKUYAMA S., SASADA T., WATANABE D., MAZUMDER M.K., KIMURA C., 2008, *Dry etching properties of boron carbon nitride (BCN) films using carbon fluoride gas*, Diamond & Related Materials, 17, 1800-1804.

BLANK V.D., SEEPUJAK A., POLYAKOV E.V., BATOV D.V., KULNITSKIY B.A., PARKHO-MENKO, 2009, *Growth and characterization of BNC nanostructures*, Carbon, 47, 3167-3174.

BOSSO J.F., GASECA G.R., 1971, *Electro-deposition process*, US Patent 3,619,398.

CHEN C.S., SHIH Y.J., HUANG Y.H., HUANG G.H., 2011, *Recovery of nickel with the addition of boric acid using an electro-deposition reactor*, Desalination and Water Treatment, 32 (1-3), 345-350.

EBRAHIMI F., BOURNE G.R., KELLY M.S., MATTHEWS T.E., 1999, *Mechanical properties of nanocrystalline nickel produced by electro-deposition*, NanoStructured Materials, 11 (3), 343-350.

ETI MINE, 2003, Pre-feasibility report summaries, Boron nitride planning and data processing department, Ankara.

ETI MINE, 2012, *Activity report*, Retrieved December 12, 2013, from <http://www.etimaden.gov.tr>

GRIGOREV O.N., BEGA N.D., LYASHENKO V.I., DUBOVIK T.V., PANASHENKO V.M., SHCHERBINA O.D., 2005, *Dependence of the structure of sintered boron carbonitride on the defect level in the starting BN powder*, Powder Metallurgy and Metal Ceramics, 44, 5-6.

GUPTA C.K., 2003, *Chemical Metallurgy: Principles and Practice*, Weinheim: Wiley-Vch, 670-710.

HUANG F.L., CAO C.B., XIANG X., LV R.T., ZHU H.S., 2004, *Synthesis of hexagonal boron carbonitride phase by solvothermal method*, Diamond & Related Materials, 13, 1757-1760.

JAIN A., ANTHONYSAMY S., ANANTHASIVANA K., RANGANATHANA R., MITTAL V., NARASIMHAN S.V., 2008, *Characterization of electrodeposited elemental boron*, Materials Characterization, 59, 890-900.

LOU H.H., HUANG Y., 2006, *Electroplating*, Encyclopedia of Chemical Processing, Taylor & Francis, 1-10.

MANNAN M.A., NAGANO M., HIRAO N., BABA Y., 2008, *Hexagonal BCN Films Prepared by RF Plasma-Enhanced CVD*, Chemistry Letter, 37 (1), 96-97.

NAIK Y.A., VENKATESHA T.V., NAYAK P.V., 2002, *Electro-deposition of zinc from chloride solution*, Turkish Journal of Chemistry, 26, 725-733.

TORRES R., CARETTI I., GAGO R., MARTIN Z., JIMENEZ I., 2007, *Bonding structure of BCN nano-powders prepared by ball milling*, Diamond & Related Materials, 16, 1450-1454.

TUFAN B., BATAR T., 2014, *Production parameters of boron nitride from boric acid by low temperature electro-deposition*, Ciencia e Tecnica (ISSN:0254-0223), 29 (10), 24-36.

ULRICH S., HOLLECK H., LEISTE H., NIEDERBERGER L., NOLD E., SELL K., 2005, *Nano scale, multi-functional coatings in the material system B-C-N-H*, Surface & Coatings Technology, 200, 7-13.

WATANABE M.O., ITOH S., MIZUSHIMA K., SASAKI T., 1996, *Bonding characterization of BC₂N thin films*, Applied Physics Letter, 68, 2962-2964.

WOHLE J., AHN H., RIE K.T., 1999, *BCN coatings on polymer substrates by plasma CVD at low temperature*, Surface and Coatings Technology, 116-119, 1166-1171.

ZHI C.Y., BAI X.D., WANG E.G., 2002, *Raman characterization of boron carbonitride nano-tubes*, Applied Physics Letter, 80, 3590-3592.

ZHUGE F., YAMANAKA S., 2008, *Ternary compound B_4CN_4 prepared by direct nitridation of B_4C* , Journal of Alloys and Compounds, 466, 299-303.

Received May 15, 2015; reviewed; accepted June 15, 2015

Short communication

SOME REMARKS ON ATTACHMENT OF A GAS BUBBLE TO ANOTHER PHASE BOTH IMMERSED IN WATER

Przemysław B. KOWALCZUK, Jan DRZYMALA

Wrocław University of Technology, Faculty of Geoengineering, Mining and Geology,
Wybrzeże Wyspianskiego 27, 50-370 Wrocław, przemyslaw.kowalcuk@pwr.edu.pl

Abstract: In this paper the importance of definition of hydrophobicity and aquaoleophilicity in terms of contact angle as well as the properties of water films in flotation and oil agglomeration were briefly presented. It was shown that the hysteresis of contact angle for a considered system depends on the way of measurement and geometry of the system due to the presence of other than excess pressure and capillary forces and buffering properties of the capillary force. It was suggested that, the measured advancing and receding contact angles should be, when possible, recalculated into the Young (rest, equilibrium) contact angle. It was discussed that quartz is not a good model of hydrophilic surface because its contact angle with a gas phase in water is not zero and that a spontaneous attachment between highly hydrophobic materials such as hydrocarbons and Teflon in dynamic system, such as flotation, does not occur.

Keywords: hydrophobicity, aquaoleophobility, contact angle, liquid film, attachment

Introduction

Attachment of a gas bubble to either solid or liquid surface immersed in water is a crucial step in many processes such as flotation (Scheludko et al., 1976) and oil agglomeration performed in the presence of air (Drzymala et al., 1986). According to the second law of thermodynamics the process of attachment can take place only if the surface is not completely wetted by water, that is when the so-called contact angle is greater than zero. Then, the Gibbs potential of the three-phase contact is negative (Fuerstenau and Raghavan, 1976). On the other hand, according to the DLVO theory for flotation systems (Yoon and Mao, 1996) the kinetics of attachment depends on the properties of the bubble-surface interfacial region, that is on liquid films, and is determined by the energy barrier height of attachment. As a result, attachment can be spontaneous, slow or completely prevented. Thus, hydrophobicity and properties of

the liquid film are the most significant factors of the bubble-surface systems phenomena. These factors are frequently imprecisely defined and considered. In this article hydrophobicity and bubble-solid surface attachment issues will be briefly discussed.

Hydrophobicity

Hydrophobicity of a solid/gas/water system can be characterized by the so-called contact angle responsible for the appearance of a capillary force, the main force of bubble-to-surface adhesion. Depending on the field of science different hydrophobicity definitions, which are based on the contact angle, are used. In the colloid science the term hydrophobicity indicates that the three-phase contact angle of the solid/gas/liquid system, measured through the aqueous phase, is greater than 90 degrees (Bico et al., 2002; Bhushan, 2012). The system is referred to as hydrophilic when the contact angle is smaller than 90°. In mineral processing it is accepted that hydrophobicity starts when the contact angle of the solid/gas/liquid system, measured through the aqueous phase, is greater than zero (Nguyen and Schulze, 2004; Drzymala, 2007). It means that hydrophilic substances have the contact angle equal to zero. Thus, the definitions of hydrophobicity and hydrophilicity, when characterized by the contact angle, should be clearly indicated in scientific papers.

As it has already been mentioned, as a rule the contact angle is expressed through the aqueous phase (Adamson, 1990) and this approach is recommended for the three-phase systems involving solid-gas-water systems. It is also recommended to use in mineral processing the term hydrophobic for systems with the contact angle greater than zero. Otherwise, we will face the problem of strange expressions such as flotation of hydrophilic materials, because most naturally floating materials and minerals, which are rendered floatable by adsorption of surface modifying reagents (collectors) have the contact angle below 90° (Wark, 1938; Kowalcuk and Drzymala, 2011).

Sometimes it is very difficult, or even impossible, to tell if a substance is hydrophobic or hydrophilic because the measured contact angle is either zero or close to zero. This is so because the numerical value of contact angle for the same material depends on the way of measurements. It may result from the presence of slightly different forces involved in establishing the contact angle and geometry of the invested system. As a result the advancing, rest, receding and equilibrium contact angles are recorded. The difference between the advancing and receding contact angles measured for the same system and geometry is called hysteresis.

In calculations and considerations when only one value of contact angle is needed it is recommended to use the equilibrium (Young) contact angle, which for systems having well defined geometry can be calculated from the maximum advancing (detachment) contact angle (Drzymala, 1994a; Kowalcuk and Drzymala, 2012).

A good example of dilemma of hydrophobicity/hydrophilic is quartz. In some reports the contact angle of pure quartz is zero (Tarasevich, 2007; Wang et al., 2014), while numerous papers report that contact angle for quartz is greater than zero (Lamb and Furlong, 1982; Gee et al., 1990; Drzymala, 1994b). In our opinion quartz should be considered as weakly hydrophobic because it has a positive advancing, equilibrium, and in some studies also receding contact angles. In addition to that, quartz can float in the presence of selected frothers near its point of zero charge (Doren et al., 1975; Drzymala et al., 2007). Dahlgren et al. (1986) demonstrated that also there is a positive contact angle for captive air bubbles on glasses, which have very similar structure and properties to quartz. These observation suggests that the lack of quartz flotation in pure water (Drzymala, 1994c; Kowalcuk, 2015) does not results from quartz hydrophilicity but from the stable aqueous films present at the quartz/bubble interface. Thus, during important investigations it should not be ignored that quartz is a weakly hydrophobic material. In the case of a need to use truly hydrophilic materials other materials, including gypsum, should be used.

On one hand it is well known that contact angle depends on the method of measurement (Shang et al., 2008; Nowak et al., 2013). On the other hand it is claimed that there is no contact angle hysteresis on molecularly smooth surfaces. The case of mercury shows that this is not true because there is always a hysteresis of contact angle in real multiphase systems (Banerji, 1981; Xu et al., 1995). It results from very obvious facts that the Young equation, which defines the so-called equilibrium contact angle, is valid only for hypothetical systems, in which only excess pressure (Laplace equation) and capillary force are present. The angle of capillary force action is equal to the equilibrium contact angle determined by the energetics (and equivalent forces) of the three involved interfaces (Young equation). In real systems additional forces are always present which are counter-balanced by increasing capillary force due to the change of the contact angle from the equilibrium to either advancing or receding (Drzymala, 1994c). As a results of the additional, specific for given system forces and geometry, the contact angles are different even for the same systems but measured either by the sessile drop or captive bubble methods. Figures 1-3 illustrate this properties for different three-phase systems.

It should be noted that in the case of solid-water-oil systems it was recommended to use the terms aquaoleophilicity and aquaoleophobicity. In such systems the contact angle should be expressed through the oil phase (Yang and Drzymala, 1986). This recommendation is based on geometrical analogy between sessile water drop and sessile oil drop.

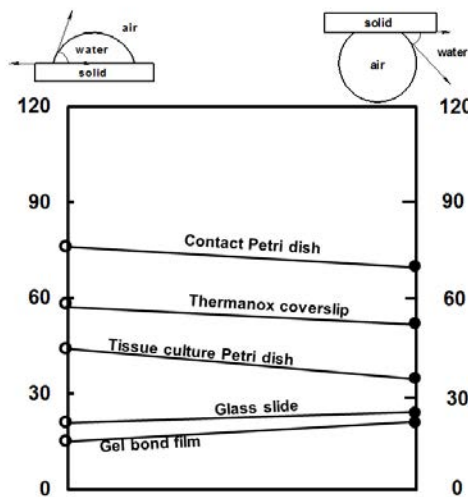


Fig. 1. Contact angle of glass-type materials measured in water drop-air-solid and air bubble-water-solid arrangements. Dependence of contact angle value on the way of contact angle measurement is not visible. Source of data: Dahlgren et al. (1986)

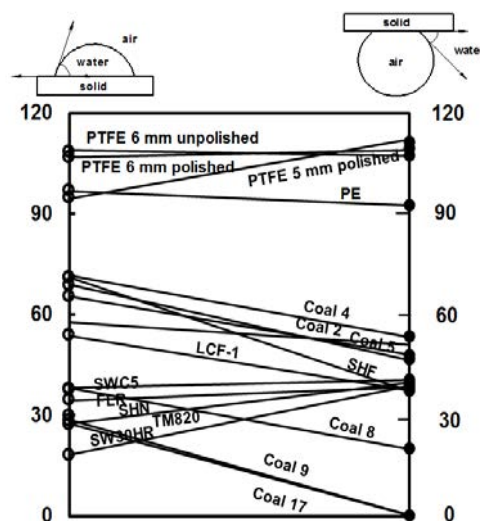


Fig. 2. Contact angle of different materials measured in water drop-air-solid and air bubble-water-solid arrangements. Dependence of contact angle value on the way of contact angle measurement is not visible.

Source of data: Drelich et al. (1996): PTFE 6 mm unpolished, PTFE 6 mm polished, PTFE 5 mm polished, PE; Gutierrez-Rodriguez (1984): Coal 2, Coal 4, Coal 5, Coal 8, Coal 9, Coal 17; Baek et al. (2012): LCF-1, SHE, SWC5, PER, SHN, TM820, SW39HR

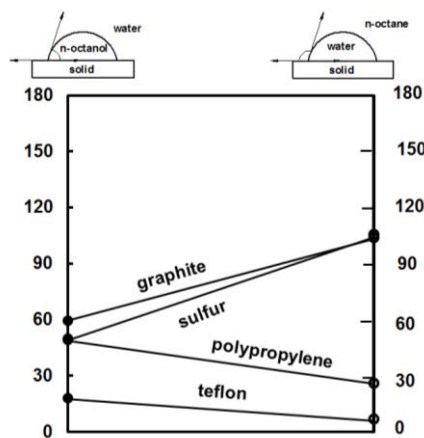


Fig. 3. Contact angle of materials measured as water drop-n-octane-solid and as n-octane drop-water-solid. Dependence of contact angle value on the way of contact angle measurement does not occur. Source of data: Janczuk and Chibowski (1983): sulfur, graphite, Teflon; Hamilton (1972), Chibowski and Holysz (1981): polypropylene

Bubble-solid surface attachment

Another important parameter of attachment of bubble to either highly hydrophobic solid surface or oleophilic material suspended in water is the kinetics of process. Wang et al. (2014) observed a spontaneous attachment of an air bubble to methylated quartz. It occurs only under static conditions since the kinetics of attachment under dynamic ones is totally different. Krasowska et al. (2006) and Kosior et al. (2011) showed that the bubble attachment to Teflon takes place only when, due to multiple unsuccessful collisions, the bubble reduces significantly its velocity. The same happens with other highly hydrophobic materials including high molecular mass hydrocarbons having contact angle up to 110°, as in the case of solid paraffin (Adamson, 1990). It was demonstrated by Medrzycka (1990) that nonvolatile highly hydrophobic hydrocarbons, including tetradecane, in the form of droplets suspended in water, do not float (Fig. 4). It means that the water film between oil drop and gas bubble is very strong.

Even though tetradecane is very hydrophobic, there is no a fast hydrocarbon-air bubble attachment during flotation. It means that the spontaneous attachment between the hydrocarbon and air bubble does not occur always and it is not present in many practical systems. Attachment occurs not spontaneously but with a certain rate due to repulsions caused by the aqueous films formed between the hydrophobic particle and air bubble. In the case of highly hydrophobic materials the attachment barrier is usually caused by electrical charges, which in the case of tetradecane droplets (Stachurski and Michalek, 1985; 1996) and bubbles (Li and Somasundaran, 1992) are both negative.

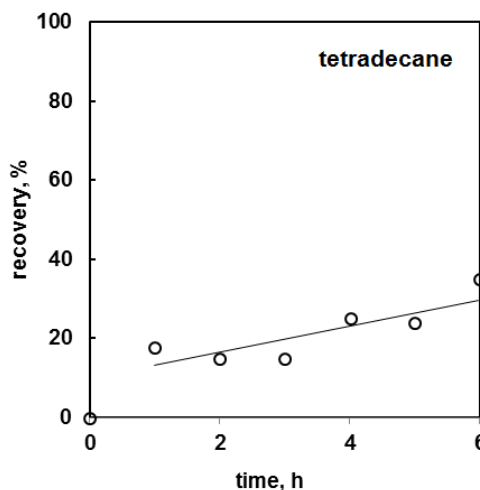


Fig. 4. Negligible flotation of suspended in water tetradecane droplets, even after a long time of flotation. No spontaneous adhesion of highly hydrophobic tetradecane to air bubbles occurs. The plot is based on the data of Medrzycka (1990)

Conclusions

Mineral processing papers dealing with hydrophobicity and aquaoleophilicity should specify the relation between these terms and contact angle. The hysteresis of contact angle for a system depends on the way of measurement and geometry (gas bubble, oil drop) of the system due to the presence of other that excess pressure and capillary forces and buffering properties of the capillary force. When possible, the measured advancing and receding contact angles should be recalculated into the Young (rest, equilibrium) contact angle.

Quartz is not a good model of hydrophilic surface because its contact angle with gas in water is not zero and that spontaneous attachment between highly hydrophobic materials such as hydrocarbons and Teflon in dynamic system such as flotation does not occur.

The presented remarks on the hydrophobicity of materials and kinetics of adhesion of highly hydrophobic materials to air bubbles should be helpful for considering these issues in research and review papers.

Acknowledgments

This work was partially financed by the National Science Centre Research Grant (2012/07/D/ST8/02622).

References

ADAMSON, A.W., 1990, *Physical chemistry of surfaces*, 5th ed., Wiley & Sons, New York.

BAEK, Y., KANG, J., THEATO, P., YOON, J., 2012, *Measuring hydrophilicity of RO membranes by contact angles via sessile drop and captive bubble method: A comparative study*, Desalination, 303, 23–28.

BANERJI, B.K., 1981, *Physical significance of contact angles*, Colloids and Polymer Sci., 259, 391-394.

BHUSHAN, B., 2012, *Biomimetics. Bioinspired hierarchical-structured surfaces for green science and technology. Biological and medical physics, Biomedical Engineering*, Springer-Verlag Berlin Heidelberg, ISBN: 978-3-642-25408-6.

BICO, J., THIELE, U., QUERE, D., 2002, *Wetting of textural surfaces*, Colloids and Surfaces A: Physicochemical and Engineering Aspects 206 (2002) 41–46.

CHIBOWSKI, E., HOLYSZ, L., 1981, *A study of n-alkane films of solids by zeta-potential measurements*, Journal of Colloid and Interface Science, 81(1), 8–13.

DAHLGREN, C., ELWING, H., MAGNUSSON, K.E., 1986, *Comparison of contact angles calculated from the diameter of sessile drops and submerged air bubbles in contact with a solid surface*, Colloids and Surfaces, 17, 295–303.

DOREN, A., VARGAS, D., GOLDFARB, J., 1975, *Nonionic surfactants as flotation collectors*, Trans. IMM, Sec. C., C-34–37.

DRELICH, J., MILLER, J.D., GOOD, R.J., 1996, *The effect of drop (bubble) size on advancing and receding contact angles for heterogeneous and rough solid surfaces as observed with sessile-drop and captive-bubble techniques*, Journal of Colloid and Interface Science, 179, 37–50.

DRZYMALA, J., 1994A, *Characterization of materials by Hallimond tube flotation. Part 2: Maximum size of floating particles and contact angle*, Int. J. Miner. Process., 42, 153–167.

DRZYMALA, J., 1994B, *Hydrophobicity and collectorless flotation of inorganic materials*, Advances in Colloid and Interface Science, 50, 143–185.

DRZYMALA, J., 1994C, *Characterization of materials by Hallimond tube flotation. Part 1: Maximum size of entrained particles*, Int. J. Miner. Process., 42, 139–152.

DRZYMALA, J., 2007, *Mineral processing. Foundations of theory and practice of metallurgy*, Ofic. Wyd. PW, Wrocław

DRZYMALA, J., MARKUSZEWSKI, R., WHEELOCK, T.D., 1986, *Influence of air on oil agglomeration of carbonaceous solids in aqueous suspension*, Inter. Miner. Process. Journal, 18, 277–286.

DRZYMALA, J., MIELCZARSKI, E., MIELCZARSKI, J.A., 2007, *Adsorption and flotation of hydrophilic and hydrophobic materials in the presence of hydrocarbon polyethylene glycol ethers*, Colloids and Surfaces A: Physicochem. Eng. Aspects, 308, 111–117.

FUERSTENAU, D.W., RAGHAVAN, S., 1976, *Some aspects of the thermodynamics of flotation*. In Flotation - A.M. Gaudin Memorial Volume, M.C. Fuerstenu Ed., AIME, New York, Chapter 3, 21–65.

GEE, M.L., HEALY, T.W., WHITE, L.R., 1990, *Hydrophobicity effects in the condensation of water films on quartz*, Journal of Colloid and Interface Science, 140(2), 450–465.

GUTIERREZ-RODRIGUEZ, J.A., 1984, *Estimating the hydrophobicity of coal*, Colloids and Surfaces, 12, 1–25.

HAMILTON, W.C., 1972, *A technique for the characterization of hydrophilic solid surfaces*, Journal of Colloid and Interface Science, 40(2), 219–222.

JANCZUK, B., CHIBOWSKI, E., 1983, *Interpretation of contact angle in solid-hydrocarbon-water system*, Journal of Colloid and Interface Science, 95(1), 268–270.

KOSIOR, D., ZAWALA, J., MALYSA, K., 2011, *When and how α -terpineol and n-octanol can inhibit the bubble attachment to hydrophobic surfaces*, Physicochem. Probl. Miner. Process., 47, 169–182.

KOWALCZUK, P.B., 2015, *Flotation and hydrophobicity of quartz in the presence of hexylamine*, Int. J. Miner. Process. 140, 66–71.

KOWALCZUK, P.B., DRZYMALA, J., 2011, *Contact angle of bubble with an immersed-in-water particle of different materials*, Ind. Eng. Chem. Res. 50(7), 4207–4211.

KOWALCZUK, P.B., DRZYMALA, J., 2012, *Surface flotation of particles on liquids. Principles and applications*, Colloids and Surfaces A: Physicochem. Eng. Aspects 393, 81–85.

KRASOWSKA, M., TERPIŁOWSKI, K., CHIBOWSKI, E., MALYSA, K., 2006, *Apparent contact angles and time of the three phase contact formation by the bubble colliding with Teflon surfaces of different roughness*, Physicochem. Probl. Miner. Process., 40, 293–306.

LAMB, R.N., FURLONG, D.N., 1982, *Controlled wettability of quartz surfaces*, J. Chem. Soc., Faraday Trans. 1, 78, 61–73.

LI, C., SOMASUNDARAN, P., 1992, *Reversal of bubble charge in multivalent inorganic salt solutions – effect of aluminium*, J. Colloid Interface Sci., 148(2), 587–591.

MEDRZYCKA, K.B., 1990, *Removal of hydrocarbons from the oil/water type emulsion in the flotation process*, Habilitation dissertation, Politechnika Gdańsk, Gdańsk, 1990 (in Polish).

NGUYEN, A.V., SCHULZE, H.J., 2004, *Colloidal science of flotation*, Marcel Dekker Inc., New York.

NOWAK, E., COMBES, G., STITT, E.H., PACEK, A.W., 2013, *A comparison of contact angle measurement techniques applied to highly porous catalyst supports*, Powder Technology, 233, 52–64.

SCHELUDKO, A., TOSHEV, B.V., BOJADJIEV, D.T., 1976, *Attachment of particles to a liquid surface (capillary theory of flotation)*, J. Chem. Soc., Faraday Trans. 1, 72, 2815–2828.

SHANG, J., FLURY, M., HARSH, J.B., ZOLLARS, R.L., 2008, *Comparison of different methods to measure contact angles of solid colloids*, Journal of Colloid and Interface Science, 328, 299–307.

STACHURSKI, J., MICHALEK, M., 1985, *The zeta potential of emulsion droplets of the aliphatic hydrocarbons in aqueous solutions*, Colloids and Surfaces, 15, 255–259.

STACHURSKI, J., MICHALEK, M., 1996, *The effect of the ζ potential on the stability of a non-polar oil-in water emulsion*, J. Colloid Interface Sci., 184, 433–436.

TARASEVICH, Y.I., 2007, *The surface energy of hydrophilic and hydrophobic adsorbents*, Colloid Journal, 69(2), 212–220.

WANG, X., YIN, X., NALASKOWSKI, J., DU, H., MILLER, J.D., 2014, *Molecular features of water films created with bubbles at silica surfaces*, Surface Innovations 3(1), 20–26.

WARK, I.W., *Principles of flotation*, Australasian Institute of Mining and Metallurgy, Melbourne, 1938.

XU, Z., LIU, Q., LING, J., 1995, *An evaluation of the van Oss-Chaudhury-Good equation and Neumann's equation of state approach with mercury substrate*, Langmuir, 11, 1044–1046.

YANG, G.C.C., DRZYMALA, J., 1986, *Aqua-oleophilicity and aqua-oleophobicity of solid surfaces*, Colloids and Surfaces, 17, 313–315.

YOON, R-H., MAO, L., 1996, *Application of extended DLVO theory, IV Derivation of flotation rate equation from first principles*, Journal of Colloid and Interface Science, 181, 613–626.

Received February 9, 2015; reviewed; accepted May 19, 2015

BEHAVIOR AND MECHANISM OF COLLOPHANE AND DOLOMITE SEPARATION USING ALKYL HYDROXAMIC ACID AS A FLOTATION COLLECTOR

Jun YU, Yingyong GE, Jingtao HOU

School of Resources and Environmental Engineering, Wuhan University of Technology, Wuhan 430070, PR China; yujun_198521@163.com;251163252@qq.com

Abstract: Flotation response of collophane and dolomite using alkyl hydroxamic acid (AH) (chelating collector) was investigated in the paper. The experiments were performed using pure and artificially mixed minerals as well as a real phosphate ore. Their separation mechanisms were studied by means of zeta potential measurements, infrared analysis, adsorption measurements, thermodynamics, and quantum chemical calculations. The results indicated that AH exhibited an excellent performance in the flotation separation of collophane from dolomite in neutral medium. The P_2O_5 grade of the concentrate increased from 19.84% to 30.51% without any other reagents when the pH value was about 7. The zeta potential and adsorption studies showed that the adsorption of AH at the cellophane/aqueous interface was greater than that at dolomite surface, which was the essential reason that separation of collophane from dolomite. The results of Fourier Transform Infrared (FTIR) spectrum and thermodynamics calculation indicated that the adsorption of AH at collophane was attributed to the chemical bonding. Moreover, AH molecule formed O-O five-membered ring with calcium ion on the collophane surface.

Keywords: hydroxamic acid, collophane, dolomite, separation mechanism

Introduction

Phosphorus, produced from phosphate ore, is an important raw material in agriculture industry (Santana et al., 2008). More than 95% of phosphate ore in the world is consumed in fertilizer industry (Santana et al., 2012). As the requirement of phosphate ore increases, high grade phosphate ore resources are exhausted. Thus, the depletion of the high grade phosphate ores attracts more attention to low grade phosphate beneficiation (Merma et al., 2013).

More than half of worldwide production of commercial phosphate is upgraded by flotation (Santana et al., 2011). The flotation technique for upgrading phosphate ore depends on the types of gangue minerals. For siliceous phosphate ore, reverse flotation technology is successfully used to separate silicate from phosphate with cationic

collector at neutral pH (Mohammakhani et al., 2011; Boulos et al., 2014). However, the calcareous phosphate ore is not easy to purify by flotation because the physicochemical characteristic of carbonate and apatite surface is similar (Abouzeid et al., 2009).

According to numerous studies, flotation is still a dominant technology to separate carbonate from phosphate ore for calcareous phosphate (Ahmed et al., 2013). In the process, carbonate as a primary impurity is separated from phosphate using fatty acid or their ramification as collector. Meanwhile, apatite is depressed by depressants such as different acids, various organic and inorganic salts (Sis et al., 2003; Boulos et al., 2014). However, the reverse flotation for calcareous phosphate confronts some difficulties because optimal pH range is acidic (Al-Fariss et al., 2014). In this case, a portion of P_2O_5 is lost due to the dissolution of phosphate in acidic medium. Moreover, a large amount of calcium and magnesium ions in the pulp precipitates with collector molecule which results in the increase in collector consumption (Dos Santos et al., 2012).

Currently, the research orientations to solve this problem can be classified into two basic types: one is to exploit the efficient depressants that can be applied in neutral medium such as microorganism, which was utilized for enhancing the separation selectivity of minerals by modifying minerals surface characteristic (Elmahdy et al., 2013). The other one is to exploit high selectivity collectors such as chelating agents (Wang et al., 2006).

Hydroxamic acid has long been known as a high selectivity chelating agent for metal cations. Although hydroxamic acid was used as a collector for separating different valuable minerals from their gangues such as scheelite, cassiterite, and diaspore (Jiang et al., 2010; Wanget al., 2013; Zhao et al., 2013), the application of hydroxamic acid to separate colophane from dolomite still needs to be studied.

Therefore, the present work aims at studying the separation behavior and mechanism of colophane and dolomite using an efficient collector—alkyl hydroxamic acid (AH). The flotation performance of the AH was evaluated by micro-flotation experiments of pure mineral, artificially mixed sample and real phosphate ore. The mechanism of the AH adsorbed on mineral surfaces was interpreted by infrared spectra, zeta potential, adsorption, thermodynamics, and quantum chemical calculation.

Materials and methods

Materials

Colophane and dolomite samples used in this study were obtained from the Zhongxiang and Wuhan in the Hubei Province, China, respectively. The pure minerals were picked with the help of microscope, and ground to 90% $-74\mu m$ fraction in a ceramic ball mill. The specific surface areas of colophane and dolomite determined by the BET test are presented in Table 1. For the zeta potential measurement and FTIR

analysis, the samples were further ground to about $-2\mu\text{m}$. The results of chemical analysis showed that the P_2O_5 content of colophane was 38.66% and MgO content of dolomite was 19.70%. Additionally, the real phosphate ore was crushed and ground to 92% $-74\mu\text{m}$ fraction and the results of chemical analyses of the real phosphate ore are given in Table 2.

Table 1. Specific surface of colophane and dolomite

Particle Size (μm)	Weight (%)	Colophane (m^2/g)	Dolomite (m^2/g)
-74	90	1.632	2.853

Table 2. Chemical analysis results of phosphate ore (mass fraction, %)

Element	P_2O_5	MgO	Fe_2O_3	Al_2O_3	CaO	SiO_2	LOI	F
Content (%)	19.84	7.84	0.69	1.02	39.26	8.94	19.12	1.66

LOI – Loss on ignition

AH was used as a collector which was synthesized with coconut oil and hydroxylamine hydrochloride. HCl and NaOH of analytical grade from Kemiou Chemical Reagent Factory China were used to regulate the pH of the system. Distilled water was used in the experiments.

Methods

Flotation experiments

The micro-flotation tests of single mineral and artificially mixed samples were performed using a XFGC-80 flotation machine with a 50 cm^3 cell. Two grams of a mineral sample was placed in the cell which then was filled with distilled water. The suspension was agitated with a rotational speed of 1600 rpm. The pH was adjusted to a desired value with addition of HCl and NaOH solutions. Then, AH ($2 \cdot 10^{-5}$ mol/dm 3) was added into the cell with 3 min conditioning time. The froth and sink products were weighed and assayed respectively after the filtration and drying, and the results were used to calculate the recovery. The experimental error for the micro-flotation experiments was obtained by conducting five flotation tests, and statistical analysis of grade and recovery data. The experimental error was found to be 5~7%.

The flotation tests of phosphate ore (400 g) were conducted in an XFD-type laboratory flotation machine with 1.0 dm^3 cell. The air flow rate was $45\text{ dm}^3/\text{h}$ and the agitation speed was 1850 rpm. The conditioning time with collector (500 g/Mg) was 3 min. The froth and sink products were weighed and assayed respectively after the filtration and drying, and the results were used to calculate the recovery. The experiments were repeated three times, and the reported values are the average of the three experiments.

Zeta potential measurements

The zeta potentials of the minerals were measured using a Brookhaven Zeta Plus Zeta Potential Analyzer (manufactured in the USA). The concentration of the mineral suspension was 0.04 wt%, and the $1 \cdot 10^{-3}$ mol/dm³ NaCl solution was used as a background electrolyte. The measurements were conducted at room temperature 25 °C. The pH value of the suspension was adjusted to a desired value using HCl and NaOH solutions. Besides, further measurements also were carried out with the addition of AH at a constant concentration. The average zeta potential values of at least five independent measurements were recorded with a measurement error of ± 2 mV.

Adsorption experiments

In this research, the amount of collector adsorbed on the mineral surfaces was measured by the solution depletion method using a UV-VIS spectrophotometer (UV775B, China). An amount of 1.0 g of pure mineral sample was placed in the 250 cm³ conical flask. After adding 50 cm³ AH solution at a constant concentration ($2.62 \cdot 10^{-4}$ mol/dm³, $3.49 \cdot 10^{-4}$ mol/dm³, $4.37 \cdot 10^{-4}$ mol/dm³, $5.24 \cdot 10^{-4}$ mol/dm³, $6.11 \cdot 10^{-4}$ mol/dm³) into the suspension, the suspension was conditioned with the collector in the water-bathing constant temperature vibrator for 1 h. Then, the solid particles were separated by centrifuge for 12 min. The concentration of the collector in the supernatant was measured using UV-VIS spectrophotometer. The collector adsorption on the mineral surface was calculated by Eq. (1)

$$\Gamma = \frac{(C_0 - C)V}{mA} \quad (1)$$

where Γ is the amount (mol/m²) of the collector adsorbed at the mineral/aqueous solution interface, C_0 and C are the initial and supernatant concentrations (mol/dm³), respectively, m is the mass (g) of the mineral sample for each test, V is the volume (dm³) of the collector solution, and A is the specific surface area (m²/g) of the particle.

FTIR measurements

Fourier Transform Infrared (FTIR) spectra ranging from 4000 to 500 cm⁻¹ were used to characterize AH and the adsorption on the mineral surface at room temperature. The pure mineral samples were ground to -2 μ m and conditioned with the collectors ($1 \cdot 10^{-2}$ mol/dm³). The pellets were prepared by mixing KBr and mineral at the mass ratio of 200/1. The spectra of the samples were obtained with KBr pellets by a Fourier transform infrared spectrometer Nicolet.

Results and discussion

Characterization of AH

In order to investigate the characteristics of the new collector, the FTIR was used, and the infrared spectra of AH is shown in Fig. 1. The IR spectrum of AH contains intensive stretching vibration of O-H with peak frequencies at 3050 cm^{-1} and 3251 cm^{-1} . The peak frequencies at 2941 cm^{-1} and 2848 cm^{-1} arise from stretching vibration absorption of $-\text{CH}_2$. The bands found at 1622 cm^{-1} , 1661 cm^{-1} , and 1771 cm^{-1} come from stretching vibration absorption of $\text{C}=\text{N}$ and $\text{C}=\text{O}$ in the collector molecule. The characteristics peaks appearing at 1424 cm^{-1} and 1436 cm^{-1} are bending vibration of $-\text{CH}_3$ and $-\text{CH}_2$, respectively. The stretching vibration absorption of $\text{N}-\text{O}$ was observed at 968 cm^{-1} and 1017 cm^{-1} . Therefore, it can be concluded that the new synthesized collector contains the characteristics absorption peaks of alkyl hydroxamic acid.

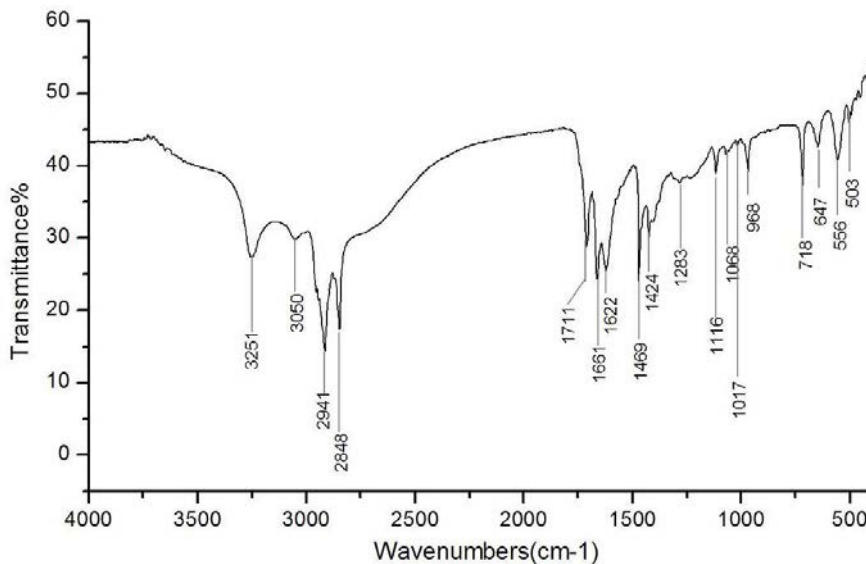


Fig. 1. FTIR spectra of AH

Flotation performance of single minerals

Figure 2 presents the flotation results of collophanite and dolomite with AH as a function of the pulp pH value. The experiments were performed at the concentration of $\text{AH} = 2 \cdot 10^{-5}\text{ mol}/\text{dm}^3$ at room temperature ($25\text{ }^\circ\text{C}$). It was observed that AH showed very good selectivity for collophanite over a wide range of pH value. The floatability difference of two minerals was obvious at the pH range between 3 and 10, and the maximum flotation recovery was obtained in the neutral medium. Additionally, when the pH was changed to 2, the flotation recovery of collophane decreased, which was due to the presence of calcium ions dissolved from collophane. The calcium ions form

water-insoluble precipitates with AH, a process that normally results in flotation values decrease (Nanthakumaret al., 2009). Therefore, it is important to control the concentration of calcium ions when AH is used as collector in the flotation process.

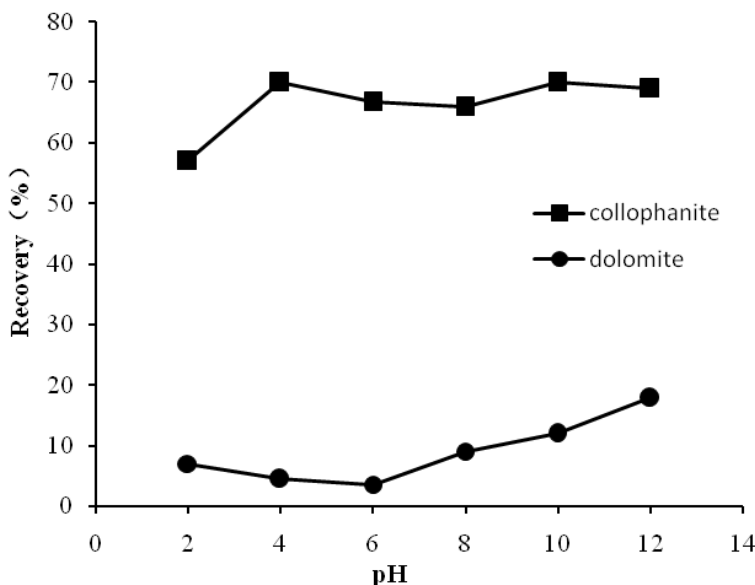


Fig. 2. Flotation results of collophanite and dolomite as a function of pH

Flotation separation of artificially mixed sample

The results of single mineral flotation tests showed that AH had a remarkable selectivity for the separating collophanite from dolomite in neutral medium. In order to further investigate the separation performance, the flotation tests on the artificially mixed sample were conducted. The artificially mixed sample was prepared by the mixing two single minerals at the mass ratio of 3/1, namely, the mixture contained 75% collophanite. Figure 3 presents the flotation results of artificially mixed sample as a function of pH value. The results indicated that the P_2O_5 grade of the concentrate increased slightly with the increase of the pH when the pH value was less than 6. After that, the P_2O_5 grade of the concentrate decreased, and the maximum value of P_2O_5 grade (32.26%) was obtained when the pH value was about 6. In addition, the P_2O_5 recovery of the concentrate reached 96.94% at maximum when the pH value was about 8. By considering the relationship between the grade and recovery, the products with 31.85% P_2O_5 grade and 94.56% P_2O_5 recovery can be obtained when the pH value was about 7.

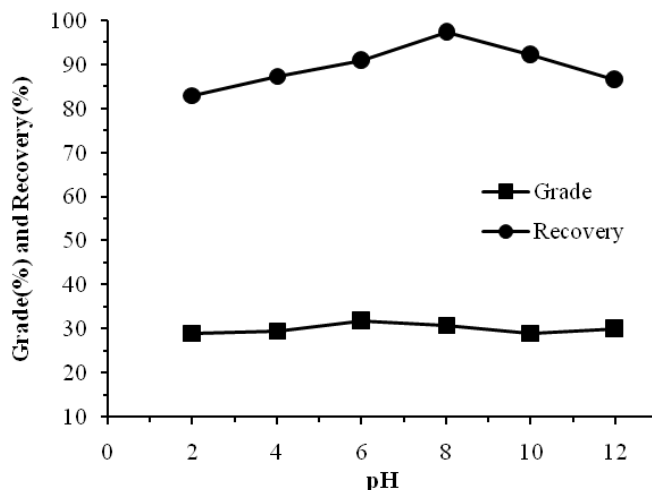


Fig. 3. Flotation results of artificial mixture as a function of pH value

Flotation performance of real ore

Figure 4 provides a flotation separation performance of the real phosphate ore obtained under different operating conditions using AH as a collector. The results showed that the P_2O_5 recovery of the concentrate decreased significantly with the P_2O_5 grade of concentrate increase. The P_2O_5 grade of concentrate was increased from 19.84% to 30.51% when the P_2O_5 recovery of concentrate decreased from 100% to 79.16%, which achieved the target grade ($\beta P_2O_5 \geq 30\%$).

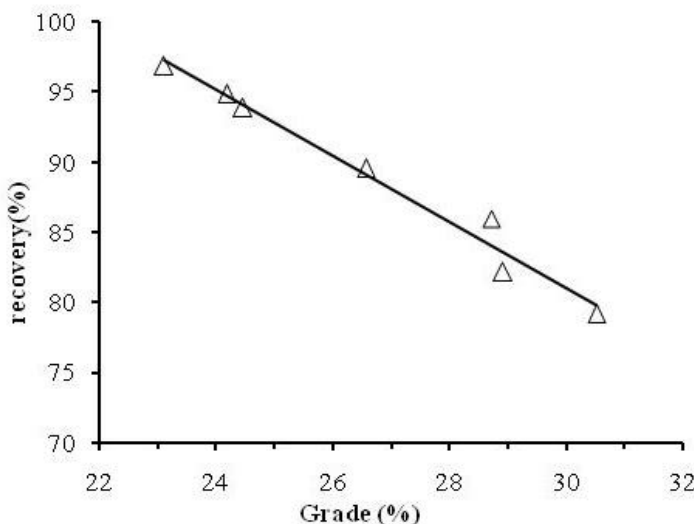


Fig. 4. Flotation results of real ore

Zeta potential measurements

The zeta potential results of collophanite in distilled water and AH solutions at different pH values are given in Fig. 5a. The zeta potential of collophanite in water was negative and decreased with the increase of the pH. Additionally, it was not possible to obtain the isoelectric point (IEP) value of collophanite. Nevertheless, IEP values of apatite between 2.0 and 8.0 are reported in the literature (Merma et al., 2013). This collophanite behavior could be explained due to its tolerance to isomorphic substitutions regardless of its origin and composition, which alter the IEP value of the mineral (Merma et al., 2013). Figure 5a also shows the zeta potential profile of the collophanite after the interaction with AH over the studied pH range. The addition of AH leads to a decrease in the zeta potential of collophanite. Moreover, the change was more pronounced at pH range between 6 and 7. It indicated that the AH molecules were adsorbed on the mineral surface.

As shown in Fig. 5b, the zeta potential of dolomite in water decreased with the increase of the pH, and the IEP of dolomite was about 4.0. Furthermore, it can be seen that the IEP of dolomite changed from 4.0 to around 3.4 in the presence of AH solution. The slight variation indicated that the amount of AH adsorbed on the dolomite surface in the aqueous AH solution was small.

Comparing the zeta potential results for two minerals, the variation of absolute value of the zeta potential for collophanite and dolomite in AH solutions as a function of pH is shown in Fig. 6. The zeta potential variation of dolomite is more significant than collophanite over the pH range between 2 and 4, which is probably because of the dissolution of the dolomite in the acidic medium. As the pH increased, the variation absolute value of zeta potential for collophanite increased and surpassed the dolomite (Fig. 6). It can be concluded that the amount of AH adsorbed on collophanite surface is more than dolomite under the same conditions, which is the essential reason that use of AH facilities separation of collophanite and dolomite.

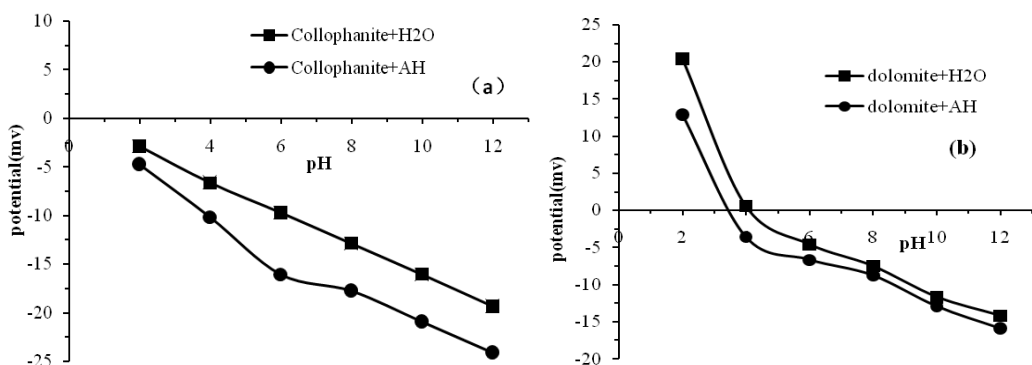


Fig. 5. Zeta potential of (a) collophanite (b) dolomite in distilled water and AH solution as a function of pH

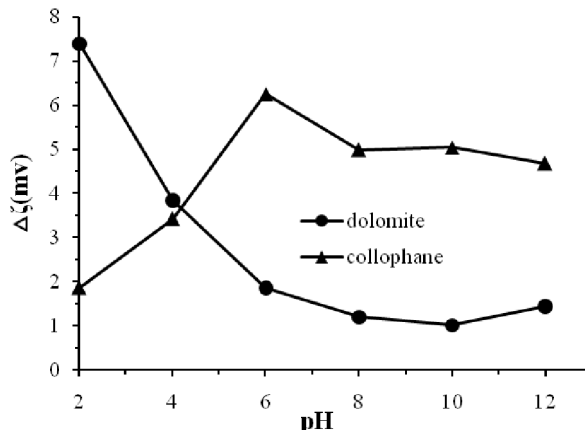


Fig. 6. Variation of absolute value of zeta potential for collophanite and dolomite in AH solution as a function of pH

FTIR analysis

In order to investigate the adsorption mechanism of AH on the mineral surfaces, the raw minerals and minerals reacting with AH were characterized by the infrared spectrometry.

The FTIR spectrum of dolomite before and after reacting with AH is shown in Fig. 7a. After the interaction with AH, the stretching vibration peaks at 1661 cm^{-1} and 1622 cm^{-1} of C=N could be observed on dolomite surface although they were weak. The characteristics peaks at 2956 cm^{-1} , 2921 cm^{-1} and 2851 cm^{-1} arise from stretching vibration of $-\text{CH}_3$ and $-\text{CH}_2$ respectively. This shows that a surface compound formed on dolomite.

Figure 7b displays the infrared spectra of collophane before and after reacting with AH. In contrast with the spectra A, the infrared spectra of collophane surface reacting with AH appears obvious characteristics peaks at 3439 cm^{-1} , 2921 cm^{-1} , 2851 cm^{-1} , 1771 cm^{-1} , 1661 cm^{-1} and 1622 cm^{-1} . The peak frequency at 3439 cm^{-1} comes from stretching vibration of O-H in H_2O molecule adsorbed on collophane surface. The characteristics peaks at 2921 cm^{-1} and 2851 cm^{-1} arise from stretching vibration of CH_2 . Additionally, there exists C=N and C=O stretching vibration at 1771 cm^{-1} , 1661 cm^{-1} and 1622 cm^{-1} . It can be concluded that there exists stable chemical compound on the collophane surface.

A comparison of infrared spectra of collophane and dolomite interaction with AH revealed that the characteristics peaks of C=N, $-\text{CH}_3$ and $-\text{CH}_2$ on collophane were stronger than those on dolomite. This indicates that the amount of AH adsorbed on collophane surface is greater than that on dolomite, which is in good agreement with the results of collector adsorption experiments (Figs. 8 and 9).

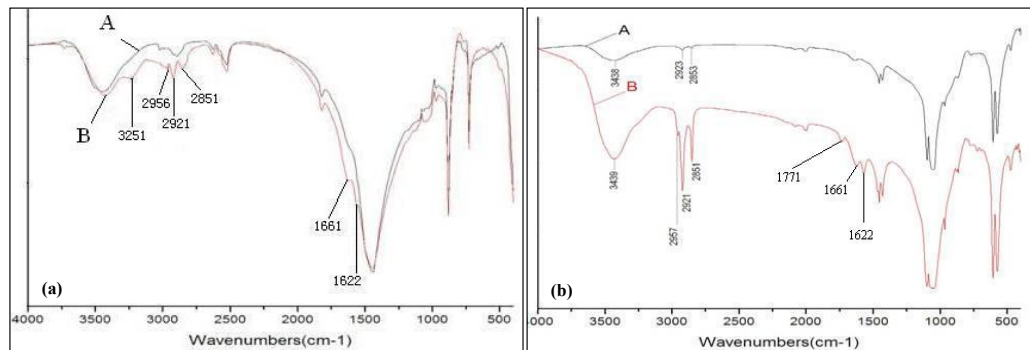


Fig. 7. FTIR spectra of (a) dolomite(b) colophane before (A) and after (B) reacting with AH

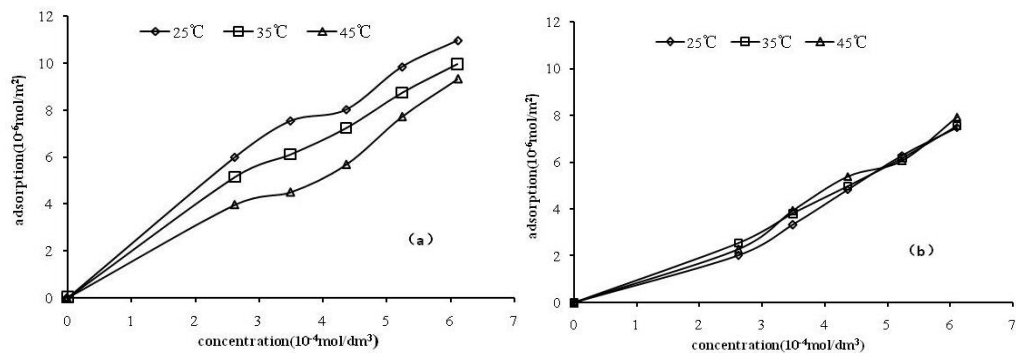


Fig. 8. Adsorption isotherms of AH on (a) colophane(b) dolomite surfaces at different temperatures

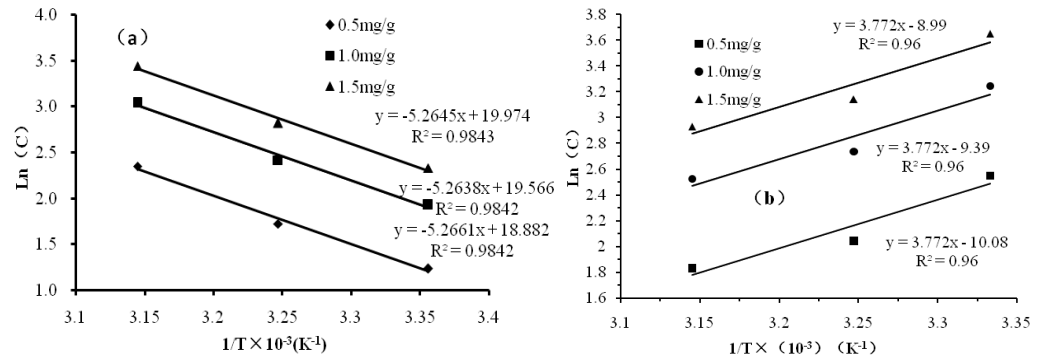


Fig. 9. Fitting curves of equivalent adsorption on (a) colophane (b) dolomite at three different levels

Adsorption experiments

The adsorption measurements of AH on the surface of colophane and dolomite as a function of AH concentration were performed in neutral medium ($\text{pH} = 6.8$). Figure 8 shows the adsorption isotherms of AH on colophane and dolomite surfaces at three different temperatures, respectively. The results indicated that the adsorption quantity

of AH on the mineral surface increased with the increasing concentration of AH for both minerals. Under the condition of room temperature, the adsorption quantity on the collophane surface was higher than that on the dolomite surface at the low concentration of AH solution. This is also verified by the results of the zeta potential measurement (see Fig. 5). For collophane, the adsorption quantity of AH decreased with the increasing temperature because the AH molecules at high temperature showed higher free energy which made them more likely to desorb from the mineral surface. Meanwhile, the free AH molecules were not easy to adsorb on the mineral surfaces due to the high kinetic energy. The situation for dolomite was opposite since the adsorption quantity of AH showed a slight increase with the increase of the temperature. Thus, AH chelating collector can be used to separate collophane from dolomite at a low collector dosage at room temperature in the direct flotation of calcareous phosphate ore.

Thermodynamic calculation

The enthalpy change (ΔH) of adsorption can be calculated using Eq. 2 (Geet et al., 2014):

$$\ln C = \frac{\Delta H}{RT} + \text{constant} \quad (2)$$

where C is the concentration of AH solution, R is constant, T temperature in kelvin, ΔH adsorption enthalpy.

The thermodynamic parameters of AH adsorption for collophane are listed in Table 3. Figure 9a shows the fitting curves of the equivalent adsorption on collophane at three different adsorption levels in term of parameters presented in Table 3. The enthalpy changes (ΔH) of adsorption were calculated as follows:

when $\Gamma = 0.5 \text{ mg/g}$, the slope of curve (K1) is equal to $-5.266 \cdot 10^3$ (Fig. 9a):

$$\Delta H_{(\Gamma=0.5 \text{ mg/g})} = -5.2661 \cdot 10^3 \times R = -5.2661 \cdot 10^3 \times 8.3145 = -43.79 \text{ kJ/mol}$$

when $\Gamma = 1.0 \text{ mg/g}$:

$$\Delta H_{(\Gamma=1.0 \text{ mg/g})} = -5.2638 \cdot 10^3 \times R = -5.2638 \cdot 10^3 \times 8.3145 = -43.766 \text{ kJ/mol}$$

when $\Gamma = 1.5 \text{ mg/g}$:

$$\Delta H_{(\Gamma=1.5 \text{ mg/g})} = -5.2646 \cdot 10^3 \times R = -5.2646 \cdot 10^3 \times 8.3145 = -43.77 \text{ kJ/mol.}$$

According to the calculation results, the enthalpy changes (ΔH) of the adsorption at three different adsorption levels are greater than 40 kJ/mol. It is believed that the adsorption process of AH is held on the surface of collophane by chemical bond. Meanwhile, the adsorption process is an exothermic reaction because the enthalpy changes of adsorption are negative.

The calculation method of enthalpy changes (ΔH) of AH adsorbed on dolomite is the same as that on collophane. The thermodynamic parameters are listed in Table 3. The fitting curves of equivalent adsorption on dolomite at three different adsorption levels are given in Fig. 9b. The enthalpy changes (ΔH) of adsorption were calculated as follows:

when $\Gamma = 0.5 \text{ mg/g}$, $K1=3.77026\cdot103$ (Fig. 9b):

$$\Delta H_{(\Gamma=0.5 \text{ mg/g})} = 3.772 \cdot 10^3 \times R = 3.772 \cdot 10^3 \times 8.3145 = 31.35 \text{ kJ/mol}$$

when $\Gamma = 1.0 \text{ mg/g}$:

$$\Delta H_{(\Gamma=1.0 \text{ mg/g})} = 3.772 \cdot 10^3 \times R = 3.772 \cdot 10^3 \times 8.3145 = 31.35 \text{ kJ/mol}$$

when $\Gamma = 1.5 \text{ mg/g}$:

$$\Delta H_{(\Gamma=1.5 \text{ mg/g})} = 3.772 \cdot 10^3 \times R = 3.772 \cdot 10^3 \times 8.3145 = 31.35 \text{ kJ/mol.}$$

The enthalpy changes (ΔH) of adsorption at three different adsorption levels are less than 40 kJ/mol. According to literature (Zhu and Zhu, 1993), the enthalpy change of physisorption is less than 9 kJ/mol, and chemisorption is larger than 40 kJ/mol. Therefore, there exists physisorption and chemisorption when AH is adsorbed on the dolomite surface. In addition, the adsorption process is an endothermic reaction which explains that the adsorption quantity of AH on dolomite surface has a slight increase with the increase in temperature (see Fig. 8).

Based on the results of the thermodynamic calculation for both minerals, it can be concluded that the adsorption behavior of AH on collophane is enhanced while the temperature decreases because the adsorption process is an exothermic reaction. However, the situation for dolomite is opposite since the adsorption process is endothermic. Therefore, the effect of separating collophane from dolomite with alkyl hydroxamic acid at room temperature is better than that at high temperature.

Table 3. Thermodynamic parameters of adsorption of AH on the collophane and dolomite surfaces in aqueous solution

Γ (mg/g)	C (mg/dm ³)			Ln C			1/T (K ⁻¹)	
	298 K	308 K	318 K	298 K	308 K	318 K		
Collophane	0.5	3.44	5.61	10.47	1.24	1.72	2.35	0.003356
	1.0	6.88	11.22	20.93	1.93	2.42	3.04	0.003247
	1.5	10.32	16.83	31.40	2.33	2.82	3.45	0.003145
Dolomite	0.5	12.83	7.73	6.25	2.551786	2.045109	1.832581	0.003333
	1.0	25.66	15.46	18.46	3.244933	2.738256	2.525729	0.003247
	1.5	38.49	23.19	27.69	3.650398	3.143721	2.931194	0.003145

Quantum chemical calculation

The optimized molecule models of two types of alkyl hydroxamic acid are presented in Fig. 10. Some selected atomic charges were calculated, and the results are presented in Table 4. The results indicate that the atomic charges of 39O and 42O are higher than other atoms in both types of AH molecules. It can be concluded that 39O and 42O atoms are easy to offer their electrons to calcium and magnesium ions on the collophane and dolomite surfaces to form ionic bond (Liu et al., 2015).

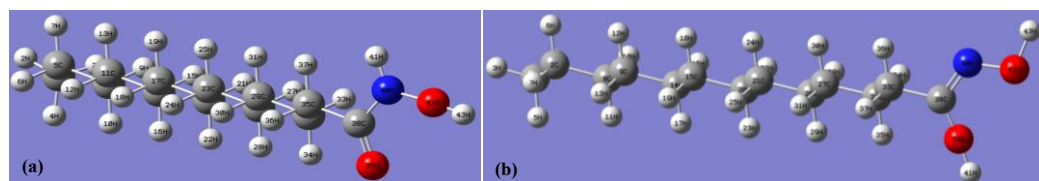


Fig. 10. Molecule model of alkylhydroxamic acid(a) AH^{-1} (b) AH^{-2}

Table 4. Selected Mulliken atomic charges of AH^{-1} and AH^{-2}

Reagent	Mulliken atomic charges
AH^{-1}	40N: -0.226683; 39O: -0.415645; 42O: -0.701150; 38C: 0.551314
AH^{-2}	40N: -0.183200; 39O: -0.709937; 42O: -0.497207; 38C: 0.544746

Figure 11 shows the schematic diagram of alkyl hydroxamic acid adsorbed on the collophane and dolomite surfaces in aqueous environment. It was also observed that two types of AH molecules form O-O five-membered ring with calcium and magnesium ions on the collophane and dolomite surfaces, respectively.

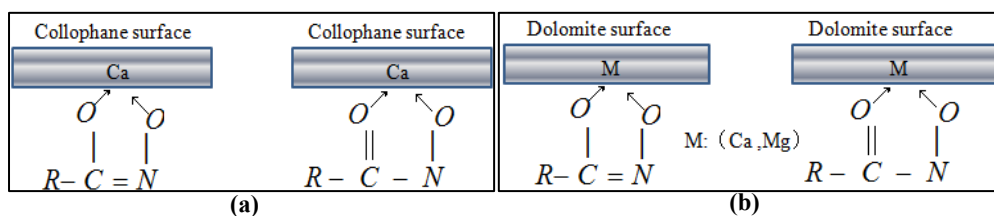


Fig. 11. Schematic diagrams of alkylhydroxamic acid adsorbed on (a) collophane
(b) dolomite surfaces in aqueous solution

Conclusions

Alkylhydroxamic acid exhibits selective collection of collophane coexisting with dolomite, allowing preferential flotation separation in neutral medium. The results of artificially mixed minerals and real phosphate ore separation show that AH can separate collophane from dolomite without any other reagents, and the concentrate

with 30.51% P_2O_5 grade and 79.16% P_2O_5 recovery can be obtained when the pH value is about 7.

Collophane has a more obvious variation of zeta potential than dolomite in AH solution when pH value is greater than 4, indicating a stronger interaction with AH. The FTIR spectra show the presence of AH on the surface of collophane, meanwhile, AH is preferably adsorb on the surface of collophane by chemical bond. The spectrum of dolomite reacting with AH is nearly similar with dolomite. Due to adsorption test and thermodynamic calculation, there exist several different adsorption behaviors between collophane and dolomite: (1) adsorbed collector density of collophane decreases significantly with the increase of temperature, while that of dolomite has a slight increase; (2) adsorbed collector density of collophane is larger than that of dolomite with low collector dosage at room temperature; (3) the process of AH adsorption on collophane is an exothermic reaction, while the situation for dolomite is opposite. Quantum chemical calculation results show that AH adsorbs onto collophane surface by chemical adsorption, which the AH molecule form O-O five-membered ring with calcium ion on the collophane surface.

Acknowledgements

The author wishes to express his most sincere appreciation to Prof. LI Chongqing and ZHANG Haifeng, who read the manuscript carefully and gave valuable advice. Tremendous thanks are owed to Mr. LIU Xiangbin for helping him with the chemical analysis.

References

ABOUZEID A.Z.M., NEGM A.T., ELGILLANI D.A., 2009, *Upgrading of calcareous phosphate ores by flotation: Effect of ore characteristics*, International Journal of Mineral Processing, 90, 81–89.

AHMED H.A.M., ALJUHANI M.S., DRZYMALA J., 2013, *Flotation after direct contact of flotation reagents with particles. Part I. Model investigations*, Physicochemical Problem of Mineral Processing, 49(2), 713–723.

AL-FARISS T.F., ARAFAT Y., ABD EL-ALEEM F.A.E., L-MIDANY A.A., 2014, *Investigating sodium sulphate as a phosphate depressant in acidic media*, Separation and Purification Technology, 124, 163–169.

BOULOS T.R., YEHIA A., IBRAHIM, S.S. and YASSIN, K.E., 2014, *A modification in the flotation process of a calcareous–siliceous phosphorite that might improve the process economics*, Minerals Engineering, 69, 97–101.

DOS SANTOS M.A., SANTANA R.C., CAPPONI F., ATAIDE C.H., BARROZO M.A.S., 2012, *Influence of the water composition on the selectivity of apatite flotation*, Separation Science and Technology, 47(4), 606–612.

ELMAHDY A.M., EL-MOFTY S.E., ABDEL-KHALEK M.A., ABDEL-KHALEK N.A., EL-MIDANY A.A., 2013, *Bacterially induced phosphate–dolomite separation using amphoteric collector*, Separation and Purification Technology, 102, 94–102.

GE Y.Y., HUANG L., XIONG X.H., YU Y.F., 2014, *Mechanism of a new collector alkyl polyamine ether adsorption on jasper and magnetite*, Journal of Central South University, 45(5), 1377–1382.

JIANG Y., ZHAO B., ZHOU X.H., ZHOU L.Y., 2010, *Flotation of diaspore and aluminosilicate minerals applying novel carboxyl hydroxamic acids as collector*, Hydrometallurgy, 104(1), 112–118.

LIU A., FAN J.C., FAN M.Q., 2014, *Quantum chemical calculations and molecular dynamics simulations of amine collector adsorption on quartz (001) surface in the aqueous solution*, International Journal of Mineral Processing, 134, 1–10.

MERMA A.G., TOREM M.L., MORAN J.J.V., MONTE M.B.M., 2013, *On the fundamental aspects of apatite and quartz flotation using a Gram positive strain as a bioreagent*, Minerals Engineering, 48, 61–67.

MOHAMMADKHANI M., NOAPARAST M., SHAFAEI S.Z., AMINI A., AMINI E., ABDOLLAHI H., 2011, *Double reverse flotation of a very low grade sedimentary phosphate rock, rich in carbonate and silicate*, International Journal of Mineral Processing, 100(3-4), 157–165.

NANTHAKUMAR B., GRIMM D., PAWLICK M., 2009, *Anionic flotation of high-iron phosphate ores – Control of process water chemistry and depression of iron minerals by starch and guar gum*, International Journal of Mineral Processing, 92(1-2), 49–57.

SANTANA R.C., DUARTE C.R., ATAIDE C.H., BARROZO M.A.S., 2011, *Flotation selectivity of phosphate ore: Effects of particle size and reagent concentration*, Separation Science and Technology, 46(9), 1511–1518.

SANTANA R.C., RIBEIRO J.A., SANTOS M.A., REIS A.S., ATAIDE C.H., BARROZO M.A.S., 2012, *Flotation of fine apatitic ore using microbubbles*, Separation and Purification Technology, 98, 402–409.

SANTANA R., FARNESE A., FORTES M., ATAIDE C., BARROZO M., 2008, *Influence of particle size and reagent dosage on the performance of apatite flotation*, Separation and Purification Technology, 64(1), 8–15.

SIS H., CHANDER S., 2003, *Reagents used in the flotation of phosphate ores: a critical review*, Minerals Engineering, 16(7), 577–585.

WANG P., QIN W., REN L.Y., WEI Q., 2013, *Solution chemistry and utilization of alkyl hydroxamic acid in flotation of fine cassiterite*, Transactions of Nonferrous Metals Society of China, 23 (6), 1789–1796.

WANG X., NGUYEN A.V., MILLER J.D., 2006, *Selective attachment and spreading of hydroxamic acid–alcohol collector mixtures in phosphate flotation*, International Journal of Mineral Processing, 78 (2), 122–130.

ZHAO G., ZHONG H., QIU X.Y., WANG S., GAO Y.D., 2013, *The DFT study of cyclohexylhydroxamic acid as a collector in scheelite flotation*, Minerals Engineering, 49, 54–60.

ZHU D., ZHU Y.S., 1993, *Dynamic study on adsorption of octylhydroxamic acid on the surfaces of cassiterite*, Mining and Metallurgical Engineering, 13(4), 41–43.

Received January 23, 2015; reviewed; accepted May 31, 2015

ROLE OF SODIUM HEXAMETAPHOSPHATE IN FLOTATION OF A NICKEL ORE

Bo FENG*, Pengcheng WANG*, Yiping LU**, Qiming FENG**

* Jiangxi Key Laboratory of Mining Engineering, Jiangxi University of Science and Technology, Ganzhou, China

** School of Mineral Processing and Bioengineering, Central South University, Changsha, China
fengbo319@163.com

Abstract: In this work, a role of sodium hexametaphosphate (SHMP) in the flotation performance of a nickel ore was studied and mechanism was discussed in detail. The results showed that the presence of lizardite interferes with the flotation performance of pentlandite. The adsorption of SHMP at the lizardite/solution interface and the removal of magnesium ions from lizardite surface overcompensated the positive charge on the lizardite particle, and made its zeta potential negative. The interaction between lizardite and pentlandite changed from attractive to repulsive in the presence of SHMP. Thus, the addition of SHMP made the mixed sample of pentlandite and lizardite more dispersed, and significantly reduced the adverse effect of lizardite on the flotation of pentlandite. However, when the content of lizardite in the mixed ore was increased, the effect of SHMP weakened. Therefore, in flotation of a nickel ore containing a large amount of lizardite (46% w/w), SHMP usage is not suitable at the roughing stage due to the fact that lizardite in the pulp will consume most of the SHMP, and hence the removal of lizardite slimes from pentlandite surface become impossible. Based upon the results, SHMP usage is found to be suitable at the cleaning stage to improve the grade of concentrate.

Keywords: nickel ore, lizardite, flotation, concentration process, pentlandite

Introduction

The Jinchuan nickel mine is the largest nickel production corporation in China. However, pentlandite ($(\text{Fe}, \text{Ni})_9\text{S}_8$) flotation in Jinchuan has historically been difficult due to the presence of large amounts of serpentine minerals which can reduce selectivity in flotation, causing loss of Ni-mineral to the tails, hence reducing the grade of concentrate and increasing transport and smelting costs as well (Edwards et al., 1980; Wellham et al., 1992; Peng and Bradshaw, 2012). The main reason for MgO -minerals degrading the flotation performance of the nickel ore is slime coating which is believed to be primarily controlled by the magnitude and sign of the surface charge

of the interacting particles as reflected by zeta potential measurements (Uddin et al., 2012; Trahar, 1981). Oppositely charged or near-neutral charged ultrafine particles tend to aggregate. Slime coating can be controlled using dispersants, which adsorb preferentially onto slimes, reversing and/or increasing the surface charge and preventing electrostatic attraction. In order to improve the flotation selectivity against MgO-minerals, sodium hexametaphosphate (SHMP), sodium silicate, carboxy methyl cellulose (CMC), and other reagents, are used to disperse slime particles of MgO type minerals from sulfide surfaces (Bremmell et al., 2005; Feng and Luo, 2013; Lu et al., 2011).

SHMP is a reagent that is commonly used to disperse the particles in the pulp. Previous research has shown that SHMP can make the mixed sample of pyrite and lizardite more disperse, and significantly reduce the adverse effect of lizardite ($Mg_6[Si_4O_{10}](OH)_8$) on flotation of pyrite (Lu et al., 2011). However, whether SHMP has the same effect in the flotation of a nickel ore or not has not been studied yet. For this purpose, the objective of this study is to find out the role of SHMP in the flotation performance of a nickel ore.

Experimental

Materials and methods

The lizardite used in this study was purchased from Donghai, Jiangsu Province, China. The pentlandite sample was prepared using “pentlandite rocks” obtained from Jinchuan, Gansu Province, China. This sample was passed through a magnetic separator three times to remove the magnetic pyrrhotite fraction. X-ray diffraction measurements and chemical analysis of the lizardite and pentlandite samples showed that there was 2% of chlorite in lizardite and minor amounts of impurities in pentlandite. Two samples were dry-ground and screened. The particle size distribution of lizardite determined using a Malvern Instruments Mastersizer showed that the sample was less than $-10\text{ }\mu\text{m}$ with a D_{50} of $3.94\text{ }\mu\text{m}$, a D_{90} of $9.62\text{ }\mu\text{m}$, and an average diameter of $6.17\text{ }\mu\text{m}$. A $-150+75\text{ }\mu\text{m}$ fraction of pentlandite was used for the flotation tests.

The nickel grade of the ore sample used in this study was 1.35%. Approximately 96% of the nickel in the ore was in the form of pentlandite, and could be recovered by true flotation. The remaining 4% of nickel distributed in non-sulfide minerals, which could only be recovered by the entrainment mechanism or as composites with pentlandite. The ore contained of 37% w/w MgO was distributed mainly in serpentine (46% w/w) and olivine (19% w/w), as determined by x-ray diffraction.

A laboratory grade sample of the flotation collector, potassium amyl xanthate (PAX), was used for the flotation of the ore and a highly purified PAX was used for the micro-flotation of pentlandite, respectively. Since the solutions of PAX slowly hydrolyse, the solutions were made freshly as required (1% by weight). MIBC was

used as a frother during the flotation. An analytical grade of KOH and HCl were used for the pH adjustment.

Methods

Grinding

The ore samples were crushed to less than 2 mm, and riffled into representative samples of 500 g. These samples were purged under nitrogen and frozen. For each flotation experiment, the samples were ground at 60% (w/w) in a mild steel rod mill in order to produce a sample in size of 65% passing 74 μm . Sodium carbonate of 5 000 g/Mg was added at the grinding stage (Feng et al., 2012a).

Flotation

A mechanical agitation flotation machine was used for the micro-flotation experiments of a mixture of pentlandite and lizardite minerals. Pentlandite (2 g) was washed in ultrasonic bath for 3 min to remove potential oxidation film before the sample was introduced to the flotation cell. The pH of the suspension was adjusted to appropriate values using KOH or HCl solutions. This was followed by the addition of stock PAX solution and MIBC for 5 min of stirring after adding each reagent, respectively. The conditioned slurry was floated for 4 min. In order to study the effect of lizardite on pentlandite flotation, lizardite was also conditioned with pentlandite particles. At this time, the changing amount of lizardite was introduced before PAX. The SHMP dispersant was also added before the addition of PAX when needed. The floated and unfloated particles were collected, filtered, and dried. The flotation recovery was calculated based on the solids weight and grade of the two products.

The bench-scale flotation tests for the nickel ore were performed in a self-aerated XFD-63 flotation cell. The volume of the cell was 1.5 dm^3 . The mill product was transferred to the flotation cell and diluted to 35% (w/w). The pulp was conditioned for 5 min after the addition of PAX (150 g/Mg) and MIBC (30 g/Mg), respectively. After the conditioning process, the flotation was started with the injection of air into the flotation cell. The air flow rate was kept as 0.1 Nm^3/h monitored with a flowmeter. A total of five concentrates were collected at individual times of 1, 3, 6, 10, and 15 min.

Zeta potential measurements

Zeta potential of particles can be determined through measuring their electrophoretic mobility. The electrophoretic mobility measurements for the particles were carried out using a zeta potentiometer (Coulter Delsa440 SX). Potassium nitrate was used as a supporting electrolyte (0.001 mol/dm³). A suspension with 0.03% (w/w) mineral, ground to D_{50} less than 5 μm , was prepared with deionized water (resistivity $0.1 \cdot 10^6 \Omega\cdot\text{cm}$), and conditioned in a conditioning cell. The suspension pH was controlled with small additions of dilute HCl or KOH. The possibility of oxidation was not prevented during the measurements in order to be consistent with the situation during the flotation. The suspension was stirred for 30 min to allow the system to equilibrate

prior to the removal of a subsample for electrophoretic mobility measurement. The electrophoretic mobility was converted to the zeta potential by the equipment (Feng et al., 2012b).

Sedimentation tests

State of aggregation/dispersion between lizardite and pentlandite can be studied by sedimentation tests. For the sedimentation tests, 0.1 g of lizardite and 1 g of pentlandite were introduced directly into a beaker. The beaker contained 100 cm³ of solution and the pH was adjusted to desired values by small additions of KOH or HCl. The suspension was then conditioned for 30 min at 25°C and transferred into a 100 cm³ of a graduated flask. The suspension was then settled for 3 min, and about 25 cm³ of supernatant liquor was pipetted out and measured by scattering turbidimeter. The dispersion of the supernatant liquor was characterized by its turbidity. The higher is the turbidity value the better the sample is dispersed (Feng et al., 2012c).

X-Ray photoelectron spectroscopy (XPS)

The surface chemical compositions of lizardite before and after interaction with SHMP were determined by XPS. To prepare the mineral sample for the XPS analysis, 1 g lizardite was mixed with SHMP in 100 cm³ distilled water at pH 9. The suspension was conditioned for 5 min, and the mineral solids were filtered, washed with distilled water through the filter funnel, and dried in a desiccator in vacuum before the XPS analysis. The XPS experiments were carried out with a Perkin-Elmer Physical Electronics Division (PHI) 5100 spectrometer using Mg K α X-ray source operated at 300 W with a pass energy of 35.75 eV (Feng et al., 2012d).

Results and discussion

Effect of SHMP on flotation performance of pentlandite depressed by lizardite

The effect of lizardite on flotation of pentlandite in the absence and presence of SHMP as a function of pH is shown in Fig. 1. It can be seen from Fig.1 that the flotation recovery of pentlandite in the absence of lizardite is very high (>80%) under acidic and neutral conditions. As the pH was increased, pentlandite recovery decreased due to formation of hydrophilic iron oxy-hydroxy species on the surface. A minimum flotation recovery was obtained at pH 12 because of stable hydrophilic Fe(OH)₃ species formed at this pH. When lizardite particles were added prior to collector addition, the recovery of pentlandite decreased with increasing pH from a maximum recovery of 86% to 8% when 2.5 g/cm³ lizardite had been added. This result illustrates that hydrophilic lizardite interferes with flotation of valuable pentlandite. The addition of SHMP could restore the recovery of pentlandite which had been depressed by lizardite. At pH value 9, where flotation of nickel sulfide ore is routinely performed, the recovery of depressed pentlandite increased from 31% to 88% when 100 mg/dm³ SHMP had been added.

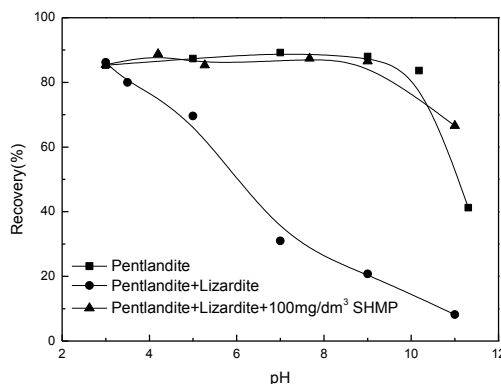


Fig. 1. Effect of SHMP on flotation performance of pentlandite in the presence of lizardite.
Test conditions: $c(\text{pentlandite}) = 50 \text{ g/cm}^3$; $c(\text{lizardite}) = 2.5 \text{ g/cm}^3$; $c(\text{PAX}) = 1 \cdot 10^{-4} \text{ mol/dm}^3$;
 $c(\text{MIBC}) = 1 \cdot 10^{-4} \text{ mol/dm}^3$; $c(\text{SHMP}) = 100 \text{ mg/dm}^3$

The effect of lizardite concentration on the flotation performance of pentlandite in the presence of 100 mg/dm^3 SHMP was studied and the result is shown in Fig. 2. The result showed that the flotation recovery of pentlandite decreased with the increase of lizardite concentration, and the addition of SHMP could significantly weaken the depression effect of lizardite on the flotation performance of pentlandite. However, when the content of lizardite in the mixed ore increased, the effect of SHMP weakened. This result illustrates that SHMP can reduce the adverse effect of lizardite on the flotation of pentlandite only when the content of lizardite in the mixed ore is not too high.

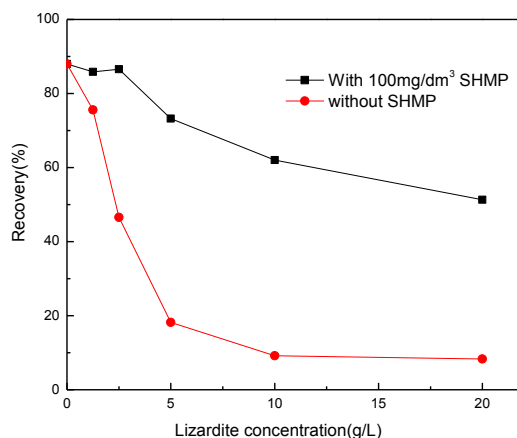


Fig. 2. Effect of lizardite concentration on flotation performance of pentlandite in the absence and presence of SHMP. $c(\text{PAX}) = 1 \cdot 10^{-4} \text{ mol/dm}^3$,
 $c(\text{MIBC}) = 1 \cdot 10^{-4} \text{ mol/dm}^3$, $c(\text{pentlandite}) = 50 \text{ g/dm}^3$

Role of SHMP in flotation performance of a nickel ore

The effect of flotation time on the recovery of a nickel ore at different SHMP dosages is shown in Fig. 3. The flotation results in Fig. 3 indicate that the recovery of pentlandite increased from 68% to 73% with the addition of 5 kg/Mg SHMP, and a further increase of the SHMP dosage produced little gain in the recovery. The effect of high intensity conditioning (HIC) method on the recovery of this nickel ore were also studied by present authors, and the Ni recovery increased by 21% (Feng et al., 2012a). This result illustrated that the hydrophilic lizardite slimes interfered with the flotation performance of pentlandite, and SHMP can eliminate this effect to some extent, but the effect was not so significant when compared with the HIC method.

Combining the results from Figs. 1 and 2, it can be concluded that a high content of lizardite in the ore (46% w/w) is the main reason that SHMP cannot do the same dispersion effect in the flotation of the nickel ore as in the mixed ore of pentlandite and lizardite.

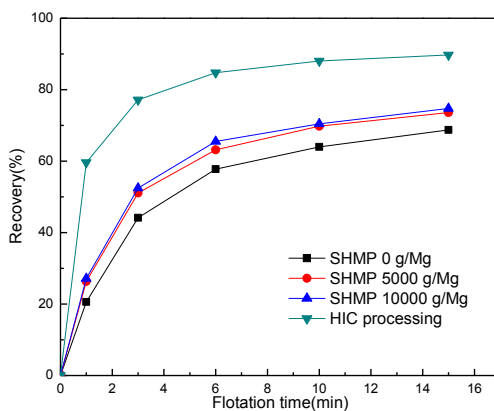


Fig. 3. Effect of SHMP on flotation performance of a nickel ore.
 $c(PAX) = 150 \text{ g/Mg}$; $c(MIBC) = 30 \text{ g/Mg}$

To study the mechanism by which SHMP increase the flotation recovery of pentlandite from a nickel ore, the effect of SHMP on surface cleaning of the nickel ore was carried out using a sieving technique developed by Chen et al. (1999a,b) and the result is shown in Fig. 4. The results showed that the amount of slimes removed from the surfaces of the coarse particles changed little with the increasing SHMP dosage. With the addition of 10 kg/Mg SHMP, there was no change in the particle size distribution for the size fraction larger than 10 μm and only the amount of slimes between the size of 4-10 μm decreased. The results indicated that SHMP was not effective in enhancing dispersion in the pulp and assisting removal of adhering slime particles from pentlandite surfaces when the lizardite content in pulp was too high.

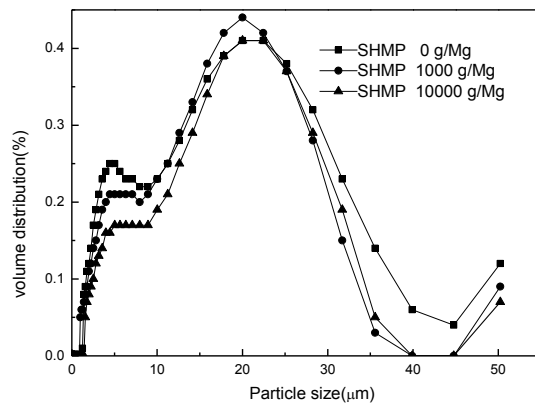


Fig. 4. Effect of SHMP on the size distribution of fines in the +75 μm sample

Flotation concentrate has to be upgraded at a nickel smelter by burning off excess of sulphur and removing iron as well as MgO as a slag phase to produce a nickel sulfide rich matte. It is critical that MgO levels in the concentrate are controlled to less than 7% to avoid processing problems occurring in the flash furnace due to the adverse impact of MgO on the melt chemistry. Therefore, the flotation concentrate of the HIC flotation experiments must be processed further.

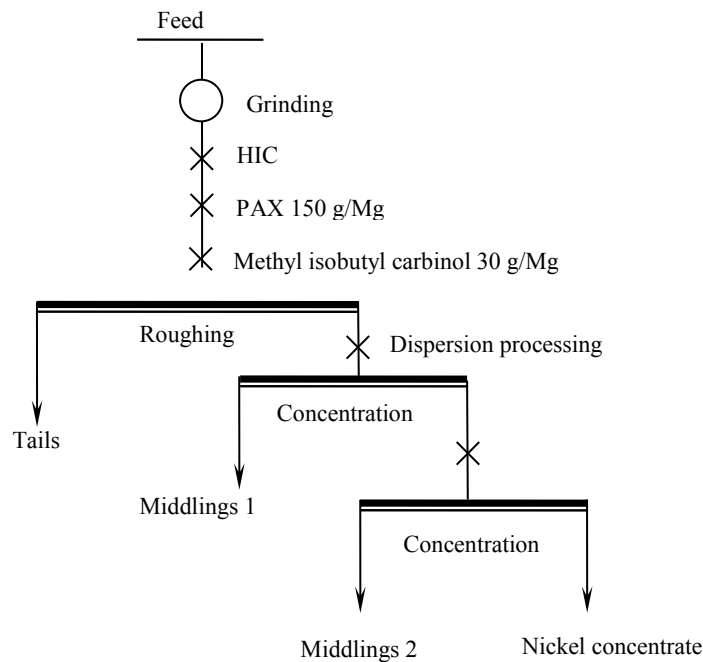


Fig. 5. Flowsheet of concentration process

The effect of different methods of dispersion processing on the nickel and MgO grade of concentrate was studied. The flotation flowsheet is shown in Fig. 5 and the results are shown in Table 1. It can be seen from Table 1 that the use of SHMP is an effective method to reduce the MgO levels in the concentrate. The results in Table 1 also show that HIC processing cannot reduce the MgO level to less than 7%.

Table 1. Result of concentration process

Dispersion processing	Products	Ratio	Ni Grade	Ni Recovery	MgO grade
HIC	Concentrate	13.78	6.89	70.18	7.77
	Middles 2	3.06	2.99	6.70	
	Middles 1	15.46	1.06	12.11	
	Tails	67.70	0.22	11.01	
	Feed	100	1.35	100.00	
CMC (1+0.5) kg/Mg	Concentrate	15.57	6.41	73.78	7.42
	Middles 2	3.63	2.31	6.20	
	Middles 1	11.79	1.01	8.80	
	Tails	69.01	0.22	11.22	
	Feed	100.00	1.35	100.00	
SHMP (1+0.5) kg/Mg	Concentrate	13.1	7.33	71.03	6.63
	Middles 2	3.21	3.15	7.48	
	Middles 1	13.47	1.01	10.06	
	Tails	70.22	0.22	11.43	
	Feed	100.00	1.35	100.00	

From the result of the batch-scale flotation, it can be concluded that the HIC is suitable at the roughing stage but not for the cleaning. The reason is that in the process of HIC, when the conditioning speed exceeds some critical value, the separation forces will be bigger than the adhesion forces between pentlandite surfaces and slimes particles, thus the slimes will be removed from pentlandite surface (Chen et al., 1999 a,b). The critical shear velocity required to detach a fine particle from the surface depends on the size of fine particle. The finer the particle at the surface is, the higher is the critical shear velocity required for the particle to be detached (Tsai et al., 1991; Phares et al., 2000). The conditioning speed of HIC processing is high enough to remove some coarse size lizardite slimes from sulfide surface. The removal of lizardite slimes will help to expose sulfide surfaces to flotation. However, there are fine slimes still attached to the surface of sulfide which cannot be removed and report into the concentrate with the sulfide. So the level of MgO in the concentrate cannot be reduced to less than 7%.

For SHMP, the situation is different. At the roughing process, there is a lot of lizardite in the pulp which will consume most of the SHMP and the removal of fine

serpentine slimes from sulfide surface by SHMP is impossible. Thus, the SHMP is not suitable at the roughing process. At the cleaning stage, most of lizardite has been reported into the tailings, and only a small amount of lizardite was present in the pulp. SHMP can interact with the lizardite slime that adsorbed on pentlandite surface and remove the lizardite slime from the pentlandite surface, thus decreasing the MgO level in the concentrate.

Mechanism of removal of lizardite slime from pentlandite surface

Surface charge is an important factor in controlling particle-particle interactions. The zeta potential values of pentlandite and lizardite as a function of pH are shown in Fig. 6. The PZC for the lizardite was pH 11.9 and the zeta potential of lizardite is positive in the pH range of 2-11.9. The surface of pentlandite is negatively charged in the pH range of 2-11.9. At pH value 9, surface potential of lizardite and pentlandite are opposite, the positively charged fine lizardite particles will attach to the negatively charged pentlandite particle surface through electrostatic attraction. The addition of SHMP makes the zeta potential of lizardite negative at all pH values measured. However, SHMP has minimal effect on zeta potential values of pentlandite. With the addition of SHMP, both pentlandite and lizardite are negatively charged, and the strong attraction force between pentlandite and lizardite surfaces is changed to the repulsion force.

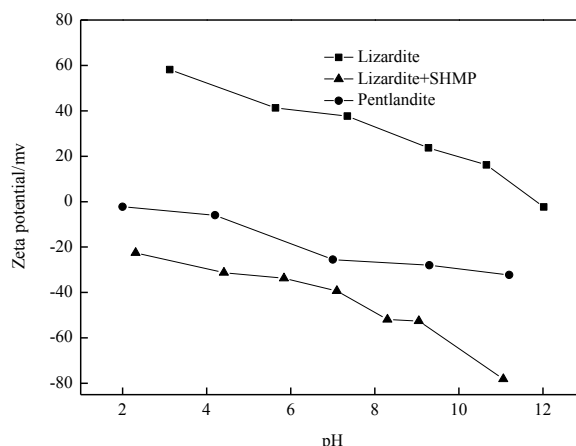


Fig. 6. Zeta potential of lizardite and pentlandite particles as a function of pH

The electrokinetic behavior of lizardite aqueous suspensions is mainly a function of the cation/anion atomic ratio on the surface. The removal of cations or the adsorption of anions on lizardite surface will result in a shift of the PZC to a lower pH (Feng et al., 2013). The dissolution and adsorption tests results in Table 2 show that the concentration of Mg cations dissolved from lizardite surface increased in the presence of SHMP. The results also show that SHMP can adsorb on the surface of lizardite.

Table 2. Dissolution and adsorption tests results of lizardite in the presence of SHMP

SHMP concentration (mg/dm ³)	Mg (mg/dm ³)	Adsorbed SHMP concentration (mg/dm ³)
0	1.27	0
100	25.06	67.3

To confirm the change of cation/anion atomic ratio on surface, the surface of lizardite sample was analysed using XPS. The atomic concentrations of the different elements present on the surface of the lizardite were determined. The results of this surface analysis are summarized in Table 3. Analysis of chemical species present on the surface of each sample by XPS indicated that the surface of the sample contained slightly less Mg in the presence of SHMP. This decreased concentration of Mg on the surfaces of lizardite is the main reason for the change of the lizardite surface charge.

Table 3. Relative atomic concentrations of the surface of lizardite using XPS

	Elements (%)	C1s	O1s	Si2p	Mg2p	Fe2p
Samples	Lizardite	13.4	53.1	9.1	23.8	0.6
	Lizardite+ SHMP	9.1	60.9	11.1	18.3	0.6

The effect of SHMP on the aggregation and dispersion behavior of pentlandite and lizardite can be also studied by sedimentation tests. The turbidity value of suspensions reflects the particle numbers of colloidal suspensions. A decrease of turbidity value indicates a decrease in particle number, which is the result of particle aggregation. The turbidity of mixed ores as a function of pH in the absence and presence of SHMP is shown in Fig. 7. It can be seen from Fig. 7 that SHMP could effectively disperse mixed ores in the pH range of 2–11, as the turbidity of mixed ores in the presence of SHMP is higher than the value in the absence of SHMP.

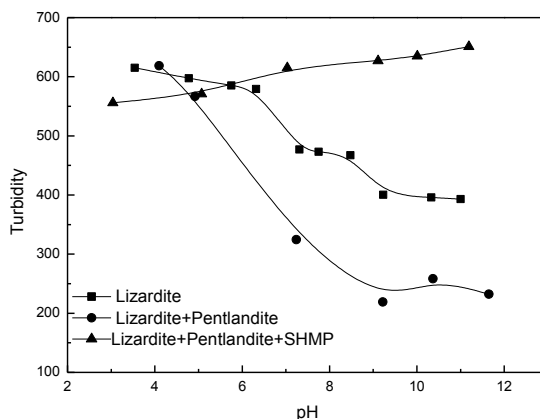


Fig. 7. Turbidity of lizardite and pentlandite as a function of pH in the presence of SHMP

Conclusions

From the results of this investigation, the following conclusions can be drawn.

1. The presence of lizardite interferes with the flotation of pentlandite by slime coating. The addition of SHMP could make the mixed sample of pentlandite and lizardite more disperse and significantly reduce the adverse effect of lizardite on the flotation of pentlandite.
2. The critical shear velocity required to detach a fine particle from pentlandite surface depends on the size of the fine particle. The very fine slimes cannot be removed by HIC and will report into the concentrate with the sulfide minerals. So HIC is suitable at the roughing stage but not for the cleaning stage.
3. The SHMP could reduce the adverse effect of lizardite on the flotation of pentlandite. However, when the content of lizardite in the mixed ore is increased, the effect of SHMP is weakened. So, SHMP is suitable for the cleaning stage to improve concentrate grade in flotation of the nickel ore.
4. The adsorption of SHMP at the lizardite/solution interface and the removal of magnesium ions overcompensates the positive charge on the lizardite particle and its zeta potential is rendered negative. The interaction between lizardite and pentlandite is changed from attractive to repulsive in the presence of SHMP.

Acknowledgements

The authors acknowledge the support of the National Natural Science Foundation of China (Nos. 51404109, 51374116), the Natural Science Foundation of Jiangxi Province (20142BAB216021) and Projects in Jiangxi province department of education (GJJ14425).

References

BREMMELL K.E., FORNASIERO D., RALSTON J., 2005, *Pentlandite-lizardite interactions and implications for their separation by flotation*, Colloids and Surfaces A: Physicochemical and Engineering Aspects, 252, 207–212.

CHEN G., GRANO S., SOBIERAJ S., RALSTON J., 1999a, *The effect of high intensity conditioning on the flotation of a nickel ore, Part 1: Size by size analysis*, Minerals Engineering, 12, 1185–1200.

CHEN G., GRANO S., SOBIERAJ S., RALSTON J., 1999b, *The effect of high intensity conditioning on the flotation of a nickel, Part 2: Mechanisms*, Minerals Engineering, 12, 1359–1373.

EDWARDS G.R., KIPKIE W.B., AGAR G.E., 1980, *The effect of slime coatings of the serpentine minerals, chrysotile and lizardite on pentlandite flotation*, International Journal of Mineral Processing, 7, 33–42.

FENG B., FENG Q., LU Y., LV P., 2012a, *The effect of conditioning methods and chain length of xanthate on the flotation of a nickel ore*, Minerals Engineering, 39, 48–50.

FENG B., LU Y., FENG Q., LI H., 2012b, *Solution chemistry of sodium silicate and implications for pyrite flotation*, Industrial & Engineering Chemistry Research, 51, 12089–12094.

FENG B., LU Y., FENG Q., ZHANG M., GU Y., 2012c, *Talc–serpentine interactions and implications for talc depression*, Minerals Engineering, 32, 68–73.

FENG B., FENG Q., LU Y., 2012d, *The effect of lizardite surface characteristics on pyrite flotation*, Applied Surface Science, 259, 153–158.

FENG B., LUO X., 2013, *The solution chemistry of carbonate and implications for pyrite flotation*, Minerals Engineering, 53, 181–183.

FENG B., LU Y.P., FENG Q.M., DING P., LUO N., 2013, *Mechanisms of surface charge development of serpentine mineral*, Transactions of Nonferrous Metals Society of China, 23, 1123–1128.

LU Y.P., ZHANG M.Q., FENG Q.M., LONG T., OU L.M., ZHANG G.F., 2011, *Effect of sodium hexametaphosphate on separation of serpentine from pyrite*, Transactions of Nonferrous Metals Society of China, 21, 208.

PENG Y., BRADSHAW D., 2012, *Mechanisms for the improved flotation of ultrafine pentlandite and its separation from lizardite in saline water*, Minerals Engineering, 36, 284–290.

PHARES D. J., SMEDLEY G.T., FLAGAN R.C., 2000, *Effect of particle size and material properties on aerodynamic resuspension from surfaces*, Journal of Aerosol Science, 31, 1335–1353.

TRAHAR W.J., 1981, *A rational interpretation of the role of particle size in flotation*, International Journal of Mineral Processing, 8, 289–327.

TSAI C.J., PUI D., LIU B., 1991, *Particle detachment from disk surfaces of computer disk drives*, Aerosol Sci., 22, 737–746.

UDDIN S., RAO S.R., MIRNEZAMI M., FINCH J.A., 2012, *Processing an ultramafic ore using fiber disintegration by acid attack*, International Journal of Mineral Processing, 102, 38–44.

WELLHAM E.J., ELBER L., YAN D.S., 1992, *The role of carboxymethyl cellulose in the flotation of a nickel sulphide transition ore*, Minerals Engineering, 5, 381–395.

Received April 30, 2015; reviewed; accepted June 9, 2015

INFLUENCE OF TYPE OF LINING IN HIGH-PRESSURE GRINDING ROLLS ON EFFECTIVENESS OF COPPER ORE COMMINUTION

**Daniel SARAMAK^{*}, Dariusz FOSZCZ^{*}, Tomasz GAWENDA^{*},
Andrzej KONIECZNY^{**}, Witold PAWŁOS^{**}**

^{*} AGH University of Science and Technology, Faculty of Mining and Geoengineering, Department of Environmental Engineering and Mineral Processing, Mickiewicza 30 Av., 30-059 Krakow, Poland, dsaramak@agh.edu.pl

^{**} KGHM "Polska Miedź" S.A., Division of Ore Processing Plant, Polkowice, ul. Kopalniana 1

Abstract: Comminution in a High-Pressure Grinding Rolls (HPGR) device is considered as one of the most efficient method to break particles, in terms of the energy utilization. Two main types of the rolls linings are applied in hard ore grinding: studded and hexagonal, which show varied characteristics of operation and have different lifetime of service. The article concerns the analysis of HPGR device operation for various linings of the rolls. Two pilot-scale test programmes were run and performance of both types of rolls was tested in terms of energy consumption, technological effects measured by means of comminution ratio, lifetime service as well as economic aspects. Results of investigation show, that much longer lifetime service was obtained for the studded rolls, while hexagonal ones are more favourable from economic scope. The feed material for the HPGR comminution tests was Polish copper ore from two divisions of processing plants of KGHM Polska Miedz S.A. Taking into account that industrial comminution operations in mining and mineral processing sector consume over 50% of total energy utilized for ore treatment operations, the problem is of a major significance, especially in terms of optimization of hard ore crushing and grinding circuits.

Keywords: HPGR, comminution, copper ore, high-pressure grinding rolls device, HPGR linings, ore processing, energy consumption

Introduction

Industrial comminution operations in mining and mineral processing sector consume over 50% of total energy utilized for total ore treatment operations. Key-aspects connected with reduction of that high share in the energy consumption concern the application of more efficient crushing and grinding technology together with more efficient utilization of the existing circuits of ore size reduction. High-pressure

grinding rolls (HPGR) technology is considered as one of the most efficient method to break particles, in terms of the energy utilization (Schoenert, 1979). The main principle of its operation is compressing of the particle bed between two counter-rotating rolls due to the high pressing force exerted on the one of rolls (called floating roll). Two main types of the rolls linings are applied in hard ore grinding: studded and hexagonal. The studded surface consists in metal ring with the pins (studs) embedded in regular distances from each other. The head of each pin protrudes above the surface of the lining, and an autogenous wear layer can be formed by ore packing itself between the studs on the roll. This layer provides a kind of shield from the abrasive impact of the material on the roll surface (Weir, 2013). The hexagonal type surface is made of hexagonal tiles fixed at the roll surface with using hot isostatic pressing technology. Area between the tiles is made of a softer material, which gets worn out, and the fine particles build an autogenous protective layer there (Sesemann et al., 2013).

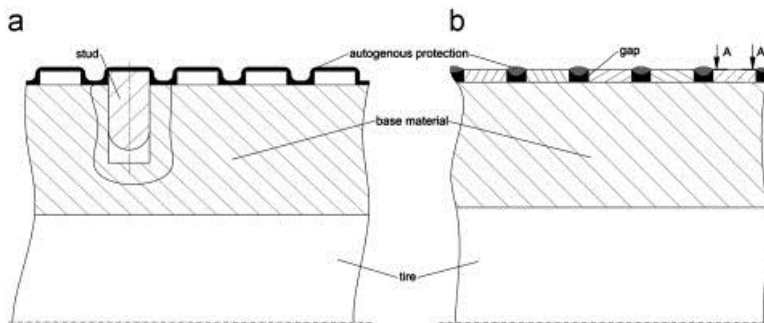


Fig.1. Two types of wear protection: studded (a) and hexagonal (b) surface

Both types of linings show varied characteristics of operation and have different lifetime of service. Data relating to lifetime operational hours for hexagonal rolls are not shown, while studded rolls are expected to operate up to 17,000 hours in coarse iron ore grinding and up to 10,000 hours in harder ore comminution, like kimberlites (Weir, 2013).

Very few data, concerning the relationship between type of lining and the effectiveness of comminution or the lifetime operation, can be found in literature. Results of some investigation (Daniel and Morell 2004, Saramak, 2012) and experience of authors show that comminution process for HPGR equipped with hexagonal rolls might show slightly lower energy consumption, while comminution ratio might be more favourable for studded rolls. On the other hand, the lifetime service of studded rolls might be longer, while cost of new set of rolls is considered to be lower for hexagonal rolls. It is however hard to state clearly, which type of roll surface is more beneficial for given type of hard ore, without relevant investigations. It is also almost impossible to draw some general conclusions, due to various factors influencing individual processing plant operation along with various ore characteristics. Lack of

respective research articles in literature, is also a significant limitation, because there are no opportunities for verification of own research.

Therefore, the main aim of the paper is to provide some comparative investigations over the performance of hexagonal and studded rolls. A pilot-scale investigative programme for copper ore, presented in the paper, concerns some selected aspects of operation of both types of linings, and the authors, to some extent, aimed to fill the gap in research within the issue. Another goal of these investigations was to learn about possible effects of copper ore HPGR comminution achieved for different types of device's linings.

Experimental programme

The pilot-scale research programme included testing the efficiency of copper ore crushing in the press equipped with different types of rolls lining. Similar research programmes were carried out by two HPGR manufacturers at the request of KGHM "Polska Miedź" S.A. The feed material for testing was copper ore from two divisions of processing plants: Rudna and Polkowice (called Rudna plant and Polkowice plant, or Rudna and Polkowice, respectively). The aims of investigations were investigations on copper ore comminution effectiveness depending the type of linings, determination of lifetime service of both types of linings, and economic assessment of two types of linings operation.

Feed material characteristics

The material from Rudna was a rod mill feed with the top size 40 mm, while ore from Polkowice constitutes the oversize product from the screen, operating on the first technological circuit. Particle size distributions of both materials are presented in Fig. 2., while ore lithologic composition and Bond's work index value are presented in Table 1.

Table 1. Feed material characteristics

	Rudna	Polkowice
Bond's work index [MJ/Mg]	50.868	40.428
Share of individual lithologic fractions [%]		
Sandstone	47	27
Shale	11	11
Dolomite	42	62

Inspecting Table 1 it can be seen that feed material from Rudna was of a higher value of Bond's work index, and sandstone content nearly 50 percent. Ore from Polkowice, in turn, contains over 60% of dolomite fraction and is characterized by lower Bond's index value for nearly 10.8 MJ/Mg, comparing to feed material from

Rudna. Various investigations show (Tumidajski et al., 2010) that diverse content of individual lithologic fractions results in different comminution effects and energy consumption. Energy consumption was given in SI units (MJ/Mg), but in industrial practice [kWh] units are used more frequently than [MJ] (1 MJ = 0.278 kWh).

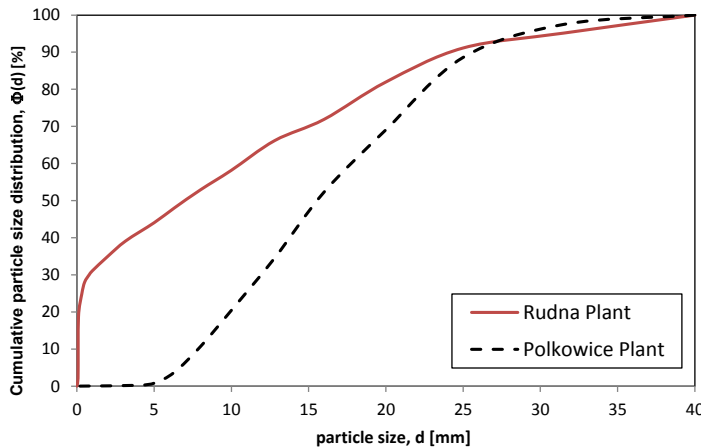


Fig. 2. Particle size distribution curves of feed materials from Rudna and Polkowice plants

Ore characteristics were supplemented with the grinding kinetics tests for both ores. The tests were carried out in a standard Bond's mill and particle size distributions of grinding products after 1, 3, 5 and 10 minutes were determined (Figs. 3 and 4), along with comminution ratios S_{50} , S_{80} and S_{95} (Table 2).

Table 2. Comminution ratio values after 1, 3, 5 and 10 minutes of grinding in laboratory Bond mill

	Comminution ratio S	Grinding time [minutes]			
		1	3	5	10
Rudna	S ₅₀	4.23	5.60	7.17	11.93
	S ₈₀	1.17	1.72	6.04	24.33
	S ₉₅	1.06	1.11	1.16	1.33
Polkowice	S ₅₀	2.42	8.86	17.33	24.67
	S ₈₀	1.11	1.32	1.77	34.10
	S ₉₅	1.05	1.08	1.15	1.27

Comparing data in Table 2 it can be noticed that more intense comminution is observed for material from Polkowice. After ten minutes of grinding particle size distribution curves of both material were similar, but comminution effectiveness measured by means of comminution degree value were higher for ore from Polkowice.

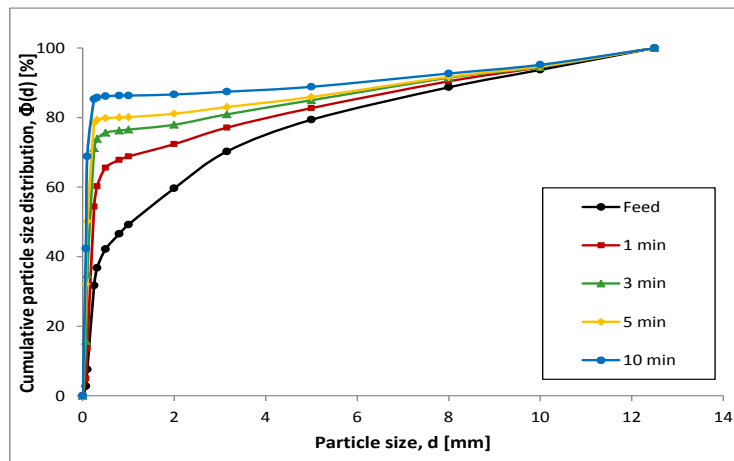


Fig. 3. Grinding kinetics for feed material from Rudna

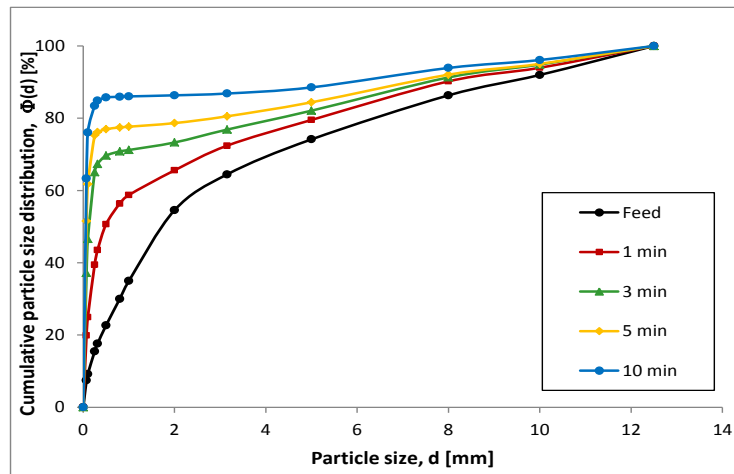


Fig. 4. Grinding kinetics for feed material from Polkowice

Results of investigations

As it was mentioned in previous section, research programme included investigations over lifetime performance of individual type of rolls; technological effectiveness in terms of comminution ratio and throughput and economic effects (energy consumption, capital cost). Manufacturers of each type of rolls have carried out tests, which enabled them to determine an approximate time of roll service when crushing Polish copper ores. Results of these tests are presented in Table 3.

Table 3. Service time of different type of HPGR linings, for ore from Rudna and Polkowice plant

Type of roll's lining	Estimated period of service [hours]	
	Rudna	Polkowice
Hexagonal	5 500	8 500
Studded	15 000	15 000

Table 3 shows that the studded linings have a much longer estimated time of service in crushing of Polish copper ore, comparing with hexagonal rolls. One can deduct that in this case hexagonal linings are sensitive to the type of ore in favor of Polkowice feed material. Studded linings, in turn, have similar time of service, regardless the ore type. In general, service time for studded rolls is 44% longer for Polkowice ore and 53% longer for Rudna feed material, comparing to hexagonal linings. The results presented in Table 3 confirm, to a some extend, incomplete literature data and information that can be found in HPGR catalogues. However, the results from Table 3 are valid only for specific type of material (here: Polish copper ore), and drawing a more general conclusions on the basis of these tests cannot be justified.

Linings lifetime service is a very significant issue, influencing the HPGR effectiveness performance, but there are also some other operating parameters of a key influence on high-pressure grinding process. The next aspect under investigation was technological effects. Table 4 presents comminution degrees obtained for both types of ore depending the type of linings.

Table 4. Comminution degrees for Rudna and Polkowice ore obtained for two types of linings under investigation

Comminution degree	Rudna		Polkowice	
	Studded	Hexagonal	Studded	Hexagonal
S ₅₀	6.66	5.70	10.31	8.53
S ₈₀	2.57	3.43	4.10	3.81
S ₉₅	1.91	2.90	1.35	2.47

The most favorable values of comminution ratio in terms of average index (S_{50}) were obtained for Polkowice ore, and comminution process in HPGR device equipped with studded rolls, was more effective. On the other hand, maximum comminution degrees (S_{95}) were more favorable for Rudna feed material and here hexagonal rolls have performed in a better manner than studded ones.

Energetic results

Energy consumption is another factor of a key significance, influencing the overall effectiveness of comminution operations. On the basis of power draw values of both HPGR devices and their productivities, the specific energy consumption index (E_{sp}) was calculated according to formula (1):

$$E_{sp} = \frac{P}{Q} \cdot \left[\frac{\text{kWh}}{\text{Mg}} \right], \quad (1)$$

where: P – total power draw during individual test [kW], Q – throughput of device [Mg/h].

Figure 5 presents the obtained results. It can be noticed, that operation of HPGR with hexagonal linings received higher energy consumption value, comparing to HPGR device with studded linings. Various values of E_{sp} were also obtained, depending on whether the feed material was from Rudna or Polkowice. In general, more favorable energetic results were achieved for ore from Rudna. Depending on the type of linings, E_{sp} values were lower by 5 and 20 per cent for hexagonal and studded linings, respectively. Studded lining might possibly consume nearly 30% less energy (for Rudna) and roughly 15% (for Polkowice) comparing to hexagonal ones.

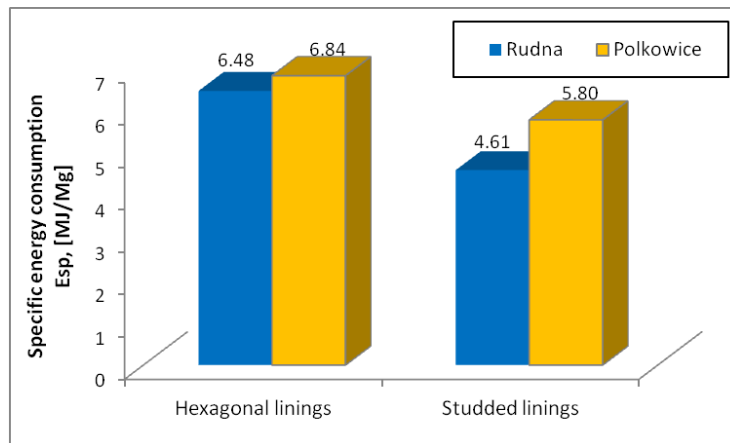


Fig. 5. E_{sp} values for HPGR equipped with studded and hexagonal linings obtained for feed material from Rudna and Polkowice plants

Table 5 presents results concerning the throughput of HPGR comminution process for both types of linings. The comparison of throughput is not an easy task, considering that both machines have operated at slightly different operating conditions, defined independently by each manufacturer. To overcome this problem the index of specific throughput (M_{dot}) was used, defined by formula (2):

$$M_{dot} = \frac{Q}{D \cdot l \cdot v}, \left[\frac{\text{Mg} \cdot \text{s}}{\text{h} \cdot \text{m}^3} \right] \quad (2)$$

where: Q – throughput [Mg/h], D – rolls diameter [m], l – width of rolls [m], v – peripheral speed of rolls [m/s].

Table 5. M_{dot} values for ore from Rudna and Polkowice, obtained in HPGR equipped with various type of linings

	Rudna		Polkowice	
	studded	hexagonal	studded	hexagonal
M_{dot} [Mg·s/h·m ³]	306	239	203	208

Even though this index is commonly used in evaluation of HPGR productivity, its interpretation might not be obvious for those who are not familiar with HPGR scaling-up procedure. However it is very important index, because it allows for comparing the productivities of HPGR with various dimensions. In general, the index characterizes a “volumetric” throughput, i.e. the throughput which can be obtained per unit of operational volume of HPGR. The higher value of the index, the more favorable productivity of HPGR is achieved for specific operational conditions and given type of feed material. Results in Table 5 show that more favorable effects of high-pressure comminution in terms of productivity were registered for studded rolls for Rudna, while for Polkowice slightly better results were observed for hexagonal rolls. In general, better throughput results were obtained for feed material from Rudna.

Assessment of HPGR product grindability

The HPGR comminution effects have a potential impact on the course of downstream grinding operations in ore enrichment circuit. According to various publications, possible energy savings in downstream grinding operations for HPGR products can reach up from 10 to 40% (Rule et al., 2008; Pahl, 1993; Fuerstenau et al., 1991).

HPGR products from each HPGR test was subject to ball mill grinding in order to determine potential benefits resulting from high-pressure compression of material in HPGR working chamber. In order to verify the results obtained for Polish copper ore, an assessment of HPGR product energy-consumption in ball mill, was performed by determination of the Bond's work index value. Results are presented in Table 6.

Table 6. Values of Bond's indices for HPGR feed and products

Material	Bond's index value [MJ/Mg]			Potential energy savings [%]	
	HPGR feed	HPGR product (studded)	HPGR product (hexagonal)	studded	hexagonal
Rudna	50.868	40.932	41.04	19.5	19.3
Polkowice	40.428	35.316	36.936	12.6	8.6

Results show that the HPGR effect, considered as lower ball mill energy consumption, is generally higher for ore from Rudna (greater than 19%), than for ore from Polkowice (from 8.6% to 12.6%). Both types of lining are capable to reduce ball mill energy consumption for the Rudna ore by more than 19%, while for the Polkowice ore, the results are more favorable for studded rolls.

Results of grinding kinetic tests, carried out in a laboratory Bond mill, are presented in Table 6. Each HPGR product was ground for 10 minutes, and its particle size composition after 1, 3, 5 and 10 minutes were determined, along with values of d_{50} , d_{80} and d_{95} .

Table 6. Ball mill grinding results for ore from Polkowice and Rudna, obtained for various types of linings

Type of ore	Grinding time [minutes]	Type of lining	S50	S80	S95
Rudna	1	studded	29.90	4.68	3.05
		hexagonal	36.21	7.97	3.40
	3	studded	43.08	6.87	3.06
		hexagonal	57.69	66.04	3.80
	5	studded	70.06	24.96	3.08
		hexagonal	82.21	86.96	4.15
	10	studded	88.02	95.36	3.17
		hexagonal	88.59	109.26	4.91
Polkowice	1	studded	32.25	4.44	2.85
		hexagonal	40.86	4.72	2.75
	3	studded	122.06	5.35	2.95
		hexagonal	125.88	6.31	2.78
	5	studded	226.25	8.07	2.98
		hexagonal	189.33	27.14	2.80
	10	studded	277.92	126.74	3.30
		hexagonal	193.69	106.70	2.84

Analyzing data in Table 6 it can be noticed that in most cases the obtained values of comminution ration were more favorable for HPGR equipped with studded rolls. The hexagonal rolls, in turn, reached better grinding effects for ore from Rudna for an average (d_{50}) and eighty-percent (d_{80}) comminution ratio.

Economic effects

Economic effect were assessed through analysis of capital costs of HPGR devices and cost of spare set of rolls. Table 7 presents respective types of costs in percentage values, because in each variant of HPGR press equipped with studded rolls appeared to be more expensive than HPGR with hexagonal linings. For purposes of more clear comparison, all costs concerning the hexagonal lining were presented as a percentage values of respective cost for studded HPGR press.

Table 7. Investment costs of HPGR devices equipped with different types of linings (percentage)

Rudna		
	studded	hexagonal
HPGR device	100%	84%
Spare rolls	100%	78%
Polkowice		
	studded	hexagonal
HPGR device	100%	65%
Spare rolls	100%	90%

In terms of economy hexagonal linings appear to be more beneficial, both for HPGR device and spare sets of rolls.

Final discussion and conclusions

The main aim of this paper was to compare the effectiveness of HPGR operation due to different linings of rolls. The obtained results show that the type of roll surface in HPGR significantly influences the high-pressure comminution process both in terms of technological effects measured through comminution ratio values, and from economic point of view. Summarizing the investigations, important conclusions may be drawn.

More favorable energetic effects were generally obtained for studded linings and for material from Rudna. In terms of throughput indices, studded rolls achieved values by 21% higher, comparing hexagonal linings, and better results were also obtained for material from Rudna.

Higher values of comminution ratio were obtained for ore from the Polkowice, however it is difficult to state unequivocally which type of linings have more favorable impact on the HPGR crushing effect. On the basis of the above research programme, it can be assumed, that comminution effects for both types of rolls are comparable.

Potential application of the HPGR devices in comminution of Polish copper ores would effect in reduction of the HPGR product grindability (lower values of Bond's working index) and energy saving in downstream ball mill grinding process.

On the basis of the above conclusions it can be stated that application of high-pressure grinding rolls into technological circuit of Polish copper ore processing should be beneficial in terms of technological and economic aspects. These investigations, however, should be rather regarded as initial research and further analysis will be necessary before potential application of HPGR. Some simulation models of HPGR performance should be developed, which enable us to characterize the effectiveness of HPGR in terms of technology, economy and ecology (Morrell et al., 1997; Tavares, 2005; Cleary et al., 2008; Saramak, 2013).

Acknowledgements

The article was written as a result of Polish Government statutory work 11.11.100.276.

References

CLEARY P.W., SINNOTT M.D., MORRISON R.D., 2008: *DEM prediction of particle flows in grinding processes*. International Journal for numerical methods in fluids, vol. 58 (3), 319–353.

DANIEL M.J., MORRELL S., 2004: *HPGR model verification and scale-up*, Minerals Engineering, vol. 17 (11/12), 1149-1161.

FUERSTENAU D.W., SHUKLA A., KAPUR P.C., 1991: *Energy consumption and product size distribution in choke-fed high-compression roll mills*. International Journal of Mineral Processing vol. 32 (1-2), 59–79.

MORRELL S., LIM W., SHI F., TONDO L., 1997: *Modelling of the HPGR crusher. Comminution Practices* (ed. Kawatra K.S.). Society for Mining, Metallurgy and Exploration Inc. (SME), Chapter 17, 117–126.

PAHL M.H., 1993: *Praxiswissen Verfahrenstechnik – Zerkleinerungstechnik*. Fachbuchverlag Leipzig/Verlag TÜV Rheinland, Köln.

RULE C.M., MINNARR D.M., SAUREMANN G.M., 2008: *HPGR – revolution in Platinum?*, 3rd Intern. Conference „Platinum in Transformation”, The Southern African Institute of Mining and Metallurgy, Johannesburg, SAIMM, 2008.

SARAMAK D., 2012: *Optimizing the performance of high-pressure grinding roll based ore enrichment circuits*, Gospodarka Surowcami Mineralnymi-Mineral Resources Management, vol. 28 (4), 87–99.

SARAMAK D., 2013: *Mathematical models of particle size distribution in simulation analysis of High-pressure grinding rolls operation*, Physicochemical Problems of Mineral Processing, vol. 49(1), 495–512.

SCHONERT K., 1979. *Aspects of the physics of breakage relevant to comminution*. In: Fourth Tewksbury Symposium, University of Melbourne, 3.1–3.30.

SESEMANNY., BROECKMANN C., HOEFTER A., 2013: *A new laboratory test for the estimation of wear in high pressure grinding rolls*, Wear, vol. 302 (1-2), 1088–1097.

TAVARES L.M., 2005, *Particle weakening in high-pressure roll grinding*. Minerals Engineering vol. 18 651-657.

TUMIDAJSKI T., KASINSKA-PILUT E., GAWENDA T., NAZIEMIEC Z., PILUT R.: 2010. Investigation of grinding process energy consumption and grindability of lithologic components of polish copper ores, Gospodarka Surowcami Mineralnymi-Mineral Resources Management, 26(1), 61-72.

WEIR 2013, Weir Minerals/KHD Humbold Wedag, First choice for HPGR technology and service (official information booklet and catalogue of the product and technology).

Received April 30, 2014; reviewed; accepted June 3, 2014

SPLIT OF MERCURY BETWEEN PRODUCTS OF COAL CLEANING VERSUS MERCURY EMISSIONS REDUCTION

Ireneusz PYKA, Krzysztof WIERZCHOWSKI

Central Institute of Mining, Plac Gwarków 1, 40-166 Katowice, Poland, kwierzchowski@gig.eu

Abstract: The article deals with the analysis of the split of mercury present in raw coals between commercial products and wastes in 21 Polish collieries producing hard steam coal (Upper Silesia Coal Basin). The coal cleaning constitutes the first step in the reduction of mercury emissions in coal utilisation (mainly combustion) processes by decreasing the charge of mercury in the commercial products in comparison to the raw coal. The ratio of this reduction depends, first of all, on the technological characteristics of raw coal, as well as on the range of the applied coal cleaning method. The charges of mercury in exploited raw coals are split in coal preparation processes (mainly coal cleaning processes) between commercial products and waste products. The mercury content in commercial products has been analysed together with the emissions from coal combustion processes. In the second case, tools for the reduction of emissions have already been employed. Characteristics of waste products, in particular the mercury content, have been under consideration to a less extent so far. Data presented in the article allows for better, broadened with the waste products, analyses, understanding and assessment of all environmental mercury originated risks, arising from coal production, including coal cleaning. Presented data generate also the need for discussion of such terms like: “mercury reduction in commercial coal products” and “mercury emissions reduction”, as the result of coal cleaning processes.

Keywords: hard coal, mercury charge, coal cleaning, mercury charge split, mercury emissions reduction

1. Introduction

The legal regulations on the reduction of mercury emissions of the coal utilization (mainly combustion) processes are already a fact (UNEP, 2013; Sloss, 2012). Further regulations are in preparation (Best Available, 2013), including the executive acts of the Minamata convention, which most probably will encompass not only the mercury emissions to the atmosphere but also other aspects, for example the gold artisanal production, as well as other potential sources of mercury transferred to the environment. Coal production and utilization are counted among those types of economic activity as a result of which large quantities of mercury enter the environment. It is estimated that in 2005 around 50% of mercury emissions originated

from coal combustion (UNEP, 2008). At the same time the high uncertainty of the mercury emission estimates is emphasized (UNEP, 2008) together with the observed decrease in the emissions. For example in Europe between 1980-2005 the mercury emissions decreased by almost 80% (Pacyna et al., 2009). Broadening of knowledge on the mercury charge in the Polish coals has enabled, among other, to recalculate and decrease the values of the reported mercury emissions (Ochrona Środowiska, 2013; Paczosa, 2014). All this points out the necessity of conducting further analysis of the anthropogenic sources of mercury emissions to the environment. Such a necessity was defined in the Minamata Convention itself, for example in Article 9 (UNEP, 2013). A significant source of mercury emissions to the environment can be the coal mining waste and in particular the coal cleaning waste. If the mercury emissions during the utilization of cleaned coal (clean coal concentrates) are to be lower than during the utilization of raw coal, then a question should be asked on the mercury split in the coal cleaning processes and on the degree of mercury pollution in the waste from these processes.

Cleaning processes are commonly applied for improving coal quality before utilization. Their application is supported by the need to minimize the pollutants charge in the used coal, which becomes of particular importance for long-distance transport of coal (Couch, 1999). Utilisation of the cleaned coal, characterized by high quality parameters, increases also the efficiency of the conversion of the chemical energy of coal to other forms of energy and decreases the costs of countermeasures to the negative environmental impact of energy production as well as the exploitation costs in power plants (Couch, 1999).

The coal cleaning methods used for removal of various pollutants and adaptation to the end-user needs, including the reduction of mercury in coal, provide another advantage. The decrease of the charge (mass) of the pollutants in coal concentrates in comparison to the raw coal must be accompanied by the transfer of a part of the charge of the pollutants to the waste. Literature provides data on the mercury content in raw coals and after cleaning (Best Available Technique, 2013; Bialecka et al., 2012; Dziok et al., 2014; Matalerz et al., 2005; Ozbayoglu, 2011; Ozbayoglu, 2013; Pyka et al., 2010a; Toole-O'Neil et al., 1999; UNEP, 2010; Zajusz-Zubek et al., 2014). Some of the publications contain data on the mercury content in the coal cleaning waste (Dziok et al., 2014; Bialecka et al., 2012; Huggins et al., 2009; Ozbayoglu, 2013; Wang et al., 2009; 2006a; 2006b) but practically no literature contains the mercury mass (charge) split between the cleaned coal and waste.

The article provides the results of the split of the mercury mass between the commercial products and waste for 21 Polish collieries producing hard steam coal and the weighted average of the split as a function of the coal cleaning range. The presented data indicate the scale of the environmental threat following the extraction and utilisation of the coal polluted by mercury. The data confirm that the threats cannot be identified solely with the mercury emissions from the coal utilisation processes.

The industrial cleaning processes of coal and other raw materials are not ideal. Their unavoidable, typical features are the losses of the carbonaceous matter to the waste. The presented data in combination with the information on the calorific value of the raw coal, cleaned coal well as the “calorific value” of the waste (i.e. energy balance of energy contained in the raw coal – the feed for the cleaning processes) allow for starting discussion on the method of an objective assessment of the reduction of mercury emissions as a result of mercury charge change in coal during coal cleaning.

Impact of coal cleaning on reduction of mercury content and charge in coal

In the UNEP (2010) document it is shown that the classic coal cleaning methods lead to around 30% decrease of the mercury charge (mass) in coal after cleaning. The application of advanced, chemical coal cleaning methods (e.g. the *K-fuel* method) can lead to a decrease of mercury charge in coal even by 70%. In another literature source, which reviews the current, already quite rich American experiences (Pavlish, 2003), various degrees of mercury content reduction in cleaned coals for various deposits– starting with practically none up to around 80% is discussed. Thus, the variability in the coal susceptibility to the reduction of mercury content as a result of coal cleaning is significant. This is confirmed by the results of other researchers (Das et al., 2013; Dziok et al., 2014; Feeley et al., 1994; Lopez-Anton et al., 2006; Ozbayoglu, 2011; Pyka et al., 2010a; Quick et al., 2002; Zajusz-Zubek et al., 2014).

It is worth pointing out that the decrease of the mercury contamination in coal after coal cleaning processes, similarly to the reduction of other contaminants, has two dimensions. The first one is the assessment of mercury content in coal before and after cleaning. The second one is the assessment of the mercury charge in coal before and after coal cleaning. For example Ozbayoglu (2013), discusses removal of mercury from raw coal in the cleaning process with the “reduction rate” of the mercury at around 53%, even though the mercury content in some of the cleaned coals, obtained in unit processes applied to various particle size fractions, was higher than in the raw coal. This is a classic example, where coal cleaning leads to the reduction of the contamination of the commercial product with mercury. The technological characteristics of the mining product indicate the lack of possibility to decrease the contaminant concentration in the cleaned coal in relation to the content (concentration) of a given pollution in the feed for cleaning processes. Similar results of industrial research for several Polish hard coal collieries were presented by Dziok et al. (2014). The analyses of the technological characteristics of several Polish hard coals (Pyka et al., 2010a) indicated that the coal cleaning in the full particle size range always leads to concentrates with lower mercury content than in the feed. It gives an incentive to some theoretical considerations. It can be assumed that during the coal cleaning processes the total energy contained in the raw coal is transferred to the commercial

products as well as the whole mercury is transferred to the commercial products. The chemical energy of the coal fuel is not lost with the waste, but also the waste is not contaminated with mercury. Despite the higher calorific value of the commercial products (pure waste was separated with no energy loss) their mercury emissions will remain the same as for raw coal, since we are dealing here with the same amount of energy and the same mercury charge (waste free of mercury). In practice the contaminants from raw mining product concentrate most often in the waste, but their discharging results in energy losses. This makes the assessment of the impact of the cleaning processes on the reduction of contaminants' emissions in coal utilization processes much more complex. Moreover, the information on the mercury content in coal and its reduction as the result of coal cleaning is incomplete. The lack of information on the mass balance of the coal cleaning process does not allow to directly estimate how much the mercury mass (charge) directed with coal to the end users was decreased.

Literature provides various methods of assessing the efficiency of decreasing the mercury content in coal cleaning processes (Dziok et al., 2014; Lopez-Anton et al., 2006; Toole-O'Neil et al., 1999; Wichlinski et al., 2013). The simplest are based on the difference between the mercury content in the cleaned coal and the raw coal. An example of including the improvement of the calorific value of the cleaned coal in relation to raw coal was proposed by Tool-O'Neil et al. (1999) in the form of the mercury reduction index:

$$\eta_{\text{Hg2}} = \frac{\frac{Hg_{\text{feed}} - Hg_{\text{concentrate}}}{Q_{i_feed}}}{\frac{Hg_{\text{feed}}}{Q_{i_feed}}} \cdot 100 \% \quad (1)$$

where: η_{Hg2} – mercury reduction index, [%],

Hg_{feed} – mercury concentration in the feed, [$\mu\text{g}/\text{kg}$],

Q_{i_feed} – calorific value of the feed, [kJ/kg],

$Hg_{\text{concentrate}}$ – mercury concentration in the cleaned coal, [$\mu\text{g}/\text{kg}$],

$Q_{i_concentrate}$ – calorific value of the cleaned coal, [kJ/kg].

The reference to the calorific value of coal before and after the cleaning process, assumed in Eq. 1 in practice leads to an overestimation of the assessment of the reduction of mercury content in coal. The equation does not include the inevitable energy loss connected with the waste in the cleaning processes. For the purpose of objectivity, the energy loss related to waste in the cleaning processes should be included and the reduction should be estimated based on some constant reference, at the best constant quantity of energy in coal before and after cleaning. (Pavlish, 2003; Smolka et al., 1999). Taking the above into consideration the equation should, in our opinion, be supplemented with coefficient γ , which would include the energy loss in waste since the commercial products composed of the cleaning products of the given raw coal lot will always "carry" lower energy than the raw coal lot:

$$\eta_{Hg2} = \frac{\frac{Hg_{feed}}{Q_{i_feed}} \frac{Hg_{concentrate}}{Q_{i_concentrate}}}{\frac{Hg_{feed}}{Q_{i_feed}}} \eta \cdot 100 \% \quad (2)$$

where: η is the energy loss in the waste.

The quoted publications (Dziok et al., 2014; Ozbayoglu, 2013, Pyka et al., 2010a), allow for drawing another significant practical conclusion. The “behavior” of mercury in the cleaning processes is a function of the particle size. The results of the tests conducted for one, narrow size fraction, are more often than not unrepresentative and do not allow to generalize on the mercury reduction in cleaning processes in the full particle size range of raw coal. Results of tests conducted on samples of heavily grounded (e.g. below 0.5 mm) coal as well as attempts of generalization on the reduction of mercury contamination of the commercial coal in the cleaning processes adopted for the full particle size range can be found in literature (Feeley et al., 1994; Guangqian et al., 2013; Ozbayoglu, 2011; Lopez-Anton et al., 2006; Quick et al., 2002)

Literature data show that the mercury content in the waste from coal cleaning is, similarly to that of the cleaned commercial coal, variable (Dziok et al., 2014; Bialecka et al., 2012; Ozbayoglu, 2011; Ozbayoglu, 2013; Pyka et al., 2010b). Generally, these values are not significantly larger than for raw coal. The mass of the waste produced in the cleaning processes is relatively large. In Poland in 2013 it was around 35 teragrams (Tg) at the coal production around 76 Tg (Paszcza et al., 2014). Thus, the contamination with mercury is a problem (Pyka et al., 2010b). Similarly to the small mercury content in the coal used on a mass scale, also the small mercury content in the waste translates into large masses (charges) of mercury being exposed to the environment.

Testing program and methodology

Samples of commercial coals of selected intermediate products (commercial products components) and waste were taken from different collieries. In order to ensure the representativeness of the data, samples of commercial products (components) were taken over the period of at least one week. The samples for analysis applying Polish Standards (2014) were prepared from individual as well as combined samples.

The basic quality parameters and the mercury content were determined according to the certified internal procedure elaborated at GIG (Poland) (No. SC-1.PB.23) applying the cold-vapor atomic absorption spectrometry. In the case of the waste, most mercury analyses were performed on the analytical samples obtained from the collieries.

For each colliery, from several to several dozens of mercury samples of the commercial product, or their basic components were analyzed. In the case of complex commercial product, the composition system was used. From 1 to 3 analysis of

mercury in the waste were performed. In order to eliminate the accidental sampling errors, the results of the laboratory tests of the basic quality parameters of the commercial products and waste were verified through comparison with the data from the online monitoring of production quality. The obtained quality data were combined with the information on the production of respective commercial products and waste per year. Due to unavailability, during the preparation of the publication, of annual data on year 2014 production, for the purpose of calculation of the mercury charge between the commercial products and waste, the data on the 2013 production were used.

The above calculations and analyses were prepared for 21 collieries producing steam coal, located in the Upper Silesian Coal Basin (USCB) in Poland. For the selected collieries the assessment of the split of energy in the raw coal between the commercial products and waste in coal cleaning process was performed. These values were used for assessment of the real reduction of the mercury content (as well as mercury emissions) resulting from coal cleaning.

The results and discussion

Figure 1 presents the results of the analysis of the split of the mercury charge in 21 steam coal mines located in the USCB in Poland. The split of the mercury mass between the commercial products and waste is provided in percent. The analyzed mines can be divided into two groups:

- collieries 1–7 (Fig. 1), in which only the coarse and middle sized coals (coarse and medium coal size fractions) are cleaned i.e. ROM coal with the particle size above 20 mm,
- collieries 8–21 (Fig. 1), in which to a smaller or larger extent also the fines are cleaned, i.e. ROM coal with the particle size below 20 mm in dedicated cleaning processes.

Colliery 6 belongs to the group of collieries in which raw fines are not cleaned. There the cleaning of coarse and middle sized coals results in transfer of only 4% of the mercury charge to the waste. The same is for colliery 4, in which over 30% of the mercury charge can be found in the waste. The fact that coal cleaning technology for the coarse and medium size fractions is similar in each of the collieries and concerns more or less the same part (mass) of the ROM coals shows a strong influence of the technological characteristics of ROM coal on the efficiency of mercury reduction.

Colliery 17 belongs to the group of collieries in which the coal cleaning concerns also the fines in which only around 15% of the mercury charge in the raw coal is directed to the waste. Despite the fact that for none of the analyzed collieries the raw fines are cleaned as a whole, in the case of two collieries (numbers 8 and 21) over 50% of the mercury charge in the raw coal is transferred to the waste. This indicates a potential for reduction of the mercury content and charge in the cleaning processes in

the analyzed Polish steam coal collieries as well as the scale of contamination of the waste with mercury.

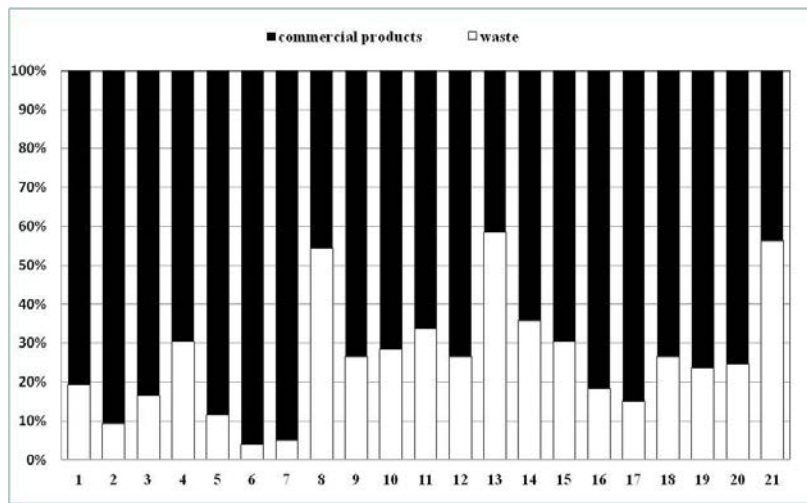


Fig. 1. Split of mercury between commercial products and waste, expressed in % in 21 of analysed collieries

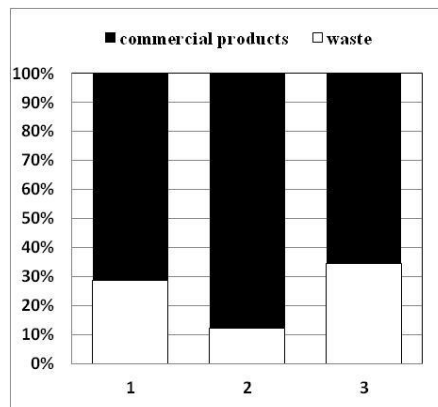


Fig. 2. Weighted mean split of mercury between commercial products and waste for 21 collieries (1) and divided between the mines in which only the coarse and medium coal size fractions are cleaned (2) as well as the fractions themselves and partly the smalls (3)

Data in Fig. 1, cumulated for all the collieries as well as divided into the two assumed colliery groups have been recalculated including the coal mass and the waste produced/generated in the analysed collieries. The results of these calculations are presented in Fig. 2. The mean mercury charge (mass) presented in Fig. 2 is the

weighted mean and illustrates in particular the impact of coal cleaning on the split of the mercury charge.

In the collieries in which only the coarse and middles sized coals are cleaned, on average around 12% of the mercury charge from the raw coal is transferred to the waste. In the collieries which also clean fines, but not in the full range, on average almost 35% of the mercury charge from raw coal leaves the cleaning plant together with waste. The part of mercury charge contained in raw coal removed with the waste for all of the analyzed collieries equals, on average, around 29%. The mercury charge in the waste, directly and objectively illustrates the additional environmental threats resulting from coal production in Poland, which should not be identified only with mercury emissions to the atmosphere.

The split of mercury charge in raw coal between the cleaned coal and waste should not be directly identified with the reduction of mercury in coal, estimated for the purpose of demonstrating the limiting of the mercury emissions through coal cleaning. Not only the mercury charge is carried with the waste, but also unavoidable losses of the energy contained in raw coal. The losses deprive us of a constant basis for treating the mercury charge split equally to the reduction of mercury emissions. There is a lack a constant basis in the form of the same amount of energy in the raw coal and the commercial products of the coal (Smolka et al., 1999). In the earlier analyses, conducted for raw coals from several of the USCB collieries (Smolka et al., 1999), it has been estimated that depending on the range of coal cleaning the energy losses can be:

- additionally from around 6.4 to over 10%, when only the coarse and middles sized coals are cleaned,
- additionally from around 6.5% to over 14% when also the fines are cleaned.

The results were taken from modeling of the coal cleaning processes which include their randomness but in the industrial processes the energy losses can be even higher. The reduction of the mercury content in coal, despite the presented significant amounts of mercury being transferred to coal waste, should be assessed including the energy losses and thus it is reasonable to apply for example in Eq. 1 coefficient η (Eq. 3) with the value smaller than 1, which includes the energy losses in the waste:

$$\eta = \frac{100 - \text{energy losses}}{100} \quad (3)$$

In practice the value of coefficient η , after being introduced into Eq. 1 results in a decrease of the value of the estimated mercury content reduction as a result of coal cleaning. Assuming the values above we see a decrease, by around 6%, when only the coarse and medium coal size fractions are cleaned, and up to over 24%, when the coarse and medium coal size fractions are cleaned together with the fines.

Conclusions

The charge of the contaminants contained in raw coal is divided in the coal cleaning processes between the commercial products and waste. In the case of mercury contained in coal, the mercury charge in the raw coal for several of the analyzed collieries is divided into the commercial products and waste on average in the ratio around 71%/29%.

Coal cleaning is an efficient method of reduction of mercury emissions to the atmosphere during its utilization. The split of mercury charge between the products and waste, especially in case of the collieries in which only the coarse and middles sized coals are cleaned, depends on coal processing technological.

The difference between the split of the mercury charge into the commercial products and waste in collieries cleaning only the coarse and middles sized coals and the collieries cleaning also the fines shows that broadening of the scope of coal cleaning leads to efficient decrease of the mercury charge in commercial coal. Thus, we obtain the confirmation that in Poland coal cleaning is a very important element of the mercury emission reduction strategy.

The mercury charge (mass) in commercial coal is the basis for the assessment of the threat of mercury emissions. These charges can be matches or even exceeded by the mercury charge in the waste from coal cleaning. This comprises another environmental issue which needs to be analyzed, and surely even addressed by preventive measures.

The results of the assessment of the mercury charge/ content in coal and in the final outcome also mercury emissions as the result of coal cleaning, conducted applying the currently used approaches do not provide fully objective information. These results suffer from the lack of a comparison basis such as the constant energy of the raw coal, partially lost with the waste. The energy losses in the waste do not allow for a direct comparison of the mercury charge in raw coal before cleaning and in the coal commercial products produced from this raw coal. These losses can exceed 24% of the energy contained in the raw coal and the mercury reduction effect in the products, in reference to the content/charge of mercury in the raw coal. Thus, also the mercury emissions reduction resulting from coal cleaning will be decreased at the same level.

Acknowledgements

The results of the determination of the mercury and ash content in the commercial products of the Polish hard coal collieries have been obtained in the realisation of a project funded in the frames of the Applied Research Program of the Polish National Centre for Research and Development *The elaboration of a data base on mercury content in domestic coal, technological guidelines of the further mercury reduction, including the defining of benchmarks for domestic indices of mercury emission* – acronym “Baza Hg”, (PBS2/A2/14/2013). The authors would like to thank the staff of the coal quality assessment departments of the respective mines for their cooperation in obtaining the samples.

References

BEST AVAILABLE TECHNIQUES (BAT), 2013, Reference Document for the Large Combustion Plants. Draft 1 (June 2013).

BIALECKA B., MICHALSKA A., 2012, *Mercury content in coal and the mining waste*. Prace Naukowe GIG, Gornictwo i Geoinżynieria 3, 73–87.

COUCH G.R., 1999, *Power from coal where to remove impurities?* IEACR/82, London, UK, IEA Coal Research.

DAS T.B., PAL S.K., GOURICHARAN T., SHARMA K.K., CHOUDHURY A., 2013, *Evaluation of Reduction Potential of Selected Heavy Metals from and Indian Coal by Conventional Coal Cleaning*. International Journal of Coal Preparation and Utilization 33, 300–312.

DZIOK T., STRUGALA A., ROZWADOWSKI A., GORECKI J., ZIOMBER S., 2014, *The variation of the mercury content in hard coal in the cleaning process*. Polityka Energetyczna Vol.17, Issue 4, 277–288.

Feeley Th.J., BARNETT W.P., HUCKO R.E., 1994, *Advanced Physical coal cleaning for controlling acid rain emissions*. Proceedings of the 12th International Coal Preparation Congress, Cracow, Poland, May 23–27. Gordon and Breach Publishers, 241–247.

GUANGQIAN Luo, JINGJING Ma, JUN Han, HONG Yao, MINGHOU X, CHENG Zhang, GANG Chen, RAJENDA Gupta, ZHENGHE Xu., 2013, *Hg occurrence in coal and its removal before coal utilization*. Fuel, 104, 70–76.

HUGGINS F.E., SEIDU L.B.A., SHAH N., HUFFMAN G.P., HONAKER R.Q., KYGER J.R., HIGGINS B.L., 2009, *Elemental modes of occurrence in an Illinois #6 coal and fractions prepared by physical separation techniques at a coal preparation plant*. International Journal of Coal Geology 78, 65–76.

LOPEZ-ANTON M. A., DI'AZ-SOMOANO M., GARCI'A, A.B., MARTI'NEZ-TARAZONA M.R., 2006, *Evaluation of mercury associations in two coals of different rank using physical separation procedures*. Fuel 85, 1389–1395.

MASTALERZ M., DROBNAIK A., 2005, *Vertical variations of mercury in Pennsylvanian coal beds from Indiana*. International Journal of Coal Geology 63, 36–57.

Ochrona Srodowiska – Environment, 2013, Glowny Urzad Statystyczny, Warszawa.

OZBAYOGLU G., 2011, *Partitioning of major and trace elements of a Turkish lignite with size and density*. Physicochem. Probl. Miner. Process. 4, 51–60.

OZBAYOGLU G., 2013, *Removal of hazardous air pollutants based on commercial coal preparation data*. Physicochem. Probl. Miner. Process. 49(2), 621–629.

PACYNA J.M., PACYNA E.G. AAS W., 2009, *Changes of emissions and atmospheric deposition of mercury, lead, and cadmium*. Atmospheric Environment 43, 117–127

PACZOSA A., 2014, *Mercury emissions to air*. Conference “ The mercury issues in Poland in view of the new global regulatory solutions.”. Polish Ministry of the Environment, Warszawa November 20th, 2014 r (in Polish).

PASZCZA H., PITURA K., 2014, *Hard coal mining in Poland in 2013*. Wiadomosci Gornicze 6, 314–324.

PAVLISH J.H., SONDREAL E.A., MANN M.D., OLSON E.S., GALBREATH K.C., LAUDAL D.L., BENSON S.A., 2003, *Status review of mercury control options for coal-fired power plants*. Fuel Processing Technology 82, 89–165.

Polish Standards (2014), PN-G-04502:2014-11: Hard coal and lignite – Sampling and preparation of the samples for laboratory tests standard.

PYKA I., WIERZCHOWSKI K., 2010a, *Technological Conditions of Mercury Content Reduction in Hard Coal Based on the ROM Coal from Several Polish Collieries*. Arch. Min. Sci., Vol. 55, 2, 349–371.

PYKA I., WIERZCHOWSKI K., 2010b, *Issues related to the mercury content in hard coal*. Gornictwo i Geoinżynieria. Vol. 34, Issue 4/1, 241–250.

QUICK W.J., IRONS R.M.A., 2002, *Trace elements partitioning during the firing of washed and untreated power stations coals*. Fuel 81, 665–657.

SLOSS L. L., 2012, *Legislation, standards and methods for mercury emissions control*. CCC/195. London, UK, IEA Clean Coal Centre.

SMOLKA W., CZAPLICKI A., PYKA I., 1999, *The cost of decreasing the SO₂ emissions in the coal cleaning plants and the flue gas desulphurisation plants*. Karbo, Energochemia, Ekologia 2, 1999.

TOOLE-O'NEIL B., TEWALT S.J., FINKELMAN R.B., AKERS D.J., 1999, *Mercury concentration in coal – unraveling the puzzle*. Fuel 78, 47–54.

UNEP (UNITED NATIONS ENVIRONMENTAL PROGRAMME), 2008, *The Global Atmospheric Mercury Assessment: Sources, Emissions and Transport*. Geneva, Switzerland,

UNEP (UNITED NATIONS ENVIRONMENT PROGRAMME), 2010, *Process Optimization Guidance for Reducing Mercury Emissions from Coal Combustion in Power Plants*. Division of Technology, Industry and Economics (DTIE) Chemicals Branch Geneva, Switzerland.

UNEP (UNITED NATIONS ENVIRONMENT PROGRAMME), 2013, Minamata Convention on Mercury (October 2013).

WANG WEN-FENG, QIN YONG, WANG JUN-YI, LI JIAN, 2009, *Partitioning of hazardous trace elements during coal preparation*. Procedia Earth and Planetary Science, 1 838–844.

WENFENG WANG, YONG QIN, SHUXUN SANG, BO JIANG, YINGHAI GUO, YANMING ZHU, XUEHAI FU, 2006a, *Partitioning of minerals and elements during preparation of Taixi coal*, China. Fuel 85, 57–67.

WENFENG WANG, YONG QIN, CHONGTAO WEI, ZHUANGFU LI, YINGHAI GUO, YANMING ZHU, 2006b, *Partitioning of elements and macerals during preparation of Antaibao coal*. International Journal of Coal Geology 68, 223–232.

WICHLINSKI M., KOBYLECKI R., BIS Z., 2013, *The investigation of mercury contents in Polish coal samples*. Archives of Environmental Protection, Vol. 39, 2, 141–150.

ZAJUSZ-ZUBEK E., KONIECZNSKI J., 2014, *Coal cleaning versus the reduction of mercury and other trace elements' emissions from coal combustion processes*. Archives of Environmental Protection, Vol. 40 1, 115–127.

Received March 4, 2015; reviewed, accepted May 7, 2015

INFLUENCE OF PARTICLE SIZE AND FEED RATE ON COAL CLEANING IN A DRY SEPARATOR

Murat KADEMLİ*, Ozcan Yıldırım GULSOY**

* Hacettepe University, Vocational School of Higher Education, Ankara, Turkey, kademli@hacettepe.edu.tr

** Hacettepe University, Department of Mining Engineering, Ankara, Turkey

Abstract: This research is concerned with the effects of particle size distribution and feed rate of feed on the coal cleaning performance of table type air separator. In tests, the lignite and hard coal samples from Mugla and Zonguldak districts in Turkey were used. The samples were tested in three different size distributions such as $-38 + 6$ mm, $-19 + 6$ mm and $-9.5 + 6$ mm. The effect of particle size was investigated together with the feed rate $2 \text{ Mg}/(\text{h}\cdot\text{m}^2)$, $1.68 \text{ Mg}/(\text{h}\cdot\text{m}^2)$ and $1.32 \text{ Mg}/(\text{h}\cdot\text{m}^2)$ and very important physical parameters of table type air separator such as, riffle height, table slope and table frequency. Results were analyzed by using the Tromp curve for indicating the effects in detail. Consequently, the results revealed that the particle size had remarkable effect on separation efficiency. The separation efficiency was, however, inversely affected as the particle size distribution became finer, and the best results were obtained in particle size distribution was $-38 + 25$ mm in both sample tested. The E_p value was 0.11 for the hard coal samples while it was 0.13 for the lignite samples.

Keywords: dry coal cleaning, particle size effect, air separator

Introduction

The classical wet coal cleaning techniques depend on density differences between coal and impurities such as, pyrite minerals and silicate minerals etc. Air-based separation technologies, like water-based methods, also separate coal and ash-bearing material according to their different relative densities (Frankland, 1995; Arslan, 2006; Chen and Wang, 2006). The pressure difference between two random points in the bed is almost equal to the difference between the hydrostatic heads of these two points, as shown in Eq. 1:

$$\Delta P = P_1 - P_2 = (h_1 - h_2) \rho, \quad (1)$$

where ΔP is the pressure drop (Pa), P_1 and P_2 are the pressures at point 1 and 2 (Pa), and ρ is the bed density (kg/m^3), h_1 and h_2 (m), are height of point 1 and point 2,

respectively. Particles with a density lower than the bed density will float to the top of the surface while higher density particles go to the bottom of the bed. This stratification process, which occurs according to density, follows Archimedes' law, as shown in equation

$$\rho_1 < \rho < \rho_2 \quad (2)$$

where ρ is the density of the fluidized bed (kg/m^3), ρ_1 and ρ_2 the densities of float and sink particles (kg/m^3), respectively (Zhenfu and Qingru, 2001).

Several of dry, density-based separators used throughout the twentieth century were developed in the period from 1910 to 1930 (Osborne, 1986). The technologies shared the same basic principle mechanisms that are commonly employed in wet cleaning separation such as, dense medium separations, pulsated air jiggling, riffled table concentration and air fluidized coal launders (Lochart, 1984; Donnelly, 1999; Sahu et al., 2009). One of the most successful applications of dry cleaning is the FGX separator which was developed by Tangshan Shengzhou Machinery Co., Ltd. in 1996. The separation principle is a combination of vibration and air and is used to develop a fluidized bed on the separator surface which is reflected in the unit's description as a "compound separator". The development of a fluidized bed eventually enhanced the separation process of the unit and the size range that can be treated (Zhenfu, et al., 2002; Kohmuench et al., 2005; Gongmin and Yunsong, 2006; Zhang et al., 2011). The apparatus which was used in tests is called "table type air separator" shares the same principles and similar design with the FGX separator with some innovative changes (Kademli and Gulsoy, 2013). The scheme of apparatus is given as Fig. 1.

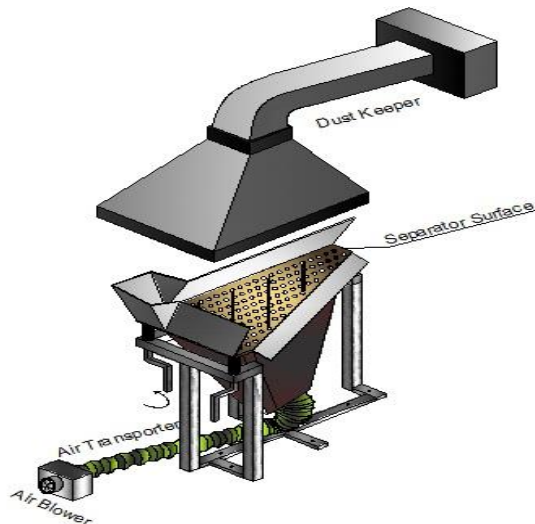


Figure 1. Scheme of apparatus

Materials and methods

The test apparatus have regular openings of 3 mm size on the table surface and air blower to supply stratification of the coal and tailings. The air blower provides air that passed holes on the table surface to fluidize and transport the light coal particles at different rates. The rate of vibration and air blowing were controlled by frequency controllers, and feed rate were controlled by an electromagnetic controller. It also has a vibrator to shake the table surface. The high-density particles (rock) move towards along riffles which direct the particles to the back of table for discharging. The riffles cause the high density particles to move towards discharge side of the table and allow the light ones to rise and to move towards concentrate. The table type air separator was chosen as an example of one simple application of dry separation methods in addition to ease of control and its ability to operate in batch mode.

In the present study, two different coal samples, lignite from Mugla and a hard coal from Zonguldak, were chosen as the test materials to indicate the effect of particle size distribution on dry coal cleaning. The proximate analyses of coal samples are given in Table 1.

Table 1. Proximate analysis of the tests samples

Samples	Original values (MJ/kg)	Dry values (MJ/kg)	Original ash content (%)	Dry ash content (%)	Original volatile material (%)	Dry volatile material (%)	Original moisture (%)
Lignite	6.17	6.82	42.56	45	37.79	40.41	6.7
Hard coal	15.65	15.94	47.32	48.08	20.04	20.36	1.59

The parameters were defined in pre-experiments as riffle height, table slope and table frequency. Besides, feed rate and particle size of feed.

According to the pre-experiments results, they were fixed their best values in accordance with results of chemical analyses. The steps of parameters that were tested in pre-experiments and fixed values are given in Table 2.

Table 2. The apparatus parameters

Name of parameter	Step 1	Step 2	Step 3	Fixed
Table frequency	45 Hz (2700 rpm)	42 Hz (2520 rpm)	39 Hz (2340 rpm)	45 Hz (2700 rpm)
Table slope	0.26 (14.6 ⁰)	0.21 (11.8 ⁰)	0.15 (8.5 ⁰)	0.15
Riffle height	1.5 cm	2 cm	2.5 cm	1.5 cm

Test methodology

The test samples were fed to the surface by using an electromagnetic feeder and two products were collected as clean coal (middling was added in concentrate) and tailing from equipment discharge units. All tests were conducted in a batch mode for each

run. For each test, the system was cleaned before using a new feed. The nine favourable experimental conditions were determined according to results of pre-experiments which are shown in Table 3. The products, clean coal and tailings, were ground to 250 μm by milling and were analyzed to find their thermal values and ash content. The influences of parameters on separation efficiency were indicated by using graphs that indicate the relationship between parameters and process recovery and also by using tromp curves to indicate the productivity. E_p and d_{50} values were calculated for different particle sizes of the samples.

Results and discussion

Analyses results of both samples are given as Table 3 and Table 4. The combustible recoveries of concentrate, total amount of removal ash contents and concentrate mass recoveries were calculated by using Eqs 3-5 respectively:

$$\text{combustible recovery} = \frac{Mc \cdot (1-Ac)}{Mf \cdot (1-Af)} 100 \quad (3)$$

$$\text{total amount of removal ash} = \frac{Mt \cdot At}{Mf \cdot Af} 100 \quad (4)$$

$$\text{concentrate mass recovery} = \frac{Mc}{Mf} 100 \quad (5)$$

where Mc is mass of clean coal (kg), Mf is mass of feed (kg), Mt is mass of tailing (kg), Ac is ash content of clean coal (%), Af is ash content of feed (%), At is ash content of tailing (%).

Table 3. Lignite sample test results

Test Number	Particle Size (mm)	Feed (Mg/h)	Concentrate (MJ/kg)	Mass of concentrate (%)	Ash of concentrate (%)	Ash of tailing (%)	Combustion recovery (%)	Removal ash (%)	Tailing (MJ/kg)
1		1.32	14.20	55.4	38.04	51.40	62.42	50.94	3.29
2	-38+6	1.68	14.16	60.5	37.41	52.09	68.85	45.72	2.94
3		2.00	12.63	65.1	38.03	53.14	73.35	41.21	2.61
4		1.32	10.11	63.4	41.56	48.56	67.37	39.50	4.14
5	-19+6	1.68	9.86	67.7	41.95	46.00	71.45	33.02	3.92
6		2.00	9.50	73.9	42.52	51.38	77.23	29.80	3.59
7		1.32	7.57	71.2	45.56	50.97	70.45	32.62	5.39
8	-9.5+6	1.68	7.46	78.7	45.73	51.39	77.66	24.33	6.72
9		2.00	7.35	85.4	45.91	52.02	83.99	16.88	3.93

Table 4. Hard coal sample test results

Test Number	Particle Size (mm)	Feed (Mg/h)	Concentrate (MJ/kg)	Mass of concentrate (%)	Ash of concentrate (%)	Ash of tailing (%)	Combustion recovery (%)	Removal ash (%)	Tailing (MJ/kg)
1		1.32	21.07	54.2	33.27	71.92	69.55	68.62	5.48
2	-38+6	1.68	20.90	59.6	33.97	73.65	75.68	61.99	5.27
3		2.00	20.15	61.5	33.98	74.42	78.08	59.69	4.85
4		1.32	17.23	60.1	36.91	75.56	74.06	61.78	5.05
5	-19+6	1.68	16.61	64.7	37.56	77.32	78.90	55.93	5.39
6		2.00	15.90	66.9	39.42	78.18	79.15	53.02	5.41
7		1.32	15.09	70.8	40.16	78.87	83.21	47.19	5.50
8	-9.5+6	1.68	14.87	76.2	41.63	80.11	89.72	39.07	5.82
9		2.00	14.21	82.9	42.01	82.26	96.72	28.82	6.37

The influences of particle size and feed rate of feed on coal cleaning process were shown in Figs 2 and 3. These figures indicate that increasing the feed rate caused a decrease in thermal values and total amount of removal ash content while mass recovery of concentrate increased. Controversially, increasing the maximum particle size of feed caused an increase in thermal values and total amount of removal ash content while mass recovery of concentrate decreased. Although different thermal values and ash contents were obtained from both coal samples with different efficiencies, the effects of parameters on the separation process were similar in both samples. In these figures, the net thermal values of clean coal were also shown in graphs to emphasize its behavior with the change in parameters.

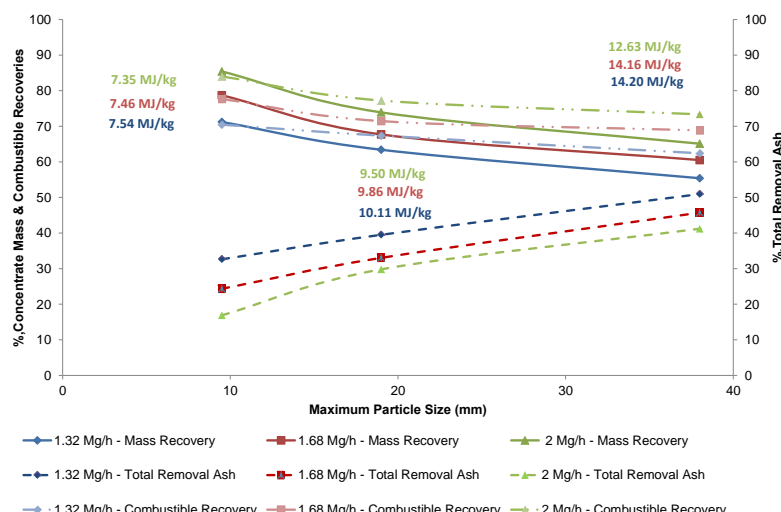


Fig. 2. Relationship between maximum particle size, feed rate and separation process of lignite sample

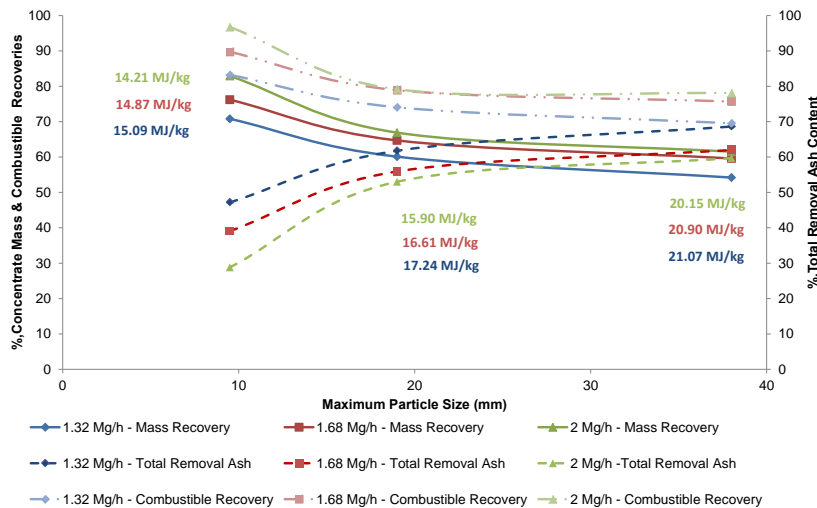
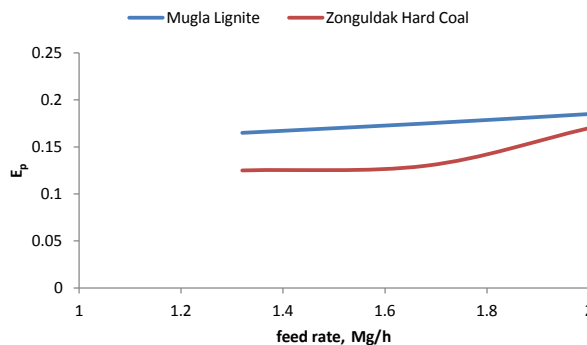


Fig. 3. Relationship between maximum particle size, feed rate and separation process of hard coal sample

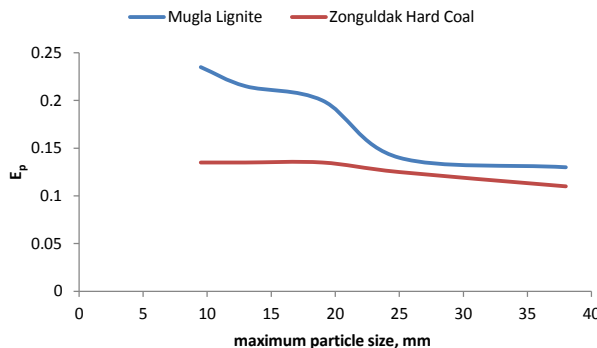
Having completed all tests, the sink-float tests were carried out with clean coal and tailings to measure the process efficiency of separation. The E_p values, which are used as a measure of the misplacement of particles in the product streams, and d_{50} , separation densities, are calculated while keeping frequency and table slope at constant values of 45 Hz and 0.15 respectively. These test conditions were chosen according to the results of tests that have low ash content and high thermal values. Also the Tromp curves for different feed rates were used to analyzed the relationship between the feed rate and separation efficiency. The best results were obtained at 1.32 $\text{Mg}/(\text{h}\cdot\text{m}^2)$ feed rates. That is why, the test condition which has $1.32 \text{ Mg}/(\text{h}\cdot\text{m}^2)$ feed rates had divided five particle size fractions for analyzing the relationship between particle size and separation efficiency. The E_p values and d_{50} (cut points) of both samples are given as Table 5. The differences of E_p values of both samples in different feed rates and different particle sizes are shown in Figs. 4 and 5, respectively. The E_p values were calculated by using Eq. 6:

$$E_p = \frac{d_{75} - d_{25}}{2} \quad (6)$$

where d_{25} and d_{75} are densities of the particles with 25% and 75% of dispersion factor, which is the probability of elutriation. E_p is the misplacement of particles in the product streams.

Fig. 4. A relationship between E_p and feed rateTable 5. E_p and d_{50} values of both samples versus feed rate

Feed Rate (Mg/h-m ²)	Lignite		Hard Coal	
	E_p	d_{50}	E_p	d_{50}
1.32	0.165	1.66	0.125	1.67
1.68	0.175	1.63	0.13	1.64
2.00	0.185	1.64	0.17	1.67

Fig. 5. Relationship with E_p values and maximum particle size

The figures and tables have shown that the particle size of the feed had more influence on separation process than the feed rate. The hard coal sample has lower E_p values than the lignite sample and the separation efficiency of lignite sample was inversely more influenced when the particle size fraction became finer than the hard coal sample. The E_p values and d_{50} (cut points) of both samples are given in Table 6 for each fraction. Also Fig. 5 shows the relationship between E_p values and maximum particle size for both samples. The figures indicated that the d_{50} (cut points) values, obtained in experiments, are similar with the wet coal cleaning methods whereas E_p

values are higher than wet coal cleaning methods which are currently used by industry. These classical wet methods usually have under 0.1 E_p values. However, other dry coal cleaning methods such as, air jigs have 0.3 E_p and 2.0 g/cm³ d_{50} values with the particle size fraction of 50–13 mm and under 13 mm (Weinstein and Snoby, 2007; Snoby et al., 2009). The FGX is a dry coal cleaning system which consists of a deck, vibrator, air chamber and hanging mechanism (Honaker et al., 2008). It is reported that the FGX system has the performance of 0.15 – 0.25 E_p and 1.78 g/cm³ – 1.98 g/cm³ d_{50} values (Gongmin and Yunsong, 2006). The results of specific study on the FGX showed that, for sub-bituminous coal, ash content was reduced from 20.79% to 8.40%. Also the low rank coal was upgraded by pneumatic table concentrator and ash content was reduced from 26% to 7% with a combustible matter recovery of 83% (Ghosh et al., 2014), whereas the table type air separator results showed that ash content was reduced 71.92% to 22.56% for hard coal with a combustible matter recovery of 78.08% while the ash content of lignite sample was reduced from 51.40% to 25.22% with a combustible matter recovery of 73.35%. The feasibility of dry cleaning system results showed that it is not suitable for lignite coal from Husamlar for the fractions of 8–5 mm and 5–3 mm (Cicek, 2008; Xia et al., 2015). Table type air separator shows similar results in the size fraction of 9.5–6 mm. The efficiency is inversely influenced with the particle size of feed in dry coal cleaning. The performance of table type air separator was slightly lower than the classical wet methods while it was higher than other dry coal cleaning methods performances. That is why it may be used in arid areas or as a pre-concentration unit in hard coal separation, especially for coarse grain sizes. All tests were repeated twice, and no meaningful differences in results were evident. So, the arithmetical averages of results are shown in paper.

Table 6. E_p and d_{50} values of both samples versus particle size fractions

Particle Size Fractions (mm)	Lignite		Hard Coal	
	E_p	d_{50}	E_p	d_{50}
–38 + 25	0.130	1.68	0.110	1.68
–25 + 19	0.140	1.69	0.125	1.65
–19 + 13	0.200	1.69	0.135	1.61
–13 + 9.5	0.215	1.66	0.135	1.72
–9.5 + 6	0.235	1.65	0.135	1.73

Conclusion

All samples used in the experiment were investigated under the same test conditions. In the lignite sample it was observed that the clean coal increased its calorific value from 6.82 MJ/kg, which is the value of the original feed, to 14.20 MJ/kg, while the value for tailing was 3.29 MJ/kg. In the hard coal samples, the values of clean coal

increased from 15.94 MJ/kg, which is value of the original feed, to 21.07 MJ/kg, while for tailing it was 5.47 MJ/kg. It was also observed that increasing the feed rate caused a decrease in concentrate values and the total amount of ash removal while the combustible recovery increased. Controversially, the increasing particle size caused an increase in concentrate values and the total amount of removal ash while combustible recovery decreased. Although, other dry coal cleaning systems provide similar results with the table type air separator, E_p values of these methods, which represent the performance of equipment, are higher (0.15, 0.25 and 0.3) than for the table type air separator. It means that table type air separator has higher performance with the lower E_p values like 0.11 for hard coal and 0.13 for lignite. It has slightly lower performance than classical wet methods while it has higher performance than other dry coal cleaning methods.

Consequently, it could be stated that the table type air separator can be used as a dry separator with high separation efficiency and high feeding capacity not only for lignite separation but also for hard coal separation process. Besides, it could use as pre-concentration unit in hard coal separation because of high quality of tailing.

Acknowledgement

The authors thank to the Scientific and Technological Research Council of Turkey for their support.

References

ARSLAN V., 2006, *Dry coal cleaning methods*. The Journal of the Chamber of Mining Engineers of Turkey – Madencilik 45 (3): 9–18.

CHEN Q., WANG H., 2006, *Clean processing and utilization of clean energy*. The Chinese Journal of Process Engineering 6: 507–511.

CICEK T., 2008, *Dry cleaning of Turkish coal*, Energy Sources Part A 30, 593 – 605.

DONNELLY J., 1999, *Potential revival of dry cleaning of coal*. The Australian Coal Review 8: 26–30.

FRANKLAND S.C., 1995, *Dry beneficiation of coal*. DTI Coal R&D Program Contractors, Report No. Coal-R063. Oxfordshire, UK: ETSU, Harwell.

GHOSH T., HONAKER R.Q., PATIL D., PAREKH B.K., 2014, *Upgrading low-rank coal using a dry, density-based separator technology*, International Journal of Coal Preparation and Utilization, 34, 198–209.

GONGMIN L., YUNSONG Y., 2006, *Development and application of FGX series compound dry cleaning system*. China Coal 1: 17–28.

HONAKER R.Q., SARACOGLU M., THOMPSON E., BRATTON R., LUTTRELL G.H., RIDHARDSON V., 2008, *Upgrading coal using a pneumatic density-based separator*, International Journal of Coal Preparation and Utilization, 28, 51 – 67.

KADEMELI M., GULSOY O.Y., 2013, *Investigation of Using Table Type Air Separators for Coal Cleaning*, International Journal of Coal Preparation and Utilization, 33:1, 1-11.

KOHMUENCH J.N., JIANG X., and RICHARDSON V.P., 2005, *Testing of the FGX compound dry coal separator*. In: Proceedings of the 22nd International Coal Preparation & Aggregate Processing Exhibition and Conference, Lexington, Kentucky, 417–431.

LOCHART N.C., 1984, *Dry beneficiation of coal*. Powder Technology 40 (1–3): 17–42.

OSBORNE D. G., 1986, *Fine coal cleaning by gravity methods: A review of current practice*, Coal Preparation 2: 207–241.

SAHU A.K., BISWAL S. K., PARIDA A., 2009, *Development of air dense medium fluidized bed technology for dry beneficiation of coal – A review*. International Journal of Coal Preparation and Utilization 29 (4): 216–241.

SNOBY R.J., THOMPSON K., MISHRA S., SNOBY B., 2009, *Dry jigging coal: Case history performance*, SME Annual Meeting and Exhibit and CMA's 111th National Western Mining Conference, 346 – 349.

WEINSTEIN R., SNOBY R.J., 2007, *Advances in dry jigging improves coal quality*, Mining Engineering, 59 :1, 29 – 34.

WENCHENG X., GUANGYUAN X., YAOLI P., 2015, *Recent advances in beneficiation for low rank coals*, Powder Technology, 277, 206 – 221.

ZHANG B., AKBARI H., YANG F., MOHANTY M. K., HIRSCHI J., 2011, *Performance optimization of the FGX dry separator for coal cleaning high-sulphur coal*. International Journal of Coal Preparation and Utilization 31 (3–4): 161–186.

ZHENFU L., QINGRU C., 2001, *Dry beneficiation technology of coal with an air dense-medium fluidized bed*, International Journal of Mineral Processing, Vol. 63, No. 3, pp. 167-175.

ZHENFU L., YAOMIN Z., QINGRU C., MAOMING F., XIUXIANG T., 2002, *Separation characteristics for fine coal of magnetically fluidized bed*. Powder Technology 79: 63–69.

Received March 17, 2015; reviewed, accepted May 15, 2015

REMOVAL OF QUINOLINE FROM AQUEOUS SOLUTIONS BY LIGNITE, COKING COAL AND ANTHRACITE. ADSORPTION ISOTHERMS AND THERMODYNAMICS

Hongxiang XU^{*}, Gen HUAGN^{*}, Xiaobing LI^{}, Lihui GAO^{**}, Yongtian WANG^{**}**

^{*} School of Chemical and Environmental Engineering, University of Mining and Technology (Beijing), Beijing, China, 100083, xuhongxiang001@163.com

^{**} School of Chemical Engineering and Technology, Chinese National Engineering Research Center of Coal Preparation and Purification, China University of Mining and Technology, Xuzhou, Jiangsu, China, 221116

Abstract: Based on the concept of circular economy, a novel method of industrial organic wastewater treatment by using adsorption on coal is introduced. Coal is used to adsorb organic pollutants from coking wastewaters. After adsorption, the coal would be used for its original purpose, its value is not reduced and the pollutant is thus recycled. Through systemic circulation of coking wastewater zero emissions can be achieved. Lignite, coking coal and anthracite were used as adsorbents in batch experiments. The quinoline removal efficiency of coal adsorption was investigated. The coking coal and anthracite exhibited properties well-suited for adsorption onto both adsorbents. The experimental data were fitted to Langmuir and Freundlich isotherms as well as Temkin, Redlich–Peterson (R-P) and Dubinin–Radushkevich (D-R) models. Both Freundlich Isotherm and D-R model provided reasonable models of the adsorption process. The thermodynamic parameters of quinoline adsorption on coking coal were calculated. The thermodynamic parameters indicated that the adsorption process is exothermic and is a physical adsorption. The ΔS° value indicated that the adsorption entropy decreased because the adsorbate molecule was under restrictions after it adsorption on the coal surface. The coal adsorption method for removing refractory organic pollutants is a great hope for achieving zero emission waste water for a coking plant.

Keywords: quinoline adsorption; coking coal; adsorption isotherms; thermodynamics

Introduction

Coking wastewater pollution is a serious problem all over the word. Coking wastewater is generated from coal coking, coal gas purification and by-product recovery processes of coking (Fang et al, 2012). It usually contains complex inorganic and organic pollutants, such as phenolic compounds, pyridine, indol, quinoline, ammonium, sulfate, cyanide, thiocyanate, polynuclear aromatic hydrocarbons and polycyclic

nitrogen-containing acyclic compounds, most of which are refractory, toxic, mutagenic and carcinogenic (Ghose, 2002; Chao et al., 2006; Lai et al., 2009). The adsorption method (Aksu and Yener, 2001; Badmus and Audu, 2009) is widely used in the treatment and recovery process of organic wastewater including coking wastewater and oily wastewater. It is very effective for removing water particulate matter and refractory organics. This method has advantages and disadvantages (Lee and Park, 1998; Magnus et al., 2000; Mall and Srivastava, 2006). How to enhance advantages and avoid disadvantages was important in this research. Coal is a complex porous medium and natural adsorbent. After adsorption, the coal would be used in its original purpose and its value was not reduced.

This research investigates the potential of adsorption for removing quinoline in simulation coking wastewater by three kinds of coals. The adsorbent properties, adsorption efficiency, adsorption isotherms and thermodynamics were investigated.

Methods and materials

Adsorbate

Quinoline with purity greater than 99.5% was purchased from Shanghai Chemical Company and used as a single component (adsorbate) in this study. According to the GC-MS analysis of coking wastewater of the Linhuan coking plant, the major organic components of coking wastewater are phenol, quinoline, pyridine and indol (Fu, 2004). The quinoline concentration of the simulated coking waste water was about $25 \text{ mg} \cdot \text{dm}^{-3}$.

Adsorbents

In this research, the three adsorbents are lignite, coking coal and anthracite. Lignite was obtained from the Shenli coal mine of Shenhua Group Co., Ltd. while coking coal and anthracite were obtained from the Linhuan coal preparation plant and Chengjiao coal preparation plant of Henan Coal Chemical Industry Group Co., Ltd, respectively. Coal was crushed, ground, sieved through a $74 \mu\text{m}$ sifter, and dried at 120°C in an oven for 2 h before to use. After drying, the adsorbent was stored in sealed glass containers.

The surface area of adsorbents was measured by surface area analyzer (BELSORP-max, BEL-JAPAN, INC). The crystalline phases present in three kinds of coal were determined via X-ray diffractometry (S8 TIGER, BRUKER AXS, German). Three kinds of coal were analyzed by the Scanning electron microscopy (SEM) (Zeiss Ultra Plus Model, Germany) to image the surface characteristic.

Batch adsorption studies

The adsorption isotherms of quinoline on three kinds of coal were investigated in batch sorption equilibrium experiments. For each experiment, fresh quinoline solutions were prepared by dissolving the quinoline material in deionized water and measuring the

concentration by UV/VIS spectroscopy (UV-4802S, Shanghai) (Lin and Dence, 1992). The adsorbents were added to the quinoline solutions in 200 cm³ sample conical flasks mounted on a shaker. The flasks were agitated at a constant speed of 200 rpm for different timings at constant temperature. Samples were collected from the flasks at predetermined time intervals for analyzing the residual concentration in the solution. The adsorption capacity of coal was calculated using the expression,

$$Q_t = \frac{(C_0 - C_t)V}{M}. \quad (1)$$

The removal efficiency of quinoline was calculated using the expression,

$$E = \frac{C_0 - C_t}{C_0} \quad (2)$$

where, Q_t (mg·g⁻¹) is the quinoline removed at time t by a unit mass of the adsorbent, C_0 (mg·dm⁻³) is the initial quinoline concentration, C_t (mg·dm⁻³) is the quinoline concentration at time t , and M (g) is coal consumption. V (cm³) is the quinoline solutions volume. The adsorption experiments, which were conducted at various time intervals and temperatures (283 K, 298 K and 313 K) to determine when the adsorption equilibrium was reached and the maximum removal of naphthalene was attained. After the equilibrium contact time, the samples were filtered and the equilibrium concentrations ascertained by spectrophotometer at the respective standard curve equations, which is 278 nm for quinoline.

Adsorption models

Both the capacity of the adsorbent and driving force of adsorption is useful for the design of a sorption treatment plant (Ho and McKay, 1999; Zhang et al., 2010). Isotherm models describe the equilibrium relationship of the adsorbate in the solid and liquid phases of the system.

The Langmuir isotherm

The Langmuir isotherm (Langmuir, 1916; Ruthven, 1984) is most widely applied sorption isotherm in the pollutant adsorption field. The Langmuir isotherm expression is given as:

$$Q_{eq} = \frac{q_m K_L C_{eq}}{1 + K_L C_{eq}} \quad (3)$$

The linear form of the Langmuir isotherm is:

$$\frac{C_{eq}}{Q_{eq}} = \frac{C_{eq}}{q_m} + \frac{1}{K_L q_m} \quad (4)$$

where, Q_{eq} (mg·g⁻¹) is the equilibrium amount of adsorbate on the solid surface; C_{eq} (mg·dm⁻³) the equilibrium amount of adsorbate in solution; K_L (dm³·mg⁻¹) is related to

the energy of adsorption and the affinity between adsorbate and adsorbent. q_m (mg·g⁻¹) is monolayer adsorption capacity (Andersson et al., 2011).

The Freundlich isotherm

The Freundlich isotherm expression is given as (Cicek et al., 2007; Sahu et al 2008):

$$Q_{eq} = K_{Fr} C_{eq}^{1/n}. \quad (5)$$

The linear form of the Freundlich isotherm is:

$$\ln Q_{eq} = \ln K_{Fr} + \left(\frac{1}{n}\right) \ln C_{eq} \quad (6)$$

where, K_{Fr} represents the adsorption capacity. $1/n$ is adsorption index, $1/n > 2$ indicates an unfavorable adsorption process. $0.1 < 1/n < 0.5$ indicates a favorable adsorption process.

The Temkin model

The Temkin model expression is given as (Basar 2006; Gunay et al., 2007):

$$Q_{eq} = \left(\frac{RT}{b_T}\right) \ln(K_T C_{eq}) . \quad (7)$$

The linear form of the Temkin model is:

$$Q_{eq} = \left(\frac{RT}{b_T}\right) \ln C_{eq} + \frac{RT \ln K_t}{b_T} . \quad (8)$$

The K_t expression is

$$K_T = \exp\left(\frac{\text{intercept}}{\text{slope}}\right) \quad (9)$$

where K_T (dm³·g⁻¹) is the equilibrium binding constant and b_T (J·mol⁻¹) is related to the heat of adsorption.

The Redlich–Peterson model

The Redlich–Peterson (R-P) model expression is given as (Redlich and Peterson, 1959; Jossens et al., 1978) :

$$Q_{eq} = \frac{K_R C_{eq}}{1 + \alpha C_{eq}^\beta} . \quad (10)$$

The linear form of the Redlich-Peterson model is:

$$\ln \left| \frac{K_R C_{eq}}{Q_{eq}} - 1 \right| = \beta \ln C_{eq} + \ln |\alpha| \quad (11)$$

where $K_R(\text{dm}^3 \cdot \text{g}^{-1})$ is constant that is varied to maximize the linear correlation coefficient R^2 , α is a constant and β is a constant in the range of 0~1.

The Dubinin-Radushkevich model

The Dubinin-Radushkevich (D-R) model expression is given as (Jossens et al., 1978):

$$Q_{\text{eq}} = Q_m \exp(-K_{\text{DR}}\varepsilon^2). \quad (12)$$

The linear form of the D-R model is:

$$\ln Q_{\text{eq}} = -K_{\text{DR}}\varepsilon^2 + \ln Q_m \quad (13)$$

$$\varepsilon = RT \ln\left(1 + \frac{1}{C_{\text{eq}}}\right) \quad (14)$$

where $K_{\text{DR}}(\text{mol} \cdot \text{kJ}^{-1})^2$ is related to the energy of sorption E ; T (K) is absolute temperature; $Q_m(\text{mg} \cdot \text{g}^{-1})$ is the largest adsorbed amount at saturation.

The mean energy of sorption E expression is:

$$E = \frac{1}{(2K_{\text{DR}})^{1/2}}. \quad (15)$$

Adsorption thermodynamics

The transformation of adsorbate from solution to the surface of adsorbent affects the thermodynamic properties of the system (Kaya et al., 2013). The free energy change of the adsorption process, ΔG° , can be calculated by:

$$\Delta G^\circ = -RT \ln k_0 \quad (16)$$

The relationship between the standard Gibbs free energy of adsorption $\Delta G^\circ(\text{kJ} \cdot \text{mol}^{-1})$, the standard enthalpy change $\Delta H^\circ(\text{kJ} \cdot \text{mol}^{-1})$ and the standard entropy change $\Delta S^\circ(\text{J} \cdot \text{mol}^{-1} \cdot \text{K}^{-1})$ is given as:

$$\Delta G^\circ = \Delta H^\circ - T\Delta S^\circ. \quad (17)$$

Combining Eqs. 16 and 17 yields:

$$\ln k_0 = \frac{\Delta S^\circ}{R} - \frac{\Delta H^\circ}{RT} \quad (18)$$

where $R(8.314 \text{ J} \cdot \text{K}^{-1} \cdot \text{mol}^{-1})$ is ideal gas constant, T (K) is absolute temperature and K_0 is partition coefficient.

Different adsorption models have different K_0 values, so the ΔG° value is also different. $\ln K_0$ can be obtained from the intercept of the straight line plots of $\ln(\frac{Q_{\text{eq}}}{C_{\text{eq}}})$ versus Q_{eq} (Khan and Singh, 1987). This method (Shu and Jia, 2005; Chandra et al.,

2007) was used to calculate the ΔG° value in this research. The straight line plots of $\ln K_0$ against $1/T$ were tested to obtain ΔH° and ΔS° , while ΔG° was obtained from Eq. 17.

Results and discussions

Chemical composition of lignite, coking coal and anthracite

The XRD of lignite, coking coal and anthracite are shown in Fig. 1–3.

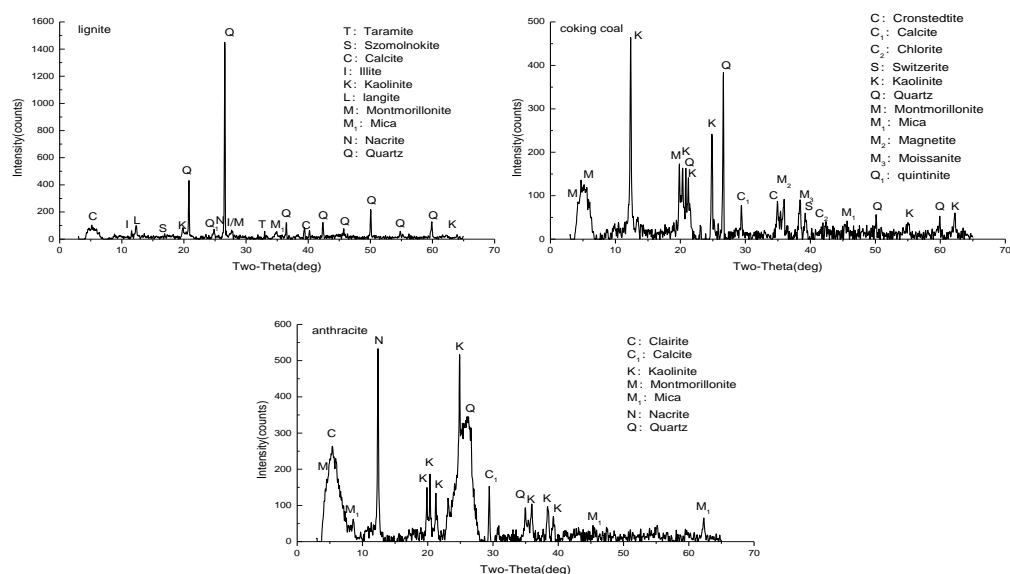


Fig. 1. X-ray Diffraction Patterns of lignite, coking coal and anthracite

Basing on the analysis, the three kinds of coal contain gangue minerals and have similar mineral compositions. The anthracite has lower content of gangue minerals than others. Based on the analysis of mineral composition content, the coal composition plays a leading role in the adsorption test. The clay minerals content also has a certain adsorption effect, but the effect is small because the content is small. The gangue minerals have a little influence on coal adsorption.

SEM analysis of adsorbents

The SEM photographs obtained for lignite, coking coal and anthracite are illustrated in Fig. 2. The three kinds of coal all have rough surfaces and pores, and they are similar. Thus, all of them may be used as an adsorbent.

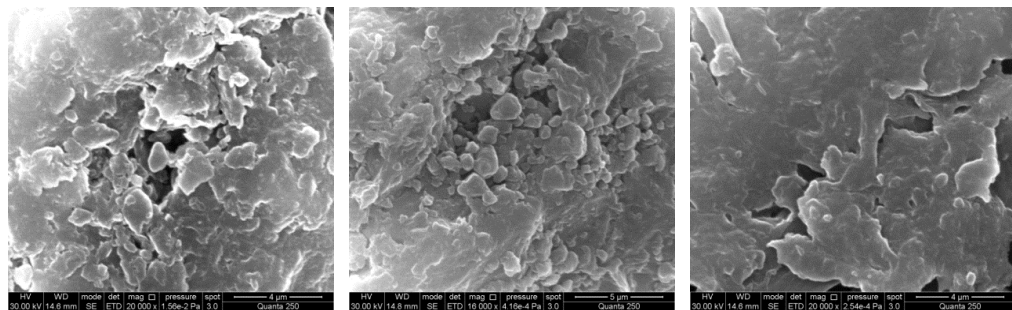


Fig. 2. SEM images of lignite (left), coking coal (middle) and anthracite (right)

The specific surface area

As shown in Table 1, the specific surface area of the lignite, coking coal and anthracite were $6.0876 \text{ m}^2 \cdot \text{g}^{-1}$, $5.7864 \text{ m}^2 \cdot \text{g}^{-1}$ and $6.1479 \text{ m}^2 \cdot \text{g}^{-1}$, respectively.

Table 1. Special surface area of lignite, coking coal and anthracite

Method	Specific surface area ($\text{m}^2 \cdot \text{g}^{-1}$)		
	Lignite	Coking coal	Anthracite
BET method	6.0876	5.7864	6.1479

The effect of adsorption time on quinoline removal efficiencies

Experimental conditions of the adsorption tests were: solution volume 100 cm^3 , quinoline concentration of solution $25 \text{ mg} \cdot \text{dm}^{-3}$, coal consumption 2.0 g , adsorption temperature 25°C . The effect of coal consumption on quinoline removal efficiencies is shown in Fig. 3.

As shown in Fig. 3, both the organic removal efficiency and adsorption capacity increased with the increasing adsorption time. At the beginning, the adsorption rate of the organic removal efficiency increased rapidly, and tended to be constant after 60 min. The shortest time for reaching adsorption equilibrium was in the case of anthracite, followed by lignite, and finally coking coal. The optimum adsorption time determined by test was 30~60 min.

The coal surface did not adsorb the organic material when the coal was just at the beginning of contact with the organic in the aqueous phase, probably because it was not fully wetted. Initially there were many sorptive sites without an adsorbant on coal surface, so the adsorption rate was higher than the desorption rate. The organic removal efficiency increased with the increasing time. The adsorption rate equalled the desorption rate when the adsorption point and the functional group were almost occupied by the organic molecule after 60 min. So, the organic removal efficiency tends to be constant after that.

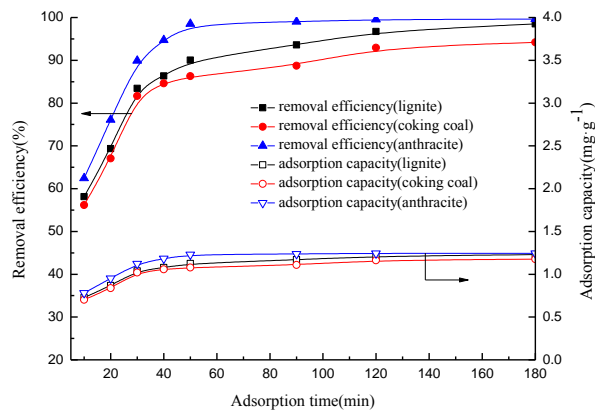


Fig. 3. The effect of adsorption time on quinolone removal efficiency

Isothermal experimental results and equilibrium modeling

Experiments were carried out for a solution volume of 100 cm³, with a quinoline concentration, coal consumption 2.0 g, adsorption temperature 25 °C and adsorption time 4 h. The results of quinoline adsorption in isothermal experiments are shown in Table 2.

Table 2. The results of quinoline adsorption isothermal experiment

Absorbent	Initial concentration / mg·dm ⁻³	5	10	20	30	50
Lignite	Equilibrium concentration / mg·dm ⁻³	0.06	0.28	1.09	1.95	4.40
	Removal efficiency / %	98.71	97.21	94.53	93.49	91.20
	Equilibrium absorption capacity / mg·g ⁻¹	0.25	0.49	0.95	1.40	2.28
Coking coal	Equilibrium concentration / mg·dm ⁻³	0.11	0.41	1.27	2.25	4.66
	Removal efficiency / %	97.85	95.92	93.67	92.49	90.69
	Equilibrium absorption capacity / mg·g ⁻¹	0.24	0.48	0.94	1.39	2.27
Anthracite	Equilibrium concentration / mg dm ⁻³	0.06	0.19	0.88	1.70	3.37
	Removal efficiency / %	98.71	98.07	95.60	94.35	93.26
	Equilibrium absorption capacity / mg·g ⁻¹	0.25	0.49	0.96	1.42	2.33

The isotherm constants were obtained by using a linear regression analysis of the quinoline adsorption isotherm. The isotherm constants and the correlation coefficients are shown in Table 3.

The curves of the calculated equilibrium amount of adsorbate on the adsorbent surface (Q_{eq}) versus the amount in solution (C_{eq}) which were used in the various models and the obtained constants are shown in Fig. 4.

Table 3. Constants and correlation coefficients obtained for the Langmuir, Freundlich, Temkin, R-P and D-R isotherm models of quinolone adsorption onto lignite, coking coal and anthracite

Adsorbent	Langmuir Isotherm			Freundlich Isotherm			
	$K_L/\text{dm}^3 \cdot \text{mg}^{-1}$	$q_m/\text{mg g}^{-1}$	R_L^a	R^2	$K_{Fr}/\text{mg g}^{-1}(\text{mg} \cdot \text{dm}^{-3})$	$1/n$	R^2
Lignite	0.5829	2.99	0.03	0.8871	0.95	0.586	0.9949
Coking coal	0.4612	3.09	0.04	0.8282	0.86	0.589	0.9943
Anthracite	0.8535	2.86	0.02	0.8247	1.12	0.544	0.8269
Redlich-Peterson (R-P) Model				Temkin Model			
	$K_R/\text{dm}^3 \cdot \text{g}^{-1}$	$\alpha/\text{dm}^3 \cdot \text{mg}^{-1}$	β	R^2	$K_T/\text{dm}^3 \cdot \text{g}^{-1}$	$b_T/\text{KJ} \cdot \text{mol}^{-1}$	R^2
Lignite	-6.381	-7.875	0.354	0.9986	2.34	4.82	0.87118
Coking coal	-1.220	-2.500	0.220	0.9999	2.22	4.92	0.82048
Anthracite	-1.658	-2.590	0.229	0.9964	2.84	5.19	0.8269
Dubinin-Radushkevich (D-R) Model							
	$K_D/(\text{mol} \cdot \text{kJ}^{-1})^2$	$E/\text{KJ} \cdot \text{mol}^{-1}$	R^2				
Lignite	-0.039	3.60	0.7363				
Coking coal	-0.056	3.00	0.7254				
Anthracite	-0.040	3.52	0.8234				

R_L^a is calculated for $C_0 = 50 \text{ mg} \cdot \text{dm}^{-3}$

A comparison of the correlation coefficients in Table 3 showed that the Redlich-Peterson model fits better quinoline adsorption on lignite, coking coal and anthracite than other models and R^2 for the three types of coals are 0.9986, 0.9999 and 0.9964, respectively. The R-P model constants results showed that the $\beta < 1$ and $|\alpha|C_{eq}^\beta > 1$, so the quinoline adsorption on lignite, coking coal and anthracite fits well the isotherm. The quinoline adsorptions on three coals also fit the Freundlich isotherm. The R_L values from the Langmuir equation were all between 0 and 1, indicating a favorable sorption process. This was supported by the $1/n$ values less than 1 obtained for the Freundlich model.

The Langmuir values of q_m , signifying adsorption capacity, were 2.99, 3.09 and 2.86 $\text{mg} \cdot \text{g}^{-1}$ for quinoline adsorption on lignite, coking coal and anthracite, respectively. According to the constant K_{Fr} , the order of rate of adsorption are anthracite > lignite > coking coal. Due to E in the range of 1.0~8.0 $\text{kJ} \cdot \text{mol}^{-1}$, the adsorption process seems to be physical (Zhang et al., 2010).

As shown in Fig. 4, the Langmuir, Freundlich, Temkin and R-P models provide better correlations than the D-R model. The Freundlich and R-P model showed the best fit of the experimental data.

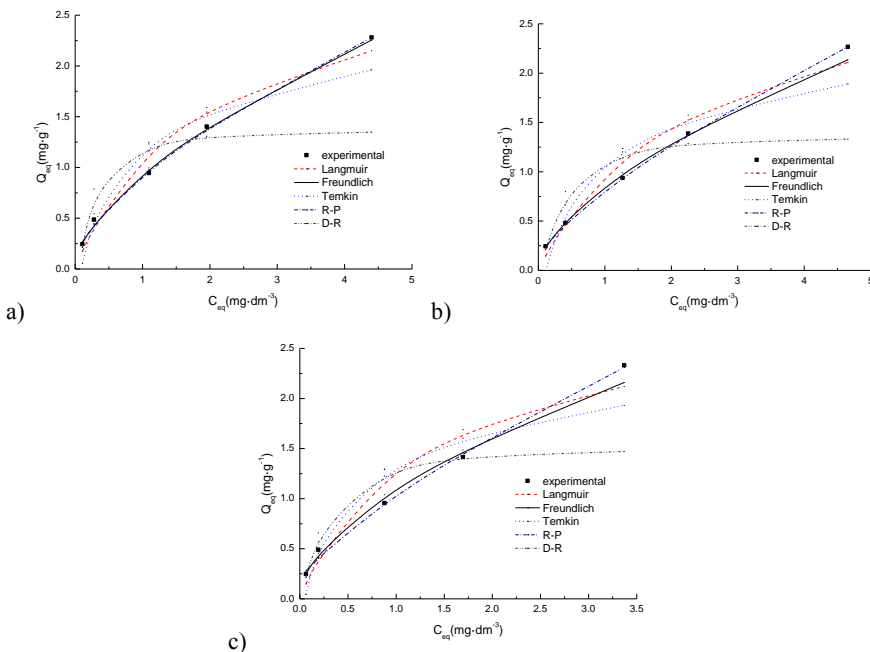


Fig. 4. Equilibrium amount of quinoline adsorbed on the adsorbent surface (Q_{eq}) at increasing equilibrium quinoline concentrations (C_{eq}) expressed by the Langmuir, Freundlich, Temkin, R-P and D-R isotherm models
 (a) adsorbent: lignite (b) adsorbent: coking coal (c) adsorbent: anthracite

Thermodynamics

According to experimental data, the relationship graph of $\ln\left(\frac{Q_{eq}}{C_{eq}}\right) - Q_{eq}$ was obtained. It is shown in Fig. 5.

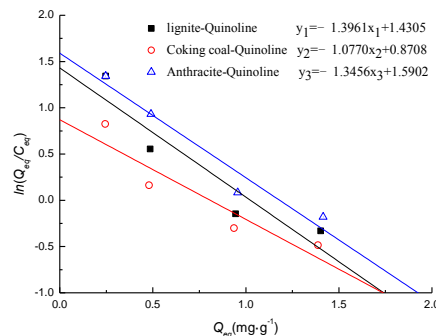


Fig. 5. Plot of $\ln\left(\frac{Q_{eq}}{C_{eq}}\right)$ versus Q_{eq} for quinoline adsorption on lignite, coking coal and anthracite

Different K_0 can affect the calculated value of thermodynamical function (Khan and Singh, 1987). Except the $\ln K_0$ which was calculated by the line of $\ln \left(\frac{Q_{eq}}{C_{eq}} \right) - Q_{eq}$, the constant K_L of Langmuir isotherm and K_{Fr} of Freundlich isotherm also can be used to calculate the ΔG° value.

Table 4. Values of $\ln K_0$ and ΔG° of adsorption on different coals

Adsorbent	T / K	$\ln \left(\frac{Q_{eq}}{C_{eq}} \right) - Q_{eq}$ line		Langmuir isotherm		Freundlich isotherm	
		$\ln K_0$	$\Delta G^\circ / \text{kJ} \cdot \text{mol}^{-1}$	$\ln K_L$	$\Delta G^\circ / \text{kJ} \cdot \text{mol}^{-1}$	$\ln K_{Fr}$	$\Delta G^\circ / \text{kJ} \cdot \text{mol}^{-1}$
Lignite	298.15	1.4305	-2.35	-0.54	1.34	-0.06	0.14
Coking coal	298.15	0.8708	-1.43	-0.77	1.92	-0.15	0.37
Anthracite	298.15	1.5902	-2.62	-0.16	0.39	0.11	-0.27

As shown in the Table 4, the process of quinoline adsorption on three coals is spontaneous and physical because the ΔG° values were below zero, and their absolute values are in the range of $0\sim 20 \text{ kJ} \cdot \text{mol}^{-1}$ (Sahu et al., 2008). For comparison, K_L and K_{Fr} , which were obtained respectively from the Langmuir model and Freundlich models, can be used to calculate ΔG° values. The ΔG° values of quinoline adsorption on lignite, coking coal and anthracite which were calculated using the equilibrium constants of the Langmuir expression where K_L were $1.34 \text{ kJ} \cdot \text{mol}^{-1}$, $1.29 \text{ kJ} \cdot \text{mol}^{-1}$ and $0.39 \text{ kJ} \cdot \text{mol}^{-1}$, respectively. It can be seen that the two ΔG° values, which were obtained using the equilibrium constants of the Langmuir and Freundlich expressions, were different from those obtained by the straight line plots of $\ln \left(\frac{Q_{eq}}{C_{eq}} \right)$ versus Q_{eq} . Consequently, the ΔG° values need to be obtained by the same procedure when

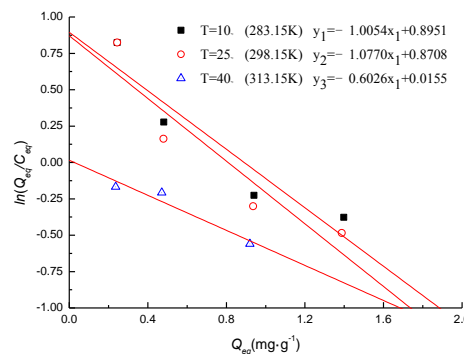


Fig. 6. Plot of $\ln \left(\frac{Q_{eq}}{C_{eq}} \right)$ versus Q_{eq} for quinoline adsorption on coking coal at different temperatures

comparing the results of various sorption tests. The ΔH° and ΔS° values of the process of quinoline adsorption on coking coal were calculated. Using the experimental data, the relationship lines of $\ln\left(\frac{Q_{eq}}{C_{eq}}\right) - Q_{eq}$ for different temperatures were obtained. It is shown in Fig. 6. The $\ln K_0$ values were used to plot of $\ln K_0$ versus $1000/T$ as is shown in Fig. 7.

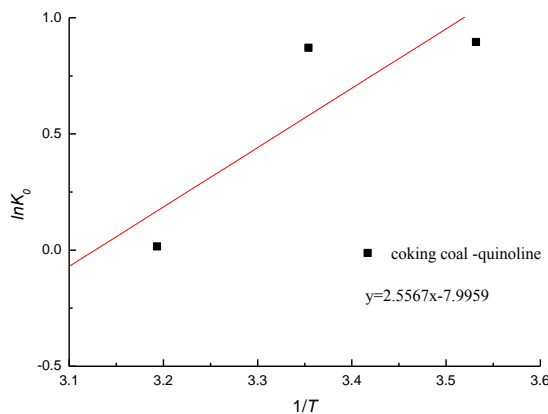


Fig. 7. Plot of $\ln K_0$ versus $1000/T$ for quinoline adsorption on coking coal

The ΔH° and ΔS° , reflecting the thermodynamics of the system for quinoline adsorption on coking coal, were determined from the slope and intercept of line in Fig. 6, respectively. The obtained values are presented in Table 5.

Table 5. Obtained values of $\ln k_0$, ΔH° , ΔS° and ΔG° for quinoline adsorption on coking coal

T (K)	$\ln k_0$	$\Delta H^\circ/\text{kJ}\cdot\text{mol}^{-1}$	$\Delta S^\circ/\text{J}\cdot\text{mol}^{-1}\cdot\text{K}^{-1}$	$\Delta G^\circ/\text{kJ}\cdot\text{mol}^{-1}$
283.15	0.8352			-1.47
298.15	0.8708	-21.27	-66.48	-1.43
333.15	0.0155			-0.03

As shown in Table 4, $\Delta H^\circ = -21.27 \text{ kJ}\cdot\text{mol}^{-1} < 0$ illustrates that the adsorption process is an exothermic reaction and also points to physical adsorption. Thus, low temperature is better for this adsorption process. $\Delta S^\circ = -66.48 \text{ J}\cdot\text{mol}^{-1}\cdot\text{K}^{-1} < 0$ indicates that the adsorption entropy decreased because the adsorbate molecule was under restrictions after it was adsorbed on the coal surface. Adsorption process is not a separate process. Even if the system entropy decreases, the total entropy, which includes the system and surrounding environment, may increase. The maximum temperature of the spontaneous adsorption process was 319.75 K, which was obtained by Eq. 18 and the values from Table 5.

Conclusions

Fitting experimental data to various equilibrium models showed that the adsorption processes follow the Freundlich isotherm. The main oxygen-containing functional groups on the three kinds of coal surface are acidic. The adsorption capacity is proportional to special surface area of coal. The rate of quinoline adsorption on anthracite is largest. Both the organic removal efficiency and adsorption capacity increased, and then tend to be constant with the increase of adsorption time. The optimum adsorption time determined by test is 30~60 min. According to the result of thermodynamics, the negative value of change in Gibbs free energy (ΔG°) indicates that adsorption of quinoline on coal is spontaneous, and that the ΔH° of quinoline adsorption on coking coal was $21.27 \text{ kJ}\cdot\text{mol}^{-1}$. Thus, the adsorption is exothermic and physical. The adsorption entropy decreased because the adsorbate molecule was under restrictions after it was adsorbed on the coal surface.

Acknowledgements

The authors are grateful to the Postgraduate Scientific Research and Innovation Projects of Jiangsu Province (No. CXLX13_954) and the Fundamental Research Funds for the Central Universities (No. 2014XT05) for their support of this project.

References

AKSU Z., YENER J., 2001, *A comparative adsorption/biosorption study of mono-chlorinated phenols onto various sorbents*, Waste Manage., 21, 695–697.

ANDERSSON K. I., ERIKSSON M., NORLGREN M., 2011, *Removal of lignin form wastewater generated by mechanical pulping using activated charcoal and fly ash: Adsorption isotherms and thermodynamics*. Ind. Eng. Chem. Res., 50, 7711–7732.

BADMUS M. A. O., AUDU T. O. K., 2009, *Periwinkle shell based granular activated carbon for treatment of chemical oxygen demand (COD) in industrial wastewater*, Can. J. Chem. Eng., 87, 69–71.

BASAR C. A., 2006, *Applicability of the various adsorption models of three dyes adsorption onto activated carbon prepared waste apricot*, J. Hazard. Mater. B, 135, 232–241.

CHANDRA T.C., MIRNA M.M., SUDARYANTO Y., ISMADJI, S., 2007, *Adsorption of basic dye onto activated carbon prepared from durian shell: Studies of adsorption equilibrium and kinetics*, Chem. Eng. J, 127, 121–129.

CHAO Y.M., TSENG I.C., CHANG J.S., 2006, *Mechanism for sludge acidification in aerobic treatment of coking wastewater*, J. Hazard. Mater., 137, 1781–1787.

CICEK F., ZER D. Ö., ZER A. Ö, 2007, *Low cost removal of reactive dyes using wheat bran*, J. Hazard. Mater. 146, 408–416.

FANG J.W., SONG X.Y., CAI C.F., TANG C.G., 2012, *Adsorption characteristics of coking coal in coking wastewater treatment*, J Anhui Univ. Technol. Sci., 25, 43–46.

FU M., 2004, *Study on Modification of Activated Carbon Fiber and Adsorptive Properties for Organic Compounds in Wastewater from Coke Plant*, Chongqing Univer., 53–55.

GHOSE M.K., 2002, *Complete physico-chemical treatment for coke plant effluents*, Water Res., 36, 1127–1134.

GUNAY A., ARSLANKAYA E., TOSUN I., 2007, *Lead removal from aqueous solution by natural and pretreated clinoptilolite: Adsorption equilibrium and kinetics*, J. Hazard. Mater., 146, 362–371.

HO Y. S., MCKAY G., 1999, *Pseudo-second order model for sorption processes*, Process Biochem., 34, 451–452.

JOSSENS L., PRAUSNITZ J.M., FRITZ W., SCHLÜNDER, E. U., MYERS, A. L., 1978, *Thermodynamics of multi-solute adsorption from dilute aqueous solutions*, Chem. Eng. Sci., 33, 1097–1099.

KAYA E.M.Ö., ÖZCAN A.S., GÖK Ö.Z., Adnan Ö., 2013, *Adsorption kinetics and isotherm parameters of naphthalene onto natural- and chemically modified bentonite from aqueous solutions*, Adsorption, 19, 879–888.

KHAN A. A., SINGH R. P., 1987, *Adsorption thermodynamics of carbofuran on Sn(IV) arsenosilicate in H^+ , Na^+ , and Ca^{2+} forms*, Colloids Surf., 24, 33–42.

LAI P., ZHAO H.Z., ZENG M., NI J.R., 2009, *Study on treatment of coking wastewater by biofilm reactors combined with zero-valent iron process*, J. Hazard. Mater., 162, 1423–1429.

LANGMUIR I., 1916, *The constitution and fundamental properties of solids and liquids*, J. Amer. Chem. Soc. 38, 2221–2223.

LEE M.W., PARK J.M., 1998, *Biological Nitrogen Removal from Coke plant Waster with External Carbon Addition*, Water Environ. Res., 70, 1090–1095.

LIN S.Y., DENCE W.C., 1992, *Ultraviolet spectrophotometry: Methods in Lignin Chemistry*, Springer-Verlag, Berlin, 217–232.

MAGNUS E., HOEL H., CARLBERG G.E., 2000, *TMP wastewater treatment, including a biological high-efficiency compact reactor: Removal and characterisation of organic components*, Nord. Pulp Pap. Res. J., 15, 37–44.

MALL I. D., SRIVASTAVA V.C., 2006, *Removal of Orange-G and Methyl Violet dyes by adsorption onto bagasse fly ash – kinetic study and equilibrium isotherm analyses*, Dyes and Pigments, 69, 210–223.

REDLICH O., PETERSON D.L., 1959, *A useful adsorption isotherm*, J. Phys. Chem., 63, 1024–1024.

RUTHVEN D.M., 1984, *Principles of adsorption and adsorption processes. A Wiley-Interscience publication*, John Wiley and Sons, 58–88.

SAHU A.K., SRIVASTAVA V.C., MALL I.D., LATAYE D.H., 2008, *Adsorption of furfural from aqueous solution onto activated carbon: Kinetic, equilibrium and thermodynamic study*, Sep. Sci. Technol., 43, 1239–1259.

SAHU A.K., MALL I.D., SRIVASTAVA V.C., 2008, *Studies on the adsorption of furfural from aqueous solutions onto low-cost bagasse fly ash*, Chem. Eng. Commun., 195, 316–335.

SHU Y.H., JIA X.S., 2005, *The mechanisms for CTMAB-bentonites to adsorb CBs from water in the adsorption kinetics and thermodynamics view*, Acta Scientiae Circumstantiae, 25, 1530–1536.

ZHANG L., LIU X.Y., JIAN X.Q., LI Q., JIANG P.L., 2010, *Adsorption properties of nano-TiO₂ for Mo(VI)*, The Chinese Journal of Nonferrous Metals., 20, 301–305.

ZHANG M.H., ZHANG Q.L., XUE B., ZHANG F., 2010, *Adsorption of organic pollutants from coking wastewater by activated coke*, Colloids Surf. A, 362, 140–146.

Received May 4, 2015; reviewed; accepted June 9, 2015

A PHYSICAL MODEL OF SEPARATION PROCESS BY MEANS OF JIGS

Agnieszka SUROWIAK, Marian BROZEK

AGH University of Science and Technology, Al. Mickiewicza 30, 30-059 Krakow, Poland
asur@agh.edu.pl, brozek@agh.edu.pl

Abstract: In the case of ideal separation of minerals, partition into products is conducted according to a specific partition feature which is, for instance, the density of raw material. Usually, enrichment in a jig is described by means of the particle density as a partition feature. However, the degree of particle loosening in the jig's bed is influenced by, among others, the particle free settling velocity. After some time of the pulsating movement duration, particle segregation along the vertical axis according to the settling velocity will occur. It can be said that the particle free settling velocity constitutes a feature characteristic of the feed heterogeneous in terms of physical and geometric properties in the jiggling process. In the article on the basis of heuristic considerations, a physical model of the partition function (recovery of the i^{th} fraction), in which interactions between particles in the working bed of the jig are taken into account, is derived. A cause of the formation of the mechanism of particle dispersion around equilibrium layers is given and the accuracy of particle partition for a narrow size fraction in two variations, i.e. in conditions when a partition feature is, accordingly, the particle density and settling velocity, is calculated. These calculations allowed for the analysis of causes of process and inherent dispersion formation which takes place during the jiggling process.

Keywords: jiggling process, physical model, Maxwell distribution, probable error, imperfection

Introduction

The condition necessary for the correct separation of particles in a separating device, a jig, is sufficient loosening of the feed particles in a working bed, leading to a proper stratification of the feed particles into subsets with similar properties (size, density, settling velocity). The diversified particle settling velocity in the working bed of the jig determines the correct course of the partition process. In order to enable the stratification of material into fractions differing in the settling velocity to occur in the jig, particles must be able to move freely between each other. Therefore, conditions of a pulsating movement must be chosen in such a way as to ensure appropriate loosening of the material layer on jig's sieve. The degree of loosening of particles in

the jig's bed is influenced by, among others, the particle free settling velocity. A distance traversed by a particle during one cycle depends on the settling velocity. Therefore, after long duration of the pulsating movement, if partition was accurate, segregation of particles will occur along the vertical axis according to the free settling velocity (Willis and Napier-Munn, 2006). Thus, it can be said that the particle free settling velocity at the accurate partition constitutes a characteristic feature of the feed heterogeneous in terms of physical and geometric properties in the partition process in the jig.

The particle partition and dispersion mechanism

A characteristic feature of partition in a jig is the free settling velocity. The particle stratification into elemental fractions (layers) occurs according to the settling velocity. The pulsating movement of liquid is a mechanism generating such partition. The movement of particles in the jig's bed is a random process. The value of a random variable denoting a particle location along the vertical axis in a non-stationary state is a function of time. Particles move between each other under deterministic forces, resulting from the pulsating movement, suffering collisions. These interactions at the moment of collisions are a source of particle dispersion around grouping centres, being a function of time, because the deterministic movement intensity is a function of time. If the pulsating movement velocity was homogeneous in the whole volume of the jig's working space and there were no interactions between particles, then in a stationary state, that is after the conducted partition, the state of ideal stratification according to the settling velocity would be achieved. However, this is not the case. Due to the heterogeneity of the liquid velocity field in the vertical direction of the jig's bed, the permeation of particles to layers improper to them occurs. It can be thus said that two independent random processes occur. One is connected to the heterogeneity of the liquid velocity field, independent of time and the other connected to particles' collisions during the deterministic particles movement with different properties to their equilibrium layers, dependent on time. The latter movement is described by the Fokker-Planck equation (Tichonov, 1968; 1973):

$$\frac{\partial f(z,t)}{\partial t} = -p \frac{\Delta z}{\Delta t} \frac{\partial f(z)}{\partial z} + \frac{1}{2} p \frac{(\Delta z)^2}{\Delta t} \frac{\partial^2 f(z,t)}{\partial z^2} \quad (1)$$

where: $f(z,t)\Delta z$ – the probability of a particle with given density to occur in a layer with thickness Δz at time t or a fraction of particles which at time t are present in layer Δz with coordinate z , p – the probability of a particle group transition from a layer to a layer.

This movement is characterised by a movement of particle grouping centres with specified settling velocities to their equilibrium layers and dispersion of those particles to adjacent layers around grouping centres, dependent on time. Particle dispersion

mechanisms in both cases are similar. They are particle interactions due to collisions. However, sources of these collisions are different. In the first case, the source of collisions is the heterogeneity of the liquid velocity field, while in the second case, the source of collisions are particle deterministic movements to their equilibrium layers with different physical and geometric properties, which the value and sense of the velocity vertical component depend on. After stratification of particles according to the settling velocity, this movement stops and this component of particle dispersion is equal to zero. However, the first component of dispersion, which is always present when there is a pulsating movement of liquid between particles, remains. This is proven by experimental facts referred to in chapter 3 according to which the standard deviation of particles with specified properties around their equilibrium centres decreases with time; however, not to zero, but after long time of separation it achieves a constant value.

The steady (stationary) state of a particle system in a jig's chamber is understood as the state in which grouping centres do not change their position over time. Then potential energy of the system would be minimal if there were no random transitions of particles connected to the heterogeneity of the liquid velocity field. Each of the random processes enumerated above generates the particles' velocity distribution independent of each other. It can be thus assumed that a random variable denoting the particle velocity in the jig's chamber is the sum of two independent random variables:

$$W = W_1 + W_2 \quad (2)$$

where: W_1 – a random variable of the particle velocity conditioned by the heterogeneity of the liquid velocity field, independent of time, W_2 – a random component of the particle velocity conditioned by a movement of particle grouping centres, dependent on time.

Random variables W_1 and W_2 have normal distributions (as a vertical component of the particle velocity distributions, which will be discussed in chapter 5). Therefore, the sum (composition) of two independent random variables with normal distributions will have normal distribution whose variance is equal to (Gerstenkorn and Sroda, 1972):

$$\sigma^2 = \sigma_1^2 + \sigma_2^2 \quad (3)$$

where: σ_1 – the standard deviation of a random variable W_1 distribution, independent on time, σ_2 – the standard deviation of a random variable W_2 distribution dependent on time.

The standard deviation in a general case depends on particles' geometric properties, the average particle density, the partition duration time and hydrodynamic conditions of the partition (Rafales – Lamarka, 1962).

Dispersing interactions and particle velocity distribution variance in stationary state

The force under the effect of which particles obtain additional kinetic energy is the force of interaction between particles. It is equal to the change in momentum of a particle in a unit of time:

$$F_T = \rho V \frac{v_p}{t} \quad (4)$$

where: ρ – particle density, V – particle volume, t – the average time between collisions, v_p – root mean square velocity of a particle conditioned by the heterogeneity of the liquid velocity field.

The average time between collisions is equal to:

$$t = \frac{\lambda}{v_p} \quad (5)$$

where: λ – the average distance covered by a particle between collisions (the average free distance) is equal to (Tichonov, 1968; 1973):

$$\lambda = \frac{1}{nS} \quad (6)$$

where: n – a number of particles in a unit of volume, S – a projective plane of a particle onto the plane perpendicular to the direction of movement.

Since the number of particles in a unit of volume is expressed by a formula:

$$n = \frac{C}{V} = \frac{6C}{k_1 \pi d_p^3}, \quad (7)$$

therefore, the average free distance is equal to:

$$\lambda = \frac{2}{3} \frac{k_1 d_p}{k_2 C} \quad (8)$$

where: C – the particle volume concentration in the jig's bed, k_1 – the volume shape coefficient of particle, k_2 – the dynamic shape coefficient of particle.

Therefore, the average time between collisions after taking expression (8) into account is as follows:

$$t = \frac{2k_1 d_p}{3k_2 C v_p}. \quad (9)$$

After the substitution of expression (9) into formula (4) we obtain:

$$F_T = \frac{\pi}{4} \rho k_2 v_p^2 d_p^2 C = 0.78 \rho k_2 v_f^2 d_p^2 C. \quad (10)$$

This force depends on the particle density. If it is assumed that the root mean square velocity of the particle movement is proportional to the additional, random value of liquid velocity v_f conditioned by the heterogeneity of the velocity field, local turbulences, that is $v_p = bv_f$ (b – proportionality coefficient) and taken into account that $C = 1 - \theta$ (θ – loosening coefficient), then:

$$F_T = 0.78 k_2 \rho b v_f^2 d_p^2 (1 - \theta). \quad (11)$$

It can be seen from formula (11) that the greater degree of loosening, the smaller the force of interactions between particles.

The following product:

$$F_T \cdot \lambda = W_L \quad (12)$$

presents the work of the dispersion force over a distance equal to the particle average free distance. Therefore, the variance σ_1^2 of the particles' velocity distribution in the stationary state is equal to (Smirnova, 1980):

$$\sigma_1^2 = \frac{F_T \lambda}{m} = \frac{0.78 k_2 b \rho v_f^2 d_p^2 (1 - \theta) \lambda}{m} \quad (13)$$

where: $m = k_1 \frac{\pi d_p^3}{6} \rho$ – the mass of a particle.

After the substitution of m into formula (13) we obtain:

$$\sigma_1^2 = \frac{1.5 k_2 b v_f^2 (1 - \theta) \lambda}{k_1 d_p}. \quad (14)$$

Variance conditioned by a movement of particle grouping centres

Experience shows that the standard deviation characterising the distribution of particles with given properties around grouping centres decreases over the partition duration time (Fig. 1). The following expressions (Tichonov, 1968; 1973):

$$p \frac{\Delta z}{\Delta t} = v \quad (15)$$

$$\frac{1}{2} p \frac{(\Delta z)^2}{\Delta t} = \frac{1}{2} v \Delta z = \sigma^2 \quad (16)$$

present the velocity of a grouping centre movement and the standard deviation, respectively. Both the velocity of movement and standard deviation are proportional to the probability of transition. This probability decreases with approaching the equilibrium layer and is expressed by the formula:

$$p = 1 - \frac{i}{n} = 1 - \frac{z_i}{z_{\max}} \quad (17)$$

where: i – layer's number, n – amount of layers, z_i – the distance from the equilibrium layer to the position of i^{th} layer, z_{\max} – the distance from the beginning of the system to the equilibrium layer (Fig. 2).

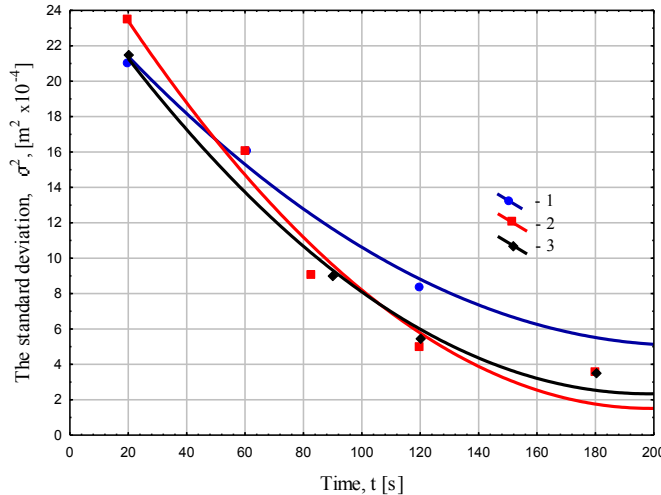


Fig. 1. Dependence of standard deviation on time:
1–3 densities accordingly 1.4–1.5; 1.6–1.7; 1.9–2.0 Mg/m³

Taking formula (17) into account, expressions (15) and (16) take the form of:

$$v = v_{\max} \left(1 - \frac{z}{z_{\max}} \right) = \frac{dz}{dt} \quad (18)$$

$$\sigma^2 = \frac{1}{2} v_{\max} \left(1 - \frac{z}{z_{\max}} \right) z_{\max} \quad (19)$$

where: v_{\max} – the maximum value of the velocity of equilibrium centre movement.

The dependence of variance on time is developed on the basis of stochastic processes is as follows (modified formula 19) (Nawrocki, 1972):

$$\sigma_z^2 = \frac{1}{2} z_{\max}^2 k^2 e^{-kt} = \frac{1}{2} z_{\max}^2 k^2 e^{-\eta} \quad (20)$$

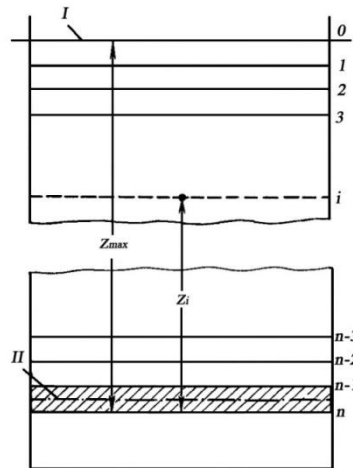


Fig. 2. System of elemental layers in a jig. I – a reference level, II – the equilibrium layer (Nawrocki, 1972)

The constant k occurring in formula (20) presents the correct velocity of a grouping centre (partition rate constant) of particles with given physical and geometric properties to its equilibrium layer. Its value should be proportional to the velocity of particle movement in conditions of constrained movement $v_{s\max}$, because the higher velocity of those particles' movement, the faster the grouping centre moves to its equilibrium layer and it should be inversely proportional to the distance of the equilibrium layer location from the feed level. At the established partition duration time determined by the process efficiency, more distant equilibrium layers will be more blurred and the boundary between centres of particle equilibrium with different properties less sharp.

Taking the above notes into account, it was assumed that the partition rate constant is equal to (Surowiak, 2007):

$$k = \frac{v_{s\max}}{z_{\max}} \quad (21)$$

where: $v_{s\max}$ – the maximum velocity of particle movement under constrained conditions.

The velocity of particle movement in constrained conditions is connected to the free settling velocity v . For Reynolds numbers $Re > 400$ and the degree of loosening θ from range (0.5-1.0), it is the following dependence (Minc, 1953):

$$v_{s\max} = \left[-0.362(1-\theta) + \sqrt{[0.362(1-\theta)]^2 + \theta^3} \right] v. \quad (22)$$

After taking the above connection and dependence presenting the settling velocity of irregular particle $v = 5.33\sqrt{x}\sqrt{d_p}\sqrt{\left(\frac{k_1}{k_2}\right)}$ into account (Brozek and Surowiak, 2010), the partition rate constant is expressed by the formula:

$$k = \frac{5.33\sqrt{xd_p}\frac{k_1}{k_2}}{z_{\max}} \left[-0.362(1-\theta) + \sqrt{[0.362(1-\theta)]^2 + \theta^3} \right] \quad (23)$$

where: $x = \frac{\rho - \rho_o}{\rho_o}$ - reduced particle density, ρ – particle density, ρ_o – medium density.

By replacing η in expression (20) from the following dependence:

$$q = \frac{Q}{bl} = \frac{3600\bar{\rho}h}{t} = \frac{3600\bar{\rho}hk}{\eta} \quad (24)$$

we obtain:

$$\sigma_z^2 = \frac{1}{2}z_{\max}^2k^2 \exp\left[-\frac{3600\bar{\rho}hk}{q}\right] \quad (25)$$

where: q – capacity per unit of jig bed surface, Q – jig capacity, $\bar{\rho}$ – mean particles density, h – height of jig's bed, b – jig bed's width, l – jig bed's length.

The dispersion function

In the non-stationary state of the particle system in the jig's chamber, the movement of random nature, resulting from collisions between particles, overlaps the particle movement conditioned by deterministic forces. Local turbulences created in spaces between particles transfer energy of whirls to particles adjacent to them (Vinogradov, 1965, after Samylin 1976). It is a source of the additional random movement between

particles. A result of this random, additional kinetic energy is the particle movement velocity distribution around the most probable value.

It was assumed that the distribution of the random particle velocity component along the vertical axis (axis z), that is the dispersion function, has the Maxwell distribution of the velocity component (Smirnova, 1980):

$$t(v) = \frac{1}{\sqrt{2\pi}\sigma} \exp\left[-\frac{(v-v_r)^2}{2\sigma^2}\right] \quad (26)$$

where: v_r – the most probable value of the particle velocity, while $\sigma^2 = \sigma_1^2 + \sigma_2^2$.

It is thus a normal distribution. Taking dependences (14) and (24) into account, the standard deviation is equal to:

$$\sigma^2 = \frac{1.5k^2bv_f^2(1-\theta)\lambda}{k_1d_p} + \frac{1}{2}z_{\max}^2k^2 \exp\left[-\frac{3600\rho_{sr}hk}{q}\right]. \quad (27)$$

After a long time of partition (infinitely long in theory), taking formula (20) into account:

$$\lim_{t \rightarrow \infty} \sigma^2 = \sigma_1^2 = \frac{1.5k_2bv_f^2(1-\theta)\lambda}{k_1d_p}. \quad (28)$$

It is the standard deviation in the stationary state. When velocity v_f goes to zero, that is when the value of the dispersing force goes to zero ($v_f \rightarrow 0$), then the standard deviation σ_1 goes to zero. The dispersion function for such a situation, that is the following limit:

$$\lim_{\sigma_1 \rightarrow 0} \frac{1}{\sqrt{2\pi}\sigma_1} \exp\left[-\frac{(v-v_r)^2}{2\sigma_1^2}\right] = \delta(v-v_r) \quad (29)$$

is equal to function δ -Dirac (Byron and Fuller, 1975), that is:

$$\lim_{v_f \rightarrow 0} t(v) = \delta(v-v_r). \quad (30)$$

It means that all particles with settling velocity v_r are in their equilibrium layer.

Partition function (recovery of the i^{th} fraction) and probable error

The partition function (recovery of the i^{th} fraction) specifying the probability of getting a particle with terminal velocity v to tailings (in the case of coal) is presented by the formula:

$$T(v) = \int_{-\infty}^v t(v)dv = \int_{-\infty}^v \exp\left[-\frac{(v-v_r)^2}{2\sigma^2}\right]dv = \varphi\left(\frac{v-v_r}{\sigma}\right) \quad (31)$$

where: φ – the Laplace function, σ – the standard deviation.

The partition function (recovery of the i^{th} fraction) expressed by formula (31) constitutes the distribution function of a normal distribution. In Fig. 3, there are presented forms of the partition curve for three values of velocity v_f in the stationary state.

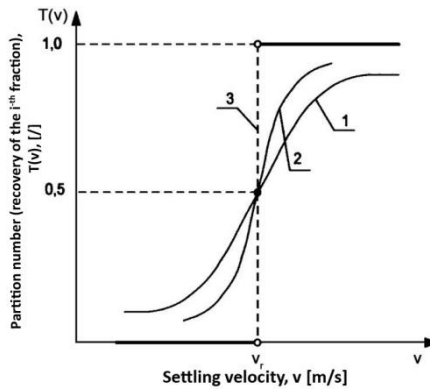


Fig. 3. Partition curve for three velocity values: $v_{1f} > v_{2f}$, $v_{3f} = 0$

The probable error being a measure of the partition accuracy according to the definition is equal to:

$$E_p = \frac{v(T=0.75) - v(T=0.25)}{2} \quad (32)$$

It is the so-called quartile deviation equal to a half of the difference between the third and first quartile and for the normal distribution it is equal to:

$$E_p = 0.67\sigma. \quad (33)$$

Taking (27) into account, the probable error is expressed by the formula:

$$E_p = 0.67 \sqrt{\frac{1.5k_2bv_f^2(1-\theta)\lambda}{k_1d_p} + \frac{1}{2}z_{\max}^2 k^2 \exp\left(-\frac{3600\bar{\rho}hk}{q}\right)}. \quad (34)$$

Based on formulas (28) and (23), the probable error in the general case depends on physical and geometric properties of a particle, the bed height, specific yield, hydrodynamic conditions of partition (through θ). It decreases with the increase in particle size, a degree of bed loosening and the partition rate constant, while it increases with the increase in the bed height. It also depends on the shape of the mixture particles.

For the stationary state:

$$E_p = 0.82v_f \sqrt{\frac{k_2 b(1-\theta)\lambda}{k_1 d_p}}. \quad (35)$$

When velocity v_f increases, then in accordance with formula (21) the standard deviation σ_1 increases. Therefore, with the unlimited increase in velocity v_f is

$$\lim_{v_f \rightarrow \infty} T(v) = \frac{1}{2}. \quad (36)$$

The partition curve has thus a form of a horizontal line, parallel to v-axis. It is equivalent to no partition. Such a situation can occur in the case of partition of fine particles with too high frequency and amplitude of the pulsating movement.

In the stationary state, particle dispersion is connected to the existence of interactions between particles conditioned by the heterogeneity of the liquid velocity field in the jig's bed which is characterised by the value of v_f . At no interactions, that is for the ideal partition, the partition function (recovery of the i^{th} fraction) with consideration of dependence (30) is expressed by the following formula (Byron and Fuller, 1975):

$$T(v) = \int_{-\infty}^v t(v)dv = \int_{-\infty}^v \delta(v - v_r)dv = H(v - v_r) \quad (37)$$

where $H(v - v_r)$ is the Heaviside function. The Heaviside function is specified as follows:

$$H(v - v_r) = \begin{cases} 0 & \text{for } v < v_r \\ 1 & \text{for } v > v_r \end{cases} \quad (38)$$

Considering the fact that according to formula (31) $T(v = v_r) = \frac{1}{2}$ the partition function at the ideal stratification is presented as follows:

$$T(v) = \begin{cases} 0 & \text{for } v < v_r \\ \frac{1}{2} & \text{for } v = v_r \\ 1 & \text{for } v > v_r \end{cases} \quad (39)$$

In Fig. 3, there is a graph of the partition curve described by formula (39) (curve 3). It is thus a curve for the ideal partition. Its equation results directly from the general equation of the dispersion function and partition function through the crossing point corresponding to the condition of the ideal partition. Particles with settling velocity $v = v_r$ with the identical probability equal to 1/2 reach the concentrate and tailing. The probable error is equal to zero.

Empirical verification

Based on data obtained from the industrial experiment which consisted in testing a fines jig upgrading bituminous coal, distributions of geometric (sizes of particles and their shape coefficients) and densimetric properties (density) of the feed particles and the partition products were calculated (Niedoba, 2013; Surowiak, 2007; Surowiak and Brozek, 2014a,b). In order to calculate the partition accuracy, the partition curve coordinates for two variations: when the partition property is the particle density and the particle settling velocity were calculated. For the purposes of this work, one size fraction 8 -10 mm was chosen and partition numbers and the partition accuracy were calculated within this size fraction for both variations.

With functions of the settling velocity distribution density in tailing and the feed in narrow size fraction 8 – 10 mm (Surowiak, 2014), it is possible to calculate partition numbers (recovery of the i^{th} fraction) for tailing and a given value of the settling velocity using the formula (Surowiak, 2007):

$$T(v) = \gamma_o \frac{h_o(v)}{h(v)} \quad (40)$$

where: $T(v)$ – a partition number (recovery of the i^{th} fraction) equal to probability of transferring particles of certain settling velocity v to tailing, γ_o – tailing yield, $h_o(v)$ – the probability density function of the settling velocity in tailing of size fraction 8–10 mm, $h(v)$ – the probability density function of the settling velocity in the feed of size fraction 8–10 mm.

For the empirical partition curve obtained in this way, a model dependence, which is expressed by the normal distribution function, is matched. From the match, a value of the probable error and value of the cut point are obtained. In Fig. 4, the partition curve obtained from the match is presented. Its equation is expressed by the following formula in accordance with dependence (31):

$$T(v) = \varphi \left(\frac{v - 0.159}{0.018} \right). \quad (41)$$

The curvilinear correlation index is greater than 0.99. The value of the cut point is equal to $v_r = 0.159$ m/s, while the probable error on the basis of formula (33) $E_p = 0.012$ m/s. Imperfection in accordance with the definition expressed by the formula is equal to $I = \frac{E_p}{v_r} = 0.076$.

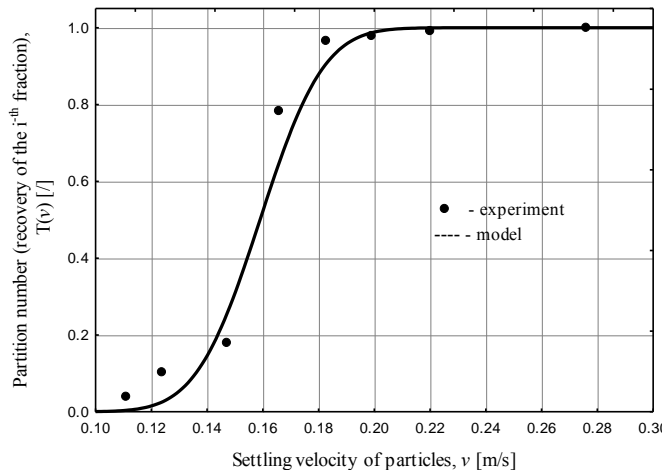


Fig. 4. Partition curve for tailing (8–10 mm size fraction)

In the practice of upgrading and evaluation of partition results in a jig, using partition curves is adopted when the partition feature is the particle density. Density is the partition feature in the case of upgrading of the monodisperse spherical particles sample. Then geometric properties have established identical values for all particles, and the settling velocity distribution depends only on the particle density distribution. Although the particle density distribution in a sample is independent of the geometric properties distribution, the evaluation of the partition accuracy of the device, in which particle stratification according to the settling velocity occurs, on the basis of density is burdened with some error due to the existence of the inherent (pre-existents) probable error, independent of the process course conditions and dependent on the geometric properties distribution.

In Fig. 5, the partition curve based on results of densimetric analyses provided in the work (Brozek and Surowiak, 2006; Surowiak, 2007) for size fraction 8–10 mm is drawn.

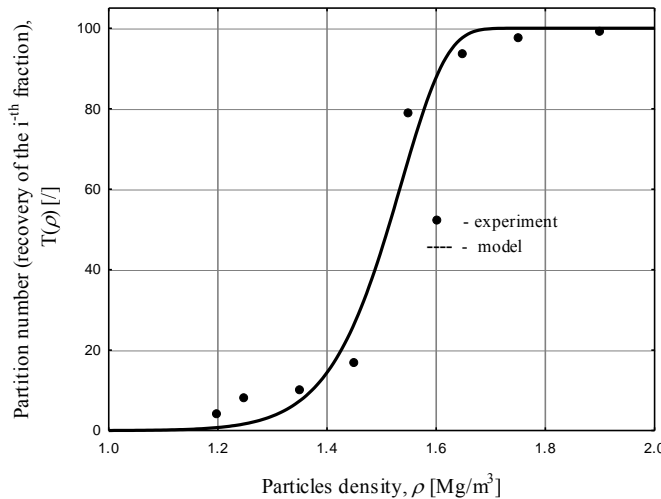


Fig. 5. Partition curve for 8–10 mm particle size fraction

As other authors' (Paul et al., 1998; Gottfried, 1978) studies have shown, partition curves for jigs with density as the partition feature are asymmetric curves and are well approximated by the Weibull distribution. Therefore, the Weibull distribution was matched to the empirical partition curve. Its equation and values of the partition density, probable error and imperfection are as follows:

$$T(\rho) = 100 \left\{ 1 - \exp \left[- \left(\frac{\rho}{1.54} \right)^{19.5} \right] \right\} \quad (42)$$

$$\rho_r = 1.505 \text{ Mg/m}^3, E_p = 0.0605 \text{ Mg/m}^3, I = 0.12.$$

In Fig. 5, the continuous curve presents the model dependence. The curvilinear correlation index is greater than 0.95. The value of imperfection in this case is greater than in a situation when partition results are analysed on the basis of the particle settling velocity. This difference is a result of the fact that the dispersion in the case of the results analysis according to density is the sum of the inherent and process dispersion. However, when partition results are analysed according to the settling velocity, there is only the process dispersion. It can be thus said that the imperfection difference is a cause coming from the inherent dispersion.

Discussion

The state in which material heterogeneous in terms of physical and geometric properties in the jig's bed is ideally stratified due to the settling velocity is the state with the lowest potential energy. It results from Mayer's energy theory. If material

partitioned itself into densimetric fractions and apart from that each fraction into particle size fractions according to the particle pyramid from the biggest to the smallest, then the layer porosity would be the highest and thus the layer height would be greater than before (Kuprin et al., 1983). Therefore, after such partition, potential energy would be greater than before partition. It is contrary to the principle of least action that processes proceed in the direction of minimum potential energy of the system. A decrease in porosity will occur when empty spaces between bigger particles are fulfilled with smaller particles. It will take place in a situation when in the ideally stratified material, as above, smaller particles with greater density move to a higher sublayer of greater particles with lower density or the other way round. There will appear the ideal stratification according to the settling velocity, whose result is the phenomenon of dispersion of particles with given density to other layers. It is the so-called inherent dispersion. It can be thus said that from the physical point of view the inherent dispersion results from the principle of minimising potential energy of the system of particles heterogeneous in terms of physical and geometric properties. It is present always when a mixture of mineral particles heterogeneous in terms of geometric properties is partitioned in a jig or other partitioning devices where the partition argument is the settling velocity. If the feed particles were spherical particles with the same diameters, then at the ideal separation there would be no dispersion of particles to layers inappropriate to them and the value of the inherent dispersion would be equal to zero.

The inherent dispersion constitutes the first mechanism of dispersion of particles with given density to other layers. Another mechanism of dispersion are mutual collisions of particles between each other due to the heterogeneity of the liquid velocity field. It is the so-called process dispersion which is always present regardless of what physical properties is the partition feature (density or settling velocity). If material heterogeneous in terms of physical and geometric properties is partitioned, then the settling velocity is the partition feature. Analysing the partition results on the basis of this feature, the lower value of imperfection is obtained because there is no inherent dispersion in this case. However, in analysing the results of such material partition with the use of the particle density as the partition feature, the greater value of imperfection is obtained because it is the result of the inherent and process dispersion's influence on the partition accuracy.

Acknowledgements

This work was performed as a part of the AGH University of Science and Technology Research Program No.11.11.100.276 project.

References

BROZEK M., SUROWIAK A., 2006. *Efektywność procesu rozdziału w osadzarce*, Górnictwo i Geoinżynieria, 30, (3/1), 29–40.

BROZEK M., SUROWIAK A., 2010. *Argument of separation at upgrading in the jig*. Archives of Mining Sciences, 55, 21–40.

BYRON F.W., FULLER R.W., 1975. *Matematyka w fizyce klasycznej i kwantowej*. PWN, Warszawa.

GERSTENKORN, T., SRODKA T., 1972. *Theory of combinations and probability calculus*, PWN, Warsaw (in Polish).

GOTTFRIED B.S., 1978. *A generalization of distribution data for characterizing the performance of float-sink coal cleaning devices*. Int. J. Mineral Processing, 5, 1-20.

KUPRIN A.I., KLESZNIN A.A., FEDORENKO G.I., 1983. *Vlijanie poroznosti na effektivnost gidravliczeskoj otsadki*, Izv. VUZ Gornyj Žurnal, 4, 129-132 (in Russian).

MINC D.M., 1953. *O skorosti stesnennogo padienia tverdyh czastic w źidkosti*, Gidrotechniczeskoe stroitelstvo, 5, 24-28 (in Russian).

NAWROCKI J., 1972. *Budowa i eksploatacja osadzarek*, Skrypt uczelniany Politechniki Śląskiej nr 408, Gliwice.

NIEDOBA T., 2013. Statistical analysis of the relationship between particle size and particle density of raw coal, *Physicochemical Problems of Mineral Processing*, 49 (1), 175-188.

PAUL A.D., MARONDE C.P., KILLMEYER R.P., 1998. *Evaluation of mathematical functions for representing partition data: a case study*, Proc. XIII ICPC, Brisbane, vol. II, 861-869.

RAFALES-LAMARKA E.E., 1962. *K teorii otsadki*, Izv. VUZ Gornyj Žurnal, 171-177 (in Russian).

SAMYLIN N.A., ZOŁOTKO A.A., POCZINOK V.V., 1976. *Otsadka*, Izd. Nedra, Moskva (in Russian).

SMIRNOVA N.A., 1980, *Methods of statistical thermodynamics in physical chemistry*, PWN, Warsaw, (in Polish).

SUROWIAK A., 2007. *Influence of particles physical and geometrical properties distribution on the separation efficiency of jigging process on the example of coal*. Ph,D Thesis, Main Library of University of Science and Technology, Cracow, Poland (in Polish).

SUROWIAK A., 2014. *Influence of particles density distributions of their settling velocity for narrow size fractions*. Mineral Resources Management, 30, 1, 105-122 (in Polish).

SUROWIAK A., BROZEK M., 2014a, *Methodology of calculation the terminal settling velocity distribution of spherical for high values of the Reynold's number*. Archives of Mining Sciences, 59, 1, 269-282.

SUROWIAK, A., BROZEK, M., 2014b, *Methodology of calculation the terminal settling velocity distribution of spherical for high values of the Reynold's number*. Archives of Mining Sciences, 59, 2, 553-562.

TICHONOV O.N., 1968. *Gravitacionnoje razdelenie mnogokomponentnyh mineralnyh smesej*, Obogashcheniye Rud, 1, 47-49 (in Russian).

TICHONOV O.N., 1973. *Vvedenie w dinamiku massoperenososa processov obogatitelnoj technologii*, Izd. Nedra, Leningrad (in Russian).

VINOGRADOV N.N., 1965. *Izuczenije mechanizma rasslojenijazieren w procesie otsadki*, Obogaszczanie uglej grawitacjonnymi metodami, Nauka (in Russian).

WILLS B.A., NAPIER-MUNN T.J., 2006. *Will's Mineral Processing Technology an introduction to the practical aspects of ore treatment and mineral recovery*, Elsevier, seventh edition, 227-229.

Received May 3, 2015; reviewed; accepted: June 29, 2015

PREG-ROBBING OF GOLD IN CHLORIDE-BROMIDE SOLUTION

Riina AHTIAINEN*, Mari LUNDSTROM**

* Outotec (Finland) Oy, riina.ahtainen@outotec.com

** Aalto University, School of Chemical Technology, Department of Materials Science and Engineering, mari.lundstrom@aalto.fi

Abstract: One of the major issue in gold chloride leaching is a tendency of gold to either precipitate or adsorb on a carbonaceous matter in an ore, i.e. preg-robbing. This paper discusses issues related to a preg-robbing phenomenon in gold hydrometallurgy, specifically in gold chloride-bromide leaching. This phenomenon has been observed in the 1800s to decrease gold recovery during gold chlorination as well as the state-of-art of gold cyanidation processes. The experiments were conducted in order to study the preg-robbing phenomenon in chloride-bromide media. The tendency of preg-robbing was demonstrated by adding carbon in a non-preg-robbing ore. It was shown that the preg-robbing tendency in the chloride-bromide media was very strong. Addition of 0.01% w/w of carbon powder into the non-preg-robbing ore decreased gold recovery from 92 to 70% and addition 5% w/w of carbon decreased gold recovery to almost zero.

Keywords: gold, leaching, pre-robbing, hydrometallurgy, carbon

Introduction

In the mid to late 1800s, there were several gold leaching processes using chlorine as an oxidizing agent. The process was typically carried out in either vats or revolving barrels and chlorine produced in either a vessel or in-situ. With time, cyanide processes took over and became an industrial standard for hydrometallurgical gold production (Marsden and House, 2006). Today, mineral resources are becoming lower in grade. At the same time, environmental regulations may change to favour non-cyanide processes.

Several cyanide-free gold chloride or gold halide leaching processes have been patented and/or tested on a demonstration plant scale, such as Intec (Moyes, 2002), HydroCopper® (Haavanlammi et al., 2007), Nippon N-Chlo/NIKKO (Ishiguro et al., 2008), Nichromet (Dundee) (Lemieux et al., 2013) and Outotec Gold Chloride

(Miettinen et al., 2013; 2014). Characteristically, these processes are operated at a concentrated chloride solution, at a redox potential around 600 mV vs. Ag/AgCl, often needing bromine addition in order to increase oxidative power and/or to keep gold chloride complex more stable in a solution.

The main challenge with using chloride as a lixiviant is related to preg-robbing, i.e. unwanted gold precipitation back to an ore during ore leaching. Almost all lixiviants are known to suffer from this phenomenon. Preg-robbing has been known for decades also in the chloride media (Rose, 1896). In the historical chlorination process, wooden barrels and seashell filter beds in contact with gold-containing solution were impregnated with some gold. It showed that gold chloride complexes were eager to precipitate on an organic carbon containing material (Aylmore, 2005).

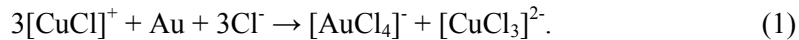
It is clear that due to environmental, health and safety issues related to use of cyanide, there is intensive research into a gold chloride leaching technology. Nowadays, there are only a few papers in the field of preg-robbing in either chloride or chloride-bromide solutions. This paper investigates the preg-robbing intensity in chloride-bromide media.

Gold chloride leaching and preg-robbing

Elemental gold is the only stable form of gold within the stability limits of water. However, in concentrated chloride (and other halide) solutions, significant dissolution as aurous and auric complexes can be achieved (Marsden and House, 2006).

It is clear that platinum group metal processes operating at potentials higher than 1.0 V easily and effectively oxidize gold. However, concentrated chloride solutions (having lower redox potentials) can also be used to leach gold. If gold dissolution is carried out in chloride solutions at ambient pressure, high reagent concentrations and temperatures are needed. The lack of a strong oxidant, such as Cl₂ used in either the historical chlorination process (Rose, 1896) or Cl₂/H₂O₂ used in platinum group metal leaching (Crundwell et al., 2011) or high pressure (Ferron et al., 2003), needs to be compensated by a high redox couple such as cupric/cuprous with a reasonable amount of complexing agent.

Gold leaching in a cupric chloride solution can proceed according to reaction:



It is also possible that gold dissolution to a trivalent chloride complex occurs via a monovalent gold complex. The stability of gold complexes varies. Gold in chloride media exists both in the monovalent state $[\text{AuCl}_2]^-$ as well as in a trivalent state $[\text{AuCl}_4]^-$ and the states are not very stable, having stability constants of 10^9 and 10^{26} , respectively. Gold bromide and cyanide complexes have a much higher stability constant, the corresponding values are 10^{12} and 10^{32} for bromide and $2 \cdot 10^{38}$ and $\sim 10^{56}$ for cyanide (Leppinen et al., 2010).

Preg-robbing is most often associated with the carbonaceous matter, such as hydrocarbons, organic acids and natural carbon. The latter are the most important species for preg-robbing. The mineralogy associated with carbonaceous gold ores can be quite variable and carbonaceous material occurs in many deposits around the world (Adams and Burger, 1998). However, the presence of carbonaceous matter does not necessarily result in poor gold recovery, but it seems to be that native carbon has similar behavior with activated carbon (Mohammadnejad et al., 2012). Amorphous carbon (free reactive carbon without crystalline structure) has been identified as the main carbon form causing preg-robbing. In contrast, a shale ore with graphitic material has been suggested to have a lower degree of preg-robbing activity (Mohammadnejad et al., 2012). In addition, hydrocarbons have been found to have only a minor effect on preg-robbing (Sibrell et al., 1990).

It is clear that in an oxidative environment, the preg-robbing effect of carbonaceous matter is substantially stronger than preg-robbing in the presence of other minerals. Silica in the form of quartz, feldspar, kaolinite and pyrophyllite as well as mechanically activated silica has been found to reduce gold chloride complexes (Mohammadnejad et al., 2012). It has been reported that the effect of mica (phyllosilicate) on preg-robbing was negligible compared to the carbonaceous matter (Adams and Burger, 1998), and it is likely that no silica-based material has as high preg-robbing intensity as carbonaceous materials. Also, other minerals can cause preg-robbing, specifically at low redox potentials (Mohammadnejad et al., 2012). In oxygen-free solutions, sulfides, such as chalcopyrite, pyrrhotite and pyrite in large amounts can cause preg-robbing, i.e. precipitation. The gold chloride complex also adsorbs on mineral surfaces such as goethite and alumina (Goodall et al., 2005).

Materials and methods

The chemical composition of non-preg-robbing gold ore used in leaching tests is presented in Table 1. The raw material was quartz-rich and sulfide-poor free-milling gold ore, having a total carbon concentration of 0.11%.

Leaching experiments were carried out both in cyanide and in chloride-bromide (halide) media at Outotec Research Center, Pori, Finland. A cyanide leaching test (Test 0) was carried out on a gold ore (Table 1) to determine a preg-robbing tendency of gold ore under investigation. The cyanide concentration used was 3 g/dm³ NaCN and pH was 10.5–11.0. The temperature was not adjusted but kept at room temperature (22 °C). The cyanide leaching experiment was conducted in a 2 dm³ glass reactor with air oxidation. Agitator used was of a four-blade impeller at a 45 degree angle. The chloride concentration used was 150 g/dm³, sodium bromide concentration 8 g/dm³ and oxygen was fed under mixer blades at a velocity of 2 dm³/min. Copper ([Cu²⁺] = 15 g/ dm³) was added into the solution to increase the oxidation potential of solution. During ten hours of leaching, the temperature was kept at 98 °C and acid concentration (HCl) at 10 g/dm³.

Table 1. Chemical composition of non-preg-robbing gold ore

Element	Raw material
Au, g/Mg	4.8
Ag, g/Mg	1.6
Al, %	11.8
C _{total} , %	0.11
Ca, %	0.63
Cu, %	0.05
Fe, %	1.6
Na, %	0.34
S, %	0.26
SiO ₂ , %	75.3

A chloride-bromide leaching test was done on the gold ore without any additives in order to demonstrate gold dissolution from the non-preg-robbing ore (Test 1). The preg-robbing phenomenon was simulated by carbon addition as finely powdered activated carbon to the gold ore with carbon addition of 0 (Test 1), 0.01 (Test 2), 0.1 (Test 3), 1 (Test 4), 5 (Test 5), and 10% w/w (Test 6).

All the gold chloride-bromide leaching experiments were conducted in a 5 dm³ titanium reactor with baffles and a reflux condenser. The agitator used was of GLS-type. Temperature was adjusted automatically and verified using a thermometer. The acid concentration was measured from the solution with automatic volumetric apparatus.

The metals content in solids was determined using an Inductive Coupled Plasma Optical Emission Spectrometry (Thermo Scientific iCAP 6000), after total dissolution. Total carbon and sulfur concentrations were determined by a combustion method. The gold content in raw materials and leach residues were determined by a fire assay analysis. Soluble gold was analyzed by Graphite Furnace Atomic Absorption Spectrometry (Varian Spectra).

Results

A cyanide leaching test (Test 0) was carried out on the gold ore to determine the preg-robbing tendency of the raw material under investigation. Figure 1 shows that the raw material used was not preg-robbing. The gold concentration in the solution during cyanide leaching (Test 0) increased as a function of time up to 24 hours. This kinetic behavior is typical for non-preg-robbing materials.

Chloride-bromide leaching (Test 1) without additional of carbon showed similar leaching behavior to cyanide leaching (Test 0). The gold concentration in solution increased over time. However, the gold leaching kinetics in chloride-bromide media was faster than in cyanide media.

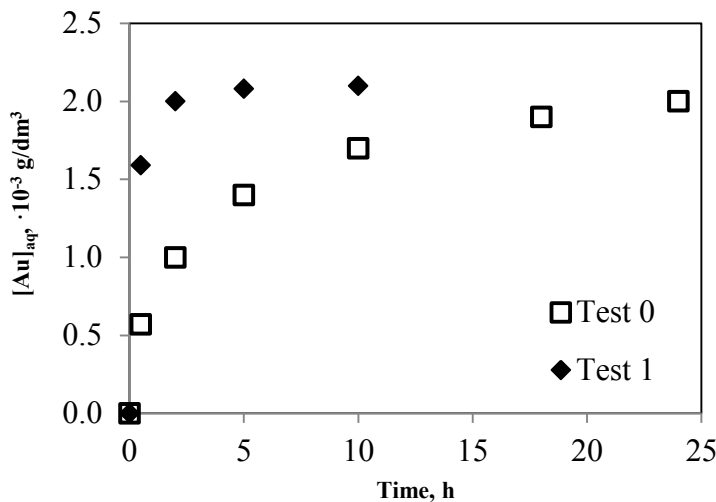


Fig. 1. Gold concentration in solution as a function of time during cyanide leaching (Test 0) and halide leaching without carbon addition (Test 1)

In leaching Tests 1-6 it was observed that the carbon content in the gold ore had a strong effect on the gold stability in the chloride-bromide solution. Figure 2 shows that the soluble gold concentration was of the same magnitude with 0 and 0.01% w/w carbon addition in the ore (Test 1 vs. Test 2). Gold from the ore could be leached and the soluble gold concentration increased as a function of time. The preg-robbing phenomenon could be seen more clearly with carbon additions of 0.1 and 1% w/w (Tests 3 and 4) as the soluble gold concentration was less than half compared to Tests 1 and 2. In addition, the soluble gold concentration decreased with time indicating some progress in preg-robbing as a function of time. This behavior is typical for preg-robbing raw materials. With carbon concentrations of 5–10% no soluble gold could be analyzed, which indicates extremely strong preg-robbing intensity.

Based on the solution analysis, carbon containing raw materials can be divided into three groups: low (with 0 and 0.01% w/w carbon), moderate (with 0.1 and 1% w/w carbon), and very high preg-robbing (with 5 and 10% w/w carbon).

It was shown that the raw material used was not originally preg-robbed (Fig. 1). Figure 3 presents gold extraction based on the solids analysis with increasing added carbon concentration in the raw material after the leaching test. In the absence of carbon, the gold extraction from originally non-preg-robbing material was 92% (Test 1). However, addition of 0.01% w/w carbon (Test 2) decreased the final gold extraction from 92% to 70%. With 0.1 (Test 3) and 1% (Test 4) carbon addition, the gold recovery was in the range of 20 to 30% and decreased to almost zero at carbon concentrations of 5-10% w/w (Tests 5-6).

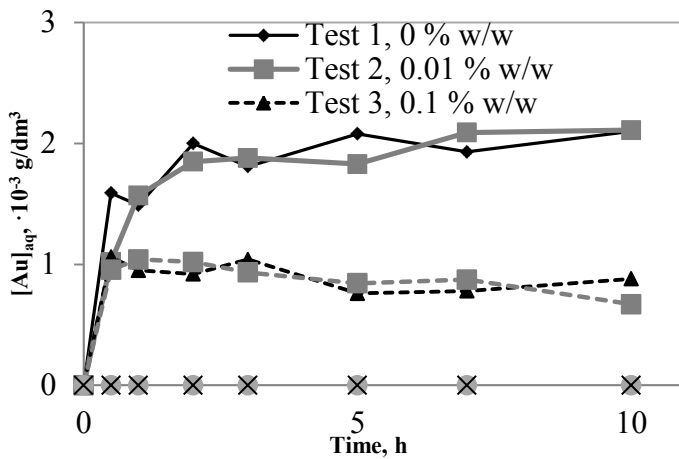


Fig. 2. Gold concentration in solution as a function of time during halide leaching.
Additional organic carbon concentrations in non-preg-robbing ore were
from 0, 0.01, 0.1, 1, 5 and 10% w/w in Tests 1, 2, 3, 4, 5 and 6, respectively

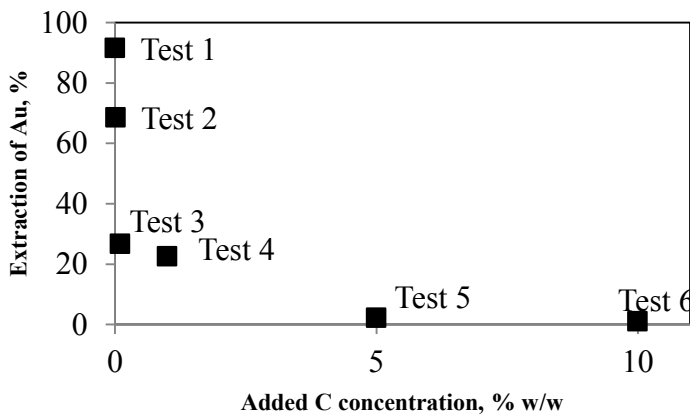


Fig. 3. Final gold extraction as a function of carbon concentration added to the ore
(added carbon 0, 0.01, 0.1, 1, 5 and 10% w/w in Tests 1, 2, 3, 4, 5, and 6, respectively).
Extraction based on solid analysis

Conclusions

Preg-robbing is mainly related to the organic carbon content in the natural ore. In addition, some minerals and clays may cause gold losses due to this phenomenon. It was experimentally shown that the raw material investigated was a non-preg-robbing material, as the gold concentration increased as a function of time in cyanide leaching up to 24 hours. The same behavior was observed in chloride-bromide media without carbon additional. The gold content in solution increasing up to 5 hours. Gold leaching

kinetics was shown to be faster in chloride-bromide media compared to cyanide media.

The preg-robbing intensity in chloride-bromide media was investigated by adding a carbon powder to the raw material, which was originally shown to be non-preg-robbing. The carbon concentration had a major effect on gold recovery. The addition of 0.01% w/w carbon decreased gold recovery from 92 to 70%, while addition of 5% carbon decreased gold recovery to close to zero.

Based on the preg-robbing demonstration test work, the carbon-containing raw materials can be divided into three groups: low (with 0 and 0.01% w/w carbon), moderate (with 0.1 and 1% w/w carbon), and very high preg-robbing (with 5 and 10% w/w carbon). The same classification can be valid for naturally preg-robbing components in ores assuming that the preg-robbing activity of ore is close to that of activated carbon.

References

ADAMS, M.D., BURGER, A.M., 1998, *Characterization and Blinding of Carbonaceous Preg-robbbers in Gold Ores*, Minerals Engineering, 11, 919-927.

AYLMORE, M.G., 2005, *Chapter 21: Alternative Lixiviants to Cyanide for Leaching Gold Ores*, in *Advances in Gold Ore Processing*, 1st ed., Adams, M.D., Elsevier, B.V., Amsterdam, Netherland, 501-539.

CRUNDWELL, F., MOATS, M., RAMACHANDRAN, v., ROBINSON, T., DAVENPORT, W.G., 2011, *Extractive Metallurgy of Nickel, Cobalt, and Platinum Group Metals*, Elsevier, Oxford.

FERRON, C.J., FLEMING, C.A., DREISINGER, D., O'KANE, T., 2003, *Chloride as an Alternative to Cyanide for the Extraction of Gold – Going Full Circle?*, TSM, Hydrometallurgy – 5th International Conference in Honor of Professor Ian Ritchie, Vol 1, eds. Young, C.A, Alfantazi, A.M., Anderson, C.G., Dreisinger, D.B., Harris, B. & James, A.

GOODALL, W.R., LEATHAM, J.D., SCALES, P.J., 2005, *New Method for Determination of Preg-robbing in Gold Ores*, Minerals Engineering, 18, 1135-1141.

HAAVANLAMMI, L., HYVÄRINEN, O., TIIHONEN, M., TONTTI, R., 2007, *Method for Recovering Gold*, Worldwide Patent 093666 A1.

ISHIGURO, Y., HOSAKA, H., YOSHIMURA, A., TAKABAYASHI, K., ABE, Y., 2008, *Process of Leaching Gold*, AU Patent 202814 B8.

LEMIEUX, D., DUBREUIL, B., LALANCETTE, J.-M., 2013, *Nichromet Cyanide-Free Process for Gold Extraction*, Presentation in World Mining Congress, Canada.

LEPPINEN, J., HYVÄRINEN, O., HEIMALA, S., PALOSAARI, V., HÄMÄLÄINEN, M., 2010, *Method for Recovering of Gold from Sulphide Concentrate*, US Patent 7785395 B2.

MARSDEN, J.O., HOUSE, C.I., 2006, *The Chemistry of Gold Extraction*, Littleton, Colorado, USA:SME.

MIETTINEN, V., HAAPALAINEN, M., AHTIAINEN, R., KARONEN, J., 2013, *Development of Gold Chloride Process*, in Proceeding ALTA 2013, pp. 187-203.

MIETTINEN, V., AHTIAINEN, R., VALKAMA, K., PAATERO, E., HIETALA, K., HAAPALAINEN, M., 2014, *Method of Preparing a Gold-Containing Solution and Process Arrangement for Recovering Gold and Silver*, Worldwide Patent 177765.

MOHAMMADNEJAD, S., PROVIS, J.L., VAN DEVENTER, J.S.J., 2012, *Reduction of Gold(III) Chloride to Gold(0) on Silicate Surfaces*, Journal of Colloid and Interface Science, 389, 252-259.

MOYES, A.J., 2002, The *Intec Copper Process, Superior and Sustainable Copper Production*, s.l.: Intec Copper, Australia.

ROSE, T.K., 1896, *The Metallurgy of Gold*, 2nd ed., British Library, Historical Print editions.

SIBRELL, P.L., WAN, R.W., MILLER, J.D., 1990, *Spectroscopic Analysis of Passivation for Carbonaceous Matter from Carlin Trend Ores*, in Proceeding World Gold '90, 335-363.

Received January 20, 2015; reviewed; accepted April 24, 2015

APPLICATION OF D-OPTIMAL DESIGN FOR OPTIMIZING COPPER-MOLYBDENUM SULPHIDES FLOTATION

Fardis NAKHAEI^{*}, Mehdi IRANNAJAD^{*}, Abbas SAM^{}, Ali JAMALZADEH^{**}**

^{*} Department of Mining & Metallurgical Engineering, Amirkabir University of Technology, Tehran, Iran, Iranajad@aut.ac.ir

^{**} Department of Mineral Processing, Engineering Faculty, Shahid Bahonar University, Kerman, Iran

Abstract: Froth flotation is widely used for concentration of base metal sulphide minerals in complex ores. One of the major challenges faced by flotation of these ores is selection of the type of flotation reagents. In this study, the D-optimal experimental design method was applied to determine the optimum conditions for flotation of copper and molybdenum in the rougher flotation circuit of the Sungun copper concentrator plant. The investigated parameters included types and dosages of collectors and frothers, diesel dosage and feed size distribution. The main effects on copper and molybdenum recoveries and grades were evaluated. Results of optimization showed that the highest possible grade and recovery were obtained for Z₁₁ as a primary collector (20 g/Mg), R407 as a first promoter collector (20 g/Mg), X231 as a second promoter collector (7 g/Mg), A65 (15 g/Mg) and Pine oil as frothers (5 g/Mg), 20 g/Mg of diesel dosage, and d_{80} of feed size was equal to 80 μ m. The analysis of variance showed that the primary promoter collector was the most significant parameter affecting the recovery of Cu, while diesel dosage and d_{80} were the most significant parameters influencing the Mo recovery.

Keywords: copper, molybdenum, flotation, chemical reagents, D-optimal, optimization

Introduction

Although it seems that porphyry copper deposits are relatively simple, the geology of porphyry copper ores is almost complex and varies significantly within the ore body. Many copper sulphide ore deposits occur with molybdenum, mainly related to pyrite and silicate gangue minerals. Flotation is one of the most complex mineral processing operation, which is mainly applied to recover both copper and molybdenum sulphides, and it is affected by a very large number of variables (Pradyumna et al., 2005).

The efficiency of flotation process is highly dependent on reagent type and dosage as well as the feed size distribution, which directly influence the product grade and

recovery. Control of reagent additions is the most important aspect of the flotation strategy in commercial plants (Bulatovic, 2007). Selection of reagent and flowsheet used in actual plant practice is usually dictated by the nature and mineralogy of the ore, type of minerals present, flotation behaviour of gangue minerals, amount and occurrence of pyrite as well as the presence of clay minerals in the ore. Reagent used for treatment of porphyry copper and molybdenum ores usually involve lime as a modifier, xanthate as the primary and secondary collectors, which include dithiophosphates, mercaptans, thionocarbamates and xanthogen formats, and frothers, such as methyl isobutyl carbonyl, TEB (alkoxy paraffin and pine oil), Dow Froth 250, Dow Froth 1012 (glycols), HP700 and HP600 (alcohols in amine oxide) (Bulatovic, 2007).

The choice of secondary collector relies on a relatively large number of factors that are (a) type of copper minerals (i.e. single copper mineral or varieties), (b) composition of gangue minerals, (c) presence and type of clay minerals as well as (d) type of frother used. There is a wide variation in selection of the type of frother, and in many operating plants mixtures of either two or more frothers are used. The importance of frothers is enormous. It helps to stabilise bubble formation in the pulp phase, creating a stable froth to allow selective drainage from the froth of entrained gangue to increase flotation kinetics (Wills, 2007). Several studies have been carried out on various reagents in recovery of minerals by flotation (Malysa et al., 1981; Guy and Jia, 2000; Laskowski et al., 2003; Harvey et al., 2005; Melo, and Laskowski, 2006; Xia and Peng, 2007). The studies clearly show the importance of chemical factors that are type of collector, frother, and pH on flotation performance. Moreover, some parameters such as aeration, hold-up and froth height can also affect the flotation performance.

The experimental design method has been illustrated to be an effective for the improvement of quality and productivity in research and development (Ilyas, 2010). It is a well-accepted technique that has been widely used for product design and process optimization in worldwide manufacturing and engineering (Kamaruddin et. al., 2004; Gopalsamy et. al., 2009; Rama and Padmanabhan, 2012; Sapakal and Telsang, 2012). Recently, the use of experimental design method has extended to include the mineral processing industry (Abali et al., 2006; Haghie et.al. 2009; Ilyas et. al., 2010; Vazifeh et al., 2010). It provides a simplified systematic and efficient methodology for process optimization. There are several advantages of statistical design of experiments over classical one variable at a time method, where one variable is varied at time. The greatest advantage of this method is saving effort in conducting experiments, saving experimental time, reducing costs and discovering significant factors quickly (Trust and Nehta, 2014). The number of experiments that need to be done is greatly reduced, compared to those required by other traditional statistical methods. One of these statistical techniques is the factorial design test, which is employed to study several factors and determine their main effects and interactions.

The main goal of the present work is to use statistical techniques to optimize the types and dosages of flotation reagents and feed size distribution in the rougher circuit of the Sungun Copper Concentrator Plant to achieve the maximum Cu and Mo grades and recoveries. By using this procedure, the main effects of these reagents on flotation performance will be determined. Different steps of optimization strategy used in this study are:

- a) designing experimental tests and performing them on laboratory scale (using D-optimal factorial design),
- b) performing an analysis of the experimental results by ANOVA to determine the significant factors influencing the flotation process,
- c) finding out optimum conditions for flotation to maximize the grade and recovery.

Experimental

Sungun copper concentrator plant

The Sungun copper ore body is located in the eastern Azerbaijan province, northwest of Iran. The total minable ore based on mine design and production scheduling is 400 Tg (400 million tons) with an average Cu grade of 0.62% (Vazifeh et al., 2010). Figure 1 shows the flotation circuit of the Sungun concentrator plant. The process consists of grinding circuit with their associated flotation circuits. The grinding circuit products with d_{80} about 90 μm are transferred to the rougher conditioner tank and then enter 12 rougher flotation tank cells, which are grouped into 6 banks of 2 cells each. Lime, collectors of Z₁₁ (isopropyl xanthate sodium) and R407 (a mixture of mercapto benzothiazole and dithiophosphate) are added to the ball mill feed. The pH level of the feed with respect to rougher is measured in this conditioner tank and then lime slurry is added. The AF65 (hydrogen-terminated polypropylene glycol) and AF70 frothers are added to the conditioner tank. Further reagents (collectors) are added to the flotation cells of 3, 5 and 9. The collector distribution pattern is 32% for ball mill feed, 32% for the third rougher flotation cell, 20% for the fifth rougher flotation cell and 16% for the ninth rougher flotation cell (Vazifeh et al., 2010).

The final plant tailing consists of the last rougher flotation bank tailing and scavenger one. The rougher and scavenger concentrates are pumped to hydrocyclone clusters. Hydrocyclone underflow, after lime addition, reports to the regrind ball mill. The hydrocyclone overflow (d_{80} about 40 μm) is transferred to two cleaner column cells. The cleaner column concentrate is transferred to the re-cleaning column cell to produce the final concentrate with a 30% (nominal) copper grade and 84% recovery.

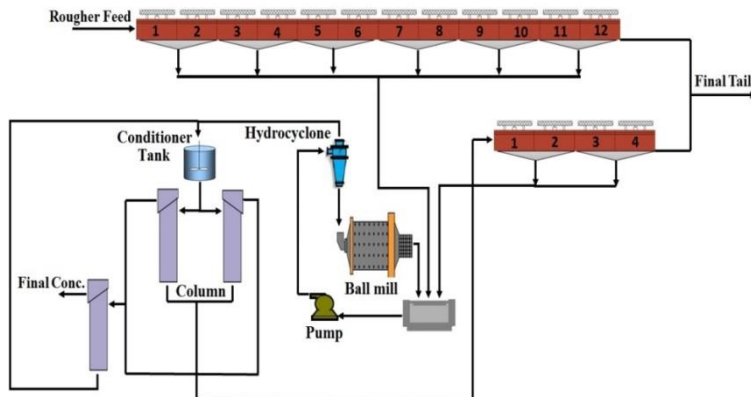


Fig. 1. The flow sheet of flotation circuit of the Sungun industrial plant

Materials

The cooper ore sample used in this study was taken from the SAG mill feed. The minerals of ores were defined by means of microscopy (Table 1). Chalcocite, chalcopyrite, covellite and pyrite were the primary sulfide minerals.

Table 1. Sulfide minerals composition (wt. %) of copper ore

Component	Cu ₂ S	CuS	CuFeS ₂	FeS ₂	MoS ₂	ZnS
%	0.262	0.341	0.426	6.55	0.023	0.424

The ore sample was ground using jaw and roll crushers as well as ball mill so that 80% of the sample reached less than 120, 100 and 80 μm for the flotation tests. The chemical analysis of sample is shown in Table 2.

Table 2. Main chemical analysis results of ore sample

Component	Cu	CuO	Fe	Mo (%)
%	0.74	0.07	3.35	0.013

Flotation reagents used in this work were: collectors: Z₁₁ (sodium isopropyl xanthate), Z₆ (potassium amyl xanthate), R407 (a mixture of mercaptobenzothiazole and dithiophosphate), Nascol (a mixture of mercaptobenzothiazole and di-n-butyl sodium dithiophosphate), Flomin 7240 (mixture of mercaptobenzothiazole and butyl sodium dithiophosphate), Flomin C4132 (isopropyl-n-ethyl thionocarbamate), X231 (thionocarbamate) and diesel (non-thiol collector); frothers: AF65 (hydrogen-terminated polypropylene glycol), DF 250 (methyl-terminated polypropylene glycols), Flomin 742 (polypropylene glycol), AF70, MIBC (methyl isobutyl carbonyl) and pine oil.

Flotation procedure

The flotation tests were performed according to the D-optimal factorial design of experiments. The considered variables in this study are: type of collectors (A, B and C), type of frothers (D and E), collector and frother dosages (H, J, K, L and M), dosage of diesel (F) and flotation feed size (G). The levels of variables are given in Table 3. The main advantage of employing D-optimal design is reduction in the number of experimental runs, which are required to evaluate multiple variables. Moreover, it has the ability to identify interactions statistically. It is able to overcome the shortcomings of the traditional formulation method (Muteki et al., 2007).

Table 3. Experimental parameters and their relative levels

Collector			Frother			Diesel	d_{80}	Reagent Dosage				
A	B	C	D	E	F	g/Mg	%	g/Mg				
Z ₁₁	R407	0	A65	A70	0	80	10	15	0	5	5	
Z ₆	Nascol	C4132	DF 250	MIBC	10	100	15	20	7	10	10	
	A7240	X231	Flomin 742	Pine Oil	20	120	20	25	15	15	15	

Since the objective of this study was to select the type and dosage of collector and frother, the region of their dosages used in 150 operating days in the plant were considered in the experimental design in all tests. Table 4 shows dosages of collectors and frothers employed in all tests.

Table 4. Ranges of collector and frother dosages used in all tests

Primary (A)	Collector (g/Mg)		Frother (g/Mg)	
	First promoter (B)	Second promoter (C)	D	E
10-20	15-25	0-15	5-15	5-15

Laboratory flotation tests were conducted in a Denver mechanical cell using 35% solids conditioned for 3 min. The pH value was then adjusted to 11.8 using lime before adding the reagent. The slurry was further conditioned after addition of each reagent, i.e. 2.5 min for the collector and 1 min for the frother. The agitation speed of 1300 rpm and flotation time of 16 min (which was scaled down from the Sungun plant rougher flotation time of 33 min) were used for all the experiments. The froth and tailing were collected, filtered, dried and analysed for copper grade and recovery calculations. Tap water was employed throughout the experiments.

The collector distribution patterns of 32, 32, 20, 16% as the current distribution in the plant, corresponding to the ball mill feed, third rougher flotation cell, fifth rougher flotation cell and ninth rougher flotation cell respectively were examined in the laboratory tests (Vazifeh et al., 2010). The froth collecting time of 16 min was divided

into 160 s for simulating the first and second rougher flotation cells, 160 s for simulating the third and fourth rougher flotation cells, 320 s for simulating the fifth to eighth rougher flotation cells and 320 s for simulating the ninth to twelfth flotation cells.

Analysis of variance

An analysis of variance (ANOVA) is a standard statistical tool that can be used to interpret experimental data. The DX7 software is used to analyse the experimental data. The analysis of variance is performed to evaluate the significance of the main effects among the investigated factors. The effect is considered to be significant if its significance level is greater than 95%, what means that the model with a P-value lower than 0.05 could be considered. To evaluate the fitness of model, a regression-based determination coefficient R^2 should be determined (Haider and Pakshirajan, 2007; Liu and Wang, 2007). When the values of R^2 are close to 1, the model offers an appropriate explanation of the variability of experimental values to the predicted values (Sayyad et al., 2007). The residuals, as differences between observed and predicted responses, are examined using the normal probability plots of the residuals. If the model is adequate, the points on the normal probability plots of the residuals should form a straight line.

Results and discussions

D-optimal factorial design

The D-optimal factorial is designed for using categorical factors as an alternative to the general factorial design method. The general factorial design builder may produce designs with more runs than are willing to run. The D-optimal design will choose an ideal subset of all possible combinations based on the specified model. The statistical design of experiments is used when the effects of several factors are to be studied in order to determine the main effects. When the effect of a factor depends on the level of another factor, two factors are said to interact. In this study, to design the experiments, the D-optimal factorial design was employed. In this paper, the main effects were taken into consideration. As illustrated in Table 5, 29 tests using D-optimal method were designed. From Table 5, it can be seen that the highest recovery of Cu of 92.03% with grade of 3.25% in the concentrate occurred in the 11th experiment run (primary collector = Z6, first promoter collector = R407, frothers = A65 and A70, diesel dosage = 0 and $d_{80} = 120 \mu\text{m}$) and the lowest recovery of copper (80.22%) with grade of 3.84% was recorded in the 5th experiment run. For Mo the maximum recovery was 77.06% with grade of 0.057% achieved in the 22rd experimental run (primary collector = Z11, first promoter collector = Nascol, second promoter collector = C4132, frothers = Flomin 742 and pine oil, diesel dosage = 20 g/Mg and $d_{80} = 80 \mu\text{m}$).

Table 5. Factorial design with results of Cu and Mo recoveries and grades in flotation tests

Run	Collector			Frother		Diesel dosage	d_{80}	Reagent Dosage				Recovery		Grade		
	A	B	C	D	E			F	G	H	J	K	L	M	Cu	Mo
						g/Mg	μm	g/Mg				%	%	%	%	%
1	z11	A7240	X231	D250	Pine Oil	10	120	15	25	7	15	10	82.27	60.97	5.89	0.053
2	z11	R407	Without	A65	A70	0	100	15	15	0	5	5	86.15	53.7	3.98	0.044
3	z6	A7240	X231	A65	A70	0	80	15	15	7	10	10	85.69	58.9	3.86	0.050
4	z6	A7240	X231	D250	MIBC	10	80	10	25	15	15	15	85.07	68.78	4.11	0.048
5	z11	A7240	X231	Flomin 742	A70	10	120	10	25	7	5	15	80.22	60.42	3.84	0.048
6	z11	Nascol	Without	A65	A70	20	100	20	15	0	10	10	87.09	58.77	4.64	0.045
7	z11	R407	Without	Flomin 742	MIBC	10	80	20	15	0	10	5	86.09	67.73	4.65	0.048
8	z6	A7240	C4132	D250	Pine Oil	20	80	10	20	7	15	10	85.15	75.03	4.31	0.052
9	z6	R407	X231	Flomin 742	MIBC	0	80	20	15	15	5	5	89.93	61.63	2.79	0.045
10	z11	R407	Without	A65	Pine Oil	20	80	15	20	7	15	5	88.99	69.77	5.14	0.046
11	z6	R407	Without	A65	A70	0	120	20	20	0	10	15	92.03	47.1	3.25	0.040
12	z6	Nascol	X231	A65	MIBC	20	120	20	20	15	5	10	89.41	58.12	3.52	0.044
13	z6	R407	C4132	Flomin 742	A70	10	100	20	15	15	15	10	88.94	67.09	3.7	0.044
14	z6	R407	X231	Flomin 742	Pine Oil	20	100	15	15	15	10	5	88.63	70.52	3.56	0.047
15	z6	R407	C4132	A65	MIBC	10	120	20	20	7	10	5	90.94	69.09	3.39	0.043
16	z6	Nascol	C4132	Flomin 742	MIBC	10	100	10	20	7	10	15	85.09	70.62	3.26	0.046
17	z11	A7240	Without	D250	MIBC	10	100	15	20	0	10	10	83.81	60.31	5.12	0.043
18	z11	Nascol	C4132	A65	Pine Oil	10	80	15	20	15	10	15	87.98	69.19	4.74	0.058
19	z11	Nascol	X231	D250	MIBC	0	100	10	15	7	15	15	85.14	58.61	4.55	0.050
20	z6	Nascol	Without	A65	A70	10	80	10	25	0	5	5	87.27	60.91	2.69	0.041
21	z11	A7240	C4132	A65	MIBC	20	120	20	15	15	10	5	82.95	64.89	5.07	0.048
22	z11	Nascol	C4132	Flomin 742	Pine Oil	20	80	10	25	7	10	10	83.57	77.06	4.5	0.057
23	z6	Nascol	Without	Flomin 742	Pine Oil	20	120	15	15	0	15	15	84.03	61.8	4.24	0.042
24	z6	A7240	Without	A65	MIBC	0	120	10	20	0	15	5	86.32	44.85	4.75	0.040
25	z6	Nascol	X231	D250	Pine Oil	10	100	20	20	7	5	5	90.91	69.12	2.82	0.048
26	z11	R407	Without	D250	MIBC	0	80	10	25	0	5	10	85.09	56.73	3.29	0.048
27	z11	R407	X231	D250	A70	20	80	15	25	15	5	15	86.99	73.77	3.1	0.051
28	z6	R407	C4132	A65	MIBC	0	100	15	20	7	5	15	89.94	61.09	3.27	0.048
29	z11	Nascol	Without	D250	A70	0	120	15	25	0	15	5	84.27	50.98	4.77	0.042

Cu recovery and grade

According to the analysis of variance (Table 6), the Fisher F -test with a very low probability values $P_{Model} < 0.05$ indicates that the models for Cu recovery and grade are highly significant. The recovery and grade models present high determination coefficients of $R^2 = 0.99$. The adjusted determination coefficients (Adj. $R^2 = 0.93$ and 0.96) are also satisfactory and confirm the significance of the models.

Table 6. Analysis of variance for Cu recovery and grade

Source		F value	P-value	Prob > F
Cu Recovery	Model	19.93	0.0018	
	A	16.80	0.0094	
	B	20.29	0.0040	
	Variables	D	10.15	0.0174
	H	9.81	0.0186	
		J	8.44	0.0249
		CV = 0.85%; $R^2 = 0.99$; Adj. $R^2 = 0.93$, C-E-F-G-K-L-M = not significant		
	Model	31.19	0.0006	
	A	138.57	< 0.0001	
Cu Grade	B	16.69	0.0061	
	Variables	D	13.82	0.0092
	E	13.18	0.0102	
		H	8.90	0.0225
		L	46.14	0.0006
	CV = 4.2%; $R^2 = 0.99$; Adj. $R^2 = 0.96$, C-F-G-J-K-L-M = not significant			

The normal probability plots of the residuals and the plots of the residuals versus the predicted response for Cu recovery and grade are shown in Figs. 2 and 3, respectively. Figure 2 shows that the residuals generally lie on a straight line referred to the normal distribution of errors. It implies that the proposed models were adequate.

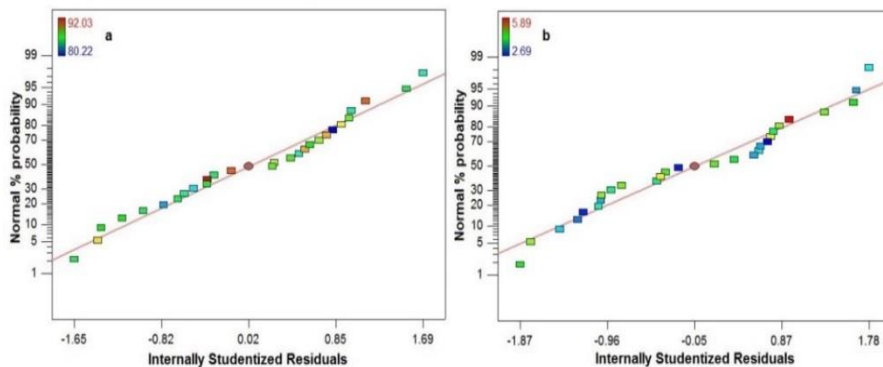


Fig. 2. Normal probability plot of residuals for Cu (left) recovery and (right) grade

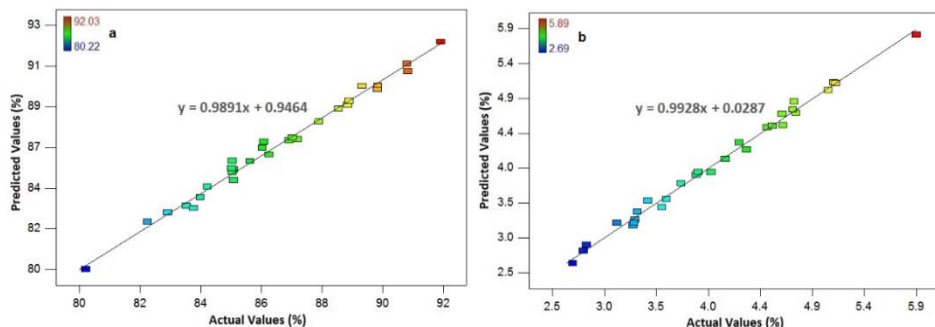


Fig. 3. Comparison of predicted and experimental results obtained for Cu (left) recovery and (right) grade

The A, B, D, H and J variables indicate a significance effect for Cu recovery. The order of influences is B > A > D > H > J. The A, B, D, E, H and L variables indicate a significant effect on the Cu grade. The order of influences is A > L > B > D > E > H. For both grade and recovery, the A, B, D and H are identified as the important factors. Figure 4 shows the effect of flotation process parameters on Cu recovery and grade. In general, lower recovery of Cu is obtained when Z_{11} rather than Z_6 is used as the collector. Also, R407 is a better choice than Nascol and A7240. According to Fig. 4, the primary promoter collector type has the maximum effect on the Cu recovery. Furthermore, the highest recovery could be achieved with the A65 as the frother. As shown in Fig. 4, the Cu recovery increased by increasing the primary collector (factor A) dosage and reached its maximum value at 20 g/Mg. Also the maximum value of Cu recovery is obtained when 20 g/Mg of the first promoter collector is employed. The first level of primary collector, third level of first promoter collector, A65 and pine oil as frothers represent the optimum levels of various turning process parameters to obtain the maximum Cu grade. The best reagent dosages are found to be 20 g/Mg of first promoter collector and 15 g/Mg of frother (factor D) to attain the maximum Cu grade.

Mo recovery and grade

In order to quantify the influence of process parameters on the Mo recovery and grade, the variance analysis is performed. The analysis of variance for Mo recovery and grade (ANOVA) is given in Table 7. Based on the results the models are significant. It is evident that the C, D, F, G, K and M variables are significant at 95% confidence level in ANOVA of Mo recovery. Also, the A, C, E and G variables are significant at 95% confidence level in ANOVA of Mo grade. The F and G variables significantly affect the Mo recovery. The order of factors from high to low contribution in Mo grade is A, G, E and C.

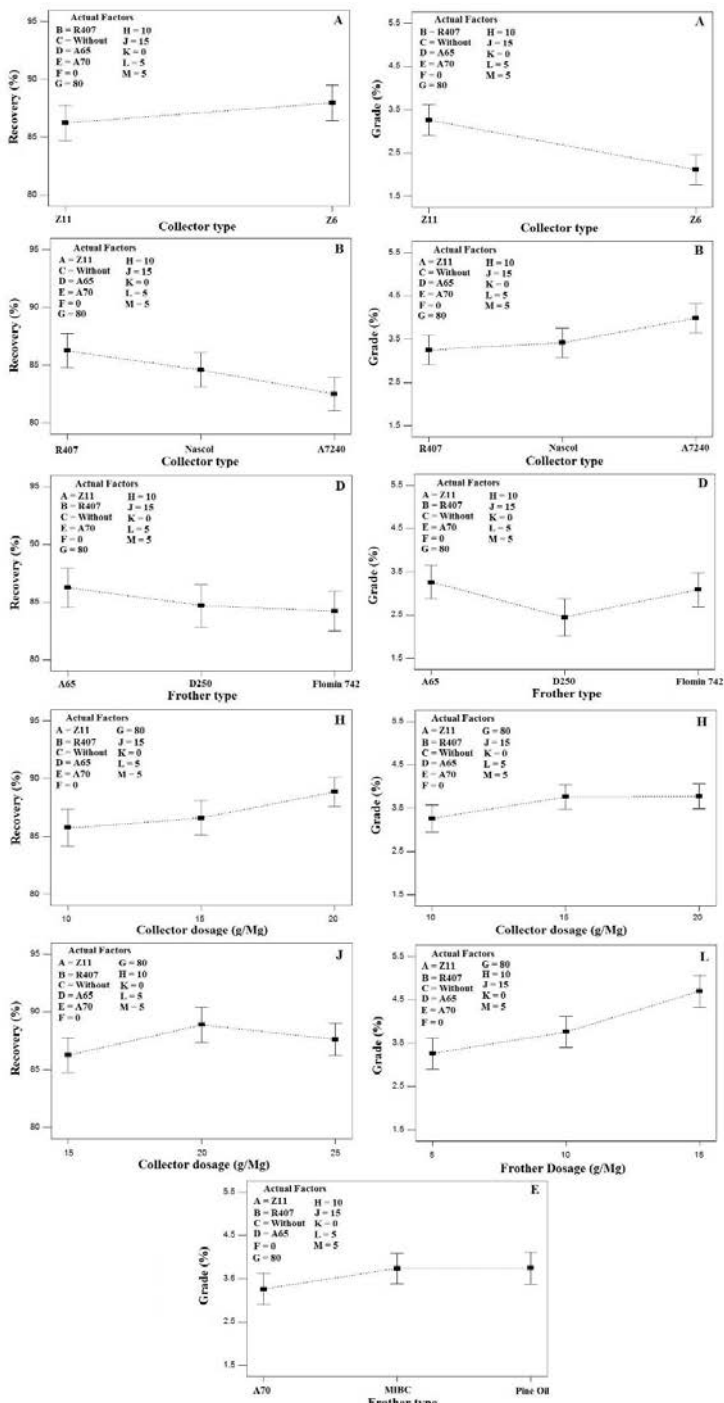


Fig. 4. Effect of process parameters on Cu recovery and grade

The design of experimental analysis assumes that the residuals are normally and independently distributed with the same variance in either each treatment or factor level. The deviation from this assumption means that the residuals contain a structure that is not accounted for the model. The residual plots given in Fig. 5 are used to check the assumption. Since the residuals lie approximately along a straight line, it is concluded that the residuals are normally and independently distributed. No particular trend in residual values against the test numbers indicates any systematic errors in the performed tests. Systematic errors cause the residual values either increase or decrease. As it is seen, the obtained model for Mo recovery and grade matches well with the performed experiments results. The observed Mo recovery and grade and their predicted values are shown in Fig. 6. The R^2 values for Mo recovery and grade are 0.99 and 0.98, respectively.

Table 7. Analysis of variance for Mo recovery and grade

Source	F value	P-value	Prob > F
Mo Recovery	Model	32.97	0.0005
	C	15.94	0.0068
	D	6.55	0.0401
	F	54.62	0.0004
	G	22.83	0.0031
	K	7.98	0.0278
	M	5.32	0.0478
	CV = 1.92%; R ² = 0.99; Adj. R ² = 0.96, A-B-E-H-J-L = not significant		
Mo Grade	Model	15.07	0.0034
	A	46.60	0.0010
	C	5.48	0.0442
	Variables	12.85	0.0107
	E	16.35	0.0064
	CV = 2.71%; R ² = 0.98; Adj. R ² = 0.92, B-D-F-H-J-K-L-M = not significant		

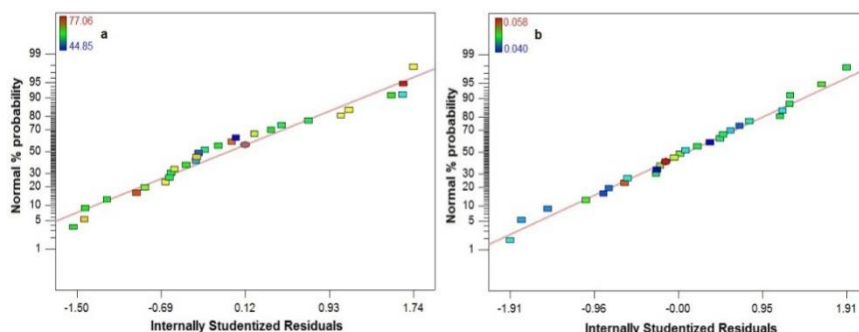


Fig. 5. Normal probability plot of residuals for Mo (left) recovery and (right) grade

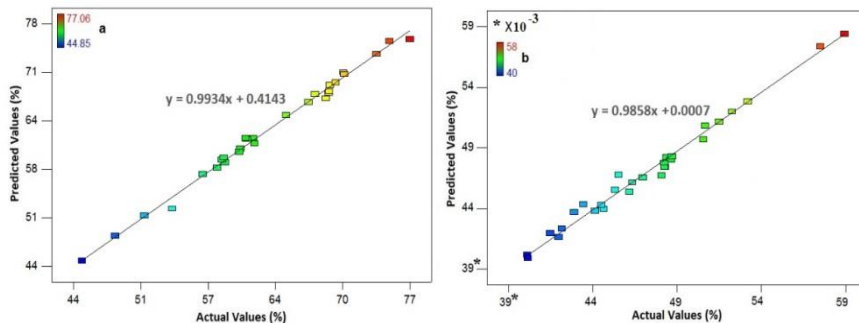


Fig. 6. Comparison of predicted and experimental results obtained for Mo (left) recovery and (right) grade

Figure 7 shows the role of effective parameters on Mo recovery and grade. The highest Mo recovery is obtained when C4132 (7 g/Mg) is used as a second promoter collector as well as the diesel dosage and d_{80} of feed are equal to 20 g/Mg and 80 μm , respectively. Also, using either Flomin 742 or DF250 with dosage of 15 g/Mg is better alternative than A65 in order to obtain high Mo recovery. In general, pine oil is a better choice than A70 and MIBC in order to make the concentrate with high Mo grade. The highest grade could be achieved with the d_{80} equal to 80 μm . As the effect of size (factor G) on recovery and grade is highly negative, the size is kept at the low level for process optimization.

Process optimization

The considered conditions for responses of optimal conditions and parameters are given in Table 8. The optimum levels of variables to maximize recovery within the studied range are obtained using the DX7 software. Table 9 shows the optimum level of each parameter to achieve the highest Cu and Mo grades and recoveries within the corresponding ranges. Based on software prediction, a product with Cu and Mo recoveries equal to 91.70 and 72.33%, respectively, will be obtained. Also, Cu and Mo grades equal to 5.67 and 0.055% respectively will be obtained. In order to verify the adequacy of the model prediction, two confirmation experiments were performed with optimal conditions. The tests results are given in Table 10. The validation tests proved the optimization results obtained from the D-optimal design experiment.

Table 8. Optimization criteria for different variables and responses

Variables	Goal
A-B-C-D-E-F-G-H-J-K-L-M	is in range
Cu recovery	maximum
Mo recovery	maximum
Cu grade	5.5-5.9
Mo grade	550-580

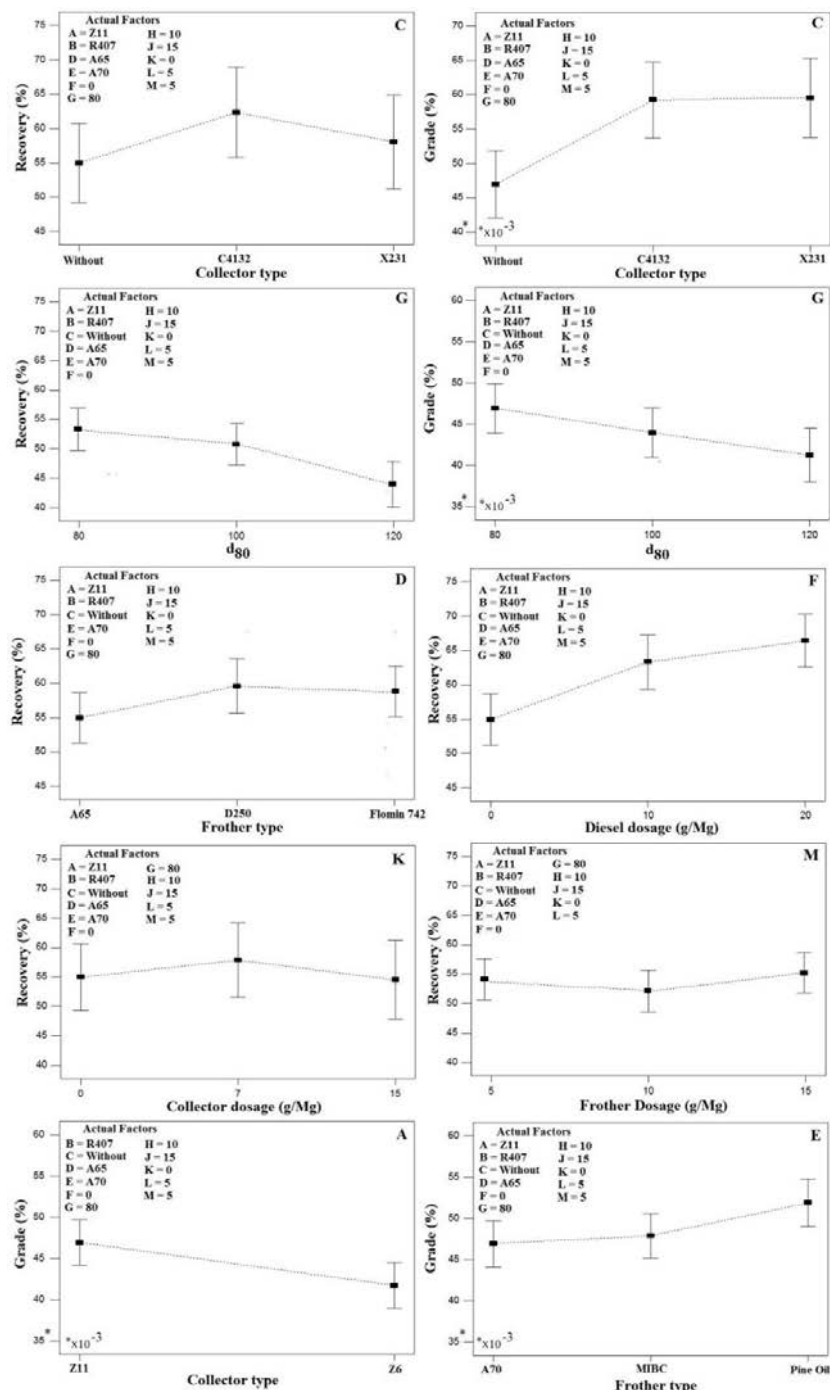


Fig. 7. Effect of process parameters on Mo recovery and grade

Table 9. Optimum level of each parameter

A	B	C	D	E	F	G	H	J	K	L	M	Recovery	Grade	Desirability		
												Cu	Mo			
					g/Mg	μm		g/Mg				%				
Z ₁₁	R407	X231	A65	Pine Oil	20	80	20	20	7	15	5	91.70	72.33	5.67	0.055	0.911

Table 10. Validation tests results with optimal condition

Test	Cu rec (%)	Mo rec (%)	Cu grade (%)	Mo grade (%)
1	90.65	70.39	5.83	0.053
2	90.42	71.18	5.54	0.054

Conclusions

In this paper, the D-optimal design method was used for modelling and optimizing grade and recovery of copper and molybdenum in the rougher flotation circuit of the Sungun copper concentrator plant. The investigated parameters included types and dosages of collectors and frothers, diesel dosage and feed size distribution. The following conclusions were drawn from the present study within the levels of process parameters selected.

1. Based on ANOVA and at 95% confidence level, the first promoter collector type had maximum effect on the Cu recovery. R407 (20 g/Mg) was a better choice than Nascol and A7240. Lower recovery of Cu was obtained when Z₁₁ rather than Z₆ was used as the collector. Higher grade of Cu was obtained when Z₁₁ rather than Z₆ was used as the collector. Also, Pine oil and A65 were better than other frothers to achieve the product with high copper grade. The best reagent dosages were found to be 20 g/Mg of the first promoter collector and 15 g/Mg of A65 to obtain the maximum Cu grade.

2. ANOVA of flotation parameters indicated that diesel dosage and d_{80} had the most significant effect on the recovery of Mo during flotation. The highest Mo recovery was obtained when C4132 (7 g/Mg) was used as the promoter collector and diesel dosage and d_{80} of feed were equal to 20 g/Mg and 80 μm, respectively. As the effect of size on recovery was highly negative, the size was kept at low level for optimizing the experiment. In general, pine oil was a better choice than A70 and MIBC in order to make the concentrate with high Mo grade. The highest Mo grade could be achieved with the feed size (d_{80}) equal to 80 μm.

3. Results of optimization showed that the highest possible Cu and Mo grades and recoveries were obtained when Z₁₁ (20 g/Mg) as the primary collector, R407 (20 g/Mg) as a first promoter collector, X231 (7 g/Mg) as the second promoter collector, A65 (15 g/Mg) and Pine oil (5 g/Mg) as frothers, 20 g/Mg of diesel dosage and d_{80} of feed size equal to 80 μm were used.

Acknowledgments

The authors would like to acknowledge the support of the Department of Research and Development of the Sarcheshmeh and Sungun Copper Plants for this research.

References

ABALI, Y., COPUR, M., YAVUZ, M., 2006. *Determination of the optimum conditions for dissolution of magnesite with H₂SO₄ solutions*, Indian Journal of Chemical Technology, Vol.13, pp. 391-397.

BULATOVIC S.M., 2007. *Handbook of flotation reagents chemistry, theory and practice: flotation of sulfide ores*. Elsevier Science & Technology.

GOPALSAMY, B.A., MONDAL, B., GHOSH, S., 2009. *Taguchi method and ANOVA: An approach for process parameters optimization of hard machining while machining hardened steel*, Journal of scientific and Industrial Research, Vol. 68, pp. 686-695

GUY, H. H., JIA, R., 2000. *An improved class of flotation frothers*, Int. J. Miner. Process, vol. 58, pp. 35–43.

HAGHI, H., GHADYANI, A., BIRANVAND, B., SHAFEI, S.Z., 2009. *Optimization of Apatite flotation using Taguchi method*, 7th industrial Minerals Symposium and Exhibition, 25-27 February, Turkey.

HAIDER, M.A., PAKSHIRAJAN, K.K. 2007. *Screening and optimization of media constituents for enhancing lipolytic by a soil microorganism using statically designed experiments*. Appl Biochem Biotech, 141: 377-390.

HARVEY, P.A., NGUYEN, A.V., JAMESON, G.J., EVANS, G.M., 2005. *Influence of sodium dodecyl sulphate and Dowfroth frothers on froth stability*, Minerals Engineering, vol. 18, pp. 311–315.

IIYAS, S., BHATTI, H.N., BHATTI, I.A., SHEIKH, M.A., and GHAURI, M.A., 2010. *Bioleaching of metal ions from low grade sulphide ore: Process optimization by using orthogonal experimental array design*, African Journal of Biotechnology, Vol. 9(19), pp. 2801-2810.

KAMARUDDIN, S., KHAN, Z.A., WAN, K.S., 2004. *The use of the Taguchi method in determining the optimum plastic injection moulding parameters for the production of a consumer product*, Jurnal Mekanikal, Bil.18, pp. 98-110.

Malysa, K., Barzyk, W., Pomianowski, A., 1981. *Influence of frothers on floatability. I. Flotation of single minerals (Quartz and synthetic chalcocite)*, International Journal of Mineral processing, vol. 8, pp. 329-343.

MUTEKI K., MACGREGOR J. F., and UEDA T., 2007. *Mixture designs and models for the simultaneous selection of ingredients and their ratios*, Chemometrics and Intelligent Laboratory Systems, vol. 86, 1, pp. 17–25.

LASKOWSKI, J. S., TLHONE, T., WILLIAMS, P., DING, K., 2003. *Fundamental properties of the polyoxypropylene alkyl ether flotation frothers*, Int. J. Miner. Process, vol. 72, pp. 289– 299.

LIU, G.C., WANG, X.L., 2007, *Optimization of critical medium components using response surface methodology for biomass and extra cellular polysaccharide production by Agaricus blazei*. Appl Microbiol Biotechnol, 74: 78–83.

MELO, F. and LASKOWSKI, J. S, 2006. *Fundamental properties of flotation frothers and their effect on flotation*, Minerals Engineering, vol. 19, pp. 766–773.

PRADYUMNA, K., NAIK, P, REDDY, S.R., VIBHUTI, N., 2005 *Interpretation of interaction effects and optimization of reagent dosages for fine coal flotation*, Int. J. Miner. Process. 75 83– 90.

RAMA, R.S. and PADMANABHAN, G., 2012. *Application of Taguchi methods and ANOVA in optimization of process parameters for metal removal rate in electrochemical machining of Al/5%SiC composites*, International Journal of engineering Research and Application (IJERA), Vol.2, Issue 3, pp. 192-197.

SAPAKAL, S.V., and TELSANG, M.T., 2012. *Parametric optimization of MIG welding using Taguchi Design Method*, International Journal of Advanced Engineering Research and Studies, Vol.1, Issue IV, pp. 28-30

SAYYAD, S.A., PANDA, B.P., JAVAD S, ALI M., 2007. *Optimization of nutrient parameters for lovastatin production by monascus purpureus MTCC 369 under submerged fermentation using response surface methodology*. Appl Microbiol Biotechnol, 73: 1054–1058.

TRUST T. M. Willie N., 2014. *Flotation of nickel-copper sulphide ore: optimisation of process parameters using Taguchi method*, Proceedings of the International Conference on Mining, Material and Metallurgical Engineering Prague, Czech Republic, August 11-12, Paper No. 113.

VAZIFEH1, Y., JORJANI1, E., BAGHERIAN A., 2010. *Optimization of reagent dosages for copper flotation using statistical technique*, Trans. Nonferrous Met. Soc. China 20, 2371–2378

XIA Y. K. and PENG, F. F., 2007. *Selection of frothers from residual organic reagents for copper-molybdenite sulfide flotation*, Int. J. Miner. Process. vol. 83, pp. 68–75.

WILLS, B. A., and NAPIER-MUNN, T. J., 2006. *An Introduction to the Practical Aspects of Ore Treatment and Mineral Recovery*, in *Wills' Mineral Processing Technology*, 7th ed., pp. 267 - 352.

Received February 17, 2015; reviewed; accepted June 20, 2015

FIRST-ORDER AND SECOND-ORDER BREAKAGE RATE OF COARSE PARTICLES IN BALL MILL GRINDING

Kianoush BARANI, Hoosein BALOCHI

Department of Mining Engineering, Lorestan University, Khorramabad, Iran, barani.k@lu.ac.ir

Abstract: It has been observed by many authors that the breakage rates of coarse particles in a ball mill slow down with increasing grinding time and deviate from the first order. In this paper it is intended to find out whether the breakage rates of coarse particles obey second-order kinetics or not. For this purpose, quartz, limestone, iron ore and a mixture of quartz/limestone (weight ratio of 1:1) were selected as a ball mill feed. The first-order breakage rate was determined for the four particle sizes of quartz, limestone, iron ore and the mixture of quartz/limestone. Results indicating good first-order kinetics were obtained with the fine-sized particles (-1.2+1 mm, -0.6+0.42 mm). However, the coarse-sized particles (-5+4 mm, -3.15+2.5 mm) showed deviations from the first order. These coarse particles were in the abnormal breakage region. The second-order breakage rate was determined for the coarse particles (-5+4 mm, -3.15+2.5 mm). It can be seen that, for both sizes and all the materials, the second-order plot had better fit than the first-order plot. Also, it can be concluded that the second-order kinetics could model the breakage of coarse particles better than the first-order kinetics, and the validity of the second-order breakage rate was increased with increasing particle size. However, it is suggested to examine the validity of the second-order breakage rate kinetics for other materials and particle sizes.

Keywords: ball mill, grinding kinetic, particle breakage

Introduction

The breakage rate equation, similar to a chemical reaction, can be expressed in a general way as follows:

$$-\frac{dm}{dt} = Sm^n \quad (1)$$

where m is the total mass, t is time, S is the breakage rate constant or selection function, and n is the order of equation.

Loveday (1967) and Austin (1971) have found experimentally that, in the case of batch grinding, the breakage rate obeys a first-order law or $n=1$. However, there is no valid reason for this.

If the total mass load in the mill is at particle size $i=1$ (single-sized particles), then for a first-order breakage process (Austin, 1971) is:

$$-\frac{dm_1}{dt} = S_1 m_1 \quad (2)$$

It is usually adequate to assume that S_1 does not vary with time. Then, with integration from $t = 0$ to t :

$$m_1(t) = m_1(0) \exp(-S_1 t) \quad (3)$$

or taking logs

$$\log(m_1(t)) = \log(m_1(0)) - \frac{S_1 t}{2.303} \quad (4)$$

where $m_1(0)$ and $m_1(t)$ are respectively the weight of particle size $i=1$ at time 0 and t and S_1 is a proportionality constant called specific rate of breakage with unit of time $^{-1}$. A plot of $\log(\frac{m_1(t)}{m_1(0)})$ versus t should give a straight line with slope $(\frac{S_1}{2.033})$.

The kinetics of breakage has been studied by many researchers, the majority of whom have classified breakage as a first-order reaction. However, it has been reported by various researchers that breakage rate deviates from the first order; this breakage is called non-first order (Austin et al., 1971; Austin et al., 1972; Austin et al., 1977; Gardner et al., 1975; Mankosa et al., 1989; Tuzun et al., 1995; Cho et al., 1996; Gao et al., 1993; Fuerstenaau et al., 2004).

It has been observed by many authors that the breakage rates of coarse particles in the ball mill slow down with increasing grinding time and deviate from the first order (Tavares et al., 2009; Austin et al., 1982; 2006). This behaviour has been often encountered for the sizes above those corresponding to the maximum breakage rate (Tavares et al., 2009) and has been called by Austin "abnormal breakage region". The deviation from the first-order grinding kinetics is resulting from either mill conditions or material properties and has been explained in the literature with two points. First, as grinding time increases, fine products accumulated in the mill cover the coarse material and prevent further grinding, which is usually encountered in fine-dry grinding and high-viscosity wet grinding and is called the "medium effect". The second point could be that the size of the material is much bigger than the grinding ball diameter. In this case, coarse particles cannot be nipped by the balls and some amount of the material behaves as a relatively weaker material, while some behaves as a relatively stronger material. It is called by Austin the "material effect", which is in contrast with an "environmental effect", by which breakage rates of all sizes slow down as fines accumulate in the charge in dry grinding (Austin and Bagga, 1981). However, it is an oversimplification of the physical phenomenon, since materials are known to have a range of fracture energies (Tavares and King, 1998; Tavares, 2007). In addition, some researchers believe machines operating prior to grinding stage effect

on the grinding breakage rate and this may cause to deviation from first order breakage rate. This can be called the 'device effect' (Tumidajski et al., 2010; Gawenda, 2013; Saramak, 2013).

Gardner and Rogers (1975) presented the mathematical formulation for milling a material which behaved as if it consisted of a mixture of soft and hard components, each breaking in a first-order manner. They noted that attaching physical significance to the two hypothesized components was avoided.

Second-order breakage rate

The kinetics of some mineral processing processes is second-order rate or between first- and second-order rates. For example, the kinetics of froth flotation obeys the second order for low-grade ores or more concentrated pulps.

In this paper, it is tried to find out whether the breakage rates of coarse particles in the abnormal breakage region obey the second order or not. If the breakage material is assumed as one reactant and the breakage rate obeys the second order ($n=2$), then Eq. 1 can be written as follows:

$$-\frac{d[m_1]}{dt} = S_1[m_1]^2 \quad (5)$$

and integration from $t = 0$ to t gives

$$\frac{m_1(0)}{m_1(t)} = 1 + m_1(0)S_1 t \quad (6)$$

where $m_1(0)$ and $m_1(t)$ are the weight of particle size $i=1$ at time 0 and t , respectively, and S_1 is a proportionality constant called specific rate of breakage with the unit of $\text{mass}^{-1} \cdot \text{time}^{-1}$. A plot of $\frac{m_1(t)}{m_1(0)}$ versus t should give a straight line with slope $(m_1(0)S_1)$ and y-intercept (1).

Materials, equipment, and procedure

Materials

The materials used in this research were quartz, limestone and iron ore. Quartz is a hard material (7 on the Mohs scale) and limestone is a soft material (3 on the Mohs scale). A mixture of quartz/limestone (weight ratio 1:1) was also prepared as the medium-soft material. Large chunks of each material (quartz, limestone and iron ore) were broken in a jaw and roll crusher. The crushed materials were first screened and then carefully sieved to obtain the single-sized particles. Four single-sized particles sizes (-5+4 mm, -3.15+2.5 mm, -1.2+1 mm, -0.6+0.42 mm) were prepared from quartz, limestone, iron ore and the quartz/limestone mixture.

Mill

Grinding tests were performed in a 20 cm×20 cm stainless steel laboratory mill. It was operated at the constant speed of 85 rpm (84 % of the critical speed). The mill charge consisted of stainless steel balls with 16 and 42 mm diameter and the total ball load weighed 8.79 kg. The volume of the ball charge with voids was 25% of the total volume of the mill.

Procedure

Dry grinding experiments were carried out using the single-sized particles of quartz, limestone, iron ore and the quartz/limestone mixture. The material weight in each experiment was 350 g. Each grinding experiment was continued for short time periods until about 90% of the material passed through the sieve (fraction). After each grinding period, the mill content was discharged and sieved for 20 min and the remaining materials were determined. Then, the whole material was returned to the mill for the next grinding period. By fitting Eqs. 4 and 6 to the experimental grinding data, the first- and second-order breakage rates of the particles sizes were determined, respectively.

Results and discussion

Figs. 1-4 show the first-order plots for various feed sizes of quartz, limestone, and the mixture of quartz/limestone and iron ore. The coefficient of determination, denoted by R^2 , which indicates how well data fit a breakage rate kinetic model was calculated and reported in Fig. 5. The results showed that R^2 decreased with increasing the particle size. The results indicated that good first-order kinetics was obtained with fine-sized particles (-1.2+1 mm, -0.6+0.42 mm). However, the coarse particle sizes (-5+4 mm, -3.15+2.5 mm) showed deviations from the first order. Figure 6 demonstrated the variation of the first-order specific rate of breakage values (S_1) against feed particle sizes. It can be seen that the coarse-sized particles were in the abnormal breakage region. As mentioned before, in the abnormal breakage region, deviation from the first-order breakage occurred, because the particles were too large to be properly nipped by the balls.

For the evaluation, the second-order breakage rate, Eq. (6), was fitted to the grinding data of the coarse particles. Figs. 7-10 show the second-order plots for the coarse feed sizes (-5+4 mm, -3.15+2.5 mm) of quartz, limestone, iron ore and the mixture of quartz/limestone. Table 1 demonstrates the comparison between the R^2 of the first- and second-order plots for the coarse particle sizes of quartz, limestone, iron ore and the mixture of quartz/limestone. It can be seen that, for both particle sizes and all the materials, the R^2 of the second-order plot was higher than that of the first order; i.e. the second-order plot had a better fit than the first-order plot, which was especially true for -5+4 mm particles and harder materials. It can be concluded that, in the

abnormal breakage region, with increasing particle size, the validity of the second-order breakage rate would be increased.

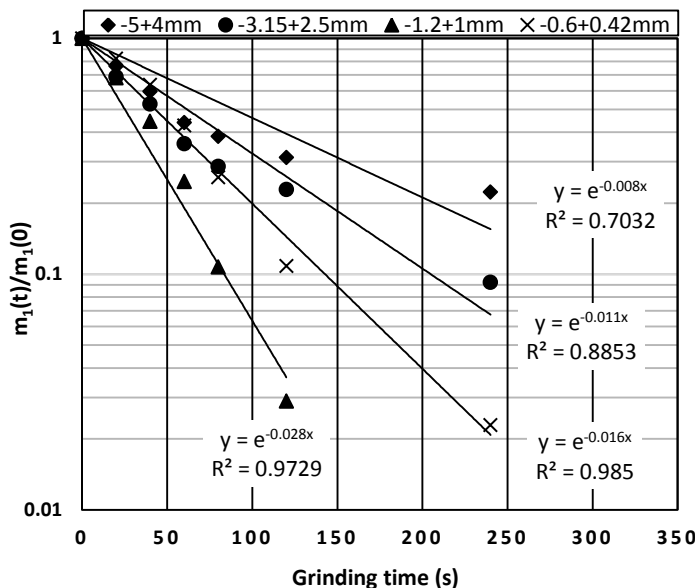


Fig. 1. First-order plots for various feed sizes of quartz

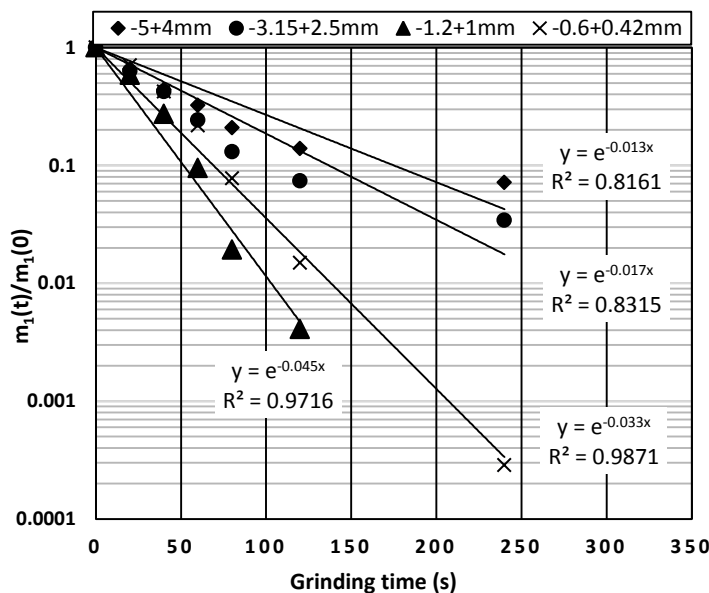


Fig. 2. First-order plots for various feed sizes of limestone

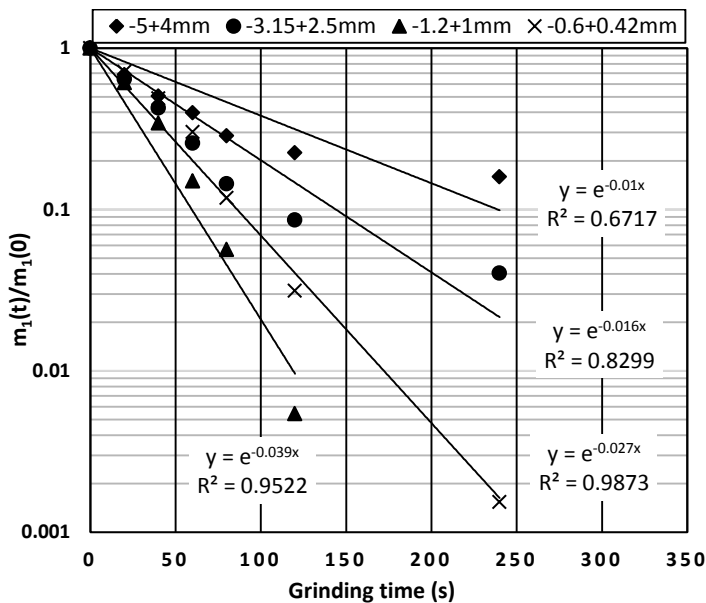


Fig. 3. First-order plots for various feed sizes of the mixture of quartz/ limestone (weight ratio of 1:1)

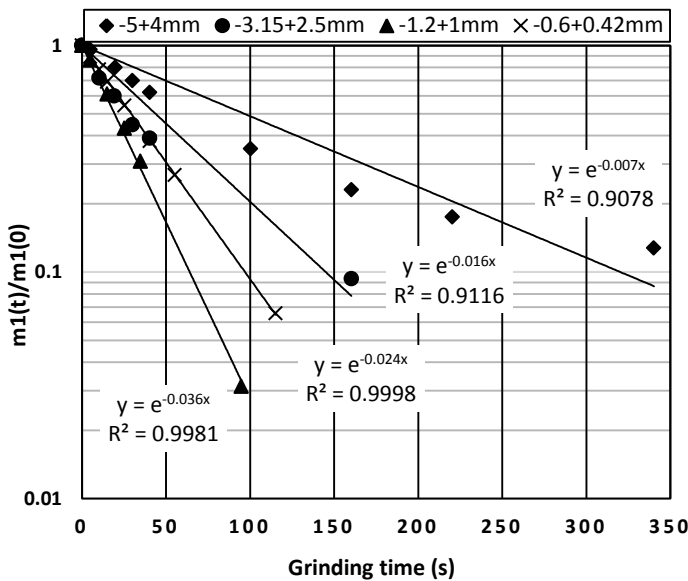


Fig. 4. First-order plots for various feed sizes of iron ore

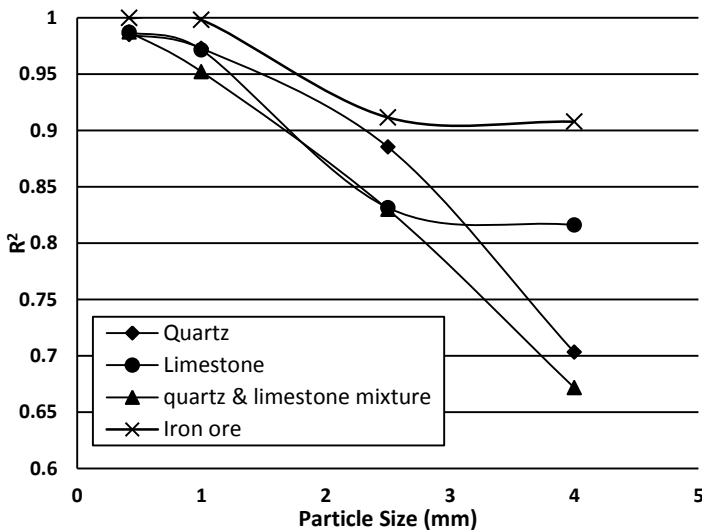
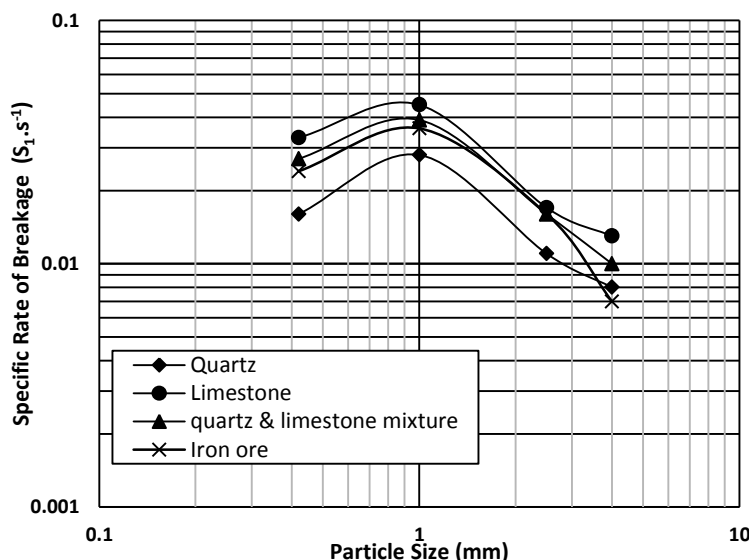
Fig. 5. R^2 of the first order kinetics model versus particle size

Fig. 6. Specific rates of breakage as function of particle size

Tavares and Carvalho (2009) showed that breakage does not necessarily follow a simple power law time, but is rather related to the complex micro-behavior of individual particles and fundamental fracture mechanics theory. The Tavares and Carvalho model is a very complex one with many parameters that are difficult to measure or nigh on impossible to back-calculate because of parameter sensitivity issues. This model is also suspect in that the breakage distribution function is based on

single particle impact tests, rather than the statistical approach advocated by Austin (1971) where the particle bed in the ball mill is treated as a statistical ensemble composing many particles.

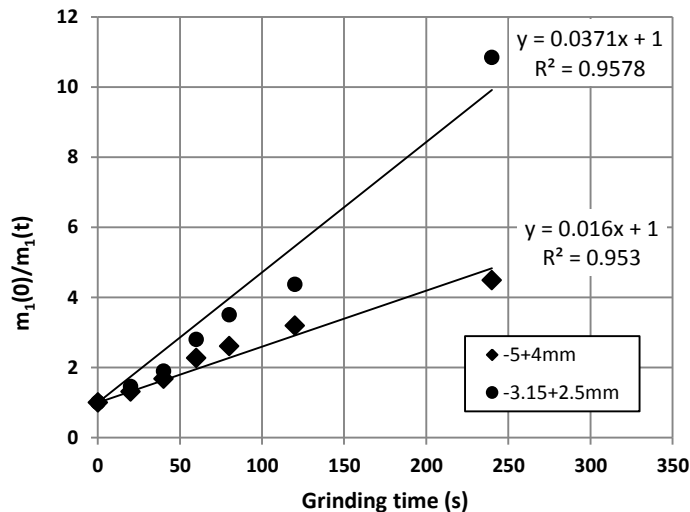


Fig. 7. Second-order plots for the coarse feed sizes of quartz

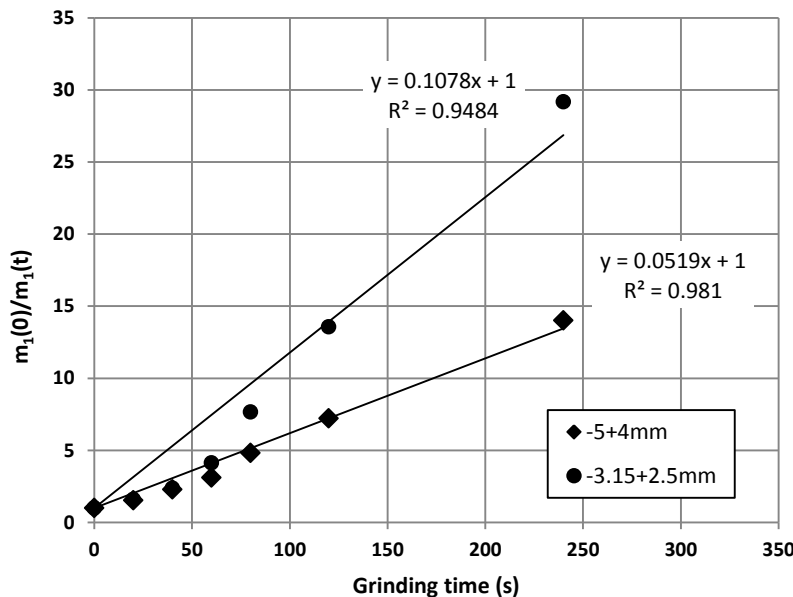


Fig. 8. Second-order plots for the coarse feed sizes of limestone

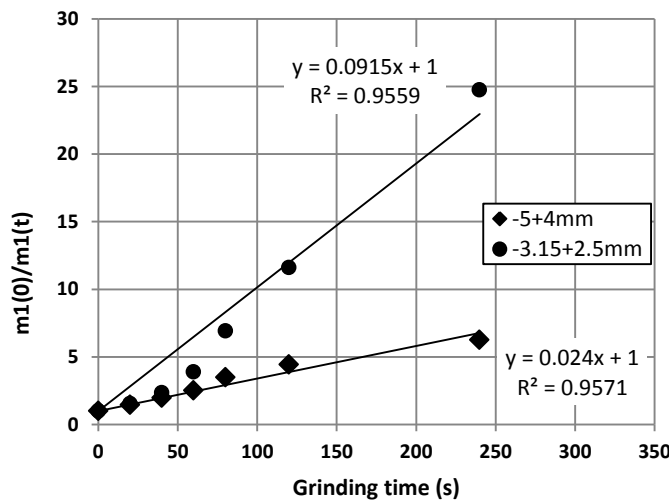


Fig. 9. Second-order plots for the coarse feed sizes of the mixture of quartz/limestone (weight ratio of 1:1)

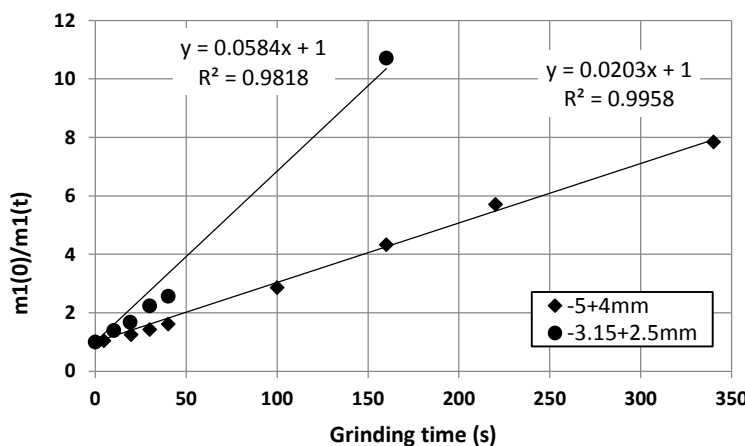


Fig. 10. Second-order plots for the coarse feed sizes of iron ore

Table 1. *R*-squared of first and second order for the coarse particles sizes

kinetic order	-5+4mm				-3.15+2.5mm			
	quartz	limestone	q&l mixture	iron ore	quartz	limestone	q&l mixture	iron ore
First-order	0.7032	0.8161	0.6717	0.9078	0.8853	0.8315	0.8299	0.9116
Second- order	0.9531	0.9810	0.9571	0.9958	0.9578	0.9484	0.9559	0.9818

Summary and conclusion

The first-order breakage rate was determined for four particle sizes of quartz, limestone, iron ore and a mixture of quartz/limestone (weight ratio of 1:1). The results indicated good first-order kinetics for fine particle sizes (-1.2+1 mm, -0.6+0.42 mm). However, the coarse particle sizes (-5+4 mm, -3.15+2.5 mm) showed deviations from the first order. These coarse particle sizes were in the abnormal breakage region. In the abnormal breakage region, deviation from first-order breakage occurred, because the particles were too large to be properly nipped by the balls.

The second-order breakage rate was determined for the coarse particles (-5+4 mm, -3.15+2.5 mm). It can be seen that, for both particles sizes and all the materials, the second-order plot had a better fit than the first-order plot, which was especially true for -5+4 mm particles and harder materials. It can be concluded that, in the abnormal breakage region, with increasing particle size, the validity of the second-order breakage rate was increased.

The results of this research showed that the second-order kinetics can model the breakage of coarse particles better than the first-order kinetics. This phenomenon was also observed by the authors of this paper for different iron ore samples. However, it is suggested to examine the validity of the second-order breakage rate kinetics for other materials and particle sizes as well.

Acknowledgements

The authors would like to thank Lorestan University for support in conducting this research.

References

AUSTIN, L.G., 1971. *Introduction to the mathematical description of grinding as a rate process*. Review Article, Powder Technology, 5(1), pp. 1-17.

AUSTIN, L.G., BHATIA, V.K., 1972. *Experimental methods for grinding studies in laboratory mills*. Powder Technology, 5(5), pp. 261-266.

AUSTIN, L.G., TRIMARCHI, T., WEYMONT, N.P., 1977. *An analysis of some cases of non-first-order breakage rates*. Powder Technology, 17, pp. 109 – 113.

AUSTIN, L.G. BAGGA, P., 1981. *An analysis of fine dry grinding in ball mills*, Powder Technology, 28, pp.83–90.

AUSTIN, L.G., SHOJI, K., BELL, D., 1982. *Rate equations for non-linear breakage in mills due to material effects*. Powder Technology, 31, pp. 127–133.

AUSTIN, L.G., JULIANELLI, K., SCHNEIDER, C.L., 2006. *Simulation of wet ball milling of iron ore at Carajas, Brazil*, International Journal of Mineral Processing, 84, pp.157-171.

CHO, H., WATERS, M.A., HOGG, R., 1996. *Investigation of the grind limit in stirred media milling*. International Journal of Mineral Processing, 44, pp. 607–615.

FUERSTENAU, D.W., DE, A., KAPUR, P.C., 2004. *Linear and nonlinear particle breakage processes in comminution systems*, International Journal of Mineral Processing, 74, pp.317–327.

GAO, M.W., FORSSBERG, E., 1993. *A study on the effect of parameters in stirred ball milling*. International Journal of Mineral Processing, 37, pp. 45–59.

GARDNER, R.P., ROGERS, R.S., 1975. *A two-component mechanistic approach for the comminution of material that exhibits heterogeneous breakage characteristics*. Powder Technology, 12(3), pp. 247-258.

GAWENDA, T., 2013. *The influence of rock raw materials comminution in various crushers and crushing stages on the quality of mineral aggregates*. Gospodarka Surowcami Mineralnymi – Mineral Resources Management, 26(1), pp. 53-65.

LOVEDAY, B.K., 1967. Journal of the South African Institute of Mining and Metallurgy, 68, 111.

MANKOSA, M.J., ADEL, G.T., YOON, R.H., 1989. *Effect of operating parameters in stirred ball mill grinding of coal*. Powder Technology, 59, pp. 255–260.

SARAMAK, D., 2013. *Mathematical models of particle size distribution in simulation analysis of high-pressure grinding roll operations*. Physicochemical Problems of Mineral Processing, 49(1), pp. 121-131.

TAVARES, L.M., KING, R.P., 1998. *Single-particle fracture under impact loading*. International Journal of Mineral Processing, 54 (1), pp.1-28.

TAVARES, L.M., 2007. *Breakage of single particles: quasi-static*. Handbook of Powder Technology, 12, pp. 3-68.

TAVARES, L.M., CARVALHO, R.M., 2009. *Modeling breakage rates of coarse particles in ball mills*. Minerals Engineering, 22, pp.650–659.

TUMIDAJSKI, T., KASINSKA-PILUT, E., GAWENDA, T., 2010. *Investigation of grinding process energy consumption and grind ability of lithological components of polish copper ores*. Gospodarka Surowcami Mineralnymi – Mineral Resources Management, 2010, 26(1), pp. 61-72.

TUZUN, M.A., LOVEDAY, B.K., HINDE, A.L., 1995. *Effect of pin tip velocity, ball density and ball size on grinding kinetics in a stirred ball mill*. International Journal of Mineral Processing, 43, pp. 179–191.

Received May 2, 2014; reviewed; accepted April 10, 2015

EFFECT OF INTERGROWN PARTICLE LIBERATION ON DIFFICULT-TO-SEPARATE COKING COAL FLOTATION

Xiahui GUI^{*}, Jiongtian LIU^{*}, Yijun CAO^{*}, Yaowen XING^{}, Yangyang DENG^{**}, Shulei LI^{**}**

^{*} Chinese National Engineering Research Center of Coal Preparation and Purification, Xuzhou 221116, Jiangsu, China, guixiahui1985@163.com

^{**} School of Chemical Engineering and Technology, China University of Mining and Technology, Xuzhou 221116, Jiangsu, China

Abstract: Flotation tests with intergrown particle liberation were conducted to explore a separation method of difficult-to-separate coking coal from the Tangshan Kailuan mine in China. The particle size distribution, density and coal petrography were investigated. The difficult-to-separate coking coal sample resulted in intergrown particles, such as non-liberated coal and rocks. Thus, intergrown coal particle liberation and re-separation tests were conducted. The results showed that grinding time had a great effect on the flotation performance. Grinding prompted coal to dissociate and improve the surface hydrophobic properties of minerals. However, heterogeneous fine silt covered the surface of coal particles when coal was ground too long. The inorganic mineral particles were over-ground and reduced the contact angle of coal. The results of coal rock dissociation and laboratory re-separation tests showed that clean coal combustible recovery increased through intergrown particle liberation and re-separation.

Keywords: *liberation, particle size, coking coal, hydrophobicity*

Introduction

This study focuses on fine coal from coking and fat coal samples. As an indispensable raw material used in a coke-making industry in China, coking and fat coal resources are quite depleted. Prime coking coal from coking and fat coal samples have reserves of approximately 100 petagrams (billion tons). Coking coal accounts for 5.39% of the total coal resources and 22.07% of coal resources for coking. Fat coal resources are scarce, accounting for only 3.38% of the total coal resources and 12.58% of coal resources for coking. China is the largest steelmaking coking coal producer and consumer in the world. China consumes nearly one petagrams of coke-making coal annually, and uses only about 10% of coking coal resources to support about half of

the world steel production. Coking and fat coals are mined faster than other types of coal. Coking and fat coals yield more than double in proportion compared with total coal resources, which rapidly reduced the country coking and fat coal resources. Coking and fat coals are becoming rare in China (Xu, 2003; Du, 2006; Ma, 2006; Wu, 2007).

The most rare coal resource in China is high-ash and difficult-to-separate coal because of the intergrowth of coal and gangue, very finely disseminated size of high-ash coal and very large supply of middle-density coal (Cheng et al., 2013; Gui et al., 2013). A large amount of middlings, which account for about 10 to 30% of raw coal, is produced by separation. The ash content of middlings is generally from 25 to 35%. Thus, middlings are only used as a fuel. An estimated two petagrams per year of coking coal is used as power coal, which causes a great waste of scarce coal resources.

Some feeds to flotation of fine coal are middlings, intergrown coal and gangue of which the surface hydrophobicity generally ranges between that of coal and inorganic minerals. The middlings of intergrown particles are recovered as either flotation concentrate or tailing, depending on their floatability. However, the content of ash in a product is generally close to the content of ash in a feed, and may enter to tailings in actual production. The flotation middlings are then obtained by classification recovery operations and used as power coal, resulting in a coking coal resource waste. The coal middlings are primarily inter-band coal, which is an accretion of minerals and coal, and has a density between that of clean coal and rock. The conventional coal preparation methods do not effectively separate interlocked minerals. Petrographic components of coal, such as macerals or group macerals, should be dissociated to obtain low-ash clean coal from fine inter-band coal. However, the existing coal slime flotation technology only performs flotation progress without dissociation (Harris, et al., 1992; Giroux, et al., 2006; Jena, et al., 2008; Jorjani, et al., 2009; Vapur et al., 2010; Gui, et al., 2012). Fu and Wang (1996) studied recovery of high-quality clean coal from flotation coal middlings. They adopted the hydrophobic flocculation flotation process to recover low-ash clean coal from coking coal middlings by pulverizing coal middlings using a JM series stirred mill. The tests showed that a concentrate with ash content of 11.32% could be obtained from coking coal middlings with 57.78% ash content and yield of 38.31%. In addition, grinding was used to increase floatability of oxidized coal and some difficult-to-separate coal (Shu et al., 2002; Man et al., 1998; Tao et al., 2009; Hu et al., 2011; Li et al., 2013; Xia et al., 2012,a ,b, 2013; Zhang and Tang, 2014).

From the perspective of coal petrology, difficultness in separating of organic and inorganic matters in coal is determined by coal slime washability, which mainly depends on the composition, particle size, density and distribution state of inorganic matter in coal. Dissociation could be easily performed when the inorganic matter is gathered in layers, large nodulars, lenticulars or monomers. However, dissociation is very difficult and leads to poor washability when mineral dissemination size is very fine and is distributed in the organic substrate as either disseminated or in thin strips or

even filled in plant cells. This study focuses on rare fat coal and explores the methods for improving coal rock liberation of middlings through the coal petrology analysis and grinding floating experiments.

Experimental

The representative -0.5 mm coal sample used for testing was obtained from the Tangshan Kailuan mine in China. The collected sample was subsampled to obtain a representative sample. The samples were selected for an X-ray diffraction test. The instrument used was a Rigaku D/Max-RA rotating anode X-ray diffraction. The working conditions were as follows: Cu target, operating voltage: 40 kV, current at 50 mA, graphite monochromator, scattering slit at 1° , slit acceptance at 0.3 mm, step scan, preset time at 0.1 s, and pace: $0.02^\circ/\text{step}$.

A SPB200 vibrating Taylor screen was used for size analysis to determine the ash content at various particle sizes. A GL-21M high-speed centrifuge was used for density analysis at a centrifuge speed of 3000 rpm. Specification of centrifuge tube was 4×250 cm 3 . Four centrifuge tubes with volumes of 250 cm 3 were arranged symmetrically in the centrifuge. The centrifugal liquid was prepared by mixing an organic solution composed of carbon tetrachloride, benzene and tribromomethane.

A ZEISS imager M1m type microscope spectrophotometer was used for coal maceral analysis and testing. The working conditions were as follows: immersion oil refractive index (Ne): 1.518 , standard material for sapphire and yttrium aluminum garnet, determination target: 90% of telocollinite and 10% of desmocollinites. The test was performed at ambient temperature (23°C).

A contact angle of coal sample was determined by fast photo-angle measurement. The coal sample was formed into a tablet under a pressure of 30 MPa for 10 seconds. The diameter and thickness of tablet were 10 and 2 mm, respectively. The contact angle of right and left sides were measured three times and the average value was considered as the final contact angle.

A crushed sample was ground in a laboratory XMB-68 type 160×200 ball mill. The mill cylinder diameter and length were 160 and 200 mm, respectively. The cylinder volume was 4.02 dm 3 , cylinder speed was 120 rpm and feeding quantity was from 300 to 800 g. The test was completed through wet grinding to simulate grinding-flotation industrial processes at the production site. An XFD 0.75 dm 3 laboratory-scale flotation machine was used for flotation tests.

The flotation concentrates were analyzed using combustible matter recovery and ash contents. The combustible matter recovery was calculated by using formula:

$$\text{Combustible matter recovery}(\%) = [M_c(100 - A_c) / M_F(100 - A_F)] \cdot 100 \quad (1)$$

where M_c and M_F are weights of concentrate and feed (%), respectively, A_c and A_F are ash contents in concentrate and feed (%), respectively

A coal rock liberation test had an open circuit flow and consisted of one rougher, one scavenger, middling liberation and re-separation. To ensure the maximum recovery of clean coal combustible matter, the scavenger process (wherein numerous hard-to-recycle intergrown particles float) was applied to the rougher tailings, followed by liberation and re-separation. Figure 1 shows the flow-sheet. Using a single factor experiment and considering comprehensive ash concentrate and clean coal combustible matter recovery, the test conditions for preparation of grinding middlings were as follows: diesel as the collector (rougher, 190 g/Mg; scavenger, 310 g/Mg), 2-octanol used as the frother (rougher, 90 g/Mg; scavenger, 125 g/Mg), stirring speed during flotation 1590 rpm, and air flow 0.37 m³/min.

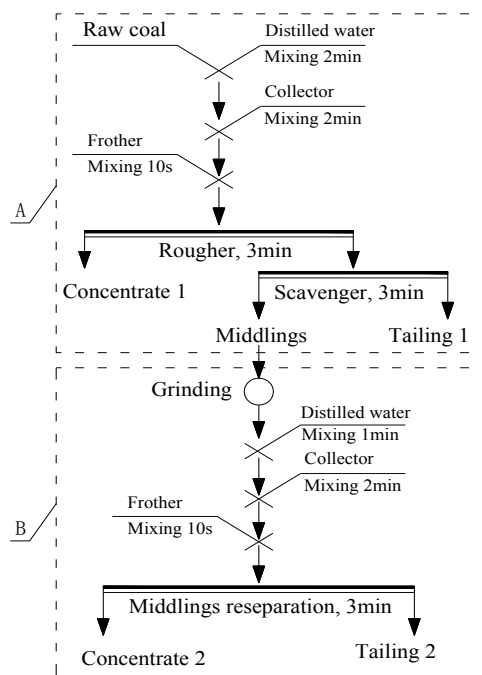


Fig. 1. Test flow-sheet

Results

Mineralogical and chemical analysis of the sample

The X-ray diffraction patterns of the -0.5 mm coal sample (Fig. 2) show that the main gangue mineral in the coal slime was kaolinite, with small amount of quartz, illite and pyrite. Kaolinite $\text{Al}_4[\text{Si}_4\text{O}_{10}](\text{OH})_8$, a very fine mineral is the major component of clay and argillaceous rocks. The exchange capacity of anions in kaolinite is relatively high. Organic reagents are adsorbed on the particle surface. It allows kaolinite to enter

easily to the concentrates through bubbles, which results in the high ash content in the concentrates.

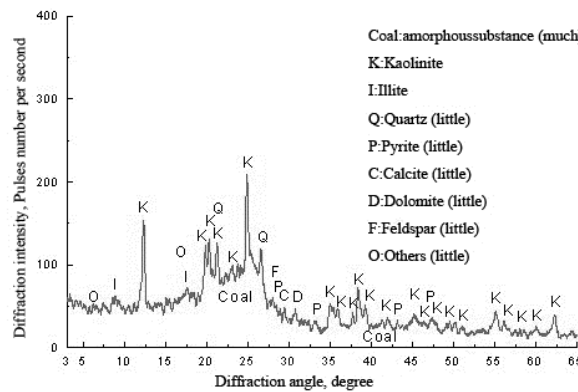


Fig. 2. X-ray diffraction patterns of -0.5mm coal sample

Density and size analyses

Figure 3 shows results of density and size analyses. It can be seen that the low density fraction of investigated coal was mainly located in the coarse particle size fraction. For instance, the density fraction less than 1.3 g/cm^3 was mainly located in particles coarser than 0.045 mm . However, the yield of density fractions from 1.3 to 1.5 g/cm^3 was uniform. The coal slime of density fractions of 1.5 – 1.8 g/cm^3 was the main cause of intergrowth of coal and gangue, which was verified in later petrological composition analysis.

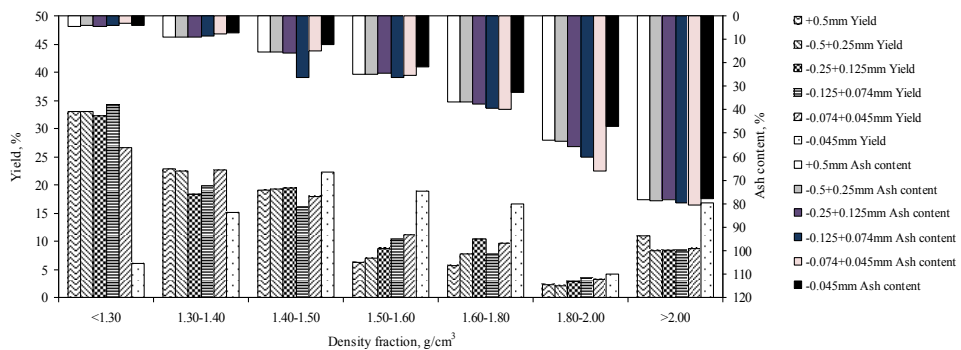


Fig. 3. Density analysis of narrow size fraction

Intergrown coarse particles easily entered the concentrates during flotation because of high desorption probability. Thus, mineral liberation prior to separation increased the recovery of combustible matter. Table 1 shows the yield and ash content of the middle density range (1.5 – 1.8 g/cm^3) of $+0.074 \text{ mm}$ size fraction. It can be seen that

the middle density range was 10.75% of raw coal with 31.50% ash content. This fraction was composed mostly of intergrown particles of coal and mineral matter. Thus, full liberation was a key to efficient separation.

Table 1. Yield and ash of middle density fraction

Density, g/cm ³	Size fraction, mm	Yield of size fraction, %	Yield of raw coal, %	Ash, %
1.5-1.8	+0.5	11.93	0.60	30.65
	-0.5+0.25	14.72	1.34	30.97
	-0.25+0.125	19.07	4.86	31.44
	-0.125+0.074	18.16	3.94	31.88
Total				10.75
				31.50

A mean-value curve can be used to show washability of coal (Fig. 4). The increasing trend of cumulative yield was weakened when the ash content was higher than 10%. The cumulative yield of five size fractions coarser than 0.045 mm, that is 0.5, 0.25–0.5, 0.125–0.25, 0.045–0.074 mm, was close for the same ash content. For a yield of about 80% the ash content was under 12%. The cumulative yield of fine size fraction (-0.045 mm) was the lowest.

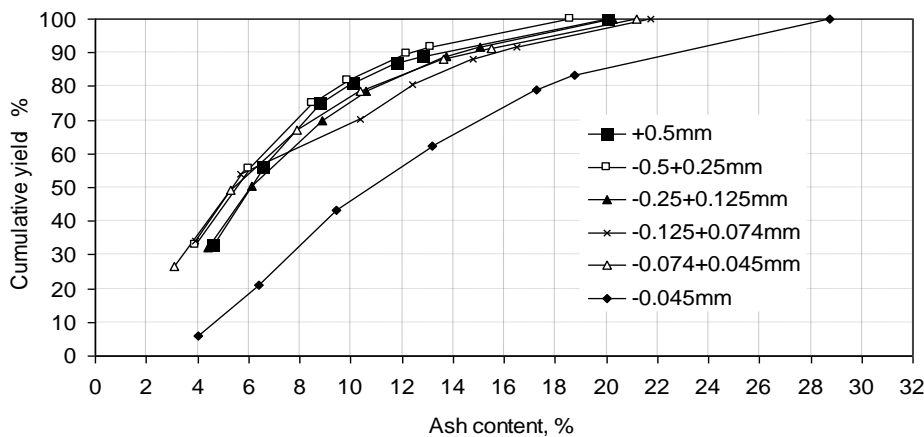


Fig. 4. Cumulative yield – ash content curve of narrow size fractions

Coal petrography

Table 2 shows that the coal sample mainly consists of vitrinite (56.34%) and inertinite (32%). The proportion of sample composition determined floatability due to differences in the physical properties of each maceral. Inertinite exhibits a very low floatability.

Table 2. Coal petrography analysis of particle sample

Sample	Organic maceral				Inorganic maceral		
	Vitrinite	Inertinite	Exinite	Clay	Pyrite	Calcite	Quartz
Content, %	56.34	32.44	1.76	6.38	2.15	—	0.93

Figure 5 shows the petrological composition of different density fractions. Inertinite, clay and pyrite contents increased with increase in density, whereas content of vitrinite gradually decreased. The majority of fine inorganic minerals in the middle density range ($1.5\text{--}2.0\text{ g/cm}^3$) were disseminated throughout the coal particles. Clay minerals always appeared to fill the plant cell in an aggregate form.

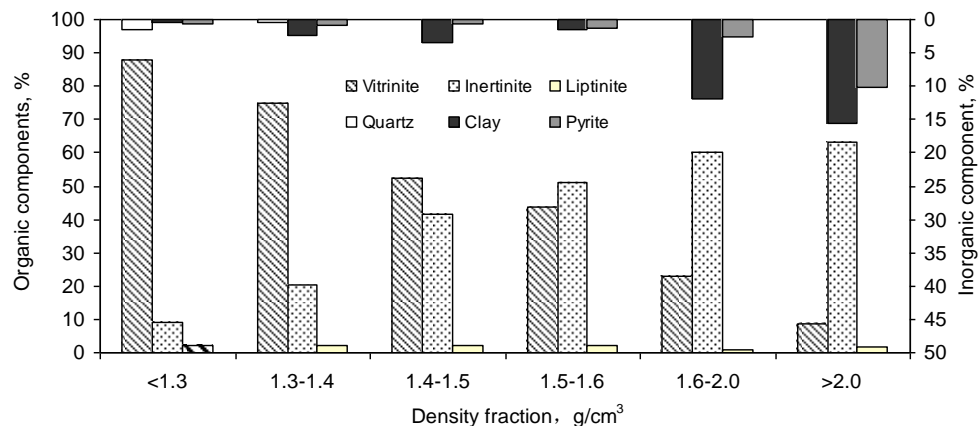


Fig. 5. Petrological composition of different density fractions

Figure 6 shows the petrological composition of different size fractions. The organic maceral content of each size fraction was very uniform. The vitrinite content ranged from 55 to 60%, and the content of inertinite was approximately 30%, with trace amounts of exinite. The content distribution of inorganic maceral was high in the coarse and fine fractions and low in the middle size fraction. A large amount of clay and quartz were disseminated in the coarse coal particles. The coal particles in $+0.125\text{ mm}$ size fraction filled the cell cavities and holes in the form of particle aggregates. The dissemination size of clay and pyrite was generally less than $10\text{ }\mu\text{m}$. Minerals almost appeared in the form of monomer in the fine particle size fraction (-0.045 mm). Dispersed clay particles of micro-fine size were occasionally observed in the coal particles (Fig. 7). The size analysis showed that the ash content of coarse size fraction was low. However, coarse coal particles disseminated with a large amount of inorganic minerals such as clay. Thus, liberation of coarse particles was clearly significant to the intensification process of fine coal.

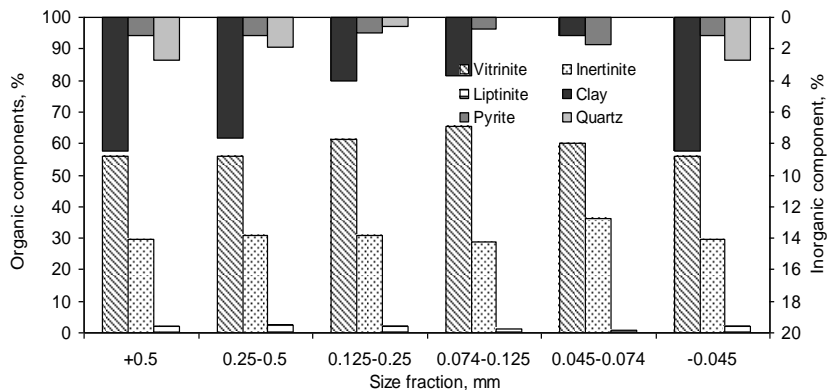


Fig. 6. Petrological composition of narrow size fractions

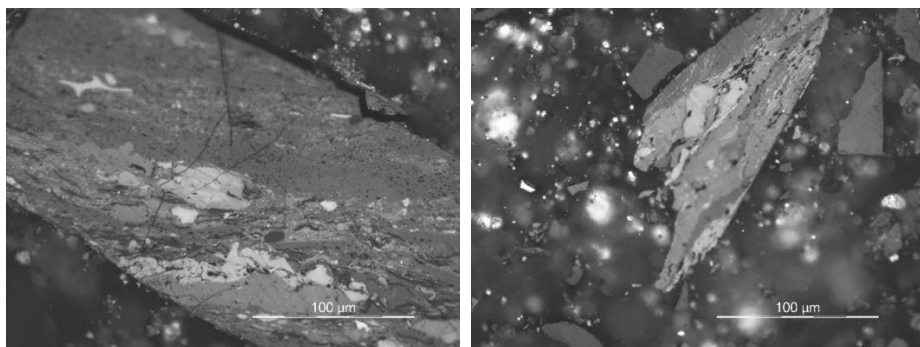


Fig. 7. Maceral composition photos of raw coal

Grinding test for the middlings

Middlings were first prepared as indicated in the flow-sheet in A-block diagram for the single-factor experiment (Fig. 1). The test conditions were as follows: 20% filling rate, 120 rpm wheeling speed, 40% grinding density, 300 g grinding dried slime, 5, 10, 15, and 20 min grinding time. Figure 8 shows changes in the yield and ash content of size fraction of -0.074 mm. The results show that the fine-sized middlings in the first 10 min were quickly reduced. The yield was 83.23% after 10 min of grinding. The slope of yield-time curve became significantly small and size reduction of materials became difficult in the next 10 min. The ash content decreased in the first 5 min. The organic matter in the coal was easier to grind than gangue. A considerable amount of low-ash clean coal among the inorganic matter was liberated and entered the next size fraction, which decreased the ash content. The decreasing trend of ash content of fine-sized fraction weakened with grinding time.

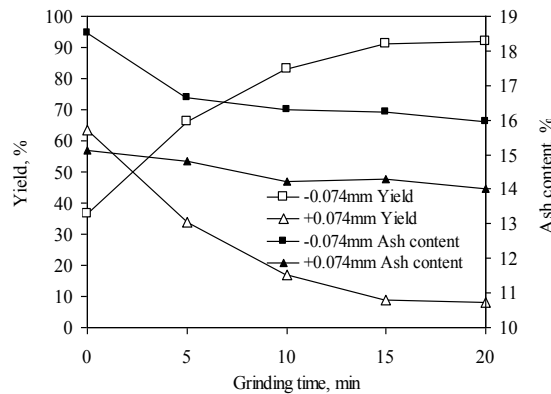


Fig. 8. Relationship between grinding time, yield and ash content

Table 3 shows that the yield of middle density fraction and ash content of low density fraction gradually decreased over grinding time. The density slightly changed when grinding time exceeded 15 min. These phenomena show that grinding was clearly effective by liberation of the middlings.

Table 3. Density analysis of different grinding times

Density fraction g/cm ³	0 min		5 min		10 min		15 min		20 min	
	Yield, %	Ash, %	Yield, %	Ash, %	Yield, %	Ash, %	Yield, %	Ash, %	Yield, %	Ash, %
<1.3	21.58	3.68	24.39	3.85	21.18	3.47	23.29	3.41	23.71	3.43
1.3-1.4	39.41	11.42	26.41	8.79	22.53	7.00	21.96	7.10	21.75	6.88
1.4-1.5	25.43	20.59	29.08	17.65	18.94	11.74	24.67	13.53	20.70	12.69
1.5-1.6	7.35	32.15	10.55	28.34	24.05	22.67	9.52	20.99	17.75	21.83
1.6-2.0	2.85	46.55	4.09	43.33	6.22	37.66	6.11	30.96	4.53	34.12
>2.0	3.38	54.04	5.48	50.60	7.08	49.85	14.45	43.73	11.56	46.66

In this work a four-factor and three-level orthogonal test was designed. The effect of different grinding conditions, such as filling rate, grinding time, wheeling speed and grinding density, on liberation of inorganic matter was comprehensively explored. Table 4 provides the results of the orthogonal test.

Table 5 shows the results of the variance analysis of yield and content of ash with density less than 1.4 g/cm³. The filling rate had the most obvious effect on the yield of clean coal. It can also be seen that the wheeling speed did not affect the yield. The grinding conditions with the greatest effect on the yield of clean coal after grinding were as follows: 20% filling rate, 130 rpm wheeling speed, 40% grinding density and 5 min grinding time. Grinding time had the most obvious effect on the ash content of clean coal. The grinding conditions with the greatest effect on the ash content of clean

coal were as follows: 40% filling rate, 120 rpm wheeling speed, 40% grinding density and 5 min grinding time.

Table 4. Data of the grinding orthogonal test

Group	Filling rate	Wheeling speed, rpm	Grinding density	Grinding time, min	-1.4 g/cm ³		+1.4 g/cm ³	
					Yield, %	Ash, %	Yield, %	Ash, %
1	20	110	30	5	24.72	8.61	75.28	19.76
2	20	120	40	10	26.32	7.08	73.68	20.78
3	20	130	50	15	23.52	7.51	76.48	19.54
4	30	110	40	15	13.61	6.52	86.39	17.81
5	30	120	50	5	15.14	7.88	84.86	18.45
6	30	130	30	10	12.44	7.04	87.56	18.08
7	40	110	50	10	19.64	7.64	80.36	18.80
8	40	120	30	15	13.90	8.20	86.10	17.71
9	40	130	40	5	27.00	14.55	73.00	16.07

Table 5. Variance analysis of clean yield and content of ash with density less than 1.4 g/cm³.

	Filling rate	Wheeling speed	Grinding density	Grinding time	Error			
					Yield, %	Ash, %	Yield, %	Ash, %
Square of deviance	187.17	14.99	9.94	8.39	42.08	5.04	41.83	18.22
Degree of freedom	2	2	2	2	2	2	2	8
<i>F</i>	2.664	1.286	2.664	0.72	0.599	0.432	0.595	1.562

F denotes the ratio of average sum of squared deviations and error average deviation squared error caused by changes in factor/level

The filling rate had different effects on the yield of low-density products. The yield of clean coal with density less than 1.4 g/cm³ decreased with increase in filling rate, whereas the ash content increased. The effect of grinding density and time on the products yield with low density were in a good agreement with each other. Thus, the optimum grinding conditions for liberation of middlings were determined to include the low filling rate and high wheeling speed.

Re-separation test of middlings

The re-separation test of liberated middlings was conducted as indicated in the flow-sheet in B block diagram of Fig. 1. The test conditions included collector (310 g/Mg), frother (125 g/Mg) and stirring speed of 1590 rpm, with flow of 0.37 m³/min. Table 6 shows the results of the test.

Table 6. Re-separation results of dissociated middling coal

Group	Filling rate, %	Wheeling speed, rpm	Grinding density, %	Grinding time, min	Clean coal		Physical Properties of feed middlings			
					Ash, %	Combustible recovery, %	Ash, %	Yield, %	Ash, %	Yield, %
8	40	120	30	15	12.28	31.49	16.37	13.90	8.20	69.99
4	30	110	40	15	12.33	37.25	16.60	13.61	6.52	93.42
3	20	130	50	15	12.25	46.57	16.49	23.52	7.51	96.73
6	30	130	30	10	12.27	46.91	16.42	12.44	7.04	85.53
2	20	120	40	10	12.04	48.45	16.50	26.32	7.08	86.39
7	40	110	50	10	11.99	61.62	16.71	19.64	7.64	70.59
1	20	110	30	5	12.18	67.87	16.43	24.72	8.61	64.79
9	40	130	40	5	12.49	76.66	16.15	27.00	14.55	45.37
5	30	120	50	5	12.51	76.72	16.17	15.14	7.88	52.46
Direct flotation	0	0	0	0	12.50	67.70	/	/	/	/

The ash content of liberated middlings was kept as 12.5% to fulfill the ash requirement of desired clean coal based on the re-separation test results of liberated middling coal (Table 6) in the Qianjiaying Coal Preparation Plant of Tangshan Kailuan Mine. The tests of Groups 1, 9, and 5 obtained the clean coal combustible recovery of approximately 70% and ash content of about 12.5%. The results of Groups 4 and Groups 8 were worsened, with the clean coal combustible recovery of just about 35% and ash content of 12.3%. The best three groups were found in the initial stage with grinding time of 10 min, whereas the worst two groups were observed at the latter stage at grinding time of 15 min. Therefore, longer grinding time did not result in higher recovery rate. The increase in grinding time led to overgrinding. A large amount of overground clay minerals covered the surface of coal particles and caused competitive adsorption of flotation reagents. It decreased the probability of collecting by bubbles the low ash content coals, resulting in low clean coal combustible matter recovery.

The grinding density had the most obvious effect on flotation. The sliming probability of clay minerals in middlings decreased as the grinding density increased. The yield of low density fraction of middlings floated after liberation increased. It suggests that high grinding density was beneficial for selective liberation of minerals. Based on the results of size analysis of liberated middlings the yield of fine particles (-0.074 mm) were: 50% in Group 1, Group 9 and Group 5, 93.42% in Group 4, 69.99% in Group 8 and 70.59% in Group 7. A significant difference existed between flotation of Groups 7 and 8, what indicated that different grinding conditions resulted in different size compositions and mineral liberations. The results of the liberation and re-separation tests for middlings showed that better flotation results were obtained when the yield of size fraction of -0.074 mm after liberation was approximately 50%.

Figure 9 shows the quantitative and qualitative flow-sheet of middling coal re-separation based on coal and rock liberation. Based on calculation of the whole flow-

sheet, the ash content of total concentrates was 12.41%, and the total concentrate combustible recovery was 75.82%. This value increased by 8.12 percentage when compared to raw coal direct flotation without liberation and re-separation of middlings.

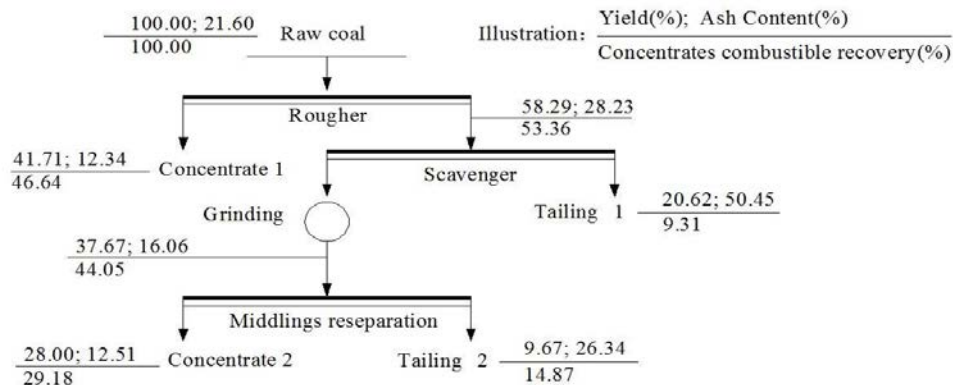


Fig. 9. Quantitative and qualitative flow-sheet of middling coal re-separation based on dissociated coal and rock

Physical characteristics of middlings

Middlings of Group 2 and Group 9, which are typical middling coal products in the grinding orthogonal test, were selected to determine mineral morphology of middling surface after dissociation. Figures 10–12 show that the content of coarse particle in middlings of Group 9 was larger than Group 8. A large number of micrometers grade clay minerals were observed on the middling coal surface and in the fissure of fractured ground particles after dissociation. Overly crushed coal particles dissociated and only little fine clay covered their smooth surfaces.

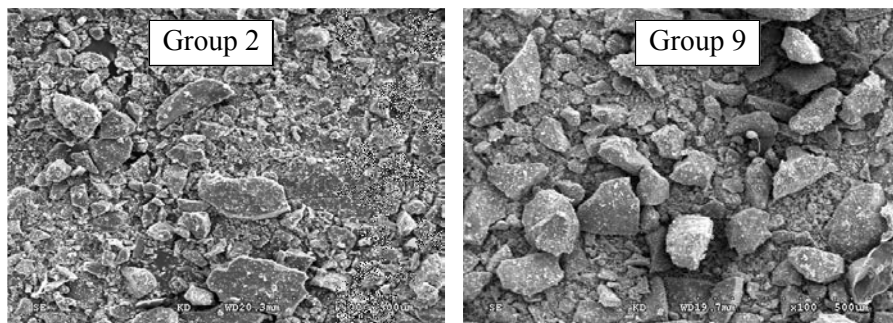


Fig.10. SEM photos of middlings of Group 2 and Group 9 coal after dissociation

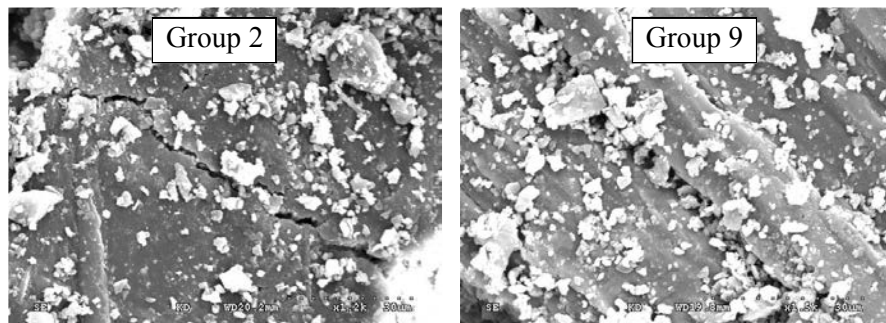


Fig. 11. Fracture SEM photos of middlings of Group 2 and Group 9 coal after dissociation

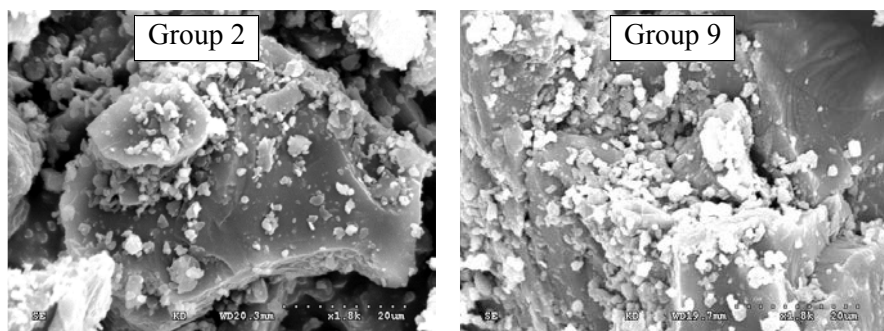


Fig. 12. Cleaves layer SEM photos of middlings of Group 2 and Group 9 coal after dissociation

Middlings of Group 9 in the grinding orthogonal test was selected for the density analysis. The petrography analysis was conducted for sample products with density less than 1.4 g/cm³ (Table 7 and Fig. 13). The liberated middlings sample had a large particle size that ranged from micrometers to millimeters. Telocollinite and desmocollinite account for 96% and 4%, respectively. Invitrinites are the primary macerals, followed by telinite and a small amount of corpovitrinite. Semivitrinite is mainly composed of half-desmocollinite and includes some half-telinite. Inertinite mainly consists of macrosome and includes small amounts of fusinite and semifusinite. Exinite is mainly composed of liptodetrinite, resinite and sporophyte. Clay minerals are finely dispersed. Sulfide minerals are mainly dispersed. Figure 13a shows that middling coal is ground into micrometers. Figure 13 b shows a large number of cracks and scratches on the particle surface, indicating that mineral grinding phenomenon occurred.

Table 7. Maceral composition of middlings of Group 9 after dissociation

Organic maceral, %					Inorganic maceral, %		
Vitrinite	Semivitrinite	Inertinite	Exinite	Clay	Sulphide	Carbonate	
83.45	3.50	10.45	1.15	1.20	0.25	—	

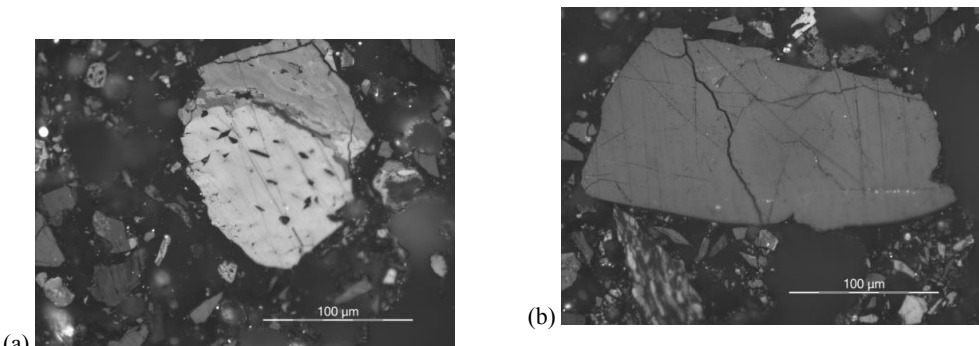


Fig. 13. Macerals map of middlings of Group 9 with density less than 1.4 g/cm^3 after dissociation

Table 9 shows that the contact angle of raw coal, measured by the sessile drop technique, was 68° , and increased to 85° with grinding time. Then, the contact angle decreased as the time increased after 15 min of grinding. This result suggests that grinding prompted coal to dissociate from the mineral and improved hydrophobic properties on its surface. However, heterogeneous fine silt covered the surfaces of coal particles when coal was ground too long. Also overground inorganic mineral particles reduced contact angle.

Table 9. Hydrophobicity of coal middlings over grinding time

Grinding time, min	0	5	10	15	20
Contact angle, $^\circ$	68	86.4	85.6	84.6	75.1

Conclusion

The results presented in this paper showed that the gangue mineral in the hard-to-separate coal slime of the Tangshan Kailuan mine was mostly kaolinite. The dominant size fraction of coal slime was -0.074 mm . The yield of middle density fraction was high and equal to 35%. The conventional separation process increased the difficulty-to-obtain high ash tailings and low ash concentrates.

The data on middling coal rock liberation in Group 9 showed that the maceral content in the low density fraction (less than 1.4 g/cm^3) was high and vitrinite enrichment was at its highest degree. Only a few inorganic minerals were found in low-density materials. Such finding was favorable to the flotation process. However, fine mud of clay minerals with high ash content was obtained during the liberation process.

The middlings coal rock liberation and re-separation tests were conducted in a laboratory scale. Grinding time had the greatest effect on the flotation performance. A high grinding density enhanced selective mineral liberation. The best flotation performance was obtained when the yield of -0.074 mm size fraction after liberation

was 50%. The clean coal combustible recovery after re-separation based on intergrown particles liberation increased by 8.12 percentage points when compared to raw coal direct flotation for the equal clean coal ash content.

Acknowledgements

This research was supported by the Fundamental Research Funds for the Central Universities (Grant no. 2014QNA26) and A Project Funded by the Priority Academic Program Development of Jiangsu Higher Education Institutions for which the authors express their appreciation.

References

CHENG, G., MA, L. Q., GUI, X. H., LIU, J. T., WANG, Y. T., 2013, *Study On Kinetic Modelling For Fine Coal Flotation*. International Journal Of Coal Preparation And Utilization, 33(1),12-25.

DU, M. H., 2006, *Coking Coal Resources And Production In China*, Coal Quality Technology, 6, 1-3.

MA, Q. Y., 2006, *Distribution Features Of Coking Coal Resources In China*, Coal Science And Technology, 32(3), 63-66.

JORJANI, E., ASADOLLAHI POORALI, H., SAM, A., CHEHREH CHELGANI, S., MESROGHLI, SH., SHAYESTEHFAR, M.R., 2009. *Prediction Of Coal Response To Froth Flotation Based On Coal Analysis Using Regression And Artificial Neural Network*. Minerals Engineering, 22(11), 970-976.

FU, X. H., WANG, Z. N., 1996, *Research On Separation Of Middlings From Prime Coal By Hydrophobic Flocculation-Flotation*, Journal Of China University Of Mining & Technology, 25(1), 57-61.

GUI, X. H., CHENG, G., LIU, J. T., CAO, Y. J., LI, S. L., HE, Q. Q., *Effects Of Energy Consumption On The Separation Performance Of Fine Coal Flotation*. Fuel Processing Technology, Vol. 115, Pp.192-200(2013).

GUI, X. H., LIU, J. T., CAO, Y. J., 2012, *Studies On Flotation Features Of A Hard-To-Float Fine Coal*, XXVI International Mineral Processing Congress , New Delhi, India, 1751-1761.

VAPUR, H., BAYAT, O., UÇURUM, M., 2010, *Coal Flotation Optimization Using Modified Flotation Parameters And Combustible Recovery In A Jameson Cell*. Energy Conversion And Management, 51(10), 1891-1897.

HU, Z. B., TAO, X. X., WANG, S. W., LI, X. X., 2011, *Decomposition Of Coal And Rock Group And Its Detection Method*,Coal Preparation Technology, 3, 4-7.

GIROUX L., KOLIJN C.J., PICHLER F.S., 2006, *Storage Of Small Samples Of Coking Coal For Thermal Rheological Tests*, Fuel Processing Technology 87(6), 547-561.

LI, Y., ZHAO, W., GUI, X., ZHANG, X., 2013. *Flotation Kinetics And Separation Selectivity Of Coal Size Fractions*. Physicochemical Problems Of Mineral Processing, 49(2), 387-395.

MAN, C. K., JACOBS, J., GIBBINS, J. R., 1998, *Selective Maceral Enrichment During Grinding And Effect Of Particle Size On Coal Devolatilisation Yields*. Fuel Processing Technology, 56, 215-227.

HARRIS, M.C., FRANZIDIS, J-P., O'CONNOR, C.T., STONESTREET, P., 1992. *An Evaluation Of The Role Of Particle Size In The Flotation Of Coal Using Different Cell Technologies*. Minerals Engineering, 5(10-12), 1225-1238.

JENA, M.S., BISWAL, S.K., DAS, S.P., REDDY, P.S.R., 2008. *Comparative Study Of The Performance Of Conventional And Column Flotation When Treating Coking Coal Fines*. Fuel Processing Technology, 89(12),1409-1415.

SHU, X. Q., WANG, Z. N., XU, J. Q., 2002, *Separation And Preparation Of Macerals In Shenshu Coal By Flotation*. Fuel Processing Technology .81, 495-501.

TAO, X. X., CAO, Y. J., LIU, J. Y., 2009, *Studies On Characteristics And Flotation Of A Hard-To-Float High-Ash Fine Coal*. The 6th International Conference On Mining Science Technology. 799-806.

WU, L. Q., 2007, *Reserves, Production, And Utilization Of Main Coking Coal Mining Areas In China*, Coal Quality Technology, 6, 20-23.

XIA, W., YANG, J., ZHAO, Y., ZHU, B., WANG, Y., 2012a, *Improving Floatability Of Taixi Anthracite Coal Of Mild Oxidation By Grinding*. Physicochemical Problems Of Mineral Processing. 48 (2), 393-401.

XIA W., YANG J., ZHU B., 2012b, *Flotation Of Oxidized Coal Dry-Ground With Collector*. Powder Technology, 228, 324-326.

XIA, W., YANG, J., LIANG, C, 2013, *A Short Review Of Improvement In Flotation Of Low Rank/Oxidized Coals By Pretreatments*. Powder Technology, 237, 1-8.

XU, Z. H., 2003, *Electro Kinetic Study Of Clay Interactions With Coal In Flotation*, International Journal Of Mineral Processing. 68, 183-196.

ZHANG, W., TANG, X., 2014, *Flotation Of Lignite Pretreated By Sorbitanmonooleate*, Physicochemical Problems Of Mineral Processing. 52 (2), 759-766.

Received April 29, 2015; reviewed; accepted June 28, 2015

DEVELOPMENT OF CHARACTERIZATION METHODS FOR ADHERENT ANODE SLIMES IN COPPER ELECTROREFINING

**Mikko KIVILUOMA, Miamari AALTONEN, Jari AROMAA,
Mari LUNDSTROM, Olof FORSEN**

Aalto University, School of Chemical Technology, PO Box 16200, FI-00076 AALTO, Finland,
mikko.kiviluoma@aalto.fi

Abstract: Adherent anode slimes can cause anode passivation in copper electrorefining and lower the efficiency of copper electrorefining. Declining concentrate grades cause larger impurity levels in anodes, thus creating larger quantities of slimes in the refining process. In order to investigate the characterization methods for adherent anode slimes in copper electrorefining, experiments were conducted for the Boliden Harjavalta Pori refinery material. Methods such as particle size determination, chemical (ICP) analysis, settling rate determination, XRD, SEM-SE, SEM-BSE and SEM-EDS were applied. In addition, adherent anode slime samples were compared to optical micrograph and SEM-BSE images of respective anode copper samples. It was shown that SEM-EDS and SEM-BSE provided precise information about phases formed during electrorefining. The settling rate and particle size had a correlation only with a copper content of anode slime. The main phases in the anode slime were copper and lead sulphates as well as copper-silver selenides. NiO was shown to be the major Ni-bearing phase in the adherent slime. Nickel, tellurium and lead had the strongest, whereas arsenic, selenium and antimony had the weakest tendency to report to the anode slime.

Keywords: anode, slime, copper, electrorefining, nickel, lead, arsenic

Introduction

The dominating trend for all metals refining processes in the 21st century is declining ore grades accompanied by increasing impurity levels. Between 2007 and 2013 there was an increase of roughly 20% in the main impurity elements of copper anodes (Moats et al., 2013). Solid phases in copper electrorefining that originate from anode impurities are referred as slimes. Anode slimes can be classified as adherent, bottom and floating slimes based on their location. These are further divided to primary and secondary slimes based on their formation mechanism (Wang et al., 2011).

The impurity elements in electrorefining report to either slimes or electrolyte. The major elements reporting to electrolyte are nickel and arsenic, whereas silver, lead, selenium and tellurium report to slimes. The dominant phases in anode slimes are complex oxides, lead sulphate and Ag-Cu selenides (Chen and Dutrizac, 1990). It has been reported that 85% of tellurium in the anode slimes exist in the Cu₂Se-Cu₂Te phase, where tellurium acts as a substitute atom for selenium. The Cu₂Se-Cu₂Te phase is rimming the complex oxide inclusions (Chen and Dutrizac, 1993; 2005). The limit for NiO formation is 0.25% nickel with suitable oxygen concentration and 0.32% nickel with any oxygen level (Forsen, 1985). Nickel may also be found in kupferglimmer, which forms at >0.3% Ni and >200 ppm Sb (Chen and Dutrizac, 1989). The formation methods of bismuth and antimony bearing compounds are not clear in electrorefining (Moats et al., 2012).

For an efficient electrorefining process the following anode slime characteristics are advantageous: (i) adequate adhesion to the surface of anode, but not too firm, (ii) rapidly sinking to the bottom of cell, and (iii) minimum amount of floating particles contaminating cathodes. The objective of this research was to develop a characterization methodology for anode slimes, and moreover to analyze the characteristics and elements excluding PGMs of adherent anode slimes.

Experimental

Adherent anode slime samples were collected from the Boliden Harjavalta's Pori refinery during March-April 2014 from 31 different anode cells, one anode lug and one adherent anode slime sample from each. The adherent anode slimes were collected before washing of anodes, at the end of the electrolysis cycle. Then, the samples were washed with water and filtered at Aalto University. After washing the filtered slime was divided into four sections. One section was dried, one used for particle size analysis and two for settling rate tests. The amount needed to perform all analyses was 50 g. Dried sections were further split into 20 fractions, using a spinning riffler (Microscal L/MSR). The split fractions were combined to create fractions for the chemical, XRD and SEM analyses.

Settling rate testing was done using a 250 cm³ measuring cylinder and slime to water concentration of 50 g/dm³. Particle size distribution was done with Malvern Mastersizer 2000, using distilled water as the dispersing agent and ultrasound to break agglomerates. The chemical analysis was done by a certified laboratory - Labtium Oy. A 0.05 g sample was leached at 90 °C with the aqua regia. The volume of the solution was 500 cm³. After leaching selected elements were analyzed with either inductively coupled plasma mass spectrometry (ICP-MS) or optical emission spectrometry (ICP-OES). Some of the slime samples were also analyzed by Boliden using x-ray fluorescence (XRF). The compounds of all samples were analyzed with a X'Pert PRO PANalytical PW3040/60 x-ray diffractometer. The used slits were FDS (fixed divergence slit, 0.5 mm), FASS (Fixed anti scatter slit, 1.0 mm), AS (automatic slit,

6.4 mm) and brass (15 mm). For SEM analyses about 2 g of dried slime sample was compressed to pellets using 7 megagram pressure. The pellets were further cast into epoxy, ground, polished and sputtered with carbon. Anode lugs were cut to 1 cm² samples, which were also ground and polished. Afterwards they were etched using the ferric chloride solution. The anode samples for SEM were not etched. The SEM used for backscatter electrons (BSE) and energy dispersive spectroscopy (EDS) was LEO model 1450 VP (manufactured by Zeiss, Germany) and Oxford Instruments INCA software. The secondary electron (SE) images were done by using the Tescan Mira 3 GMH microscope. Olympus PMG3 was used as the optical microscope.

Results

Copper anode

The average anode compositions used in this research are given in Table 1. The anode nickel content varied between 2000 and 5000 ppm. This concentration range favors formation of NiO-particles in anodes, which further report to anode slimes. Also the antimony level was sufficient in every anode to support kupferglimmer formation.

Table 1. Average anode and adherent anode slime chemical compositions of 31 anodes and adherent anode slimes determined by ICP-MS and ICP-OES

	Anode [ppm]	Slime [%]
Ag	1409	21.05
Pb	666	8.35
As	2481	5.40
Sb	492	3.73
Bi	536	5.48
Ni	3071	2.96
Te	249	1.50
Se	606	6.48
O ₂	1919	-
Cu	Bal.	17.70

Because of high variation in impurity levels, some distinctive differences were found in an anode microstructure using the combination of optical microscopy and SEM-BSE. Fig. 1 shows dendrites formed during cooling and impurities formed along grain boundaries. The darker areas between the dendrites are the eutectic phase that solidified last. However, the different impurities could not be identified from the optical image in Fig. 1. With the subsequent use of SEM-BSE (Fig. 2), the oxide impurity particles could be identified. The main impurity is Cu₂O that is clearly visible as dark grey areas in Fig. 2, and the other oxide impurities with high molar masses are white. Because NiO has lower molar mass than the copper matrix, it is seen as a dark

phase and can be identified from its crystal shape. Figure 2 also shows that that the oxide-phase (5) solidified between two Cu_2O inclusions and encapsulated them as one. Other phases in the anodes, not visible in Fig. 2, were as following: $\text{Cu}_2(\text{Se},\text{Te})$, kupferglimmer and Cu_2O . $\text{Cu}_2(\text{Se},\text{Te})$ was present in connection to other phases, kupferglimmer as a separate inclusion and Cu_2O as the most common impurity.

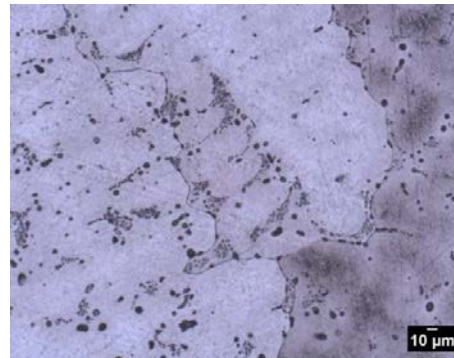


Fig. 1. Anode micrograph, 20x magnification, etched with ferric chloride.
Dendrites formed in cooling and impurities at grain boundaries

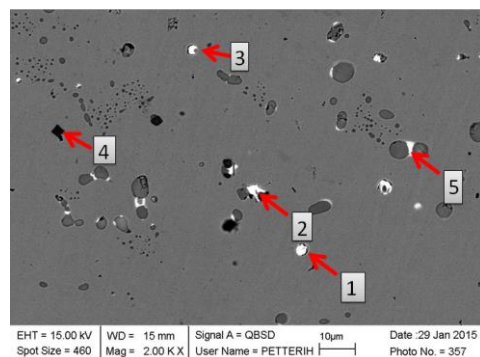


Fig. 2. SEM-BSE image of the same anode as in Fig. 1. (1) and (3) Bi-Pb-As-Sb-Cu oxide,
(2) Pb-As-Cu oxide, (4) NiO, (5) Pb-As-Sb-Cu-Ni oxide

Adherent slime chemistry

The correlation between anode composition and anode slime composition was calculated from chemical analyses (Table 2). The strongest correlation was observed between nickel, lead and tellurium contents. This suggests that most of nickel in anode slimes exists as non-soluble NiO as well as lead and tellurium also remain in the adherent slimes. The negative correlation of bismuth suggests that it remains dissolved in the electrolyte.

Table 2. Correlation between anode and adherent anode slime compositions

Ag	0.32	Bi	-0.23
Pb	0.51	Ni	0.72
As	0.18	Te	0.58
Sb	0.16	Se	0.17

There is also some correlation between other elements in anode slimes. Tellurium is present as a substitute atom in selenides. In the present study, the correlation between tellurium and selenium contents in anode slimes is 0.90. Another strong correlation of 0.86 is between bismuth and antimony in the anode slimes. Typical bismuth and antimony bearing compounds in the anode slimes are bismuth bearing antimonates (Moats et al., 2012). The chemical analysis of elements was further supported by the SEM-EDS analysis. The objective was to compare the chemical information given by EDS and chemical analysis. With EDS the high variation of nickel in the anode slimes (0.3-12.5 %) could be explained to be caused by NiO particles in some adherent slimes. From Figure 3 it can be seen that the adherent slime consists of more than 10 different phases and particles of 5-20 μm , with some enclosed phases. The results of EDS analysis are presented in Table 3. The advantage of EDS is opportunity to identify the elements in previously mentioned enclosed phases, such as gold in copper sulphate (3, Fig. 3).

The XRD analysis also showed that PbSO_4 is present in every anode slime sample. In addition the analysis confirmed the presence of NiO in the anode slime samples. Every sample with nickel content of >2% contained NiO-particles. The XRD analysis was also capable to identify kupferglimmer, which is challenging to detect from SEM-BSE images.

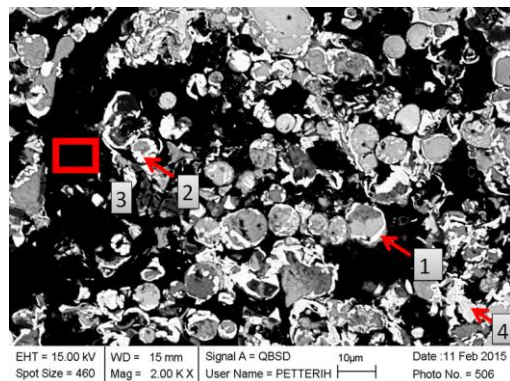


Fig. 3. SEM-BSE image of anode slime sample, (1) and (2) $\text{Ag}_2(\text{Se},\text{Te})$, (3) copper oxide - CuSO_4 , (4) $\text{CuAg}(\text{Se},\text{Te})$

Table 3. EDS-analysis of anode slime sample presented in Fig. 3

Analysis	O	S	Cu	As	Se	Ag	Sb	Te	Au	Pb	Total
1	3.4	0.2	3.4		19.5	62.8		8.1	0.6		98.0
2	8.4	0.8	3.6		17.0	60.6		7.6		4.4	102.4
3	15.4	3.1	47.9	6.7	3.7	5.3	1.3	0.8	2.3		86.5
4	3.9	0.8	12.3	1.0	21.2	48.4		8.1		4.1	99.8

Adherent slime imaging

The main imaging method for adherent anode slimes was SEM-BSE, which was used to determine different phases in the anode slime sample. Some samples were also examined with SEM-SE, in which the overall morphology of sample could be investigated. It was noticed that SEM-BSE is more applicable for characterization, especially with the EDS-detector. It is also noted that the precise use of the BSE-detector for anode slimes benefits from possibility to also use the SE-detector, which is normally found in a SEM-instrument. Figure 4 shows clearly that basing on the SEM-BSE different phases can be found in the anode slimes.

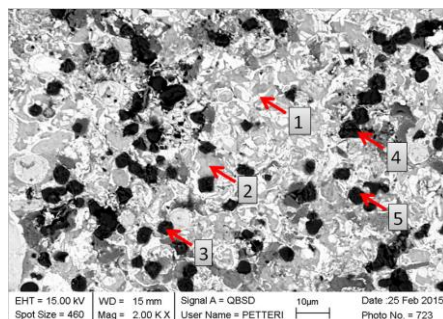


Fig. 4. SEM-BSE image of anode slime sample with NiO-particles.
(1) Cu-As-Sb-Pb –oxide, (2) Cu-As-Pb-Sb –oxide, (3), (4) and (5) NiO

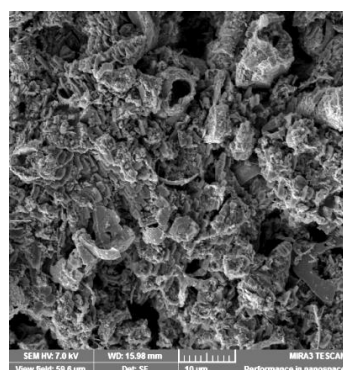


Fig. 5. SEM-SE image of anode slime sample,
which was not ground prior to imaging

Some of the anode slime samples were imaged using SEM-SE without treating the sample surface and an example is shown in Fig. 5. The image shows the slime topography clearly, but does not provide information regarding phase composition.

Adherent slime physical characteristics

An adherent slime was tested for physical characteristics with two different methods: the particle size analysis and settling rate test. The particle size analysis provided quantitative results with $d(0.1)$, $d(0.5)$ and $d(0.9)$ (in μm) and the settling rate test quantitative results in the form of sediment column height. The sediment column heights were further interpreted to three settling rate classes: slow, intermediate and fast. Using 250 mm initial column height, the slimes with fast settling rate reached final height in one minute, intermediate in two and slow in three minutes. From 27 tested slime samples, 11 referred to have fast settling, 14 intermediate settling and 2 slow settling. The particle size analysis was done for the anode slimes and the average sizes were $d(0.1)$ 3.9 ± 0.6 μm , $d(0.5)$ 13.3 ± 1.6 μm , and $d(0.9)$ 29.7 ± 4.5 μm . The particle sizes were not found to have a clear correlation with the settling rates. The most clear correlation was that the samples with slow settling rate had smaller $d(0.1)$ and $d(0.5)$ particle sizes. The average size of $d(0.1)$ was 9 μm for slow settling, whereas 3.9-4.2 μm for intermediate and fast settling. The size of $d(0.5)$ was 10.7 μm for intermediate and 13.4-14.2 μm for fast settling.

From the results it was found, that the increasing copper content of anode slimes correlated positively (0.74) with increasing particle size, especially in particle sizes of $d(0.1)$ and $d(0.5)$. Increasing lead and silver correlated negatively (-0.55), indicating smaller particle sizes. Hence, it was shown, that the chemical composition of adherent anode slime had the effect on the particle sizes. Using the information from the SEM-BSE images, it was shown that the copper sulphate particles were generally larger than lead sulphate and silver selenide particles. The copper content averages for slow, intermediate and fast settling rates were, 8.0 ± 2.1 , 15.8 ± 3.9 and $22.5\pm2.6\%$, respectively, showing that the copper content has the effect on the settling rate of anode slimes.

Conclusions

Characterization methods for adherent anode slimes were investigated in the current research. It was found that the most informative anode slime characterization for slime behavior in electrorefining is achieved by the chemical analysis of anode slimes supported with settling rate tests, XRD-analysis, SEM-BSE imaging and SEM-EDS analysis. The particle size analysis provided some additional information. Optical microscopy and SEM-SE imaging were not considered to be providing valuable characterization.

The anode lugs and corresponding adherent anode slimes were compared. It was shown that there is a strong correlation between nickel, lead and tellurium in the anode

and anode slime content. The high nickel concentration (> 2%) in anode slimes was shown to consist mostly of NiO-particles.

Particle size analysis showed that the chemical composition of anode slime has the effect on the particle size distribution. The copper content correlated positively with the small particle size. Higher copper content indicated on the large particle sizes $d(0.1)$ and $d(0.5)$, while higher silver and lead compositions indicated on smaller particle sizes. Increasing copper content of anode slime was shown to increase the settling rate of anode slime. The advantageous characteristics of anode slimes for efficient electrorefining were achieved with high copper and low lead and silver contents.

Acknowledgements

This work has been performed within the “*System integrated metals processing*” (SIMP) project coordinated by the Finnish Metals and Engineering Competence Cluster FIMECC Ltd. The authors are grateful for Boliden Harjavalta Copper Refinery for permission to publish the results.

References

CHEN T.T., DUTRIZAC J.E., 1989. *Minerological Characterization of Anode Slimes - IV. Copper-Nickel-Antimony Oxide ("Kupferglimmer") in CCR Anodes and Anode Slimes*. Canadian Metallurgical Quarterly, 28(2), 127-134.

CHEN T.T., DUTRIZAC J.E., 1990. *The Mineralogy of Copper Electrorefining*. Journal of Metals, 42(8), 39-44.

CHEN T.T., DUTRIZAC J.E., 1993. *The Minerological Characterization of Tellurium in Copper Anodes*. Metallurgical Transactions B, 24B, 997-1007.

CHEN T.T., DUTRIZAC J.E., 2005. *Mineralogical characterization of a Copper Anode and the Anode slimes from the La Caridad Copper Refinery of Mexicana de Cobre*, Metallurgical and materials Transactions B, 36B, 229-240

FORSEN O., 1985. *The behaviour of nickel and antimony in oxygen-bearing copper anodes in electrolytic refining*. Doctoral thesis. Helsinki University of Technology. Espoo, Finland.

MOATS M., ROBINSON T., WANG S., FILZWIESER A., SIEGMUND A., DAVENPORT W., 2013. *Global Survey of Copper Electrorefining Operations and Practices*. Abel, R. & Delgado, C. (eds.) Proceedings of Copper 2013, Volume V, Electrowinning / Electrorefining. Santiago, Chile. 307-318.

MOATS M.S., WANG S., KIM D., 2012. *A Review of the Behavior and Deportment of Lead, Bismuth, Antimony and Arsenic in Copper Electrorefining*. Wang, S. & Dutrizac, J. E. & Free, M. L., Hwang, J. Y., Kim, D. (eds.). T. T. Chen Honorary Symposium on Hydrometallurgy, Electrometallurgy and Materials Characterization. Hoboken, New Jersey, USA. 3-21.

WANG X., CHEN Q., YIN Z., WANG M., XIAO B., ZHANG F. 2011. *Homogenous precipitation of As, Sb and Bi impurities in copper electrolyte during electrorefining*. Hydrometallurgy, 105, 355-358.

Received May 3, 2015; reviewed; accepted July 14, 2015

PROPERTIES OF FATTY ACID/DODECYLAMINE MIXTURES AND THEIR APPLICATION IN STEAM COAL REVERSE FLOTATION

Liang SHEN^{*}, Huaifa WANG^{*, **}

^{*} College of Mining Engineering, Taiyuan University of Technology, Taiyuan 030024, Shanxi, China

^{**} Key Laboratory of Coal Science and Technology of Ministry of Education and Shanxi Province, Taiyuan University of Technology, Taiyuan 030024, Shanxi, China, Corresponding author, tyut01@126.com

Abstract: A series of surfactant mixtures which consist of DAH (dodecylamine hydrochloride) and fatty acids (FAD) were made in this study. The characteristics of these fatty acids/DAH mixtures, including surface tension, critical micelle concentration (CMC) and adsorption onto coal were investigated. The reverse flotation results with these fatty acids/DAH mixtures (FAD) and DAH were compared with each other. Experimental results showed that the fatty acids/ DAH mixtures have lower CMC and γ_{cmc} than DAH. The adsorption test indicated that more amine molecules would adsorb preferentially onto the bubbles surface in FAD solutions than that in DAH solutions. Reverse flotation results showed that about 50% surfactant dosage was saved under the same froth product yield. Only 28% froth product yield was obtained in the presence of 1.66 kg/Mg DAH. However, when 0.83 kg/Mg hexadecanoic acid/DAH mixture (C16D) surfactant was used, the froth product yield reached 29%. Dodecanoic acid/DAH mixture (C12D) surfactant a showed better performance with a high mineral matter recovery similar to that with tetradecanoic acid/DAH mixture (C14D) and higher combustible recovery than with C14D and C16D.

Keywords: steam coal, surfactant mixture, reverse flotation, fatty acids, surface activity

Introduction

Even though the coal reverse flotation process has some obvious advantages over forward flotation and a development period of around 50 years starting from 1960s, it is still an established route neither for ash reduction nor for pyrite removal. This indicates that there is scope of improvement and more work needs to be done in order to bring the process to the commercialization stage. The idea of reverse flotation was first patented by Eveson in 1961. The concept was further developed for the selective removal of pyritic sulphur from US coals by several investigators (Baker et al., 1973; Miller, 1973, 1975, 1978; Miller and Deurbrouck, 1982; Lin, 1982; Miller et al.,

1984). Consequently, the study of reverse flotation of coal with a motive to lower the ash content of coal was carried out by many scientists and researchers (Stonestreet and Franzidis, 1988, 1989, 1992; Pawlik and Laskowski, 2003a, 2003b; Ding and Laskowski, 2006a, b; Patil and Laskowski, 2008, Zhang et al., 2013; Ozturk and Temel, 2013; Xia and Yang, 2013a; Zhang and Liu, 2015).

The driving force behind the works done so far to develop reverse flotation as a viable processing tool to produce clean coal is the advantages associated with it. Coal makes up around 60% to 80% of the flotation feed and as the coal rises, with it gangue particles also rise which cannot be avoided. This problem is known as ash entrainment which is inevitable during direct flotation and adversely affects the quality of product (Angadi and Suresh, 2005; Angadi et al., 2012). Here coal reverse flotation can provide a good substitute as the gangue particles are floated with some coal entrainment. But in comparison to ash entrainment, coal entrainment will be less significant due to the coarser size of coal particles and smaller physical mass transfer of coal into the froth. Another benefit is the reduction of mass transfer as the gangue material makes up 15% to 35% of the feed. So the concentrate mass is lowered and the overall carrying capacity of the froth is reduced which implies that reverse flotation can be carried out at higher pulp densities and using small sized equipment. The gangue minerals in comparison to coal have a consistent chemical composition and well defined structures which impart them uniform floatability. Above all, these coal reverse flotation may prove to be a better option for coals with poor floatability characteristics which do not give sufficient recovery with forward flotation.

With the increasingly serious air pollution in China, coal slime in steam coal preparation plants need to be upgraded with flotation technology. However, it is difficult to float these coal slimes in conventional coal flotation processes due to its low hydrophobicity. Compared with flotation of coal slimes in coking coal preparation plants, a certain amount of ash reduction can be acceptable for coal slimes in steam coal preparation plant. Therefore, reverse flotation of steam coal slimes should be more suitable.

Although coal reverse flotation displays these advantages, it is still not brought to the commercialization stage. The main obstacle is the huge dosage and the expensive price of the collector. Thus, many scientists and researchers have studied on many ways to decrease the dosage of the collector. According to the papers by Pawlik and Laskowski (2003b) and Ding and Laskowski (2006a), dodecyltrimethyl ammonium chloride (DTAC) was used as collector which showed good separation but not at dosage lower than 6 kg/Mg. They found that for hydrophilic oxidized and sub bituminous coals high dosages of amine (around 4 ~ 6 kg/Mg), were needed to initiate the reaction. In addition, they found that the use of PAM (polyacrylamide) along with the zero-conditioning method brought down the amine dosage from 6 kg/Mg to 1.375 kg/Mg at rejection yield more than 80% (Ding and Laskowski, 2006b). In this paper, mixtures of DAH (dodecylamine hydrochloride) and fatty acids were made and used as mineral collectors. Generally, surfactant mixtures can have a number of synergistic

advantages over the use of a single surfactant type. Many studies have been conducted on mixed micellar systems that consist of two surfactants (Fang et al., 2003; Penfold et al., 1996; Xiao et al., 2000; Rubingh and Jones, 1982; Xue et al., 2009). Among various surfactant combinations, mixed cationic–nonionic surfactants are of great interest because of their strong synergistic effects on the interfacial properties and spontaneous vesicle formation behavior in aqueous phases (Desai and Dixit, 1996; Penfold et al., 1997; Vora et al., 1999). A system that contains two surfactants of different charge is called a catanionic system. The attraction between the different charged head groups will lead to a decrease in the area per head group (Herrington et al., 1993). However, there are limited studies on the application of surfactant mixtures in coal reverse flotation.

In this paper, five different fatty acids were mixed with DAH respectively. The characteristics of these fatty acids/DAH mixtures, including surface tension, critical micelle concentration (CMC) and adsorption onto coal were investigated. And the reverse flotation results with these fatty acids/DAH mixtures and DAH were compared with each other. In this paper, gangue minerals are floated into froth as froth products, clean coals are left in flotation pulp as concentrate.

Experiment method and procedure

Samples and reagents

Coal samples were obtained from the Steam Coal Preparation Plant in the Shanxi Province. The over 0.5mm size materials were removed. The proximate analysis of coal samples (air-dried) is given in Table 1, where M_{ad} is the moisture content, V_{ad} the volatile content, FC_{ad} the fixed carbon content, A_{ad} the ash content, and S_t is the total sulfur content.

Table 1. Proximate analysis of oxidized coal sample (air dried)

M_{ad} (%)	V_{ad} (%)	FC_{ad} (%)	A_{ad} (%)	S_t (%)
6.02	30.47	38.01	25.5	0.8

The size composition of coal samples is given in Table 2. The weight of -0.04mm size fraction is the highest which is 68.34%. Meanwhile, the ash content of -0.04mm size fraction is the highest which is 33.01%. The size composition of coal samples indicates that the coal is primarily made up of fine coals with high ash content.

X-ray diffraction is used to study the composition of coal samples. The XRD test was performed at room temperature. The samples were ground to $-50\mu\text{m}$. The step size of the test is 0.01° and the speed is $8^\circ/\text{min}$. The scanned area is $5^\circ \sim 80^\circ$.

Table 2. Size composition of coal samples

Size fraction (%)	Weight (%)	Ash content (%)
-0.5 + 0.25	3.25	8.66
-0.25 + 0.125	9.38	9.52
-0.125 + 0.074	9.45	9.88
-0.074+0.045	9.58	10.21
-0.045	68.34	33.01
Total	100.00	25.65

Figure 1 showed that the main gangue mineral in the coal sample is kaolinite and quartz. The IEP of kaolinite was at pH 1.8. And the IEP of quartz was 2.7. Thus, in these experiments they could be floated by cationic collector.

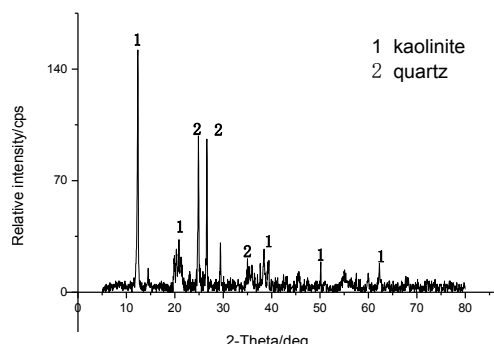


Fig. 1. X-ray diffraction patterns of the sample

The analytically grade DDA (dodecylamine) used in this study was obtained from the Tianjin Guangfu Chemical Research Institute. Hydrochloric acid (HCl) and sodium hydroxide (NaOH) were used as pH regulators. HCl and NaOH used in this study were of analytical grade obtained from Aladdin Reagent (China). DDA neutralized with HCl regarded as DAH, the solution concentration was 0.135 mol/dm³. Reagent grade fatty acids and dextrin were supplied by Aladdin Reagent. The following fatty acids were used: n-octanoic acid, C8 (purity ≥98%), n-capric acid, C10 (purity ≥98%), dodecanoic acid, C12 (purity ≥98%), tetradecanoic acid, C14 (purity ≥98%) and hexadecanoic acid, C16 (purity ≥98%). All surfactants and fatty acids were used as received. The full names and abbreviations of all reagents were listed in Table 3. Each fatty acid was mixed with 50 cm³ DAH solution and stirred with a magnetic stirrer at 50 °C until a homogeneous mixture was obtained. The pHs of the mixtures were 3.8–4.1 and the molar ratio of DAH and fatty acid was 1:1.

Table 3. Reagents

Full name	Abbreviation
Dodecylamine	DDA
Hydrochloric acid	HCl
Sodium hydroxide	NaOH
Dodecylamine Hydrochloride	DAH
Fatty acid/DAH mixture	FAD
n-octanoic acid/DAH mixture	C8D
n-capric acid/DAH mixture	C10D
Dodecanoic acid/DAH mixture	C12D
Tetradecanoic acid/DAH mixture	C14D
Hexadecanoic acid/DAH mixture	C16D

Methods

Surface tension measurement

Surface tension measurements were determined at pH=5 by the du Nouy ring method using a LAUDA (TEIC) Tensiometer (Germany). The instrument was calibrated against double distilled water. Measurements were made at intervals of a few minutes until successive values agreed within a standard deviation of 0.1mN/m or less. The CMC values were determined graphically as the intersection point of the two linear portions of the plot (Li et al., 2000).

Adsorption experiments

In these tests, 1 g of the clean coals were preconditioned for 20 min with 25 cm³ of tap water in 100 cm³ glass bottles, placed in a magnetic stirrer at 800 rpm, to ensure complete wetting of the solids. Then 1 cm³ of solutions of different concentrations were added to each sample and the mixtures were conditioned for 1 h at pH=5 which was sufficient to achieve adsorption equilibrium. Then the centrifugate of the solution was used for cationic collector concentration test. Cationic collector concentration was measured using the Eosin Y method (limit of detection less than 10.0 mg/dm³)(Qin and Tan, 2006). The absorbance of DAH-Eosin Y complex was measured with a UV/Vis spectrometer at 516.5 ± 0.5 nm in a 1.0 cm long quartz cuvette respectively. The amount of collector adsorbed was calculated using the expression:

$$n_{ads} = \frac{(C_0 - C_{eq})V}{m} \quad (1)$$

where n_{ads} is the adsorption quantity of collector per gram of coal, C_0 is the initial concentration of collector, C_{eq} is the concentration of collector at a given time after

adsorption, V is the volume of the solution and m is the weight of coal sample. The standard curve of DAH solution was showed in Fig. 2.

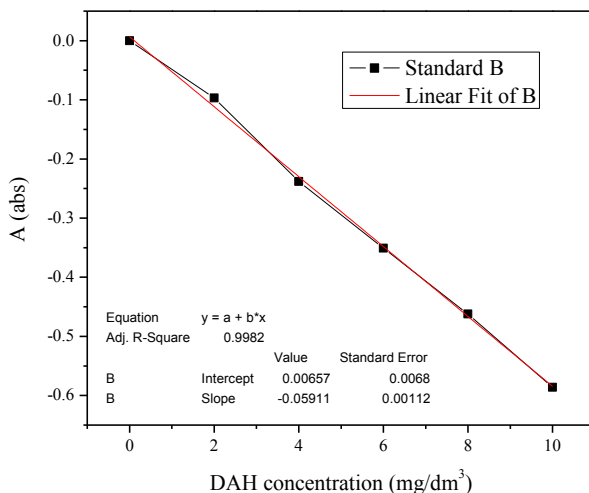


Fig. 2. Standard curve of DAH solution (pH = 5)

Adsorption of DAH and FADs on bubbles

In these tests, different dosages of DAH and FADs were added to a 1 dm³ XFD laboratory flotation cell, respectively. The concentrations of the collectors were 0.27 mmol/dm³, 0.35 mmol/dm³, 0.43 mmol/dm³ and 0.54 mmol/dm³. The impeller speed is 1800 rpm, which produced an aeration rate of 1.33 dm³/min. The bubbles were collected after 5mins and the concentrations of surfactants in the flotation cell were then measured using the Eosin Y method.

Reverse flotation test

Reverse flotation tests were carried out in a 1 dm³ XFD laboratory flotation cell. In all flotation tests, a 60 g sample was used. The impeller speed in both conditioning and flotation processes is 1800 rpm, which produced an aeration rate of 1.33 dm³/min. The coal sample was first prewetted in flotation cell for 1 min. Then pH was adjusted with HCl at pH = 5. Dextrin was added to flotation slurry and conditioned for 2 min. Then collector was added and conditioned for 1 min. Each flotation test was performed for 5 min. The dosage of dextrin was 0.8 kg/Mg. The dosages of collectors were 0.83 kg/Mg, 1.08 kg/Mg, 1.33 kg/Mg, and 1.66 kg/Mg corresponding to 0.27 mmol/dm³, 0.35 mmol/dm³, 0.43 mmol/dm³ and 0.54 mmol/dm³.

Results and discussion

Surface activity of DAH and FADs

The results of surface tension (γ) measurements of DAH and FADs are shown in Fig. 3. Surface tension decreases rapidly with increasing concentration and each curve has a level off point at the concentration corresponding to critical micelle concentration CMC, then remains at an almost constant value at higher concentration. Figure 3 shows that the surface activity of the surfactant increased with the increasing of hydrocarbon chain length of the fatty acids. The critical micelle concentration (CMC) and the surface tension at CMC, γ_{cmc} , were showed in Table 4. Generally, increasing the hydrocarbon chain of the surfactant leads to the surfactant molecules being more hydrophobic. As a result, surfactants with longer hydrocarbon chains have a driving force for the aggregation, and thus dramatically reduce the solution CMC. At air/water interface, the minimum surface area per adsorbed FAD molecule, A_{min} was obtained from the excess surface concentration Γ_{max} using the equation:

$$A_{min} = \frac{1}{\Gamma_{max} N_A} \quad (2)$$

where Γ_{max} is the excess surface concentration (mol/cm^2), the excess surface concentration Γ_{max} can be calculated from the Gibbs isotherm, according to the equation below:

$$\Gamma_{max} = -\frac{d\gamma}{RTd(\ln C)} \quad (3)$$

Here γ is the surface tension in N/m , R is gas constant ($8.314 \text{ J}/\text{mol K}$), T is the absolute temperature and C is the molar concentration of surfactant (mol/dm^3). The term $[dC/d(\ln C)]$ is the slope of $\gamma-\ln C$ plot before the CMC. The values of CMC, surface tension at CMC and Amin of FAD are listed in Table 4.

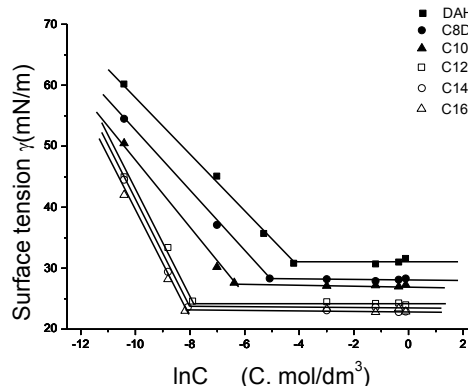


Fig. 3. Surface tension of DAH and FADs solutions in tap water ($\text{pH} = 5$)

From the relation between Γ_{\max} , A_{\min} and FADs, it is evident that the Γ_{\max} in the adsorbed state at liquid/air interface became larger as the length of fatty acid chain increased. It means that more surfactants would adsorb on the liquid/air interface. And the decrease of the A_{\min} indicated that the surfactants molecules adsorbed more closed in the adsorption layer.

Table 4. Surface parameters of DAH and FADs (the values of the CMC, surface tension at CMC, γ_{cmc} , the average area per surfactant molecule, A_{\min} and the excess surface concentration, Γ_{\max})

Reagent	CMC(mol/dm ³)	γ_{cmc} (mN/m)	Γ_{\max} /(mol/cm ²)	A_{\min} /nm ²
DAH	$1.5 \cdot 10^{-2}$	31.2	$1.88 \cdot 10^{-10}$	0.88
C8D	$6.2 \cdot 10^{-3}$	28.1	$1.96 \cdot 10^{-10}$	0.84
C10D	$1.7 \cdot 10^{-3}$	27.3	$2.27 \cdot 10^{-10}$	0.73
C12D	$3.7 \cdot 10^{-4}$	24.1	$3.36 \cdot 10^{-10}$	0.49
C14D	$3.1 \cdot 10^{-4}$	23.7	$3.58 \cdot 10^{-10}$	0.46
C16D	$2.8 \cdot 10^{-4}$	22.9	$3.65 \cdot 10^{-10}$	0.45

Adsorption of DAH and FADs onto coal

The adsorption density of DAH and FADs on clean coals was shown in Fig. 4. As it illustrated, the adsorption density of DAH and FADs on coal increased with the increase of the equilibrium concentration. The shapes of adsorption isotherms of DAH and FADs on coals were similar to each other. At low concentration, the surfactants adsorb as individual molecules through some interactions between the negatively charged sites on the coal surfaces and the positively charged amine cations. With the increasing of the equilibrium concentration near the CMC, the adsorption density increased intensely due to the interactions between the hydrocarbon chains. Meanwhile, the adsorption density of FADs on the coal was higher than that of DAH. It may cause by the interactions between the hydrocarbon chains of DAH and fatty acids.

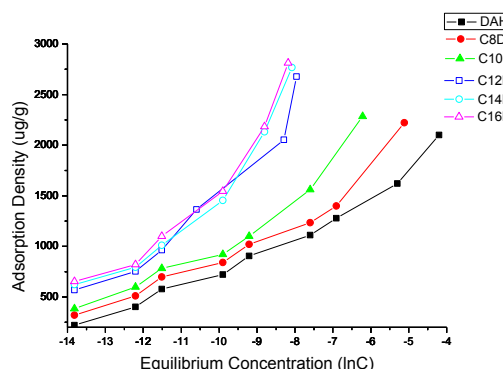


Fig. 4. Adsorption isotherms of DAH and FADs onto coals (pH = 5)

Adsorption of DAH and FADs on bubbles

The adsorption results of DAH and FADs on bubbles are shown in Fig. 5. As it illustrated, the FADs surfactants were much easier to adsorb on the bubbles surface. The adsorption amount of C16D surfactant on bubble surface was almost six times more than that of DAH.

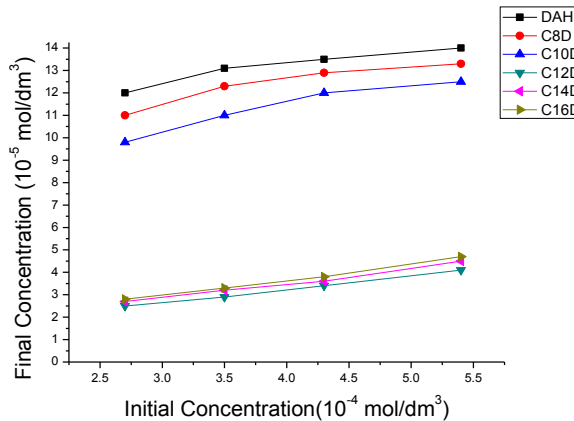


Fig. 5. Adsorption of DAH and FADs surfactants on bubbles (pH = 5)

A probable interaction mechanism of DAH and fatty acid was proposed. Figure 6 shows the schematic representation of the structure of adsorption layer at pH 5. According to the proposed structure, the fatty acid molecules adsorb between the DAH molecules in the adsorption layer and, thus, decrease significantly the average area per surfactant molecule in the adsorption layer. It conformed to the results of surface tension test. Based on the proposed structure of the adsorption layer, we can explain why the FADs showed a stronger collectivity than DAH. The “bubble transfer” hypothesis has been proposed by other researchers (Digre and Sandvik, 1968). They postulated that during a real flotation process, amine molecules are transferred onto particles surfaces by repeated collisions with the amine-coated air bubbles. So air bubbles indeed act as “amine carriers” (Pawlak and Laskowski, 2003a). In FADs solutions, more amine molecules would adsorb onto bubbles surfaces than that in DAH solutions. Thus, it can enhance the adhering of particles onto bubbles surface and prevent the desorbing. As a result, a high froth product yield would be obtained. Zero-condition time concept in reverse flotation was proposed by Laskowski. He pointed that using the DTAB-coated bubbles in coal reverse flotation would lead to a decrease in DTAB consumption and increase the froth product yield. Amine-coated bubbles would be more easily to adhere to the particles in flotation process.

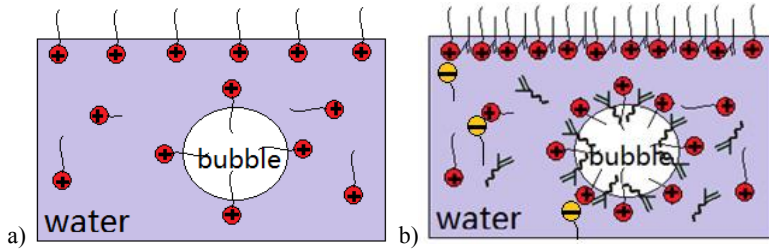


Fig. 6. Schematic presentation of structure of adsorption layer at pH 5
(a) Bubbles in DAH solution, (b) Bubbles in FADs solutions

Reverse flotation results

The reverse flotation results were shown in Fig. 7. It can be seen in Fig. 7a that the FADs showed stronger collectivity than DAH. Only 28% froth product yield was obtained in the presence of 1.66 kg/Mg DAH. However, when 0.83 kg/Mg C16D surfactant was used, the froth product yield reached 29%. About 50% surfactant dosage was saved under the same froth product yield.

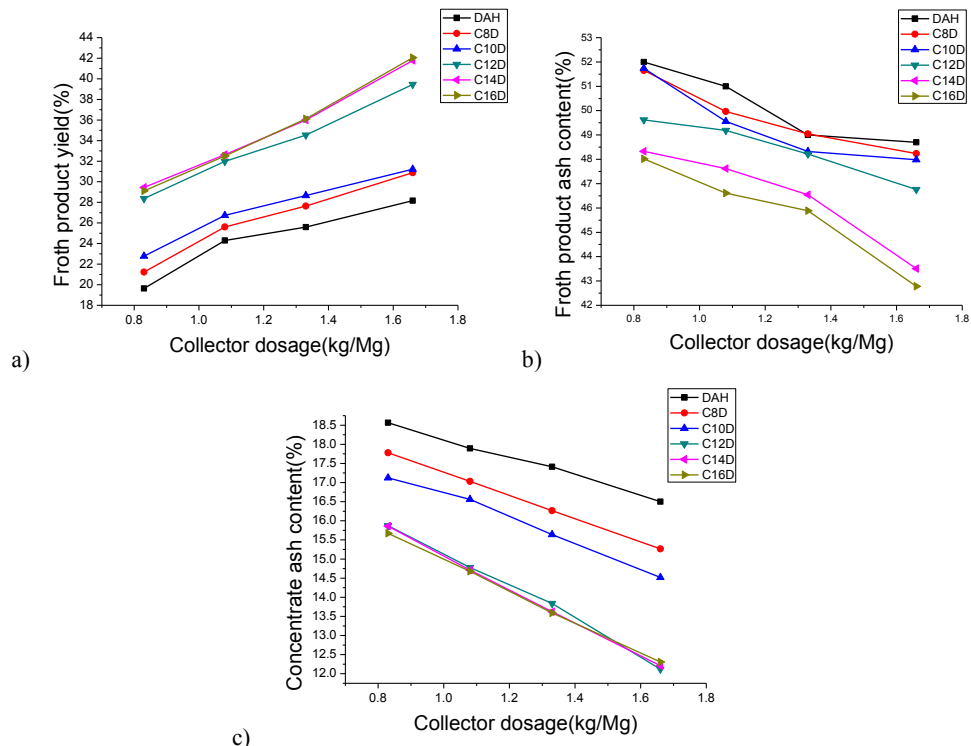


Fig. 7. Reverse flotation results in the presence of DAH and FADs (pH = 5)
(a. Froth product yield b. Froth product ash content. c. Concentrate ash content
in the presence of DAH and FADs)

Figure 7b showed that the selectivity of the FADs decreased with the increasing of hydrocarbon chain length of the fatty acids. This was consistent with the adsorption test results in Fig. 4. The adsorption amount of FADs on coals increased with the increasing of hydrocarbon chain length of the fatty acids.

Table 5. Reverse flotation results

Surfactant name	Dosage (kg/Mg)	Froth product yield (%)	Froth product ash content (%)	Concentrate yield (%)	Concentrate ash content (%)	Mineral matter recovery (%)	Combustible recovery (%)
DAH	0.83	20	52.00	80	18.56	41	87
	1.08	24	51.00	76	17.17	49	84
	1.33	26	49.00	74	17.41	49	82
	1.66	28	48.70	72	16.50	54	81
C8D	0.83	21	51.65	79	17.78	44	86
	1.08	26	49.97	74	17.03	50	83
	1.33	28	49.04	72	16.27	54	81
	1.66	31	48.24	69	15.27	59	79
C10D	0.83	23	51.74	77	17.12	47	85
	1.08	27	48.46	73	16.56	52	82
	1.33	29	48.32	71	15.64	55	80
	1.66	31	47.98	69	14.52	60	78
C12D	0.83	28	49.62	72	15.87	55	81
	1.08	32	49.19	68	14.78	61	78
	1.33	35	48.21	65	13.84	65	76
	1.66	39	46.76	61	12.12	72	72
C14D	0.83	29	48.33	71	15.86	56	80
	1.08	33	47.62	67	14.71	61	77
	1.33	36	46.54	64	13.62	66	74
	1.66	42	43.51	58	12.21	72	68
C16D	0.83	29	48.02	71	15.67	56	80
	1.08	33	46.61	67	14.68	60	77
	1.33	36	45.89	64	13.59	66	74
	1.66	42	42.78	58	12.31	72	68

Lower concentrate ash content can be obtained in the presence of FADs. As Fig. 7c showed that 12.31% concentrate ash content was obtained when C16D was used comparing with 16.50% of that in the presence of DAH only. The reverse flotation results of DAH and FADs were shown in Table 5. It can be seen that the mineral matter and combustible recoveries in the presence of 1.66 kg/Mg DAH were 54% and

81%, while 55% mineral matter recovery and 81% combustible recovery were obtained in the presence of 0.83 kg/Mg C12D. And the highest mineral matter recovery 72% in these experiments was obtained in the presence of 1.66 kg/Mg C14D. However, taking the both evaluation indicators into consideration, C12D surfactant showed a better performance that high mineral matter recovery near C14D and higher combustible recovery than C14D and C16D. In addition, less weight of C12 would be used under the same molar ratio (DAH : Fatty acid = 1:1) due to its lower molecular weight than C14 and C16.

Conclusion

This study investigated the properties of DAH and fatty acids/DAH mixtures. In addition, their effects on coal reverse flotation were also investigated. Based on the results, the following conclusions can be presented.

1. Surface tension measurements indicated that the fatty acids/DAH mixtures can obtain a much lower CMC and γ_{cmc} than DAH and the surface activity of the FADs increased with the increasing of hydrocarbon chain length of the fatty acids.
2. Adsorption experiments showed that the adsorption density of DAH and FADs on clean coal increased with the increase of the equilibrium concentration and the adsorption density of FADs on the coal was higher than that of DAH.
3. Adsorption of DAH and FADs on bubbles revealed that the FADs surfactants were more easily to adsorb on the bubbles surface. The adsorption amount of C16D surfactant on bubble surface was almost six times more than that of DAH and a probable interaction mechanism of DAH and fatty acid in solution was proposed.
4. Reverse flotation results showed that the FADs surfactants have stronger collectivity than DAH and that C12D showed better performance with a high mineral matter recovery similar to that with C14D as well as higher combustible recovery than with C14D and C16D.
5. For some difficult-to-float coals such as oxidized coal and lignite, forward flotation is not suitable. Many scientists have studied on improving the flotation behavior using both forward flotation and reverse flotation methods (Xia and Yang, 2013a; Zhang and Tang, 2014; Zhang and Liu, 2015). In most of the works it was observed that the trend of reagent consumption is towards the higher side (Xia and Yang, 2013a; Zhang and Liu, 2015; Ding and Laskowski 2006a). This paper proposed a new way to reduce about 50% collector consumption in steam coal reverse flotation and make reverse flotation to be an alternative way for upgrading difficult-to-float coal.
6. Kaolinite and quartz are usually treated as gangue minerals in many other mineral flotation processes. Therefore, the mixture of DAH/fatty acids used in this study may also be used in the reverse flotation process of other minerals such as iron ores and bauxite.

References

ANGADI, S.I., SURESH, N., 2005. *A kinetic model for the prediction of water reporting to the froth products in batch flotation*. Trans. Inst. Min. Metall. Sect. C, 114, 225–232.

ANGADI, S.I., JEON, HO-SEOK, NIKKAM, S., 2012. *Experimental analysis of solids and water flow to the coal flotation froths*. Int. J. Miner. Process, 110–111, 62–70.

BAKER, A.F., MILLER, K.J., DUERBRAUCK, A.W., 1973. *Desulphurization of froth flotation*. Proceedings 6th Int. Coal Prep. Congress, Paris, March, 1973.

DESAI, T.R., DIXIT, S.G., 1996. *Interaction and viscous properties of aqueous solutions of mixed cationic and nonionic surfactants*. J. Colloid Interface Sci, 177, 471–477.

DING, K., LASKOWSKI, J.S., 2006a. *Coal reverse flotation. Part I: separation of a mixture of subbituminous coal and gangue minerals*. Miner. Eng. 19, 72–78.

DING, K., LASKOWSKI, J.S., 2006b. *Coal reverse flotation. Part II: cleaning of a subbituminous coal*. Miner. Eng. 19, 79–86.

DIGRE, M., SANDVIK, K.L., 1968. *Adsorption of Amine on Quartz Through Bubble Interaction*. Transactions IMM, sec. C, 77, 61–64.

FANG X., ZHAO S., MAO S., YU J., DU Y., 2003. *Mixed micelles of cationic–nonionic surfactants: NMR self-diffusion studies of Triton X-100 and cetyltrimethylammonium bromide in aqueous solution*. Colloid Polym. Sci. 281, 455–460.

HERRINGTON, K.J., KALER., MILLER, D.D., ZASADZINSKI, J.A., CHIRUVOLU, S., 1993. *Phase behavior of aqueous mixtures of dodecyltrimethylammonium bromide (DTAB) and sodium dodecyl sulfate (SDS)*. Journal of Physical Chemistry, 97 (51), 13792–13802

LIN, C.H., 1982. *Characterisation of Pyrites in Reverse Flotation Products*. (PhD Thesis) University of Utah

LI M, RHARBI Y, HUANG X, WINNIK M., 2000. *Small variations in the composition and properties of triton X-100*. J Colloid Interface Sci 230:135–139

MILLER, K.J., 1973. *Flotation of Pyrite From Coal: Pilot Plant Study*. (USBM, RI, 7822).

MILLER, K.J., 1975. *Coal–pyrite flotation*. Trans. AIME, 258, 30.

MILLER, K.J., 1978. *Desulphurization of Various Midwestern Coals by Flotation* (USBM, RI, 8262).

MILLER, J.D., LIU, C.L., CHANG, S.S., 1984. *Co-adsorption phenomena in the separation of pyrite from coal by reverse flotation*. Coal Prep, 1, 21.

MILLER, K.J., DEURBROUCK, A.W., 1982. *Froth Flotation to Desulphurize Coal in “Physical Cleaning of Coal”*. Marcel Dekker, New York, 255.

OZTURK, F.P., TEMEL, H.A., 2013. *Reverse flotation in Muş-Elmakaya lignite beneficiation*. Energy Sources Part A, 35 (8), 695–705.

PATIL, D.P., LASKOWSKI, J.S., 2008. *Development of zero conditioning procedure for coal reverse flotation*. Miner. Eng. 21, 373–379.

PAWLIK, M., LASKOWSKI, J.S., 2003a. *Coal Reverse Flotation—Part I. Adsorption of Dodecyltrimethyl Ammonium Bromide and Humic Acids onto Coal and Silica*. Coal Prep, 23, 91–112.

PAWLIK, M., LASKOWSKI, J.S., 2003b. *Coal reverse flotation—part II. Batch flotation tests*. Coal Prep, 23, 113–127.

PENFOLD, J., STAPLES, E., CUMMINS, P., THOMAS, R., SIMISTER, E., LU, J., 1996. *Adsorption of mixed cationic–non-ionic surfactants at the air/water interface*. J. Chem. Soc. Faraday Trans, 92, 1773–1779.

PENFOLD, J., STAPLES, E., TUCKER, I., THOMPSON, L., 1997. *Adsorption of mixed cationic and nonionic surfactants at the hydrophilic silicon surface from aqueous solution: Studied by specular neutron reflection*. Langmuir, 13, 6638–6643.

QIN, Z.H., TAN, R., 2006. *Spectrophotometric method for determination of cationic surfactants with eosin Y and its reaction mechanism*. Chin. J. Anal. Lab, 25 (10), 110–114.

RUBINGH, D., JONES, T., 1982. *Mechanism of detergency in systems containing cationic and nonionic surfactants*, Ind. Eng. Chem. Prod. Res. Dev. 21, 176–182.

SOMASUNDARAN, P., 1968. *The Relationship Between Adsorption at Different Interfaces and Flotation Behavior*. Transactions SME, 241, 105–108.

STONESTREET, P., FRANZIDIS, J.P., 1988. *Reverse flotation of coal—a novel way for the beneficiation of coal fines*. Miner. Eng. 1, 343–349.

STONESTREET, P., FRANZIDIS, J.P., 1989. *Development of the reverse coal flotation process: depression of coal in the concentrates*. Miner. Eng. 2, 393–402.

STONESTREET, P., FRANZIDIS, J.P., 1992. *Development of the reverse coal flotation process: application to column flotation*. Miner. Eng. 5, 1041–1051.

VORA S., GEORGE A., DESAI H., BAHADUR P., 1999. *Mixed micelles of some anionic–anionic, cationic–cationic, and ionic–nonionic surfactants in aqueous media*, J. Surfactant Deterg, 2, 213–221.

XUEFEN, Z., GUIWU, L., XIAOMING, W., HONG Y., 2009. *Molecular dynamics investigation into the adsorption of oil–water–surfactant mixture on quartz*, Appl. Surf. Sci. 255, 6493–6498.

XIAO, J.X., SIVARS, U., TJERNELD, F., 2000. *Phase behavior and protein partitioning in aqueous two-phase systems of cationic–anionic surfactant mixtures*, J. Chromatogr. B Biomed. Sci. Appl. 743, 327–338.

XIA, W., YANG, J., 2013a. *Reverse flotation of Taixi oxidized coal*. Energy Fuels, 27 (12), 7324–7329.

ZHANG, H., LIU, J., CAO, Y., WANG, Y., 2013. *Effects of particle size on lignite reverse flotation kinetics in the presence of sodium chloride*. Powder Technol. 246, 658–663.

ZHANG, HAIJUN., LIU, QINGXIA., 2015. *Lignite cleaning in NaCl solutions by the reverse flotation technique*. Physicochem. Probl. Miner. Process. 51 (2), 695–706.

ZHANG, W.J., TANG, X.Y., 2014. *Flotation of lignite pretreated by sorbitan monooleate*. Physicochem. Probl. Miner. Process. 50 (2), 759–766.

Received August 26, 2014; reviewed; accepted May 11, 2015

FLOTATION OF LONG FLAME COAL PRETREATED BY POLYOXYETHYLENE SORBITAN MONOSTEARATE

Chao NI, Guangyuan XIE, Zhiyuan LI, Xiangning BU, Yaoli PENG, Jie SHA

Key Laboratory of Coal Processing and Efficient Utilization (Ministry of Education), School of Chemical Engineering and Technology, China University of Mining and Technology, Xuzhou 221116, Jiangsu, China, xgywl@163.com(G. Xie)

Abstract: In this investigation, polyoxyethylene sorbitan monostearate (Tween 60) was used to improve flotation of fine long flame coal. The flotation recovery of long flame coal could be increased when long flame coal was either pretreated or conditioned with Tween 60 in a flotation cell for a period before the addition of collector. Fourier Transform Infrared (FTIR) technique was used to indicate surface properties of long flame coal. The results of FTIR show that there are many oxygen functional groups on the surface. Contact angle measurements were used to indicate changes in hydrophobicity of coal surface before and after Tween 60 and/or diesel pretreatments. The results of contact angle measurements show that hydrophobicity of coal can be increased by Tween 60. Tween 60 can also enhance adsorption of diesel on the coal surface, and hence floatability of long flame coal can be further improved. Tween 60 primarily enhances the flotation recovery of low density coal fractions (<1.5 and $1.5\text{--}1.8 \text{ kg/dm}^3$). However, the increase in flotation recovery is less significant with an excessive addition of Tween 60.

Keywords: flotation, hydrophobicity, low rank coal, Tween 60, pretreatment

Introduction

Flotation is widely used in beneficiation of fine coal slimes ($<0.5 \text{ mm}$) and is based on the difference in hydrophobicity between coal matter and minerals. It is well known that coal particles are usually much more hydrophobic than gangue ones (Drzymala, 2007). During conventional flotation processes, coal particles are floated into the froth, which is treated as a clean coal after dewatering processes, whereas hydrophilic particles are retained in a system and transported to tailings.

It is well recognized that low rank coals, such as peat, lignite and long flame coal are difficult to float using common oily collectors. However, universal oily collectors after special treatments, such as emulsification and addition of oxygenated functional groups into collector molecule can significantly improve flotation of low rank coals

(Jia et al., 2000; Boylu and Laskowski, 2007). The addition of pitch in a dry grinding process of low rank coal before flotation enhance the combustible matter recovery and reduce the ash content of clean coal (Atesok and Celik, 2000). A low temperature heating process can be also useful for improvement in hydrophobicity of lignite (Celik and Seyhan, 1995; Ye et al., 1988; Cinar, 2009). Floatability of low rank coal can be improved by microwave pretreatment since microwave pretreatment reduces the moisture content of low rank coal (Ozbayoglu et al., 2009). The low moisture content might be beneficial to the flotation performance of lignite. Furthermore, microwave treatment was also used to improve Taixi oxidized coal flotation since both dehydration and oxidation reactions could occur on the oxidized coal surface after microwave radiation (Xia et al., 2013).

Surfactants are widely used in food processing technology since they can decrease the surface tension of solutions. Thus, surfactants are also applied in improvements in low rank coal flotation (Burkin and Bramley, 1963; Aston et al., 1981; Chander et al., 1987; Moxton et al., 1987; Yu et al., 1990; Jia et al., 2000; Sahbaz, 2013). In some cases, surfactants added at low concentration can make low rank coal more hydrophobic, whereas, at high concentration, they can decrease hydrophobicity of low rank coal (Zhang and Tang, 2014). On the other hand Kowalcuk et al. (2015) showed that frothers do not change the real hydrophobicity of particles, but they improve their effective hydrophobicity. Furthermore, the foaming ability and froth stability can be improved by addition of surfactants into flotation processes (Aktas and Woodburn, 1995; Pugh, 1996; Cho and Laskowski, 2002; Ozmak and Aktas, 2006; Kosior et al., 2011).

In this investigation, polyoxyethylene sorbitan monostearate (Tween 60) was used to improve flotation of low rank coal slimes (long flame coal). The effect of different Tween 60 dosages on the flotation performance of long flame coal was investigated. Fourier Transform Infrared (FTIR) technique was used to indicate the surface properties of long flame coal. Contact angle measurements were used to indicate the changes in hydrophobicity of coal surface before and after Tween 60 and diesel pretreatments. In this paper, Tween 60 will be found to be a good promoter in the flotation of long flame coal.

Materials and methods

Materials

Long flame coal samples were obtained from the Shandong Province of China. The proximate composition of coal samples is shown in Table 1, where M^{ad} is the moisture content, V^{ad} volatile content, FC^{ad} fixed carbon content, and A^{ad} is the ash content on an air dry basis.

The particle size distribution of coal samples is shown in Table 2. It indicates that the yield of <0.045 mm size fraction with an ash content of 43.40% plays the most important role in the size distribution of this coal samples. It is deduced that the coal

samples contain a certain number of heterogeneous minerals, which might deteriorate the flotation performance of combustible matters due to the particle interaction in the flotation system (Bokanyi, 1996).

Table 1. Proximate composition of coal samples

M ^{ad} (%)	A ^{ad} (%)	FC ^{ad} (%)	V ^{ad} (%)
8.63	35.09	23.35	32.93

Table 2. Particle size distribution of coal samples

Size fraction (mm)	Mass (%)	Ash content (%)	Cumulative	
			Yield (%)	Ash content (%)
0.5-0.25	1.79	7.43	1.79	7.43
0.25-0.125	8.17	11.45	9.97	10.73
0.125-0.074	14.96	20.15	24.93	16.38
0.074-0.045	8.51	24.93	33.44	18.56
<0.045	66.56	43.40	100.00	35.09

The density distribution of coal samples is shown in Table 3. It indicates that the materials with the density smaller than 1.6 kg/dm³ are clean coal with the ash content of 8.84%. The yield of 1.6-1.8 kg/dm³ density fraction is 25.83% with 29.18% ash content, which demonstrates there is a certain number of composite particles in the coal sample (Dyrkacz and Horwitz, 1982; Luttrell et al., 2000). In addition, the yield of >1.8 kg/dm³ density fraction takes the largest proportion at 43.72% with the ash content of 56.88% in the density distribution. The high density particles are mainly gangue particles. It indicates that a low ash content clean coal may be difficult to obtain due to the contamination of fine gangue particles (Zheng et al., 2005).

Table 3. Density distribution of coal samples

Density fraction (kg/dm ³)	Mass (%)	Ash content (%)	Cumulative lights	
			Yield (%)	Ash content (%)
<1.3	1.54	2.99	1.54	2.99
1.3-1.4	5.74	4.58	7.28	4.24
1.4-1.5	13.18	7.75	20.46	6.50
1.5-1.6	9.99	13.64	30.45	8.84
1.6-1.8	25.83	29.18	56.28	18.18
>1.8	43.72	56.85	100.00	35.09

Methods

FTIR measurements

A Perkin Elmer Spectrum 2000 model spectrometer was used for Fourier Transform Infrared (FTIR) analyses, and the spectrum was obtained at 2 cm^{-1} resolution in the interval between 4000 and 400 cm^{-1} . The FTIR spectra of coal samples were obtained with analytical grade KBr pellets. The ratio of the coal to KBr was 1 to 100.

Flotation tests

Diesel and 2-octanol were used as the collector and frother, respectively. The flotation tests were conducted in a 1.5 dm^3 XFD flotation cell using 90 g of coal for each flotation test. The impeller speed of flotation machine was kept as 1800 rpm, and airflow rate was $4.0\text{ dm}^3/\text{min}$. Collector dosage was 2 kg/Mg coal, and frother dosage was 1 kg/Mg coal. Tween 60 dosages were 1, 2, 3, 4, 5 and 6 kg/Mg coal. Both 2-octanol and Tween 60 were obtained from Sinopharm Chemical Reagent Co. Ltd of China, and they were in analytical grades. Diesel was industrial product grade, which was obtained from a coal preparation plant of China.

For each test, the pulp was first agitated in the flotation cell for 2 min, and then Tween 60 was added and agitated for an additional 3 min. After this, diesel was added to the pulp and agitated for another 2 min. Then, the frother was added, and the pulp was conditioned for the next 30 seconds. At last, the air inlet was opened and the froth products were collected.

The flotation concentrates were analyzed using two parameters: the combustible matter recovery and ash content. The combustible matter recovery can be calculated by using formula:

$$\text{Combustible Matter Recovery (\%)} = \frac{M_C(100 - A_C)}{M_F(100 - A_F)} \cdot 100 \quad (1)$$

where M_C and M_F are concentrate and feed yields (%), respectively, A_C and A_F are ash contents in concentrate and feed (%), respectively.

Contact angle measurements

Coal samples before and after Tween 60 and diesel pretreatments were firstly pressed to tablets. Four types of coal tablets were investigated: raw coal tablet (without any pretreatment), coal pretreated by Tween 60 only (3 kg/Mg), coal pretreated by diesel only (2 kg/Mg) and coal pretreated by both Tween 60 and diesel (Tween 60 1, 2, 3, 4, 5 and 6 kg/Mg, diesel 2 kg/Mg).

The coal samples were pretreated in a 1.5 dm^3 XFD flotation cell at a speed of 1800 rpm, and the pulp density was 60 g/dm^3 . When the coal sample was pretreated by Tween 60 only, the pulp was first agitated in the flotation cell for 2 min, and then Tween 60 was added and agitated for an additional 5 min. Afterwards, the pulp was filtered, and dried at a temperature of below 40 degrees. The process of coal samples

pretreatment by diesel only was the same with that by Tween 60 only. However, when the coal sample was pretreated by Tween 60 and diesel together, the Tween 60 was added into the pulp and agitated for 3 min first. Then diesel was added into the pulp and agitated for another 2 min.

The tablets of coal samples were measured by the sessile drop method using a water contact angle analyzer (JC2000D) such as a water droplet on the surface of coal tablets in the air. Static contact angles were adopted to determine hydrophobicity of coal samples. Each coal sample was measured three times and the average value of contact angles was used in this investigation.

Results and Discussion

The FTIR spectrum obtained for the long flame coal (Fig. 1) shows CH_3 and CH_2 regions at 2927 cm^{-1} and 2852 cm^{-1} , respectively. The peak at 1447 cm^{-1} is $-\text{CH}_3$ stretching vibration. The peaks around 1112 cm^{-1} , 1278 cm^{-1} and 1035 cm^{-1} may be attributable to C-O-C vibration (Sun et al., 2010). The peak at 3400 cm^{-1} is for OH, and peaks at 1607 cm^{-1} may be for C=O or COOH functional groups. The peaks around 800 cm^{-1} and 697 cm^{-1} usually indicate the presence of benzene rings. The peaks at 3695 cm^{-1} and 3623 cm^{-1} can be considered as attributable to the kaolin mineral. The peak at 3050 cm^{-1} may be C-C=C (olefins) stretching vibration. It indicates that the long flame coal sample represents a really low rank coal. Long flame coal has many oxygen bearing functional groups which are hydrophilic. Meanwhile, long flame coal as low rank coal is usually difficult to float with common oily collectors since there are many oxygenated functional groups on low rank coal surface (Zhang and Tang, 2014).

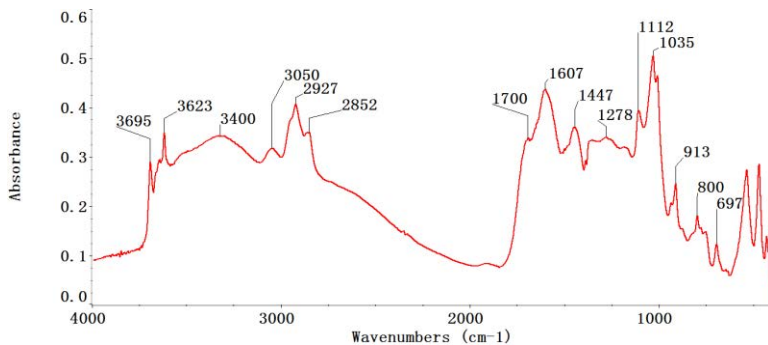


Fig. 1. FTIR spectrum of long flame coal

Figure 2 shows that the combustible matter recovery increases with the increase of Tween 60 dosage, while Tween 60 dosage is less than 3 kg/Mg . After then, the combustible matter recovery decreases with the increasing Tween 60 dosage. The concentrate ash content decreases with the increase of Tween 60 dosage (while Tween 60 dosage is less than 2 kg/Mg). The ash content of concentrate then shows no change

with the increasing Tween 60 dosage. It indicates that the hydrophobicity of long flame coal surface may be effectively enhanced by Tween 60 at low dosages (optimal dosage is 3 kg/Mg). Under a higher dosage of Tween 60, the flotation performance of the coal samples deteriorates.

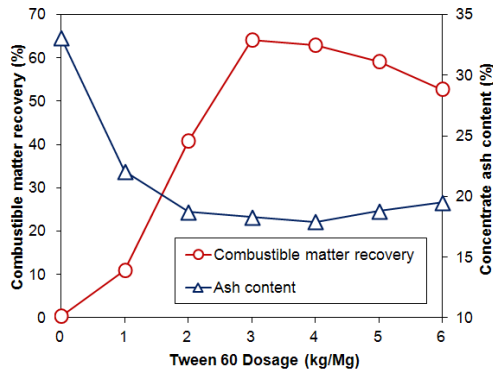


Fig. 2. Flotation results at different Tween 60 dosages

The concentrate at Tween 60 dosage of 3 kg/Mg was collected and screened into five size fractions, 0.5-0.25, 0.25-0.125, 0.125-0.074, 0.074-0.045 and <0.045 mm. The combustible matter recoveries and ash contents for different size fractions were obtained calculating that the flotation feed of each size fraction was regarded as 100%.

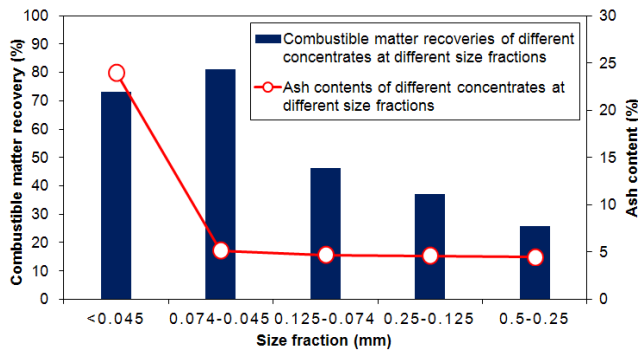


Fig. 3. Combustible matter recovery and ash content of concentrates with different size fractions at Tween dosage of 3 kg/Mg

Figure 3 shows that the combustible matter recovery increases with the decrease of size fraction but it has a little decrease, while the size fraction is <0.045 mm. The ash content increases with decrease of size fraction steadily. As shown in Fig. 3, the ash content of <0.045 mm size fraction is about 24%, while the ash contents of other size fractions are about only 4~5%. It indicates that the selectivity of <0.045 mm size fraction is lower than those of other size fractions. The combustible matter recovery of

0.074-0.045 size fraction is the highest, around 80%, with the ash content of about 5%. This is the size fraction with the best flotation performance. The high ash content of <0.045 mm size fraction increases the ash content of total concentrate since the particles of size below 0.045 mm show a very low selectivity and are recovered by various ways, including entrainment, entrapment and slime coatings (Trahar, 1981).

In order to investigate the effect of Tween 60 dosage on the flotation recovery of coal fines of different density fractions (<1.5, 1.5-1.8 and >1.8 kg/dm³), the concentrates at different Tween 60 dosages were collected and treated by a sink-float test using organic heavy liquids. As it shown in Fig. 4, the combustible matter recoveries of <1.5 and 1.5-1.8 kg/dm³ density fractions increase with increase of Tween 60 dosage but it has a little decrease while Tween dosage is higher than 3 kg/Mg. A higher Tween 60 dosage has a deleterious effect on the flotation recovery of low ash content coals (<1.5 and 1.5-1.8 kg/dm³). The combustible matter recovery of >1.8 kg/dm³ density fraction increases with the increase of Tween 60 dosage but with little range. The addition of Tween 60 can enhance the recovery of low density coal fractions (<1.5 and 1.5-1.8 kg/dm³) much more than that of high density coal fraction (>1.8 kg/dm³). Therefore, Tween 60 may be used as a good promoter in the flotation of long flame coal.

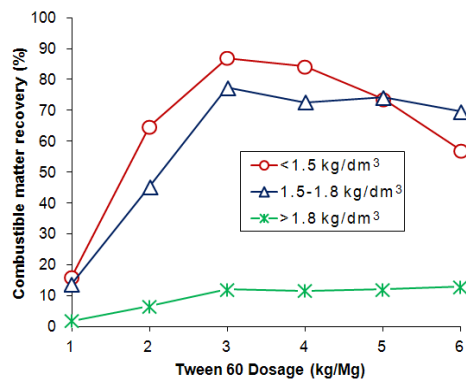


Fig. 4. Combustible matter recovery of various density fractions at different Tween 60 dosages

As shown in Fig. 5, the static contact angle of raw coal is about 43°, pretreated by Tween 60 only is about 51°, pretreated by diesel only is also about 51°, while the contact angle of coal pretreated by both Tween 60 (3 kg/Mg) and diesel is about 59°. Figure 6 shows that the contact angles increase with the increase of Tween 60 dosages when the Tween 60 dosage is less than 4 kg/Mg. After then, the contact angles decrease with the increasing Tween 60 dosages. However, it is clear that the contact angles at the Tween 60 dosage of more than 1 kg/Mg (include 1 kg/Mg) are greater than 51°, which demonstrates that the contact angle of coal sample pretreated by

Tween 60 and diesel together is greater than that of the coal sample pretreated by diesel only.

The results of contact angle measurements indicate that the hydrophobicity of coal surface can be improved by Tween 60, i.e. the contact angle increases from 43° to 51° . The collector (diesel) also can improve the hydrophobicity of coal surface, i.e. the contact angle increases from 43° to 51° . If the coal is pretreated by Tween firstly and then the pretreated coal is conditioned with collector (diesel), the hydrophobicity of coal surface can be further improved, i.e. the contact angles at all Tween 60 dosages are greater than 51° , and the maximum contact angle is up to approximately 60° . It indicates that Tween 60 has a good effect on the flotation improvement.

Tween 60 may screen the hydrophilic functional groups and hence increase the hydrophobicity of coal surface. The addition of Tween 60 may also enhance dispersion of the collector (diesel). The enhanced spread collector may adsorb on the coal surface more effectively, and hence the coal surface hydrophobicity will be further improved (Sis and Chander, 2003; Dey, 2012). However, the hydrophobicity of coal surface decreases at higher dosages of Tween 60 since higher dosages of Tween 60 might screen the coal surface and forms bilayer adsorption (Zhang and Tang, 2014). As a result, the flotation performance of coal samples at higher Tween 60 dosages was a little lower than that at proper Tween 60 dosages as shown in Fig. 2.

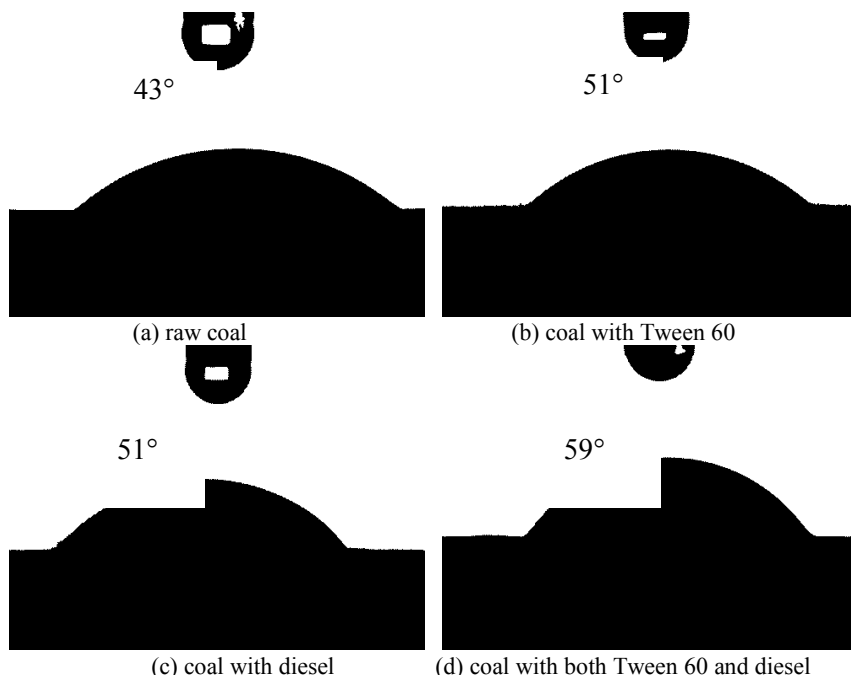


Fig. 5. Static contact angles of different coal tablets

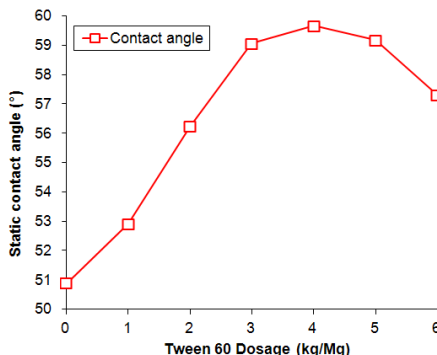


Fig. 6. Static contact angles of coal samples pretreated by Tween 60 and diesel (2 kg/Mg) together at different Tween 60 dosages

Conclusions

(1) The FTIR spectrum of long flame coal shows that there are many oxygen bearing functional groups, which are hydrophilic. Long flame coal is of a low rank and hence it is difficult to float it with common oily collectors.

(2) Flotation tests indicate that the flotation recovery of long flame coal can be improved by the addition of polyoxyethylene sorbitan monostearate (Tween 60) before flotation processes. The Tween 60 dosage is very important in the flotation recovery. The optimal Tween 60 dosage was found to be 3 kg/Mg in this investigation.

(3) Tween 60 can enhance the flotation of 0.5-0.25, 0.25-0.125, 0.125-0.074 mm size fractions. However, the high ash content of <0.045 mm size fraction increases the ash content of total concentrate since the particles of sizes below 0.045 mm show a very low selectivity. Meanwhile, Tween 60 can enhance the flotation recovery of low density coal fractions (<1.5 and 1.5-1.8 kg/dm³) much more than that of high density coal fraction (>1.8 kg/dm³).

(4) Tween 60 may screen the hydrophilic functional groups and hence increase the hydrophobicity of coal surface. The contact angle of coal pretreated by both Tween 60 and diesel is greater than 51°, while that of coal pretreated by diesel only is just about 51°. The addition of Tween 60 may also enhance dispersion of collector (diesel). The enhanced spread collector may adsorb on the coal surface effectively. Tween 60 can be used as a good promoter in the flotation of long flame coal.

Acknowledgments

This work was supported by the National Natural Science Foundation of China (51374205, 51474213). We also want to thank the support of A Project Funded by the Priority Academic Program Development of Jiangsu Higher Education Institutions.

References

AKTAS Z., WOODBURN E. T., 1995. *The effect of non-ionic reagent adsorption on the froth structure and flotation performance of two low rank British coals*. Powder Technology, 83(2), 149–158.

ASTON J.R., DEACON M.J., FURLONG D.N., HELY T.W., LAU A.C.M., 1981. *The chemistry of non-ionic surfactants, preparation processes*. Proceedings of the first Australian coal preparation congress, Newcastle, Australia, 358–378.

ATESOK G., CELIK M.S., 2000. *A new flotation scheme for a difficult-to-float coal using pitch additive in dry grinding*. Fuel, 79(12), 1509–1513.

BOKANYI L., 1996. *Kinetic Model for Flotation Systems with Particle Interaction*. In: New Trends in Coal Preparation Technologies and Equipment. Edited by W.S. Blaschke. Gordon and Breach Publishers, Amsterdam, pp. 731–736.

BOYLU F., LASKOWSKI J. S., 2007. *Rate of water transfer to flotation froth in the flotation of low-rank coal that also requires the use of oily collector*. International Journal of Mineral Processing, 83(3), 125–131.

BURKIN A.R., BRAMLEY J.V., 1963. *Flotation with insoluble reagents II, effect of surface active reagents on the spreading of oil at coal–water interface*. Journal of Applied Chemistry, 13, 417–422.

CELIK M.S., SEYHAN K., 1995. *Effect of heat treatment on the flotation of Turkish lignites*. International Journal of Coal Preparation and Utilization, 16, 65–79.

CHANDER S., MOHAL B., APLAN F.F., 1987. *Wetting behavior of coal in the presence of some non-ionic surfactants*. Journal of Applied Chemistry, 13, 205–216.

CHO Y.S., LASKOWSKI J.S., 2002. *Effect of flotation frothers on bubble size and foam stability*. Int. J. Miner. Process. 64, 69–80.

CINAR M., 2009. *Floatability and desulfurization of a low-rank (Turkish) coal by low-temperature heat treatment*. Fuel Processing Technology, 90(10), 1300–1304.

DEY S., 2012. *Enhancement in hydrophobicity of low rank coal by surfactants—A critical overview*. Fuel Processing Technology, 94(1), 151–158.

DRZYMALA J., 2007. *Mineral processing: foundations of theory and practice of metallurgy*. Wroclaw University of Technology, Oficyna Wyd. PWr., Wroclaw, 2007, 507 pages, <http://wwwdbc.wroc.pl/dlibra/docmetadata?id=2070&from=publication>

DYRKACZ G. R., HORWITZ E. P., 1982. *Separation of coal macerals*. Fuel, 61(1), 3–12.

JIA R., HARRIS G.H., FUERSTENAU D.W., 2000. *An improved class of universal collectors for the flotation of oxidized and for low-rank coal*. International Journal of Mineral Processing, 58, 99–118.

KOSIOR D., ZAWALA J., MALYSA K., 2011. *When and how α -terpineol and *n*-octanol can inhibit the bubble attachment to hydrophobic surfaces*. Physicochem. Problems Mineral Process, 47, 169–182.

KOWALCZUK P.B., MROCKO D., DRZYMALA J., 2015. *Influence of frother type and dose on collectorless flotation of copper-bearing shale in a flotation column*. Physicochem. Probl. Miner. Process, 51(2), 547–558.

LUTTRELL G. H., KOHMUENCH J. N., YOON R. H., 2000. *An evaluation of coal preparation technologies for controlling trace element emissions*. Fuel Processing Technology, 65, 407–422.

MOXTON N.T., KEAST-JONES B., NICOL S.K., 1987. *Insoluble oils in coal flotation: the effects of surface spreading and pore penetration*. International Journal of Mineral Processing, 21, 261–274.

OZBAYOGLU G., DEPCI T., ATAMAN N., 2009. *Effect of Microwave Radiation on Coal Flotation*. Energy Sources Part A-Recovery Utilization And Environmental Effects, 31(6), 492–499.

OZMAK M., AKTAS Z., 2006. *Coal froth flotation: Effects of reagent adsorption on the froth structure*. Energy & Fuels, 20(3), 1123–1130.

PUGH R. J., 1996. *Foaming, foam films, antifoaming and defoaming*. Advances in Colloid and Interface Science, 64, 67–142.

SAHBAZ O., 2013. *Determining optimal conditions for lignite flotation by design of experiments and the halbich upgrading curve*. Physicochemical Problems of Mineral Processing, 49(2), 535–546.

SIS H., CHANDER S., 2003. *Reagents used in the flotation of phosphate ores: a critical review*. Minerals Engineering, 16(7), 577–585.

SUN W., OUYANG K., ZHANG L., HUA Y., CHEN C., 2010. *Preparation of hydrolyzate of hogwash oil (HHO) and its application in separating diaspore from kaolinite*. Minerals Engineering, 23, 670–675.

TRAHAR W. J., 1981. *A rational interpretation of the role of particle size in flotation*. International Journal of Mineral Processing, 8(4), 289–327.

XIA W., YANG J., LIANG C., 2013. *A short review of improvement in flotation of low rank/oxidized coals by pretreatments*. Powder Technology, 237, 1–8.

YE Y., JIN R., MILLER, J. D., 1988. *Thermal treatment of low-rank coal and its relationship to flotation response*. Coal preparation, 6(1-2), 1–16.

YU Q., YE Y., MILLER J.D., 1990. *A study of surfactant/oil emulsion for fine coal flotation*. Advances in Fine Particles Processing, Springer, 344–355.

ZHANG W., TANG X., 2014. *Flotation of Lignite Pretreated by Sorbitan Monooleate*. Physicochemical Problems of Mineral Processing, 50(2), 759–766.

ZHENG X., FRANZIDIS J. P., JOHNSON N. W., MANLAPIG E. V., 2005. *Modelling of entrainment in industrial flotation cells: the effect of solids suspension*. Minerals Engineering, 18(1), 51–58.

Received January 27, 2015; reviewed; accepted July 27, 2015

EXPERIMENTAL STUDY ON TRIBOELECTROSTATIC BENEFICIATION OF WET FLY ASH USING MICROWAVE HEATING

**Haisheng LI, Yinghua CHEN, Xinxi ZHANG, Yuemin ZHAO, Youjun TAO,
Chaoyong LI, Xin HE**

Key Laboratory of Coal Processing and Efficient Utilization (Ministry of Education), School of Chemical Engineering and Technology, China University of Mining and Technology, Xuzhou 221116, Jiangsu, China,
cyhlhs@163.com (H. Li), zhangxinxi@126.com (X. Zhang)

Abstract: Triboelectrostatic beneficiation, as a physical method, of fly ash cannot only meet the technical requirements of fly ash application but also recycle of an unburned carbon as a useful energy source. The aim of this study was to investigate the feasibility of improving efficiency of triboelectrostatic beneficiation of wet fly ash using microwave heating. The wet fly ash with different moisture contents had an average loss-on-ignition of 12.56%. The fly ash samples were heated in a microwave oven before the experiments. The experimental conditions were electric field voltage of 40 kV and air flux ranging from 12 to 30 m³/h. The influence of the microwave heating on the wet fly ash triboelectrostatic beneficiation was discussed under the conditions of different microwave intensity and irradiation time. The results indicated that the removal rate and recycle rate of the unburned carbon showed a significant increase performance as the wet fly ash was processed by the microwave heating which was attributed to changes of moisture contents and dielectric constants caused by the microwave heating. The feasibility had been verified according to the experimental study on fly ash with different moisture contents. It can be concluded that the microwave heating process was efficiently applied for the wet fly ash triboelectrostatic beneficiation.

Keywords: wet fly ash, triboelectrostatic beneficiation, microwave heating, efficiency

Introduction

Fly ash is a solid waste produced by coal-fired power plants, and it can be harmful to the environment because of air pollution, groundwater contamination etc. On the other hand, it is also a sort of useful resource (Hwang et al., 2002) and several researchers have focused on the utilization of fly ash (Soong et al., 2001; Huang et al., 2003). At present, the fly ash has been widely used as a kind of additive for building materials.

The influence of carbon content on the building materials was proven by some previous studies (Kim et al., 2001; Cangialosi et al., 2010).

Removal unburned carbon from fly ash can be achieved using flotation and electrostatic separations. Flotation is an effective method to remove unburned carbon from fly ash (Cao et al., 2012; Huang et al., 2003). However, the pretreatment technique of flotation needs a lot of water, and the post-processing needs dehydration equipment. Accordingly, the equipment investment and energy consumption should be taken into consideration. The follow-up use of fly ash production obtained by flotation is difficult because of low activity. Moreover, the flotation reagents will cause the environmental pollution. By contrast, the electrostatic separation has an obvious advantage over the flotation. As also known from literature, the triboelectrostatic separation has been studied as a cost-effective solution for fly ash beneficiation (Ban et al., 1997). Therefore, it is suitable to be used especially for the water-deficient area.

Recent two investigations were focused on questions regarding ash triboelectrostatic beneficiation. On one hand, the separation efficiency should be improved to obtain high-quality ash product with low carbon content (Cangialosi et al., 2008). On the other hand, the recovery efficiency of unburned carbon needs to be enhanced with the improvement of their awareness of energy resources (Li et al., 2012). Removal of unburned carbon from wet fly ash is difficult to achieve in a continuous operation at low temperature and high relative humidity. Especially in some southern regions of China, the fly ash collected by a dry method will absorb a bit of moisture during the winter or rainy weather. In some places, the fly ash produced by coal-fired power plants is collected by a wet method. Therefore, humid fly ash is generally processed by a dryer.

The temperature and moisture content has an important effect on the wet fly ash triboelectrostatic beneficiation. The relative humidity and temperature of air flow used to convey fly ash particles have an impact on the electrical charging process. As the particle size decreased, the influence of air humidity and surface moisture would be more important. The particles less than 45 μm had a four-fold change in their separability once changing their surface moisture contents (Cangialosi et al., 2006). An experimental methodology was introduced to measure electrical charge distributions of fly ash particles exposed to weather conditions for six months. It is suggested that removal of surface moisture would be beneficial to improve the efficiency of the fly ash triboelectrostatic beneficiation (Cangialosi et al., 2009). Also, the configuration of tribo-charger and the operational parameters have an important influence on the fly ash triboelectrostatic beneficiation (Li et al., 2015). The temperature field inside the tribo-device can reflect the efficiency of friction and collision indirectly. The tribo-charger was optimized by infrared thermography experiments (Li et al., 2013). A remarkable increase in separation efficiency was obtained after heating fly ash with loss-on-ignition (*LOI*) content below 15%. The adhesive forces between coal and ash caused by moisture adsorption may be a factor influencing triboelectrostatic beneficiation performance for the wet fly ash (Cangialosi et al., 2006).

In general, the heating of mineral particles is utilized in a microwave oven. In recent literature, the mixed oxide powders were prepared by the microwave heating before the experiments (Kato, 2012). Microwave heating of mineral ores offers a mechanism to induce fractures around grain boundaries. The process was influenced by microwave power and thermal expansion coefficient (Ali et al., 2010). The effect of microwave treatment on the processing of mineral ores was investigated through simulations of microwave heating (Ali et al., 2011).

Obviously, the microwave heating would be more efficient than others. The wet fly ash processed by the microwave heating has several technical advantages. Firstly, the microwave heating is uniform and fast. The temperature of particles will rise, and the moisture distribution of their surface will change. Secondly, the charged process has a close relationship with the collision and vibration of the particles caused by the microwave heating. Thirdly, the temperature and moisture contents of particles can be controlled by the adjustable parameters of the microwave heating. Finally, the microwave heating operated in a closed environment will not produce dust pollution. Thus, it could be used as a pre-process for wet fly ash particles during the triboelectrostatic beneficiation. In this context, the aim of this study was to discuss the feasibility of realizing the wet fly ash triboelectrostatic beneficiation efficiently using microwave heating. The experimental results can provide some references for the engineering applications.

Experimental

Materials

The fly ash used in this study was obtained from a thermal power station of the Fujian province in China. A 30 kg portion of representative sample was divided into 30 portions uniformly. The particle size of the wet fly ash was obtained by a sieve analysis as $-74+38\text{ }\mu\text{m}$. The content of unburned carbon in the wet fly ash was obtained by the *LOI* analysis.

The samples exposed to the atmosphere can absorb moisture. The relative air humidity ranges from 48% to 90%. During this period of time, two samples of wet fly ash were collected and put into a sealed container before the experiments. The moisture contents of two samples were 4.37% and 8.23%, respectively. The wet fly ash had an average *LOI* of 12.65%.

The wet fly ash processed by a microwave oven before the experiments was weighted with an electronic scale. Then, the particles were put on the glass disc uniformly, and the glass disc was heated inside a microwave oven. The experimental conditions in this study were the microwave intensity (60%, 80%, and 100%) and irradiation time (30, 60, and 120 s). The microwave intensity was adjusted by a knob installed on the control panel. The maximal power of the microwave oven was 800 W. The microwave intensity is different from the output power of the microwave oven. The heating intensity is defined by manufacturers. It is only selected by the user and can't be

measured. The heating intensity of 100% indicates that the heating process is continuous. As the heating intensity is smaller than 100%, the heating process is discontinuous. There has been a close relation between the heating intensity and irradiation time. Meanwhile, the irradiation time was monitored by a timer.

Feasibility analysis

The dielectric constant of wet fly ash is larger than that of dry fly ash because of the moisture content. As the wet fly ash is processed by the microwave heating, the dielectric constant will gradually decrease because of the increase in temperature and the decrease in surface moisture. This can lead to reducing of electrical conductivity. The charge transfer can be prevented for the charged particles. It is effective to improve the charged efficiency. Therefore, the higher temperature caused by the microwave heating is conducive to the wet fly ash triboelectrostatic beneficiation. The feasibility of wet fly ash triboelectrostatic beneficiation using microwave heating was analyzed according to the experimental temperature and dielectric constant of particles.

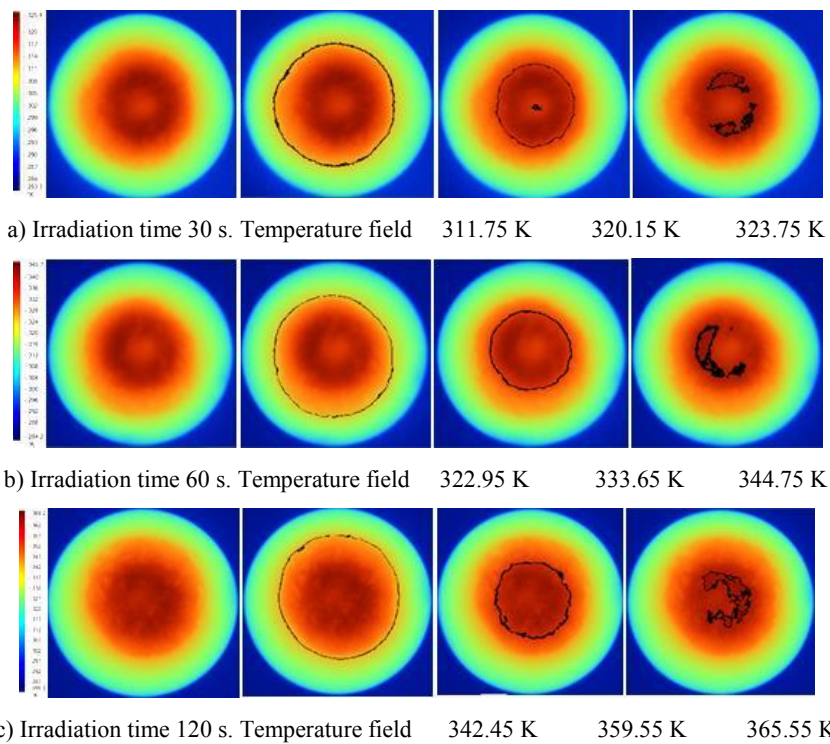


Fig. 1. Isothermal point distribution of temperature field

As the microwave intensity was 100%, the temperature distributions of the fly ash particles were detected by an infrared thermal imager of Ti10 made by FLUKE. The irradiation time was 30, 60, and 120 s. The experimental results analyzed by a software

are seen in Fig. 1. The temperature gradually decreased from inside to outside. The distribution of external isothermal region was circular, and that of central was uneven. The agglomeration of the wet fly ash particles was destroyed due to the vibration of the particles caused by the microwave heating. The longer the microwave time was, the better the particles dispersion would be.

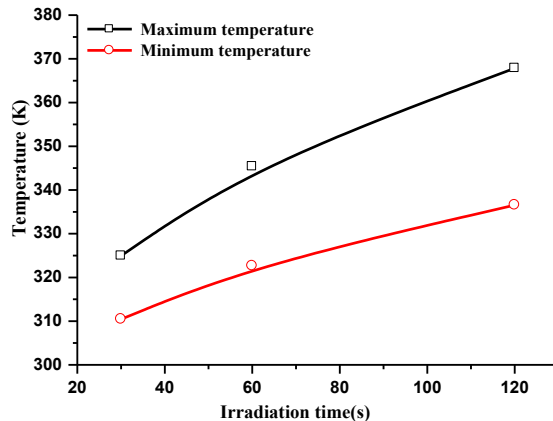


Fig. 2. Relationship between the temperature and irradiation time

A testing system of the dielectric constant is shown in Fig. 3. Two capacitance plates were put inside a metal cover. Three terminals were available for connecting safety ground and measuring instrument. A digital capacitance meter was connected with two electrodes. The measuring device was placed in a thermostat during the experiments. The capacitance was C_0 and C for the plates filled with vacuum and wet fly ash, respectively. The dielectric constant can be calculated as below:

$$\varepsilon = \frac{C}{C_0} \times 100\% \quad (1)$$

The relationship between the dielectric constant and irradiation time is illustrated in Fig. 4. The dielectric constant increased proportionally to the moisture content. The irradiation time of 0 s indicated the unprocessed wet fly ash. The dielectric constants of the particles having moisture contents 2.34%, 5.65%, and 10.23% were 5.29%, 24.02%, and 56.33%, respectively, at the irradiation time 0. The microwave heating reduced the surface moisture of wet the fly ash particles. When the irradiation time was 120 s, the dielectric constant values of the particles decreased to 4.13%, 17.21%, and 39.24%, respectively. The effect of the microwave heating on the dielectric constant values was more obvious with the increase of moisture content. With the increase of the irradiation time, the temperature of the particles increased and the dielectric constant values decreased gradually. Accordingly, the decrease of dielectric constants caused by the microwave heating reduced the electrical conductivity. As the charged particles

contacted with each other, it was difficult to realize the transfer of particles surface charge.

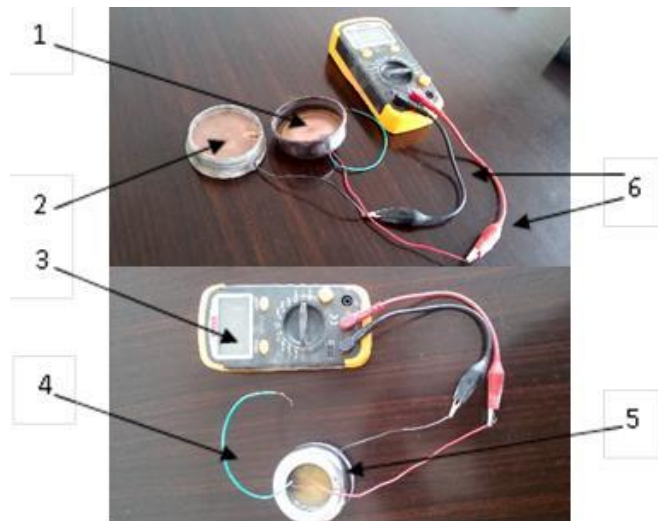


Fig. 3. The testing system of dielectric constant. 1. Positive electrode, 2. Negative electrode, 3. Digital capacitance meter, 4. Ground wire, 5. Metal cover, 6. Wires

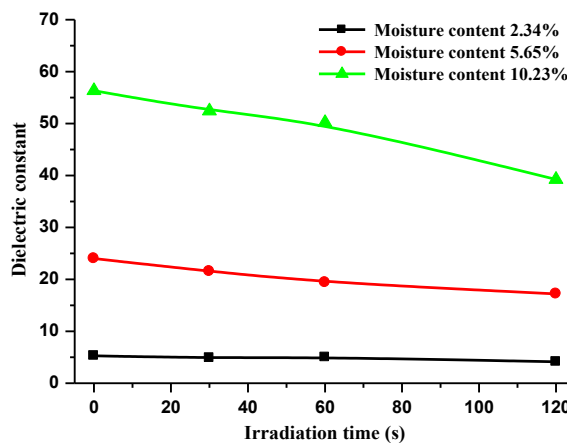


Fig. 4. Relationship between the dielectric constant and irradiation time

Experimental system

An experimental system of fly ash triboelectrostatic beneficiation is demonstrated in Fig. 5. A fan was controlled by a frequency changer in order to obtain the airflow with the flux ranging from 12 to 30 m^3/h . The wet fly ash particles were fed by a vibrator feeder with a controller and sucked into the pipeline. The medium temperature was 283.65 K, and the relative air humidity was 56.5%. The fly ash particles were carried by

the airflow produced by the fan. The particles were obtained different charges because of collision and friction inside a tribo-charger. The unburned carbon and the ash carried the opposite charge. The charged particles were injected into the high-voltage static field of 40 KV under the action of the airflow. The voltage was controlled by a power regulator. The motion of carbon and ash particles was in the opposite direction due to the electric field force. While the unburned carbon particles were recycled on the positive plate, the high-quality ash products with low carbon content were collected on the negative plate.

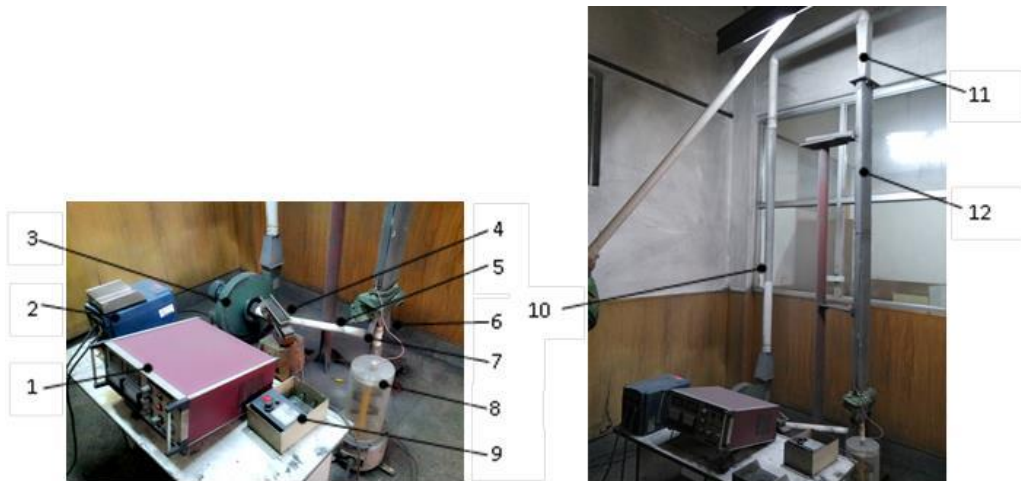


Fig. 5. Experimental system of wet fly ash triboelectrostatic beneficiation. 1. Power regulator, 2. Frequency changer, 3. Fan, 4. Vibrator feeder, 5. Delivery pipe, 6. Positive products 7. Negative products 8. High voltage power supply, 9. Controller of vibrating feeder, 10. Gas-solid mixing pipeline, 11. Tribo-charger, 12. Electric field

Experimental methodology

The efficiency of removal unburned carbon is evaluated by the *LOI* and recycle rate of the unburned carbon (*REC*). The recycling of unburned carbon was estimated by the removal rate of the unburned carbon (*REM*).

The *LOI* is calculated as follows:

$$LOI(\%) = \frac{M_0 - M_1}{M_0} \times 100\% \quad (2)$$

where M_0 is the mass of unbaked fly ash and crucible, g; M_1 is the mass of baked ash and crucible, g.

The *REM* and *REC* are defined as follows:

$$REM(\%) = \frac{LOI_s - LOI_-}{LOI_s} \times 100\% \quad (3)$$

$$REC(\%) = \frac{M_+}{M} \times \frac{LOI_+ - LOI_s}{LOI_s} \times 100\% \quad (4)$$

where LOI_s is defined as the LOI of fly ash sample before experiment, LOI_+ and LOI_- describes the LOI of fly ash obtained from the positive and negative plate, respectively. The mass of fly ash collected from the positive plate is M_+ , g. The mass of wet fly ash for each experiment is M_- .

Results and discussion

Influence of microwave intensity

The influence of the microwave intensity on the wet fly ash triboelectrostatic beneficiation was obtained at the irradiation time of 60 s and the moisture content of 4.37%. With the increase of the microwave intensity, the heating time during the same period was longer. The temperature of the particles increased gradually, and it caused reduction of the surface moisture and dielectric constant of the particles. Therefore, it helped the separation of the charged particles. Comparisons of LOI with different microwave intensity values are illustrated in Fig. 6.

The LOI_+ increased in proportion to the air flux, whether the fly ash was processed or not, while it was reversed for the negative plate. With the increase of air flux, the difference of LOI_+ between untreated and heated process decreased gradually, while that of LOI_- increased. It suggested that the increase of air flux was conducive to improving the efficiency of fly ash triboelectrostatic beneficiation. The LOI_+ increased from 16.06% to 20.78% for the untreated fly ash, while the LOI_- decreased from 9.68% to 8.48% as the air flux rose from 12 to 30 m^3/h . As the wet fly ash was processed with microwave intensity of 100% and air flux of 30 m^3/h , and the LOI of positive and negative plates was 22.07% and 6.98%, respectively. Under the condition of the same air flux, the microwave intensity was proportional to the LOI_+ . The results were opposite for the negative plate. As the microwave intensity was increased from 60% to 100%, and air flux was 30 m^3/h , the LOI_+ increased from 20.36% to 22.07%, while the LOI_- decreased from 7.95% to 6.98%.

The comparison of efficiency under different microwave intensity is shown in Fig. 7. The air flux and microwave intensity were in direct proportion to REM and REC . As the microwave intensity was 60% and air flux of 12 m^3/h , the REM and REC of wet fly ash processed by the microwave were 31.70% and 18.47%, while those of untreated were 23.48% and 11.59%, respectively. With the increasing of air flux, the difference of REM between heated and untreated was more obvious than that of REC . As the air flux ranging from 12 to 30 m^3/h , the REM increased from 37.15% to 44.82%, and the REC

increased from 24.31% to 29.40% with the microwave intensity of 100%. The maximum value of *REM* and *REC* was obtained under the condition of air flux of 30 m³/h and microwave intensity of 100%.

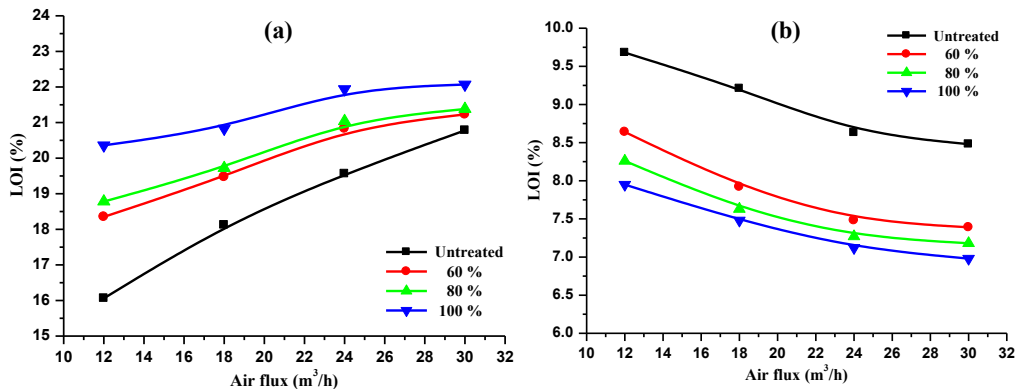


Fig. 6. Comparison of *LOI* under different microwave intensity values.

(a) Positive plate, (b) Negative plate

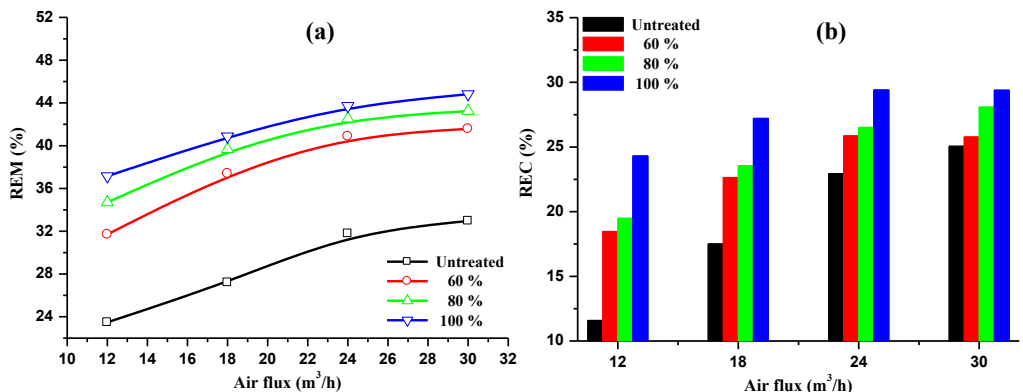


Fig. 7. Comparison of *REM* and *REC* under different microwave intensity. (a) *REM*, (b) *REC*

Influence of irradiation time

The irradiation time had an impact on the dielectric constant. A strong correlation between the irradiation time and temperature of the particles was observed according to the feasibility analysis. The decrease in the surface moisture caused by the microwave heating reduced the dielectric constant and the conductivity of the particles. The separation efficiency of charged particles was improved because the capacity of particles charge storage was enhanced. Figure 8 shows the comparison of *LOI* under the different irradiation time. The microwave intensity was 100%, and the moisture content of materials was 4.37%.

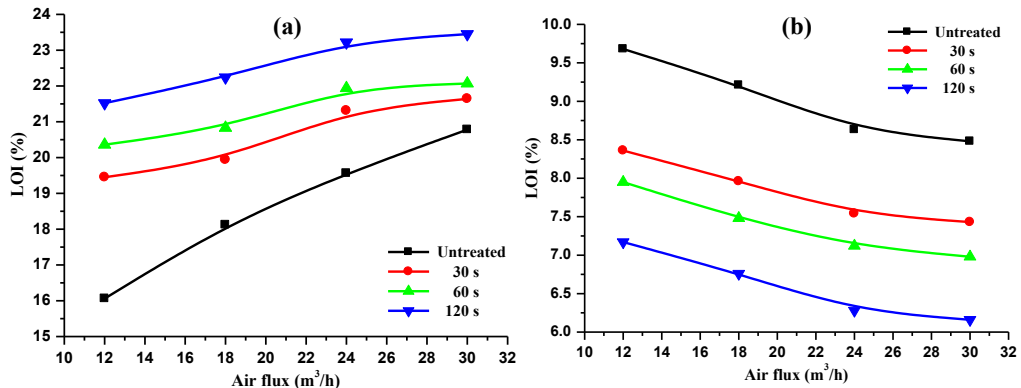


Fig. 8. Comparison of LOI under different irradiation time. (a) Positive plate, (b) Negative plate

With the increase of air flux, the difference of LOI_+ between heated and untreated fly ash was decreased gradually, while that of LOI was increased slowly. The LOI_+ of heated and untreated was 19.45% and 16.06% as the air flux of 12 m³/h and the irradiation time of 30s, while the LOI was 8.36% and 9.68%, respectively. When the irradiation time was 120 s, the LOI_+ increased from 21.52% to 23.45% as the air flux rose from 12 to 30 m³/h. The LOI decreased from 7.17% to 6.16%. As the irradiation time increased from 30 s to 120 s, the LOI_+ increased from 21.64% to 23.45% with the air flux 30 m³/h. Meanwhile, the LOI decreased from 7.43% to 6.16%. Thus, the irradiation time had an important effect on the triboelectrostatic beneficiation of wet fly ash.

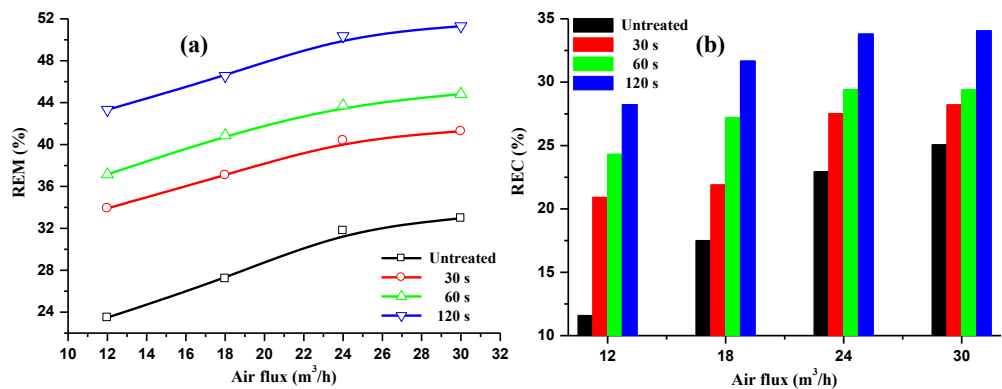


Fig. 9. Comparison of REM and REC under different irradiation time. (a) REM , (b) REC

The comparison of REM and REC under the different irradiation time is shown in Fig. 9. It can be seen there that the efficiency of removal and recovery was improved by the increase of irradiation time. As for the heated and untreated materials, the REM difference increased with the increasing of the air flux, and it was reversed to the REC .

As the irradiation time of 120 s and the air flux of 12 m³/h, the *REM* of heated and untreated was 43.32% and 23.48%, while the *REC* was 28.23% and 11.59%. As the air flux rose to 24 m³/h, the *REM* and *REC* of heated increased to 50.36% and 33.80%, and those of untreated increased to 31.78% and 22.94%, respectively. The longer the irradiation time was, the higher the *REM* and *REC* would be. As the air flux of 30 m³/h and irradiation time of 120 s, the *REM* and *REC* of heated increased to 51.30% and 34.06%, respectively. The wet fly ash triboelectrostatic beneficiation was realized efficiently.

Influence of moisture content

The higher the moisture content is, the larger the dielectric constant is. When the particles contact each other, it is easy to transfer and cancel the electrical charge for the same and different charged particles. This is not conducive to electrical charging process and particles separation. The microwave heating can improve the separation efficiency according to reduction of the moisture content and dielectric constant of the particles. Two samples with different moisture contents were processed by the microwave heating. The feasibility of improving the efficiency of wet fly ash triboelectrostatic beneficiation was verified by the experimental results. The comparison of *LOI* between two samples with different moisture contents is presented in Fig. 10. The operational conditions were the microwave intensity of 100% and the irradiation time of 120 s.

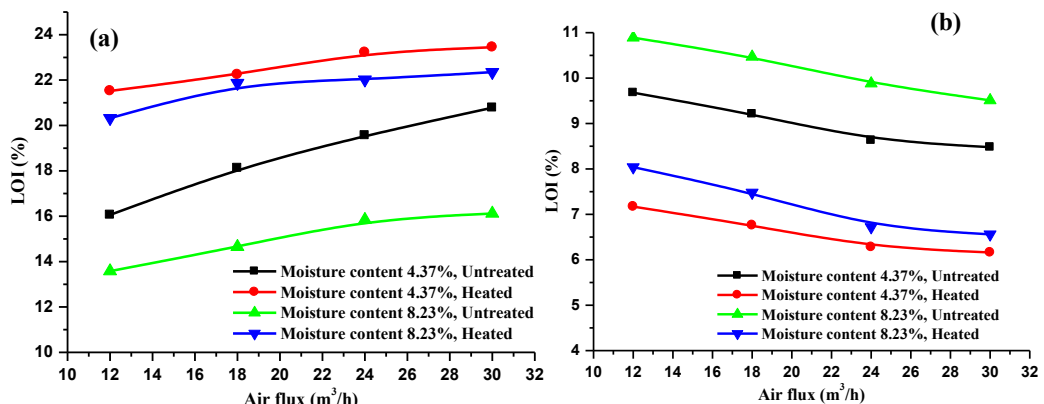


Fig. 10. Comparison of *LOI* for wet fly ash with different moisture content.

(a) Positive plate, (b) Negative plate

The *LOI*₊ and *LOI* of two samples obviously changed according to the difference of *LOI* between two plates. As for the fly ash with moisture content 4.37% and 8.23%, the *LOI*₊ of untreated was 20.78% and 16.12% for the air flux of 30 m³/h. When the wet fly ash with the moisture content of 4.37% was heated, the *LOI*₊ increased from 20.78% to 23.45%. Moreover, in the case of the wet fly ash with the moisture content 8.23%, the

LOI_+ increased from 16.12% to 22.35% because of the heating process. When the fly ash is processed by microwave heating, the LOI of fly ash with moisture content 4.37% decreased from 8.48% to 6.16%, while the moisture content 8.23% decreased from 9.51% to 6.56%.

A comparison of the efficiencies of beneficiation of wet fly ash with different moisture contents is shown in Fig. 11. The REM and REC increased markedly under the action of microwave heating. At the same operating conditions, the REM and REC of the sample with the moisture content of 4.37% were higher than those with the moisture content of 8.23%. The difference between two samples decreased gradually with the increasing of air flux. The REM of untreated fly ash with moisture content 4.37% increased from 23.49% to 32.96% as the air flux increased from 12 to 30 m^3/h whereas that of heated increased from 43.32% to 51.30%. The REM of untreated and heated increased to 24.82% and 48.14% for the wet fly ash with the moisture content 8.23%. As for the two samples with the moisture contents of 4.37% and 8.23%, the REC of untreated was 11.59% and 3.73% as the air flux was 12 m^3/h whereas that of heated was 28.23% and 26.55%. When the air flux increased to 30 m^3/h , the REC of heated was 8.99% and 20.71% higher than those of unheated. Therefore, the microwave heating can improve the efficiency of wet fly ash triboelectrostatic beneficiation according to the obvious difference between REM and REC .

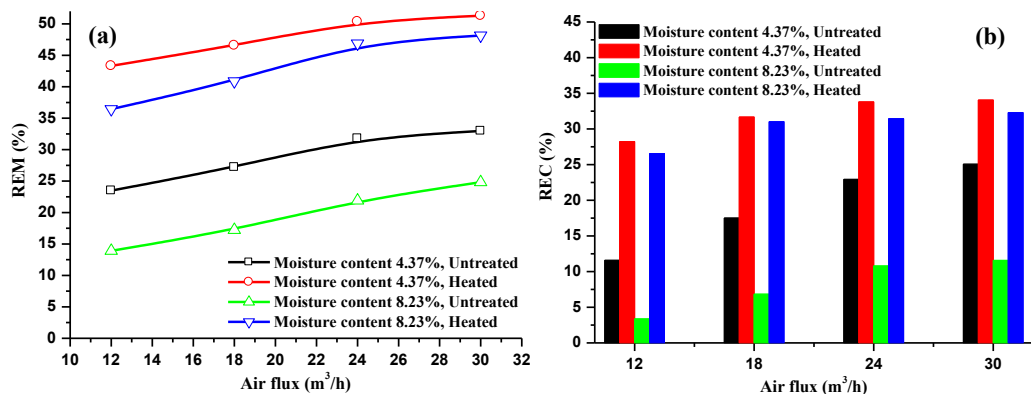


Fig. 11. Comparison of REM and REC for wet fly ash with different moisture content. (a) REM , (b) REC

Conclusions

An experimental study was conducted to study the feasibility of improving efficiency of wet fly ash triboelectrostatic beneficiation using microwave heating. The following major conclusions can be drawn from this study.

(1) Microwave heating can increase surface temperature and decrease moisture content of particles. The reduction of dielectric constant and conductivity caused by microwave heating has a positive effect on the electrical charging process. Furthermore, it is difficult to transfer and cancel electrical charges of the particles with the same and

different charges. Therefore, the charged efficiency can be improved by microwave heating.

(2) The difference between the LOI_+ and LOI under the same condition was noticeable as the wet fly ash was processed by the microwave heating. With the increase of the air flux, the microwave intensity and irradiation time, the REM and REC showed a significant increase. The results showed that the microwave heating was an effective method to improve the efficiency of triboelectrostatic beneficiation of wet fly ash. The separation process using the microwave heating can not only obtain the ash-rich products with lower carbon content but also improve the recovery rate of unburned carbon.

(3) According to the experimental study on wet fly ash with different moisture contents, the microwave heating is feasible to improve the efficiency of wet fly ash triboelectrostatic beneficiation. As for the fly ash with moisture content of 4.37% and 8.23%, the REM and REC increased obviously under the operating conditions at air flux of $30\text{ m}^3/\text{h}$, microwave intensity of 100% and irradiation time of 120 s. Finally, it can be concluded that these results will provide a technical reference for an industrial application of the wet fly ash triboelectrostatic beneficiation.

Acknowledgments

The financial support provided by “the Fundamental Research Funds for the Central Universities” (Project2014QNB12), “China Postdoctoral Science Foundation” (Project2014M560466), “Postdoctoral Science Foundation of Jiangsu Province” (Project1401054B) and “A Project Funded by the Priority Academic Program Development of Jiangsu Higher Education Institutions” for this work is gratefully acknowledged.

References

- ALI A.Y., BRADSHAW S.M., 2010, *Bonded-particle modelling of microwave-induced damage in ore particles*, Minerals Engineering, 23, 780-790.
- ALI A.Y., BRADSHAW S.M., 2011, *Confined particle bed breakage of microwave treated and untreated ores*, Minerals Engineering, 24, 1625-1630.
- BAN H., LI, TIAN X., HOWER J.C., SCHAEFER J.L., STENCEL J.M, 1997, *Dry triboelectrostatic beneficiation of fly ash*, Fuel, 76, 801-805.
- CANGIALOSI F., NOTARNICOLA M., LIBERTI L., CARAMUSCIO P., BELZ G., GURUPIRA T.Z., STENCEL J.M, 2006, *Significance of surface moisture removal on triboelectrostatic beneficiation of fly ash*, Fuel, 85, 2286-2293.
- CANGIALOSI F., NOTARNICOLA M., LIBERTI L., STENCEL J.M, 2008, *The effects of particle concentration and charge exchange on fly ash beneficiation with pneumatic triboelectrostatic separation*, Separation and Purification Technology, 62, 240-248.
- CANGIALOSI F., NOTARNICOLA M., LIBERTI L., 2009, *The role of weathering on fly ash charge distribution during triboelectrostatic beneficiation*, Journal of Hazardous Materials, 164, 683-688.
- CANGIALOSI F., INTINI G., LIBERTI L., NOTARNICOLA M., DI CANI, F., 2010, *Activated coal fly ash as improved mineral addition in cement and concrete*, 2nd International Conference on Sustainable Construction Materials and Technologies, 1431-1439.

CAO Y.J., LI G.S., LIU J.T., ZHANG H.J., ZHAI X., 2012, *Removal of unburned carbon from fly ash using a cyclonic-static microbubble flotation column*, Journal of the South African Institute of Mining and Metallurgy, 112, 891-896.

HUANG Y., TAKAOKA M., TAKEDA N., 2003, *Removal of unburned carbon from municipal solid waste fly ash by column flotation*, Waste Management, 23, 307-313.

HWANG J. Y., SUN X., LI Z., 2002, *Unburned carbon from fly ash for mercury adsorption: I. Separation and characterization of unburned carbon*, Journal of Minerals and Materials Characterization and Engineering, 1, 39-60.

KATO Y., 2012, *Wet granulation of mixed oxide powders de-nitrated by the microwave heating*, Journal of Nuclear Science and Technology, 49, 999-1009.

KIM J.K., CHO H.C., KIM S.C., 2001, *Removal of unburned carbon from coal fly ash using a pneumatic triboelectrostatic separator*, Journal of Environment Science and Health, Part A, 36, 1709-1724.

Li H.S., Chen Y.H., Wu K.B., Zhang X.X., 2013. *Particle collision during the tribo-electrostatic beneficiation of fly ash based on infrared thermography*. Journal of the South African Institute of Mining and Metallurgy, 113(12), 899-904.

LI H.S., CHEN Y.H., ZHAO Y.M., ZHANG X.X., WU K.B., 2015. *The effect of the cross-sectional shape of friction rods on the triboelectrostatic beneficiation of fly ash*, International Journal of Coal Preparation and Utilization, 35(3), 113-124.

Li H.S., Chen Y.H., Wu K.B., Wu T., Zhang X.X., 2015. *Experimental study on influencing factors of axial clearance for scroll compressor*, International Journal of Refrigeration, 54, 38-44.

LI H.S., ZHANG X.X., CHEN Y.H., 2012, *Collision characteristics of particles in the friction device of triboelectrostatic separator*, Journal of China University of Mining & Technology, 41, 607-612. (In Chinese)

SOONG Y., SCHOFFSTALL M.R., LINK T.A., 2001, *Triboelectrostatic beneficiation of fly ash*, Fuel, 80, 879-884.

Received March 13, 2015; reviewed; accepted July 31, 2015

KINETIC GRINDING TEST APPROACH TO ESTIMATE THE BALL MILL WORK INDEX

Hojjat H. GHAREHGHELAGH

Hacettepe University Department of Mining Engineering, 06800 Beytepe Ankara, Turkey
h.h.qaraqislaq@hacettepe.edu.tr

Abstract: The standard Bond method is the most acceptable method for designing and selecting ball/rod mills described by their basic parameter called work index (W_i). The standard Bond method is a tedious time consuming procedure requiring at least 7–10 grinding cycles, so that many researchers have tried to simplify this method to be able to perform a rapid calculation of a work index. This study aims to develop a new approach toward estimating the Bond ball mill work index (BBWI) by applying a series of kinetic grinding tests with Bond standard mill. Establishing a series of relationships between grinding parameters and Bond equation parameters, this approach is fast and practical due to eliminating laboratory control steps while reducing the number of milling steps. In this scope, thirteen ore samples were used to compare W_i values obtained by standard Bond method with those of the proposed kinetic approach. The kinetic periods were determined as 0.33, 1, 2, 4 and 8 minutes. The results of kinetic tests were found to be logical and acceptable as they were so close to the values obtained by Bond standard method, for all samples error was $\leq 2.60\%$. It was therefore concluded that the proposed approach could be considered as a simple yet practical alternative for the standard Bond method.

Keywords: work index, Bond method, kinetic grinding test, grindability, ball mill

Introduction

The standard Bond (1952; 1961) method is widely used in the course of design, selection, scale up, energy calculation and performance evaluation of grinding circuits in mineral processing industry. This is mainly owed to the wide and valid database this method uses to derive its empirical equation (Bond, 1952; 1960; 1961). The most important parameter in this empirical equation is the Bond work index (W_i) which expresses the resistance of a material to comminution. In mineral industry, this is generally used for comparing the resistance of different materials in milling, estimating the required energy for milling (Levin, 1989) and mill scaling-up (Man, 2002).

The W_i parameter is obtained from Bond's ball mill grindability test (Bond, 1961). This test is performed according to the standard Bond procedure which proposed model is presented in Eq. 1. This standard grindability test simulates a closed-cycle dry grinding and screening process, which continues to carry out until the steady state condition of 250% circulating load is obtained. This grindability test is conducted in a Bond ball mill of $\phi D/L = 0.3048/0.3048$ m dimensions at the speed of 70 rpm. The mill is loaded with 21.125 kg standard sized balls and 700 cm³ of grinded materials to under 3.35 mm. The test procedure takes from 7 to 10 grinding cycles with the required amount of material for whole procedure being approximately 10 kg. Once steady state condition is achieved, the work index, W_i , can be calculated according to the following Eq. 1.

$$W_i = \frac{48.95}{D^{0.23} G_{bp}^{0.82} \left(\frac{10}{\sqrt{P_{80}}} - \frac{10}{\sqrt{F_{80}}} \right)} , \frac{kWh}{Mg} . \quad (1)$$

Determining W_i via the standard Bond method needs careful grinding cycles and screen procedures. However, these are tedious time-consuming procedures with potential errors in sieving steps. Considering the difficulties of the standard Bond method in the course of determining W^i , a number of simpler and faster alternative methods have been developed by various researchers (Berry and Bruce, 1966; Smith and Lee, 1968; Horst and Bassarar, 1977; Karra, 1981; Yap et al., 1982; Armstrong, 1986; Magdalinosic, 1989; Nematollahi, 1994; Aksani and Sonmez, 2000; Deniz and Ozdag, 2003; Yalcin et al., 2004; Ipek et al., 2005; Ahmadi and Shahsavar, 2009; Ahmadi et al., 2013).

The aim of this study is to develop a new approach to estimate the Bond ball mill work index (BBWI) using a combination of Bond standard mill and initial test conditions by conducting kinetic grinding tests. The proposed approach differs from the previous methods in that it determines the required grinding parameters for calculating work index by the resultant distributions from the sieve analysis of the kinetic grinding tests, with no need to the control step using the 106 μ m sieve. Although the same methodology was used for all materials, different relationships were established depending on the material. The kinetic method is implemented in two steps: 1) conducting laboratory grinding tests, and 2) calculation process in which the relationships between laboratory and Bond equation parameters are established.

Method and material

The experimental conditions of kinetic grinding tests together with mill specifications are given in Table 1. Except for grinding time, revolution numbers, sample amount and sieving procedures, all other operational conditions were set according to the standard Bond procedure.

Table 1. Conditions of kinetic grinding test and mill specifications
(more in Appendix A)

D_m , cm	30.48
L_m , cm	30.48
V , rpm	70
C_v	0.91
J_B , %	19.27
M_B , kg	21.125
d_B , mm	36.38
Geometry of mill liner	smooth
Grinding type	dry
V_{ore} , cm ³	700
T , min	0.33, 1, 2, 4, 8

Thirteen samples of different ores and materials such as copper, iron and clinkers were collected for testing. According to the Bond method, these samples were prepared via repeated crushing in a laboratory jaw crusher following by sieving into appropriate sizes (100% < 3.35mm). Then, a representative feed sample of 700 cm³ was taken followed by measuring its weight (W). Particle size distribution of feed sample was measured, so that F_{80} , $F_{(-106)}$ and G_{feed} were determined.

The proposed method

The test procedure shown in Fig. 1 performs in the followings steps.

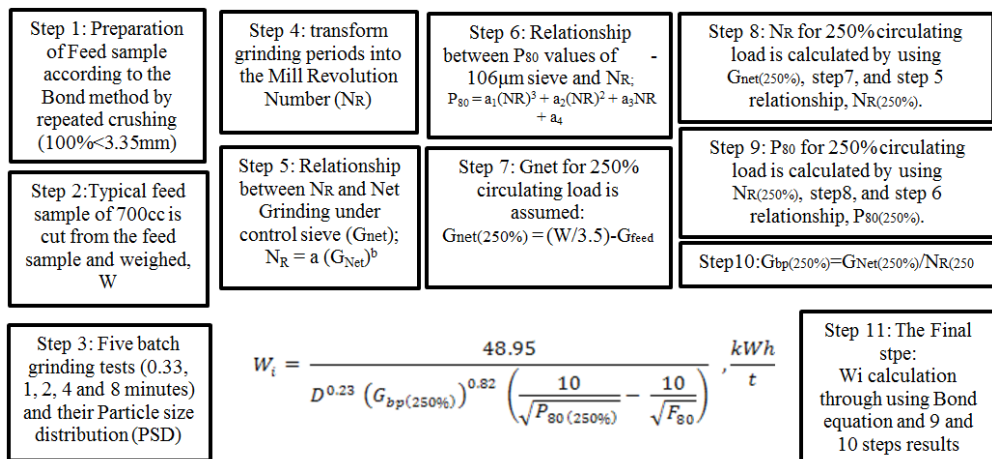


Fig. 1. Kinetic grinding approach procedure for BBWI calculation

Kinetic grinding

Exactly 700 cm³ of 100% passing 3.35 mm material from each sample was progressively ground in periods of 0.33, 1, 2, 4, and 8 minutes. Our experience has shown that the required number of revolutions to achieve the circulating load of 250% is most likely to be between 200 to 300 rotations. However, it will be suitable to select a grinding time of 8 minutes (560 cycles) to ensure achieving the desired condition while creating an additional point to reduce the associated errors to the fitted model. After each grinding step, the mill contents were removed and dry sized. Particle size distributions were recorded for fresh feed as well as the product obtained at the end of each grinding step. As an example, particle size distributions of hematite sample are presented in Fig. 2. The $G_{tot(i)}$, $G_{Net(i)}$ and $P_{80(i)}$ were determined graphically and numerically for each grinding step.

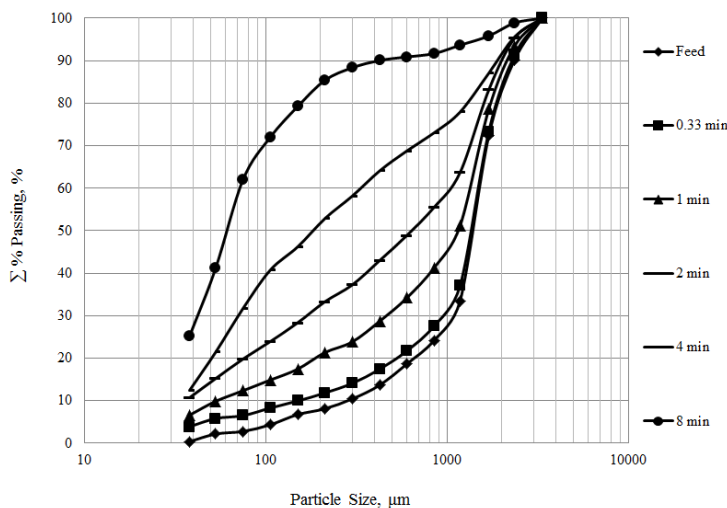


Fig. 2. Kinetic grinding results, hematite sample

$t - N_R$ conversion

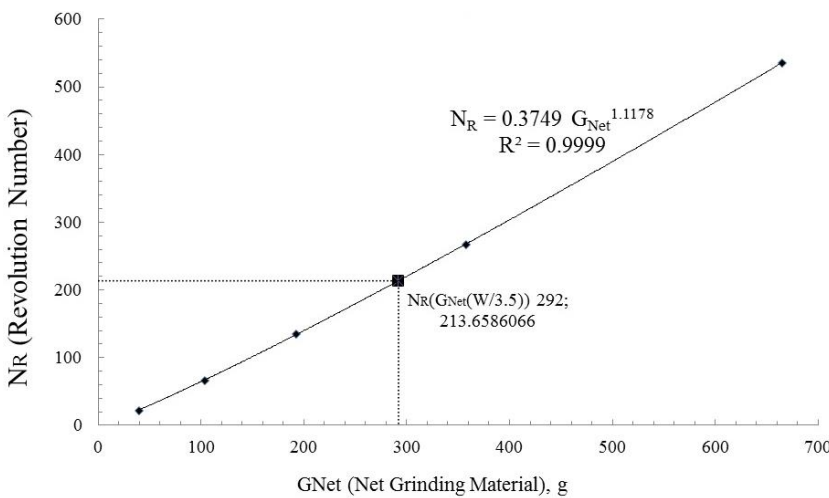
Referring to the mill speed, 70 rpm, the grinding period (t) was converted into the mill revolution number (N_R).

Relationship between N_R and G_{Net}

In this step, a relationship was established between N_R and G_{Net} using non-linear least squares fitting techniques. The value of G_{Net} was estimated for each N_R using particle size distribution graphs obtained from the kinetic grinding tests in section 3.1, ($N_{R(i)}$, $G_{Net(i)}$). An exponential relationship was found between N_R and G_{Net} with the corresponding equations presented in Table 3 for all samples. Figure 3 shows $N_R - G_{Net}$ relation of hematite sample, as an example.

Table 3. Obtained N_R - G_{Net} equations for all samples

Sample No.	Ore type	N_R - G_{Net}	R^2
1	Bauxite	$N_R = 0.3883 G_{Net}^{1.0624}$	0.9995
2	Hematite	$N_R = 0.3749 G_{Net}^{1.1178}$	1.0000
3	Chromite1	$N_R = 0.4171 G_{Net}^{1.0984}$	0.9945
4	Chromite2	$N_R = 0.4396 G_{Net}^{1.0899}$	0.9998
5	Chalcopyrite1	$N_R = 0.5518 G_{Net}^{1.0371}$	0.9985
6	Chalcopyrite2	$N_R = 0.4673 G_{Net}^{1.0489}$	0.9983
7	Clinker1	$N_R = 0.6346 G_{Net}^{1.033}$	0.9982
8	Clinker2	$N_R = 0.5097 G_{Net}^{1.0574}$	0.9991
9	Dolomite	$N_R = 0.5004 G_{Net}^{1.0486}$	0.9986
10	Magnetite	$N_R = 0.3955 G_{Net}^{1.0784}$	0.9995
11	Limestone1	$N_R = 0.5937 G_{Net}^{1.032}$	0.9982
12	Limestone2	$N_R = 0.7076 G_{Net}^{0.9845}$	0.9989
13	Quartzite	$N_R = 0.3523 G_{Net}^{1.1083}$	0.9954

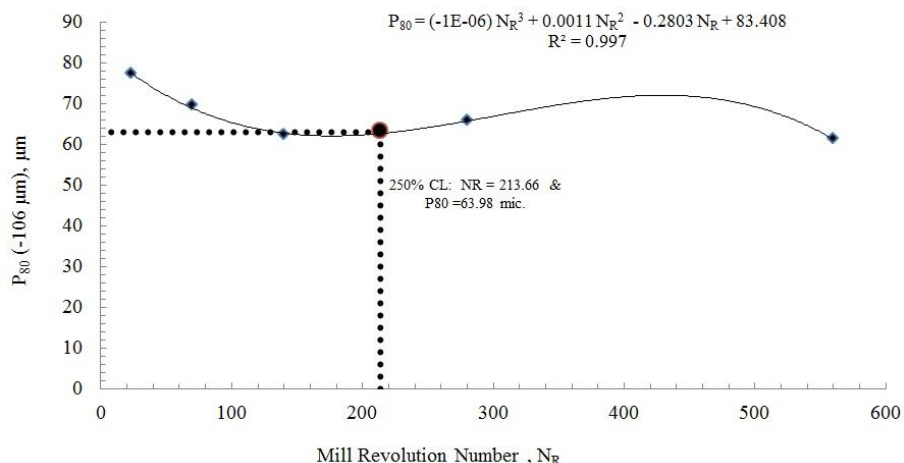
Fig. 3. N_R - G_{Net} relationships, hematite sample

Relationship between N_R and P_{80}

Based on non-linear least squares fitting techniques, relationships among P_{80} values, $P_{80(i)}$, and N_R values were established. These are polynomial relationships presented in Table 4 for all samples. Figure 4 shows the relationship between P_{80} and N_R for the Hematite sample, as an example. In order to avoid extraneous oscillations in the cubic relationship established between N_R and P_{80} , a linear interpolation might be preferred. In Fig. 4, P_{80} increases with $N_{R(280)}$ possibly because of the agglomeration of fine particles.

Table 4. Obtained $P_{80} - N_R$ equations for all samples

Sample No.	Ore type	$P_{80} - N_R$	R^2
1	Bauxite	$P_{80} = (-2E-06) N_R^3 + 0.0014 N_R^2 - 0.3094 N_R + 87.923$	0.968
2	Hematite	$P_{80} = (-1E-06) N_R^3 + 0.0011 N_R^2 - 0.2803 N_R + 83.408$	0.9971
3	Chromite1	$P_{80} = (-2E-06) N_R^3 + 0.0017 N_R^2 - 0.3394 N_R + 93.704$	0.9647
4	Chromite2	$P_{80} = (-9E-07) N_R^3 + 0.0008 N_R^2 - 0.1858 N_R + 95.371$	0.9876
5	Chalcopyrite1	$P_{80} = (-2E-06) N_R^3 + 0.0015 N_R^2 - 0.3097 N_R + 91.002$	0.982
6	Chalcopyrite2	$P_{80} = (-2E-06) N_R^3 + 0.0015 N_R^2 - 0.3464 N_R + 102.7$	0.9956
7	Clinker1	$P_{80} = (-1E-06) N_R^3 + 0.0012 N_R^2 - 0.2643 N_R + 95.144$	0.9834
8	Clinker2	$P_{80} = (-1E-06) N_R^3 + 0.0012 N_R^2 - 0.2426 N_R + 92.183$	0.9967
9	Dolomite	$P_{80} = (-1E-06) N_R^3 + 0.0011 N_R^2 - 0.2607 N_R + 97.003$	0.9831
10	Magnetite	$P_{80} = (-2E-06) N_R^3 + 0.0016 N_R^2 - 0.3955 N_R + 102.23$	0.9808
11	Limestone1	$P_{80} = (-1E-06) N_R^3 + 0.0011 N_R^2 - 0.2605 N_R + 94.201$	0.9788
12	Limestone2	$P_{80} = (-1E-06) N_R^3 + 0.0011 N_R^2 - 0.2836 N_R + 104.38$	0.9868
13	Quartzite	$P_{80} = (-1E-06) N_R^3 + 0.0009 N_R^2 - 0.1658 N_R + 67.834$	0.9566

Fig. 4. $P_{80} - N_R$ relationships, hematite sample

Estimation of P_{80} and N_R for 250% circulating load

In the standard Bond grindability method, the CL of the grinding cycle is considered to be 250%. It means that the total charge in the mill is 350% or 3.5 times the fresh feed. Considering the weight W for all samples in the standard Bond grindability test, the purpose of the test will be to keep the passed amount of grinded material through the controlled sieve constant at $W/3.5$. Therefore, in order to reach the equilibrium grinding condition when CL is 250%, the G_{Net} must be equal to $G_{Net(250\%)} = \left(\frac{W}{3.5}\right) \times$

$\left(\frac{100 - F_{(-106)}}{100}\right)$. This is taken as the base-assumption-factor. The value of N_R for 250% CL , $N_{R(250\%)}$, is determined by using $G_{Net} - N_R$ plot or relationship, while the value of P_{80} for 250% CL , $P_{80(250\%)}$, is determined by using $N_R - P_{80}$ plot or relationship.

Estimation of $G_{bp(250\%)}$

The value of G_{bp} can be calculated by means of obtained N_R and G_{Net} values for 250% circulating load, $G_{bp(250\%)} = G_{Net(250\%)} / N_{R(250\%)}$.

Calculation of $BBWI (W_i)$

Finally, the $BBWI$ or W_i can be calculated using the Bond equation (Eq. 1) and the estimated $G_{bp(250\%)}$ and $P_{80(250\%)}$ parameters for kinetic grinding tests.

Table 5. Comparison of standard Bond method and kinetic tests results

Sample No.	Ore type	Used Method	P_{80}	G_{bp} , g/rev	W_i , kWh/t	Error, %
1	Bauxite	kinetic test	66.42	1.771	10.321	-1.47066
		Bond Standard	65.21	1.779	10.172	
2	Hematite	kinetic test	63.48	1.374	12.525	0.04788
		Bond Standard	62.97	1.365	12.531	
3	Chromite1	kinetic test	81.30	1.358	14.330	-1.76406
		Bond Standard	81.09	1.384	14.082	
4	Chromite2	kinetic test	83.83	1.360	14.649	-1.04807
		Bond Standard	81.56	1.349	14.497	
5	Chalcopyrite1	kinetic test	74.44	1.460	13.054	0.733376
		Bond Standard	75.11	1.457	13.150	
6	Chalcopyrite2	kinetic test	78.03	1.601	12.298	0.951632
		Bond Standard	78.62	1.592	12.416	
7	Clinker1	kinetic test	87.78	1.304	15.471	0.985496
		Bond Standard	85.24	1.260	15.625	
8	Clinker2	kinetic test	86.74	1.410	14.865	0.898863
		Bond Standard	87.02	1.398	14.999	
9	Dolomite	kinetic test	82.45	1.505	13.479	-1.73527
		Bond Standard	80.56	1.510	13.249	
10	Magnetite	kinetic test	71.31	1.598	11.806	2.590589
		Bond Standard	73.25	1.579	12.120	
11	Limestone1	kinetic test	79.66	1.400	13.998	-0.01085
		Bond Standard	79.48	1.398	13.997	
12	Limestone2	kinetic test	86.16	1.548	13.646	0.584285
		Bond Standard	87.22	1.551	13.727	
13	Quartzite	kinetic test	62.40	1.527	11.238	0.387378
		Bond Standard	64.39	1.555	11.282	

Comparison of the results of standard method and the kinetic tests

Once the calculations were conducted, a comparison was performed between the results of the standard Bond method and those of kinetic tests and presented in Table 5. The complete W_i estimation procedure using the kinetic method is presented in Appendix A.

Results and discussion

In this study, a new approach was developed toward determination of the work index based on kinetic tests and Bond standard conditions. The G_{Net} value for 250% CL was assumed as $G_{Net(250\%)} = \left(\frac{W}{3.5}\right) \times \left(\frac{100 - F(-10^6)}{100}\right)$. This assumption was taken as the base-assumption-factor of the current study. The Bond method along with the kinetic approach was used to determine the work indices of different materials within thirteen samples. The results showed that the obtained values for work indices by means of kinetic tests were in good agreement with those of the standard Bond method, for all samples: error $\leq 2.60\%$, indicating usefulness of the Base-Assumption-Factor for estimation of W_i . The proposed procedure included five batch grinding tests, their sieve analyses in laboratory and the calculation process according to laboratory results and the Bond equation. This method is fast and practical as it eliminates laboratory control steps and reduces the number of milling steps. It also reduces the required weight of material from about 10 kg to approximately 1.5 kg. Due to these results and the simplicity of the method, the new developed approach can be used instead of the standard Bond method. It should be carefully noted that if an ore sample contains small amounts of very hard fractions, it will be necessary to apply a full Bond test to accumulate these fractions. This approach gives a raise to the possibility of using the collected data to change the test screen size and the assumed circulating load without collecting further data. This issue will be discussed in future studies.

Acknowledgments

The author gratefully acknowledges the financial support provided by the Turkish Scientific and Technical Research Council (TÜBİTAK) under grant No: B.02.1.TBT.0.06.01.00-215.01-847/6116 for 2215 program.

Appendix A. Determination of the Bond work index using the kinetic method

In order to determine Bond work index of a material, firstly, it must be prepared according to the Bond standard method. The kinetic method uses the same mill operating under the same conditions as those in Bond standard procedure, except for the grinding time, revolution numbers, sample amount and sieving procedure. Specifications of hematite sample, as an example, are presented in Table A.1.

Table A.1. Specifications of hematite sample

V_{ore, cm^3}	W, g	$F_{80}, \mu\text{m}$	$F_{(-106)}, \%$	$CL, \%$	$W/3.5, \text{g}$
700	1022	1983	4.89	250	292.00

Calculation of W_i through the proposed kinetic method was performed at five grinding cycles. The sieve analysis of the fresh feed and these grinding cycles were measured and plotted. The obtained graph for the hematite sample is presented in Fig. 2, as an example. Then, the calculation procedure was conducted as follows:

1. for a 250% circulating load, the net grinded material was $G_{Net(250\%)} = \left(\frac{W}{3.5}\right) \times \left(\frac{100 - F_{(-106)}}{100}\right) = 279.27 \text{ g}$
2. each grinding period, t , was converted into a Mill Revolution Number, N_R
3. for each N_R , the values of G_{Net} and P_{80} were estimated through using particle size distribution graphs shown in Fig. 2
4. for hematite samples, an exponential relationship was established between N_R and G_{Net} ($N_R = 0.3749 G_{Net}^{1.1178}$, Fig. 3), so that
5. $N_{R(250\%)} = 0.3749 \times (279.27)^{1.1178} = 203.27 \text{ rev}$
6. for hematite sample, the following polynomial relationship was established between N_R and P_{80} : $P_{80} = (-1E - 06)N_R^3 + 0.0011 N_R^2 - 0.2803N_R + 83.408$, Fig. 4, so that the P_{80} value for $N_{R(250\%)}$ was calculated as $P_{80(250\%)} = 63.48 \mu\text{m}$
7. the grindability factor, G_{bp} , could be calculated by means of obtained N_R and G_{Net} for 250% circulating load: $G_{bp(250\%)} = (G_{Net(250\%)})/N_{R(250\%)} = 279.27/203.27 = 1.374 \text{ g/rev}$
8. finally, the Bond equation was used to determine the work index, which was equal to 12.525 (kWh/Mg) in our example.

Nomenclature	
$BBWI$	Bond Ball Mill Work Index (kWh/Mg)
CL	Circulating Load (%)
C_v	Mill speed (fraction of critical)
D	Control sieve size = 106 μm
d_B	Ball top size (mm)
D_m	Inner diameter of mill (cm)
$F_{(-106)}$	Amount of -106 μm in the mil Feed, before grinding, (%)
F_{80}	80% passing size of the mill feed, before grinding, (μm)
G_{bp}	Grindability factor (g/rev)
$G_{bp(250\%)}$	Grindability factor for 250% circulating Bond ball mill work index load (g/rev)
G_{feed}	Weight of -106 μm material in the mill feed, before grinding, (g)
G_{Net}	Net grinding material of -106 μm (g)
$G_{Net(250\%)}$	Net grinding material under control sieve for 250% circulating load (g)

$G_{Net(i)}$	Weight of net grinding material of -106 μm for any step that is equal to $G_{tot(i)}$ minus G_{feed} for $i=1,2,..,5$
$G_{tot(i)}$	Weight of -106 μm material in the mill product at any step (g)
J_B	Ball load (% by volume)
L_m	Inner length of mill (cm)
M_B	Total mass of balls (kg)
N_R	Mill revolution numbers
$N_{R(250\%)}$	NR for 250% circulating load
$N_{R(i)}$	amount of revolution number for each step, $i = 1, 2, \dots, 5$
P_{80}	80% passing size of the final product (μm)
$P_{80(250\%)}$	P80 for 250% circulating load
$P_{80(i)}$	80% passing size of the -106 μm material for any step for $i=1,2,..,5$ (μm)
R^2	R-squared or coefficient of determination
t	Grinding period (min)
V	Mill speed (rpm)
V_{ore}	Ore volume, required material (cm ³)
W	Mass of mill content (g)
$W/3.5$	Weight of material for 250% circulating load (g)
W_i	Work index (kWh/Mg)

References

AHMADI R., HASHEMZADEHFINI M., AMIRI PARIAN M., 2013, *Rapid determination of Bond rod-mill work index by modeling the grinding kinetics*, Advanced Powder Technology 24, 441–445.

AHMADI R., SHAHSAVARI SH., 2009, *Procedure for determination of ball Bond work index in the commercial operations*, Minerals Engineering 22, 104–106.

AKSANI B., SONMEZ B., 2000, *Simulation of Bond Grindability Test by Using Cumulative Based Kinetic Model*, Minerals Engineering 13 (No. 6), 673-677.

ARMSTRONG D.G., 1986, *An alternative grindability test: an improvement of the Bond procedure*, International Journal of Mineral Processing 16, 197–208.

BERRY T.F., BRUCE R.W., 1966, *A simple method of determining the grindability of ores*, Can. Min. J. 87, 63–65.

BOND F.C., 1952, *The Third Theory of Comminution*, Transaction AIME (Mining) 193, 484-494.

BOND F.C., 1960, *Three Principles of Comminution*, Mining Congress Journal (August), 53-56.

BOND F.C., 1961, *Crushing and Grinding Calculation*, British Chemical Engineering 6 (June & Aug.), 378-385 & 543-548.

DENIZ V., OZDAG H., 2003, *A new approach to Bond grindability and work index: dynamic elastic parameters*, Minerals Engineering 16 (3), 211– 217.

HORST W.E., BASSAREAR J.H., 1977, *Use of simplified ore grindability technique to evaluate plant performance*, Trans. Soc. Min. Eng. (AIME) 260, 348–351.

IPEK H., UCBAS Y., HOSTEN C., 2005, *The bond work index of mixture of ceramic raw materials*, Mineral Engineering 18, 981-983.

KARRA V.K., 1981, *Simulation of Bond grindability tests*, CIM Bull. 74, 195–199.

LEVIN J., 1989, *Observation on the Bond Standard Grindability Test and a Proposal for a Standard Grindability Test for Fine Materials*, Journal of South African Institute of Mining and Metallurgy 1, 13-21.

MAGDALINOVIC N., 1989, *A procedure for rapid determination of the Bond work index*, International Journal of Mineral Processing 27 (1-2), 125-132.

MAN Y.T., 2002, *Why is the Bond Ball Mill Grindability Test done the way it is done?*, European journal of mineral processing and environmental protection 2, 34-39.

NEMATOLLAHI H., 1994, *New size laboratory ball mill for Bond work index determination*, Minerals Engineering, 352-353.

SMITH R.W., LEE K.H., 1968, *A comparison of data from Bond type simulated closed-circuit and batch type grindability tests*, Trans. Soc. Min. Eng. (AIME) 24, 91-99.

YALCIN T., IDUSUYI E., JOHNSON R., STURGESSION C., 2004, *A simulation study of sulphur grindability in a batch ball mill*, Powder Technology 146 (Issue 3), 193-199.

YAP R.F., SEPULVEDA J.L., JAUREGUI R., 1982, *Determination of the Bond work index using an ordinary laboratory batch ball mill: Designing and Installation of comminution circuits*, Soc. Min. Eng. (AIME), 176-203.

Received June 12, 2015; reviewed; accepted August 7, 2015

SYNERGISTIC SOLVENT EXTRACTION OF Co(II) AND Li(I) FROM AQUEOUS CHLORIDE SOLUTIONS WITH MIXTURE OF CYANEX 272 AND TBP

Beata POSPIECH

Department of Chemistry, Czestochowa University of Technology, Armii Krajowej 19, 42-200 Czestochowa, Poland, e-mail: b.pospiech@wip.pcz.pl

Abstract: In this work, separation of cobalt(II) over lithium(I) ions from aqueous chloride solutions by synergistic solvent extraction (SX) has been studied. A synergistic mixture of commercial extractants such as bis(2,4,4-trimethylpentyl)phosphinic acid (Cyanex 272) and tributyl phosphate (TBP) in kerosene was used as a selective extractant. The investigations were first performed to select optimal conditions for the effective separation including pH of the aqueous phase as well as concentration of synergistic mixture. High selective solvent extraction of cobalt(II) over lithium(I) from chloride solution has been achieved by the mixture of 0.1 M Cyanex 272 and 0.05 M TBP in kerosene while efficient Co(II) stripping has been performed by 0.5 M sulphuric acid.

Keywords: cobalt(II), lithium(I), Cyanex 272, TBP, synergistic extraction

Introduction

Cobalt is a strategic metal, which has many industrial uses. This metal is less available and thus more costly than other transition metals, such as manganese, iron and nickel (Chagnes and Pospiech, 2013). On the other hand, lithium application in batteries has expanded significantly in recent years, because rechargeable lithium-ion batteries (LIBs) have increasingly been used in portable electronic devices, such as: mobile telephones, laptops, video-cameras, etc. They are also used to provide constant electric current for electric automobiles (Pospiech, 2014a). Many investigations have been carried out to recover valuable metals from the waste LIBs by hydrometallurgical technologies, which include the following stages: crushing, physical separation and leaching. The processing of wastes containing metals for their recovery and separation is very important due to the essential two aspects – economic and environmental (Chmielewski et al., 1997; Pospiech 2013; Pospiech 2014a). The solutions after

leaching of LIBs are subjected to separation processes, i.e. precipitation of impurities, solvent extraction, adsorption and ion-exchange to isolate and concentrate the valuable metals. The separation stage is necessary since it enables the next step of the obtaining pure metal or compounds of this metal (Kolodynska et al. 2008; Pospiech 2010; Pospiech 2015).

Solvent extraction processes are very often used for separation of ferrous metals ions from wastewater (Wionczyk 2013; Ochromowicz and Chmielewski 2013) and leach liquors (Chagnes and Pospiech, 2013). This technique requires appropriate extractants whose aim is to provide high selectivity and efficiency of this process. The organophosphorous acids, such as: Cyanex 272, Cyanex 301 and Cynex 302 (Preston, 1982; Gega et al., 2001; Kozlowski et al., 2006) and amines (Marchese et al., 1995) were studied for the extraction of Co(II) from aqueous chloride and sulphate solutions. The specific extraction of cobalt(II) ions with Cyanex 272 have been reported in numerous publications (Rickelton and Boyle, 1988; Gandhi et al. 1993, Swain et al. 2007). However, instead of a single extractant, we can used a mixture of extractants, which may give rise to synergistic effects and better efficiency and selectivity of metal ions extraction from aqueous solutions (Pospiech 2014). In addition, we may observe that the extractive capability of a mixture of extractants is greater than the sum of their individual extractive capabilities (Zhu et al. 2012; Pospiech 2014b, Pospiech and Chagnes, 2015). Synergistic effects have been studied in the extraction of Co(II) and Ni(II) using the sodium salts of D2EHPA, PC88A and Cyanex 272 and their mixtures (Devi et al., 1994; Sarangi et al., 1999) as well as a mixture of D2EHPA and 5-dodecylsalicylaldoxyme (Zhang et al., 2001). The main advantage of mixed extractant systems over developing new reagents is that the reagents are already commercially available (Pospiech and Chagnes, 2015).

The most important aim of this paper was the separation of Co(II) and Li(I) from aqueous chloride solutions using a synergistic mixture of Cyanex 272 and TBP. Up to now, the proposed synergistic mixture was not applied as a selective extractant in solvent extraction of Co(II). The effects of pH, extractant concentrations in the organic phase as well as the concentration of sulphuric acid in the stripping phase on the extraction percent and selectivity with the mixture of Cyanex 272 and TBP have been studied.

Experimental

Inorganic chemicals. Cobalt chloride $\text{CoCl}_2 \cdot 6\text{H}_2\text{O}$, lithium chloride LiCl , sulphuric acid (H_2SO_4), were of analytical grade and were purchased from POCh (Gliwice, Poland). Aqueous solutions were prepared with deionized water (conductivity of 0.1 $\mu\text{S}/\text{cm}$ at 25 °C). The aqueous phase containing 0.01 M Co(II) and 0.01 M Li(I) was used for the investigation.

Organic reagents. Bis(2,4,4-trimethylpentyl)phosphinic acid (Cyanex 272) and tributyl phosphate (TBP) were of analytical reagent grade (Fluka) and used without further purification.

Solvent extraction. It was carried out as reported in an earlier paper (Pospiech and Chagnes, 2015). Equal volumes of organic and aqueous phases (phase volume ratio O/A=1) were mechanically shaken for 20 minutes at 25±2 °C. Then the aqueous phase was separated from the organic phase. Equilibrium pH of aqueous phases were measured with an Elmetron CX-731 pH-meter equipped with a glass electrode (Hydromet, Poland). Metal ions concentrations in aqueous phases were analyzed with AAS Solaar 939 (Unicam) spectrophotometer (AAS – Atomic Absorption Spectrometry). The concentration of metal ions in aqueous phases was determined before and after solvent extraction for calculating extraction efficiency and after stripping for calculating stripping efficiency. The concentrations of metals in organic phases were deduced by mass balance. Each experiment was carried out in triplicate and the error did not exceed 5%. Distribution ratio (D) and extraction percent (% E) were defined as follows:

$$D = \frac{[M]_{org}}{[M]_{aq}} \quad (1)$$

$$\% E = \frac{D}{D + 1} \cdot 100\% \quad (2)$$

where $[M]_{org}$ and $[M]_{aq}$ denote metal concentrations in the organic and aqueous phases after solvent extraction, respectively.

Selectivity coefficient ($S_{M1/M2}$) for M_1 over M_2 was calculated as follows:

$$S_{M1/M2} = \frac{D_{M1}}{D_{M2}} \quad (3)$$

ΔD and SC were defined as follows to evaluate synergistic effect:

$$\Delta D = D_{mix} - (D_{Cyanex272} + D_{TBP}) \quad (4)$$

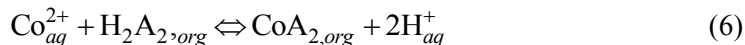
$$SC = \frac{D_{mix}}{D_{Cyanex272} + D_{TBP}} \quad (5)$$

where D_{mix} is the distribution ratio by the mixture of Cyanex 272 and TBP, $D_{Cyanex272}$ and D_{TBP} are distribution ratios by Cyanex 272 alone and TBP alone, respectively.

Results and discussion

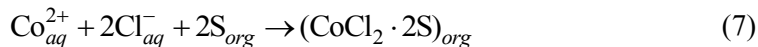
Effect of equilibrium pH on Co(II) and Li(I) solvent extraction

Although the solvent extraction studies of cobalt(II) by Cyanex 272 have been reported, but report regarding extraction of this metal ions using mixture of Cyanex 272 and TBP by solvent extraction technique has not been showed yet. Cyanex 272, a cationic exchanger, extracts Co(II) from aqueous solution according to the following reaction (Swain et al., 2007):



where “aq” and “org” denote aqueous and organic phases, respectively.

On the other hand, TBP is a kind of neutral, solvating extractant which has been used in the separation of many metal ions. This extractant can be also a modifier in the extraction process (Li et al., 2007). The ability of TBP to chemically react with bis(2,4,4-trimethylpentyl)phosphinic acid (the active reagent in Cyanex 272) to generate butyl ester species (butyl phosphinate; butyl bis(2,4,4-trimethylpentyl) phosphinate) was reported by Barnard et al., (2014). In this work, the presence of neutral donor TBP as synergistic agent was studied and discussed. Solvating agents such as TBP also extract Co(II) from chloride acidic media according to the following reaction:



where S is TBP.

The effect of equilibrium pH on the competitive solvent extraction of Co(II) and Li(I) from aqueous chloride solutions at pH ranging from 3.5 to 5.8 by 0.1 M Cyanex 272 in kerosene, 0.05 M TBP in kerosene and the mixture of 0.1 M Cyanex 272 and 0.05 M TBP in kerosene is shown in Fig. 1. The increase of the equilibrium pH from 3.5 to 5.8 is responsible for an increase of Co(II) extraction by these extractants. This figure also shows that the use of mixture containing Cyanex 272 and TBP, instead of TBP alone or Cyanex 272 alone, improves the extraction efficiency of Co(II) and at a minor extent of Li(I) from aqueous chloride solution. Conversely, then no significant variation of solvent extraction efficiency of Li(I) vs. pH is observed. Taken account the literature date concerning the participation of a neutral donor molecule (S) in the extracted species of synergistic extraction process (Rafighi et al., 2010), the following corresponding mechanism of Co(II) extraction can be written as:



Further studies are necessary to confirm the suggested reaction for the studied mixture consisting of cationic extractant (Cyanex 272) and solvating extractant (TBP).

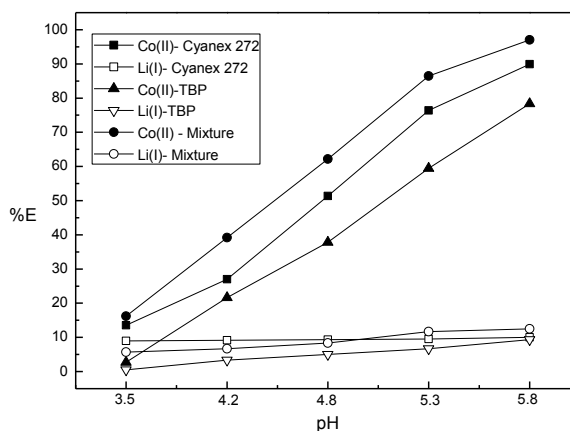


Fig. 1. Extraction percent of Co(II) and Li(I) as a function of equilibrium pH by 0.1 M Cyanex 272 in kerosene, 0.05 M TBP in kerosene and mixture of 0.1 M Cyanex 272 and 0.05 M TBP in kerosene. Aqueous phase: 0.01 M Co(II) and 0.01 M Li(I)

Table 1 shows that distribution ratios of Co(II) are significantly higher in the range of pH values between 3.5 and 5.8, while distribution ratio of Li(I) remains low when Cyanex 272-TBP mixture is used instead of Cyanex 272 or TBP alone. A synergistic phenomenon occurs during the recovery of Co(II) from chloride solutions with mixtures of Cyanex 272 and TBP whereas an antagonist effect is observed in the case of Li(I) solvent extraction throughout the studied pH range (Table 1). The obtained synergism can be expressed in terms of synergistic coefficient (SC) (Eq. 5). The formation of adduct species may be responsible for an increase of the extraction properties of Co(II) when Cyanex 272 and TBP mixture is used. In addition to the very high distribution ratios of Co(II), the use of mixtures of Cyanex 272 and TBP appears very interesting because the selectivity coefficients are much more higher with these mixtures compared to those obtained with Cyanex 272 or TBP alone in kerosene (Fig. 2). In this present work, the use of mixtures of Cyanex 272 and TBP appears as very effective method for Co(II) and Li(I) separation. Indeed, the results evidence the presence of synergistic effect in the competitive solvent extraction of Co(II) from chloride solutions containing Li(I) ions. The obtained selectivity coefficients of Co(II) over Li(I) ($S_{Co/Li}$) with this system are significantly higher in comparison with those obtained with Cyanex 272 or TBP alone. The similar synergistic effect was observed by Batchu et al. (2014) during solvent extraction of Mn(II) from H_2SO_4 solutions with Cyanex 301, TBP and their binary mixture. They reported that the observed synergism may be due to the increased lipophilic nature of extracted complex by the addition of TBP. Therefore, the addition of TBP has shown synergistic effect. In the earlier work (Pospiech and Chagnes, 2015) the synergistic effect was described during solvent extraction of Zn(II) and Cu(II) from chloride solutions with the mixture of Cyanex 272 and Aliquat 336. There it can be observed that the obtained selectivity coefficients

of Zn(II) over Cu(II) ($S_{Zn/Cu}$) from hydrochloric acid and acidic sodium chloride solutions by mixtures of Cyanex 272 and Aliquat 336 are about twice greater than those obtained with Aliquat 336 alone.

Table 1. Variation of the distribution ratio of Co(II) and Li(I) as a function of pH. Organic phase: 0.1 M Cyanex 272, 0.05 M TBP and a mixture of 0.1 M Cyanex 272 and 0.05 M TBP in kerosene; aqueous phase: initially 0.01 M Co(II) and 0.01 M Li(I). $D_{Cyanex272}$ – distribution ratio by Cyanex 272 alone; D_{TBP} – distribution ratio by TBP alone; $D_{mixture}$ – distribution ratio by the mixture of Cyanex 272 and TBP; SC – synergistic coefficient

pH	$D_{Cyanex\ 272}$	D_{TBP}	$D_{mixture}$	ΔD	SC
3.5	Co(II)	0.156	0.028	0.194	0.010
4.2		0.360	0.253	0.644	0.031
4.8		1.015	0.571	1.642	0.056
5.3		3.238	1.466	6.400	1.700
5.8		8.919	3.625	32.64	20.10
3.5	Li(I)	0.099	0.005	0.060	-0.044
4.2		0.101	0.034	0.071	-0.064
4.8		0.103	0.053	0.091	-0.065
5.3		0.105	0.071	0.132	-0.044
5.8		0.111	0.103	0.143	-0.071

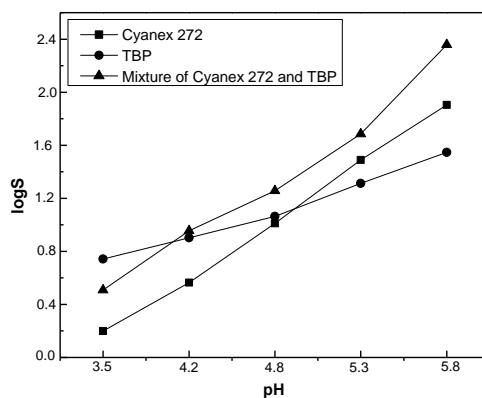


Fig. 2. Logarithm of selectivity coefficient of Co(II) over Li(I) vs. pH under the same experimental conditions as in Fig. 1

Influence of Cyanex 272 and TBP concentrations on Co(II) and Li(I) solvent extraction

Solvent extractions of 0.01 M Co(II) and 0.01 M Li(I) from chloride aqueous solution by Cyanex 272 mixed with TBP in kerosene has been studied as a function of TBP concentration at constant concentration of Cyanex 272. As shown in Fig. 3, the

addition of 0.05 M TBP 336 into 0.1 M Cyanex 272 in kerosene is responsible for an increase of Co(II) extraction percent from 89% to 97% and an increase of Co(II) distribution ratio from 8.9 to 32.6. Conversely, Li(I) distribution ratio and extraction percent remain low in the presence of TBP in 0.1M Cyanex 272 in kerosene. This distribution ratio of Li(I) increases very slightly and reaches 0.14 in the presence of 0.05 M TBP in the mixture contained 0.1 M Cyanex 272 (Table 2). The logarithm of the selectivity coefficient increases from 1.9 to 2.4, when TBP concentration in the mixture varies from 0 to 0.06 M. Above 0.05 M concentration of TBP, distribution ratios of Co(II) and Li(I) are slightly decrease.

Table 2. Selectivity coefficient of Co(II) over Li(I) as a function of TBP concentration.

Organic phase: mixture of 0.1 M Cyanex 272 and various concentrations of TBP in kerosene;
 aqueous phase: 0.01 M Co(II) and 0.01 M Li(I). $D_{\text{Co(II)}}$ – distribution ratio of cobalt(II);
 $D_{\text{Li(I)}}$ – distribution ratio of lithium(I); $\log S_{\text{Co/Li}}$ – logarithm of selectivity coefficient of Co(II) over Li(I)

[TBP], M	$D_{\text{Co(II)}}$	$D_{\text{Li(I)}}$	$\log S_{\text{Co/Li}}$
0.00	8.91	0.11	1.9
0.01	15.3	0.12	2.1
0.02	19.7	0.12	2.2
0.03	24.1	0.13	2.3
0.04	29.8	0.13	2.4
0.05	32.6	0.14	2.4
0.06	31.4	0.12	2.4

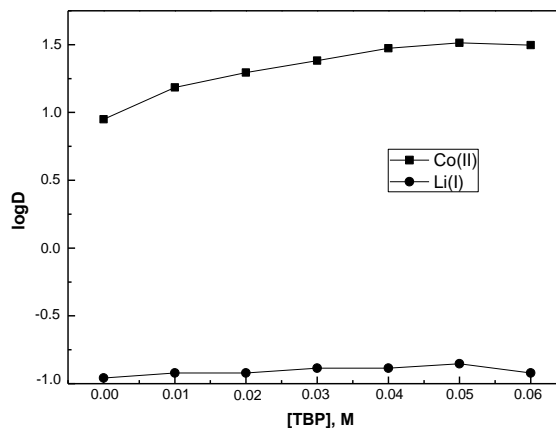


Fig. 3. Logarithm of distribution ratios of Co(II) and Li(I) vs. TBP concentration.

Aqueous phase: 0.01 M Co(II), 0.01 M Li(I); organic phase: 0.1 M Cyanex 272 and different concentration of TBP in kerosene

Banda et al. (2012) reported separation of rare earth elements by Cyanex 272 and its mixture with other extractants (TBP, TOPO, Cyanex 301, Alamine 308). They also

observed synergistic effects with the combination of Cyanex 272 and TBP, which led to complete separation of Pr(III) and Nd(III) over La(III).

The next series of investigations was carried out with the mixture containing 0.05 M TBP and different concentrations of Cyanex 272. The concentration of Cyanex 272 in the mixture of TBP was changed from 0.01 to 0.2 M. Table 3 shows the variation in the distribution ratios (D) of Co(II) and Li(I) from aqueous solutions as a function of Cyanex 272 concentration in the mixture of 0.05 M TBP.

Table 3. Selectivity coefficient of Co(II) over Li(I) as a function of Cyanex 272 concentration.
 Organic phase: mixture of 0.05 M TBP and various concentrations of Cyanex 272 in kerosene;
 aqueous phase: 0.01 M Co(II) and 0.01 M Li(I). $D_{\text{Co(II)}}$ – distribution ratio of cobalt(II);
 $D_{\text{Li(I)}}$ – distribution ratio of lithium(I); $\log S_{\text{Co/Li}}$ – logarithm of selectivity coefficient of Co(II) over Li(I)

[Cyanex 272], M	$D_{\text{Co(II)}}$	$D_{\text{Li(I)}}$	$\log S_{\text{Co/Li}}$
0.00	3.63	0.10	1.5
0.01	4.86	0.12	1.6
0.05	15.1	0.12	2.1
0.08	26.4	0.13	2.3
0.10	32.6	0.14	2.4
0.20	32.0	0.14	2.4

As can be seen from Table 3, distribution ratios of Co(II) and Li(I) reach 3.63 and 0.10, respectively by 0.05 M TBP single in kerosene (Table 3). The distribution ratio of Co(II) increases significantly from 3.63 to 32.6 with increasing Cyanex 272 concentration up to 0.1 M. We can also see that, the addition of Cyanex 272 in 0.05 M TBP cause increase in the logarithm of the separation coefficient of Co(II) towards Li(I) ($S_{\text{Co/Li}}$) from 1.5 to 2.4.

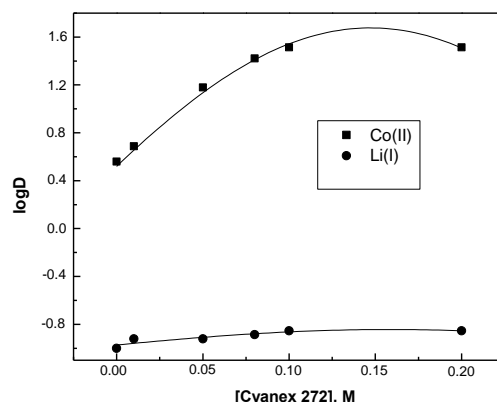


Fig. 4. Logarithm of distribution ratios of Co(II) and Li(I) vs. Cyanex 272 concentration.

Aqueous phase: 0.01 M Co(II), 0.01 M Li(I); organic phase: 0.05 M TBP and different concentration of Cyanex 272 in kerosene

Figure 4 shows the logarithm of distribution ratios of Co(II) and Li(I) vs Cyanex 272 concentration. It indicates that $\log D$ of Co(II) increases with increase of this extractant concentration. Above 0.1 M concentration of Cyanex 272 further increase in distribution ratio of Co(II) is not observed. On the other hand the extraction of Li(I) was low and only slightly changed with Cyanex 272 concentration increase in mixture with TBP. The highest extraction selectivity was obtained using 0.1 M Cyanex 272 and 0.05 M TBP in kerosene.

Stripping investigation

The stripping investigations were carried out in order to determine the appropriate concentration of H_2SO_4 required for stripping Co(II) from the loaded organic phase. A range of 0-1M acid concentration was investigated. Stripping investigations were carried out on the organic solution consisting of the mixture of 0.1 M Cyanex 272 and 0.05 M TBP in kerosene containing Co(II) and Li(I) after extraction from aqueous solution. In order to evaluate the stripping percent by sulphuric acid, extraction solvent was first contacted with an aqueous solution containing 0.01 M Co(II) and 0.01 M Li(II) by mixture of 0.1 M Cyanex 272 and 0.05 M TBP at phase volume ratio O:A=1. After settlement, the organic phase was separated from aqueous phase. Organic phase was then contacted with the stripping solution (deionized water and sulphuric acid solutions) at phase volume ratio O:A=1 at 25 ± 2 °C. After shaking, organic and aqueous phases were separated and metal concentrations in aqueous phases were determined by AAS in order to calculate stripping percent.

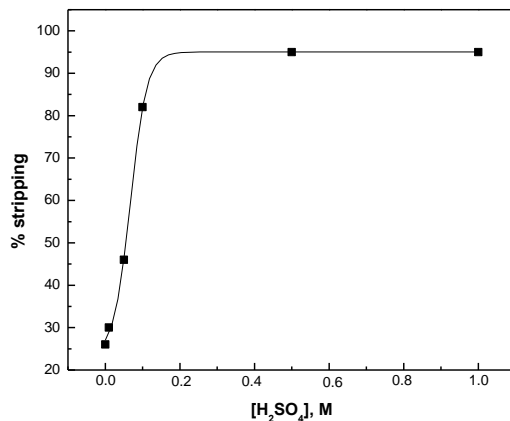


Fig. 5. Co(II) stripping percent by water and sulfuric acid from 0.1 M Cyanex 272 and 0.05 M TBP mixtures in kerosene previously loaded by contacting the extraction solvent with an aqueous phase containing 0.01 M Co(II) and 0.01 M Li(I).

The results are presented in Fig. 5. As can be observed the stripping was highly selective since no Li(I) was found in the stripping solution. Figure 5 shows that maximum stripping of Co(II) was obtained with 0.5 M H_2SO_4 . This solution can be

considered as a promising stripping agent since it leads to good stripping of Co(II) (95%). Further increase of this acid concentration has no significant effect on cobalt(II) stripping.

Conclusions

The extraction system Cyanex 272-TBP can be recommended for the separation of Co(II) and Li(I) from chloride solutions with regard to the high values of separation coefficients. Co(II) ions were successfully separated from Li(I) in a synergistic solvent extraction process using the mixture of 0.1 M Cyanex 272 and 0.05 M TBP. The obtained selectivity coefficient of Co(II) over Li(I) ($S_{Co/Li}$) by this mixture is significantly greater than those obtained with Cyanex 272 or TBP alone. This mixture exhibits no synergistic effects for Li(I) which provides possibilities for Co(II) and Li(I) separations at a proper ratio of extractants. Sulfuric acid at 0.5 M concentration, appears as the good stripping agent with a stripping efficiency of about 95% at room temperature. Finally, the separation system presented in this paper can be useful for the separation of Co(II) and Li(I) from aqueous chloride solutions. These metal ions are present in the leach liquor from hydrometallurgical recycling of spent lithium-ion batteries (LIBs). This type of batteries is considered as an attractive secondary resource of valuable metals such as cobalt and lithium (Sun and Qiu, 2011, Zeng et al., 2014; Wang et al., 2014). Their effective recovery is possible only after separation process of metal ions from solution after leaching of the spent batteries in hydrometallurgical technology (Xu and al., 2008). In this work, the proposed novel synergistic mixture offers an efficient way to separate metal ions. Therefore this separation process by synergistic solvent extraction can be very important for the recycling of LIBs by hydrometallurgical method.

The results of the study were presented during 42nd International Conference of Slovak Society of Chemical Engineering, May 25-29, 2015.

References

BANDA R., JEON H., LEE M., 2012, *Solvent extraction separation of Pr and Nd from chloride solution containing La using Cyanex 272 and its mixture with other extractants*. Sep. Purif. Technol. 98, 481-487.

BARNARD K.R., KELLY N.J., SHIERS D.W., 2014, *Chemical reactivity between bis(2-ethylhexyl) phosphoric acid (D2EHPA) and tributyl phosphate*. Hydrometallurgy, 146, 1-7.

BATCHU N.K., SONU CH.H., LEE M.S., 2014, Solvent extraction equilibrium and modeling studies of manganese from sulfate solutions by a mixture of Cyanex 301 and TBP. Hydrometallurgy, 144-145, 1-6.

CHAGNES A., POSPIECH B., 2013, *A brief review on hydrometallurgical technologies for recycling spent lithium-ion batteries*. J. Chem. Technol. Biotechnol., 88 (7) 1191-1199.

CHMIELEWSKI A.G., URBAŃSKI T.S., MIGDAŁ W., 1997, *Separation technologies for metals recovery from industrial wastes*. Hydrometallurgy, 45, 333-344.

DEVI N.B., NATHSARMA K.C., CHAKRAVORTTY V., 1994, *Sodium salts of D2EHPA, PC-88A and Cyanex 272 and their mixtures as extractants for cobalt(II)*. Hydrometallurgy, 34, 331-342.

GANDHI M.N., DEORKAR N.V., KHOPKAR S.M., 1993, *Solvent extraction separation of cobalt(II) from nickel(II) and other metals with Cyanex 272*. Talanta, 40, 1535-1539.

GEWA J., WALKOWIAK W., GAJDA B., 2001. Separation of Co(II) and Ni(II) ions by supported and hybrid liquid membrane. Sep. Purif. Technol. 22-23, 551-558.

KOŁODYNSKA D., HUBICKA H., HUBICKI Z., 2008, *Sorption of heavy metal ions from aqueous in the presence of EDTA on monodisperse anion exchangers*. Desalination, 227, 150.

KOZŁOWSKI C.A., KOZŁOWSKA J., PELŁOWSKI W., WALKOWIAK W., 2006. *Separation of cobalt-60, strontium-90, and cesium-137 radioisotopes by competitive transport across polymer inclusion membranes with organophosphorous acids*. Desalination 198, 149-156.

LI W., WANG X., MENG S., LI D., XIONG Y., 2007, *Extraction and separation of yttrium from the rare earths with sec-octylphenoxy acetic acid in chloride media*. Sep. Purif. Technol., 54, 164-169.

MARCHESE J., CAMPEDROS M., A., COSTA A., 1995. *Transport and separation of cobalt, nickel and copper ions with Alamine 336 liquid membranes*. J. Chem. Tech. Biotechnol., 64, 293-297.

OCHROMOWICZ K., CHMIELEWSKI T., 2013. *Solvent extraction of copper(II) from concentrated leach liquors*, Physicochem. Probl. Miner. Process. 49(1), 357-367..

POSPIECH B., 2010, *Studies on iron(III) removal from chloride aqueous solutions by solvent extraction and transport through polymer inclusion membranes with D2EHPA*, Physicochem. Probl. Miner. Process., 44, 195-204.

POSPIECH B., 2013, *Hydrometallurgical recovery of cobalt(II) from acidic chloride solutions by transport through polymer inclusion membranes*. Physicochem. Probl. Miner. Process., 49, 641-649.

POSPIECH B., 2014(a), *Selective recovery of cobalt(II) towards lithium(I) from chloride media by transport across polymer inclusion membrane with triisooctylamine*. Pol. J. Chem. Technol. 16, 15-20.

POSPIECH B., 2014(b), *Synergistic solvent extraction and transport of Zn(II) and Cu(II) across polymer inclusion membranes with mixture of TOPO and Aliquat 336*. Sep. Sci. Technol. 49, 1706-1712.

POSPIECH B., 2015, *Highly efficient facilitated membrane transport of palladium(II) ions from hydrochloric acid solutions through plasticizer membranes with Cyanex 471X*. Physicochem. Probl. Min. Process., 51, 281-291.

POSPIECH B., CHAGNES A., 2015, *Highly selective solvent extraction of Zn(II) and Cu(II) from acidic aqueous chloride solutions with mixture of Cyanex 272 and Aliquat 336*. Sep. Sci. Technol. 50, 1302-1309.

PRESTON J.S., 1982, *Solvent extraction of cobalt and nickel by organophosphorus acids. Comparison of phosphoric, phosphonic and phosphinic acid systems*. Hydrometallurgy 9, 115-133.

RAFIGHI P., YAFTIAN M.R., NOSHIRANZADEH N., 2010, *Solvent extraction of cobalt(II) ions; cooperation of oximes and neutral donors*. Sep. Purif. Technol., 75, 32-38.

RICKELTON W.A., BOYLE R.J., 1988, *Solvent extraction with organophosphines commercial & potential applications*. Sep. Sci. Technol., 23, 227-1250.

SARANGI K., REDDY B.R., DAS R.P., 1999, *Extraction studies of cobalt(II) and nickel(II) from chloride solutions using Na-Cyanex 272. Separation of Co(II)/Ni(II) by the sodium salts of D2EHPA, PC88A and Cyanex 272 and their mixtures*. Hydrometallurgy, 52, 253-265.

SUN L., QIU K., 2011, *Vacuum pyrolysis and hydrometallurgical process for the recovery of valuable metals from spent lithium-ion batteries*. J. Hazard. Mater., 194, 378-384.

SWAIN B., JEONG J., LEE J., LEE G., 2007, *Extraction of Co(II) by supported liquid membrane and solvent extraction using Cyanex 272 as an extractant: A comparison study*. J. Membr. Sci., 288, 139-148.

WANG X., GAUSTAD G., BABBITT C.W., RICHA K., 2014, *Economies of scale for future lithium-ion battery recycling infrastructure*, Resour. Conserv. Recy., 83, 53-62.

WIONCZYK B., 2013, *Kinetic modeling of chromium(III) extraction with Aliquat 336 from alkaline aqueous solutions containing chlorides*, Physicochem. Probl. Miner. Process. 49(2), 2013, 587-605.

XU J., THOMS H.R., FRANCIS R.W., LUM K.R., WANG J., LIANG B., 2008, A review of processes and technologies for the recycling of lithium-ion secondary batteries, J. Power Sources, 177, 512-527.

ZENG X., LI J., SINGH N., 2014, *Recycling of Spent Lithium-Ion Battery: a Critical Review*, Environ. Sci. Technol., 44, 1129-1165.

ZHAN G.P., YOKOYAMA T., SUZUKI T.M., INOUE K., 2001, *The synergistic extraction of nickel and cobalt with a mixture of di(2-ethylhexyl) phosphoric acid and 5-dodecylsalicylaldoxime*. Hydrometallurgy 61, 223-227.

ZHU Z.; ZHANG W.; CHENG C.Y., 2012, *A synergistic solvent extraction system for separating copper from iron in high chloride concentration solutions*. Hydrometallurgy, 113-114, 155-159.

Received April 24, 2015; reviewed; accepted August 13, 2015

EFFECT OF MOISTURE CONTENT IN COAL DUST ON FILTRATION AND CLEANING PERFORMANCE OF FILTERS

Jianlong LI^{*,**}, Shihang LI^{*,**}, Fubao ZHOU^{*,***,***}

^{*} Key Laboratory of Gas and Fire Control for Coal Mines, Ministry of Education, China University of Mining and Technology, Xuzhou 221116, China, zfbcumt@gmail.com, f.zhou@cumt.edu.cn (Fubao Zhou)

^{**} School of Safety Engineering, China University of Mining and Technology, Xuzhou 221116, China

^{***} State Key Laboratory of Coal Resources and Mine Safety, China University of Mining and Technology, Xuzhou 221116, China

Abstract: A large amount of fugitive coal dust is generated during the mining, transportation, and processing of coal. The moisture content of the coal dust has a significant influence on the dust collection performance of filters, although relatively few studies on this phenomenon exist. This study deals with six groups of coal dust samples with moisture contents ranging from 0 to 12 wt.% and tested the pressure drop as the coal dust was deposited onto three different types of filters. The specific resistance, compression coefficient, and porosity of the coal dust cake were analyzed, and the cake/filter adhesive force was tested using the reverse flow cleaning method. This research demonstrates that the influence of the moisture content on the specific resistance, compression coefficient, and porosity of the coal dust cake can be divided into two phases (according to the critical moisture content of 4 wt.%): first, as the moisture content increased from 0 to 4 wt.%, the cake resistance and compression coefficient increased and the cake porosity decreased; and second, as the moisture content increased from 4 to 12 wt.%, the cake resistance and compression coefficient decreased and the porosity increased. The coated and repellent filters possessed a lower adhesive force on the coal dust cake than the conventional filter. The comparison of all three of the filters revealed that the adhesive force between the repellent filter and the dust cake was the least sensitive to the moisture content.

Keywords: coal dust, moisture content, filtration, compressibility, adhesive force

Introduction

Throughout the mining, transportation, and processing of coal, a large amount of fugitive coal dust is inevitably generated. Human exposure to coal dust results in pneumoconiosis with an initiation and progression of pulmonary fibrosis. Other dangers associated with coal dust include serious explosion hazard and quite severe

environmental pollution (Demir and Kursun, 2012; Finkelman et al., 2002; Ozbayoglu, 2013). Filter-type collection is commonly utilized for coal dust control and possesses a high collection efficiency, especially for fine dust (Cecala et al., 2012, Li et al., 2015).

Moisture exists in coal at various levels that change constantly during its transportation and processing. The moisture content influences the physical properties of the coal dust particles and thereby influences the dust collector performance factors, such as the filtration pressure drop and the filter regeneration efficiency. Under particularly high dust concentration conditions, water spraying is typically conducted along with the filter-type collection methods, which increases the moisture content of the coal dust and significantly influences the effectiveness of the dust filtration.

Previous studies have mostly focused on the influence of the particle size, shape, and/or chemical composition during the filtration and cleaning processes (Choi et al., 2002; Park et al., 2007; Salazar-Banda et al., 2012). The previous findings generally agree that the filtration pressure drop increases and dust cake porosity decreases with a decrease in the particle size (Kim et al., 2008; Lupion et al., 2014) and that the more irregular particles tend to form a higher pressure drop and are more compressible (Choi et al., 2002). The effects of the chemical composition on the filter cake strength and adhesion were much more varied, and these have also been studied at length (Lupion et al., 2014; Salazar-Banda et al., 2012). Few studies have investigated the effect of the dust moisture content on the filter performance (Joubert et al., 2010).

It should be noted that many researchers have studied the influence of air humidity on the clogging and cleaning performance of flat filters (Gupta et al., 1993; Joubert et al., 2010; Joubert et al., 2011; Park et al., 2007). The air humidity changes the increasing rate of the pressure drop, alters the particulate deposition pattern, and changes the particle-to-particle adhesive force. To a certain extent, air humidity also affects the moisture content in the dust and vice versa. Because coal is a hydrophobic material, it is not readily deliquesced by capillary condensation in humid air. The primary deliquescent mechanism in coal is molecular diffusion, which requires a lengthy amount of time as moisture diffuses from open air into the pores of dust particulates. Furthermore, air humidity mainly affects the filtration air flow and the surface properties of the dust. The moisture content may be more likely to affect the density of the dust than its surface properties.

This paper focuses on the influence of the coal dust moisture content on the filtration and cleaning performance of filters. Six groups of coal dust samples with moisture contents ranging from 0 to 12 wt.% were prepared, and the filtration pressure drop during coal dust deposition was measured on three types of filters. The specific resistance, compression coefficient, and porosity of the coal dust cake were analyzed. The adhesive force between the dust cake and the filter was also studied utilizing the reverse flow cleaning method.

Theory

Gas filtration

During the filtration of dust-laden air, particulates are captured and deposited onto the filter. A dust cake forms on the surface of the filter, and this cake traps most of the particulates within it. In general, the total filter pressure drop (ΔP_T) can be considered the sum of the pressure drop in the filter medium (ΔP_F) and the pressure drop across the dust cake (ΔP_C), as expressed in Eq. (1) (Chen et al., 2012; Cheng and Tsai, 1998):

$$\Delta P_T = \Delta P_F + \Delta P_C = k_1 v_f + k_2 v_f W \quad (1)$$

where k_1 is the resistance of the filter (Pa·s/m), k_2 is the specific resistance of the cake (1/s), v_f is the face velocity of filtration (m/s), and W is the dust mass deposited per unit area (kg/m²).

The filter drag (S) represents the value of the pressure drop across the dust cake and is expressed as follows:

$$S = \Delta P_C / v_f = k_2 W \quad (2)$$

where the specific resistance k_2 can be expressed by the following equation (Cheng and Tsai, 1998; Choi et al., 2002):

$$k_2 = f v_f^n \quad (3)$$

where f and n are constants and n indicates the dust cake compressibility in terms of the filtration velocity.

The dust cake specific resistance k_2 has a relation to the porosity ε and can be expressed as (Choi et al., 2002; Neiva et al., 1999):

$$k_2 = 180(1 - \varepsilon) \varepsilon^{-3} (\rho_p \phi_s^2 d_s)^{-1} \mu \quad (4)$$

where ε is the cake porosity, ρ_p is the true density of the dust (g/cm³), d_s is the Sauter mean particle size (μm), ϕ_s is the particle sphericity and μ is the viscosity of air (kg/(s·m)). The specific resistance k_2 is determined based on the pressure drop test data and the calculations according to Eq. (2); once the specific resistance has been determined, the cake porosity ε can be calculated according to Eq. (4).

In general, the mass of the dust loading onto the filter is a function of the variable filtration pressure drop (Choi et al., 2002; Joubert et al., 2010). However, the density of a dust particulate distinctly changes with a change in the moisture content, rendering it not appropriate to employ mass loading as the variable when studying the

influence of moisture content in dust as a function of the drop in the filter pressure. To this effect, the dust's true volume deposited per unit area was utilized as the filtration variable in this study. Equations (1) and (2) were rewritten accordingly and are expressed as follows:

$$\Delta P_T = \Delta P_F + \Delta P_C = k_1 v_f + k_2' v_f V \quad (5)$$

$$S = \Delta P_C / v_f = k_2' V \quad (6)$$

where V ($= W / \rho_P$) is the dust true volume deposited per unit area (m^3/m^2), k_2' is the specific resistance of the cake in the true volume mode ($\text{Pa}\cdot\text{s}/\text{m}^2$), and k_2' can be expressed by the equation $k_2' = f' V_f^n$, where f' is a constant. Additionally, $k_2 = k_2 \rho_P$ and $f' = f \rho_P$.

Adhesive force

As far as reverse flow cleaning, a method suggested by Seville et al. (1989) has proven appropriate for the estimation of the cake/filter adhesive force by observing a flow of gas in the direction opposite to that of filtration. The cake behaves similarly as in the filtration cycle when the cleaning air flow is below the critical removal velocity. Rupture occurs in the cake/filter surface as the critical velocity is reached. The pressure drop through the filter and cake can be written as

$$\Delta P_{Tc} = k_1 v_c + \Delta P_{Cc} \quad (7)$$

where ΔP_{Tc} is the pressure drop on the cleaning (Pa), v_c is the face velocity of the cleaning gas (m/s), and ΔP_{Cc} is the pressure drop in the cake (Pa). Under these conditions, ΔP_{Cc} represents the cake/filter adhesive force per unit area.

The Seville method is widely used to determine the adhesive force and provides satisfactory results (Salazar-Banda et al., 2012; Tanabe et al., 2011).

Experimental

Equipment set-up and procedure

A diagram of the experimental set-up is shown in Fig. 1. The equipment consisted of a dust feeder, test chamber, pressure drop recorder, air flow meter, and exhaust fan. The test filter was installed perpendicularly to the direction of the air flow in the filtration chamber and possessed a total filtration area of 78.5 cm^2 . The air flow face velocity in the chamber could be tuned to $1.5 - 8.8 \text{ cm/s}$ by adjusting the regulation valve.

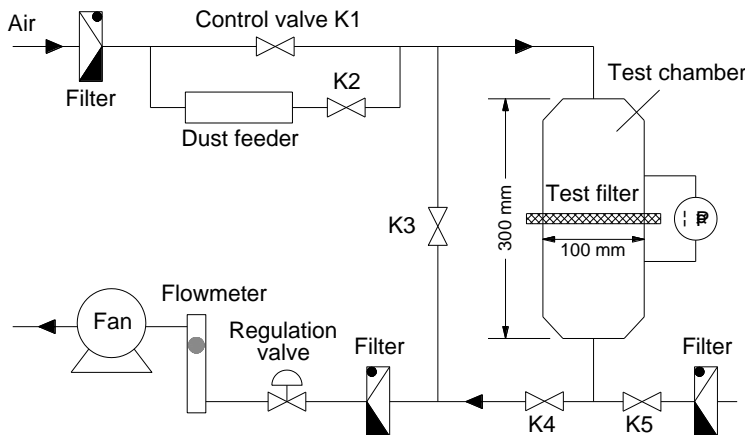


Fig. 1. Sketch of the experimental set-up

The values of the pressure drop during the dust clogging and reverse flow cleaning were recorded using this experimental set-up. The room temperature was maintained at 9–15 °C, and the air humidity was maintained between 50 and 65% during each test period. In the filtration mode, four filtration velocity levels, i.e., 3.50, 4.24, 4.97 and 5.28 cm/s, were selected for the test. First, the control valves K1 and K2 were opened, and the rest were closed. Next, the fan was started. And the flow velocity was adjusted to the desired value using the regulation valve. Dust was then added into the feeder (hard operations were performed in the isovolumetric adding mode, and the dust was added 15 times for each clogging period in the isogravimetric mode in increments of 0.1 ± 0.005 g). Dust was entrained by the air flow when the K2 valve was opened and the K1 valve was closed. The dust-laden air was then flowed into the test chamber, and the air flow was switched from valve K2 to valve K1. The desired filtration velocity was maintained for 30 s to obtain a stable dust cake, and the pressure drop was then recorded. Subsequent dust additions were conducted utilizing the same method.

After dust addition was performed 15 times, the experimental system was switched to the reverse flow cleaning mode for the adhesive force testing. First, the control valves K1, K2, and K4 were closed, and the K3 and K5 valves were opened. The removal velocity was increased incrementally from 1.5 to 2.6, 3.5, 4.4, 5.3, 6.2, and 7.1 cm/s. The pressure drop during cleaning was recorded after a duration of 30 s at each step.

Test filters

Three filters were selected for testing. The first filter was a conventional filter, which is a non-woven long staple polyester medium with a thermo-bonded surface – this type of medium is one of the most extensively used in the industry and is favored for its small pressure drop and reasonable price. The second filter was a coated filter,

which is a non-woven polyester medium coated with a fine polytetrafluoroethylene (PTFE) membrane. For a surface treatment with microporous layers, this type of medium provides highly effective filtration. The third filter was a repellent filter, a non-woven polyester medium with a water-repellent treatment. Scanning electron microscope (SEM) views of the filter media are shown in Fig. 2, and the filter properties are presented in Table 1.

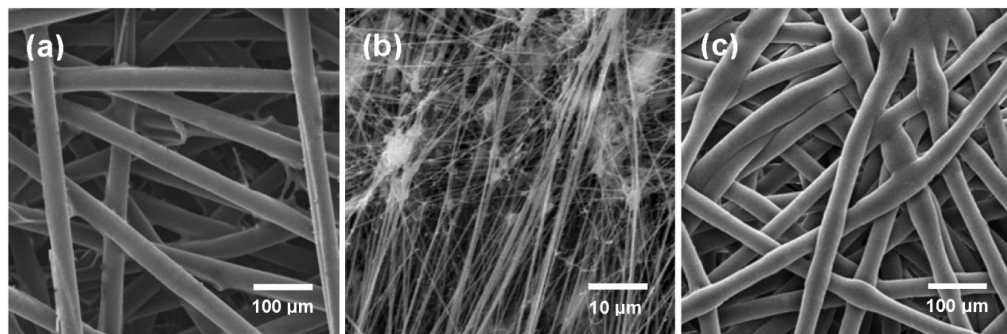


Fig. 2. SEM views of the surface of the (a) conventional, (b) coated, and (c) repellent filter media

Table 1. Filter properties

Parameters	Conventional filter	Coated filter	Repellent filter
Surface treatment	Thermo-bonding	Microporous coating	Water repellent
Surface mass (g/m ²)	240 ± 3	255 ± 5	260 ± 5
Thickness (mm)	0.50 ± 0.05	0.62 ± 0.05	0.55 ± 0.05
Fiber diameter*(μm)	18.41 ± 1.5	0.19 ± 0.20	19.82 ± 3.0
Resistance (Pa·s/cm)	8.91	42.57	19.93

*Calculated from the 20 fibers shown in the SEM images

Coal dust

In this research, coal dust with a diameter of less than 75 μm (the typical particle size of fugitive coal dust,) was collected after the jet coal sample from the Yuejin Coal Mine (Yima City, Henan Province, China) was crushed and ground. The coal dust sample was first dried at 110 °C for 3 h to remove the total moisture, according to the procedure established by the Chinese National Standard the Determination of Total Moisture (GB/T 211-2007). The sample was then divided into six groups, five of which were sprayed with different amounts of water to obtain coal dust samples with moisture contents of 2 wt.%, 4 wt.%, 6 wt.%, 8 wt.% and 12 wt.%. The moist dust samples were sealed and stored for a month to ensure a uniform distribution of moisture in the dust particulates. The moisture content values of each dust sample

were tested before the filtration testing, and the relative biases were less than 3%. Particle size distributions were obtained using a Microtrac S3500 Particle Size Analyzer in the dry measurement mode (Table 2). The particle size was not notably affected by a moisture content between 0 and 12 wt.%. The repose angles of the dust were also measured using a BT-1000 Powder Integrative Characteristics Tester.

Table 2. Properties of the coal dust

M (wt.%)	ρ_P (g/cm ³)	d_{50} (μm)	d_s (μm)	φ_s (-)	Repose angle (°)
0	1.394	34.92	29.86	0.782	36.8
2	1.470	35.33	29.84	0.778	41.7
4	1.443	35.76	30.05	0.779	47.6
6	1.461	35.78	30.06	0.782	50.4
8	1.478	36.06	30.11	0.808	54.1
12	1.532	36.37	30.16	0.811	59.9

Results and discussion

Effect on filtration pressure drop

Figure 3 shows where the filtration pressure drops changed with the dust load and moisture content for the conventional filter. The pressure drop increased with the dust load. During the clogging process of a clean filter, this increase in pressure drop generally exhibited three stages (Mao et al., 2008), which is described as follows. Stage I is characterized by an accelerating increase in the rate of the pressure drop. Stage II is characterized by a decelerating increase. Stage III is characterized by a constant increase. Stage I provides mostly deep filtration where dust particulates deposit inside the filter. Stage II acts as a transition from deep to surface filtration where some particulates deposit inside and some deposit onto the surface of the filter. Stage III is the surface filtration stage in which the first dust layer has formed on the surface of the filter and subsequent particulates are captured by this layer. All three stages were clearly observable during our tests, as can be observed in Fig. 3 and in accordance with previous reports (Mao et al., 2006; Mao et al., 2008). The pressure drop values increased with similar tendencies for differing moisture contents.

A comparison of the filtration pressure drop curves for different moisture contents demonstrated that the overall pressure drop increased as the moisture content increased from 0 to 4 wt.%. For the moisture content in the range of 4 to 12 wt.%, the pressure drop decreased as the moisture content increased. To further investigate the pressure drop as it changed with changes in the moisture content, the pressure drop values were extracted under a loaded dust true volume $V = 10 \times 10^{-5}$ m³/m² for the conventional, coated, and repellent filter conditions (Fig. 4). The pressure drop for the conventional, coated, and repellent filters showed similar variation tendencies – first an increase and then a subsequent decrease with increasing moisture content – with a

maximum pressure drop value at $M = 4$ wt.%. The differences in the filtration pressure drop between these three filters were mainly attributable to the resistance of each filter itself.

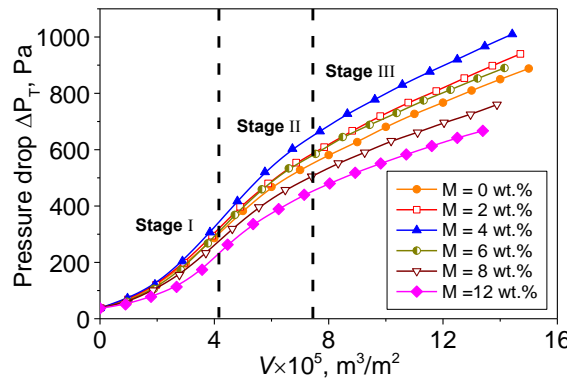


Fig. 3. Filtration pressure drop of a loaded conventional filter as a function of moisture content in coal dust (M = moisture content)

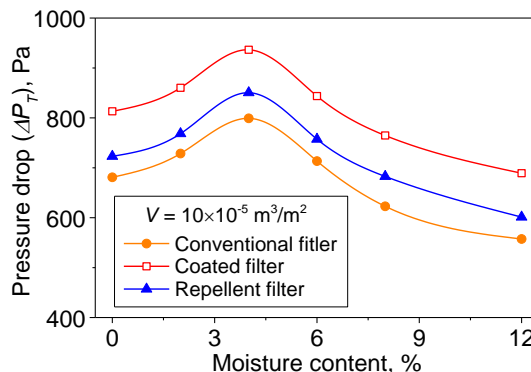


Fig. 4. Filtration pressure drop as a function of the moisture content when a loaded dust true volume $V = 10 \times 10^{-5} \text{ m}^3/\text{m}^2$ was utilized for the conventional, coated, and repellent filters

Effect on dust cake

S - V curves showing the effects of the face velocities in the range of 3.50 to 5.28 cm/s and the moisture contents in the range of 0 to 12 wt.% for the conventional filter are shown in Fig. 5. As can be found in Fig. 5, the increase in the filter drag (S) with a dust load (V) in Stage I and Stage II was not linear. It means that the dust cake compressibility (n) was not constant with the dust load according to the equations $S = \Delta P_C / V_f = k_2 V$ and $k_2 = f' V_f^n$. This is because, in Stage I and Stage II, most or some of the dust particulates deposited inside of the filter rather than be captured by the dust layer, which has a complex influence on the formation of the dust cake.

However, in stage III, almost all of the dust particulates deposited on the dust layer and a constant value of the dust cake compressibility was obtained. Therefore, Stage III of the filtration test was the focus for a clear comparison of the dust cake compressibility for the different moisture contents and filtration velocities. The results of the calculated k_2 are shown in Fig. 6a.

For the same moisture content, the cake specific resistance k_2 increased with the filtration velocity; for the same filtration velocity, k_2 first increased and then decreased as the moisture content increased, with the maximum at 4 wt.%.

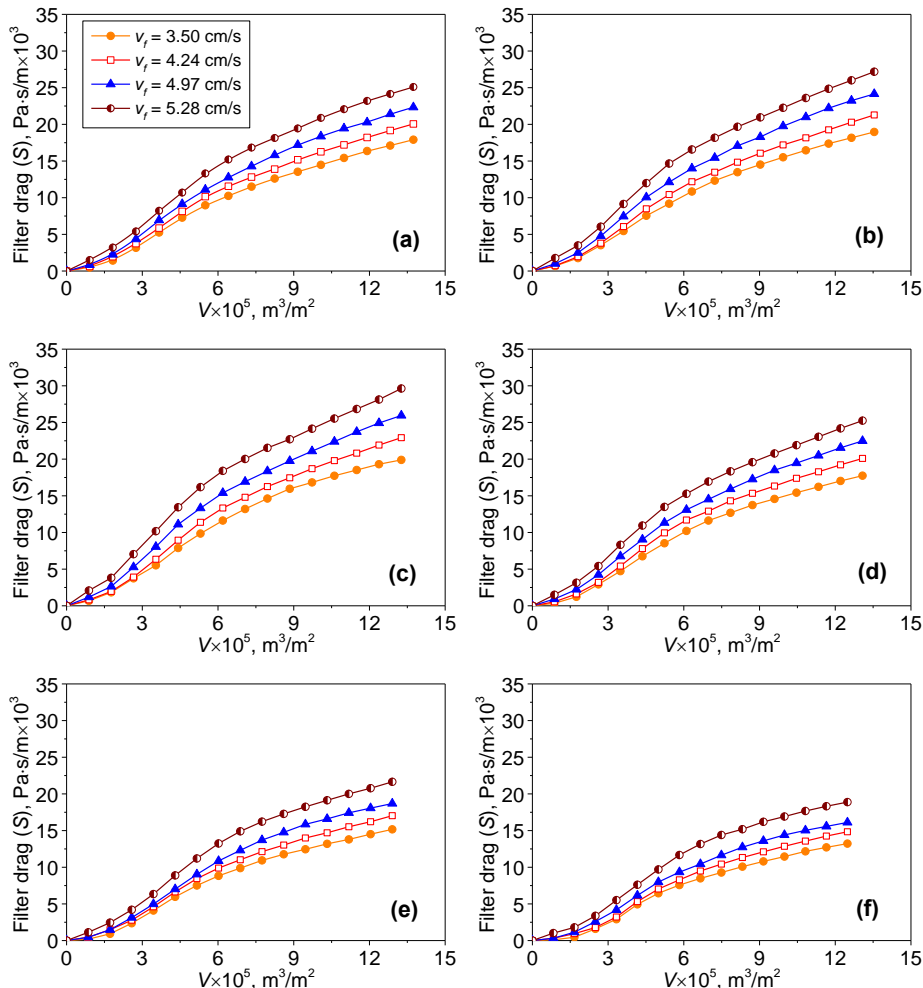


Fig. 5. S - V curves showing the effects of the face velocities for the conventional filter:
 (a) moisture content = 0 wt.%, (b) 2 wt.%, (c) 4 wt.%, (d) 6 wt.%, (e) 8 wt.%, and (f) 12 wt.%

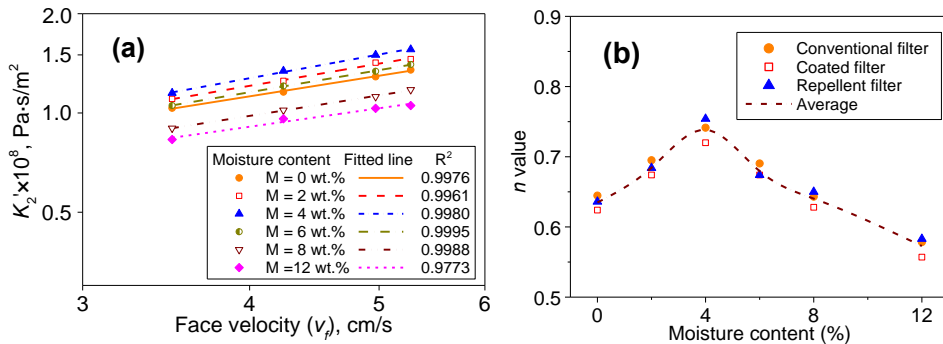


Fig. 6. Correlation curves of (a) the specific resistance k_2' as a function of the face velocity, and (b) the compression coefficient n , which was obtained from the relationship between k_2' and v_f , as a function of moisture content

Based upon the changes in the k_2' value, which corresponded with the filtration velocity, as well as the known relationship $k_2' = f' v_f^n$, the values of the compression coefficient n were determined through curve fitting, as shown in Fig. 6a. In the same manner, the values of the compression coefficient n on the coated and repellent filter conditions were obtained, as shown in Fig. 6b. The compression coefficient n was stable in all three filter conditions. The average n values were 0.635, 0.684, 0.738, 0.679, 0.640, and 0.573 for moisture contents M = 0 %, 2 wt.%, 4 wt.%, 6 wt.%, 8 wt.%, 12 wt.%, respectively, demonstrating that the compression coefficient first increased and then decreased with a corresponding increase in the moisture content, with a maximum at 4 wt.%.

The values of the cake porosity ε were also calculated using Eq. (4) ($\mu = 1.8 \times 10^{-5}$ kg·s⁻¹·m⁻¹), as shown in Fig. 7. The cake porosity ε first decreased and then increased with a corresponding increase in the moisture content, and its minimum was obtained at a moisture content of 4 wt.%.

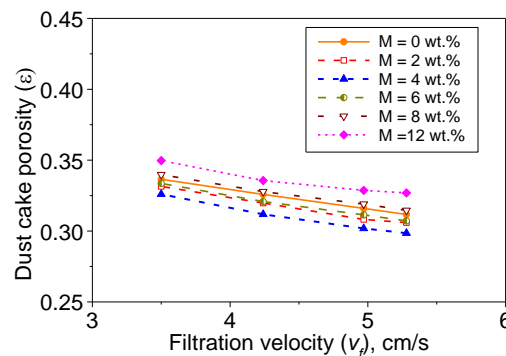


Fig. 7. Correlation curves of porosity ε with moisture content

Previous researchers (Joubert et al., 2010; 2011) have studied the effects of air humidity on the filtration pressure drop and have found that the pressure drop and dust cake porosity decreased monotonously with an increase in the air humidity. They posited that the particle-to-particle adhesive force increased with increasing relative humidity, where depositing particles were less effectively squeezed and a more open cake was formed, lowering the pressure drop for a given amount of particulate loading. This finding suggests that the effects of the dust moisture content and the air humidity on the filtration performance should be different. To better understand this difference, it is necessary to analyze the forces which act upon the dust particles during filtration.

During dust filtration, once a particle makes contact with the surface of a previously deposited particle, it is subject to mainly compression forces (including wind force F_w and inertial force F_i) and resistant forces (mainly including a friction force F_f , adhesive force F_a , and a braced force F_b) from the deposited particle. The contribution of gravity is considered negligible for the small particles in this study. It was also assumed that particles do not bounce upon colliding.

The relationship between these forces is detailed in Fig. 8. The friction force was calculated by $F_f = \beta \cdot [F_a + (F_w + F_i) \cdot \cos\theta]$, where β is the friction coefficient of the two contacting particles with values usually between 0 and 1, and θ is the angle between the line connecting the centers of the two contacting particles and the vertical line with values between 0° and 90° . The compression force can be divided into a normal force and a shear force. When the shear compression force is larger than the friction force, the particle will slide down, i.e., the forces meet the following discriminant:

$$(F_w + F_i) \cdot \sin\theta > \beta \cdot [F_a + (F_w + F_i) \cdot \cos\theta] \quad (8)$$

Otherwise, the particle will not move.

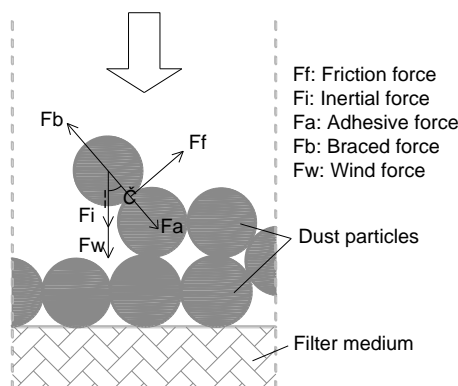


Fig. 8. Relationship between the forces acting on a particle in a dust cake

Under the conditions set by Eq. 8, the value range of θ decreases with an increasing adhesive force F_a and a friction coefficient β . In the statistical sense, this suggests that fewer particles can slide down and the dust cake compressibility decreases. At the same time, the value range of θ increases with an increase in the compression force ($F_w + F_i$), and this causes more particles to slide down and the cake compressibility to increase.

An increase in the moisture content primarily increases the particle density, the friction coefficient (reflected by the repose angle shown in Table 2, where a higher repose angle means a greater friction coefficient,) and the surface adhesiveness (Joubert et al., 2010), which consequently increases the inertial force F_i , friction force F_f , and the adhesive force F_a as well. Under the same filtration velocity conditions, the wind force F_w can be considered the same due to the similar particle sizes of the coal dust with different moisture contents (Table 2). It is easy to assume that in relatively low moisture content conditions, the dust particle surface friction coefficient and adhesiveness do not increase as dramatically as the density and that a sharper increase in the inertial force over the friction/adhesive forces renders the dust cake more compressed. With a moisture content between 4 and 12 wt.%, the dust particle surface friction coefficient and the adhesiveness increases more obviously than the density, forming a more open cake. This suggests that as the moisture content increases from 0 to 4 wt.% the dust cake structure is more compact, and as moisture content increases from 4 wt.% to 12 wt.%, the cake structure tends to be loose. Fig. 9 depicts this phenomenon between the dust particles (simplified as spheres with a uniform size with a moisture content of 0 %, 4 wt.%, and 12 wt.%).

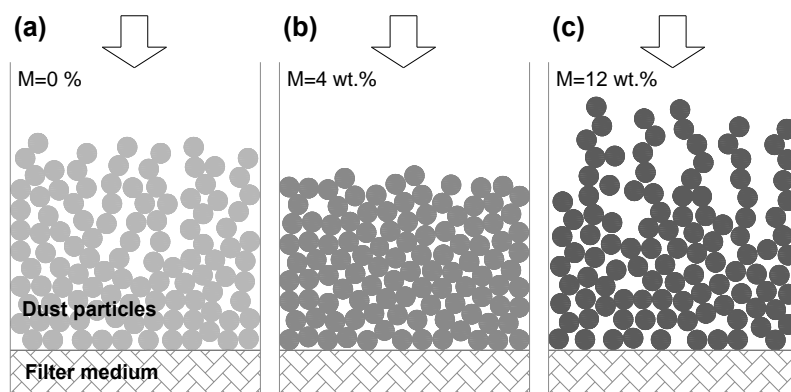


Fig. 9. Deposition morphology of the coal dust cake

Compared to the moisture content, the effect of air humidity on the dust focuses mostly on the particle surface. As the air humidity increases, the friction and adhesive forces increase more than the inertial force, causing the degree of cake compression to increase monotonously. To this effect, the differences between the influences on the

dust filtration performance between the moisture content in the dust and air humidity are most likely caused by discrepancies in the particle density, surface friction, and particle-to-particle adhesive force.

Effect on cake/filter adhesive force

Figure 10a shows the pressure drop across the conventional filter as a function of the cleaning velocity where the filtration velocity was $v_f = 4.24$ cm/s. The pressure drop values that corresponded with the conditions of moisture content $M = 0\%$ and 2 wt.% with a velocity of $v_c = 1.5$ cm/s and $M = 4\%$, 6 wt.%, 8 wt.%, and 12 wt.% with $v_c = 1.5$ and 2.6 cm/s did not match the fitted line of the pressure drop values corresponding to the same moisture content conditions with higher velocities (unfitted data in Fig. 10a). The unmatched values corresponded to non-ruptured dust cakes on the filter; in other words, the corresponding velocities were under the critical removal velocity. The adhesive force can be calculated after the rupture occurs on the cake/filter surface, according to Eq. (7). For the conventional filter, the values of the cake/filter adhesive force per unit area ΔP_{C_c} were 143.59, 147.13, 152.87, 163.85, 175.06, and 218.52 Pa for moisture contents of 0%, 2 wt.%, 4 wt.%, 6 wt.%, 8 wt.%, and 12 wt.%, respectively. The cake/filter adhesive force was obtained in the same manner for the coated and repellent filters.

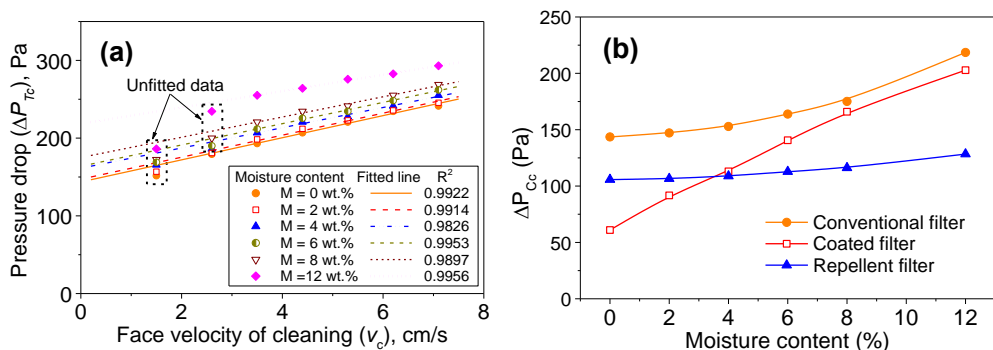


Fig. 10. Pressure drop upon cleaning where the filtration face velocity $v_f = 4.24$ cm/s: (a) total pressure drop as a function of the cleaning face velocity, obtained using conventional filter, and (b) pressure drop in the cake as a function of the moisture content for the conventional, coated, and repellent filters

The cake/filter adhesive forces for the three filters are shown in Fig. 10b. The cake/filter adhesive forces increased with an increase in the moisture content in the range of 0–12 wt.% for all three filters, and the adhesive forces for the coated and repellent filters were lower than for the conventional filter. For a moisture content between 0–4 wt.%, the coated filter possessed the lowest adhesive force with the coal dust cake, while for a moisture content between 4 wt.% and 12 wt.%, the repellent filter possessed the lowest.

The adhesive force increased by 1.52 times for a conventional filter when the moisture content increased from 0 to 12 wt.%, 2.90 times for the coated filter, and 1.21 times for the repellent filter – basically, for all three filters, the adhesive force was the most sensitive to the moisture content between the dust cake and the coated filter and the most insensitive between the cake and the repellent filter.

Conclusions

1. The filtration pressure drop ΔP , cake specific resistance k_2' , and compression coefficient n first increased and then decreased with an increase in the moisture content in the coal dust, and maximum values were observed with a moisture content $M = 4$ wt.%. In contrast, the cake porosity ε first decreased and then increased, also reaching a maximum value at $M = 4$ wt.%.
2. The moisture content of the dust showed notable differences from the air humidity in terms of influencing the dust cake resistance, compressibility, and porosity, and this could be attributed to the discrepant changes in the particle density, surface friction, and particle-to-particle adhesive force.
3. The adhesive force between the coal dust cake and conventional filter was larger than the force between the cake and the coated or repellent filter for moisture contents M between 0 and 12 wt.%. At $M = 0\text{--}4$ wt.%, however, the lowest adhesive force was found between the coal dust and the coated filter, and for $M = 4\text{--}12$ wt.%, the repellent filter presented the lowest adhesive force. The adhesive force was observed to be most sensitive to the moisture content between the dust cake and the coated filter and least sensitive to the moisture content between the cake and the repellent filter.

Acknowledgments

This work was supported by the Program for Changjiang Scholars and Innovative Research Team in University (IRT13098), the Fundamental Research Funds for the Central Universities (2014XT02, 2014ZDPY03), and the Qing Lan Project of Jiangsu Province. This work is also a project funded by the Priority Academic Program Development of Jiangsu Higher Education Institutions.

References

CECALA, A. B., O'BRIEN, A. D., SCHALL, J., COLINET, J. F., FOX, W. R., FRANTA, R. J., JOY, J., REED, W. R., REESER, P. W., ROUNDS, J. R., SCHULTZ, M. J., 2012, *Dust control handbook for industrial minerals mining and processing*, NIOSH RI 2012-112.

CHEN, Y. S., HSIAU, S. S., LEE, H. Y., CHYOU, Y. P., 2012, *Filtration of dust particulates using a new filter system with louvers and sublouvers*, Fuel, 99, 118–128.

CHENG, Y. H., TSAI, C. J., 1998, *Factors Influencing Pressure Drop through a Dust Cake during Filtration*, Aerosol Sci. Tech. 29, 315–328.

CHOI, J. H., HA, S. J., BAK, Y. C., PARK, Y. O., 2002, *Particle size effect on the filtration drag of fly ash from a coal power plant*, Korean J. Chem. Eng. 19, 1085–1090.

CHOI J.H., HA S. J., PARK Y.O., 2002, *The effect of particle shape on the pressure drop across the dust cake*, Korean J. Chem. Eng. 19, 711–717.

DEMIR I., KURSUN I., 2012, *Investigation of radioactive content of Manisa-Soma and Istanbul-Agacli coals (Turkey)*, Physicochem. Probl. Miner. Process. 2, 341–353.

FINKELMAN R.B., OREM W., CASTRANOVA V., TATU C.A., BELKIN H.E., ZHENG B., LERCH H.E., MAHARAJ S.V., BATES A.L., 2002, *Health impacts of coal and coal use: possible solutions*, Int. J. Coal Geol. 50, 425–443.

GUPTA A., NOVICK V.J., BISWAS P., MONSON P.R., 1993, *Effect of humidity and particle hygroscopicity on the mass loading capacity of high efficiency particulate air (HEPA) filters*, Aerosol Sci. Tech. 19, 94–107.

JOUBERT A., LABORDE J.C., BOUILLOUX L., CHAZELET S., THOMAS D., 2010, *Influence of Humidity on Clogging of Flat and Pleated HEPA Filters*, Aerosol Sci. Tech. 44, 1065–1076.

JOUBERT A., LABORDE J.C., BOUILLOUX L., CHAZELET S., THOMAS D., 2011, *Modelling the pressure drop across HEPA filters during cake filtration in the presence of humidity*, Chem. Eng. J. 166, 616–623.

KIM J.H., LIANG Y., SAKONG K.M., CHOI J.H., BAK Y.C., 2008, *Temperature effect on the pressure drop across the cake of coal gasification ash formed on a ceramic filter*, Powder Technol. 181, 67–73.

LI J.L., LI S.H., ZHOU F.B., 2015, *Effect of cone installation in a pleated filter cartridge during pulse-jet cleaning*, Powder Technol. 284, 245–252.

LUPION M., RODRIGUEZ-GALAN M., ALONSO-FARIÑAS B., ORTIZ F.G., 2014, *Investigation into the parameters of influence on dust cake porosity in hot gas filtration*, Powder Technol. 264, 592–598.

MAO N., OTANI Y., YAO Y., KANAOKA C., 2006, *Modeling the filtration process with a flat-type fabric filter*, Adv. Powder Technol. 17, 237–256.

MAO N., YAO Y., HATA M., WADA M., KANAOKA C., 2008, *Comparison of filter cleaning performance between VDI and JIS testing rigs for cleanable fabric filter*, Powder Technol. 180, 109–114.

NEIVA A.C.B., GOLDSTEIN JR. L., CALVO P., ROMEO L.M., ARAUPO J., 1999, *Modelling cake compressibility on gas filtration*, XV Congreso Brasileño de Ingeniería Mecánica, 1–15.

OZBAYOGLU G., 2013, *Removal of hazardous air pollutants based on commercial coal preparation plant data*, Physicochem. Probl. Miner. Process. 2, 621–629.

PARK O.H., YOO G.J., SEUNG B.J., 2007, *A lab-scale study on the humidity conditioning of flue gas for improving fabric filter performance*, Korean J. Chem. Eng. 24, 717–722.

SALAZAR-BANDA G.R., LUCAS R.D., COURY J.R., AGUIAR M.L., 2012, *The Influence of Particulate Matter and Filtration Conditions on the Cleaning of Fabric Filters*, Sep. Sci. Technol. 48, 223–233.

SEVILLE J.P.K., CHEUNG W., CLIFT R., 1989, *A patchy-cleaning interpretation of dust cake release from non-woven fabrics*, Filtr. Separat. 26, 187–190.

TANABE E.H., BARROS P.M., RODRIGUES K.B., AGUIAR M.L., 2011, *Experimental investigation of deposition and removal of particles during gas filtration with various fabric filters*, Sep. Purif. Technol. 80, 187–195.

Received April 21, 2015; reviewed; accepted July 31, 2015

REMOVAL OF Pb(II) AND Cd(II) IONS FROM AQUEOUS SOLUTIONS WITH SELECTED ORGANIC WASTES

Agnieszka BOZECKA*, Piotr BOZECKI**,
Stanisława SANAK-RYDLEWSKA*

* AGH University of Science and Technology, Faculty of Mining and Geoengineering, Al. Mickiewicza 30, 30-059 Cracow, Poland, gala@agh.edu.pl (Agnieszka Bozecka)

** AGH University of Science and Technology, Faculty of Geology, Geophysics and Environmental Protection, Al. Mickiewicza 30, 30-059 Cracow, Poland

Abstract: The authors investigated sorption of Pb(II) and Cd(II) ions from aqueous solutions on selected natural wastes: sunflower hulls, walnut shells and plum stones. The chemical and physical structure of the surface of these sorbents was determined using infrared spectrometry and scanning electron microscopy. The most favourable physicochemical parameters of the sorption processes were also defined. The sorption of Pb(II) and Cd(II) ions was described according to the Langmuir and Freundlich models. It has been shown that the adsorbents studied can be effectively used in removing heavy metals from aqueous solutions. The sunflower hulls have the highest sorption capacity for Pb(II) and Cd(II) ions. It is equal to 36.93 mg/g for the Pb(II) ions and 19.93 mg/g Cd(II) ions. The calculated values of thermodynamic functions indicate a spontaneous ($\Delta G^\circ < 0$) and exothermic ($\Delta H^\circ < 0$) nature of the sorption processes. A participation of ion exchange in these processes is significant. Desorption tests confirm that the adsorbed heavy metals can be recovered and the sorbent materials after regeneration can be reused.

Keywords: biosorption, Pb(II), Cd(II), organic wastes, adsorption isotherms

Introduction

Water pollution with heavy metals is now one of the most important environmental threats. These metals have harmful effects on living organisms, which are related to their carcinogenic and mutagenic properties and the ability of the metals to bioaccumulation (Senczuk, 1999).

For water and waste water purification from heavy metals a number of conventional methods are used, such as chemical precipitation (Alvarez et al., 2007; Ghosh et al., 2011), ion exchange (Kocaoba, 2007; Rao et al., 2010) and adsorption on active carbon (Sulaymon et al., 2009; Tajar et al., 2009; Machida et al., 2012). The methods are widespread and have many advantages. However, due to their limitations

and high cost of application (especially in low concentration of contaminants) they also have some disadvantages. Therefore, new alternatives that will combine efficiency with economy should be searched for. Natural sorbents give perspectives to meet those requirements. Among them both dead organic matter and living micro-organisms may be mentioned. Sorption capacity of this type of organic materials to heavy metals ions is significant, which was lately confirmed, e.g. by Qi and Aldrich (2008), Sari and Tuzen (2008), Uluozlu et al. (2008), Gupta et al. (2009), Saeed et al. (2009), Azouaou et al. (2010), Blazquez et al. (2011).

The aim of the study was to experimentally confirm the possibility of using organic waste, such as sunflower hulls, walnut shells and plum stones, for the removal of Pb(II) and Cd(II) ions from aqueous solutions in single-component systems. The influence of selected physical and chemical parameters of organic materials on the sorption processes has been determined and the possibility of their regenerating examined. Other investigations conducted to elucidate the mechanism of binding heavy metals from solutions involved determining the chemical and physical structure of the organics used. The sorption processes have been described using well-known models of sorption and the maximum sorption capacity of the materials tested has been calculated.

Materials and methods

Three natural sorbents were used in the study: sunflower (*Helianthus L.*) hulls, walnut (*Juglans regia L.*) shells and plum (*Prunus domestica L.*) stones, the latter free from seeds. The material was washed, dried, ground and sieved to obtain the grain fraction below 0.5 mm (fraction was selected based on results obtained in earlier studies). Then it was purified by treating with 10^{-3} M nitric and hydrochloric acids solutions, followed by washing with reverse osmosis water until the pH attained that of the pure reverse osmosis water, i.e., about 6.0, and then dried at 323K.

Sorption experiments were performed in beakers containing 100 cm³ of a test solution into which known weights of the sorbent (sample weights: 0.3, 0.5, 0.7, 1.0 and 1.5 g) were added. The initial Pb(II) and Cd(II) ion concentrations ranged from 6.3 mg/dm³ to 109.4 mg/dm³. Metals were added as the water solutions of Pb(NO₃)₂ and Cd(NO₃)₂ 4H₂O (p.p.a.). All the experiments run at a constant ionic strength of 0.02 mol/dm³, which was adjusted with a solution of KNO₃ at a concentration of 0.04M. The range of initial pH of the test solutions was from 2.0 to 5.0 (\pm 0.1) (its value was adjusted with 0.1M HNO₃).

All the solutions with the sorbents added were continuously stirred for one hour (in this time the system reached equilibrium) with a mechanical stirrer at 120 rpm at the constant temperature 298 \pm 0.5 K. In addition, the studies of a temperature effect were conducted in the range 293-313 \pm 0.5 K (Bozecka, 2013).

The desorption process was studied for the sunflower hulls and walnut shells used earlier to remove Pb(II) and Cd(II) ion from the solutions whose initial concentrations

of Pb and Cd were 15.6 mg/dm³. The sorbents were regenerated with 50 cm³ 0.2M solutions of HNO₃ or HCl. The experimental conditions were the same as in the case of the sorption process. The progress of the desorption effectiveness was determined after 15, 30, 45 and 60 minutes of the tests.

The final concentration of Pb(II) and Cd(II) ions in a solution after sorption and regeneration was determined by the flow coulometry method using an EcaFlow 150 GLP (POL-EKO, Poland). Before the measurements, all the samples were filtered to remove solid particles. Three measurements were performed for each sample. The values of equilibrium concentrations shown in Tables 1-4 are arithmetic averages.

The sorption capacity was calculated from the formula presented below:

$$Q = \frac{V(c_0 - c_{eq})}{m} \quad (1)$$

where: Q – content of the Cd(II) ions in the sorbent (mg/g); V – the volume of the solution (dm³); c_0 and c_{eq} – the initial and final concentrations of Cd(II) ions (mg/dm³); m – the dry mass of the adsorbent (g).

Identification of surface functional groups was carried out using infrared absorption spectra recorded with BIO-RAD FTIR spectrometer (model FTS-165) for the samples prior to and after sorption (each sample had an initial concentration of 109.4 mg/dm³ of Pb or Cd cations). The frequency range was 4000-400 cm⁻¹ and a resolution 4 cm⁻¹. The pellets were made from a mixture of a dried sorbent and the spectrally pure potassium bromide (at the ratio 1:400) pressed at 10 MPa.

The morphology of the selected organic sorbents was determined using a scanning electron microscope FEI Quanta 200 FEG. The analyses were supplemented by microchemical assays using an EDS spectrometer. The tests were carried out on starting (i.e. untreated) samples and on the samples after the sorption process.

Results and discussion

Determination of the chemical and physical structure of the sorbents

The surface morphology images of the sorbents prior to and after the sorption process and the corresponding EDS spectra (Figs 1(a-f) and 2(a-h), respectively) show that lead and the cadmium are below detection limits in the starting materials.

Both elements are present on the surface of the samples used in the sorption tests (Fig. 2a-h), but there are no traces of microprecipitated Pb and Cd compounds. In some areas, however, there are indications of the sorption involving mainly the ion exchange mechanism (e.g. Fig. 2a, c and e). Distribution of adsorbates on the surface is random, which may indicate their heterogeneity (Bozecka, 2013; Bozecka et al., 2014a).

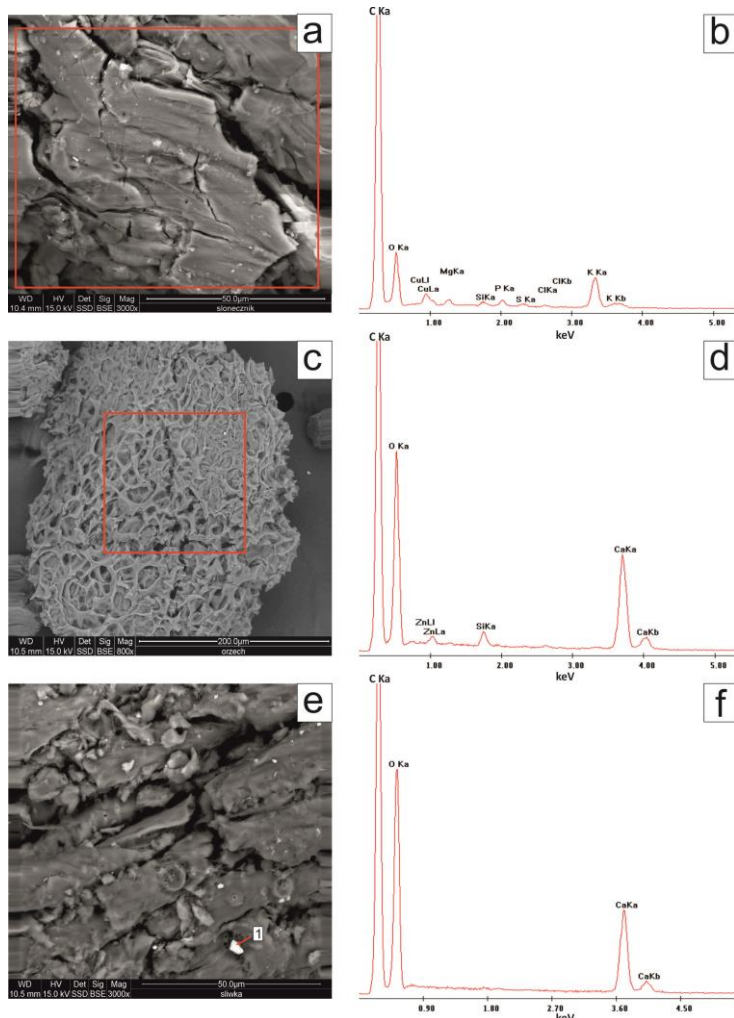


Fig. 1. Examples of SEM images with EDS spectra obtained for samples of starting sunflower hulls (a, b), walnut shells (c, d) and plum stones (e, f) (Bozecka, 2013; Bozecka et al., 2014a)

The presence of functional groups in the starting samples can be traced in the IR spectra (Fig. 3). They show strong absorption bands at approximately 3420 cm^{-1} , which can be attributed to stretching vibrations of the OH groups present in alcohols and phenols or to intramolecular hydrogen bonds of carbohydrates, present in organic compounds (presumably cellulose, hemicellulose and lignin). The bands occurring in all the tested materials in the range of approximately $2930\text{--}2840\text{ cm}^{-1}$ can probably be related to the CH stretching vibrations of alkyl groups.

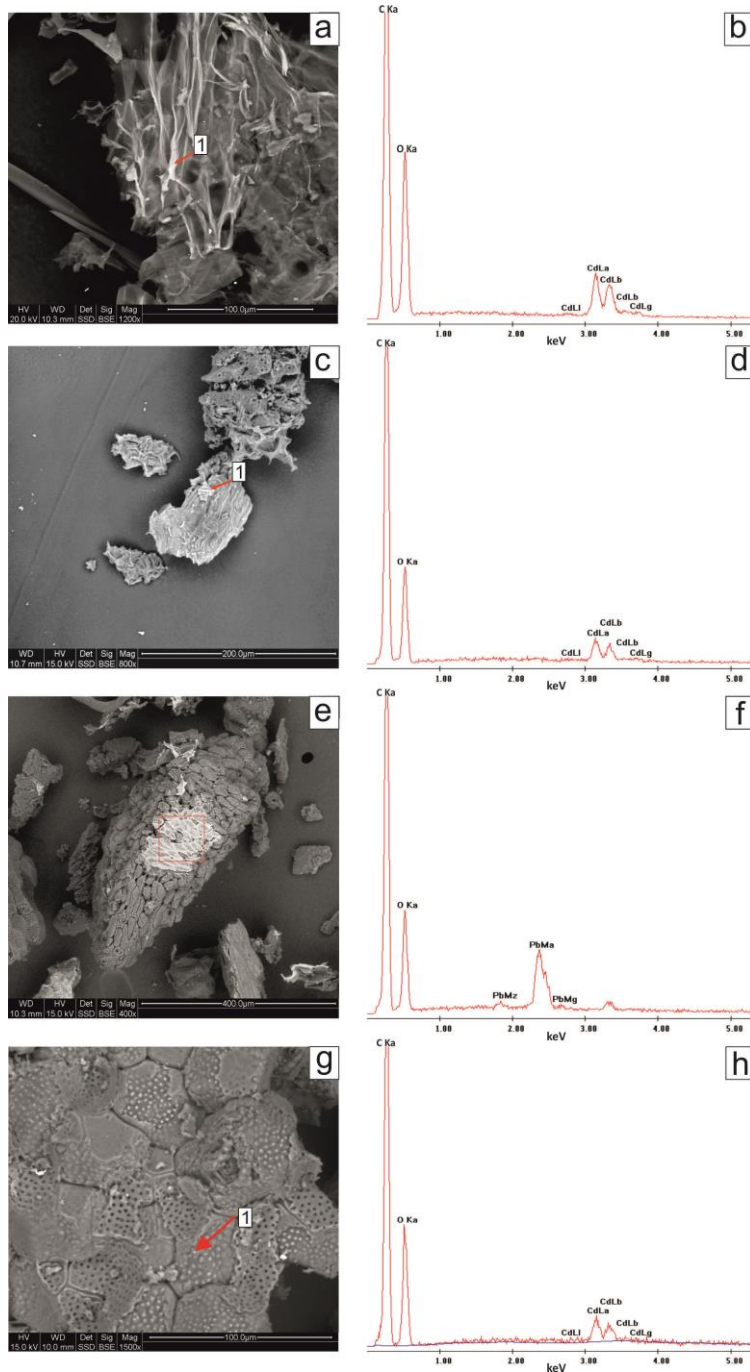


Fig. 2. Examples of SEM images with spectra EDS obtained for samples of sunflower hulls (a, b), walnut shells (c, d) and plum stones (e-h) after sorption of the Pb(II) and Cd(II) ions
 (Bozecka, 2013; Bozecka et al., 2014a)

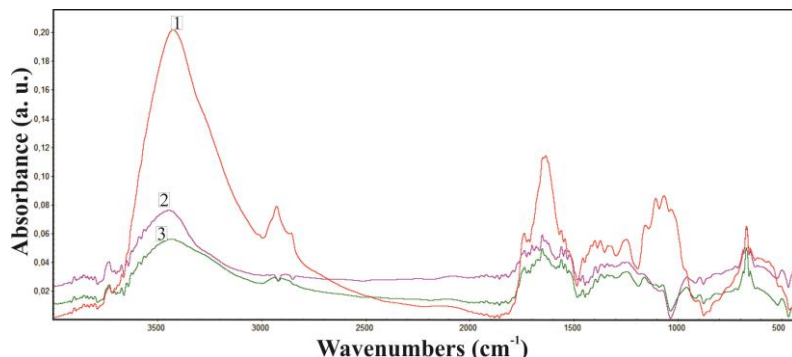


Fig. 3. Comparison of the IR spectra of starting samples of sunflower hulls (1), walnut shells (2) and plum stones (3) (after Bozecka, 2013; Bozecka et al., 2014a, b)

Another band, pronounced mainly in the walnut shells and plum stones at approximately 1740 cm^{-1} may be attributed to the vibrations of C=O carbonyl compounds (carboxylic compounds, esters, ketones, aldehydes, etc.). The presence of the esters, alcohols and phenols is also indicated by the bands in the range 1300-1000 cm^{-1} interpreted as the stretching vibrations of C-O groups.

The bands in the region of approximately 1650 cm^{-1} may be attributed to the stretching vibration of C=O groups and the bending vibration of the N-H amide group. The amines manifests their presence by the band in the range approximately 1650-1580 cm^{-1} , also attributed to the N-H bending.

Absorption in the range approximately 1600-1400 cm^{-1} indicates probably the presence of aromatic compounds. In addition, the bands between 900 and 675 cm^{-1} may be interpreted also as aromatic bands resulting from the bending vibrations out of the plane of the C-H (Uluozlu et al., 2008; Azouaou et al., 2010; Bozecka, 2013; Bozecka et al., 2014a; Bozecka et al., 2014b).

The effects of the functional groups mentioned above on the sorption mechanism of Pb(II) and Cd(II) ions have been interpreted on the IR spectra of the samples after the sorption (Figure 4a, b, c). The intensity of all the characteristic absorption bands, including those of the OH groups (alcohols, phenols, carboxylic acids), C = O (carboxylic compounds, esters, ketones, aldehydes, etc.), and amino and amide groups decreased (Figure 4 a, b, c). Such a distinct intensity reduction occurring at all band frequencies may indicate an adhesion of the Pb(II) and Cd(II) ions that block the access to organic groups.

The strongest change in the band intensity is observed at approximately 3420 cm^{-1} for the sunflower hulls (Fig. 4a). Therefore, it can be concluded that this material is the most efficient sorbent of Pb(II) and Cd(II) ions assuming that the O-H groups are involved in the investigated sorption process. Such a conclusion is consistent with the results discussed in Section 3.2.4, which demonstrate that the sunflower hulls in comparison with other materials have the highest relative capability to remove cations.

Apart from the O–H groups, the carbonyl group C=O (carboxylic compounds, esters, ketones, aldehydes, etc.) and the amine or amide groups may also play an important role in the sorption of Pb(II) and Cd(II) ions. A significant intensity reduction of the bands at the frequencies characteristic of these organic groups may point to their blocking by the Pb(II) and Cd(II) ions adsorbed from the solution. The spectra also confirm that the sorption processes also involve the ion exchange mechanism (Bozecka, 2013; Bozecka et al., 2014a, b).

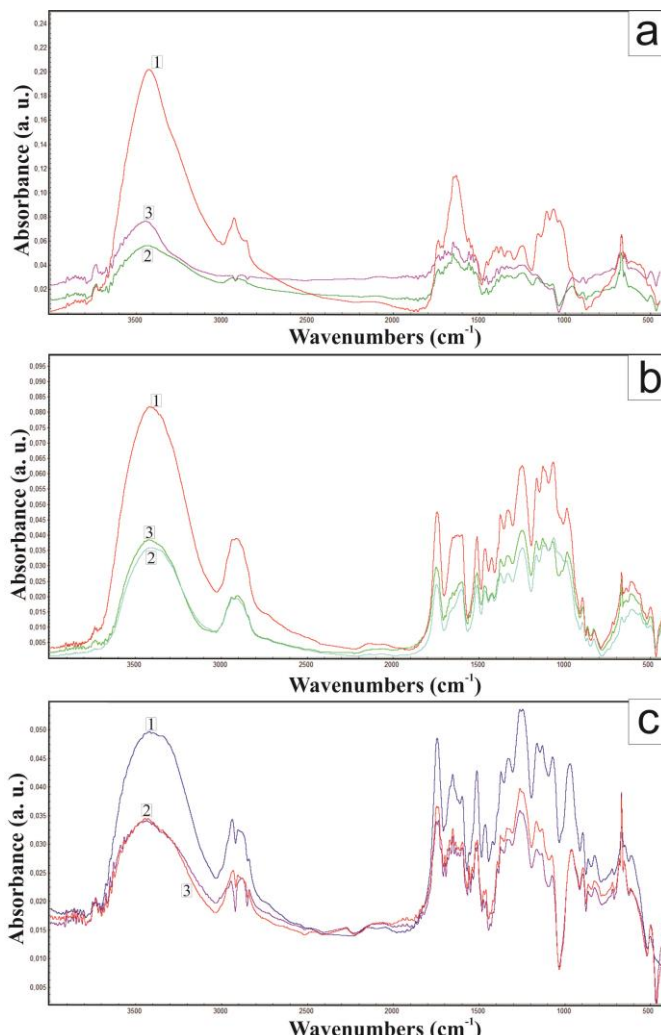


Fig. 4. Comparison of IR spectra obtained for sunflower hulls (a), walnut shells (b) and of plum stones (c) prior to (1) and after sorption of Pb(II) (2) or Cd(II) (3) ions (Bozecka, 2013; Bozecka et al., 2014a, b)

Sorption process of Pb(II) and Cd(II) ions from aqueous solutions

Impact of sorbent mass

Sorption was measured in the samples with the mass 0.3, 0.5, 0.7, 1.0 and 1.5 g (Fig. 5). All the sorbents remove from aqueous solutions an increasing amount of the Pb(II) and Cd(II) ions with an increasing weight of the sample until a maximum sorption at a sorbent mass of 0.5 g is reached. A further increase of the sorbent mass does not significantly affect the amount of the ions adsorbed. Presumably, it is associated with sorbent particle aggregation in the solution, which can reduce an access of the cations to the surface active centres of the sorbent (Uluzlu et al., 2008; Gala (Bozecka) and Sanak-Rydlewsk, 2011; Bozecka, 2013; Bozecka and Sanak-Rydlewsk, 2011, 2015).

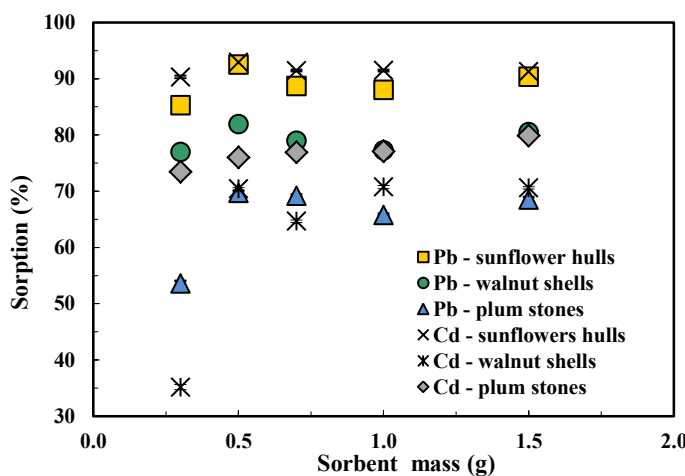


Fig. 5. The influence of the sorbent mass on sorption of the Pb(II) and Cd(II) ions on sunflower hulls, walnut shells and plum stones ($c_o = 15.63 \text{ mg/dm}^3$; pH 4.0 ± 0.1 ; sorbent's particle size class $< 0.5 \text{ mm}$; ionic strength 0.02 mol/dm^3 ; temperature $(298 \pm 0.5) \text{ K}$; time of sorption 1 h; mixing speed 120 rpm) (Bozecka, 2013)

Impact of initial pH of solutions

The sorption of the Pb(II) and Cd(II) ions in the function of the initial pH of the solution was tested for the pH values 2.0, 3.0, 4.0 and 5.0 (Fig 6).

The efficiency of sorption of the Pb(II) and Cd(II) ions by all the materials increases with the pH until it reaches a maximum in the solutions with pH of about 4.0. At pH higher than 5.0 a sorption efficiency noticeably decreases. Only is a little weaker the sorption efficiency of the Pb(II) ions on the walnut shells and sunflower hulls, but its reason is not currently possible for a clear interpretation.

The reduction in the sorption efficiency, both below and above pH of 4.0, is most likely associated with an electrostatic charge accumulated on the surface of the sorbents. The type and amount of this charge depends on the pH of the solution and on

the functional groups on the surface of sorbents (Bansal and Goyal, 2009; Gala (Bozecka) and Sanak-Rydlewska, 2011; Bozecka, 2013; Bozecka and Sanak-Rydlewska, 2011, 2015).

The initial pH of the solution determines the form of the Pb and Cd ions in the solution. In a strongly acidic solution, lead and cadmium are mainly in the form of cations. The gradual increase of the pH leads to the formation of complex ions, followed by precipitation of $\text{Pb}(\text{OH})_2$ and $\text{Cd}(\text{OH})_2$.

Studying the effect of the solution pH on sorption of the Pb(II) and Cd(II) ions, the differences between the starting and the equilibrium pH values were noted. For example, in case of the sunflower hulls and Pb(II) ions the starting pH was 2.08, 3.04, 4.00 and 4.98, while after sorption the values were 2.78, 4.45, 5.23, and 5.34, respectively.

The sorption, hydrolysis and ionization processes explain the changes in pH. The equations 1 and 2, showing the hydrolysis degree of the Pb(II) and Cd(II) ions, indicate that at the time of their attachment to the surface of a sorbent the reaction equilibrium moves to the left. This leads to a reduction of protons in the solution and a pH increase. With the increase of the starting pH value (up to value of zero point charge – pH_{Zpc}), the sorption capacity increases and the pH reaches an equilibrium state

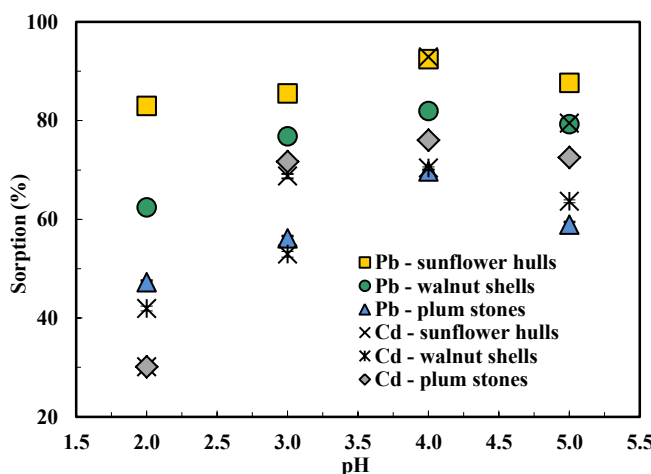


Fig. 6. The effect of pH on sorption of the Pb(II) and Cd(II) ions on sunflower hulls, walnut shells and plum stones ($c_o = 15.63 \text{ mg}/\text{dm}^3$; sorbent mass 0.5 g; sorbent's particle size class $< 0.5 \text{ mm}$; ionic strength $0.02 \text{ mol}/\text{dm}^3$; temperature $(298 \pm 0.5)\text{K}$; time of sorption 1 h; mixing speed 120 rpm) (Bozecka, 2013)

As soon as the $\text{Pb}(\text{OH})^+$ or $\text{Cd}(\text{OH})^+$ ions are adsorbed, the reaction equilibrium moves to the right, thereby increasing the concentration of protons and acidifying the solution:



As mentioned before, the Pb(II) and Cd(II) ions in water are subject to hydrolysis and complexation, thus the protons generated increase the acidity of the solutions. They may also be acidified as a result of hydrolysis and ionization of the functional groups present on the surface of the sorbents. However, the impact of these processes appears to be insignificant and can be ignored (Bozecka, 2013).

Impact of solution temperature

An impact of temperature on the sorption process of the Pb(II) and Cd(II) ions was tested between 293K and 313K. Other conditions were the same as in the previous series.

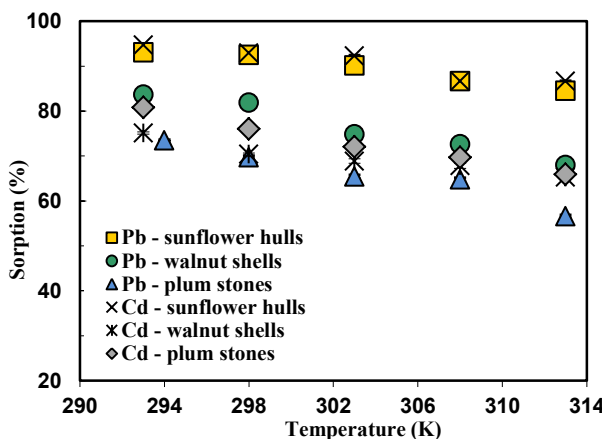


Fig. 7. The impact of the temperature on sorption of the Pb(II) and Cd(II) ions by sunflower hulls, walnut shells and plum stones ($c_0 = 15.63 \text{ mg/dm}^3$; sorbent mass 0.5 g; sorbent's particle size class $< 0.5 \text{ mm}$; ionic strength 0.02 mol/dm^3 ; pH of 4.0 ± 0.1 ; time of sorption 1 h; mixing speed 120 rpm) (Bozecka, 2013)

An increase of the temperature reduced sorption of the Pb(II) and Cd(II) ions (Fig. 7). This indicates the exothermic nature of the processes investigated. The decline in a sorption efficiency may be due to a destruction of the active sites present on the surface of the sorbents or shifting the equilibrium in favour of desorption of the Pb(II) and Cd(II) ions from the surface to a solution (Uluzlu et al., 2008). At higher temperatures, the kinetic energy of the adsorbed molecules increases, which may hinder their connection to the surface (Gala (Bozecka) and Sanak-Rydlewska, 2011; Bozecka, 2013; Bozecka and Sanak-Rydlewska, 2011; 2015).

Based on the experimental data and known thermodynamic relations, the changes of the standard free energy (ΔG°), standard enthalpy (ΔH°) and standard entropy (ΔS°)

have been calculated using the following equation (Meena et al., 2008; Uluzlu et al., 2008; Bozecka, 2013)

$$\Delta G^\circ = -RT \ln K'_c \quad (2)$$

where: R – ideal gas constant ($8.314 \cdot 10^{-3}$ kJ/mol K), T – temperature (K), K'_c – equilibrium constant, defined as the ratio of the concentration of metal ions on the sorbent c_a , to the concentration of ions in the solution c_{eq} , after reaching equilibrium of the sorption process.

The K'_c constant was determined for the lowest, experimental concentration of the metal (Han et al., 2005):

$$\Delta G^\circ = \Delta H^\circ - T \Delta S^\circ \quad (3)$$

$$\ln K'_c = \frac{\Delta S^\circ}{R} - \frac{\Delta H^\circ}{RT} \quad (4)$$

The change of the standard free energy (ΔG°) was calculated from the equation 3. For all the investigated samples and in the whole range of the selected temperatures, the calculated ΔG° is characterized by negative values (Table 1), which proves that the process is spontaneous.

The changes of standard enthalpy and entropy of the system were determined based on Eq. 4, plotting the K'_c graphs as a function of $1/T$ (Fig. 8). The values of ΔH° and ΔS° were determined from the slope and intersection of the y-axis by the linear graphs.

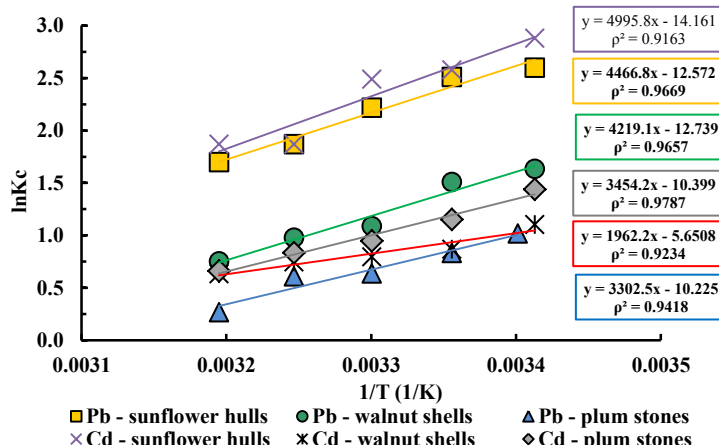


Fig. 8. Relationship between $\ln K'_c$ and $1/T$ for sorption of the Pb(II) and Cd(II) ions on the sunflower hulls, walnut shells and plum stones (after Bozecka, 2013)

The calculated change of the standard enthalpy (ΔH°) in the systems studied reaches negative values (Table 1), confirming the exothermic nature of the process. When $\Delta H^\circ < 0$, the dependence $\ln K'_c = f(1/T)$ is an increasing function ($a > 0$), i.e. with an increasing temperature both the sorption and the value of the equilibrium constant decrease (Fig. 5).

The changes of the standard entropy (ΔS°) of the systems also have negative values (Table 1). The molecules in the adsorbed state have less freedom degrees than those in the solution, which results in a decrease of entropy (Bozecka, 2013).

Table 1. Thermodynamic functions describing the sorption of Pb(II) and Cd(II) ions from aqueous solutions by sunflower hulls (S), walnut shells (O) and plum stones (P) (Bozecka, 2013)

Function (kJ/mol)	Materials	Temperature (K)											
		293	298	300	303	308	313	293	298	300	303		
		Pb(II)						Cd(II)					
ΔG°	S	-6.33	-6.22	-5.58	-4.79	-4.42	-6.33	-7.01	-6.38	-5.90	-4.78	-4.87	-7.01
	O	-3.98	-3.74	-2.74	-2.50	-1.96	-3.98	-2.69	-2.15	-2.00	-1.91	-1.65	-2.69
	P	-2.49	-2.06	-1.61	-1.56	-0.69	-2.49	-3.51	-2.86	-2.39	-2.14	-1.72	-3.51
ΔH°	S					-37.14						-41.62	
	O					-35.08						-16.30	
	P					-27.46						-28.72	
ΔS°	S					-0.10						-0.12	
	O					-0.11						-0.05	
	P					-0.09						-0.09	

A description of the sorption of Pb(II) and Cd(II) ions with selected adsorption models

To evaluate the maximum sorption capacity of the sorbents studied toward the Pb(II) and Cd(II) ions, the authors applied commonly used adsorption models of Langmuir and Freundlich.

The Langmuir theory assumes that the surface of the adsorbent is homogeneous. Adsorption in the system is located, which means that the molecule cannot move freely across the surface. Lateral interactions between the adsorbed molecules are irrelevant. It is, therefore, a monolayer adsorption (Bansal and Goyal, 2009). The Langmuir model is described by the following equation:

$$Q = \frac{q_{\max} b \cdot c_{eq}}{(1 + b \cdot c_{eq})} \quad (5)$$

where: q_{\max} (mg/g) and b (dm³/mg) are the Langmuir constants.

The parameter q_{\max} is the maximum sorption capacity of the sorbent, i.e. the maximum amount of cations needed to form a complete monolayer (Han et al., 2005).

The constant b represents the energy of adsorption. This parameter is very useful, because it determines the sorbents affinity toward the substances removed. The higher the value of the constant b , the higher the affinity of the sorbent towards cations and the steeper the Langmuir isotherm. In general, a good sorbent should be characterised by high values of both the constants q_{max} and b (Meena et al., 2008).

The values of the coefficients q_{max} and b in the Langmuir equation were determined based on their linear form:

$$\frac{1}{Q} = \frac{1}{q_{max}b} \cdot \left(\frac{1}{c_{eq}} + b \right) \quad (6)$$

The Freundlich equation has an experimental nature, well describing the adsorption on heterogeneous surfaces and microporous adsorbents. The Freundlich model is described by the following equation:

$$Q = K \cdot c_{eq}^{1/n} \quad (7)$$

where K and n are the Freundlich constants.

The Freundlich parameter K allows the assessment of the maximum sorption capacity of the sorbent and the parameter n is defined as the affinity constant or the binding strength. The smaller the value of $1/n$, the greater heterogeneity energy of an adsorption system (Bansal and Goyal, 2009).

To calculate the constants K and n of the Freundlich equation, the logarithmic form of this equation is used:

$$\log Q = \log K + \frac{1}{n} \cdot \log c_{eq} \quad (8)$$

The resulting values of the coefficients of the Langmuir and the Freundlich isotherms together with their uncertainties and correlation coefficients ρ are summarized in Tables 2 and 3.

The values of the Langmuir and Freundlich constants confirm that of the three materials studied the sunflower hulls is the best sorbent for removing the Pb(II) and Cd(II) ions from water solutions. It is characterized by the highest values of the parameter q_{max} that expresses the capacity of the monolayer; the parameter b that determines its affinity for removing ions and for the constant K . The coefficient n in the Freundlich isotherm for all the materials is in the range from 1 to 10. That proves that the sorption processes investigated are "beneficial" (Meena et al., 2008; Gala (Bozecka) and Sanak-Rydlewsk, 2011; Bozecka, 2013; Bozecka and Sanak-Rydlewsk, 2011; 2015).

Table 2. Coefficients of the Langmuir isotherm and the uncertainty resulting for sorption of the Pb(II) and Cd(II) ions on sunflower hulls (S), walnut shells (O) and the plum stones (P) (Bożęcka, 2013)

Cation	Materials	q_{max} (mg/g)	Δq_{max} (mg/g)	b (dm ³ /mg)	Δb (dm ³ /mg)	P
Pb(II)	S	36.93	0.76	0.1512	0.0002	0.9740
	O	23.08	0.52	0.03343	0.00006	0.9837
	P	21.23	0.47	0.03457	0.00005	0.9796
Cd(II)	S	19.93	0.51	0.2264	0.0002	0.9869
	O	17.17	0.54	0.03272	0.00008	0.9485
	P	17.98	0.39	0.0777	0.0001	0.9613

Table 3. Coefficients of the Freundlich isotherm and the uncertainty resulting for sorption of the Pb(II) and Cd(II) ions on sunflower hulls (S), walnut shells (O) and the plum stones (P) (Bożęcka, 2013)

Cation	Materials	K (dm ³ /mg)	ΔK (dm ³ /mg)	n	Δn	ρ
Pb(II)	S	4.43	0.06	1.35	0.02	0.9467
	O	0.95	0.02	1.36	0.01	0.9860
	P	0.78	0.02	1.31	0.01	0.9936
Cd(II)	S	3.10	0.04	1.60	0.02	0.9627
	O	1.22	0.02	1.82	0.02	0.9831
	P	1.27	0.02	1.44	0.01	0.9813

Sorption capacity of tested materials in relation to the lead and cadmium ions are comparable to other organic and inorganic sorbents (Bożęcka, 2013; Gupta et al., 2009).

Equilibrium study on desorption of the Pb(II) and Cd(II) ions

The desorption process was studied on two sorbents, namely sunflower hulls and walnut shells, using the 0.2M solutions of nitric(V) and hydrochloric acids. The results are summarized in Table 4.

Desorption of the Pb(II) and Cd(II) ions from the surface of the two natural sorbents proceeds relatively fast. The desorption equilibrium in almost all cases was reached after 30 minutes. An extension of the desorption time practically does not significantly affect the recovery of lead and cadmium.

A comparison of the desorption efficiencies indicates that HNO₃ is more effective for the Pb(II) ions and sunflower hulls. For walnut shells there are no significant differences between the results. For both acids the desorption efficiency is high and approximates 94%.

The Pb(II) ions are desorbed more efficiently from the surfaces of sunflower hulls in comparison to walnut shells.

Table 4. Desorption of the Pb(II) and Cd(II) ions from the surface of sunflower hulls and walnut shells using nitric(V) and hydrochloric acids depending on the duration of the process

Regenerator	Materials	Regeneration time (min)							
		15	30	45	60	15	30	45	60
		Desorption (%)							
0.2 M HNO ₃	S	79.49	83.36	84.56	84.61	45.41	49.21	49.23	51.03
	O	90.54	93.04	92.53	93.37	39.06	41.73	41.89	42.28
0.2 M HCl	S	68.11	69.33	69.45	69.33	64.53	65.87	67.08	68.08
	O	90.24	91.42	94.40	94.02	36.94	39.17	39.66	39.78

The recovery of cadmium is much lower than that of lead. It is 68.08% for HCl and 51.03% for HNO₃ in case of sunflower hulls and 39.78% for HCl and 42.28% for HNO₃ in the case of walnut shells. Desorption of the Cd(II) ions from sunflower hulls is more efficient than that from walnut shells.

The results confirm that protons in the solutions at pH<2.0 have a greater ability to attach to the sorbent surface groups than the cations of a heavy metal (Bozecka, 2013)

Conclusions

1. Sunflower hulls, walnut shells and plum stones can be effectively used for the removal of heavy metals ions from water and underpin for further research.
2. Sorption capacity of this materials in relation to the lead and cadmium ions are comparable to other organic and inorganic sorbents (Bozecka, 2013; Gupta et al., 2009).
3. Used sorption method have many advantages, which include: low cost both of purchasing and of process itself and management possibility of unwanted waste, which storage is a major environmental problem. Another advantage of used method is reusability of studied materials as well as the recovery possibility of adsorbed heavy metals.
4. Ion exchange processes are dependent on the surface construction of the sorbents used and also on the ionic radius of a metal considered
5. The best sorption properties have been revealed by sunflower hulls. In their case q_{max} was 36.93 mg/g for the Pb(II) ions and 19.93 mg/g for the Cd(II) ions.
6. The microchemical analysis indicates that lead and cadmium are not present in the starting sorbent samples. No traces of microprecipitation of lead and cadmium were observed in scanning images. In turn, there are several areas that confirm that the sorption processes involve mainly the ion exchange mechanism.
7. Among the surface functional groups, the -OH group (from alcohols, phenols, carboxylic acids), the carbonyl group C=O (from carboxylic compounds, esters, ketones, aldehydes etc.) and the amine or amide groups have been found to dominate.

8. The calculated values of thermodynamic functions indicate the spontaneous ($\Delta G^\circ < 0$) and exothermic ($\Delta H^\circ < 0$) nature of the sorption and desorption processes on the organic sorbents studied.

9. After their acid regeneration, the sunflower hulls and walnut shells can be used again to remove the Pb(II) and Cd(II) ions from aqueous solutions.

References

ALVAREZ M.T., CRESPO C., 2007, *Mattiasson, B. Precipitation of Zn(II), Cu(II) and Pb(II) at bench-scale using biogenic hydrogen sulfide from the utilization of volatile fatty acids*, Chemosphere. 66, 1677–1683.

AZOUAOUI N., SADAQUI Z., DJAAFRI A., MOKADDEM H., 2010, *Adsorption of cadmium from aqueous solution onto untreated coffee grounds: Equilibrium, kinetics and thermodynamics*, J. Hazard. Mater. 184, 126–134.

BANSAL R.C., GOYAL M., 2005, *Activated Carbon Adsorption*, CRC Press.

BLÁZQUEZ G., MARTÍN-LARA M. A., TENORIO G., CALERO M., 2011, *Batch biosorption of lead(II) from aqueous solutions by olive tree pruning waste: Equilibrium, kinetics and thermodynamic study*, Chem. Eng. J. 168, 170–177.

BOZECKA A., 2013, *Usuwanie jonów metali toksycznych z roztworów wodnych za pomocą odpadów organicznych*. PhD Thesis, AGH-UST University of Science and Technology, not published.

BOZECKA A., BOZECKI P., SANAK-RYDLEWSKA S., 2014a, *Badanie chemicznej i fizycznej struktury powierzchni sorbentów naturalnych wykorzystanych do usuwania jonów Pb²⁺ i Cd²⁺ z roztworów wodnych w układach jedno- i dwuskładnikowych*, Przem. Chem. 93, 374–383.

BOZECKA A., BOZECKI P., SANAK-RYDLEWSKA S., 2014b, *Study of chemical surface structure of natural sorbents used for removing of Pb²⁺ ions from model aqueous solutions (Part II)*, Arch. Min. Sci. 59, 217–223.

BOZECKA A., SANAK-RYDLEWSKA S., 2011, *Removal of Pb²⁺ ions from aqueous solutions on plum stones crushed to particle size below 0,5 mm*, Arch. Min. Sci. 56, 71–80.

BOZECKA A., SANAK-RYDLEWSKA S., 2015, *Sorption of Cd²⁺ ions from aqueous solutions on organic wastes*, Arch. Min. Sci. 60, 455–464.

GALA (BOZECKA) A., SANAK-RYDLEWSKA S., 2011, *A comparison of Pb²⁺ sorption from aqueous solutions on walnut shells and plum stones*, Polish J. Environ. Stud. 20, 877–883.

GHOSH P., SAMANTA A.N., RAY S., 2011, *Reduction of COD and removal of Zn²⁺ from rayon industry wastewater by combined electro-fenton treatment and chemical precipitation*, Desalination 266, 213–217.

GUPTA S., KUMAR D., GAUR J.P., 2009, *Kinetic and isotherm modeling of lead(II) sorption onto some waste plant materials*. Chemical Engineering Journal, 148, 226–233

HAN R., ZHANG J., ZOU W., SHI J., LIU H., 2005, *Equilibrium biosorption isotherm for lead ion on chaff*, J. Hazard. Mater. 125, 266–271.

KOCAOBA S., 2007, *Comparison of Amberlite IR 120 and dolomite's performances for removal of heavy metals*, J. Hazard. Mater. 147, 488–96.

MACHIDA M., FOTOOGHI B., AMAMO Y., MERCIER L., 2012, *Cadmium(II) and lead(II) adsorption onto hetero-atom functional mesoporous silica and activated carbon*, Appl. Surf. Sci. 258, 7389–7394.

MEENA A.K., KADIRVELU K., MISHRAA G.K., RAJAGOPAL C., NAGAR P.N., 2008, *Adsorption of Pb(II) and Cd(II) metal ions from aqueous solutions by mustard husk*, J. Hazard. Mater. 150, 619–625.

QI B.C., ALDRICH C., 2008, *Biosorption of heavy metals from aqueous solutions with tobacco dust*, *Bioresour. Technol.* 99, 5595–601.

RAO K.S., CHAUDHURY G.R., MISHRA B.K., 2010, *Kinetics and equilibrium studies for the removal of cadmium ions from aqueous solutions using Duolite ES 467 resin*, *Int. J. Miner. Process.* 97, 68–73.

SAEED A., IQBAL M., HOLL W.H., 2009, *Kinetics, equilibrium and mechanism of Cd²⁺ removal from aqueous solution by mungbean husk*, *J. Hazard. Mater.* 168, 1467–75.

SARI A., TUZEN M., 2008, *Biosorption of Pb(II) and Cd(II) from aqueous solution using green alga (Ulva lactuca) biomass*, *J. Hazard. Mater.* 152, 302–8.

SENCZUK W., 1999, *Toksykologia*. Wydawnictwo Lekarskie PZWL. Warszawa.

SULAYMON A.H., ABID B.A., AL-NAJAR J.A., 2009, *Removal of lead copper chromium and cobalt ions onto granular activated carbon in batch and fixed-bed adsorbers*, *Chem. Eng. J.* 155, 647–653.

TAJAR A., KAGHAZCHI T., SOLEIMANI M., 2009, *Adsorption of cadmium from aqueous solutions on sulfurized activated carbon prepared from nut shells*, *J. Hazard. Mater.* 165, 1159–64.

ULUOZLU O.D., SARI A., TUZEN M., SOYLUK M., 2008, *Biosorption of Pb(II) and Cr(III) from aqueous solution by lichen (Parmelina tiliaceae) biomass*, *Bioresour. Technol.* 99, 2972–80.

Received June 6, 2015; reviewed; accepted August 19, 2015

REMOVAL OF QUINOLINE FROM AQUEOUS SOLUTIONS BY LIGNITE, COKING COAL AND ANTHRACITE. ADSORPTION KINETICS

Hongxiang XU^{*}, Yongtian WANG^{}, Gen HUAGN^{*}, Guixia FAN^{***},**
Lihui GAO^{}, Xiaobing LI^{**}**

^{*} School of Chemical and Environmental Engineering, University of Mining and Technology (Beijing), Beijing, China, 100083, xuhongxiang001@163.com

^{**} School of Chemical Engineering and Technology, Chinese National Engineering Research Center of Coal Preparation and Purification, China University of Mining and Technology, Xuzhou, Jiangsu, China, 221116.

^{***} School of Chemical Engineering and Energy, Zhengzhou University, Zhengzhou, China, 450001

Abstract: Basing on the concept of circular economy, a novel method of industrial organic wastewater treatment by using adsorption on coal is introduced. Coal is used to adsorb organic pollutants from coking wastewaters. After adsorption, the coal would be used in its original purpose, as its value was not reduced and the pollutant was reused. Through the systemic circulation of coking wastewater zero emissions can be achieved. Lignite, coking coal and anthracite were used as adsorbents in batch experiments. The quinoline removal efficiency of coal adsorption was investigated. Both the coking coal and anthracite exhibited properties well-suited for quinoline adsorption removal. The experimental data were fitted to the pseudo-first- order and pseudo-second-order kinetic equations as well as intraparticle diffusion and Bangham models. An attempt was made to find the rate-limiting step involved in the adsorption processes. Both boundary-layer diffusion and intraparticle diffusion are likely involved in the rate-limiting mechanisms. Effect of pH on coal adsorptions by coking coal was investigated. The process of quinoline adsorption on coal was researched. The coal adsorption method for removing refractory organic pollutants is a great hope for achieving wastewater zero emission for coking plants.

Keywords: quinoline adsorption, coking coal, kinetics, adsorption activation energy, coal adsorption

Introduction

Coking wastewater usually contains high concentrations of ammonia, sulfide, phenol, quinoline, pyridine, indol, and other organic compounds, which makes it difficult to treat because most of those compounds are refractory, highly concentrated mutative and carcinogenic and produce long-term environmental and ecological impacts (Lai et al., 2009; Chen et al., 2009; Fang et al., 2012).

Adsorption is the most convenient and effective technique to remove organic compounds from coking wastewater (Aksu and Yener, 2001; Badmus and Audu, 2009; Lorenc-Grabowska et al., 2013), but there also are some problems including the high cost of adsorbent and adsorbent regeneration, sludge may be produced which may cause other environment problem, and finally adsorbent regeneration loss (Mall and Srivastava, 2006; Ahmaruzzaman, 2008; Belhachemi and Addoun, 2012). Therefore, methods that enhance advantages and avoid disadvantage of adsorption were important in this research. Coal is a complex porous medium and natural adsorbent. After adsorption, the coal may be used in its original purpose and its value was not reduced (Li et al., 2015).

This research investigates the adsorption behavior of quinoline related substances found in simulated coking plant wastewater. The characters of adsorbents are investigated by using FTIR and BET. Lignite, coking coal and anthracite were compared with respect to adsorption capacity and process kinetics by various fitting models. The effect of pH on special surface area and coal adsorption efficiency were also investigated.

Methods and materials

Adsorbate and adsorbents

Adsorbate used in this paper is quinoline, and adsorbents investigated are lignite, coking coal and anthracite which used in this experiment. The characterization of the adsorbent has been previously published (Xu et al., 2016).

Batch adsorption studies

The adsorption kinetics of quinoline on three kinds of coal was investigated in batch sorption experiments and described previously (Xu et al., 2016). The adsorption capacity of coal was calculated using the expression

$$Q_t = \frac{(C_0 - C_t)V}{M}. \quad (1)$$

The removal efficiency of quinoline was calculated using the expression,

$$E = \frac{C_0 - C_t}{C_0} \times 100\% \quad (2)$$

where, Q_t ($\text{mg} \cdot \text{g}^{-1}$) is the quinoline removed at time t by a unit mass of the adsorbent, C_0 ($\text{mg} \cdot \text{dm}^{-3}$) is the initial quinoline concentration, C_t ($\text{mg} \cdot \text{dm}^{-3}$) is the quinoline concentration at time t , and M (g) is coal consumption. V (cm^{-3}) is the quinoline solutions volume.

During experiments, the solution pH was carefully adjusted to a range between 1 and 11 by adding small amounts of HCl ($0.1 \text{ mol} \cdot \text{dm}^{-3}$) or NaOH ($0.1 \text{ mol} \cdot \text{dm}^{-3}$) solution and it was measured using a pH-meter (S20, Mettler Toledo), while quinoline

solutions contained in 100 cm³ conical flasks closed with glass stoppers to avoid evaporation were stirred using a mechanical magnetic stirrer. The blank experiments were also carried out to observe the effect of vaporization of quinoline. The amount of vaporization during the experiments was subtracted from the experimental data.

The adsorption experiments, which were conducted at various time intervals and temperatures (283K, 298K and 313K) to determine when the adsorption equilibrium was reached and the maximum removal of naphthalene was attained. After the equilibrium contact time, the samples were filtered and the equilibrium concentrations measured by UV/VIS spectroscopy at the respective standard curve equations, which is 278 nm for quinoline, as described by Lin and Dence (1992).

Adsorption kinetic models

The whole adsorption rate is decided by the slowest step, so to improve that step can increase the whole adsorption rate. To know which step control the rate of adsorption is very important to research (Poot et al., 1978; Rodriguez et al., 2009; Zhang et al., 2010) the adsorption process and improve the adsorption efficiency. Here, kinetic models were used to investigate the mechanism of sorption and potential rate controlling steps.

Pseudo-first-order kinetic equation

The Lagergren pseudo-first-order rate expression is given as (Ho and Mckay, 1999; Lataye et al., 2006 Hwang et al., 2011):

$$\frac{dQ_t}{dt} = k_1(Q_{eq} - Q_t). \quad (3)$$

The integration form of the pseudo-first order kinetic equation is:

$$Q_t = Q_{eq}(1 - e^{-k_1 t}). \quad (4)$$

The line form of the pseudo-first order kinetic equation is:

$$\log(Q_{eq} - Q_t) = \log Q_{eq} - \left[\left(\frac{k_1}{2.303} \right) t \right]. \quad (5)$$

The boundary conditions $Q_t = 0$ at $t = 0$ and $Q_t = Q_{eq}$ at $t = t$, where, Q_t (mg·g⁻¹) is the amount of quinoline adsorbed at time t (min); k_1 (min⁻¹) is the pseudo-first-order rate constant.

Pseudo-second-order kinetic equation

The pseudo-second-order kinetic equation which was presented by Ho and Mckay, (1988; 2002), Azizian (2004), Chowdury et al. (2011) is expressed as:

$$\frac{dQ_t}{dt} = k_2(Q_{eq} - Q_t)^2 \quad (6)$$

where, k_2 (g·mg⁻¹·min⁻¹) is the pseudo-second-order rate constant.

The integration form of the pseudo-second-order kinetic equation is:

$$\frac{1}{(Q_{eq} - Q_t)} = \frac{1}{Q_{eq}} + k_2 t \quad (7)$$

while linear form of the pseudo-second-order kinetic equation is:

$$\frac{t}{Q_t} = \frac{1}{k_2 Q_{eq}^2} + \frac{t}{Q_{eq}}. \quad (8)$$

A special feature of the pseudo-second-order rate expression is that the initial sorption rate at $t = 0$, sometimes denoted as h ($\text{mg} \cdot \text{g}^{-1} \text{ min}^{-1}$) (Srivastava, 2005; Andersson 2011). The initial sorption rate h can be calculated by:

$$h = k_2 \times Q_{eq}^2. \quad (9)$$

The intraparticle diffusion model

The intraparticle diffusion kinetic equation which was presented by Weber and Morris (1963) (Yu et al., 1996) and is expressed as:

$$Q_t = k_3 t^{0.5} + m \quad (10)$$

where k_3 ($\text{mg} \cdot \text{g}^{-1} \cdot \text{min}^{-0.5}$) is the intraparticle diffusion rate constant, and m ($\text{mg} \cdot \text{g}^{-1}$) is the intercept which indicates the boundary layer thickness. The larger the intercept is, the greater the boundary effect is (Weber and Morris, 1963; Kumar et al., 2003).

The Bangham model

The kinetic equation presented by Bangham (Sze and Mackay, 2010) is expressed as:

$$\frac{dQ_t}{dt} = k_4 (C_0 - Q_t m) \gamma t^{\gamma-1}. \quad (11)$$

The integration form of the Bangham model is:

$$Q_t = \left(\frac{C_0}{m} \right) - \frac{C_0}{m \exp(k_4 m t^\gamma)}. \quad (12)$$

The line form of the Bangham model is:

$$\log \log \left(\frac{C_0}{C_0 - Q_t m} \right) = \log \left(\frac{k_4 m}{2.3} \right) + \gamma \log t. \quad (13)$$

The boundary conditions is $Q_t = 0$ at $t = 0$ and $Q_t = Q_{eq}$ at $t = t$, where, m ($\text{mg} \cdot \text{dm}^{-3}$) is adsorbent concentration, K_4 is proportionality constant and γ is a constant (Yu et al., 1997; Kaya et al., 2013).

Results and discussion

Chemical composition of lignite, coking coal and anthracite

The chemical composition of the lignite, coking coal and anthracite which was obtained by XRF are shown in Table 1.

Table 1. Chemical composition of the lignite, coking coal and anthracite

Title		Na ₂ O	TiO ₂	K ₂ O	S	MgO	Fe ₂ O ₃	CaO	Al ₂ O ₃	SiO ₂
Concentration %	lignite	0.15	0.20	0.47	0.65	0.69	1.28	1.62	4.68	12.90
	coking coal	0.07	0.33	0.21	0.85	0.16	0.73	0.64	5.54	8.07
	anthracite	0.10	0.33	0.06	0.79	0.14	0.63	0.68	4.62	5.48

As shown in Table 1, the sum content of three parts including calcium oxide, alumina and monox in lignite was highest, was 19.91%, those were three main components of ash. The sum content of three parts in coking coal and anthracite were 14.25% and 10.78%, respectively. There may be a large number of silicon and aluminum active adsorption site on lignite surface because that the content of silicon and aluminum are large. So the main gangue mineral in lignite was quartz, which was accord with the XRD previously described Xu et al. (2016).

The special surface area

The special surface area of the lignite, coking coal and anthracite were $6.0876 \text{ m}^2 \cdot \text{g}^{-1}$, $5.7864 \text{ m}^2 \cdot \text{g}^{-1}$ and $6.1479 \text{ m}^2 \cdot \text{g}^{-1}$, respectively, as determined previously (Xu et al., 2016).

Effect of pH on special surface area

The effect of pH on special surface area for coking coal is shown in Fig. 1. As shown in Fig. 1, the special surface area of coking coal decreased as the pH value increased from 2.0 to 6.0, the special surface area remains approximately constant as the pH value increased from 6.0 to 8.0, the special surface area rapidly decreased after pH 8.0. Due to both most of oxygen-containing functional group on the coal surface and hydrochloric acid solutions acidity, there is no chemical reaction, so the coal macromolecular structure has not changed after the coal was treated by hydrochloric acid solutions, and thus the basic structure of the coal sample also has not change (Wang et al., 2012). Because the sulfate and alkali soluble minerals on the coal surface were washed away by solutions of hydrochloric acid and some concave and convex points on the coal surface were formed, the special surface area of the coal increased as shown in Fig. 1. The special surface area of the coal increased slightly because some acidic minerals on the coal surface were dissolved after the coal was treated by solutions of sodium hydroxide solution of known pH value. Meanwhile on the coal surface, the sodium hydroxide may react with the oxygen containing functional groups

and in addition some organic matter and minerals may dissolved, and thus some part of the pore collapsed after the reaction reached a certain point which decreased the special surface area of the coal. The specific surface area increase and reduction is flat around 7.5 pH value. The specific surface area decreased after 8.0 pH value because the reduction part of special surface area was bigger than increase part.

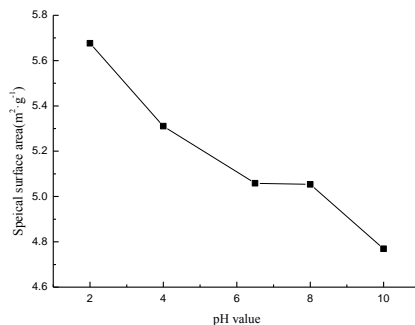


Fig. 1. Effect of pH on the specific surface area of coking coal at 25 °C

Effect of pH on coal adsorption

The effect of pH on the adsorption capacity and the quinoline removal efficiency for lignite, coking coal and anthracite coal are shown in Fig. 2.

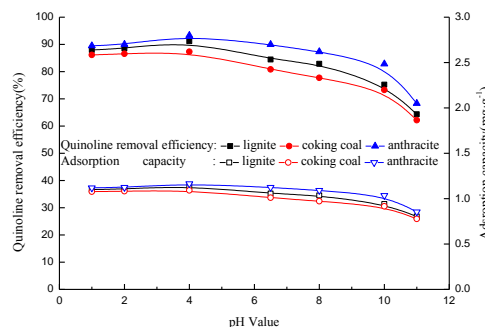


Fig. 2. The influence of pH value to the adsorption capacity and the quinoline removal efficiencies for lignite, coking coal and anthracite

As shown in Fig. 2, the maximum quinoline removal for three kinds of coal was found to beat around pH value of 4.0. Coal adsorption increased at pH values range from 1.0 to 4.0, after that it slightly decreased up to pH = 11 due to that the specific surface area decreased with the PH values from 1 to 11 according to the specific surface area measurements. The optimum adsorption pH value determined by test is 4.

Kinetic models

The equation constants were obtained from the experimental data by applying linear regression analysis to the linear forms of the model equations (Fig. 3) and are reported, together with the correlation coefficients by using Origin 8.5 and 1stOp software, in Table 1.

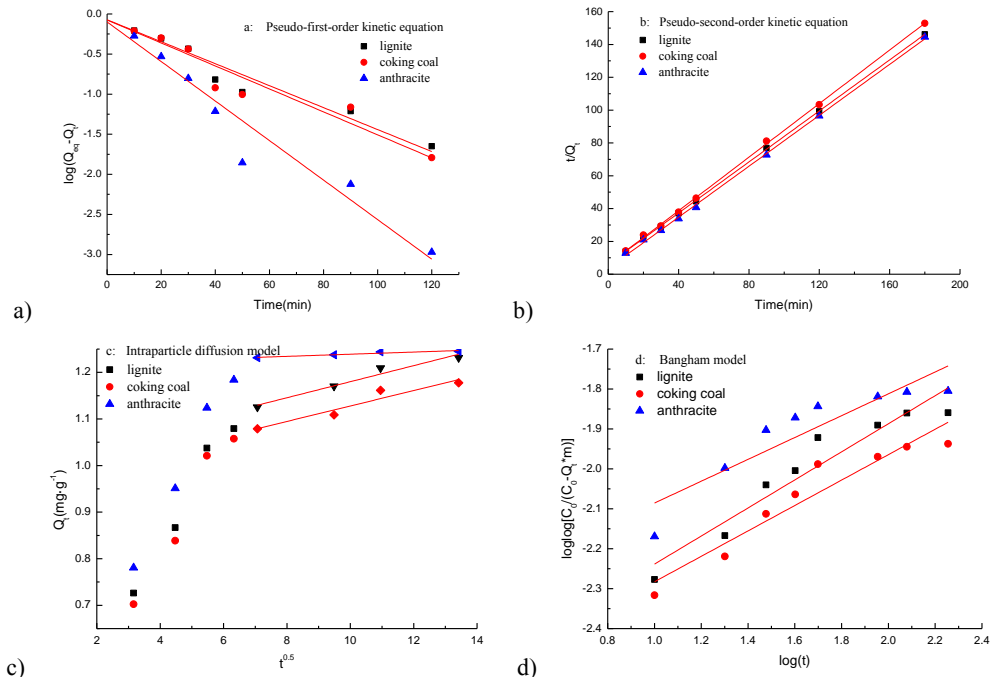


Fig. 3. Adaptation of experimental data on quinoline adsorption onto lignite, coking coal and anthracite using four kinetic models: a) pseudo-first-order equation, b) pseudo-second order equation, c) intraparticle diffusion model, and d) Bangham model

As shown in Fig. 3, it can be seen that the pseudo-first-order rate equation provided a poor fit to the experimental data. However, according to Gerente et al. (2007), this model is generally restricted to only the initial 20~40% of the adsorption capacity and the equation needs further modifications for longer sorption times. Nevertheless, the pseudo-second-order rate expression showed the best fit to the experimental data because all of three R^2 are larger than 0.999.

The pseudo-second-order rate equation also yielded $Q_{eq(calc)}$ values close to the obtained $Q_{eq(exp)}$ results (Table 2). Therefore, sorption of quinoline onto lignite, coking coal and anthracite was more appropriately approximated by the pseudo-second-order rate model. The values of h , representing the initial sorption rate, were obtained from the pseudo-second-order rate expression. The sequence of the obtained

k_2 value was anthracite > coking coal > lignite, implying that sequence of the sorption process was anthracite > coking coal > lignite. The reason is that the special surface area of anthracite is largest and the special surface area of lignite is smallest in three kinds of coal.

Table 2. Constants and correlation coefficients obtained by liner regression

Adsorbents	Pseudo-first-order kinetics model			
	$Q_{eq(exp)}/\text{mg}\cdot\text{g}^{-1}$	$Q_{eq(calc)}/\text{mg}\cdot\text{g}^{-1}$	K_1/min^{-1}	R^2
lignite	1.23	0.85	0.0316	0.9480
coking coal	1.19	0.95	0.0268	0.9021
anthracite	1.27	0.79	0.0568	0.9323
Adsorbents	Pseudo-second-order kinetics model			
	$Q_{eq(calc)}/\text{mg}\cdot\text{g}^{-1}$	$K_2/\text{g}\cdot\text{mg}^{-1}\cdot\text{min}^{-1}$	$h/\text{mg}\cdot\text{g}^{-1}\cdot\text{min}^{-1}$	R^2
lignite	1.25	0.1118	0.185	0.9999
coking coal	1.24	0.1014	0.157	0.9998
anthracite	1.28	0.2038	0.330	0.9996
Adsorbents	Intraparticle diffusion model			
	$K_3/\text{mg}\cdot\text{g}^{-1}\cdot\text{min}^{-0.5}$	intercept		R^2
lignite	0.0172	1.0078		0.9464
coking coal	0.0166	0.9621		0.8872
anthracite	0.0023	1.2159		0.8515
Adsorbents	Bangham model			
	K_4	γ	R^2	
lignite	0.0105	0.1825	0.8621	
coking coal	0.0104	0.1753	0.8254	
anthracite	0.0124	0.1580	0.7314	

In the intraparticle diffusion model, if the line goes through the origin, the intraparticle diffusion is the only rate-controlling step. If the line does not go through the origin, the rate-controlling step depends not only on the intraparticle diffusion but also on other steps, such as the boundary-layer mass transfer and internal mass transfer (Gupta et al., 1988; 2003). So the effects of intraparticle diffusion and boundary-layer diffusion on the sorption rate can be determined from the intraparticle diffusion model (Fig. 3-c). The Bangham model yielded relatively low correlation coefficients, which confirmed that intraparticle diffusion is not the only rate-limiting step, and the rate of adsorption could be controlled by several processes, all of which might be operated simultaneously.

Adsorption activation energy calculation

The adsorption activation energy of quinoline adsorption on coking coal was calculated. The quinoline adsorption on coking coal belongs to pseudo-second order kinetic equation according to the results of kinetic model calculation. So the k_2 of pseudo-second order kinetic equation was adsorption rate constant of adsorption reaction. The core of the absolute reaction rate theory is that an activated complex energy barrier is formed when reactants transfer to products. The same may be considered when an adsorption site is activated after overcoming the sorption barrier. So the theory of absolute reaction rate may be transplanted to the study of adsorption kinetics (Kathialagan and Viraraghavan, 2002). The adsorption rate constant k_2 was used to replace the reaction rate constant of Arrhenius equation. Using the assumption that the activation enthalpy and the activation entropy changes affected by temperature were small in the process of adsorption and can thus be ignored, according to the Arrhenius formula the following equation was obtained (Chandra et al., 2007)

$$k_2 = k_0 \exp\left(-\frac{E_a}{RT}\right) \quad (14)$$

where, k_2 refers to the rate constants of adsorption reaction, $\text{g}\cdot\text{mg}^{-1}\cdot\text{min}^{-1}$; k_0 refers to frequency factor; E_a refers to activation energy, $\text{kJ}\cdot\text{mol}^{-1}$. R refers to ideal gas constant, $8.314 \text{ J}\cdot\text{K}^{-1}\cdot\text{mol}^{-1}$; T refers to temperature, K .

To calculate the logarithm of the above equation the following equation was obtained:

$$\ln k_2 = \ln k_0 - \frac{E_a}{RT}. \quad (15)$$

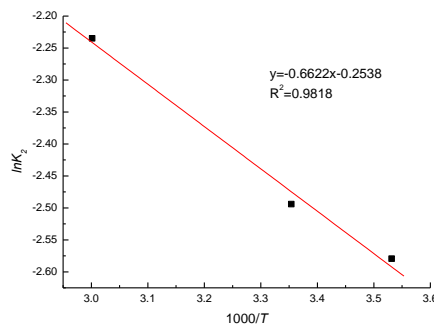


Fig. 4. Plot of $\ln k_2$ versus $1000/T$ for quinoline adsorption on coking coal

A straight line was plotted through linear regression for $10^3/T$ and $\ln k_2$ as shown in Fig. 4. The equation of straight line is $\ln k_2 = -0.6622/T - 0.2538$ ($R^2=0.9818$). The activation energy of adsorption E_a ($E_a = 5.51 \text{ kJ}\cdot\text{mol}^{-1}$) was obtained from the slope of the linear.

Generally, the activation energy of physical adsorption was 5~40 kJ·mol⁻¹ (Li et al., 2002) and the activation energy of chemical adsorption is greater than 83.72 kJ·mol⁻¹ (Shu and Jia, 2005). Thus, the quinoline adsorption on coking coal belongs to physical adsorption because the activation energy of adsorption was small.

Conclusions

Fitting of experimental data to various kinetic models showed that the process of quinoline adsorption onto three kinds of coal follows pseudo-second-order rate kinetics. The rate of quinoline adsorption on anthracite is largest. The special surface of coking coal increased after the coal was washed by the hydrochloric acid solutions. So the optimum adsorption pH value determined by test is 4. The rate of quinoline adsorption on anthracite is largest. The Bangham model confirmed that intraparticle diffusion is not the only rate-limiting step of the sorption processes, but that boundary-layer diffusion was likely to be involved as well. The activation energy of quinoline adsorption on coking coal E_a was 5.51 kJ·mol⁻¹, and the quinoline adsorption on coking coal belongs to physical adsorption. The adsorption kinetic research of the coal adsorption method is not only an important investigation for improving the efficiency of organic pollutant removal, but also has significant meanings for achieving wastewater zero emission for coal coking plants in the future.

Acknowledgements

This work was supported by the Fundamental Research Funds for the Central Universities; National Natural Science Foundation of China under Grant (NO. 51504262); Postgraduate Scientific Research and Innovation Projects of Jiangsu Province under Grant (NO. 2011QNB08).

References

AHMARUZZAMAN M., 2008, *Adsorption of phenolic compounds on low-cost adsorbents: A review*, Adv. Colloid Interface Sci., 143, 48–67.

AKSU Z., YENER J., 2001, *A comparative adsorption/biosorption study of mono-chlorinated phenols onto various sorbents*, Waste Manage., 21, 695–697.

ANDERSSON K.I., ERIKSSON M., NORSTRÖM M., 2011, *Removal of Lignin from Wastewater Generated by Mechanical Pulping Using Activated Charcoal and Fly Ash: Adsorption Kinetics*. Ind. Eng. Chem. Res. 50, 7733–7739

AZIZIAN S., 2004, *Kinetic models of sorption: a theoretical analysis*, J. Colloid Interface Sci. 276, 47–52.

BADMUS M.A.O., AUDU T.O.K., 2009, *Periwinkle shell based granular activated carbon for treatment of chemical oxygen demand (COD) in industrial wastewater*, Can. J. Chem. Eng., 87, 69–71.

BELHACHEMI M., ADDOUN F., 2012, *Adsorption of congo red onto activated carbons having different surface properties: studies of kinetics and adsorption equilibrium*, Desalin. and Water Treat., 37, 122–129

CHANDRA T.C., MIRNA M.M., SUDARYANTO Y., ISMADJI S., 2007, *Adsorption of basic dye onto activated carbon prepared from durian shell: Studies of adsorption equilibrium and kinetics*, Chem. Eng. J. 127, 121–129.

CHOWDURY S., MISHRA R., SAHA P., KUSHWAHA P., 2011, *Adsorption thermodynamics, kinetics and isosteric heat of adsorption of malachite green onto chemically modified rice husk*, Desalination, 265, 159–168.

CHEN T.H., HUANG X.M., PAN M., JIN S., PENG S.C., FALLGREN P.H., 2009, *Treatment of coking wastewater by using manganese and magnesium ores*, J. Hazard. Mater., 168, 843–847.

FANG J.W., SONG X.Y., CAI C.F., TANG C.G., 2012, *Adsorption characteristics of coking coal in coking wastewater treatment*, J Anhui Univier. Technolo. Sci., 25, 43–46.

FU M., 2004, *Study on Modification of Activated Carbon Fiber and Adsorptive Properties for Organic Compounds in Wastewater from Coke Plant*, Chongqing Univer., pp. 53–55.

GERENTE C., LEE V.K.C., CLOIREC C.P.L., MCKAY G., 2007, *Application of chitosan for the removal of metals from wastewaters by adsorption: Mechanisms and models review*, Crit. Rev. Environ. Sci. Technol., 37, 41–127.

GUPTA V.K., MOHAN D., SHARMA S., 1988, *Removal of lead from wastewater using bagasse fly ash–A sugar industry waste material*, Sep. Sci. Technol., 33, 1331–1343.

GUPTA V.K., SHARMA S., 2003, *Removal of zinc from aqueous solutions using bagasse fly ash a low cost adsorbent*, Ind. Eng. Chem. Res., 42, 6619–6624.

HO Y.S., MCKAY G., 1988, *Sorption of dye from aqueous solution by peat*, Chem. Eng. J., 70(2), 115–124.

HO Y.S., MCKAY G., 1999, *The sorption of lead(II) ions on peat*, Water Res., 33, 578–479.

HO Y.S., MCKAY G., 2002, *Application of kinetic models to the sorption of copper (II) on to peat*, Adsorpt. Sci. Technol., 20, 797–815.

HWANG Y.H., KIM D.G., SHIN H.S., 2011, *Mechanism study of nitrate reduction by nano zero valent iron*, J. Hazard. Mater., 185, 1513–1521.

KATHIALAGAN T., VIRARAGHAVAN T., 2002, *Adsorption of cadmium from aqueous solution by perlite*, J. Hazard. Mater. B, 94, 291–303.

KAYA E.M.Ö., ÖZACAN A.S., GÖK Ö.Z., ÖZCAN A., 2013, *Adsorption kinetics and isotherm parameters of naphthalene onto natural– and chemically modified bentonite from aqueous solutions*. Adsorption, 19, 879–888.

KUMAR A., KUMAR S., KUMAR S., 2003, *Adsorption of resorcinol and catechol on granular activated carbon: equilibrium and kinetics*, Carbon, 41, 3015–3025.

LAI P., ZHAO H.Z., ZENG M., NI J.R., 2009, *Study on treatment of coking wastewater by biofilm reactors combined with zero–valent iron process*, J. Hazard. Mater., 162, 1423–1429.

SAHU A.K., SRIVASTAVA V.C., MALL I.D., LATAYE D.H., 2008, *Adsorption of furfural from aqueous solution onto activated carbon:Kinetic, equilibrium and thermodynamic study*. Sep. Sci. Technol., 43, 1239–1259.

SHU Y.H., JIA X.S., 2005, *The mechanisms for CTMAB–bentonites to adsorb CBs from water in the adsorption kinetics and thermodynamics view*, Acta Scientiae Circumstantiae, 25, 1530–1536.

LATAYE D.H., MISHRA I.M., MALL I.D., 2006, *Removal of Pyridine from Aqueous Solution by Adsorption on Bagasse Fly Ash*, Ind. Eng. Chem. Res., 45, 3934–3943.

LEE M.W., PARK J.M., 1998, *Biological Nitrogen Removal from Coke plant Waster with External Carbon Addition*, Water Environ. Res., 70, 1090–1095.

LI X.H., LIU J.T., WANG Y.T., XU H.X., CAO Y.J., DENG X.W., 2015, *Separation of oil from wastewater by coal adsorption-column flotation*, Sep. Sci. Technol., 50, 583–591.

LIN S.Y., DENCE W.C., 1992, *Ultraviolet spectrophotometry: Methods in Lignin Chemistry*, Springer-Verlag, Berlin, pp. 217–232.

LORENC-GRBOWSKA K., GRYGLEWICZ G., DIEZ M.A., 2013, *Kinetics and equilibrium study of phenol adsorption on nitrogen-enriched activated carbons*, Fuel 114, 235–243

MALL I.D., SRIVASTAVA V.C., AGARWA N.K., 2006, *Removal of Orange-G and Methyl Violet dyes by adsorption onto bagasse fly ash—kinetic study and equilibrium isotherm analyses*, Dyes Pigments, 69, 210–223

POOTS V.J.P., MCKAY G., HEALY J.J., 1978, *Removal of basic dye from effluent using wood as an adsorbent*, J. Water Pollut. Control Fed., 50, 926–928.

RODRIGUEZ A., GARCIA J., OVEJERO G., Mestanza M., 2009, *Adsorption of anionic and cationic dyes on activated carbon from aqueous solutions: Equilibrium and kinetics*, J. Hazard. Mater., 172, 1311–1312.

SRIVASTAVA V.C., MALL I. D., MISHRA I. M, 2005, *Treatment of pulp and paper mill wastewaters with poly aluminium chloride and bagasse fly ash*, Colloids Surf. A, 260, 17–18.

SZE M.F.F., MCKAY G., 2010, *An adsorption diffusion model for removal of para-chlorophenol by activated carbon derived from bituminous coal*, Environ. Pollut., 158, 1669–1674.

WANG M.J., FU C.H., CHANG L.P., XIE K.C., 2012, *Effect of fractional step acid treatment process on the structure and pyrolysis characteristics of Ximeng brown coal*, J. Fuel Chem. Technol., 40, 906–911.

WEBER W.J., MORRIS J.C., 1963, *Kinetics of adsorption on carbon from solution*, J. Sanit. Eng. Div. Am. Soc. Civ. Engrs. 89, 31–59.

XU H.X., HUANG G., LI X.B., GAO L.H., WANG Y.T., 2016, *Removal of quinoline from aqueous solutions by lignite, coking coal and anthracite. Adsorption isotherms and thermodynamics*. Physicochem. Probl. Miner. Process., 52(1), 214-227.

YU H.Q., GU G.W., SONG L.P., 1996, *The effect of fill mode on the performance of sequencing-batch reactors treating various wastewaters*, Bioresour. Technol., 58, 46–55.

YU H.Q., GU G.W., SONG L.P., 1997, *Post treatment of effluent from coke-plant wastewater treatment system in sequencing batch reactors*, J. Environ. Eng., 123, 305–308.

Received September 14, 2014; reviewed; accepted July 7, 2015

RECOVERY OF COPPER FROM SMELTING SLAG BY SULPHATION ROASTING AND WATER LEACHING

Mile D. DIMITRIJEVIC*, **Daniela M. UROSEVIC****, **Zoran D. JANKOVIC*****,
Snezana M. MILIC*

* University of Belgrade, Technical Faculty at Bor, P.O. Box 50, 19210 Bor, Serbia
e-mail: mdimitrijevic@tf.bor.ac.rs

** Mining and Metallurgical Institute, Zeleni Bulevar 35, 19210 Bor, Serbia

*** University of Toronto, CFIE, 33 St. George Street, Toronto, Ontario, Canada M5S 2E3

Abstract: In this work extraction of copper and iron from a reverberatory furnace slag was studied. A two-step extraction procedure was followed. The first step was roasting of the slag in the presence of sulphuric acid at temperatures between 150 and 800 °C. The second step was leaching of the resulting calcine with distilled water. The maximum copper extraction of about 94% was achieved. In this case, the slag was roasted at 250 °C with sulphuric acid higher of about 33% than that stoichiometrically required, followed by water leaching of calcine at 50 °C. About 55% of iron was also dissolved under these conditions. On the other hand, for the calcine obtained at sulphation temperature of 600 °C, extraction of copper in a water leaching stage was still relatively high (about 79%), whereas that of iron was comparatively low (about 6%). Dissolution of copper and iron from the calcine was found to be very fast and was complete within the first few minutes. The water temperature in the leaching step was found to have no effect on extraction of copper and iron from the calcine in the range of 30 to 85 °C.

Keywords: copper, slag, sulphation, roasting, acid baking, leaching

Introduction

The environmental burden of waste disposal and decreasing metal ore grades make a strong case for implementation of alternative processes for metal recovery and metal recycling (Ochromowicz and Chmielewski, 2010; Schlesinger et al., 2011; Franegard et al., 2013; Chmielewski, 2015). It has been estimated that landfills and other waste repositories (e.g., tailing ponds and slag heaps) around the world contain about 300 teragrams (Tg) of copper, which corresponds to more than 30% of the known remaining reserves (Kapur and Graedel, 2006). The situation is similar for other base metals, which has motivated a great deal of research on the base metal tailings over the past few years (Aromaa et al., 2013; Chen et al., 2014; Muravyov et al., 2014).

Likewise, studies on various non-ferrous slags has almost tripled since the early 1990s (Piatak et al., 2015).

Pyrometallurgical production of copper generates two slags: smelting furnace slag and converter slag which contain 0.5-2% Cu and 2-8% Cu, respectively. The following three methods are generally utilized for recovering the copper from these slags on an industrial scale: (i) recycling of the converter slag to the smelting furnace, (ii) cleaning of smelting and/or converter slags in electric furnaces and (iii) flotation. Metallic copper and sulphide copper present in these slags can be floated very effectively, provided that the mineral grains are large enough to be liberated by conventional crushing and grinding (Shen and Forssberg, 2003; Schlesinger et al., 2011).

The reverberatory furnace slag that has been discarded in the vicinity of the Bor Copper Smelter, Serbia, is currently processed by flotation at the nearby Bor Copper Concentrator. The copper recovery was rather low (about 40%) mainly due to the presence of oxide copper and insufficient mineral liberation. In our previous work, we investigated the technical feasibility of increasing copper recovery by leaching and flotation of slag tailings using sulphuric acid solutions, without or with the addition of either ferric sulphate or hydrogen peroxide. However, the maximum copper extraction attained with the slag was modest at about 63%, whereas that obtained with the slag flotation tailings was as low as 33% (Urosevic et al., 2015). Accordingly, the objective of the present work was to investigate whether the introduction of a pyrometallurgical pre-treatment step to break down the slag structure, thereby rendering copper-containing phases amenable to leaching, would result in an increase in copper recovery.

Several studies on the recovery of metal values from various copper-containing slags by either chloriding or sulphation roasting followed by water leaching were reported. Thus, ammonium chloride was studied as a chloriding agent (D'yachenko et al., 2013; Nadirov et al., 2013), whereas the sulphating agents included ammonium sulphate (Sukla et al., 1986; Hamamci and Ziyadanogullari, 1991), ferric sulphate (Altundogan and Tumen, 1997), pyrite (Tumen and Bailey, 1990) and sulphuric acid (Sukla et al., 1986; Hamamci and Ziyadanogullari, 1991; Arslan and Arslan, 2002). However, all of these slags contained, in addition to copper, significant amounts of either cobalt or nickel or both. The slag studied in this paper is different from the previous studies since it contains no cobalt and very little nickel.

Based on the above mentioned studies, sulphuric acid appears to be the best pre-treatment agent. Sulphuric acid has been utilized as the sulphation agent for various materials, and the sulphation process has also been referred to as acid baking, in particular when applied at temperatures up to 400 °C (Kul et al., 2008; Kim et al., 2009; Safarzadeh et al., 2012). Therefore, in the present work, roasting with sulphuric acid was adopted as a pretreatment step prior to the water leaching step.

Materials and experimental methods

Experiments were conducted using a reverberatory furnace slag from the Bor Copper Concentrator, Serbia. The slag was sampled from the crushing line before entering the milling section of the concentrator. The sample was ground to pass through a 75 µm sieve. Quantitative determination of elements in the sample was performed by the gravimetric analysis, volumetric analysis and atomic absorption spectrophotometry (FAAS/GFAAS). The chemical composition of the sample is given in Table 1.

Table 1. Chemical composition of the smelting slag (wt. %)

Constituent	Cu total	Cu oxides	Cu sulphides	Fe total	SiO ₂	Al ₂ O ₃	Fe ₂ O ₃	FeO	Fe ₃ O ₄	CaO	MgO
Content	0.97	0.15	0.82	39.09	33.75	3.78	8.05	33.80	9.39	6.00	1.66

XRD characterization of slag indicated that the major crystalline phases are magnetite, olivines (among which fayalite was found to be the most abundant), pyroxene and granate (Urosevic et al, 2015). Based on quantitative mineralogical analysis, the mineral composition was determined to be as follows: Cu-Fe-S sulphide solid solution, chalcocite (Cu₂S), covelite (CuS), pyrite (FeS₂), troilite (FeS), metallic copper, cuprite (Cu₂O), magnetite (Fe₃O₄), and gangue minerals. The sulphide content was 2.75%. The gangue minerals comprise fayalite glass, various dendritic ferrites and refractory aggregates. The mineral composition of these materials varies widely and is dependent on various factors (pH, Eh, cooling rate, number of crystallization centres, composition of the starting minerals, etc.). Among the copper sulphide minerals, the most abundant are complex compositions of the bornite-chalcocite (digenite), that is, Cu₅FeS₄-Cu₂S(Cu₉S₅) sulphide solid solution system. This system has continuous mixing series in all ratios, from temperatures of 300°C up to melting and formation of sulphide glass. With decreasing temperature, either metastable chalcopyrite (CuFeS₂) sulphide solid solution in bornite or chalcocite (digenite) sulphide solid solution in bornite are formed. They are formed in the absence of oxygen, when the sulphide minerals become trapped within the glass and start to crystallize as the temperature decreases. They occur most frequently as either inclusions or emulsions in the fayalite-glass phase (Fig. 1a). Most commonly, they are spherical in shape, from elongated to spindle-shaped drops of various cross sections (Fig. 1b). Slag minerals are characterized by microcrystal, coarse crystal and, most commonly, glass-like structures with the appearance of various eutectic dendrites and skeletons (fayalite, ferrites, magnetite, etc.), which is shown in Figs. 1c and 1d.

Roasting experiments were performed in a porcelain crucible. In each experiment, 5 g of slag was placed in the crucible. Then, a certain amount of sulphuric acid was added to the slag and thoroughly mixed. The crucible was transferred to a muffle furnace, which was preheated to the required temperature. The standard roasting experimental conditions were as follows: an amount of sulphuric acid larger by 33%

than that stoichiometrically required, a roasting temperature of 350 °C and a roasting time of 1 h. The calcine was cooled and ground prior to leaching.

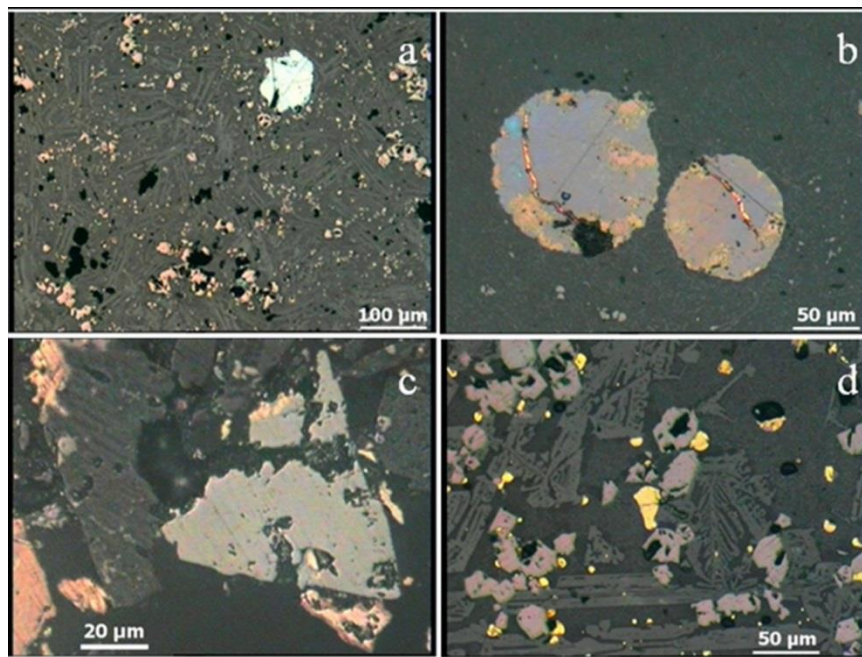


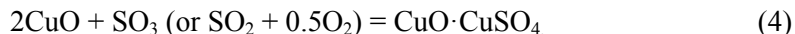
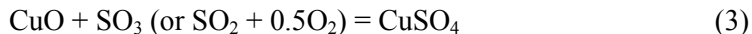
Fig. 1. Photomicrographs of smelting slag (reflected light, air, II N); (a) droplet and/or emulsion inclusions of sulphide solid solution in fayalite-glass matrix, (b) circular sections of complex sulphides of Cu-Fe-S system, (c) skeletal growth of magnetite from silicate melt, (d) coarse crystal aggregate of smelting slag with clearly distinguishable areas of troilite (yellow), magnetite (light-brown) and fayalite dendrite in glass

Leaching experiments at room temperature were conducted in a glass beaker using a magnetic stirrer, whereas those at set temperatures were performed in a three-necked glass reactor immersed in a thermostatic water bath and fitted with a glass stirrer, condenser and thermometer. The sample was leached with 150 cm³ of distilled water. Standard conditions for the leaching experiments were as follows: leaching time of 30 min and stirring speed of 350 min⁻¹. Sampling was performed by taking 1 cm³ of the leach liquor with a pipette. The leach liquor sample was filtered and the filtrate was transferred to a 50 cm³ volumetric flask. The flask was filled with distilled water to the mark. The diluted solution was acidified to prevent metal precipitation. The diluted, acidified solution was analyzed by atomic absorption spectrophotometry. All the experiments were repeated at least two times and some of them several times to establish the reproducibility of the results.

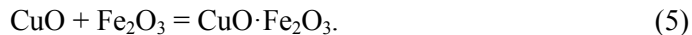
Results and discussion

Roasting

Roasting with sulphuric acid results in production of metal sulphates which are readily soluble in water. The reactions occurring during sulphation roasting of metallic copper and copper compounds may be represented as follows (Altundogan and Tumen, 1997):



Reactions similar to those presented in Eqs. 2 to 4 may be written for compounds containing ferrous iron (i.e., FeO and FeSO_4), whereas additional equations need to be considered in the case of compounds containing ferric iron (i.e., Fe_2O_3 and $\text{Fe}_2(\text{SO}_4)_3$). In addition, ferrites may be formed according to the following reaction (Tumen and Bailey, 1990):



The effect of sulphuric acid dosage in the roasting stage on extraction of copper and iron in the subsequent leaching stage was studied by addition of 5 g of slag to different quantities of concentrated sulphuric acid (2, 3, 4, and 5 cm^3) followed by roasting the mixture. The stoichiometric requirement of sulphuric acid (96%, $\rho=1.84 \text{ g/cm}^3$) was calculated to be 3 cm^3 based on the amount of copper and iron phases present in the slag. Roasting was performed at 350 °C for a duration of 1 h. The resulting calcine was leached with distilled water at room temperature.

As can be seen in Table 2, sulphuric acid dosage had no effect on the copper and iron extractions obtained, except for a dosage equal to 67% of the stoichiometric requirement, where the extractions were slightly lower. The subsequent roasting experiments were performed with an amount of sulphuric acid corresponding to 133% of that stoichiometrically required in order to ensure complete dissolution of copper.

Table 2. Effect of sulphuric acid dosage in roasting on extraction of copper and iron in leaching

$\text{H}_2\text{SO}_4, \text{cm}^3$	2	3	4	5
H_2SO_4 dosage ^a , %	67	100	133	167
Cu extraction, %	81.73	87.75	86.54	87.94
Fe extraction, %	46.90	49.74	48.90	51.17

^a percentage of stoichiometric requirement of sulphuric acid

The effect of roasting time on extraction of copper and iron in the subsequent leaching stage was investigated using calcines roasted at 350 °C for 0.5, 1, 2, 3, and 4 h. The calcines were obtained by roasting slag with an amount of sulphuric acid equal to 133% of the stoichiometric requirement. The leaching experiments were conducted at room temperature. The copper and iron extractions obtained in these experiments are shown in Table 3. It can be seen that increasing the duration of roasting from 0.5 h to 4 h had no effect on copper and iron extraction. Further roasting experiments were conducted for 1 h as in some of the experiments the roasting temperature was lower than 350 °C.

Table 3. Effect of roasting time on extraction of copper and iron in leaching

Time, h	0.5	1	2	3	4
Cu extraction, %	87.26	86.54	88.13	87.75	86.54
Fe extraction, %	49.31	48.90	49.74	49.74	48.30

The effect of roasting temperature on extraction of copper and iron in the subsequent leaching stage was studied in a relatively wide temperature range of 150 to 800 °C. Following roasting with a quantity of sulphuric acid corresponding to 133% of the stoichiometric requirement for 1 h, the calcines were cooled, ground and leached with distilled water at 50 °C. The results obtained are presented in Table 4 and Fig. 2. It can be seen that copper extractions are similar (between 91.35 and 93.74%) for the calcines obtained in the temperature range of 200 to 550 °C and decrease for temperature higher than 600 °C. The iron recoveries are rather high (between 51.17% and 57.32%) in the temperature range of 200 to 450 °C and start to decline at 500 °C. Also, the pH values of the leach solution gradually increase with increasing roasting temperature (Table 4).

The effect of roasting temperature higher than 400 °C on copper and iron extraction obtained in the subsequent leaching step can be compared with the data presented in the literature. Hamamci and Ziyandogulari (1991) and Arslan and Arslan (2002) found that roasting in the presence of sulphuric acid conducted at temperatures up to 300 °C did not decrease the copper and iron recovery. Sukla et al. (1986) conducted experiments at temperatures up to 600 °C but nevertheless found no decline in copper extraction, which remained close to 100% at temperatures higher than 150 °C. Moreover, they observed the maximum iron extraction of about 85% at roasting temperature of 50 °C, which then decreased gradually to about 50% at 400 °C, and thereafter remained unchanged. This behaviour is in contrast to that found in the present study where iron extraction decreased slightly from 60 to 54% at temperature between 100 and 400 °C, and then sharply dropped from 51 to 6% at temperature between 450 and 600 °C (Fig. 2).

Table 4. Effect of roasting temperature on extraction of copper and iron as well as on pH of leach solutions in the leaching stage

T, °C	Cu extraction, %	Fe extraction, %	pH
150	79.32	59.69	1.49
200	89.78	57.32	1.66
250	93.74	54.72	2.17
300	92.98	53.59	2.32
350	93.74	53.30	2.42
400	93.18	53.72	2.48
450	92.70	51.17	2.50
500	92.31	42.64	2.53
550	92.62	38.37	2.58
600	79.32	5.97	2.66
650	51.05	1.34	3.33
700	34.85	0.024	4.27
800	2.16	0.008	5.39

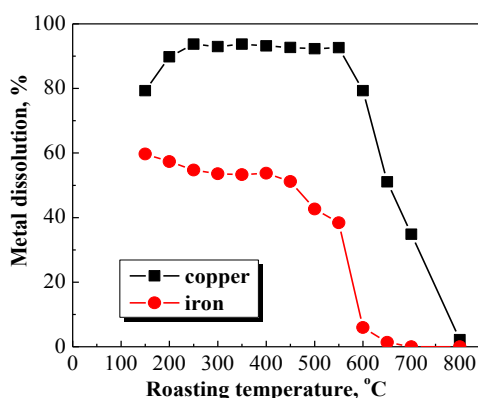
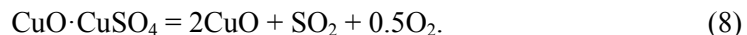
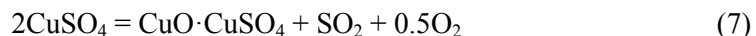


Fig. 2. Copper and iron extractions attained upon water leaching of calcines obtained at different roasting temperatures

Tumen and Bailey (1990) investigating roasting with pyrite and ferric sulphate reported results which are similar to those found in the present study. Tumen and Bailey (1990), after roasting reverberatory furnace slag without pyrite, observed the maximum copper extraction of about 78% at 550 °C, which thereafter steadily decreased to a value close to zero at 750 °C. In addition, they reported the maximum iron extraction of 4% at 450 °C, which decreased gradually to essentially zero at 650 °C. Altundogan and Tumen (1997) reported the maximum copper extraction of about 90% following roasting at 500 °C, which then decreased, first slightly to 85% at 600 °C, then sharply to practically zero at 700 °C. With regard to behaviour of iron,

Altundogan and Tumen (1997) followed the concentration of iron in the leach solution (in contrast to extraction of iron due to iron added in the form of ferric sulphate) and observed steady decline in the iron concentration from about 28 g/dm³ for a roasting temperature of 450 °C to close to zero g/dm³ for 650 °C.

These decreased metal recoveries at high temperatures may be due to the transformation of water-soluble copper and iron sulphates to copper and iron compounds which are not soluble in water. Thus, the decomposition temperature of copper sulphate is 650 °C, whereas that of iron sulphate is 480 °C (Tumen and Bailey, 1990; Altundogan and Tumen, 1997). These temperatures are consistent with the data presented in Table 4 and Fig. 2. Decomposition of iron and copper sulphates may be illustrated by the following reactions (Tumen and Bailey, 1990):



Also, the lower metal recoveries at high temperatures may be attributed to evaporation of sulphuric acid (the boiling point of sulphuric acid is 337 °C) (Sukla et al., 1986; Altundogan and Tumen, 1997). This explanation is in line with the increase in pH of leach solutions with temperature presented in Table 4.

Finally, the lower extractions of iron obtained for higher roasting temperatures may be due to precipitation of ferric iron, which can start to occur at pH 2 (Gupta, 2003).

Sulphation roasting at 550 °C was conducted not only for 1 h but also for 2, 3 and 4 h. The intent was to determine how the increase in roasting time would affect extraction of copper and iron. The results are given in Table 5. The copper extraction obtained was unaffected, whereas that of iron slightly decreased with increasing roasting time, that is, from 38.37 for 1 h to 31.98% for 4 h.

Table 5. Effect of time at roasting temperature of 550 °C on extraction of copper and iron in leaching

Time, h	1	2	3	4
Cu extraction, %	92.62	91.85	92.09	92.70
Fe extraction, %	38.37	36.14	33.51	31.98

In terms of selectivity, the optimum roasting temperature appears to be 600 °C as this temperature leads to a sharp drop in extraction of iron. On the other hand, with regard to the maximum extraction of copper, the optimum roasting temperature seems to be 250 °C as this temperature results in the highest copper extraction. However, a process including the roasting step at 250 °C would normally involve an iron removal step prior to the recovery of copper from the leach solution.

XRD analysis of the calcine produced at 550 °C revealed the presence of hematite, maghemite and magnetite crystalline phases. However, it should be noted that the

phase composition was difficult to determine due to a very high content of amorphous material.

Leaching

Four samples of slag weighing 1, 5, 10 and 20 g were roasted with the appropriate quantity of sulphuric acid under the standard experimental conditions. After cooling and grinding the calcines, they were leached with 150 dm³ distilled water at temperature of 50 °C. By performing nine roasting experiments at 350 °C, the mass of calcine was found to be by 45.3% larger than the initial mass of slag. Therefore, the solid-to-liquid ratios in the leaching stage were approximately 1:100, 1:20, 1:10 and 1:5. The results are given in Table 6.

Table 6. Effect of solid-to-liquid ratio in leaching on copper and iron extractions

Solid : Liquid	Cu extraction, %	Fe extraction, %
1 : 100	92.30	52.50
1 : 20	93.74	53.30
1 : 10	88.94	51.17
1 : 5	76.92	46.33

As seen in Table 6, the copper and iron extractions are unaffected in dilute slurries, whereas thicker slurries lead to a decrease in extractions. It should be noted that the increased mass of the calcine with respect to the initial mass of slag is dependent on the roasting temperature. Thus, the mass increase is 33.4 and 9.3% at roasting temperatures of 550 °C and 650 °C, respectively. This trend may be attributed to conversion of copper and iron sulphates to the corresponding oxides.

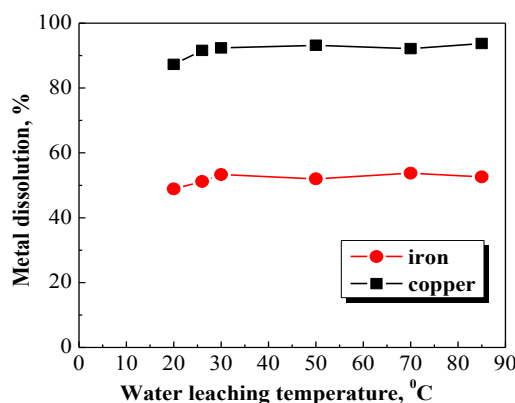


Fig. 3. Copper and iron extractions at different water leaching temperatures

Water leaching of the calcine, which was produced by roasting under standard experimental conditions, was conducted at different temperatures of 20, 26, 30, 50, 70 and 85 °C for a duration of 30 min to elucidate the effect of water temperature on extraction of copper and iron. The results illustrated in Figure 3 show that water temperature has a negligible effect on the dissolution of copper and iron above 30 °C. It can be also concluded that the copper-bearing compounds formed during sulphation roasting of the calcine are readily soluble in water.

The copper and iron extractions obtained during leaching of calcine, which was produced under standard roasting conditions, with distilled water at 50 °C are shown in Table 7 as a function of leaching time. The results indicate that leaching time has essentially no effect on extraction of copper and iron after 15 min of leaching.

Table 7. Effect of leaching time on extraction of copper and iron

Time, min	Cu extraction, %	Fe extraction, %
15	92.65	52.92
30	93.74	53.30
60	94.05	53.72
90	93.15	52.86

For this reason, experiments with shorter leaching times were then conducted, namely: 1, 3, 5, and 10 min. The experimental procedure was changed so that 1 cm³ of leach liquor was sampled directly from the leach slurry (i.e. without stopping the mixing) at the time intervals noted above. The samples were filtered into 50 cm³ volumetric flasks and analysed. As these experiments demonstrated that the copper and iron extractions obtained were stable and did not change with time after 3 min of leaching, a series of experiments was performed at different temperatures (as noted above under the effect of water leaching temperature). The duration of these experiments was 5 min, and the samples were taken every minute according to the same direct sampling procedure as that explained above. These experiments showed the same trend, that is, copper and iron extractions obtained were maximum after 2-3 min of leaching and thereafter remained unchanged. It should be also noted that copper and iron extractions after 1-2 min of reaction were only about 4% lower than those listed in Table 7, which implies very fast leaching kinetics of copper and iron from the calcine.

Process flowsheet

A simplified process flowsheet for the recovery of copper from the reverberatory furnace slag using sulphation roasting (i.e., acid baking) and water leaching is shown in Figure 4. Assuming that the calcine was produced at 350 °C and subsequently water leached at 20% solids (i.e., at a solid-to-liquid ratio of 1:5), then it can also be assumed that copper and iron extractions of 77% and 46%, respectively, could be achieved (see Table 6). Based on this data, it can be calculated that the concentrations

of copper and iron in the pregnant leach solution would be about 1 g/dm^3 and 24 g/dm^3 , respectively. This concentration of copper would be high enough for solvent extraction with oxime based reagents such as LIX[®] 84-I or LIX[®] 984N, but iron would have to be reduced to levels below about 2 g/dm^3 prior to the copper solvent extraction step (Schlesinger et al., 2011). However, despite the fact that the proposed process flowsheet appears to be technically feasible, it is less likely that it would be financially viable as compared to dump leach operations with similar copper tenors.

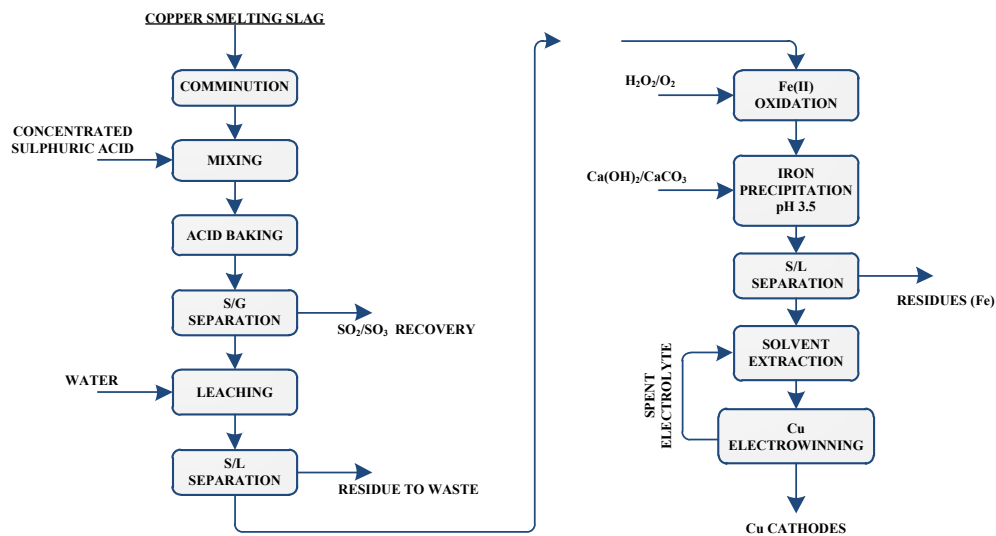


Fig. 4. Flowsheet for the recovery of copper from smelting slag

Conclusion

Treatment of smelting slag by the combined sulphation roasting-water leaching procedure resulted in high copper extractions. However, high copper extractions were accompanied by rather high iron extractions, which is unfavourable in terms of further treatment of the leach liquor. In terms of selectivity, the optimum sulphation temperature was determined to be $600 \text{ }^\circ\text{C}$. For the calcine produced at this temperature, the copper extraction attained was relatively high (about 79%), whereas that of iron was comparatively low (about 6%). On the other hand, with regard to the maximum extraction of copper, the optimum sulphation temperature was found to be $250 \text{ }^\circ\text{C}$ as this temperature resulted in the highest copper extraction (about 94%). However, in this case, the iron extraction obtained was comparatively high (about 55%). The temperature of the leach water had no effect on the copper and iron extractions obtained, except for temperatures below $30 \text{ }^\circ\text{C}$, where extractions were slightly lower.

Acknowledgements

The authors acknowledge financial support from the Ministry of Science and Technological Development of Serbia (Project no. 172031). The authors also thank Dr. Slobodan Radosavljevic, the Institute for Technology of Nuclear and Other Mineral Raw Materials, Serbia, for providing mineralogical characterization.

References

ALTUNDOGAN H.S., TUMEN F., 1997. *Metal recovery from copper converter slag by roasting with ferric sulphate*. Hydrometallurgy, 44, 261-267.

AROMAA J., MAKINEN J., VEPSALINEN H., KAARTINEN T., WAHLSTROM M., FORSEN O., 2013. *Comparison of chemical and biological leaching of sulfide tailings*. Physicochemical Problems of Mineral Processing 49, 607-620.

ARSLAN C., ARSLAN F., 2002. *Recovery of copper, cobalt, and zinc from copper smelter and converter slags*. Hydrometallurgy 67, 1-7.

CHEN T., LEI C., YAN B., XIAO X., 2014. *Metal recovery from the copper sulfide tailing with leaching and fractional precipitation technology*. Hydrometallurgy 147-148, 178-182.

CHMIELEWSKI T., 2015. *Development of a hydrometallurgical technology for production of metals from KGHM Polska Miedz S.A. concentrates*. Physicochemical Problems of Mineral Processing 51, 335-350.

D'YACHENKO A.N., KRAIDENKO R.I., PORYVAI E.B., CHEGRINTSEV S.N., 2013. *Breakdown of copper-smelting slags with ammonium chloride*. Russian Journal of Non-Ferrous Metals 54, 425-428.

FRANDEGARD P., KROOK J., SVENSSON N., EKLUND M., 2013. *A novel approach for environmental evaluation of landfill mining*. Journal of Cleaner Production 55, 24-34.

GUPTA C.K., 2003. *Chemical Metallurgy*, Wiley-VCH, Weinheim, pp. 537-539.

HAMAMCI C., ZIYADANOGLU B., 1991. *Effect of roasting with ammonium sulfate and sulfuric acid on the extraction of copper and cobalt from copper converter slag*. Separation Science and Technology 26, 1147-1154.

KAPUR A., GRAEDEL T.E., 2006. *Copper mines above and below the ground*. Environmental Science and Technology 40, 3135-3141.

KIM H.-I., PARK K.-H., MISHRA D., 2009. *Influence of sulfuric acid baking on leaching of spent Ni-Mo/Al₂O₃ hydro-processing catalyst*. Hydrometallurgy 98, 192-195.

KUL M., TOPKAYA Y., KARAKAYA I., 2008. *Rare earth double sulfates from pre-concentrated bastnasite*. Hydrometallurgy 93, 129-135.

MURAVYOV M.I., BULAEV A.G., KONDRAEVA T.F., 2014. *Complex treatment of mining and metallurgical wastes for recovery of base metals*. Minerals Engineering 64, 63-66.

NADIROV R.K., SYZDYKOVA L.I., ZHUSUPOVA A.K., USSERBAAEV M.T., 2013. *Recovery of value metals from copper smelter slag by ammonium chloride treatment*. International Journal of Mineral Processing 124, 145-149.

OCHROMOWICZ K., CHMIELEWSKI T., 2010. *Solvent extraction in hydrometallurgical processing of Polish copper concentrates*. Physicochemical Problems of Mineral Processing 46, 207-218.

PIATAK N.M., PARSONS M.B., SEAL II R.S., 2015. *Characteristics and environmental aspects of slag: A review*. Applied Geochemistry 57, 236-266.

SAFARZADEH M.S., MOATS M.S., MILLER J.D., 2012. *Evaluation of sulfuric acid baking and leaching of enargite concentrates*. Minerals and Metallurgical Processing 29, 97-102.

SCHLESINGER M.E., KING M.J., SOLE K.C., DAVENPORT W.G., 2011. *Extractive Metallurgy of Copper*, 5th ed., Elsevier, Amsterdam, pp. 191-201.

SHEN H., FORSSBERG E., 2003. *An overview of recovery of metals from slags*. Waste Management 23, 933-949.

SUKLA L.B., PANDA S.C., JENA P.K., 1986. *Recovery of cobalt, nickel and copper from converter slag through roasting with ammonium sulphate and sulphuric acid*. Hydrometallurgy 16, 153-165.

TUMEN F., BAILEY N.T., 1990. *Recovery of metal values from copper smelter slags by roasting with pyrite*. Hydrometallurgy, 25, 317-328.

UROSEVIC D.M., DIMITRIJEVIC M.D., JANKOVIC Z.D., ANTIC V.A., 2015. *Recovery of copper from copper slag and copper slag flotation tailings by oxidative leaching*. Physicochemical Problems of Mineral Processing, 51, 73-82.

Received December 17, 2015; reviewed; accepted May 29, 2015

PRETREATMENT OF COKING WASTEWATER BY AN ADSORPTION PROCESS USING FINE COKING COAL

Lihui GAO*, Shulei LI*, Yongtian WANG **, Xiahui GUI **, Hongxiang XU*

* School of Chemical Engineering and Technology, China University of Mining and Technology, Xuzhou 221116, Jiangsu, China, gaolihui0709@126.com (L. Gao),

** Chinese National Engineering Research Center of Coal Preparation and Purification, Xuzhou 221116, Jiangsu, China, wyt9495@126.com (Y. Wang)

Abstract: A new technique for pretreatment of coking wastewater is introduced based on the concept of circular economy. Coal is fed into a coking system after adsorption. This study validates the feasibility of using coking coal to adsorb organic pollutants in coking wastewater. The sorption kinetics and equilibrium sorption isotherms of coking coal for removal of chemical oxygen demand (COD) and phenol from coking wastewater was also discussed in this paper. Gas chromatograph/mass spectroscopy (GC/MS) was used to detect changes in the quality of coking wastewater. The results showed that when coking coal dosage was 120 g/dm³, 65% of COD and 34% of phenol in waste water can be removed after 40 min of agitation. The surface functional groups of coking coal before and after adsorption were observed with a Fourier transform infrared spectrometer. The kinetics of COD and phenol adsorption from coking wastewater by coking coal fitted the pseudo second-order model. The adsorption process of coking coal can be classified into two categories, namely, rapid and slow. The Freundlich isotherm provided a better fit with all adsorption isotherms than the Langmuir isotherm. Coking coal could be a suitable low-cost adsorbent for recalcitrant organic pollutants.

Keywords: coking coal, coking wastewater, adsorption, COD, phenol

Introduction

Coking wastewater is a type of highly concentrated organic wastewater generated from a process of making coke, purifying coal gas and recovering coke products (Wu and Zhu, 2012). Coking wastewater is a kind of intractable wastewater which is composed of complex inorganic and organic contaminants such as ammonia, cyanide, sulfate, phenolic compounds, polycyclic aromatic hydrocarbons and polycyclic nitrogen (Zhou, 2010; Burmistrz and Burmistrz, 2013; Burmistrz et al., 2014). The high concentration of chemical oxygen demand (COD) and phenol in coking

wastewater causes significant harm to water and soil (Sun et al., 2008). Thus, coking wastewater must be treated appropriately prior to discharge.

Current treatment methods for coking wastewater generally adopt pretreatment–biological treatment–advanced treatment. Different biodegradation techniques have been proposed for treatment of coking wastewater including anaerobic-anoxic-oxic membrane bioreactor, sequential batch reactor, activated sludge and moving bed biofilm reactors (Staib and Lant, 2006; Maranon et al., 2007; Zhao et al., 2009). Nevertheless, coexistence of toxic compounds in coking wastewater can cause inhibitory effects on the biodegradation process. Hence, it is very important to choose appropriate methods for coking wastewater pretreatment to improve the treatment efficiency of biological processes. As a consequence, multiple pretreatment processes have been studied such as catalytic oxidation treatment (Oulego et al., 2014), flocculation treatment (Pi et al., 2009), Fenton oxidation process (Lai and Zhao, 2012; Zhu, 2012) and others. Although these methods work on coking wastewater, the complexity of operation and high energy consumption make them impractical to be applied at an industrial scale.

Adsorption is an effective technique for removal of organic pollutants from coking wastewater (Vazquez et al., 2007; Burmistrz et al., 2014). Adsorbents are the key part of this technique. In the past years, some conventional adsorbents (e.g., activated carbon, zeolite, resins, silica gels, coke dust, lignite, and bottom ash) were usually applied to adsorb pollutions. Nowadays, their shortcomings of low adsorption capacity and high regeneration energy consumption requirements, however, restrict their extensive applications.

In this study a new technique for coking wastewater treatment is introduced in which coal was utilized to adsorb organic pollutants in coking wastewater based on a treatment proprietary process disclosed previously (Wang et al., 2014). In this process (Fig. 1), coal is fed into the coking system and wastewater is poured into biological treatment after adsorption. The process facilitates coking coal recycling. This paper focuses on the feasibility of using coking coal to adsorb organic pollutants from coking wastewater.

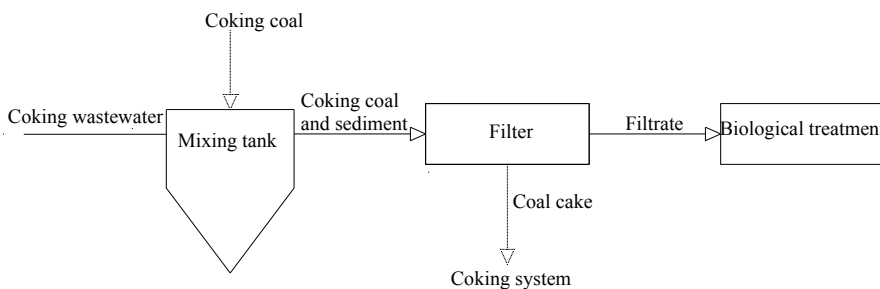


Fig. 1. Schematic of plant for coking wastewater treatment

Materials and methods

Coking wastewater and coal

The coking wastewater used in the experiments was obtained from Huayu Coke Plant, China. It was treated by ammonia distillation. The wastewater (pH value of 9.56) was deep brown in color and emitted a foul odor. Table 1 shows the analytical results of the coking wastewater sample.

Table 1. Water quality of coking wastewater

Parameter	Value
Color	Deep brown
pH	9.56
COD (g/dm ³)	7.600
Phenol (mg/dm ³)	418.35
Ammonia (mg/dm ³)	118.50

Coking coal was also obtained from the Huayu Coke Plant, China. The particle size ranged from 0.5 to 30 mm. The samples were ground and screened to produce different particle sizes, such as +0.5, 0.5–0.25, 0.25–0.125, 0.125–0.074 and –0.074 mm. The mineral components, functional groups of the coal surface were analyzed with an X ray diffractometer (D8 ADVANCE, Bruker, Germany), a Fourier transform infrared spectrometer (VERTEX 80/80v, Bruker, Germany), respectively.

Through the XRD analysis, coking coal was mainly composed of amorphous coal with some minerals including quartz, kaolinite, illite and pyrite. Coal composition has an important role in adsorption although minerals also have some adsorption capacity, they can be ignored because of their low contents.

Experimental methods

Different quantities of coking coal with a specific size were added into a 250 cm³ triangular flask and 100 cm³ coking wastewater was then added. H₂SO₄ (1:10) was utilized to adjust the pH value. All the experiments were conducted in a water bath shaker for different adsorption times at 25 °C. After adsorption, the water samples were centrifuged at 3000 rpm for 10 min. The supernate was analyzed for chemical oxygen demand (COD), ammonia, and phenol removal.

An orthogonal test was implemented to examine the effect of particle size (A), coal dosage (B), coking wastewater pH value (C) and adsorption time (D) (Table 2). The experiment was designed according to the L₂₅ (5⁶) table (Table 3). The optimum experimental condition was determined based on the removal rate of COD, ammonia, and phenol.

Table 2. Factors and levels of orthogonal experiment

Level	Factors			
	A particle (mm)	B dosage (g)	C pH	D adsorption time (min)
1	$A_1 = -0.074$	$B_1 = 8$	$C_1 = 2$	$D_1 = 10$
2	$A_2 = 0.074\text{--}0.125$	$B_2 = 10$	$C_2 = 4$	$D_2 = 20$
3	$A_3 = 0.125\text{--}0.25$	$B_3 = 12$	$C_3 = 5$	$D_3 = 40$
4	$A_4 = 0.25\text{--}0.5$	$B_4 = 15$	$C_4 = 6$	$D_4 = 100$
5	$A_5 = +0.5$	$B_5 = 20$	$C_5 = 7$	$D_5 = 150$

Table 3. $L_{25}(5^6)$ orthogonal array

	A	B	C	D	E	F	G
Exp.	Particle Size (mm)	Dosage (g)	pH	Adsorption Time (min)	The removal rate of ammonium (%)	The removal rate of Phenol (%)	The removal rate of COD (%)
1	A_1	B_1	C_1	D_1	8.48	23.59	47.37
2	A_1	B_2	C_2	D_2	14.14	33.58	73.68
3	A_1	B_3	C_3	D_3	6.50	39.02	78.43
4	A_1	B_4	C_4	D_4	14.89	28.46	51.47
5	A_1	B_5	C_5	D_5	9.79	31.65	56.86
6	A_2	B_1	C_2	D_3	4.04	15.43	78.43
7	A_2	B_2	C_3	D_4	11.46	16.33	52.07
8	A_2	B_3	C_4	D_5	10.23	23.39	56.86
9	A_2	B_4	C_5	D_1	5.80	26.54	51.84
10	A_2	B_5	C_1	D_2	3.86	28.21	63.16
11	A_3	B_1	C_3	D_5	6.28	13.61	62.25
12	A_3	B_2	C_4	D_1	6.68	26.95	47.37
13	A_3	B_3	C_5	D_2	15.37	23.59	57.89
14	A_3	B_4	C_1	D_3	4.57	24.06	69.43
15	A_3	B_5	C_2	D_4	15.33	26.76	67.64
16	A_4	B_1	C_4	D_2	20.29	9.98	60.16
17	A_4	B_2	C_5	D_3	5.27	8.17	46.07
18	A_4	B_3	C_1	D_4	6.28	10.89	69.43
19	A_4	B_4	C_2	D_5	8.04	10.80	66.43
20	A_4	B_5	C_3	D_1	5.53	13.61	63.16
21	A_5	B_1	C_5	D_4	11.73	8.17	68.04
22	A_5	B_2	C_1	D_5	9.27	17.24	62.25
23	A_5	B_3	C_2	D_1	4.57	15.43	67.68
24	A_5	B_4	C_3	D_2	10.32	16.54	52.63
25	A_5	B_5	C_4	D_3	3.95	11.80	40.68

Table 3 provides a description of the L_{25} orthogonal array involving four factors (A – D), each at five levels. The first column in this array contains the number of experiments; factors A – D are arbitrarily assigned to columns 2–5, respectively. The table suggests that 25 trials of experiments are required, with the level of each factor for each trial run indicated in the array. Elements A_i , B_i , C_i , and D_i for $i = 1, 2, \dots, 5$ represent the level of each factor. The vertical column represents the experimental factors to be studied using the array. Each column contains five assignments at each level (1, 2, 3, 4, or 5) for the corresponding factors. The last three columns are the experiment results under a corresponding combination of the factor levels. Parameters can be set easily by allocating variable levels to the individual columns. Thus, parameter setting is implemented by merely selecting an orthogonal array; this process is highly convenient (Chen et al, 2007).

Coking wastewater (100 cm^3) was placed in a 250 cm^3 triangular flask. The experiments were conducted at the optimum experimental conditions at different adsorption times of 10, 20, 30, 40, 60, and 90 min in a water bath shaker at 25°C . After adsorption, the water samples were centrifuged at 3000 rpm for 10 min. The supernate was then further analyzed.

Coking wastewater (100 cm^3) was poured into a 250 cm^3 triangular flask with different initial concentrations ranging from 3.040 to 6.840 g/dm^3 . The experiments were conducted at the optimum experimental conditions in a water bath shaker with a temperature of 25°C . Post adsorption water samples were centrifuged at 3000 rpm for 10 min and the supernate was then further analyzed.

The COD, ammonia, and phenol contents of the wastewater samples were determined by potassium dichromate oxidation, salicylic acid spectrophotometry, and 4-AAP spectrophotometric method, respectively followed by the relevant standards (National Environment Bureau Water and Wastewater Monitoring Analysis Committee, 2002).

Results and discussion

Orthogonal experiment results

One assumption in the experiments was that any two factors do not interact with each other. The superiority and the degree of the influence (sensitivity) of each design factor R (Eq. 1) can easily be determined according to Table 4. The sensitivity of factor C was highest, and factors A , B , and D had a less significant influence, because R_C was significantly larger than R_A , R_B , and R_D . The best combination of each factor level for COD removal was when K (Eq. 2) has the largest value, namely, A_1 , B_3 , C_2 , and D_3 .

The five ordered degree values, with the E (removal rate of COD) of each factor in the same level (i), were added. The corresponding average value K_i and range R were calculated as follows:

$$R = k_{\max} - k_{\min} \quad (1)$$

$$K_i = \frac{\Sigma E}{5} \quad (2)$$

where R reflects the effect of the factors on the removal rate of COD. A factor with high R suggests a strong effect on the removal rate of COD. In Eq. 2 K_i represents the effect of level i of each factor on the removal rate of COD. A high K_i value suggests good removal rate. K_{\max} is the highest value among K_i values of each factor, whereas K_{\min} is the minimum value.

Table 4. Analysis of COD removal rate

The removal rate of COD/%				
	Particle size/mm A	dosage/g B	pH C	Adsorption time/min D
\bar{K}_1	61.56	63.25	62.33	55.48
\bar{K}_2	60.47	56.29	70.77	61.50
\bar{K}_3	60.92	66.06	61.71	62.61
\bar{K}_4	61.05	58.36	51.31	61.73
\bar{K}_5	58.26	58.30	56.14	60.93
R	3.31	9.77	19.46	7.12
S _i	33.14	328.01	1069.03	161.49

Table 5 shows that the sensitivity of factor A was the highest followed by D , C , B , and had weaker influence because R_A was significantly larger than R_B , R_C , and R_D . The best combination for phenol removal was thus A_1 , B_3 , C_1 , and D_2 .

Table 5. Analysis of phenol removal rate

The removal rate of phenol/%				
	Particle size/mm A	dosage/g B	pH C	Adsorption time/min D
\bar{K}_1	31.26	14.16	20.80	21.22
\bar{K}_2	21.98	20.45	20.40	22.38
\bar{K}_3	22.99	22.46	19.82	19.70
\bar{K}_4	10.69	21.28	20.12	18.12
\bar{K}_5	13.84	22.41	19.62	19.34
R	20.57	8.31	1.17	4.26
S _i	1321.14	238.71	4.34	55.52

Table 6 shows that the sensitivity of factor D was the highest. A , B , and C had a weaker influence because R_D was significantly larger than R_A , R_B , and R_C . So the best combination for ammonia removal was A_1 , B_1 , C_4 , and D_2 .

Table 6. Analysis of ammonia removal rate

The removal rate of ammonia/%				
	Particle size/mm A	dosage/g B	pH C	Adsorption time/min D
\bar{K}_1	10.76	10.16	6.49	6.21
\bar{K}_2	7.08	9.36	9.22	12.80
\bar{K}_3	9.65	8.59	8.02	4.87
\bar{K}_4	9.08	8.72	11.21	11.94
\bar{K}_5	7.97	7.69	9.59	8.72
R	3.68	2.47	4.72	7.93
S_i	41.19	17.00	62.43	239.69

The result of orthogonal experiment revealed that the optimum conditions for COD, ammonia, and phenol removal were different. Because phenol and ammonia are relatively simple compounds, they are more easily to be removed during the downstream treatment processes (Burmistrz et al., 2014; Gu et al., 2014). Furthermore, phenol as an organic compound, is part of COD. And the biodegradation inhibitors (PAHs and oil substances) assesses by means of COD (Burmistrz et al., 2014). Removal of those components provides better conditions for the microorganisms in the activated sludge and intensified biodegradation, nitrification and denitrification process. So the optimum adsorption condition for coking coal pretreatment was determined as A_1 , B_3 , C_2 , and D_3 .

Optimum experimental conditions

Figure 2 shows that the removal rate of COD reached 65% after adsorption. The pH value of water sample was 6.99, which was beneficial for degradation in the following biological treatment. Thus, adsorption with coking coal is an efficient method to treat coking wastewater.

Figure 3 presents the gas chromatograms of coking wastewater before and after adsorption. Numerous aromatic compounds were detected in the water sample, among which the content of phenol was the highest. Only four types of organic compounds were detected in the absorbed water sample, including phenol, 2-methylphenol, 4-methyphenol and aniline. Many organic compounds, particularly large molecular organic components, were not found in the post treatment sample indicating that most organic compounds, particularly those with complicated structures, can be removed by

using coking coal as the adsorbent. Large molecular organic components usually possess a challenge for biodegradation. Thus, the absorbed coking wastewater is beneficial for the following biological degradation treatment, making it easier for the sewage treatment plant to meet the emission standards.



Fig. 2. Water quality of coking wastewater before and after adsorption
gas chromatograph/mass spectroscopy analysis

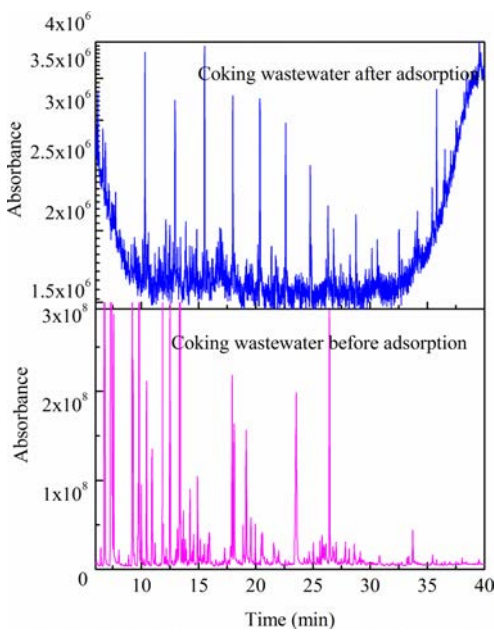


Fig. 3. Gas chromatograms of coking wastewater before and after adsorption

Figure 4 and infrared spectroscopic analysis (Liu et al, 1999) reveal that the major functional groups of coking coal are $-\text{OH}$, $\text{C}=\text{O}$, $-\text{CH}_2$, and CH_3 . Table 7 shows the adsorption peak of this pattern. As shown in Fig. 4 the location of peaks before and after adsorption was similar. The absorbance by coking coal after adsorption was

higher than that of using raw coal. The surface of coking coal did not exhibit a new adsorption peak but did show fluctuations in the original position after adsorption. Therefore, this adsorption may mainly be a physical process.

Coking and caking capacities are extremely important indicators for the coking material. However, these indicators are not related to the content of coal surface functional groups (Zhang, 2009). Thus, the use of coking coal for coking after adsorption have no effect on the quality of coke and other products (data not shown).

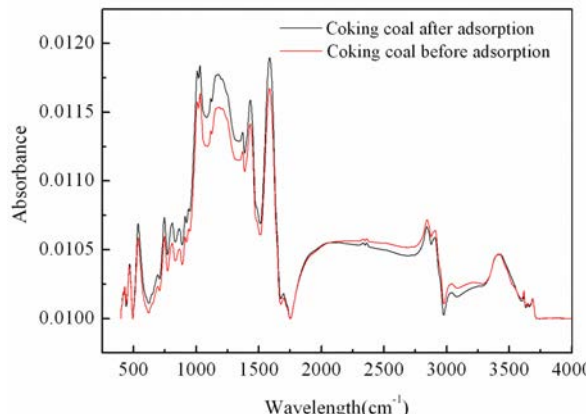


Fig. 4. FTIR analysis patterns of coking coal before and after adsorption

Table 7. Functional groups of every adsorption peak

Wavelength (cm ⁻¹)	Functional group
>4000	—
3800~3600	free hydroxyl
3500~3400	hydroxyl of intramolecular association
2920	-CH ₃
2910~2850	-CH ₃
2760~2300	-OH
1600	C=O; C=C
1450	-CH ₂ 、 -CH ₃
1380	-CH ₃
1300~1100	C-O
860-700	CH
540	-S-S-
475	-S-H
420	FeS ₂

Sorption kinetics

Pseudo first-order (Eq. 3, Fig. 5) and second-order (Eq. 5, Fig. 6) models were employed to examine the mechanism of COD and phenol adsorption by coking coal. The adsorption mechanism of ammonia was not detected because of the low removal rate.

The pseudo first-order model can be expressed as (Lagergren, 1898):

$$\frac{dp_t}{dt} = k_1 (q_1 - q_t) \quad (3)$$

where q_1 (mg·g⁻¹) is the amount of COD and phenol adsorbed at equilibrium, q_t (mg·g⁻¹) is the amount of COD adsorbed at time t (min), and k_1 (min⁻¹) is the equilibrium rate constant of pseudo first-order sorption. The integrated form of the pseudo first-order model is:

$$\log(q_1 - q_t) = \log q_1 - \frac{k_1 t}{2.303} \quad (4)$$

The straight line plots of $\log(q_1 - q_t)$ against t were tested to obtain the parameters of k_1 and q_1 .

The pseudo second-order model can be expressed as (Ho and McKay, 1999):

$$\frac{dp_t}{dt} = k_2 (q_2 - q_t)^2 \quad (5)$$

where q_2 (mg·g⁻¹) is the amount of COD and phenol adsorbed at equilibrium, k_2 (g·mg⁻¹·min⁻¹) is the equilibrium rate constant of pseudo second-order sorption. The integrated form of the pseudo second-order model is:

$$\frac{t}{q_t} = \frac{1}{k_2 q_2^2} + \frac{1}{q_2} t \quad (6)$$

Initial sorption rate h (mg·g⁻¹·min⁻¹) can be calculated by:

$$h = k_2 q_2^2. \quad (7)$$

The straight line plots of t/q_t against t were tested to obtain the parameters of k_2 , h , and q_2 .

The kinetic adsorption data on the adsorption of COD and phenol by coking coal were analyzed with the first-order and second-order models. The fitting results shown in Table 8 present better compliance with the pseudo second-order model. The regression coefficients for the linear plots are high (Table 8) and equal to 0.9993 and 0.998.

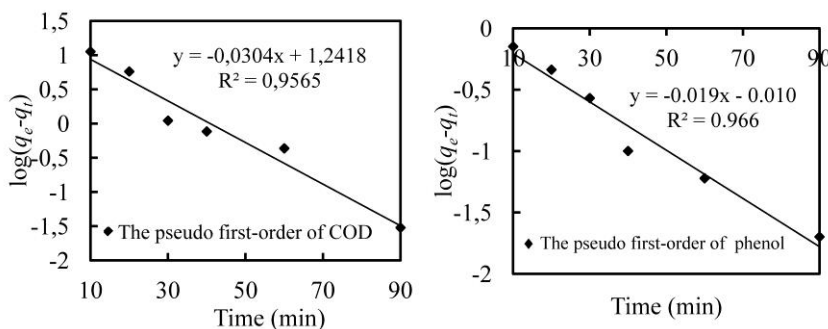


Fig. 5. The pseudo first-order of COD (left) and phenol (right)

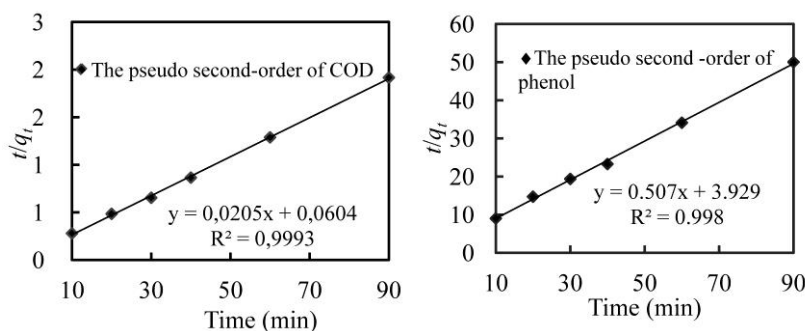


Fig. 6. The pseudo second-order of COD (left) and phenol (right)

Table 8. Kinetics parameters for adsorption of COD and phenol onto coking coal

Components	q_e^{exp} (mg·g ⁻¹)	Pseudo-first order model			Pseudo-second order model		
		q_e (mg·g ⁻¹)	k_1 (min ⁻¹)	R^2_1	q_e (mg·g ⁻¹)	k_2 (g·mg ⁻¹ ·min ⁻¹)	R^2_2
COD	47.03	17.45	0.013	0.9565	48.78	0.006958	0.9993
phenol	1.82	0.98	0.0086	0.9664	1.97	0.06552	0.9985

Figure 7 presents the kinetic curves of coking coal. It shows that the sorption capacity increased rapidly in the first 10 min before slowing down till it reached equilibrium at 40 min. Hu et al. (2008) reported that active carbon adsorbed coking wastewater can be divided into two phases, one involving a rapid adsorption process, and the second being a slow adsorption process. Figure 4 indicates that the adsorption of coking coal in the present study can also be divided into two processes, namely, rapid and slow process, respectively.

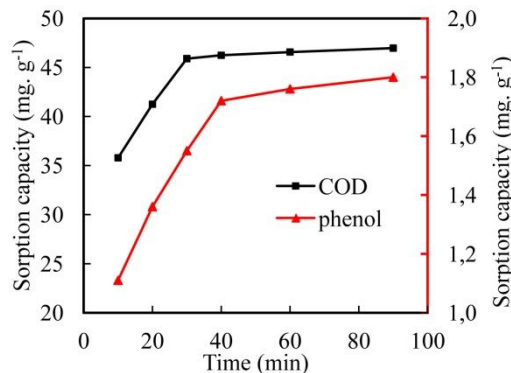


Fig. 7. Kinetic curves of COD and phenol onto coking coal

Equilibrium isotherms

The COD and phenol adsorbed by coking coal are in equilibrium with the COD and phenol in the bulk solution under constant temperature. The saturated monolayer isotherm is represented as the Langmuir isotherm as follows (Langmuir, 1916):

$$q_e = \frac{q_m k_a C_e}{1 + K_a C_e} \quad (8)$$

where C_e (mg/dm³) is the equilibrium concentration, q_e (mg·g⁻¹) is the equilibrium amount of COD adsorbed, q_m (mg·g⁻¹) is q_e for a complete monolayer, and K_a (dm³·mg⁻¹) is the sorption equilibrium constant. The Langmuir isotherm can be linearized into (Kinniburgh, 1986):

$$\frac{C_e}{q_e} = \frac{1}{q_m} C_e + \frac{1}{K_a q_m} \quad (9)$$

The empirical Freundlich isotherm (Freundlich, 1906) can be derived based on adsorption on the heterogeneous surface by assuming a logarithmic decrease in the enthalpy of sorption with the increase in the fraction of occupied sites

$$q_e = K_F C_e^{\frac{1}{n}} \quad (10)$$

where K_F and $1/n$ are the Freundlich constant characteristics of the system and indicate the sorption capacity and sorption intensity, respectively. The formula can be linearized in logarithmic form as:

$$\log q_e = \log K_F + \frac{1}{n} \log C_e \quad (11)$$

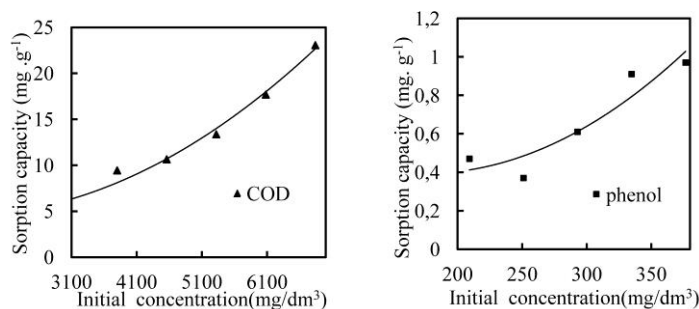


Fig. 8. Isotherm curves of COD (right) and phenol (left) onto coking coal

Table 9. Isotherm parameters for adsorption of COD and phenol onto coking coal

Adsorption isotherm	COD			Phenol		
	q_{m1}	K_{a1}	R^2_1	q_{m1}	K_{a2}	R^2_2
Langmuir	-92.59	2.6×10^{-5}	0.8265	2.556	0.0017	0.618
Freundlich	K_{F1}	n_1	R^2_3	K_{F1}	n_1	R^2_4
	0.0187	0.889	0.8713	234.96	1.416	0.63

Figure 8 shows the isotherm curves of COD and phenol adsorbed by coking coal at different initial concentrations. The equilibrium sorption capacity increased with an increasing initial concentration. Different isotherms were utilized to fit the experimental results as shown in Table 9. The correlation coefficients for the Freundlich isotherm are higher than those for the Langmuir isotherm. However, all the values of R^2 are smaller than 0.99 probably because of the complexity of coking wastewater composition. Therefore, the adsorption type of coking wastewater adsorbed by coking coal could be a combination of physical and chemical adsorption.

Conclusion

Coking coal is a kind of material suited for adsorbing organic compounds in coking wastewater. When the dosage of coking coal was 120 g/dm³, pH value of coking wastewater was 4.65% of chemical oxygen demand (COD) and 34% of phenol could be removed after 40 min agitation. Gas chromatograph/mass spectroscopy (GC/MS) results showed that most large molecular organic components could be adsorbed by coking coal. The kinetics of COD and phenol adsorption from coking wastewater by coking coal fitted the pseudo second-order model. The Freundlich isotherm provided a better fit with all adsorption isotherms than the Langmuir isotherm.

Acknowledgements

This research was supported by China National Fundamental Research Funds for the Central Universities under Grant No. 2014XT05.

References

BURMISTRZ P., ROZWADOWSKI A., BURMISTRZ M., KARCZ A., 2014, *Coke dust enhance coke plant wastewater treatment*, Chemosphere, 117, 278-284

BURMISTRZ P., BURMISTRZ M., 2013, *Distribution of polycyclic aromatic hydrocarbons in coke plant wastewater*. Water Sci. Technol., 68, 2414-2420.

CHEN Y., ZHANG J., YANG C., 2007, *The workspace mapping with deficient-DOF space for the PUMA 560 robot and its exoskeleton arm by using orthogonal experiment design method*, Robotics and Computer-Integrated Manufacturing, 23, 478- 487

FREUNDLICH H., 1906, *Über die adsorption in losungen*, Zeitschriftfur Physikalische Chemie (Leipzig), 57A, 385-470.

GU Q., SUN T., WU G., LI M., QIU W., 2014, *Influence of carrier filling ratio on the performance of moving bed biofilm reactor in treating coking wastewater*, Bioresource Technology, 166, 72-78

HO Y., MCKAY G., 1999, *Pseudo-second order model for sorption processes*, Process Biochem., 34, 451-465.

HU J., XIAO J., REN Y., 2008, *Adsorption Process of Organic Contaminant in Untreated Coking Wastewater by Powdered Activated Carbon*, Environmental Science, 6, 1567-1571.

KINNIBURGH D., 1986, *General purpose adsorption isotherms*, Environ. Sci. Technol., 20, 895-904.

LAI P., ZHAO H., 2012, *Study on Advanced Treatment of Coking Wastewater by Fenton Oxidation Process*, Conteporary Chemical Industry, 41(1), 11-14.

LIU G., QIU G., HU Y., 1999, *Study on infrared spedtra of coals*, Journal of Central South University, 30(4), 371-373.

LAGERGREN S., 1898, *Zur theorie der sogenannten adsorption geloster stoffe*, Kungliga Svenska Vetenskapsakademiens, Handlingar, 24, 1-39.

LANGMUIR I., 1916, *The constitution and fundamental properties of solids and liquids*, J. Am. Chem. Soc., 38, 2221-2295.

MARANON E., VAZQUEZ I., RODRIGUEZ J., CASTRILLON L., FEMANDEZ Y., LOPEZ H., 2008, *Treatment of coke wastewater in sequential batch reactor(SBR) at pilot plant scale*, Bioresource Technology, 99, 4192-4198.

NATIONAL ENVIRONMENT BUREAU WATER AND WASTEWATER MONITORING ANALYSIS COMMITTEE, 2002, *Water and Wastewater Monitoring Analysis Method*, fourth ed, Beijing :Chinese Environment Science Publisher.

OULEGO P., COLLADO S., GARRIDO L., LACA A., RENDUELES M., DIAZ M., 2014, *Wet oxidation of real coke wastewater containing high thiocyanate Concentration*, Journal of Environmental Management, 132, 16-23.

PI K., LUO Y., GONG W., 2009, *A Case study of A/O Coupled with Flocculation for Phenol and Cyanide Wastewater Treatment*, Journal of Hubei University of Technology, 1 (24), 17-19.

STAIB C., LANT P., 2006, *Thiocyanate degradation during activated sludge treatment of coke-ovens wastewater*, Biochemical Engineering Journal, 34, 122-130.

SUN W., QU Y., YU Q., 2008, *Adsorption of organic pollutants from coking and papermaking wastewaters by bottom ash*, Journal of Hazardous Materials, 15 VAZQUEZ I., RODRIGUEZ-

IGLESIAS J., MARANON E., CASTRILLON L., ALVAREZ M., 2007, *Removal of residual phenols from coke wastewater by adsorption*, Journal of Hazardous Materials,147, 395-400.

WANG Y., LIU L., ZHANG M., TONG J., ZHOU J., ZHANG H., GAO L., 2014, *A Process of coking wastewater treatment*, Chinese patent,10101496.7.4, 595-601.

WU Z., ZHU L., 2012, *Removal of polycyclic aromatic hydrocarbons and phenols from coking wastewater by simultaneously synthesized organobentonite in a one-step process*, Journal of Environmental Sciences. 24 (2), 248-253.

ZHOU M., 2010, *The screening and degradation characteristics study on predominant bacterias to hard-biodegradable organics in Coking wastewater*, Ph.D. dissertation,Wuhan: Wuhan University of Science and Technology.

ZHAO W., HUANG X., LEE D., 2009, *Enhanced treatment of coke plant wastewater using an anaerobic-anoxic-oxic membrance bioreactor system*, Separation and Purification Technology, 66, 279-286.

ZHU X., 2012, *Studies on Characteristics Mechanism and Effluent Biotoxicity for Enhanced Treatment of Coking Wastewater*, Ph.D. dissertation, Beijing:Tsinghua University.

ZHANG S., 2009, *Coal Chemistry*, Xuzhou: The China University of Mining and Technology press.

Received April 22, 2015; reviewed; accepted July 29, 2015

DISSOLUTION OF ALKALINE BATTERIES IN REDUCTIVE ACIDIC MEDIA

Bihter ZEYTUNCU

Istanbul Technical University, Applied Research Center of Materials Science and Production Technology,
34469, Istanbul, Turkey, bihter_zeytuncu@hotmail.com

Abstract: In this paper, recovery of manganese and zinc from alkaline battery paste by leaching under atmospheric condition using elemental sulfur as a reductive agent and sulfuric acid was investigated. Different dissolution parameters, acid concentrations, liquid-to-solid ratios, reaction temperatures, leaching times and amounts of elemental sulfur were studied in detail. According to results, the Mn dissolution in reductive acidic media was an intermediate-controlled process with activation energy of 10.21 ± 2.60 kJ/mol. After the leaching step, Mn and Zn were selectively precipitated from the leaching solution using sodium hydroxide. After solid/liquid separation, manganese(II,III) oxide (Mn_3O_4) was obtained by drying at 105 °C in air. Next, Mn_3O_4 was converted to manganese(IV) oxide (MnO_2) by heating at 800 °C in air. After that the solution containing $Zn(OH)_4^{2-}$ was treated with sulfuric acid to form zinc hydroxide, separated and next converted to zinc oxide by heating at 600 °C in air. The final products were characterized by XRD. The results showed that the proposed process can be effectively used for recovery of Mn and Zn from alkaline batteries.

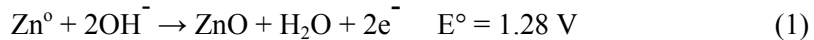
Keywords: alkaline battery, manganese, zinc, reductive leaching, sulfur

Introduction

The growth of the world population in the last decades and the economic explosion of countries have caused an increase in consumption and in the amount of the wastes of end-of-life (EOL) products (e.g. zinc–carbon and alkaline batteries) (Crompton, 2000; Levenspiel, 1972; Pistoia et al., 2001). Owing to increasing environmental concerns and raw material consumptions, worldwide stringent regulations are being demanded for waste materials. In a long term, land filling of spent batteries is not an effective disposal method mainly due to limited storage capacities, hazardous waste issues, increasing landfill costs, and the increasing need for metal recoveries (Bernardes et al., 2004; Pistoia et al., 2001).

The alkaline batteries basically are made from metallic zinc and manganese oxide (Bernardes et al., 2004; Crompton, 2000; Sayilgan et al., 2009). While battery is in use, the metallic zinc is oxidized to zinc oxide and the manganese(IV) oxide is converted to manganese(III) oxide. It is known that the reaction of these elements with sulfuric acid occurs when they are divalent. The trivalent or tetravalent manganese does not react with sulfuric acid. This situation was observed using an E-pH diagram in a study by Gega and Walkowiak (2011).

The chemical reaction in the battery is given by Eqs 1-3 (Lide, 2004; Sayilgan et al., 2009):

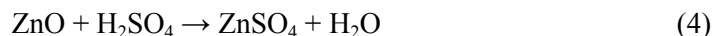


with the overall reaction



Until recently, numerous studies have been conducted on the recycling of spent alkaline and zinc–carbon batteries. Various technologies have been devised for the treatment of the spent batteries wastes including pyrometallurgical (reductive melting) and hydrometallurgical (leaching and electrolysis). The pyrometallurgical processes are widely used for the recovery of metals from the spent batteries (Bernardes et al., 2004; Sayilgan et al., 2009). However, hydrometallurgical processes have some inherent advantages including relatively simpler operation, less energy demand, and no gas emissions (Sayilgan et al., 2009).

According to Eq. 4, zinc oxide completely dissolves in sulfuric acid aqueous solution but manganese(IV) and manganese(III) oxide do not (Sayilgan et al., 2010; Veloso et al., 2005). The reactions are:



Therefore, to improve the dissolution efficiency of manganese oxides to soluble Mn ions, a reducing agent is required. Recently, numerous reductants in acid media have been investigated for waste batteries and manganese ores. The organic reductant, such as lactose (Veglio et al., 2000), sucrose (Tian et al., 2010; Veglio and Toro, 1994; Veglio et al., 2000), corncob (Tian et al., 2010), oxalic acid (Ghafarizadeh et al., 2011; Sahoo et al., 2001; Sayilgan et al., 2010), ascorbic acid (Kursunoglu and Kaya, 2014; Sayilgan et al., 2010) cellulose (Sanigok and Bayramoglu, 1988), alcohols (Trifoni et al., 2001) were used. The inorganic reductant, for example, are hydrogen

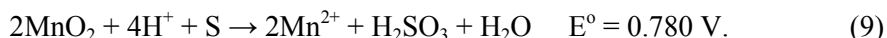
peroxide (Allen and Corwin, 1989; Ghafarizadeh et al., 2011; Jiang et al., 2004; Veloso et al., 2005) and activated carbon powder (Kursunoglu and Kaya, 2013), SO₂ (Avraamides et al., 2006; Ferella et al., 2008; Zhang and Cheng, 2007a).

After leaching, several separation methods can be used such as liquid-liquid extraction (Bernardes et al., 2004; Sayilgan et al., 2009; Zhang and Cheng, 2007c), precipitation (Kursunoglu and Kaya, 2014; Lasheen et al., 2009; Sayilgan et al., 2010; Veglio et al., 2000; Veloso et al., 2005; Zhang and Cheng, 2007c), and electro-winning (Sayilgan et al., 2010; Zhang and Cheng, 2007b).

In the present work, the recovery of zinc and manganese from alkaline paste by sulfuric acid leaching in the presence of elemental sulfur as the reducing agent, which has not been reported in the literature, was investigated. According to Eq. 7, 8 and 9, manganese dioxide completely dissolves in acid aqueous solution via elemental sulfur:



with the overall reaction



The following parameters were studied to determine dissolution kinetics of manganese and zinc in this system: amount of reducing agent, concentration of sulfuric acid, liquid/solid ratio, time and temperature. In addition, precipitation studies were conducted to reveal structure of manganese and zinc hydroxide. These products were characterized by XRD.

Materials and methods

Various alkaline batteries (Varta, Duracell, Maxwell, Sony, and Panasonic) were used in the study. Their composition is given in Table 1. Plastic and metallic cases were removed according to the manual procedure depicted by Bernardes et al. (2004). All the chemicals used were of analytical reagent grade (AR) and were obtained from Merck.

Table 1. Composition of alkaline batteries paste used in investigations

Component	Weight, %
Metallic Case	30.78
Battery Paste	55.32
Membrane and Plastics	5.25
Others	8.65

In order to determine the composition of the battery paste, three samples were analyzed for Mn, Zn and other elements by AAS (Perkin Elmer Analyst 800) using a

standard protocol. The batteries were crushed, leached with water, dried, ground, sieved and homogenized using a three-dimensional shaker.

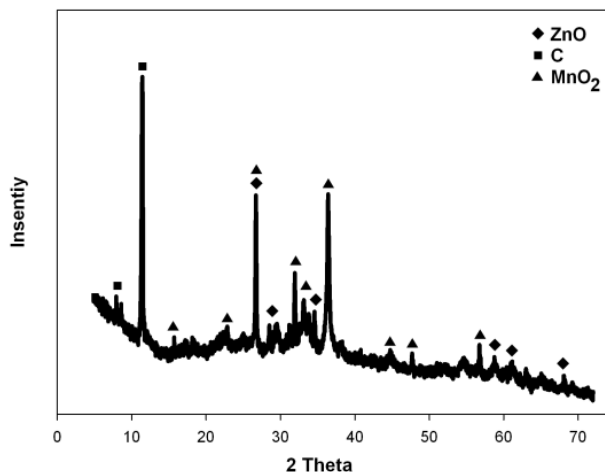


Fig. 1. XRD pattern of spent battery paste

The chemical composition and X-ray diffraction (XRD) pattern are given in Table 2 and Fig. 1, respectively. Figure 1 shows that MnO₂, ZnO and C were the major phases in the alkaline battery paste. Leaching experiments were performed in a 0.5 dm³ capacity three-neck borosilicate tempered glass reactor fitted reflux condenser and continuously stirred. The system was refluxed to prevent evaporation losses. The reactor was heated in an oil bath with provision to control the bath temperature to maintaining the reactor temperature within ± 1 °C (Fig. 2).

Table 2. Chemical composition of alkaline battery paste used in this study

Elements	Weight %
Mn	34.27
Zn	26.41
C	16.35
O	22.93
S	0.02
Fe	0.01
Pb	<0.01
Cd	N.D.*
Hg	N.D.*

*Not Detected

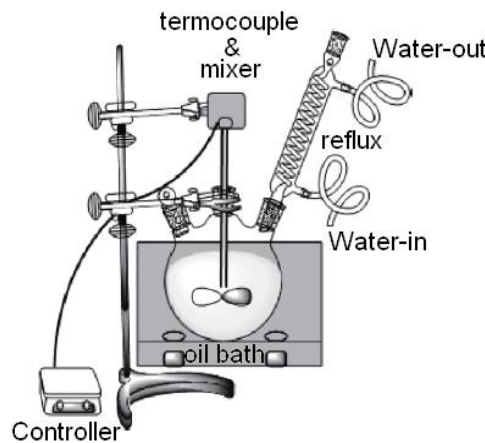


Fig. 2. Leaching reactor

At the end of each experiment, a solid/liquid separation was performed through a Whatman quantitative filter paper (ashless, grade 42, diameter 125 mm, 2.5 μm , slow filter paper).

The recovery was calculated using the following formula:

$$\text{Recovery, \%} = [M_t / (W \cdot M_i)] \cdot 100 \quad (10)$$

where, W is the weight of the powder, M_i is the metal content of the powder and M_t is the metal amount in solution at the end of the experiment.

In order to understand the leaching behavior of the manganese from the battery paste, a kinetic study was performed. In the precipitation section, Mn and Zn were transformed into hydroxides using sodium hydroxide solution. At the end of the precipitation experiments, solid/liquid separation was performed. After dried process at 105 °C in air, the obtained the solid product Mn_3O_4 was converted to MnO_2 by heating at 800 °C in air. The $\text{Zn}(\text{OH})_4^{2-}$ solution subsequently was treated with sulfuric acid to obtain $\text{Zn}(\text{OH})_2$. Zinc hydroxide was converted to zinc oxide by heating at 600 °C in air.

For each experiment, 25 cm³ of leaching solution with 4.0 M NaOH solution was employed using various solution pH. To determine chemical structure of the products, XRD analyses were performed.

Result and discussion

Effect of reducing agent

The recovery of Mn and Zn was assessed using a series of quantity of reducing agent (Fig. 3). The leaching experiments of alkaline battery paste was performed by varying the amount of elemental sulfur from 0 to 1.5 g with H₂SO₄ concentration of 2.0 M, L/S

ratio of 6:1, leaching temperature of 80 °C, time of 90 min. As can be seen in Fig. 3, the manganese recovery increased with increasing amount of the reducing agent. The conversion of Mn^{4+}/Mn^{3+} to Mn^{2+} under reductive condition is thermodynamically more favorable when the reducing-to-manganese(IV) ion ratio is high (Eqs 5, 6, 7, 8 and 9). This result is in agreement with a study by Sayilgan et al. (2010), who recovered manganese using various reducing agent described herein.

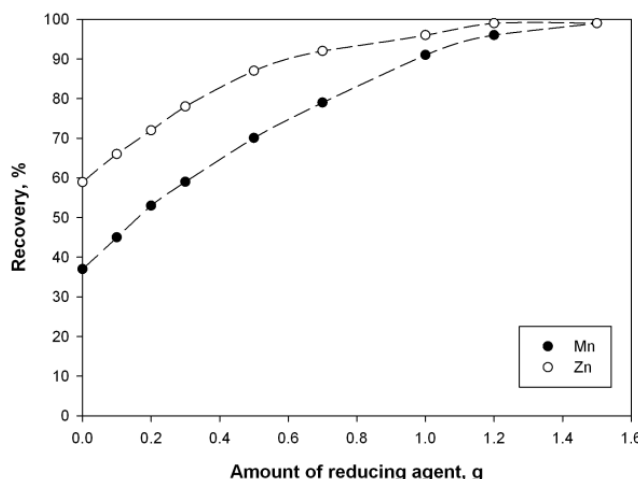


Fig. 3. Effect of reducing agent quantity on manganese and zinc recovery

It is known that zinc recovery is not dependent on the amount of reducing agent, because the reaction of zinc with sulfuric acid is thermodynamically more favorable ($\Delta G^\circ = -555$ kJ/mol) (Lide, 2004). As can be seen in Fig. 3 for zinc, the recovery percentage increases when the amount of reductant quantity is increased because of more sulfate ions in media therefore, leaching power of sulfuric acid was increased. The Mn recovery also increased with increasing amount of quantity of the reducing agent. When the high quantities of reducing agent were used (such as 1.2 g S), the manganese recovery percentage was still below 100%. This result showed that acid concentration and reaction times were inadequate and the reaction should be done at higher temperatures. The amount of reducing agent of 0.5 g was selected for all subsequent experiments.

Effect of acid concentration

In this experimental series, the alkaline battery paste was treated by varying H_2SO_4 concentration from 1.0 to 4.0 M with quantity of S from 0.5 g, L/S ratio of 6:1, leaching temperature of 80 °C, and time of leaching 90 min. As can be seen from Fig. 4, the recovery of zinc increased with an increasing amount of H_2SO_4 up to 2.0 M.

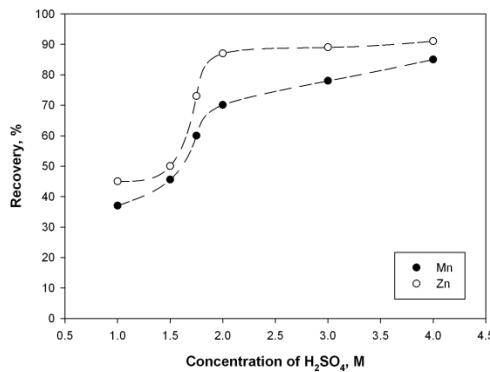


Fig. 4. Effect of sulfuric acid concentration on manganese and zinc recovery

The recovery of manganese continues to increase with increasing H_2SO_4 concentration because more acidic media and sulfate anion improved the dissolution of manganese. At a sulfuric acid concentration of 1.0 M, low zinc and manganese recoveries were obtained because acid concentration is not sufficient to dissolve zinc from the alkaline battery paste. A similar trend for the effect of acid concentration was observed in a study by Kursunoglu and Kaya (2014). It is understood that acid concentration considerably affects zinc and manganese recovery percentages.

Effect of liquid to solid ratio

The experiments were performed to understand the effects of liquid to solid ratio on the manganese and zinc recovery. The alkaline battery paste leaching was carried out by varying the liquid-to-solid ratio (L/S) from 4.0 to 10.0 with quantity of S equal to 0.5 g, H_2SO_4 concentration of 2.0 M, leaching temperature of 80 °C, and time of 90 min.

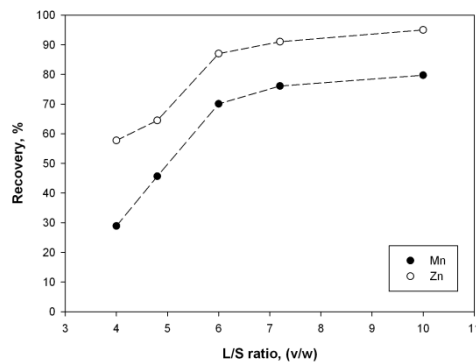


Fig. 5. Effect of liquid to solid ratio on manganese and zinc recovery

According to experimental results presented in Fig. 5, it was found that the Mn and Zn recovery increased until the liquid-to-solid ratio was 6, where 71% of manganese and 87% of zinc was recovered. At the ratio higher than 6, there is no significant increase of recovery of these metals.

Effect of time and temperature

To determine the effect of time and temperature, the L/S ratio of 6.0, 0.5 g S, and H_2SO_4 concentration of 2.0 M was selected. Figures 6a and 6b display the variation in Zn and Mn recovery as a function of time at various temperatures, respectively. As can be seen from Fig. 6a, that when the temperature was increased from 70 to 100 °C at 30 min, the Mn recovery increased from 41% to 61%. Thus, the manganese recovery increased by 20%, indicating that the temperature plays a significant role in the recovery of Mn from alkaline batteries paste.

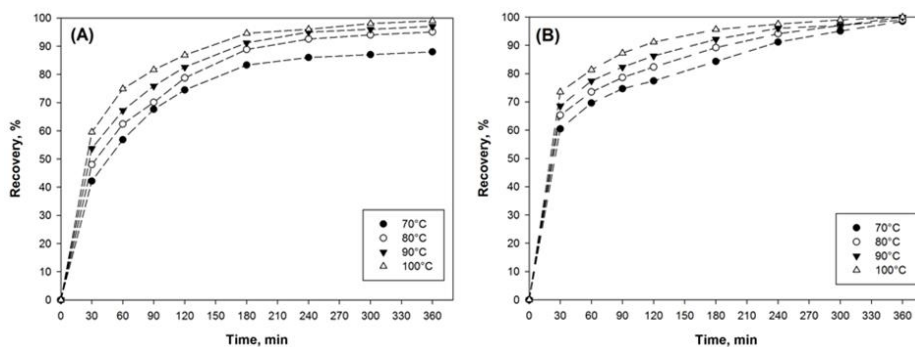


Fig. 6. Effect of temperature and time on recovery of manganese (a) and zinc (b)

The leaching time has a significant role in the recovery of manganese from the alkaline battery paste. For example, 42% recovery of Mn was obtained after 30 min at 70 °C. However, under the same conditions, 83% recovery of manganese was attained when the leaching time was prolonged to 180 min. The 83% recovery of manganese was found after 90 min at 100 °C. In addition to this, recovery of +95% was obtained for 180 min at 100 °C under the same conditions. With the exclusion of the results for 70 °C, after 240 min of reaction time no significant change was obtained. A similar result for the effect of time and temperature was found by Tang et al. (2014). As shown in Fig. 6b, +99% of zinc was dissolved at 80-100 °C. These results show that increasing temperature results in a higher recovery. After 300 minutes of leaching, the recovery of zinc was leveled off.

Leaching kinetics study of manganese

The leaching kinetic data provide reaction order based either on differential rate law or integrated rate. In our experiments, several mathematical models were studied for

temperatures from 70 to 100 °C. The kinetic studies showed that a good fit was provided by the shrinking core model $[1 - (2/3)X - (1-X)^{2/3}]$ (Fig. 7a., Eq. 11).

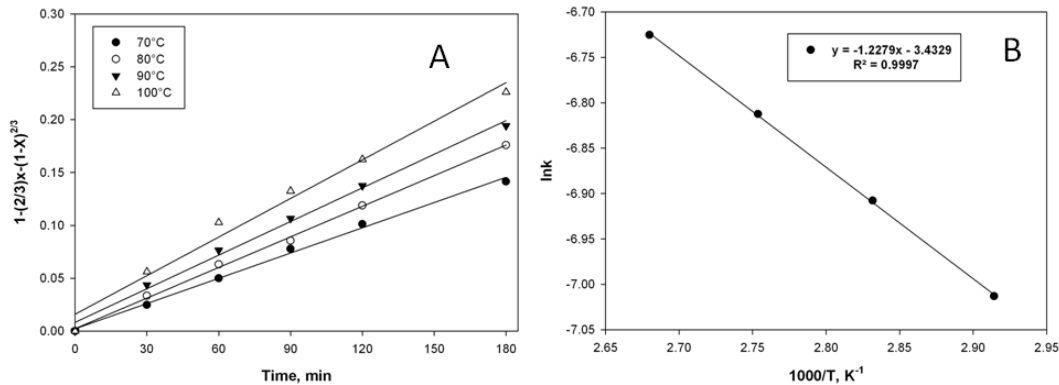


Fig. 7. a) Relationship between $[1 - (2/3)X - (1-X)^{2/3}]$ and time as a function of temperature, b) activation energy of manganese leaching

$$kt = 1 - (2/3)X - (1-X)^{2/3} \quad (11)$$

where k is rate constant, t time (min), X fraction of leached Mn.

The activation energy (E_a) was calculated using the Arrhenius equation, according to the following formula:

$$\ln k = \ln A - E_a/RT \quad (12)$$

where R is the gas constant and T is the temperature (K).

Figure 7b shows the Arrhenius plot of $\ln k$ versus $1000/T$ for Mn dissolution. The activation energy for manganese was calculated to be 10.21 ± 2.60 kJ/mol, which indicates that this is an intermediate-controlled process (Jiang et al., 2004; Kursunoglu and Kaya, 2014; Tang et al., 2014).

Selective precipitation of manganese and zinc using sodium hydroxide

The optimum leaching results were obtained under the condition of 120 min reaction time, in the mixture of 25 g battery paste with 2.0 M H_2SO_4 at 100 °C. After that, two hundred alkaline battery pastes were leached under these optimum conditions. After Mn and Zn were dissolved in the acid solution, it was diluted to 2 dm^3 with distilled-deionized water. The solution contained 42.04 g/dm^3 Mn^{2+} and 32.94 g/dm^3 Zn^{2+} . The pH was 1.10. It was treated with sodium hydroxide to yield $Mn(OH)_2$ and $Zn(OH)_2$. For each experiment, 25 cm^3 of the leaching solution was employed with 4.0 M NaOH solution in a falcon tube for 90 min at 200 rpm.

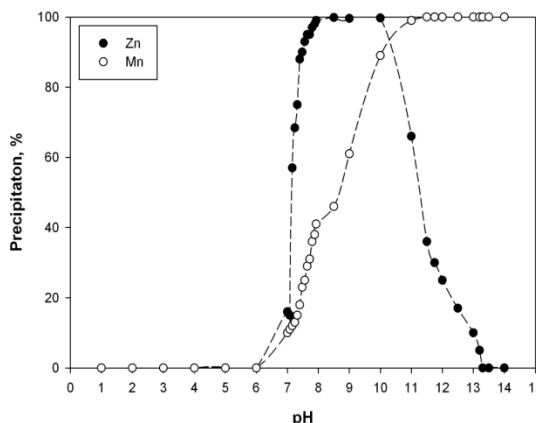
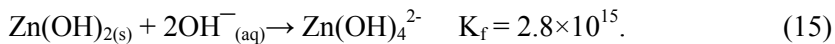
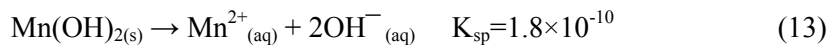


Fig. 9. Precipitation of manganese and zinc as a function of solution pH

According to Eqs. 13 and 14 (Lide, 2004), $\text{Mn}(\text{OH})_2$ and $\text{Zn}(\text{OH})_2$ have low solubility product. However, zinc shows an amphoteric character and re-dissolves in the sodium hydroxide solution to form a zinc hydroxide complex (Eq. 15) as a zincate ($\text{Zn}(\text{OH})_4^{2-}$)



The effect of pH on precipitation of Mn and Zn were investigated and the results are illustrated in Fig. 9. Based on the results obtained, a flow sheet for separation of Mn and Zn was developed and tested. Evidently (Fig. 9) Zn and Mn were not separated at the neutral pH value. However, $\text{Zn}(\text{OH})_2$ dissolves again at pH values greater than 10.5 because the Zn^{2+} ions dissolve under highly basic conditions, unlike Mn(II), which forms a complex stable even to pH 14.

The precipitated manganese compounds were rinsed with cold water five times and then dried for 2 h at 105 °C in air. It was observed that dried $\text{Mn}(\text{OH})_2$ compound was convert to Mn_3O_4 (Fig. 10a) (Reidies, 1990; Peng et al., 2010).

Normally, it is expected that manganese hydroxide occurs with the reaction of manganese sulfate and sodium hydroxide. However, interestingly, it was found that manganese hydroxide just occurred in liquid solution. After solid/liquid separation, the solid was converted to manganese(II,III) oxide by air immediately. Because precipitated manganese(II) hydroxide is oxidized at room temperature by air or oxygen to trivalent, tetravalent manganese oxides in the presence of traces of alkali, while conversion to manganates (i.e., the tetra, penta- and hexavalent states) requires much higher temperatures and high alkali concentrations (180°C for 60–70% NaOH or KOH) (Reidies, 1990; Peng et al., 2010). Furthermore, Eh-pH diagram is the evidence of this situation (Fig. 10b).

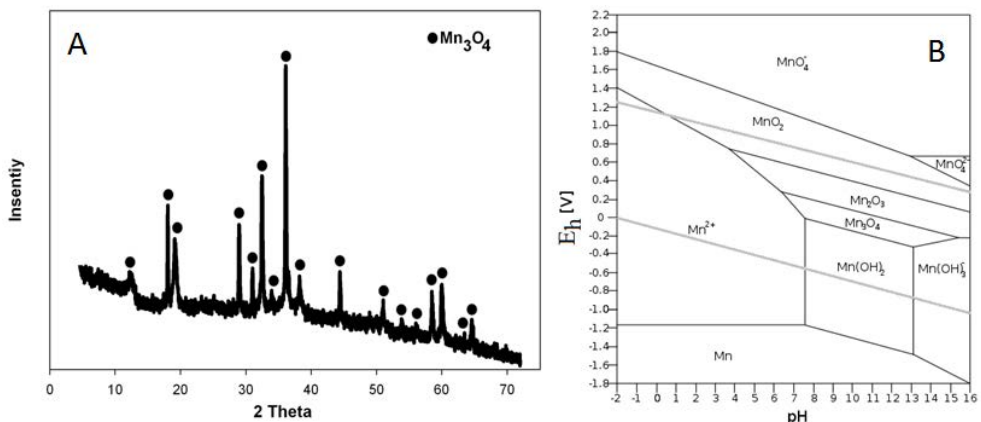


Fig. 10. XRD pattern of Mn₃O₄ (a) and manganese Eh-pH diagram (b)

As seen from Eh-pH diagram, the equilibrium between Mn(OH)₂ and the Mn₃O₄ is:



The net standard free-energy change in this equilibrium, ΔG° is 89.745 kJ/mol, and standard electrode potential can be calculated from the relation

$$E^\circ = -\frac{\Delta G^\circ}{nF} = 0.466 \text{ V}. \quad (17)$$

The value for the oxidation potential of the system when the participating substances are not at unit activity can be compared from the Nernst equation

$$Eh = 0.466 + \frac{0.0592}{2} \log \frac{[\text{Mn}_3\text{O}_4][\text{H}_2\text{O}]^2[\text{H}^+]^2}{[\text{Mn}(\text{OH})_2]^3}. \quad (18)$$

The equation may then be simplified to

$$Eh = 0.466 - 0.0592 \text{ pH}. \quad (19)$$

The vertical boundaries already drawn in Fig. 11 determine the lateral extent of the Mn(OH)₂ field. At a pH of 12.3, the Eh becomes -0.26 V, and at a pH of 11.4 the Eh value is -0.22 V.

A line connecting these points is then drawn to define the border between Mn(OH)₂ and Mn₃O₄ (Dhaouadi et al., 2012; Al Sagheer et al., 1999; Kirillov et al., 2009). The Mn₃O₄ oxide was heated to 800 °C to yield manganese(IV) oxide (MnO₂) under air atmosphere (Zhang and Cheng, 2007c). The XRD pattern of the MnO₂ is displayed in Fig. 12a.

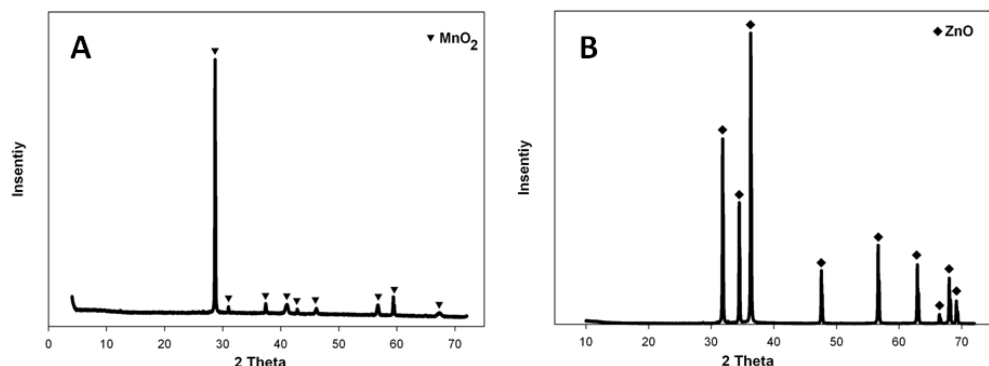


Fig. 12. XRD pattern of a) MnO_2 and b) ZnO

After the manganese was recovered, the author attempted to recover Zn as hydroxide. First, the $\text{Zn}(\text{OH})_4^{2-}$ solution was treated with diluted H_2SO_4 to yield $\text{Zn}(\text{OH})_2$. And then, the zinc hydroxide was rinsed with cold water five times and subsequently dried for 2 h at 105 °C. The resulted white-yellow powder precipitated in 99%. Then, zinc oxide was obtained by calcinations at 500 °C for 3 h (Aktas and Morcali, 2011). The XRD pattern of the product (ZnO) is shown in Fig.12b.

Conclusion

In this work a combined recovery process was proposed to separate zinc and manganese from spent alkaline batteries, which included reductive leaching of manganese in 2 M sulfuric acid medium in the presence of elemental sulfur. The results have shown that it is possible to leach Mn and Zn from the alkaline battery paste with a recovery of +98% using the mixture of 25 g battery paste, 150 cm^3 of 2 M H_2SO_4 at 100 °C and 120 min reaction time. The activation energy of Mn leaching was 10.21 ± 2.60 kJ/mol. Moreover, selective separation of Mn and Zn were studied. Selective precipitation of manganese using NaOH solutions in a neutral leaching step as precipitant agent was studied to separate Zn and Mn from the liquors produced in the acidic leaching step. Subsequently, metal oxides (e.g. MnO_2 , ZnO) were obtained with the help of sodium hydroxide after conversion to metal oxides, which was confirmed by XRD, by heating. From these products, it is possible to make other valuable products.

Acknowledgements

The author wishes to thank Tubitak for financial support. Grateful acknowledgements are given to Dr. Mehmet Hakan Morcali from Istanbul Technical University for valuable discussion.

References

AKTAS S., MORCALI M., 2011. *Recovery of mercury from spent silver oxide button cells*. Minerals and Metallurgical Processing 28, 198-203.

AL SAGHEER F.A., HASAN M. A., PASUPULETY L., ZAKI M. I., 1999. *Low-temperature synthesis of Hausmannite Mn_3O_4* . Journal of materials science letters, 18(3), 209-211.

ALLEN J.P., CORWIN R.R., 1989. *Process for acid leaching of manganese oxide ores aided by hydrogen peroxide*. Google Patents.

AVRAAMIDES J., SENANAYAKE G., CLEGG R., 2006. *Sulfur dioxide leaching of spent zinc–carbon-battery scrap*. Journal of Power Sources 159, 1488-1493.

BERNARDES A.M., ESPINOSA D.C.R., TENORIO J.A.S., 2004. *Recycling of batteries: a review of current processes and technologies*. Journal of Power Sources 130, 291-298.

CROMPTON T.P.J., 2000. Battery Reference Book. Elsevier Science.

DHAOUADI H., GHODBANE O., HOSNI F., TOUATI F., 2012. *Mn_3O_4 Nanoparticles: Synthesis, Characterization, and Dielectric Properties*. ISRN Spectroscopy, 2012.

FERELLA F., DE MICHELIS I., VEGLIÒ F., 2008. *Process for the recycling of alkaline and zinc–carbon spent batteries*. Journal of Power Sources 183, 805-811.

GEGLA J., WALKOWIAK W., 2011. *Leaching of zinc and manganese from used up zinc–carbon batteries using aqueous sulfuric acid solutions*. Physicochemical Problems of Mineral Processing 46, 155-162.

GHAFARIZADEH B., RASHCHI F., VAHIDI E., 2011. *Recovery of manganese from electric arc furnace dust of ferromanganese production units by reductive leaching*. Minerals Engineering 24, 174-176.

JIANG T., YANG Y., HUANG Z., ZHANG B., QIU G., 2004. *Leaching kinetics of pyrolusite from manganese–silver ores in the presence of hydrogen peroxide*. Hydrometallurgy 72, 129-138.

KIRILLOV S.A., ALEKSANDROVA V.S., LISNYCHA T.V., DZANASHVILI D.I., KHAINAKOV S.A., GARCÍA J.R., PENDELYUK O.I., 2009. *Oxidation of synthetic hausmannite (Mn_3O_4) to manganese ($MnOOH$)*. Journal of Molecular Structure, 928(1), 89-94.

KURSUNOGLU S., KAYA M., 2013. *Recovery of Manganese from Spent Batteries Using Activated Carbon Powder as Reductant in Sulfuric Acid Solution*. Asian Journal of Chemistry 25, 1975-1980.

KURSUNOGLU S., KAYA M., 2014. *Dissolution and Precipitation of Zinc and Manganese Obtained from Spent Zinc-Carbon and Alkaline Battery Powder*. Physicochemical Problems of Mineral Processing 50, 41-55.

LASHEEN T.A., EL-HAZEK M.N., HELAL A.S., EL-NAGAR W., 2009. *Recovery of manganese using molasses as reductant in nitric acid solution*. International Journal of Mineral Processing 92, 109-114.

LEVENSPIEL O., 1972. Chemical reaction engineering. Wiley New York etc.

LIDE D.R., 2004. CRC handbook of chemistry and physics. CRC press.

PENG T., XU L., CHEN H., 2010. *Preparation and characterization of high specific surface area Mn_3O_4 from electrolytic manganese residue*. Central European Journal of Chemistry, 8(5), 1059-1068.

PISTOIA G., WIAUX J.P., WOLSKY S.P., 2001. Used Battery Collection and Recycling. Elsevier Science.

REIDIES A.H., 1990. *Manganese compounds*. Ullmann's Encyclopedia of Industrial Chemistry. http://dx.doi.org/10.1002/14356007.a16_123

SAHOO R.N., NAIK P.K., DAS S.C., 2001. *Leaching of manganese from low-grade manganese ore using oxalic acid as reductant in sulphuric acid solution*. Hydrometallurgy 62, 157-163.

SANIGOK U., BAYRAMOGLU M., 1988. *Bench-scale manganese sulfate production from low-grade pyrolusite ores.-Part III*. Chimica Acta Turcica 16, 9-20.

SAYILGAN E., KUKRER T., CIVELEKOGLU G., FERELLA F., AKCIL A., VEGLIO F., KITIS M., 2009. *A review of technologies for the recovery of metals from spent alkaline and zinc–carbon batteries*. *Hydrometallurgy* 97, 158-166.

SAYILGAN E., KUKRER T., YIGIT N.O., CIVELEKOGLU G., KITIS M., 2010. *Acidic leaching and precipitation of zinc and manganese from spent battery powders using various reductants*. *J Hazard Mater* 173, 137-143.

TANG Q., ZHONG H., WANG S., LI J.Z., LIU G.Y., 2014. *Reductive leaching of manganese oxide ores using waste tea as reductant in sulfuric acid solution*. *Transactions of Nonferrous Metals Society of China* 24, 861-867.

TIAN X.K., WEN X.X., YANG C., LIANG Y.J., PI Z.B., WANG Y.X., 2010. *Reductive leaching of manganese from low-grade manganese dioxide ores using corncobs as reductant in sulfuric acid solution*. *Hydrometallurgy* 100, 157-160.

TRIFONI M., TORO L., VEGLIO F., 2001. *Reductive leaching of manganeseiferous ores by glucose and H₂SO₄: effect of alcohols*. *Hydrometallurgy* 59, 1-14.

VEGLIO F., TORO L., 1994. *Fractional factorial experiments in the development of manganese dioxide leaching by sucrose in sulphuric acid solutions*. *Hydrometallurgy* 36, 215-230.

VEGLIO F., VOLPE I., TRIFONI M., TORO L., 2000. *Surface response methodology and preliminary process analysis in the study of manganeseiferous ore leaching by using whey or lactose in sulfuric acid solutions*. *Industrial & engineering chemistry research* 39, 2947-2953.

VELOSO L.R.S., RODRIGUES L.E.O.C., FERREIRA D.A., MAGALHAES F.S., MANSUR M.B., 2005. *Development of a hydrometallurgical route for the recovery of zinc and manganese from spent alkaline batteries*. *Journal of Power Sources* 152, 295-302.

ZHANG W., CHENG C.Y., 2007a. *Manganese metallurgy review. Part I: Leaching of ores/secondary materials and recovery of electrolytic/chemical manganese dioxide*. *Hydrometallurgy* 89, 137-159.

ZHANG W., CHENG C.Y., 2007b. *Manganese metallurgy review. Part I: Leaching of ores/secondary materials and recovery of electrolytic/chemical manganese dioxide*. *Hydrometallurgy* 89, 137-159.

ZHANG W.S., CHENG C.Y., 2007c. *Manganese metallurgy review. Part II: Manganese separation and recovery from solution*. *Hydrometallurgy* 89, 160-177.

Received May 15, 2015; reviewed; accepted October 1, 2015

STRUCTURE AND SURFACE ENERGY OF BOTH FLUORITE HALVES AFTER CLEAVING ALONG SELECTED CRYSTALLOGRAPHIC PLANES

Mikołaj Jan JANICKI, Jan DRZYMALA, Przemysław B. KOWALCZUK

Wroclaw University of Technology, Faculty of Geoengineering, Mining and Geology, 50-370 Wroclaw,
Wybrzeze Wyspianskiego 27, mikolaj.janicki@pwr.edu.pl, przemyslaw.kowalcuk@pwr.edu.pl

Abstract: The density functional theory, supported with a commercial software, was used to compute the geometry and surface energy of fluorite cleaved along the (111), (110) and (100) planes. In the case of cleaving a piece of fluorite along the (111) plane the two newly created surfaces are identical consisting of fluorite ions with the surface energy equal to 0.384 J/m². Cleaving fluorite along the (110) plane also provides identical halves and, both contain one Ca ion next to two F ions, with the surface energy equal to 0.723 J/m². When cleaving takes place along the (100) plane, it creates two corresponding halves with different surface structures. One half, having only surface Ca ions (100^{Ca}) has the surface energy equal to 0.866 J/m², while the surface energy of the second half, having only F surface ions (100^F), is 0.458 J/m². Different structures and energies of the corresponding fluorite surfaces, that is (100^{Ca}) and (100^F) planes, should have an impact on their chemical properties, including hydrophobicity expressed by contact angle. The calculations performed in the paper also showed that reorganization of fluorite surfaces after cleaving was insignificant for all of the investigated planes.

Keywords: fluorite, fluoride, surface energy, interfacial energy, cleaving, reorganization, surface ions

Introduction

Fluorite is an important industrial mineral which is commonly used for production of aluminum, hydrofluoric acid, glasses, enamels, optical windows, spectroscopic mirrors etc. (Janczuk et al., 1993; Wu and Forsling, 1995; Reichling et al., 1996; Schick et al., 2004). Recovery of fluorite from mineral resources is achieved mostly by flotation (Fulton and Miller, 2006).

Fluorite contains calcium Ca²⁺ and fluoride F⁻ ions having radii of 0.112 and 0.133 nm, respectively (Shannon and Prewitt, 1969). The electronegativity of fluorine is 3.98 being the greatest on the Pauling scale, while the electronegativity of calcium is 1.00 (Pauling, 1960). The difference in electronegativity is equal to 2.98 indicating a highly ionic character of crystalline CaF₂.

Fluorite is a naturally hydrophobic mineral (Bakakin, 1960; Barskij, 1984; Janczuk et al., 1993; Drzymala 1994a, 1994b; Zawala et al., 2007, 2008; Gao et al., 2011; Zhang et al., 2014). According to these papers the hydrophobicity, characterized by the so-called contact angle, depends on many parameters, including fluorite color, origin, pH of aqueous solution and crystallographic plane. The maximum difference of about 100° in hydrophobicity of various treated and untreated fluorite specimens was observed by Janczuk et al. (1993), who reported that this mineral formed with water contact angles from 0° to 100.6°. These values agree well with theoretical considerations according to which the maximum hydrophobicity of fluorite is 104°, when only dispersive forces operate in the fluorite-water drop system (Drzymala, 1994a), while for pure (110) and (100) fluorite planes the non-equilibrium contact angle is zero (Zhang et al., 2014). However, upon equilibration with water, the (100) and (110) planes become hydrophobic (Zhang et al., 2012, 2014).

There is one more aspect of fluorite hydrophobicity. When a piece of fluorite is split into halves, the newly created two surfaces are not necessarily identical in arrangement of surface ions. It can be seen, for instance, in the paper of Tasker (1979), who plotted schematic representation of stacking sequence in the fluorite structure for different planes, including not identical (100) planes. In other studies the surface structure differences of the fluorite (100) plane were not recognized (Maldonado et al., 2013), while Zhang et al. (2014) once showed Ca ions on the top of the (100) plane and next F ions forming the (100) surface. Therefore, the aim of this paper is to examine the structure of fluorite after cleaving along certain planes and to calculate their surface energies taking into account surface ions reorganization. The surface structures of the two newly created surfaces formed by cleaving a lump of crystal fluorite along the (111), (110) and (100) planes and their surface energies are considered in this paper.

It should be noticed that perfect octahedral cleavage of fluorite occurs along four (111) planes and parting (poor) is observed on the (110) planes (Anthony et al., 2015). According to Vitov and Konstantitov (2001) splitting fluorite provides not only (111) but also (100) and (110) planes. Indistinct parting or cleavage on (110) was also mentioned by Palache et al. (1951). According to Minerals.net (2015) octahedral (111) cleavage fragments are flat with triangular shaped pieces, while cubic (100) and (110) cleavage fragments are flat with three dimensional rectangles.

Calculations

The calculations of fluorite primitive cell parameters and relaxation of the surface ions after cleaving were performed using the density functional theory (DFT) as well as the Perdew–Burke–Ernzerhof (PBE) functional (Perdew et al., 1996) and the CRYSTAL09 software package (Dovesi et al., 2009). The calculations are based on the pob_TZVP_2012 functions, which describe molecular orbital of Ca and F atoms as linear combinations (Peintinger et al., 2012). The Brillouin zone integrations were

performed on a special k -point mesh generated by the Monkhorst–Pack scheme ($9 \times 9 \times 9$) in the bulk (Monkhorst et al., 1973). The sampling of the Brillouin zone for the surfaces was performed with an $8 \times 8 \times 1$ Monkhorst–Pack k -point mesh (Maldonado et al., 2013).

The Amsterdam Density Functional (ADF) computational chemistry package was used for determination of the surface energy ($\gamma^{(hkl)}$) of fluorite planes after cleavage (Velde et al., 2001). The calculations were performed using the periodic density functional theory (DFT) employing the generalized gradient approximation (GGA) with the Perdew–Burke–Ernzerhof (PBE) functional for CaF_2 and two-dimensional translational symmetry. The following equation (Maldonado et al., 2013) was used

$$\gamma^{(hkl)} = \frac{1}{2} \left[\frac{E_n^{(hkl)} - n \cdot \left\{ \frac{1}{p} (E_n^{(hkl)} - E_{n-p}^{(hkl)}) \right\}}{A^{(hkl)}} \right],$$

where $E_n^{(hkl)}$ is the total energy of the n -layer slab with the Miller index (hkl) and factor 1/2 accounts for the presence of two surfaces at either side of the slab. Symbol p stands for number of rows of atoms in a terrace of any stepped surface and $A^{(hkl)}$ is the unit cell surface area.

Results and discussion

Basic fluorite structure parameters include the length of translation vectors (a, b, c), interaxial angles (α, β, γ) and distance between calcium and fluoride ions. These parameters determine the primitive cell of fluorite (Strunz, 1970). In the bulk structure of fluorite the distance between the layer of fluoride ions (F^-) and the next layer of calcium ions (Ca^{2+}) in the case of the (111) plane is 0.0788 nm, while the distance of third layer of fluoride ions from the first layer is 0.1577 nm (Schreyer et al., 2014). In the case of the (110) plane the distance between each layer containing both Ca and F ions is 0.1932 nm (Schreyer et al., 2014). The (100) plane is formed by separate layers of F and Ca ions, which are 0.1366 nm apart (Schreyer et al., 2014). Our calculations provided parameters of the primitive cell of fluorite which well agree with the literature experimental data (Table 1).

Table 1. Experimental and calculated parameters of fluorite cell

	α, β, γ [°]	a, b, c [nm]	Length of Ca–F bond [nm]
Experimental (Schreyer et al., 2014)	90	0.5463	0.2365
Calculated (this paper)	90	0.5475	0.2371

Splitting a piece of fluorite provides new surfaces. There is also reorganization of surface ions forming the surface in relation to the bulk structure (Leeuw et al., 2000). Our calculation indicated that the relaxation of the surface ions of fluorite is not

significant because the change of the Ca-F bond length, when the surface is formed, is less than 3.5%. The results of calculations of the relaxation of surface ions for (111), (110) and (100) planes of fluorite are shown in Table 2. To indicate the ions forming the surface, the hkl symbol of the considered plane was supplemented with the chemical name of the ion or ions. Therefore, for instance the (111) plane consisting of only F ions was denoted as (111^F). Details regarding the surface structures created by splitting fluorite along different planes will be discussed further in this work.

Table 2. Calculated relaxation of ions forming different surfaces of fluorite

Plane	Ca-F bond length between atoms of the first and second layers [nm]	Ca-F bond length change based on bond lengths before and after relaxation [%]
(111 ^F)	0.2346	1.04
(110 ^{CaF₂})	0.2413	1.78
(100 ^{Ca})	0.2304	2.82
(100 ^F)	0.2285	3.51

Knowing the arrangement of ions in the bulk structure of fluorite and extend of the relaxation of fluoride and calcium ions present on the surface of the considered planes, we can plot the fluorite surface structures for the (100), (110) and (111) planes. Figures 1a-c show the inner fluorite structure as well as the surface structures of both halves created by cleaving and relaxation. It can be seen that cleaving fluorite along the (111) plane provides identical halves (Fig. 1a) with fluoride ions forming the surface (111^F). Similar situation occurs for the (110) plane (Fig. 1b). In this case both halves contain fluoride and calcium ions (110^{CaF₂}) in the same proportion 2:1 as in the CaF₂ molecule. However, the situation is different in the case of the fluorite (100) plane (Fig. 1c). Splitting along the (100) plane leads to two entirely different surfaces. One of them consists of Ca (100^{Ca}), while the second one with fluoride (100^F) ions.

Since the halves produced by splitting along the (100) plane of fluorite are very different, their properties, especially the surface energies, are expected to be different. Initially the calculations of the surface energies were performed for the (111) and (110) planes to check the accuracy of determination. Table 3 shows that the calculated energies of the (111) and (110) planes of fluorite are similar to those reported by Maldonado et al. (2013). In the case of the (100) plane the surface energy of the half covered with the Ca ions (100^{Ca}) is equal to 0.866 J/m², while the surface energy of the second half with the fluoride atoms (100^F) is 0.458 J/m². Thus, there is a significant difference in the surface energies of the created halves. As a result, it should be expected that the hydrophobicity of both halves can be different. Perhaps, the difference in the contact angles of the fluorite (100) plane observed by Zhang et al. (2014) (0°) and by Gao et al. (2012) (32.4°) was caused by measuring contact angle for not the same but corresponding halves.

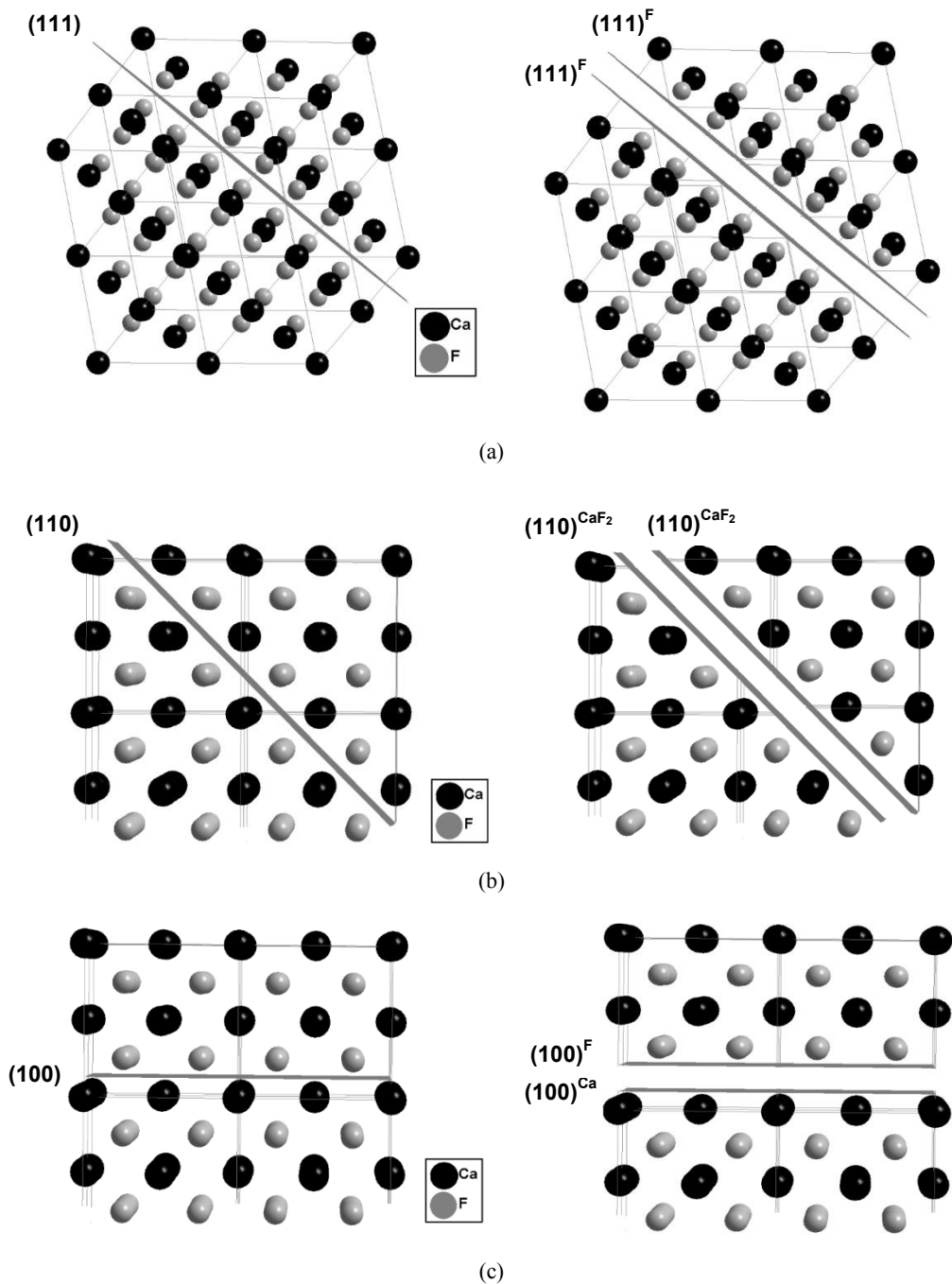


Fig. 1. Primitive cells (left) and surface structures (right) of fluorite split into halves along a) (111), b) (110), and c) (100) planes

Table 3. Calculated surface energies of different planes of fluorite

Cleavage planes	surface energy, J/m ² (this work)	surface energy, J/m ² (Maldonado et al., 2013)*
(111 ^F)	0.384	0.392
(110 ^{CaF₂})	0.723	0.613
(100 ^{Ca})	0.866	0.840
(100 ^F)	0.458	n/a

*recalculated from the eV/f.u. units

Theoretically, it is possible to split a piece of fluorite along the (100) plane to create halves having both fluoride and calcium ions on their surfaces. However, this is very unlikely because it would create electrical charge and holes (about 50% of the surface) on both halves. In addition to that, the removal of atoms would require breaking chemical bonds. Impossibility to form one half with (111^F) surface plane and the second with (111^{Ca}) surface plane was discussed by Tasker (1979), who pointed out that such cleaving would create a great dipole moment leading to a significant surface ions reorganization.

According to Tasker (1979) splitting fluorite along the (100) plane provides two different surfaces, both having dipole moments, and thus requiring serious relaxation, while our calculations for these surfaces point to a small reorganization. This discrepancy requires further considerations.

A comparison of the surface energies of different fluorite surfaces indicates that planes containing either only calcium or calcium and fluorine have the surface energy value in the vicinity of 0.8 J/m², while planes containing only fluoride ions have the surface energy equal to about 0.4 J/m².

Conclusions

The paper shows that splitting a piece of fluorite along a selected plane provides halves which, after a slight reorganization in comparison to the bulk structure, can be either identical or different. The same structure of the corresponding halves was found for the (111) and (110) planes. In the case of the (100) plane, splitting provides halves of different structures. The first one with only fluoride ions (100^F) forming the the surface has the surface energy equal to 0.458 J/m², while the second one with only calcium atom forming the surface (100^{Ca}) has the surface energy equal to 0.866 J/m². Thus, there is a significant difference in the surface energy and it should be expected that the hydrophobicity of both halves are different.

Acknowledgements

The paper was partially financed by the Polish Governmental Statutory Works Program S50167. Calculations were carried out at the Wroclaw Centre for Networking and Supercomputing within grant No. 012. Figures was rendered by Diamond - Crystal and Molecular Structure Visualization Crystal

Impact - Dr. H. Putz & Dr. K. Brandenburg GbR, Kreuzherrenstr. 102, 53227 Bonn, Germany
<http://www.crystalimpact.com/diamond>

References

ANTHONY J. W., BIDEAUX R. A., BLADH K.W., NICHOLS M.C. (EDS). "Fluorite". *Handbook of Mineralogy (PDF). III (Halides, Hydroxides, Oxides)*. Chantilly, VA, US: Mineralogical Society of America. ISBN 0962209724. Retrieved September 25, 2015

BAKAKIN V.V., 1960. *The relationship between the structure of minerals and their flotation properties*. Journal of Structural Chemistry 1(2), 149-155.

BARSKIJ L.A., 1984. *Principles of Mineralogy*, Izd. Nauka, Moscow (in Russian).

DOVESI R., SAUNDERS V.R., ROETTI C., ORLANDO R., ZICOVICH-WILSON C.M., PASCALE F., CIVALLERI B., DOLL K., HARRISON N.M., BUSH I.J., D'ARCO P., LLUNELL M., 2009. CRYSTAL09, (2009) CRYSTAL09 User's Manual. University of Torino, Torin.

DRZYMALA J. 1994a. *Hydrophobicity and collectorless flotation of inorganic materials*. Advances in Colloid and Interface Science 50, 143–185.

DRZYMALA J. 1994b. *Characterization of materials by Hallimond tube flotation. Part 1: maximum size of entrained particles*. International Journal of Mineral Processing 42, 139–152.

FULTON III, R.B., MILLER, M.M., 2006. *Fluorspar*. In: *Industrial Minerals and Rocks*, 7th ed., J.E., Kopel, N.C. Trivedi, J.M., Barker, S.T., Krukowski (eds), SME, Littleton, Colorado, USA.

GAO Z., SUN W., HU Y., LIU X., 2012, *Anisotropic surface broken bond properties and wettability of calcite and fluorite crystals*, Transactions of Nonferrous Metals Society of China 22, 1203–1208.

HOY A.R., BUNKER P.R., 1979. *A precise solution of the rotation bending Schrödinger equation for a triatomic molecule with application to the water molecule*. Journal of Molecular Spectroscopy 74(1), 1–8.

JANCZUK B., BRUQUE J.M., GONZALEZ-MARTIN M.L., MORENO DEL POZO J., 1993. *Wettability and surface tension of fluorite*. Colloids and Surfaces A: Physicochemical and Engineering Aspects 75, 163–168.

LEEUW N.H., PURTON J.A., PARKER S.C., WATSON G.W., KRESSE G., 2000. *Density functional theory calculations of adsorption of water at calcium oxide and calcium fluoride surfaces*. Surface Science 452, 9–19.

MALDONADO P., GODINHO J.R.A., EVINS L.Z., OPPENEER P.M., 2013. *Ab Initio Prediction of surface stability of fluorite materials and experimental verification*. The Journal of Physical Chemistry C 117, 6639–6650.

MINERALS.NET, 2015, <http://www.minerals.net/mineral/fluorite.aspx>.

MONKHORST H.J., PACK D.J., 1976. *Special points for Brillouin-zone integrations*. Physical Review B 13, 5188.

PALACHE, C. BERMAN, H., AND FRONDEL, C., 1951, The System of Mineralogy, Volume II, seventh edition: John Wiley & Sons, New York, 1124 p.

PAULING L., 1960. *The Nature of the Chemical Bond*, 3rd ed. Cornell University.

PEINTINGER M.F., OLIVEIRA D.V., BREDO T., 2012. *Consistent Gaussian Basis Sets of Triple-Zeta Valence with Polarization Quality for Solid-State Calculations*. Journal of Computational Chemistry 34(6), 451–459.

PERDEW J.P., BURKE K., ERNZERHOF M., 1996. *Generalized Gradient Approximation Made Simple*. Physical Review Letters 77 (18), 3865–3868.

REICHLING M., WILSON R. M., BENNEWITZ R., WILLIAMS R. T., GOGOLL S., STENZEL E., MATTHIAS E., 1996. *Surface colloid evolution during low-energy electron irradiation of CaF₂ (111)*. Surface Science 366(3), 531–544.

SCHICK M., DABRINGHAUS H., WANDELT, K., 2004. *Macrosteps on CaF₂ (111)*. Journal of Physics: Condensed Matter 16(6), L33–L37.

SCHREYER M., GUO L., THIRUNAHARI S., GAO F., GARLAND M., 2014. *Simultaneous determination of several crystal structures from powder mixtures: the combination of powder X-ray diffraction, band-target entropy minimization and Rietveld methods*. Journal of Applied Crystallography 47, 659–667.

SHANNON R.D., PREWITT C.T., 1969. *Effective ionic radii in oxides and fluorides*. Acta Crystallographica B25, 925–946.

STRUNZ H., 1970. *Mineralogische Tabellen*, Leipzig, 5th edition, Akad Verlagsges, Leipzig.

TASKER P. W., 1979. *The stability of ionic crystal surfaces*, Journal of Physics C: Solid State Physics 12, 4977–4983.

VELDE G.T., BICKELHAUPT F.M., BAERENDS E.J., GUERRA C.F., VAN GISBERGEN S.J.A., SNIJDERS J. G., ZIEGLER T., 2000. *Chemistry with ADF*, Journal of Computational Chemistry 22(9), 931–967.

VITOV O., KONSTANTITOV L., 2001. *Method for determining the cleavability of fluorite*. Comptes rendus de l'Académie bulgare des Sciences, 54(3), 55–458.

WU L., FORSLING W., 1995. *Surface complexation of calcium minerals in aqueous solution. III. Ion exchange and acid-base properties of hydrous fluorite surfaces*. Journal of Colloid and Interface Science 174(1), 178–184.

ZAWALA J., DRZYMALA J., MALYSA K., 2007. *Natural hydrophobicity and flotation of fluorite*. Physicochemical Problems of Mineral Processing 41, 5–11.

ZAWALA J., DRZYMALA J., MALYSA K., 2008. *An investigation into the mechanism of the three-phase contact formation at fluorite surface by colliding bubble*. International Journal of Mineral Processing 88, 72–79.

ZHANG X., WANG X., MILLER J.D., 2014. *Wetting of selected fluorite surfaces by water*. Surface Innovations 3, 39–48.

ZHANG X., WANG X., YIN X., DU H., MILLER. J.D., 2012. *Interfacial Chemistry features of selected fluorite surfaces*. In: Separation Technologies for minerals, coal, and earth resources, C.A. Young and G.H. Luttrell (eds.). Soc. Mining, Metallurgy and Exploration, 627–634.

Received June 6, 2015; reviewed; accepted August 25, 2015

ACTIVATED LIGNIN AND AMINOSILANE-GRAFTED SILICA AS PRECURSORS IN HYBRID MATERIAL PRODUCTION

**Lukasz KŁAPISZEWSKI^{*}, Tadeusz Jan SZALATY, Jakub ZDARTA,
Teofil JESIONOWSKI**

Poznan University of Technology, Faculty of Chemical Technology, Institute of Chemical Technology and Engineering, Berdychowo 4, PL-60965, Poznan, Poland

* e-mail: lukasz.klapiszewski@put.poznan.pl, phone: +48 616653747, fax: +48 616653649

Abstract: Functional inorganic-organic hybrids were synthesized using as a precursor silica with the addition of an appropriate amount of lignin as components. Three types of silica were applied as the support: the commercial silicas Syloid 244 and Aerosil 200, and hydrated silica precipitated in a polar system. The silicon dioxide was initially functionalized with aminosilane to activate the surface, and then the silica-based material was combined with lignin oxidized using hydrogen peroxide. The obtained inorganic-organic hybrids underwent physicochemical and dispersive-morphological analysis, with comparison of the results depending on the composition of the test samples. In addition, particle size distributions were determined and the surface structure of the products assessed by scanning electron microscopy. The presence of functional groups was also determined by FTIR spectroscopy. The thermal analysis of the silica/lignin materials was also performed, as well as the elemental and colorimetric analyses, which indirectly confirmed the correctness of the synthesis process. Hybrid materials with the most favorable dispersive and morphological properties were obtained by adding a small amount of biopolymer. The thermogravimetric analysis of the SiO_2 /lignin hybrids indicated their good thermal stability. With increasing quantity of lignin per 100 parts by weight of silica matrix, progressive deterioration in the thermal stability of the materials was observed.

Keywords: SiO_2 /lignin hybrids, silica, lignin, lignin activation, thermal stability, hybrid material

Introduction

Silica/lignin hybrid materials are novel products with applications in many branches. The presence in the lignin molecule of many different functional groups containing oxygen enables the functionalization of its surface with SiO_2 . This process is accompanied by the creation of a greater number of active sites, which increase the capacity to adsorb hazardous metal ions, organic compounds and many harmful

substances (Hasegawa et al., 1999, Telysheva et al., 2009, Klapiszewski et al., 2015). The high adsorption capacity gives rise to prospective applications especially in protection of the environment. Silica/lignin materials can be used as promising advanced functional products, which are generally characterized as those materials which possess particular native properties and functions of their own (Klapiszewski et al., 2013a). The prevalence and natural character of lignin in combination with silica makes it an excellent filler for polymeric materials, which allows desired properties of the product to be obtained (Bula et al., 2015). Additionally, the composites can be used in electrochemistry, as modified electrodes, as well as for manufacture of electrochemical sensors and electroanalyzers (Lota and Milczarek, 2011, Jasionowski et al., 2014a, Jasionowski et al., 2014b). Moreover, this hybrid material can be used as a precursor of advanced composites, e.g. in preparation of silicon carbide of high purity, lignin/SiO₂/TiO₂ and lignin/titania hybrids as precursors for Si–Ti–C–O fibers (Hasegawa et al., 1998, Hasegawa et al., 1999, Mishra et al., 2009).

Silica, in general, is an amorphous substance, with high chemical resistance, and therefore products of extremely high quality can be manufactured. A number of preparation techniques are used, which differ in terms of either the type of reagents or properties of the final product. Amongst many methods of silica preparation, the most commonly used are the flame process (Bergna and Roberts 2006, Wypych, 2010), hydrolysis and condensation of alkoxides developed by Stober (Stober et al., 1968), precipitation from aqueous sodium silicate solutions (Zurawska et al., 2003) and co-precipitation from emulsion systems (Jasionowski, 2001, Jasionowski, 2009). High demand for silica and its widespread use are linked to its valuable physicochemical properties and highly developed surface area. The fumed silica is made from primary particles with the spherical shape and size of approximately 20 nm, which form a chain structure of agglomerates. Generally, the surface has hydrophilic character due to the presence of silanol groups in the amount of 5-6 OH/nm². It is a high activity product mainly used as a thixotropic agent, additive for paints and a material of toothpaste and pharmaceuticals. In turn, the precipitated silicas as well as silica gels have a much smaller degree of particle dispersion. The amount of silanol groups on nm² for precipitated silicas is about 15. They are commonly used as components of rubber compounds. In contrast, silica gels are materials mostly dedicated to adsorption processes or used as carriers. An additional advantage is the potential for surface functionalization to modify its chemical and physical character and extend the range of possible applications of synthetically obtained silicas (Krysztafkiewicz et al., 1997, Tertykh et al., 2003, Jasionowski et al., 2010, Tertykh et al., 2013).

Lignin is a naturally occurring aromatic cross-linked polymer made up of three main phenylpropane units, namely coniferyl, sinapyl and *p*-coumaryl alcohols (Donaldson, 2001, Meister, 2002, Ralph et al., 2004). The composition of each lignin monomer differs significantly depending on the type of plant material. Three types are commonly known: softwood (gymnosperm), hardwood (angiosperm), and grass or annual plant (graminaceous) lignin (Kadokawa, 2013).

In plants, lignin acts as a biological barrier and as a glue that binds hemicelluloses and celluloses in a cell wall. It is used as a composite filler, surfactant or dispersant additive, and as a component in binders and coatings. Lignin as a primary substance (wood) is insoluble in water, although it can be dissolved in acetone, pyridine and dimethyl sulfoxide (DMSO). It is easily decomposed in nature by the chemical action of enzymes. Lignin undergoes reactions of oxidation, reduction, bleaching and hydrolysis. The reactivity is due to its ability to form reactive intermediates derived from hydroxyl-phenyl groups (Boerjan, 2003, Vanholme, 2010). This complex compound can be selectively modified in an oxidative functionalization process due to the presence of a large number of side-chain aliphatic –OH groups, terminal phenolic groups and reactive benzylic positions (Crestini, 2010).

Over many years various chemical oxidants of lignin have been investigated. Strong oxidizing agents break up the aromatic ring, whereas milder ones cause changes only in the side chains. Oxidation has a significant influence on surface activation of lignin when hydroxyl groups are abundant. When these hydroxyl groups are oxidized, carbonyl groups are formed, which are more susceptible to reactions than hydroxyl groups. Moreover, this process improves the hydrophilicity of lignin (Kadokawa, 2013). Oxidative valorization of lignin can be performed in various ways.

Activated hydrogen peroxide oxidizes phenols or methoxybenzene to regiosomeric benzoquinones. Phenolic model compounds are converted into monoaromatic benzoic acid derivative, phenyl methyl ketone derivative, syringol and unsaturated lactone. Additionally, the ring cleavage reactions occur. Transformation of neolignans undergoing demethylation oxidation of the benzylic position, and the reaction where the ring is opened are also present. Oxidation of phenolic substrates requires extreme process conditions with an excess of toxic oxidant, but methyltrioxorhenium (MTO) is able to activate hydrogen peroxide under mild conditions (Lange, 2013).

Other compounds used to activate either molecular oxygen or hydrogen peroxide include salen complexes, especially cobalt with salen. During this oxidation process, from basic cynamic ester and complex phenolic and non-phenolic phenylcoumaranes, there are obtained benzoquinone derivatives, alkyl–phenyl ketones, benzoic acid derivatives and benzofuran, respectively (Lange 2013).

Oxidation can be carried out in the presence of $[\text{Co}(\text{salen})]$ complexes with addition of ionic liquid. Various chemical oxidation reactions of lignin in ionic liquid have been investigated over many years. Scientists have used the fact that lignin is freely soluble in ionic liquids and catalytic oxidation of lignin has been carried out. Zakzeski et al. (2010, 2011) performed oxidation of lignin using 1-ethyl-3-methylimidazolium diethylphosphate ($[\text{Emim}][\text{DEP}]$), cobalt catalyst and molecular oxygen under mild conditions. $\text{CoCl}_2 \cdot 6\text{H}_2\text{O}$ in Emim DEP proved particularly effectiveness for oxidation. Based on ATR-IR spectroscopy it was shown that the catalyst oxidized benzyl and other alcohols rapidly occur in lignin, but they leave phenolic functionality and 5-5', β -O-4 and phenylcoumaran linkages intact (Zakzeski et al., 2010). The $\text{Co}/[\text{Emim}][\text{DEP}]$ catalyst system represents a potential method in a

biorefinery scheme because it is able to increase the functionality of lignin (Zakzeski et al., 2011).

Oxidative valorization of lignin mainly proceeds in the presence of enzymes, such as laccases, lignin peroxidases (LP) and manganese dependent peroxidases (MnP). Synthetic metalloporphyrins are used as biomimetic systems for enzymes, like LP and MnP, and are oxidized with highly efficient metallo-oxo species similar to those in LP I and LP II. Highly functionalized porphyrins bearing aryl substituents in the meso-positions of the ring act as catalyst systems to oxidants, while careful modification of the nature of the meso-substituents can affect the redox potential and solubility of the complexes (Crestini, 1999).

Lignin can be effectively oxidized by porphyrin catalysts such as cationic manganese-meso-tetra(*N*-methylpyridinio)porphorin-pentaacetate $\text{TP}_y\text{MePMn}(\text{MeCOO})_5$, which in this process leads to products such as benzoquinones, benzyl alcohols, and phenyl alkyl ketones in acidic environments (pH 3–6). All porphyrin catalysts such as anionic manganese and iron meso-tetra(2,6-dichloro-3-sulfonatophenyl) porphyrin chlorides (TDCSPPMnCl and TDCSPPFeCl), respectively, anionic meso-tetra-4-sulfonatophenyl porphyrin chloride (TSPPMnCl), and the previously mentioned cationic manganese meso-tetra(*N*-methylpyridinio)-porphorin-pentaacetate ($\text{TP}_y\text{MePMn}(\text{MeCOO})_5$), despite the different metal centers and porphyrin moieties, undergo comparable reaction mechanisms and produce comparable products (Lange, 2013).

In this paper a trial was undertaken to synthesize and characterize silica/lignin hybrid materials. For the first time, hydrogen peroxide was used to oxidize the appropriate functional groups in lignin and increase the affinity of the biopolymer to the aminosilane-grafted silica. The effectiveness of combination of silica with lignin was confirmed by the FTIR spectroscopy and elemental analysis, and also indirectly by the colorimetric analysis. The hybrid systems were examined by determining their dispersive (NIBS technique), morphological (SEM images) and thermal (TGA analysis) properties. In the near future, these studies will lead to the potential use of these systems in a variety of applications.

Experimental

Preparation of hydrated silica in a polar medium

The product was synthesized by means of a reaction of aqueous solution of sodium silicate (Vitrosilicon S.A., Poland) with 5 % sulfuric acid (Chempur, Poland) (Fig. 1). A reactor containing 100 cm³ of aqueous solution of hydrophobizing agent (0.2 g Rokanol K7 – PCC Rokita, Poland), was placed into a water bath (85 °C). To this system 9.8 g sodium sulfate (Chempur, Poland) was added. In the next step, the sodium silicate solution at a constant rate of 8 cm³/min, and 5 % solution of sulfuric acid at the desired rate of 4 cm³/min were added. The system was intensively stirred and the process was conducted for about 1 h. The obtained silica was filtered by suction and washed several times with water. A white precipitate was placed in a

crystallizer and subjected to convective drying at 105 °C for about 24 h. More details are given in our previously published work (Klapiszewski et al., 2012).

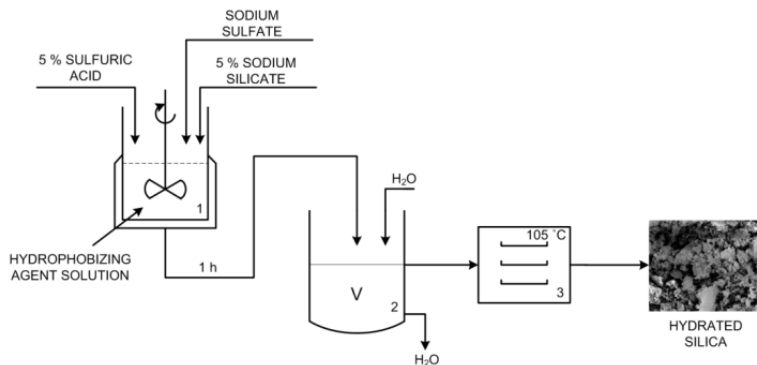


Fig. 1. Technological process for production of silica in a polar medium
(1 – mixing device, 2 – vacuum filter, 3 – convection dryer)

Functionalization of silica surface using aminosilane

In this study, the commercial silicas Aerosil 200 (Evonik Industries AG, Germany) and Syloid 244 (W.R. Grace Co., USA) were used. The three types of tested silicas (Aerosil 200, Syloid 244 and hydrated SiO_2) were subjected to grafting with a water/methanol solution (1:4, v/v) containing *N*-(2-aminoethyl)-3-aminopropyltrimethoxysilane (in a quantity of 5 parts by weight per 100 parts of SiO_2). The solution was applied on the surface of the silica using an atomizer, mixing thoroughly after each application. The modified silica was dried for 24 h at 105 °C (see Figure 2). A precise description of modification is contained in our previous publications (Jesionowski and Krysztafkiewicz, 2000; Jesionowski et al., 2010).

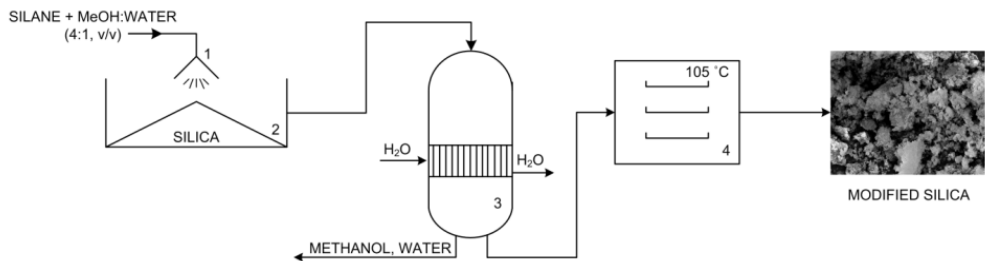


Fig. 2. Functionalization of silica surface by aminosilane
(1 – atomizer, 2 – reactor, 3 – vacuum evaporator, 4 – convection dryer)

Preparation of silica/lignin hybrids using lignin oxidized by H_2O_2

The first step in modification of silica with kraft lignin (L) was preparation of 7.5 % solution of hydrogen peroxide, into which an appropriate amount of lignin was

introduced. Kraft lignin was purchased from Sigma-Aldrich (Germany). The BET surface area of lignin was $1 \text{ m}^2/\text{g}$, while the pore size was equal to 12.1 nm. Lignin had a particle size in the range of 1990-2670 and 3580-5560 nm. The process of activation of lignin was carried out without light. The solution of lignin prepared in this way was stirred for about 20 min. In the second step, aminosilane-modified silica (Aerosil 200 (A), Syloid 244 (S) or hydrated silica (H)) was added to the prepared reaction mixture, and then the reacting system was constantly stirred for 1 h. The obtained product (silica/lignin hybrid material) was placed in a convective dryer to evaporate water and dried overnight at 50 °C. The amounts of the precursors used for silica/lignin samples obtained are summarized in Table 1.

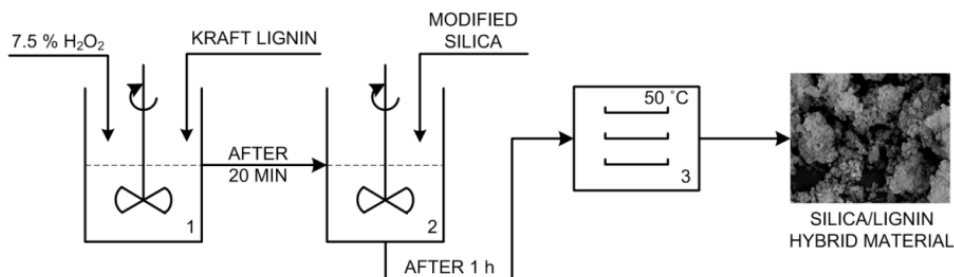


Fig. 3. Technological process for production of silica/lignin hybrid material
(1, 2 – reactor, 3 – convection dryer)

Table 1. The amounts of precursors used to obtain a silica/lignin hybrid materials

Sample	Content of lignin in relation to the modified silica matrix (wt./wt.)	Amount of kraft lignin (g)	Amount of silica (Syloid 244 / Aerosil 200 / hydrated silica (g)
SL 1 / AL 1 / HL 1	3	0.15	
SL 2 / AL 2 / HL 2	10	0.5	
SL 3 / AL 3 / HL 3	20	1.0	5.0
SL 4 / AL 4 / HL 4	50	2.5	

Evaluation of physicochemical properties

The dispersive and morphological properties of the silica/lignin hybrid materials were characterized by particle size determination using a Zetasizer Nano ZS (0.6–6000 nm) instrument (Malvern Instruments Ltd., UK), operating based on the non-invasive backscattering (NIBS) technique. To obtain information on dispersion, particle morphology and type of agglomeration in the samples as well as images from a scanning electron microscope (Zeiss EVO40, Germany) were used. Prior to tests, the samples were coated with Au for 5 seconds using a Balzers PV205P coater.

The elemental contents of the products were established with the use of a Vario EL Cube instrument made by Elementar Analysensysteme GmbH (Germany), which is capable of registering the percentage content of carbon, hydrogen, nitrogen and sulfur in samples after high-temperature combustion. The results are obtained by averaging three measurements with an error of $\pm 0.01\%$.

Fourier transform infrared spectroscopy (FTIR), using a Vertex 70 spectrometer (Bruker, Germany), was used to prove the presence of expected functional groups. The materials were analyzed in the form of tablets, made by pressing a mixture of anhydrous KBr (ca. 0.1 g) and 1 mg of the tested substance in a special steel ring under a pressure of approximately 10 MPa. The tests were performed over a wavenumber range of 4000–400 cm^{-1} (at a resolution of 0.5 cm^{-1}).

A thermogravimetric analyzer (TGA, model Jupiter STA 449F3, made by Netzsch, Germany) was used to investigate the thermal stability of the samples. The measurements were carried out under liquid nitrogen (10 cm^3/min) at a heating rate of 10 $^{\circ}\text{C}/\text{min}$ over a temperature range of 25–1000 $^{\circ}\text{C}$, with an initial sample weight of approximately 5 mg.

Colorimetric characterization of the silica/lignin hybrid materials was carried out by using a Specbos 4000 colorimeter (YETI Technische Instrumente GmbH, Germany). The results are given in the *CIE Lab* system, where L^* denotes lightness; $+a^*$, $-a^*$, $+b^*$, $-b^*$ contribution of red, green, yellow and blue, respectively. The total change in color is denoted by dE .

Results and discussion

Dispersive-morphological properties

Synthesis of silica/lignin hybrids was carried out using three types of silica (Syloid 244, Aerosil 200, and specially prepared hydrated silica), the surface of which was initially modified by aminosilane. Each of the three types of silica (Table 2), the presence of single primary particles of nanometric size, which tend to create aggregates ($<1\ \mu\text{m}$), as well as agglomerates ($>1\ \mu\text{m}$), can be noticed. In the process of hybrid material synthesis, a constant quantity of silica was used, with the addition of appropriate quantities of lignin and H_2O_2 oxidant. The SEM images of silicas and kraft lignin used have already been presented in our previous publications (Kłapiszewski et al., 2013b, Kłapiszewski et al., 2014, Jasionowski et al., 2014b).

The particle size distributions obtained for the silica/lignin hybrid materials are nano- and micrometric (Table 2). The primary particles in sample SL 1 have sizes in the range of 79–142 nm, and comparable results were recorded for samples SL 2 and SL 3. Slightly higher particle sizes equal to 142–220 nm were obtained with the hybrid material containing the largest quantity of lignin (50 parts by weight). These particles showed a tendency to form agglomerates. It was shown that the higher the quantity of lignin in the material, the greater is this tendency. The size of the agglomerates is 1480–4150 nm in the first sample, and 1480–5560 nm in the last one.

Table 2. Particle size distribution for precursors and for obtained silica/lignin hybrid materials

Sample	Type of silica	Content of lignin in relation to the modified silica matrix (wt./wt.)	Particle size distribution (Zetasizer Nano ZS) (nm)
Syloid 244	Syloid 244		39-68; 1720-2300
Syloid 244 + aminosilane	Syloid 244		51-79; 1720-2670
Aerosil 200	Aerosil 200		68-106; 1480-3370
Aerosil 200 + aminosilane	Aerosil 200	-	79-142; 1720-4150
Hydrated silica	Hydrated silica		44-59; 1110-5560
Hydrated silica + aminosilane	Hydrated silica		59-106; 1480-5560
Lignin	-		1990-2670; 3580-5560
SL 1		3	79-142; 1480 4150
SL 2	Syloid 244	10	91-122; 1280-4800
SL 3	Syloid 244	20	91-142; 1280-5560
SL 4	Syloid 244	50	142-220; 1480-5560
AL 1		3	79-106; 1110-4800
AL 2	Aerosil 200	10	106-142; 1280-5560
AL 3	Aerosil 200	20	91-220; 2300-5560
AL 4	Aerosil 200	50	122-295; 1720-5560
HL 1		3	79-220; 1990-5560
HL 2	Hydrated silica	10	91-295; 2300-5560
HL 3	Hydrated silica	20	91-342; 2670-5560
HL 4	Hydrated silica	50	106-342; 2670-5560

The analysis using a Zetasizer Nano ZS apparatus, as well as the SEM images (Fig. 4), confirm a tendency of particles to form agglomerative systems. Particles of the composites exhibit irregular shapes.

In the further study, hybrid samples were prepared from a different commercial silica Aerosil 200, for which SEM images are shown in Fig. 5. The particle sizes, which were obtained, are relatively higher than those for the samples based on the previous silica, particularly in the case of the composite containing the greatest amount of lignin. The particles of this product show a tendency to form the agglomerates of size 1720–5560 nm and a slightly greater. This tendency is exhibited in this case by the hybrid material containing 20 parts by weight of lignin. The best dispersive-morphological properties were recorded for the material containing 3 parts by weight of lignin per 100 parts silica. The diameters are in the range 79–106 nm, with a tendency towards agglomeration in the range of 1110–4800 nm (Table 2).

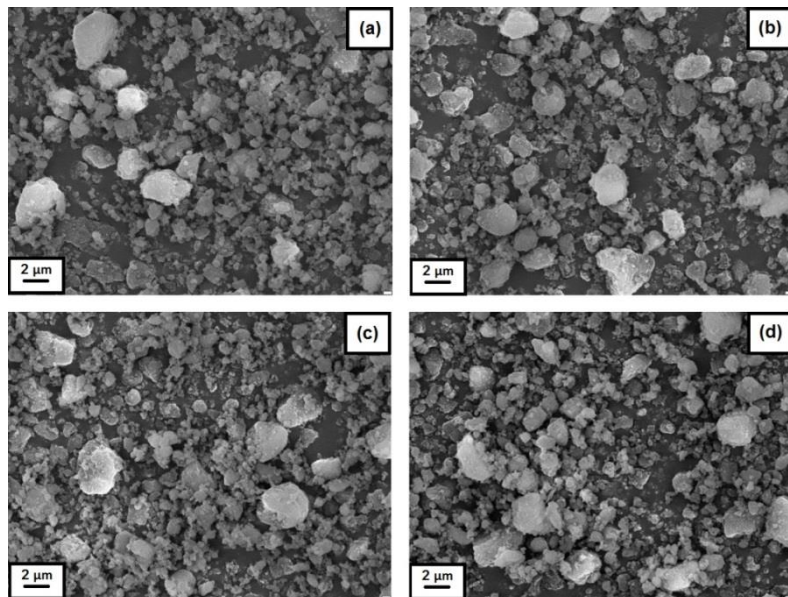


Fig. 4. SEM images of the silica/lignin hybrid materials labeled as (a) SL 1, (b) SL 2, (c) SL 3 and (d) SL 4

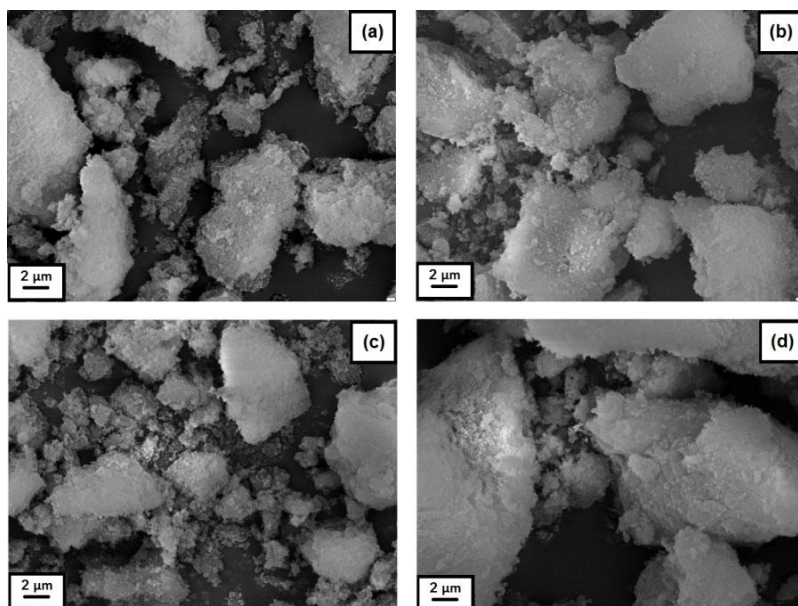


Fig. 5. SEM images of the silica/lignin hybrid materials labeled as (a) AL 1, (b) AL 2, (c) AL 3 and (d) AL 4

The SEM images (Fig. 5) indicate the presence of particles with irregular shapes. In addition, the presence of primary particles and a large number of secondary agglomerates was confirmed. As the quantity of lignin relative to the silica matrix increases, the individual molecules show a greater tendency to form the agglomerates.

Table 2 shows results of the dispersive properties of hybrids based on hydrated silica, recorded on a Zetasizer Nano ZS. The data show the products to have greater heterogeneity than the previously analyzed samples based on commercial silica. This finding is confirmed by the wide range of particle size distribution. A range of 79–220 nm was recorded for HL 1, rising with increasing quantity of biopolymer in the sample, up to 106–342 nm for the sample HL 4. With increasing content of lignin, the hybrid samples show an increasing tendency towards agglomeration, similarly to the previous samples. The particles based on hydrated silica show a markedly greater tendency to form agglomerates, but in each of these products the agglomerates reach a size of 5560 nm. The results are confirmed by the SEM images (Fig. 6) showing the presence of small particle agglomerates and larger clusters. The SEM images indicate the presence of particles of irregular shapes.

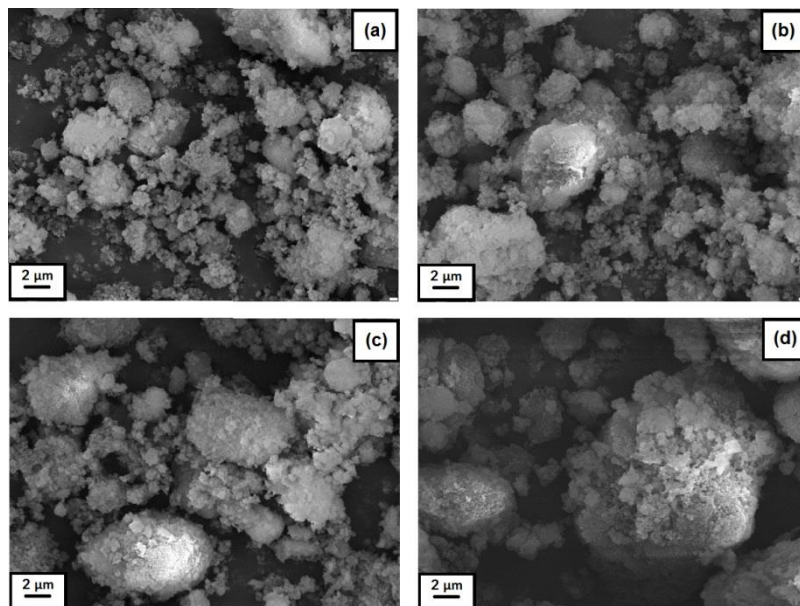


Fig. 6. SEM images of silica/lignin hybrids based on hydrated silica:
 (a) HL 1, (b) HL 2, (c) HL 3 and (d) HL 4

The pure silicas have nanometric particles with tendency to aggregation and agglomeration. A small addition of lignin in silica/lignin hybrids already causes a slight increase in the particle size. Moreover, with increasing content of lignin the amount of agglomerates increases, as shown by the data from Zetasizer Nano ZS (Table 2) and SEM images (Figs. 4-6). It should be mentioned that the commercial

kraft lignin used in the study contains the particles of sizes representing a wide range, what indicates the possibility of large agglomerates formation.

Elemental analysis

Based on the results of elemental analysis, the contents of nitrogen, carbon, hydrogen and sulfur in the analyzed samples were determined. The results given in Table 3, indirectly confirm the effectiveness of the methodology for silica/lignin hybrid synthesis. The results show that after modification of silica using aminosilane the content of nitrogen increased to 0.52% for Syloid 244, 0.54% for Aerosil 200 and 0.55% for hydrated silica). It indicates on indirect evidence of the presence of this element in the used silane. Lignin contains in its structure approximately 3 % by mass of sulfur, derived from the kraft process. The increase in the quantity of this element with increasing lignin content in the hybrid materials serves as evidence of successful interconnection of the biopolymer with the modified silica surface. The analyzed samples were found to contain quantities of nitrogen, which comes from the silica modifier. In comparison to the aminosilane-grafted silica samples the percentage content of nitrogen for silica/lignin hybrid materials slightly decreased. As the weight contribution of lignin in proportion to silica increases, an increase in carbon and hydrogen content being the main building elements of the biopolymer structure was observed. The results given in Table 2 support the conclusion that, based on all of the silicas used, expected and desirable hybrid systems were obtained. Hydrated silica appears to be the best support, since it shows the highest increase in the content of individual elements as the lignin contribution rises. For a sample containing 50 parts by weight of kraft lignin per 100 parts of hydrated silica, a carbon contribution of 10.98% was recorded, which is greater than the value for product HL 1 (C = 3.01%). Moreover, attention should be paid to the results of the elemental analysis of pure silicas. In this case, there is a clear similarity in the results for the carbon and hydrogen contents. The low content of these elements indicates the high purity of silicas used in the research. The results of this analysis indirectly confirm the effective interconnection of each type of silica with kraft lignin, which supports the correctness of the methodology used in the experiments.

FTIR spectroscopy

The FTIR analysis was performed to identify the functional groups present in the structure of silica, lignin and selected SiO_2 /lignin hybrid materials. The measurements were performed for samples of silica/lignin hybrids containing 3, 10, 20 and 50 parts by weight of lignin per 100 parts SiO_2 , obtained using commercial silicas and hydrated silica with the addition of lignin oxidized with H_2O_2 .

Table 3. Elemental content of nitrogen, carbon, hydrogen and sulfur in precursors and silica/lignin hybrids

Sample	N	Elemental content (%)		
		C	H	S
Syloid 244	—	0.19	0.13	—
Syloid 244 + aminosilane	0.52	1.32	1.42	—
Aerosil 200	—	0.11	0.12	—
Aerosil 200 + aminosilane	0.54	1.23	1.29	—
Hydrated silica	—	0.19	0.10	—
Hydrated silica + aminosilane	0.55	1.37	1.61	—
Lignin	—	42.2	5.02	3.14
SL 1	0.32	2.31	1.23	0.12
SL 2	0.30	4.32	1.30	0.28
SL 3	0.26	5.81	1.33	0.53
SL 4	0.21	9.83	1.40	0.81
AL 1	0.35	2.53	1.31	0.14
AL 2	0.33	5.01	1.38	0.31
AL 3	0.29	6.63	1.40	0.56
AL 4	0.27	10.03	1.49	0.93
HL 1	0.36	3.01	1.34	0.16
HL 2	0.33	5.89	1.45	0.38
HL 3	0.30	7.05	1.49	0.71
HL 4	0.28	10.98	1.56	1.08

The spectra of the pure silicas (Fig. 7a shows a single common spectrum for Aerosil and Syloid silicas because of their very great similarity) reveal the presence of physically bound water, as confirmed by the broad band in the range 3600–3200 cm⁻¹ coming from stretching vibrations of O–H groups. Additionally, a band at wavenumber 1650 cm⁻¹ is caused by bending vibrations of the same group. The bands that occur at 1200–1000 and 810 cm⁻¹ are attributed to stretching vibrations of Si–O–Si. Stretching vibrations of Si–OH give rise to bands at wavenumber 960 cm⁻¹, while the bands at 490 cm⁻¹ are attributed to stretching vibrations of Si–O. The results are consistent with data presented elsewhere (Roy et al., 2010, Kłapiszewski et al., 2013b, Szwarc-Rzepka et al., 2013).

The FTIR spectrum of kraft lignin is presented in Fig. 7a. The results show the presence of stretching vibrations of O–H groups in the range 3600–3200 cm⁻¹, and stretching vibrations of C–H (–CH₂, –CH₃) at 2950–2820 cm⁻¹. Stretching vibrations from the ketone group C=O produce the bands at 1710–1550 cm⁻¹, while those at 1600, 1510 and 1420 cm⁻¹ are attributed to stretching vibrations of the C–C, C=C bonds in the aromatic skeleton. Stretching vibrations of ether groups (C–O–C) appear at 1100–1000 cm⁻¹, and other bands in the range 1360–1200 cm⁻¹ correspond to stretching vibrations of C–O (C–O(H), C–O(Ar)). Below 1000 cm⁻¹ the spectrum contains bands attributed to in-plane and out-of-plane vibrations of aromatic C–H bonds. The presented analysis of kraft lignin is in agreement with previously published data (Kłapiszewski et al., 2013b; Tejado et al., 2007).

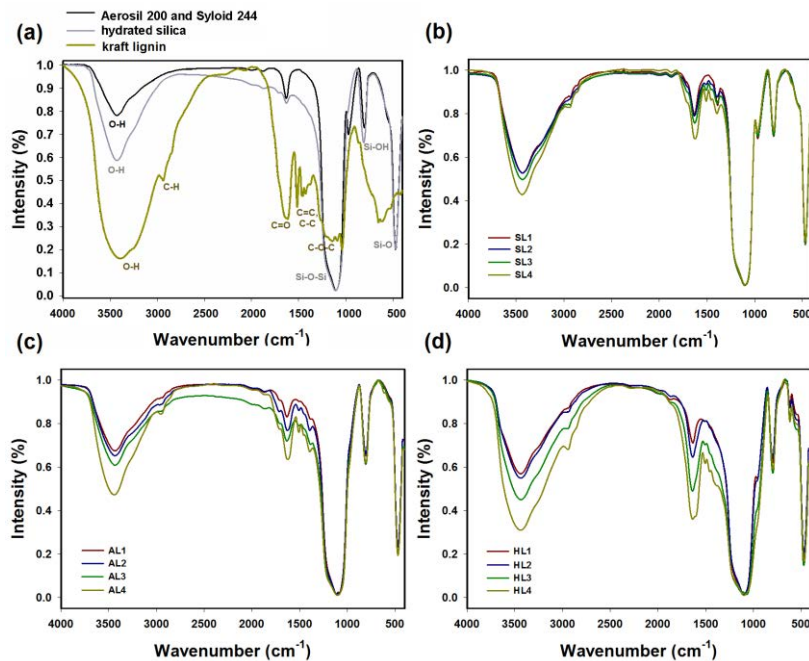


Fig. 7. FTIR spectra of precursors (a) and silica/lignin hybrids based on Syloid 244 (b), Aerosil 200 (c) and hydrated silica (d)

Selected SiO_2 /lignin hybrids were also analyzed. The analyzed samples contain 3, 10, 20 and 50 parts by weight of lignin oxidized by hydrogen peroxide per 100 parts SiO_2 . Based on the FTIR spectra (see Figs. 7b-d), the presence of characteristic functional groups was verified. The spectra reveal the presence of the characteristic bonds coming from silica: Si–O–Si symmetric stretching vibrations at 1200–1050 cm^{-1} and asymmetric stretching vibrations at 800 cm^{-1} . The bands at 960 cm^{-1} are attributed to stretching vibrations of Si–OH, and bending vibrations of Si–O appear at 485 cm^{-1} . An important broad band in the range of 3600–3200 cm^{-1} comes from stretching vibrations of O–H groups, which occur in the structure of both lignin and silica. Moreover the functional groups observed in pure lignin are present: C–H bonds at 3000–2800 cm^{-1} and different types of carbon atom bonds in the range of 1650–1300 cm^{-1} . The number of C=O, O–C–O and O=C–O bonds was greater than in kraft lignin.

The FTIR spectra presented in Figs. 7b and 7c belong to hybrids based on the commercial silicas Syloid 244 and Aerosil 200 respectively. Based on the FTIR spectra for the pure precursors and for the materials obtained, it is observed that the intensity of bands was greater in the hybrids than in the pure materials. This confirms the effectiveness of the proposed method of synthesis, which is associated with an increase in the intensity of the bands corresponding to the relevant functional groups. Furthermore, the intensity of bands increases with increasing the content of lignin in

the hybrid material, and larger intensities were observed with the use of hydrated silica (Fig. 7d). The proposed mechanisms for combination of silica with lignin (a biopolymer activated using sodium periodate) were described by Jesionowski et al. (2014 b).

TGA analysis

Thermal stability measurements of silica, lignin and inorganic-organic materials were performed. The resulting thermogravimetric curves show the mass loss of samples caused by the transitions that occur as the temperature increases.

Figure 8a shows the TGA curves obtained for the precursors used. Syloid 244 silica shows high thermal stability. A mass loss was observed at 100 °C (of about 5 %; all types of silica gave similar TGA curves, so only the curve for Syloid 244 is shown), associated with the loss of water structurally bound with the precursor. In the case of lignin the thermogravimetric curve shows a clearly larger mass loss in comparison with silica. The TGA curve recorded for lignin indicates a significant mass loss of about 65 % relative to the initial mass of the sample. The first small mass loss of about 10 % taking place at 20–150 °C is mainly a result of the removal of water bound to the lignin surface. The second, larger mass loss of about 35 % taking place in the range 200–600 °C is related to the complex thermal decomposition of lignin, involving the formation of new bonds as a consequence of crosslinking reactions. The third mass loss of about 15 % observed in the range 600–1000 °C is interpreted as a consequence of the partial elimination of carbon fragments caused by fragmentation of the molecules in uncontrolled and undetermined reactions.

Figure 8b shows the thermogravimetric curves of silica/lignin hybrids based on Syloid 244. Sample SL 4, which has the highest content of lignin in proportion to silica among the analyzed products, showed the lowest thermal stability. An increasing content of lignin in the product causes a decrease in thermal stability, as indicated by the larger mass loss. The shape of the TGA curves is similar to that obtained for pure lignin; in the case of the materials there are again present three visible stages, the most visible in the sample with 50 parts by weight of lignin. The product containing 3 parts of lignin exhibits the smallest mass loss.

Additional confirmation of the decreasing thermal stability with increasing lignin content is provided by the TGA curves for hybrids based on Aerosil 200 (Fig. 8c). These results show that composites based on this silica have the best thermal stability when the lignin content is the smallest.

Hybrids based on hydrated silica (Fig. 8d) exhibit poorer thermal stability than samples containing the commercial silicas Syloid 244 and Aerosil 200 (Figs. 8b and 8c). A common feature is that the mass loss is larger with an increase in lignin content in every case. In this case, however, mass loss is observed at lower temperatures than with the previous samples.

The final hybrid materials show rather greater thermal stability than is exhibited by pure lignin. In summary, the thermal analysis showed that the higher the content of

lignin in the product, the poorer its thermal stability. Moreover, with an increase in lignin content, the TGA curves become more similar to those of pure lignin, and the mass loss is larger. This may be caused by either a lack of oxidation or degradation of the materials. As regards the type of silica used, the best properties are exhibited by the commercial silica Aerosil 200, and the worst by hydrated silica. These results may indicate that the synthesis of lignin with hydrated silica is less effective in hybrid formation than the method using commercial silica. The attractive TGA results obtained at this stage of the study suggest that the silica/lignin products can be used as a new generation of polymer fillers.

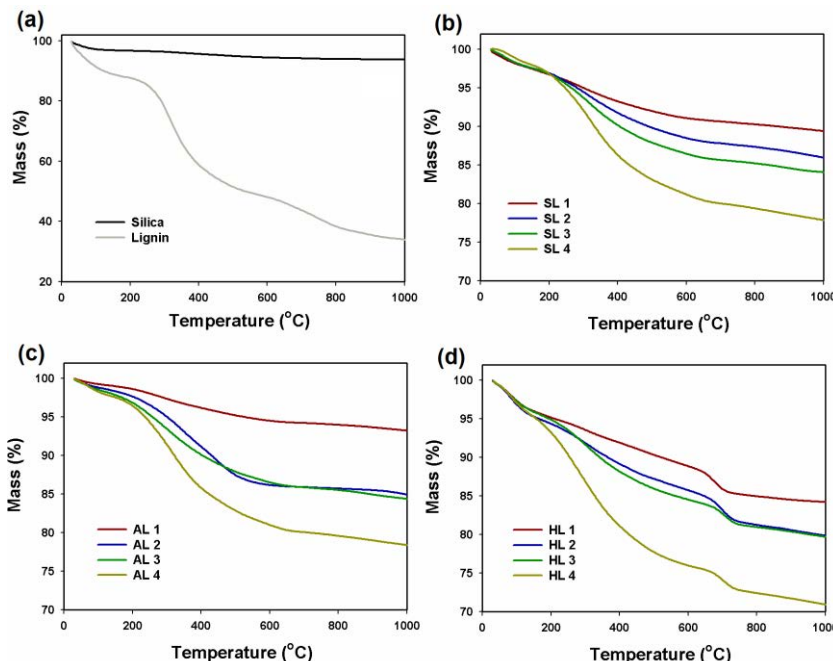


Fig. 8. Thermal stability of silica and lignin (a) and silica/lignin hybrids based on Syloid 244 (b), Aerosil 200 (c) and hydrated silica (d)

Colorimetric analysis

For the synthesized silica/lignin products as well as for the initial precursors, the colorimetric analysis was carried out using the $CIE L^*a^*b^*$ color system. The results obtained for the pure precursors are given in Table 4. Silica is white, while lignin is a dark-brown solid. The parameter L^* , which determines lightness, shows that the highest lightness is provided by the commercial silica Aerosil 200 (93.78), a very similar value is recorded for Syloid 244, and slightly worse results are obtained in the case of hydrated silica (92.93). Because of its dark color, the lightness value of lignin is 41.26. In the case of the parameters a^* and b^* , reflecting the contribution of red and

yellow color in the sample, the lowest values are obtained for the hydrated silica, with increased values for the commercial silicas, while for pure lignin the values are 10.16 (a^*) and 25.92 (b^*). Another important parameter in the colorimetric analysis is the dE variable, which determines the total color change.

Table 4. Colorimetric data for silicas, lignin and SiO_2 /lignin products

Sample	Colorimetric data			
	L^*	a^*	b^*	dE
Syloid 244	93.63	0.22	2.13	-
Syloid 244 + aminosilane	93.58	0.22	2.15	-
Aerosil 200	93.78	0.24	2.55	-
Aerosil 200 + aminosilane	93.72	0.23	2.54	-
Hydrated silica	92.93	0.18	2.01	-
Hydrated silica + aminosilane	92.90	0.19	1.97	-
Lignin	41.26	10.16	25.92	-
SL 1	88.91	3.56	10.31	13.85
SL 2	82.35	3.98	12.37	15.91
SL 3	75.34	4.53	13.77	19.43
SL 4	71.15	5.53	15.01	21.98
AL 1	87.35	3.05	9.89	13.15
AL 2	81.19	4.18	11.93	16.03
AL 3	77.03	4.87	14.87	17.93
AL 4	72.83	6.13	15.93	22.19
HL 1	86.05	2.95	9.93	13.98
HL 2	80.15	4.03	12.33	15.32
HL 3	75.98	4.78	16.66	19.97
HL 4	70.01	6.90	17.17	24.88

Table 4 contains data obtained from the colorimetric analysis of silica/lignin materials. The samples were prepared by addition of different quantities of lignin oxidized by H_2O_2 to the selected type of silica. Modification of silica with aminosilane had no effect on lightness of the unmodified SiO_2 sample. Surface functionalization of silica using an appropriate amount of lignin solution caused a significant decrease in the lightness parameter L^* . For example, the reference sample (unmodified Syloid 244) had a value of $L^*=93.63$. Modification by different quantities of lignin caused a decrease in the parameter to $L^*=88.91$ for sample SL 1 and to $L^*=71.15$ for SL 4. A decrease in these values was also observed in the case of other samples, regardless of the type of silica.

The parameters a^* and b^* reflect the change in the contribution of the colors red and yellow, respectively, as a result of modification of silica by kraft lignin. The

colorimetric analysis shows an increase in the contribution of red color with an increase in the lignin content of the sample. The change in the contribution of yellow is not so significant, but also shows a slight upward trend. This can be seen in the color of the obtained biomaterials – from light beige to dark brown. The dE parameter was used to describe the complete change of color. This also confirms the correctness of the measurements performed, as the value initially increases with increasing content of lignin in the product. The greatest differences can be seen between the samples containing 3 and 50 parts by weight of lignin per 100 parts silica, for which the respective values of dE are 13.98 (HL 1) and 24.88 (HL 4).

The colorimetric analysis showed that a small addition of lignin causes a significant change in all of the listed parameters describing the color space *CIE L*a*b**, with respect to the initial silica used as the point of reference. Lower values of the lightness L^* , and higher values of the parameters a^* and b^* , were recorded for the hybrids based on hydrated silica in comparison with those based on commercial silicas. These changes are conditioned by, among other things, the types of SiO_2 used, as shown by the data in Table 4.

Conclusions

The proposed method of preparation of silica/lignin hybrids, based on silica surface-functionalized with H_2O_2 oxidized lignin solution, makes it possible to obtain a product with defined physicochemical and dispersive-morphological properties.

The particle size distributions and SEM images of silica/lignin hybrids indicate that an increase in the proportion of lignin in the material reduces the quantity of individual primary particles of small size, at the expense of the formation of larger groups of units. Products with the most favorable dispersive-morphological properties were obtained by adding a small amount of lignin.

The effectiveness of preparation of silica/lignin materials was confirmed by FTIR spectra. This analysis shows that the process for the preparation of the materials proceeded correctly. With an increase in the quantity of lignin used, better combination with the silica matrix was observed. The efficiency of precursors combination was also confirmed by the elemental analysis.

The thermogravimetric analysis of products indicates their good thermal stability in comparison with pure lignin. With an increasing quantity of lignin per 100 parts by weight of silica matrix, a progressive decline in the thermal stability of the materials was observed. The results obtained from the thermal analysis indicate that the hybrids created based on silica and lignin will successfully find application as novel polymer fillers.

The colorimetric analysis showed that a small addition of lignin significantly alters the color parameters in the colorimetric system *CIE L*a*b** with respect to the initial silica used as the reference point. Moreover, values of parameter L^* indicated a decrease in lightness with increasing quantity of lignin in the material. An increase in

the lignin content of the hybrid materials also led to an increase in contribution of red color (parameter a^*).

Acknowledgements

The study was financed within the National Science Centre Poland funds according to decision no. DEC-2013/09/B/ST8/00159.

References

BERGNA H.E., ROBERTS W.O., 2006, *Colloidal Silica: Fundamentals and Applications*, Taylor & Francis Group, Boca Raton.

BOERJAN W., RALPH J., BAUCHER M., 2003, *Lignin biosynthesis*. Annual Review of Plant Biology, 54, 519–546.

BULA K., KŁAPISZEWSKI L., JESIONOWSKI T., 2015, *A novel functional silica/lignin hybrid material as a potential bio-based polypropylene filler*. Polymer Composites, 36, 913–922.

CRESTINI C., SALADINO R., TAGLIATESTA P., BOSCHI T., 1999, *Biomimetic degradation of lignin and lignin model compounds by synthetic anionic and cationic water soluble manganese and iron porphyrins*. Bioorganic & Medicinal Chemistry, 7, 1897–1905.

CRESTINI C., CRUCIANELLI M., ORLANDI M., SALADINO R., 2010, *Oxidative strategies in lignin chemistry: A new environmental friendly approach for the functionalization of lignin and lignocellulosic fibers*. Catalysis Today, 156, 8–22.

DONALDSON L.A., 2001, *Lignification and lignin topochemistry – an ultrastructural view*. Phytochemistry, 57, 859–873.

HASEGAWA I., FUKUDA Y., OKADA T., KAJIWARA M., 1998, *Lignin-silica-titania hybrids as precursors for Si-Ti-C-O fibers*. Journal of Sol-Gel Science and Technology, 13, 485–488.

HASEGAWA I., FUJII Y.S., YAMADA K., KARIYA C., TAKAYAMA T., 1999, *Lignin–silica hybrids as precursors for silicon carbide*. Journal of Applied Polymer Science, 73, 1321–1328.

JESIONOWSKI T., KRYSZTAFKIEWICZ A., 2000, *Comparison of the techniques used to modify amorphous hydrated silica*. Journal of Non-Crystalline Solids, 277, 45–57.

JESIONOWSKI T., 2001, *Preparation of colloidal silica from sodium metasilicate solution and sulphuric acid in emulsion medium*. Colloids and Surfaces A: Physicochemical and Engineering Aspects, 190, 153–165.

JESIONOWSKI T., 2009, *Preparation of spherical silica in emulsion systems using the co-precipitation technique*. Materials Chemistry and Physics, 113, 839–849.

JESIONOWSKI T., CIESIELCZYK F., KRYSZTAFKIEWICZ A., 2010, *Influence of selected alkoxysilanes on dispersive properties and surface chemistry of spherical silica precipitated in emulsion media*. Materials Chemistry and Physics, 119, 65–74.

JESIONOWSKI T., KŁAPISZEWSKI L., MILCZAREK G., 2014a, *Structural and electrochemical properties of multifunctional silica/lignin materials*. Materials Chemistry and Physics, 147, 1049–1057.

JESIONOWSKI T., KŁAPISZEWSKI L., MILCZAREK G., 2014b, *Kraft lignin and silica as precursors of advanced composite materials and electroactive blends*. Journal of Materials Science, 49, 1376–1385.

KADOKAWA J., 2013, *Applications of Ionic Liquids in Lignin Chemistry*, InTech, Rijeka.

KLAPISZEWSKI L., MADRAWSKA M., JESIONOWSKI T., 2012, *Preparation and characterisation of hydrated silica/lignin biocomposites*. Physicochemical Problems of Mineral Processing, 48, 463–473.

KLAPISZEWSKI L., NOWACKA M., SZWARC-RZEPKA K., JESIONOWSKI T., 2013a, *Advanced biocomposites based on silica and lignin precursors*. Physicochemical Problems of Mineral Processing, 49, 463–473.

KLAPISZEWSKI L., NOWACKA M., MILCZAREK G., JESIONOWSKI T., 2013b, *Physicochemical and electrokinetic properties of silica/lignin biocomposites*. Carbohydrate Polymers, 94, 345–355.

KLAPISZEWSKI L., ZDARTA J., SZATKOWSKI T., WYSOKOWSKI M., NOWACKA M., SZWARC-RZEPKA K., BARTCZAK P., SIWIŃSKA-STAFANSKA K., EHRLICH H., JESIONOWSKI T., 2014, *Silica/lignosulfonate hybrid materials: Preparation and characterization*. Central European Journal of Chemistry, 12, 719–735.

KLAPISZEWSKI L., BARTCZAK P., WYSOKOWSKI M., JANKOWSKA M., KABAT K., JESIONOWSKI T., 2015, *Silica conjugated with kraft lignin and its use as a novel 'green' sorbent for hazardous metal ions removal*. Chemical Engineering Journal, 260, 684–693.

KRYSZTAFKIEWICZ A., RAGER B., JESIONOWSKI T., 1997, *The effect of surface modification on physicochemical properties of precipitated silica*. Journal of Materials Science, 32, 1333–1339.

LANGE H., DECINA S., CRESTINI C., 2013, *Oxidative upgrade of lignin – Recent routes reviewed*. European Polymer Journal, 49, 1151–1173.

LOTA G., MILCZAREK G., 2011, *The effect of lignosulfonates as electrolyte additives on the electrochemical performance of supercapacitors*. Electrochemistry Communications, 13, 470–473.

MEISTER J.J., 2002, *Modification of lignin*. Journal of Macromolecular Science C: Polymer Reviews, 42, 235–289.

MISHRA S.B., MISHRA A.K., KRAUSE R.W., MAMBA B.B., 2009, *Synthesis of silicon carbide nanowires from a hybrid of amorphous biopolymer and sol-gel derived silica*. Journal of the American Ceramic Society, 92, 3052–3058.

RALPH J., LUNDQUIST K., BRUNOW G., LU F., KIM H., SCHATZ P.F., MARITA J.M., HATFIELD R.D., RALPH S.A., CHRISTENSEN J.H., BOERJAN W., 2004, *Lignins: Natural polymers from oxidative coupling of 4-hydroxyphenylpropanoids*. Phytochemistry Reviews, 3, 29–60.

ROY S., DIXIT C.K., WOOLLEY R., McCRAITH B.D., O'KENNEDY R., McDONAGH C., 2010, *Novel multiparametric approach to elucidate the surface amine-silanization reaction profile on fluorescent silica nanoparticles*. Langmuir, 26, 18125–18134.

STÖBER W., FINK A., BOHN E., 1968, *Controlled growth of monodisperse silica spheres in the micron size range*. Journal of Colloid and Interface Science, 26, 62–69.

SZWARC-RZEPKA K., CIESIELCZYK F., JESIONOWSKI T., 2013, *Preparation and physicochemical properties of functionalized silica/octamethacryl-silsesquioxane hybrid systems*. Journal of Nanomaterials, Article ID 674237, 1–15.

TEJADO A., PENA C., LABIDI J., ECHEVERRIA J.M., MONDRAGON I., 2007, *Physico-chemical characterization of lignin from different sources for use in phenol-formaldehyde resin synthesis*. Bioresource Technology, 98, 1655–1663.

TELYSHEVA G., DIZHBITE T., EVTUGUIN D., MIRONOVA-ULMANE N., LEBEDEVA G., ANDERSONE A., BIKOVENS O., CHIRKOVA J., BELKOVA L., 2009, *Design of siliceous lignins – novel organic/inorganic hybrid sorbent materials*. Scripta Materialia, 60, 687–690.

TERTYKH V.A., YANISHPOLSKII V.V., BOL'BUKH Y., 2003, *Synthesis and characterization of functional chemically modified silica fillers*. Macromolecular Symposia, 194, 141–146.

TERTYKH V.A., IVASHCHENKO N.A., YANISHPOLSKII V.V., KHAINAKOV S.A., 2013, *Platinum nanoparticles on the surface of silica modified with silicon hydride groups*. Materials Science & Engineering Technology, 44, 239–243.

VANHOLME R., DEMEDTS B., MORREEL K., RALPH J., BOERJAN W., 2010, *Lignin biosynthesis and structure*. Plant Physiology, 153, 895–905.

WYPYCH G., 2010, *Handbook of Fillers*, ChemTec Publishing, Toronto.

ZAKZESKI J., JONGERIUS A.L., WECKHUYSEN B.M., 2010, *Transition metal catalysed oxidation of Alcell lignin, soda lignin, and lignin model compounds in ionic liquid*. Green Chemistry, 12, 1225–1236.

ZAKZESKI J., BRUIJNINEX P.C.A., WECKHUYSEN B.M., 2011, *In situ spectroscopic investigation of the cobalt-catalyzed oxidation of lignin model compounds in ionic liquids*. Green Chemistry, 13, 671–680.

ZURAWSKA J., KRYSZTAFKIEWICZ A., JESIONOWSKI T., 2003, *Active silicas obtained by precipitation from mixtures of sodium metasilicate and ammonium chloride solutions*. Journal of Chemical Technology and Biotechnology, 78, 534–541.

Received May 1, 2015; reviewed; accepted September 26, 2015

PRESSURE ACID LEACHING OF SPHALERITE CONCENTRATE. MODELING AND OPTIMIZATION BY RESPONSE SURFACE METHODOLOGY

Erkan GULER

Dokuz Eylul University, Faculty of Engineering, Mining Engineering Department, 35390, Buca, Izmir, Turkey
eguler@deu.edu.tr

Abstract: The zinc leaching from sphalerite concentrate using oxygen under pressure in sulfuric acid solution was primarily studied and evaluated. The effects of important leaching parameters such as oxygen partial pressure, temperature, solid/liquid ratio and leaching time on leaching efficiency, Zn concentration and Fe extraction were investigated. Response surface methodology based on central composite rotatable design technique was used to optimize the leaching process parameters in order to obtain a suitable leach solution with high Zn leaching efficiency considering further processes such as precipitation of contaminating metal ions and electrolysis. The optimum leaching condition for maximum Zn leaching efficiency and Zn concentration with minimum Fe extraction was determined as follows: oxygen partial pressure of 12 bars, temperature of 150 °C, solid/liquid ratio of 0.20 and leaching time of 89.16 minutes. The achieved experimental results for Zn leaching efficiency, Zn concentration and Fe extraction under the optimum conditions were as 94%, 80 g/dm³ and 8.1% respectively. The experimental results corresponded well with the predicted results of quadratic polynomial models.

Keywords: *pressure leaching, sphalerite concentrate, optimization, response surface methodology, central composite rotatable design*

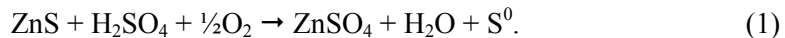
Introduction

Zinc sulfide is a predominant form of zinc in the earth crust and sphalerite (ZnS) is the most important mineral among them. Many processes have been developed over decades and at present, nearly 80–85% of total zinc production is carried out by hydrometallurgical processes which include roasting, leaching and electrowinning steps (RLE). In order to prevent the increase in investment and operating costs, zinc sulfide ore is concentrated using froth flotation in practice. Sphalerite concentrates contain approximately 50% Zn. The concentrated sphalerite is roasted to produce zinc oxide followed by leaching with weak sulfuric acid and solution purification from

other metal impurities using succession of appropriate methods. After this step, high purity metallic zinc is produced by electrolysis.

Roasting stage of the process has some major drawbacks. During calcination, SO_2 is released causing environmental pollution. In addition, iron combines with zinc to form zinc ferrite (ZnFe_2O_4) which cannot be leached in weak acid solution. Bypassing the roasting stage for metallic zinc production is mostly preferred from economic and environmental perspective. For this purpose, two alternative processes were proposed in the 1970's and several different leaching studies have been accomplished by many researchers in the course of time: Direct atmospheric leaching in which sphalerite concentrates are leached directly with some oxidizing agents such as acids (Copur, 2002), alkalis (Zhang et al., 2008), ferric salts (Crundwell, 1987; Dutrizac, 1992; Jin et al., 1993; Palencia Perez and Dutrizac, 1991; Santos et al., 2010), hydrogen peroxide (Balaz and Ebert, 1991), oxygen, ammonium, sodium and potassium persulfates (Babu et al., 2002), manganese dioxide (Rao and Paramguru, 1998), and bacteria (da Silva, 2004; Gomez et al., 1997; Haghshenas et al., 2012); and pressure leaching carried out using oxygen under pressure with similarly contributing some oxidizing agents in autoclaves (Baldwin and Demopoulos, 1995; Dehghan et al., 2008; Gu et al., 2010; Harvey et al., 1993; Li et al., 2010a; Xie et al., 2007).

The pressure leaching has been commercially used in several zinc ore/concentrate leaching plants (Filippou, 2004; Ozberk et al., 1995). As an environmentally friendly and economical technology, high pressure leaching is an alternative to conventional RLE route. The pressure leaching reaction of sphalerite is shown in Eq. 1:



Reaction (1) is slow in absence of dissolved iron, which facilitates the oxygen transfer (Au-Yeung and Bolton, 1986; Crundwell, 1998). In order to dissolve sphalerite, which is a semiconductor with a wide band gap, by an oxidative mechanism, electron must be removed from the bonding orbitals by the oxidant in solution (Crundwell, 2013). In the absence of iron species in solution, dissolved oxygen reacts at the mineral surface to form intermediate oxides (e.g. H_2O_2 and HO_2). This results in a relatively slow discharge of oxygen due to the strength of the oxygen-oxygen double bond (Wadsworth, 1972). In case the presence of iron and oxygen in solution, an electrochemical reaction is occurred at the mineral surface. $\text{Fe}^{3+}/\text{Fe}^{2+}$ redox couple dominates the surface potential of the mineral. During the dissolution reaction ferric iron reduces to form ferrous iron, then ferrous iron is oxidized to ferric iron by dissolved oxygen in solution (Verbaan and Crundwell, 1986).

Despite the reaction mechanism of sphalerite has been investigated in detail (Crundwell, 1987; Verbaan and Crundwell, 1986) and determined that the reaction kinetics depend on the iron content of the crude ore or concentrate of sphalerite (Palencia Perez and Dutrizac, 1991), the influence of experimental parameters and their interactions on the process results are not exactly figured out yet.

Conventionally, the study of the effects of experimental parameters on pressure acid leaching of sphalerite is carried out using an approach where one parameter at a time is varied. The effect of each experimental parameter is evaluated by altering the level of one parameter at a time while keeping the levels of the other parameters constant. However, this approach is very inadequate and does not provide any information about interactions between experimental parameters in a process. These interactions can be easily detected when a factorial design – through the use of methods such as response surface methodology (RSM) – is performed. In addition, factorial design provides more accurate estimation of the effects of the variables than the “one parameter at a time” approach with the same number of experimental runs (Liu et al., 2011). However, only a few cases of RSM application have been introduced in sphalerite leaching process (Dehghan et al., 2008; Haghshenas et al., 2012; Massacci et al., 1998).

The present study intends to assess the effects of parameters such as oxygen partial pressure, temperature, liquid/solid ratio and leaching time to identify the optimum pressure acid leaching conditions of sphalerite with highest Zn leaching efficiency, highest Zn concentration, lowest Fe extraction and quantify interactions between aforementioned parameters through response surface methodology based on the central composite rotatable design (CCRD).

Materials and methods

The concentrate was obtained from a sphalerite flotation plant in Western Turkey. Wet sample was dried at room temperature until it reached a constant weight. Samples were taken from the air-dried concentrate for sieving, chemical, XRD (Rigaku D/Max-2200 model diffractometer using $\text{CuK}\alpha$ radiation) and SEM-EDS (Jeol JXA-733 Superprobe) analysis. The chemical and mineralogical composition of the concentrate is presented in Table 1 and Fig. 1 respectively. The main mineralogical phases in sample are sphalerite and small quantities of pyrite, pyrrhotite, galena and quartz.

Table 1. Chemical composition of sphalerite concentrate (mass fraction, %)

Zn	Fe	Pb	Si	Al	Cu	Ca	Cd	Mg	Mn	S
42.71	11.21	2.39	1.01	0.20	0.18	0.18	0.16	0.11	0.10	34.26

The leaching solution was prepared by diluting concentrated sulfuric acid with distilled water in order to obtain a concentration of $1.5 \text{ mol}\cdot\text{dm}^{-3}$; then $0.1 \text{ g}\cdot\text{dm}^{-3}$ of sodium lignin sulfonate was added to the solution as sulfur dispersant. The leaching experiments were conducted in a 1-dm^3 titanium autoclave (Parr Inc., USA). The autoclave was equipped with a heating mantle, a PID temperature controller, a variable speed stirrer operated at 600 rpm, a sampling dip tube and an internally mounted serpentine type cooling coil. Pre-calculated amount of sphalerite concentrate

(-150 μm) was added into 500 cm^3 leaching solution. The reaction vessel was heated up to a pre-set temperature. The oxygen was admitted at the pre-set temperature and the partial pressure of oxygen was adjusted to the desired level and maintained constant during the whole experiment.

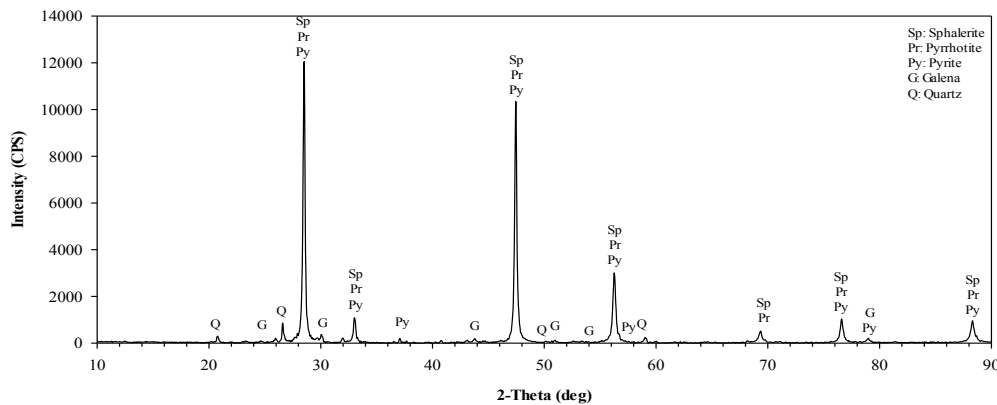


Fig. 1. XRD pattern of sphalerite concentrate

In the experiments, 20–30 cm^3 of slurry was sampled by a sampling dip tube. The slurry was cooled down immediately and filtrated by a 0.45 μm PTFE syringe filter. Metal ions content of the filtrate was analyzed by an ICP-OES (Varian 710-ES).

Representative samples were used in all experiments. All chemicals used were of analytical grade and all solutions were prepared with distilled water.

RSM is a statistical and mathematical technique utilized for multiple regression analysis using quantitative data obtained from properly designed experiments to solve multi-variable equations simultaneously. This method is useful for designing experiments, model building, evaluating the effects of experimental parameters and determining optimum conditions for desirable responses. Central composite rotatable design (CCRD), one of the techniques in RSM, is used extensively in building the second order response surface models (Li et al., 2010b).

A CCRD comprises 2^k factorial points (coded as ± 1), augmented by $2k$ star points (coded as $\pm \alpha$) and n_c center points (coded as 0). The parameter k is the number of controllable experimental parameters and α equals to $(2^k)^{1/4}$.

In this study, the sphalerite concentrate was leached using oxygen pressure leaching. The experiments are designed by varying the leaching parameters using the CCRD. The experimental parameters are (i) x_1 , oxygen partial pressure, (ii) x_2 , temperature, (iii) x_3 , solid/liquid ratio and (iv) x_4 , leaching time. The codes and levels of the experimental parameters studied in the experiments are listed in Table 2.

The behavior of the system can be explained by the following second order polynomial equation:

$$Y = \beta_0 + \sum_{i=1}^k \beta_i x_i + \sum_{i=1}^k \beta_{ii} x_i^2 + \sum_{i=1}^{k-1} \sum_{j=2}^k \beta_{ij} x_i x_j + \varepsilon \quad (2)$$

where Y is the predicted response, x_i and x_j are the experimental parameters, β_0 is the intercept term, β_i is the linear effects, β_{ii} is the squared effect, and β_{ij} is the interaction term (Aghaie et al., 2009).

Table 2. Codes and levels of experimental parameters for central composite rotatable design

Parameters	Symbol	Codes and Levels				
		-2	-1	0	+1	+2
Oxygen partial pressure (bar)	x_1	3	6	9	12	15
Temperature (°C)	x_2	105	120	135	150	165
Solid/liquid ratio	x_3	0.05	0.10	0.15	0.20	0.25
Leaching time (min)	x_4	15	40	65	90	115

In order to determine Zn extraction and concentration, and Fe extraction, pregnant leach solution was analyzed using ICP-OES. Metal extractions were calculated using metal concentration values obtained by ICP. In order to estimate the best parameter combination, both Zn extraction and concentration were selected as responses due to the experiments designed for different solid/liquid ratios.

The acid amount was selected by taking into consideration the previous investigations and the results of some pretesting. Xie et al. (2007) reported that Zn leaching rate decreases abnormally with a rise in initial sulfuric acid concentration. If the amount of sulfuric acid added in experiment is over twice the stoichiometric amount, the abnormality occurs. Therefore, the initial acid concentration was adjusted as 1.5 mol dm⁻³ which was between 1.15-fold and 2.30-fold in stoichiometric amount depending on the solid/liquid ratio.

Free acid (H₂SO₄) concentration was analyzed by the method described in the study by Kaya and Topkaya (2011) with the intent of determining the amount of acid remained after reaction in pregnant leach solution. The titration process in the method was conducted using Metrohm 842 Titrando model automatic titrator.

The polynomial equations for the responses were validated by the statistical test known as analysis of variance (ANOVA) for determination of the significance of each term in equations and also to estimate the goodness of fit in each case. Three-dimensional response surface graphs were plotted using Design Expert (version 7.0) software for the experimental results in order to determine the individual and interaction effects of the experimental parameters.

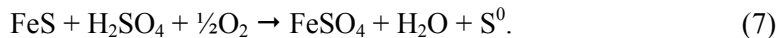
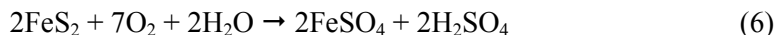
Results and discussion

Process mechanism

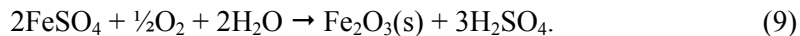
The net reaction of sphalerite dissolution (Eq. 1.) is the sum of the three reactions (Eqs 3–5) with the presence of dissolved iron in the acidic sulfate solution (Jan et al., 1976)



According to Eq. 5. there should be Fe^{3+} ions in the leaching solution for the removal of H_2S . In the case when the $\text{Fe}^{3+}/\text{Fe}^{2+}$ ions are not initially added to the solution, all of the needed Fe^{3+} ions are provided by the iron minerals in the concentrate such as pyrite and pyrrhotite. Dissolution of iron occurs as stated in the reactions listed below in the case of pyrite and pyrrhotite presence in the concentrate



Dissolved iron precipitates as jarosite and/or hematite in acidic sulfate solutions due to the hydrolysis of ferric iron at elevated temperature depending on the acidity and the amount of metal sulfate and monovalent cations in the leaching system (Acharya et al., 1992; Yue et al., 2014). Net reactions of the hydronium jarosite and hematite precipitations are stated below



Effects of oxygen pressure, temperature, solid/liquid ratio and leaching time

The CCRD method, which is very popular design for fitting second-order response surfaces, was applied in 30 leaching tests with appropriate combinations of the four parameters (oxygen partial pressure, temperature, solid/liquid ratio and leaching time). Experimental design matrix for CCRD with experimental responses is given in Table 3. The relative standard deviation of the experimental responses was calculated as below 3.66% with 6 replications at central levels of parameters.

The highest zinc extraction (> 94%) was achieved at 90 minutes with highest levels of oxygen partial pressure, temperature and solid/liquid ratio (Exp. 16).

By performing multiple regression analyses on the experimental responses, the experimental results of the CCRD designs were fitted with second-order polynomial equations for each response group. Thus, according to Eq. 2., the predicted models for Zn leaching efficiency, Zn concentrate in leach solution and Fe extraction are described in the following equations in terms of coded factors (between -2 and +2), respectively:

$$\begin{aligned} \text{Zn Leaching Efficiency (\%)} = & 78.02 + 4.34x_1 + 13.11x_2 + 6.47x_3 + 11.12x_4 - 1.41x_1x_2 + \\ & 1.43x_1x_3 - 1.68x_1x_4 + 1.21x_2x_3 - 4.74x_2x_4 + 0.35x_3x_4 - 1.96x_1^2 - 5.48x_2^2 - 1.99x_3^2 - 4.34x_4^2 \quad (10) \end{aligned}$$

$$\text{Zn Concentration (g dm}^{-3}) = 49.98 + 2.98x_1 + 8.57x_2 + 18.28x_3 + 7.18x_4 - 0.92x_1x_2 + 1.75x_1x_3 - 1.15x_1x_4 + 3.67x_2x_3 - 3.03x_2x_4 + 2.41x_3x_4 - 1.23x_1^2 - 3.49x_2^2 + 0.044x_3^2 - 2.76x_4^2 \quad (11)$$

$$\text{Fe Extraction (\%)} = 75.38 + 1.92x_1 - 4.17x_2 - 16.00x_3 + 2.74x_4 - 1.22x_1x_2 - 2.68x_1x_3 + 0.31x_1x_4 - 13.88x_2x_3 - 3.51x_2x_4 - 4.26x_3x_4 - 2.34x_1^2 - 7.58x_2^2 - 10.29x_3^2 - 6.12x_4^2 \quad (12)$$

Table 3. Experimental design matrix for CCRD with experimental results

Exp. #	O ₂ partial pressure (bar)	Temp. (°C)	Solid/liquid ratio (w/v)	Leaching time (min)	Zn Leaching efficiency (%)	Zn Concentration (g dm ⁻³)	Fe Extraction (%)	Free Acid Concentration (mol dm ⁻³)
1	6	120	0.10	40	26.65	11.38	43.00	1.186
2	6	120	0.10	90	57.74	24.66	61.73	0.931
3	6	120	0.20	40	32.86	28.07	45.96	0.743
4	6	120	0.20	90	67.33	57.51	57.87	0.174
5	6	150	0.10	40	62.68	26.77	67.47	0.894
6	6	150	0.10	90	76.44	32.65	74.45	0.808
7	6	150	0.20	40	74.69	63.80	26.85	0.160
8	6	150	0.20	90	90.56	77.36	6.45	0.259
9	12	120	0.10	40	36.05	15.40	50.52	1.142
10	12	120	0.10	90	63.63	27.18	71.49	0.884
11	12	120	0.20	40	50.49	43.13	53.45	0.440
12	12	120	0.20	90	77.06	65.82	49.56	0.151
13	12	150	0.10	40	68.65	29.32	72.86	1.132
14	12	150	0.10	90	75.14	32.09	79.94	1.044
15	12	150	0.20	40	86.50	73.89	10.74	0.239
16	12	150	0.20	90	94.18	80.45	8.68	0.276
17	3	135	0.15	65	58.24	37.31	58.40	0.631
18	15	135	0.15	65	78.93	50.57	74.66	0.358
19	9	135	0.15	15	33.18	21.26	44.80	0.966
20	9	135	0.15	115	84.91	54.40	58.00	0.355
21	9	135	0.05	65	56.27	12.02	65.24	1.109
22	9	135	0.25	65	80.62	86.08	4.16	0.096
23	9	105	0.15	65	30.11	19.29	49.08	1.195
24	9	165	0.15	65	78.88	50.53	42.06	0.613
25-30	9	135	0.15	65	78.02±1.99	49.98±1.27	75.38±2.76	0.361±0.009

The ANOVA confirmed that the models for all responses are statistically significant even at confidence level of 99.99% (p-value <0.0001). According to the results of ANOVA for Zn leaching efficiency, all the first and second order terms of independent parameters are significant. The relative significance of these parameters for the Zn leaching efficiency is in the order of temperature, leaching time, solid/liquid

ratio and oxygen partial pressure (P_{O_2}). The statistical analysis results of the interaction terms show that there are significant interactions among leaching time with both P_{O_2} and temperature at 95% confidence level (p -value < 0.05). For Zn concentration, all the first and second order terms of independent parameters are significant except the second term of solid/liquid ratio. The relative significance of these parameters is descending orders of solid/liquid ratio, temperature, leaching time and P_{O_2} . For Fe extraction, the exception is the first term of P_{O_2} and descending order of relative significance of parameters is solid/liquid ratio, temperature and leaching time. There are significant interactions for both Zn concentration and Fe extraction among solid/liquid ratio with all other parameters and among temperature with leaching time at 95% confidence level.

The predicted values versus the experimental data for the Zn leaching efficiency, Zn concentration in leach solution and Fe extraction are shown in Fig. 2. The figures indicate that the predicted values are quite proximate to the actual values and Eq. (10), (11) and (12) are well fitted to the experimental data.

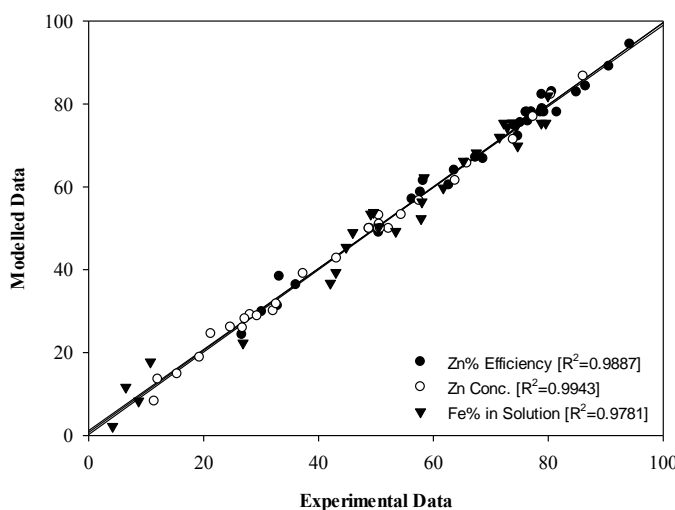


Fig. 2. Experimental vs. modeled data of all responses

The vapor pressures of sulfuric acid solution were determined initially under experimental conditions. Addition of oxygen was performed to obtain the desired level of P_{O_2} . Some increase in Zn efficiency was observed with increasing P_{O_2} under all experimental conditions other than long leaching time, high temperature and low S/L ratio. This exception may occur due to encapsulated particles by molten sulfur at elevated temperature. At low S/L ratio; increasing P_{O_2} results in increasing Fe extraction independently of temperature and leaching time. Fe extraction tends to decrease in the long term in despite of increasing in the short term with increasing P_{O_2} at low temperature and high S/L ratio.

The leaching temperature is a significant thermodynamic factor. In general, rising the leaching temperature increases the leach kinetics. Figure 3. illustrates typical temperature effect on reaction rate of the zinc extraction from the sphalerite concentrate. An increase in the temperature from 105 °C to 165 °C enhanced the initial reaction rate (Fig. 3) and Zn efficiency from 39% to 80% at 90 minutes (Exp.23→Exp.24) (Table 3) as expected. Similarly, Fe extraction increases with increasing temperature at low S/L ratio conditions. But leaching temperature has adverse effect at high S/L ratio conditions, so dissolved iron sharply decreases in the solution (e.g. from 58% to 6.5%) due to precipitation of iron as both jarosite and hematite form with increasing temperature (Exp. 4→Exp. 8) (Table 3).

Effect of S/L ratio on the leaching system should be evaluated from different perspectives such as amount of iron minerals entered to the system, initial acid concentration to concentrate ratio, acid concentration changing during the process, dissolved metal sulfate concentration which influence zinc dissolution rate, zinc sulfate concentration, amounts of both precipitated and remained iron in the solution.

Fe^{3+} ion which is a strong oxidizing agent ($E_{\text{Fe}^{3+}/\text{Fe}^{2+}} = 0.771$ V) plays a crucial role for dissolution reactions of many sulfide minerals (Yazici and Deveci, 2014). Concordantly, the amount of iron minerals entering the leaching system -the initial solid/liquid ratio- is very significant for dissolution of zinc in case non-existence of dissolved iron initially. In analogy to leaching temperature, increasing S/L ratio enhances Zn leaching efficiency under all experimental conditions. Positive effect of high iron concentration on zinc leaching efficiency and in connection with zinc extraction can be explicitly seen at low temperature where iron precipitation is slower than iron dissolution. Iron extraction shows tendency to stay steady or decrease in percent at low temperature and all P_{O_2} levels, but to increase approximately 2-fold in concentration, with increasing S/L ratio. Hence, Zn leaching efficiency enhances in parallel with increasing iron concentration (e.g. from 0.14 mol dm⁻³ to 0.20 mol dm⁻³) in the solution (i.e Exp. 10→Exp. 12). Crundwell (1988), also concluded that iron content of the concentrate affects the rate of Zn extraction.

Essentially, a rise in Zn leaching rate is expected by increasing the initial sulfuric acid concentration. However, previous investigations indicate that if the initial sulfuric acid amount is twice over the stoichiometric amount, the reaction given in Eq. 5. will go the left and more H_2S hindering the dissolution of zinc will be produced (Jan et al., 1976; Xie et al., 2007). Xie et al. (2007) concluded in their study that at higher $\text{H}_2\text{SO}_4/\text{concentrate}$ ratios (>4:1), Zn leaching rate decreased with increasing $\text{H}_2\text{SO}_4/\text{concentrate}$ ratio. Figure 4a shows that initial zinc dissolution kinetics enhances with decreasing initial acid concentration even at $\text{H}_2\text{SO}_4/\text{concentrate}$ ratios of <1:1.

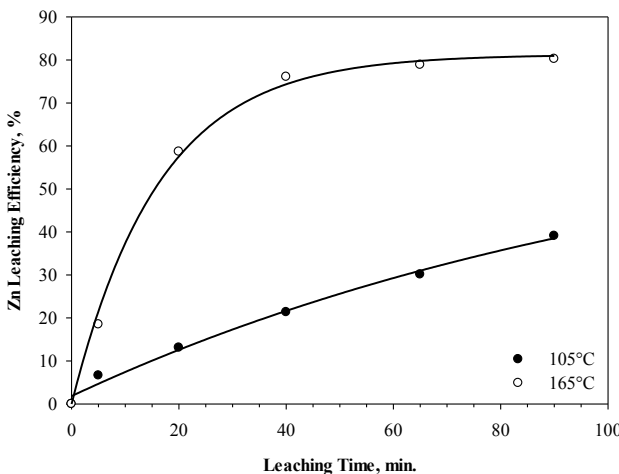


Fig. 3. Dissolution kinetics of zinc from sphalerite concentrate (P_{O_2} : 9 bar, S/L ratio: 0.15 (w/v))

Acid concentration level in the solution is controlled by the dissolution of zinc and iron minerals. Dissolutions of sphalerite and pyrrhotite are acid consuming reactions (Eq. (1) and (7)) where dissolution of pyrite dissolution produces acid (Eq. (6)). Free acid concentration of solution decreases as long as zinc dissolves which ends up with increasing pH. Under all experimental conditions, increasing S/L ratio induces decreasing of free acid concentration in the solution in parallel with increasing Zn concentration (Table 3).

Lack of acid in the system leads to start precipitation of iron. Dutrizac and Jambor (2000) reported that hydronium jarosite formed at pH range between 0.4 to 1.4 and temperature between 100 °C to 160 °C. In addition, ferric sulfates can precipitate as hematite at elevated temperature depending on pH and divalent metal sulfate (such as $ZnSO_4$, $MgSO_4$) concentration (Reid and Papangelakis, 2006; Tozawa and Sasaki, 1986). Increasing S/L ratio paves the way for precipitation of iron due to decreasing of free acidity and increasing $ZnSO_4$ concentration simultaneously. On the other hand, precipitation of iron produces some acid (Eq. (8) and (9)). Thus, acid concentration is stabilized between 0.15-0.25 mol dm^{-3} till all iron in the solution precipitates (Table 3). Figure 4. illustrates the total precipitation of iron after 20 minutes in 0.5/1 H_2SO_4 /concentrate ratio which reveals the fact that zinc extraction reduces correspondingly. A similar trend can also be determined for the results gathered for the 0.75/1 H_2SO_4 /concentrate ratio. However, a significant amount of iron remaining in the solution occurs for the 1/1 H_2SO_4 /concentrate ratio while zinc dissolution proceeds.

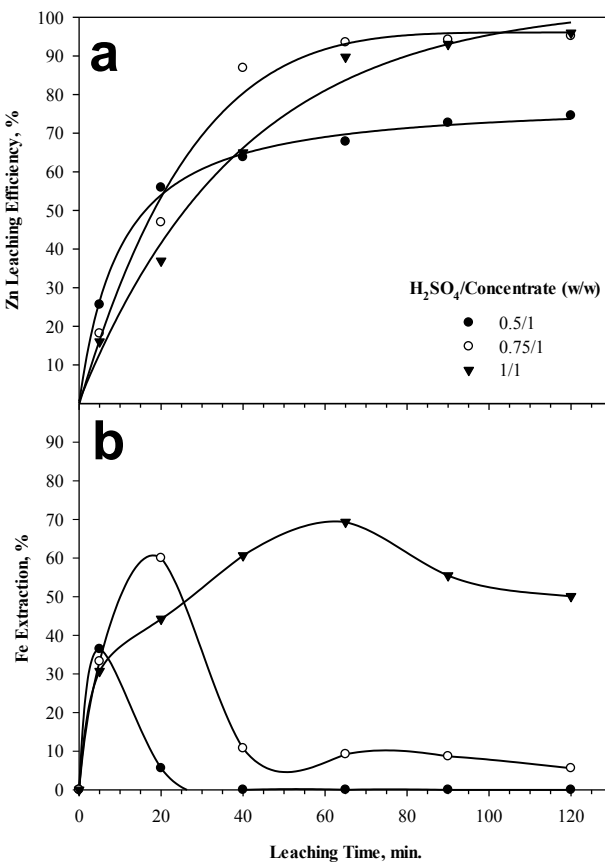


Fig. 4. Effect of initial acid concentration on Zn leaching efficiency (a) and Fe extraction (b) (temp: 150°C, S/L: 0.20 (w/v), P_{O_2} : 12 bar)

In order to comprehend the interaction effects of parameters on Zn leaching efficiency, three-dimensional (3D) graphs for the predicted responses were plotted in Fig. 5 basing on Eq. 10. It can be observed in Fig. 5a that temperature and leaching time have individually and simultaneously important effect on the Zn leaching efficiency. P_{O_2} has limited effect at all levels of leaching time (Fig. 5b.) and temperature (Fig. 5d.) and at low level of the solid/liquid ratio (Fig. 5c.). However, P_{O_2} and the solid/liquid ratio have synergistic effect on the extraction of zinc at their higher levels.

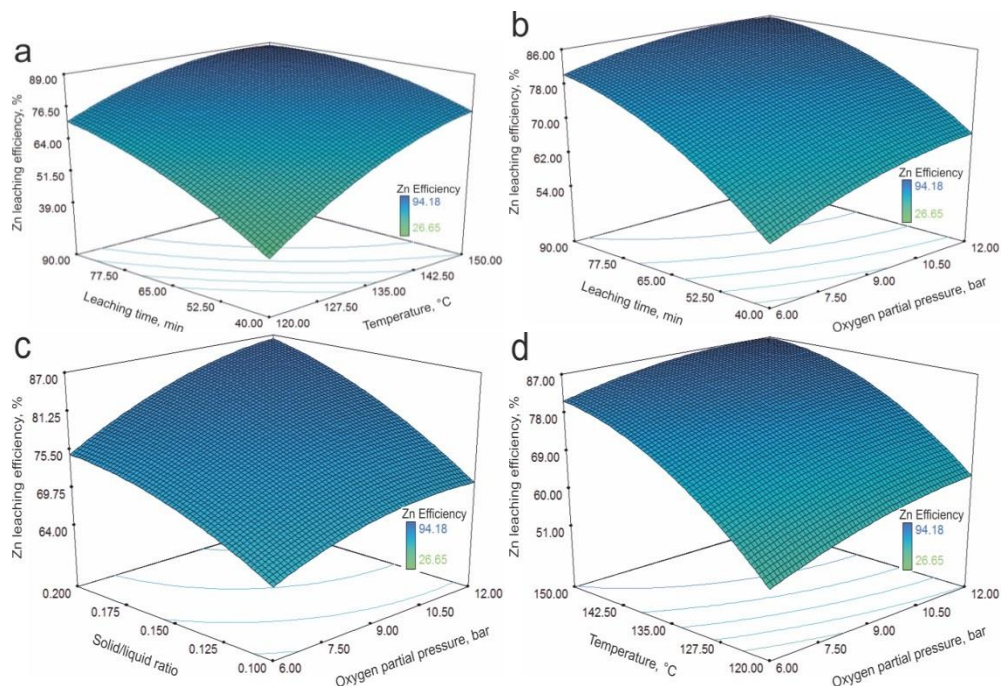


Fig. 5. Response surface plots showing the simultaneous effects of dual parameters on Zn leaching efficiency (other parameters are held at center level), (a) temperature and leaching time, (b) P_{O_2} and leaching time, (c) P_{O_2} and solid/liquid ratio, (d) P_{O_2} and temperature

Optimization of process parameters and confirmation test

One of the main objectives of this research is to determine an optimum leaching process condition with highest Zn leaching efficiency and Zn concentration in the solution and lowest Fe extraction. The optimization of process parameters are not only limited to Zn the leaching efficiency. Hence the amount of Fe dissolved triggers the loss of Zn in the electrolyte during iron precipitation process due to co-precipitation of zinc in iron oxides (Sinclair, 2005). Besides, it is known that the lower the Zn concentration in the electrolyte, the higher becomes the energy consumption during electrolysis (Alfantazi and Dreisinger, 2001; Mahon et al., 2014). The optimum conditions of the pressure acid leaching of sphalerite in two cases were determined using Design Expert software version 7.0 and presented in Table 4.

In the first case, the conditions were adjusted according to lower required energy and P_{O_2} , short process time and high capacity intending to achieve the maximum Zn efficiency and concentration with minimum Fe extraction. According to this scenario, the optimum conditions are identified as P_{O_2} at 6 bars, temperature at 139.65 °C, solid/liquid ratio at 0.20 and leaching time at 61.52 minutes. Under these conditions, Zn efficiency of 77.42%, Zn concentration of 64.67 g dm⁻³ and Fe extraction of 41.86% were predicted. On the other hand, to achieve the maximum Zn efficiency and

concentration with minimum Fe extraction, the four mentioned parameters were all kept in the range in the second case. As for the second scenario, Zn efficiency of 94.56%, Zn concentration of 82.28 g dm^{-3} and Fe extraction of 8.88% were predicted with the optimum conditions listed in Table 4. By comparison of the cases, the target differentiation in the parameters particularly influenced Zn leaching efficiency and Fe extraction positively for the second case. In addition, there has been observed a slight increase in Zn concentration. Also, the desirability value of Case 2 increased significantly compared to Case 1 (0.669 to 0.971). Accordingly, the optimum experimental conditions for pressure acid leaching of sphalerite were stated as for Case 2.

Table 4. Optimum leaching conditions and predicted results

Parameters/Responses	Case 1		Case 2	
	Target	Optimum Value	Target	Optimum Value
Oxygen Partial Pressure (bar)	Minimize	6	In range	12
Temperature (°C)	Minimize	139.65	In range	150
Solid/liquid ratio	Maximize	0.20	In range	0.20
Leaching time (min)	Minimize	61.52	In range	89.16
Zn leaching efficiency (%)	Maximize	77.42	Maximize	94.56
Zn concentration ($\text{g}\cdot\text{dm}^{-3}$)	Maximize	64.67	Maximize	82.28
Fe extraction (%)	Minimize	41.86	Minimize	8.88
Desirability		0.669		0.971

The experimental results of three confirmation tests were gathered by applying the conditions of Case 2 to determine the error margin between predicted and actual results. As shown in Table 5., there are only small differences between the predicted and actual results indicating the successful validation of the proposed models. The relative standard deviation of the confirmation tests data was calculated as below 3.19%.

Table 5. Average results of model validation at optimum leaching conditions

O_2 partial pressure, bar	Temp, °C	Solid/liquid ratio	Leaching time, min.	Zn leaching efficiency, %		Zn concentration, $\text{g}\cdot\text{dm}^{-3}$		Fe extraction, %	
				Predicted	Actual	Predicted	Actual	Predicted	Actual
12	150	0.20	89.16	94.56	93.86 \pm 1.25	82.28	80.17 \pm 1.07	8.88	8.14 \pm 0.26

The partial effect of each parameter on zinc efficiency, zinc concentration and iron extraction, based on the equations of the models, was investigated at the optimum levels of other remaining parameters, respectively (Fig. 6). For instance, to determine the partial effect of the S/L ratio, the other three parameters were fixed at their specific optimum levels and so its influence on zinc efficiency, zinc concentration and iron extraction was determined for the three different levels of the S/L ratio, accordingly.

Consequently, Fig. 6. indicates that the most significant parameter affecting the results is the change of S/L ratio by far, followed by temperature at specific optimum levels of other parameters.

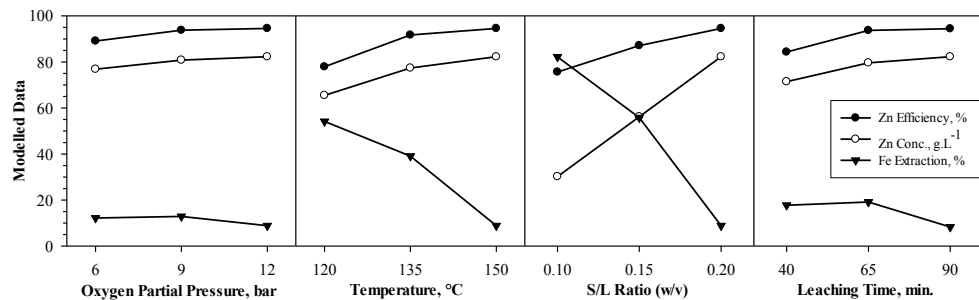


Fig. 6. Effects of parameters on modeled data at optimum conditions

The XRD pattern of the residue obtained after leaching at optimum conditions is shown in Fig. 7. The observed phase formations revealed that elemental sulfur forms as a result of sphalerite and pyrite leaching. The dissolved iron precipitated in the form of hydronium jarosite and hematite where anglesite precipitated from dissolved galena. Quartz and small amount of sphalerite remained as undissolved in the residue. In addition, SEM and EDS analyses conducted on zinc concentrate and leach residue obtained at optimum conditions confirmed the indications reached by XRD analyses (Fig. 8).

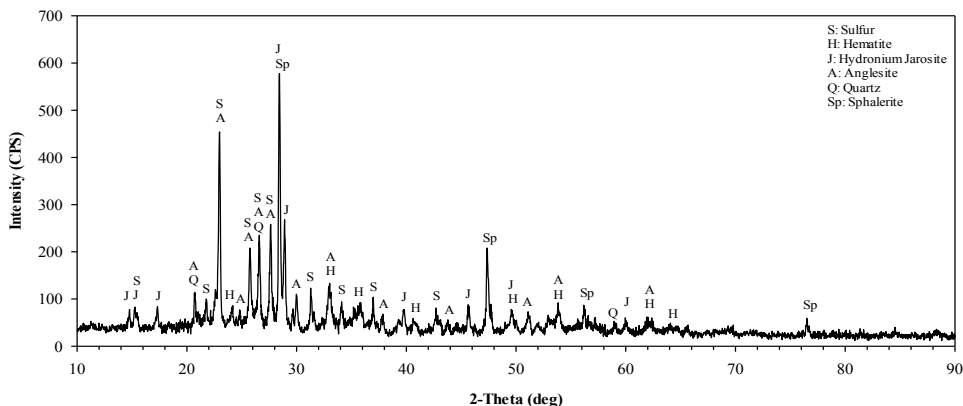


Fig. 7. XRD pattern of the residue obtained after leaching at optimum conditions

Response surface interpolation is a significant method due to facilitating the minimization of parameters which affect input cost, efficiency maximization and product quality that will influence further processes costs. Hence, the parameters of

obtaining high quality product with high efficiency and lowest cost can be optimized by this method.

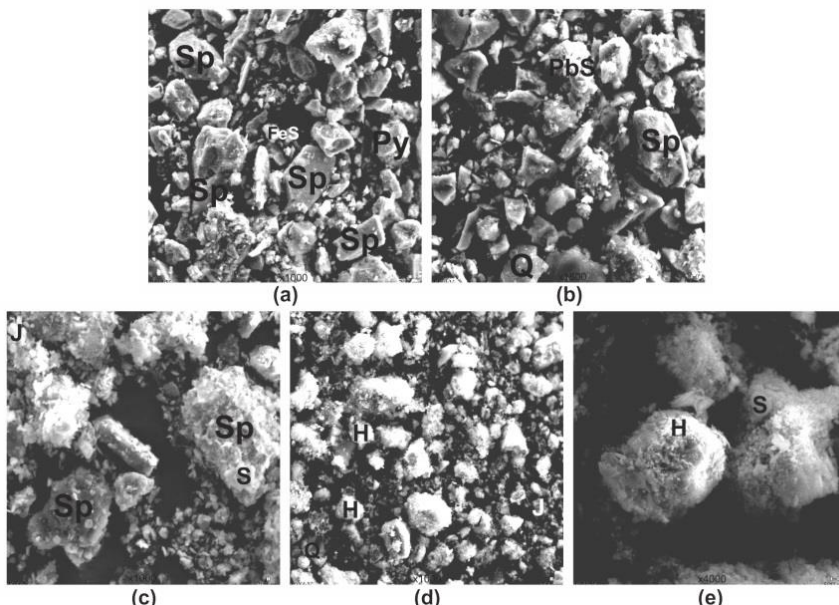


Fig. 8. SEM photographs of sphalerite concentrate and leach residues: (a) and (b) concentrate, (c) residue at 120 °C, (d) and (e) residue at optimum conditions, (Sp: sphalerite, Py: pyrite, FeS: pyrrhotite, Q: quartz, PbS: galena, H: hematite, J: jarosite, S: sulfur).

Variation of the concentrate or ore feed is one of the most important problems in mineral processing and hydrometallurgy plants. In such a case, there is a possibility of the process economics to be affected negatively whereas the efficiency and product quality may be reduced due to variable process conditions. Response surface method may be also facilitated to optimize process parameters when the concentrate or ore feed composition changes. Thus, reduction in efficiency and product quality can be prevented by responding to the process parameters.

Conclusions

The following results may be drawn from the presented study.

1. The four experimental parameters affecting Zn leaching efficiency in the pressure acid leaching process of sphalerite concentrate were all (temperature, leaching time, solid/liquid ratio and P_{O_2}) revealed as statistically significant (in descending significance order). Increasing the level of these parameters enhanced the zinc efficiency and concentrations and also precipitation of dissolved iron.

2. Dissolution of zinc is a fast reaction when dissolved iron and oxygen are present in the solution at elevated temperature.

3. Solid/liquid ratio was determined as the most crucial parameter affecting the amount of iron entering the system, free acid concentration level during the process and dissolved metal sulfate concentration. In order to obtain selective zinc electrolyte with high efficiency and concentration, initial acid/concentrate ratio should be adjusted properly.

4. The most significant interaction terms on Zn leaching efficiency were determined as leaching time vs. temperature and leaching time vs. P_{O_2} .

5. The optimum level of P_{O_2} during the leaching process was identified to be dependent on all the levels of temperature, solid/liquid ratio and leaching time. The increases in temperature, solid/liquid ratio and leaching time levels simultaneously diminished the importance of P_{O_2} control during the leaching process.

6. The indicated optimum leaching conditions for sphalerite concentrate were P_{O_2} of 12 bars, temperature of 150 °C, solid/liquid ratio of 0.20 and leaching time of 89.16 minutes. The achieved Zn leaching efficiency, Zn concentration and Fe extraction were 94.56%, 82.28 g·dm⁻³ and 8.88%, respectively.

Acknowledgements

The author wish to thank Assoc. Prof. Abdullah Seyrankaya and Prof. Haci Deveci for their support and insightful technical comments on the paper. Assist. Prof. Hatice Yilmaz is also acknowledged for her support in mineralogical analyses. Special thanks must go to Dr. Baran Tufan and Assist. Prof. Mert Y. Yardimci for their help in particular for proof reading.

References

ACHARYA, S., ANAND, S., DAS, R.P., 1992, *Iron rejection through jarosite precipitation during acid pressure leaching of zinc leach residue*. Hydrometallurgy, 31(1-2), 101-110.

AGHAIE, E., PAZOUKI, M., HOSSEINI, M.R., RANJBAR, M., GHAVIPANJEH, F., 2009, *Response surface methodology (RSM) analysis of organic acid production for kaolin beneficiation by Aspergillus niger*. Chemical Engineering Journal, 147(2-3), 245-251.

ALFANTAZI, A.M., DREISINGER, D.B., 2001, *The role of zinc and sulfuric acid concentrations on zinc electrowinning from industrial sulfate based electrolyte*. J Appl Electrochem, 31(6), 641-646.

AU-YEUNG, S.C.F., BOLTON, G.L., 1986. *Iron control in the processes developed at Sherritt Gordon Mines*, In *International Symposium on Iron Control in Hydrometallurgy*, eds. Dutrizac, J. E., Monhemius, A. J. E. Horwood Toronto, Ont., pp. 131-151.

BABU, M.N., SAHU, K.K., PANDEY, B.D., 2002, *Zinc recovery from sphalerite concentrate by direct oxidative leaching with ammonium, sodium and potassium persulphates*. Hydrometallurgy, 64(2), 119-129.

BALAZ, P., EBERT, I., 1991, *Oxidative leaching of mechanically activated sphalerite*. Hydrometallurgy, 27(2), 141-150.

BALDWIN, S.A., DEMOPOULOS, G.P., 1995, *Assessment of alternative iron sources in the pressure leaching of zinc concentrates using a reactor model*. Hydrometallurgy, 39(1-3), 147-162.

COPUR, M., 2002, *An optimization study of dissolution of Zn and Cu in ZnS concentrate with HNO₃ solutions*. Chemical and Biochemical Engineering Quarterly, 16(4), 191-197.

CRUNDWELL, F.K., 1987, *Kinetics and mechanisms of the oxidative dissolution of a zinc sulphide concentrate in ferric sulphate solutions*. Hydrometallurgy, 19(2), 227-242.

CRUNDWELL, F.K., 1988, *Effect of iron impurity in zinc sulfide concentrates on the rate of dissolution*. AIChE Journal, 34(7), 1128-1134.

CRUNDWELL, F.K., 1998, *The indirect mechanism of bacterial leaching*. Mineral Processing and Extractive Metallurgy Review, 19(1), 117-128.

CRUNDWELL, F.K., 2013, *The dissolution and leaching of minerals*. Hydrometallurgy, 139, 132-148.

DA SILVA, G., 2004, *Relative importance of diffusion and reaction control during the bacterial and ferric sulphate leaching of zinc sulphide*. Hydrometallurgy, 73(3-4), 313-324.

DEHGHAN, R., NOAPARAST, M., KOLAHDOOZAN, M., MOUSAVI, S.M., 2008, *Statistical evaluation and optimization of factors affecting the leaching performance of a sphalerite concentrate*. International Journal of Mineral Processing, 89(1-4), 9-16.

DUTRIZAC, J.E., 1992, *The leaching of sulphide minerals in chloride media*. Hydrometallurgy, 29(1-3), 1-45.

DUTRIZAC, J.E., JAMBOR, J.L., 2000, *Jarosites and their application in hydrometallurgy*. Rev Mineral Geochem, 40, 405-452.

FILIPPOU, D., 2004, *Hydrometallurgical processes for the primary processing of zinc*. Mineral Processing and Extractive Metallurgy Review, 25(3), 205-252.

GOMEZ, C., LIMPO, J.L., DELUIS, A., BLAZQUEZ, M.L., GONZALEZ, F., BALLESTER, A., 1997, *Hydrometallurgy of bulk concentrates of Spanish complex sulphides: Chemical and bacterial leaching*. Can Metall Quart, 36(1), 15-23.

GU, Y., ZHANG, T.A., LIU, Y., MU, W.Z., ZHANG, W.G., DOU, Z.H., JIANG, X.L., 2010, *Pressure acid leaching of zinc sulfide concentrate*. T Nonferr Metal Soc, 20, S136-S140.

HAGHSHENAS, D.F., BONAKDARPOUR, B., ALAMDARI, E.K., NASERNEJAD, B., 2012, *Optimization of physicochemical parameters for bioleaching of sphalerite by Acidithiobacillus ferrooxidans using shaking bioreactors*. Hydrometallurgy, 111, 22-28.

HARVEY, T.J., YEN, W.T., PATERSON, J.G., 1993, *A kinetic investigation into the pressure oxidation of sphalerite from a complex concentrate*. Minerals Engineering, 6(8-10), 949-967.

JAN, R.J., HEPWORTH, M.T., FOX, V.G., 1976, *A kinetic study on the pressure leaching of sphalerite*. Metallurgical Transactions B, 7(3), 353-361.

JIN, Z.M., WARREN, G.W., HENEIN, H., 1993, *An Investigation of the electrochemical nature of the ferric-chloride leaching of sphalerite*. International Journal of Mineral Processing, 37(3-4), 223-238.

KAYA, S., TOPKAYA, Y.A., 2011, *High pressure acid leaching of a refractory lateritic nickel ore*. Minerals Engineering, 24(11), 1188-1197.

LI, C.X., WEI, C., XU, H.S., LI, M.T., LI, X.B., DENG, Z.G., FAN, G., 2010a, *Oxidative pressure leaching of sphalerite concentrate with high indium and iron content in sulfuric acid medium*. Hydrometallurgy, 102(1-4), 91-94.

LI, D., PARK, K.H., WU, Z., GUO, X.Y., 2010b, *Response surface design for nickel recovery from laterite by sulfation-roasting-leaching process*. T Nonferr Metal Soc, 20, S92-S96.

LIU, J., WEN, S.M., LIU, D., LV, M.Y., LIU, L.J., 2011, *Response surface methodology for optimization of copper leaching from a low-grade flotation middling*. Miner Metall Proc, 28(3), 139-145.

MAHON, M., PENG, S., ALFANTAZI, A., 2014, *Application and optimisation studies of a zinc electrowinning process simulation*. Can J Chem Eng, 92(4), 633-642.

MASSACCI, P., RECINELLA, M., PIGA, L., 1998, *Factorial experiments for selective leaching of zinc sulphide in ferric sulphate media*. International Journal of Mineral Processing, 53(4), 213-224.

OZBERK, E., CHALKLEY, M.E., COLLINS, M.J., MASTERS, I.M., 1995, *Commercial applications of the sherritt zinc pressure leach process and iron disposal*. Mineral Processing and Extractive Metallurgy Review, 15(1-4), 115-133.

PALENCIA PEREZ, I., DUTRIZAC, J.E., 1991, *The effect of the iron content of sphalerite on its rate of dissolution in ferric sulphate and ferric chloride media*. Hydrometallurgy, 26(2), 211-232.

RAO, K.S., PARAMGURU, R.K., 1998, *Dissolution of sphalerite (ZnS) in acidic ferric sulfate solution in the presence of manganese dioxide*. Miner Metall Proc, 15(1), 29-34.

REID, M., PAPANGELAKIS, V.G., 2006. *New data on hematite solubility in sulphuric acid solutions from 130 to 270°C*, In *Iron Control Technologies*, eds. Dutrizac, J. E., Riveros, P. A. Canadian Institute of Mining, Metallurgy and Petroleum, Montreal, QC, pp. 673-686.

SANTOS, S.M.C., MACHADO, R.M., CORREIA, M.J.N., REIS, M.T.A., ISMAEL, M.R.C., CARVALHO, J.M.R., 2010, *Ferric sulphate/chloride leaching of zinc and minor elements from a sphalerite concentrate*. Minerals Engineering, 23(8), 606-615.

SINCLAIR, R.J., 2005, *The extractive metallurgy of zinc*. The Australasian Institute of Mining and Metallurgy, Australia.

TOZAWA, K., SASAKI, K., 1986. *Effect of coexisting sulphates on precipitation of ferric oxide from ferric sulphate solutions at elevated temperatures*, In *Iron Control in Hydrometallurgy*, eds. Dutrizac, J. E., Monhemius, A. J. Ellis Horwood Limited, Toronto, ON, pp. 454-476.

VERBAAN, B., CRUNDWELL, F.K., 1986, *An electrochemical model for the leaching of a sphalerite concentrate*. Hydrometallurgy, 16(3), 345-359.

WADSWORTH, M.E., 1972, *Advances in the leaching of sulphide minerals*. Miner. Sci. Eng., 4(4), 36-47.

XIE, K.Q., YANG, X.W., WANG, J.K., YAN, J.F., SHEN, Q.F., 2007, *Kinetic study on pressure leaching of high iron sphalerite concentrate*. T Nonferr Metal Soc, 17(1), 187-194.

YAZICI, E.Y., DEVECI, H., 2014, *Ferric sulphate leaching of metals from waste printed circuit boards*. International Journal of Mineral Processing, 133, 39-45.

YUE, G., ZHAO, L., OLVERA, O.G., ASSELIN, E., 2014, *Speciation of the H₂SO₄-Fe²(SO₄)₃-FeSO₄-H₂O system and development of an expression to predict the redox potential of the Fe³⁺/Fe²⁺ couple up to 150°C*. Hydrometallurgy, 147-148, 196-209.

ZHANG, C.L., ZHAO, Y.C., GUO, C.X., HUANG, X., LI, H.J., 2008, *Leaching of zinc sulfide in alkaline solution via chemical conversion with lead carbonate*. Hydrometallurgy, 90(1), 19-25.

Received July 3, 2015; reviewed; accepted October 4, 2015

REACTIVITY OF MARBLE WASTES FOR POTENTIAL UTILIZATION IN WET FLUE GAS DESULPHURIZATION

N. Emre ALTUN

Middle East Technical University, Mining Engineering Department, 06800, Ankara, Turkey
ealtun@metu.edu.tr

Abstract: Wastes of most marble types are distinguished with their superior CaCO_3 content and potential to utilize them as an alternative to limestone. Control of SO_2 using marble wastes in wet flue gas desulphurization (WFGD) units of coal fired thermal power plants is an important opportunity. In this study, nine types of marble wastes were evaluated in terms of their ability to dissolution (reactivity) in an acidic environment. The reactivity was expressed as fractional conversion with time with respect to the chemical composition and particle distribution of wastes as well as temperature and pH of solution. Dissolution reaction rate constants were also computed. Reactivity of the wastes varied significantly with chemical compositions of the marble types. The same marble type displayed different dissolution profiles as a function of test conditions (fineness, temperature, pH). Higher contents of CaCO_3 and Fe_2O_3 positively influenced dissolution ability and rates, whereas increased MgCO_3 content had adverse effects. The changes in particle size, temperature and pH influenced the reactivity. The reactivity increased with decreasing particle size. Also, higher temperature and increased acidity favored dissolution ability of the marble wastes. Our results showed that under optimized conditions marble wastes, having a higher content of CaCO_3 and low content of MgCO_3 , are potential SO_2 sorbent alternative.

Keywords: marble, reactivity, thermal power production, SO_2 , desulphurization

Introduction

Coal is the largest fossil fuel resource in the growing energy needs of the globe. Despite the importance of coal fired thermal power plants in power production, it is also the source of major concerns such as SO_2 emission. For SO_2 emission, post-combustion SO_2 capture through wet flue gas desulphurization (WFGD) systems is mostly used (Kaminski, 2003). In these systems, a calcareous sorbent, mainly limestone, put into a slurry form, is used for SO_2 abatement (Zhao et al., 2007). The sorbent particles in the slurry dissolve and react with SO_2 . A dissolution behavior of the calcareous sorbents, i.e. their ability to dissolution determines the extent the sorbent would impose alkalinity and react with the acid generated due to SO_2 .

dissolution in water (Brown et al., 2010). Susceptibility of the sorbent to dissolution is directly related with the efficiency of desulphurization, the design of the WFGD system as well as the economics and environmental foot print of SO₂ control (Ukawa et al., 1993; Stumpf et al., 1984).

In simulation scale, dissolution of calcareous material in acidic solution resembles the interaction between sorbent and SO₂ in WFGD (Ukawa et al., 1993; Ahlbeck et al., 1995; Hosten and Gulsun, 2004; Siagi and Mbarawa, 2009; Brown et al., 2010). Determination of dissolution ability and dissolution rate of the calcareous sorbent allows an accurate determination of the reactivity of the sorbent and assessment of alternative sorbents for full-scale implementation.

In exploitation of rock blocks, and particularly in marble quarrying, the overall efficiency is extremely low. Geological factors and obstacles, deficiencies during quarrying and processing and technical limitations contribute to generation of massive amounts of marble wastes in various forms. This problem and several associated impacts have been emphasized by several researchers (Davini, 1992; Davini, 2000; Gulsun, 2003; Altun, 2014; Duzyol, 2015). The idea of evaluation of various waste materials as an alternative to limestone, particularly for environmental engineering processes, is not new (Kupich and Girczys, 2008) and use of marble wastes as a limestone supplement could be treated as a similar opportunity. Most marble types can be considered as calcareous stones, not only petrographically, but also on the basis of high CaCO₃ content. At this point the potential of utilization of these wastes arises as an alternative sorbent to limestone in the WFGD systems. Evaluation, particularly the reactivity of marble wastes under different conditions, is a critical aspect to propose such an opportunity. Research on evaluation of marble wastes as a potential SO₂ sorbent is fairly limited except a few studies by Davini (1992 and 2000) and Altun (2014).

This work aims to assess dissolution behavior (reactivity) and reaction rates of marble wastes under various conditions. Wastes of different marble types from the Aegean Region of Turkey were subjected to detailed reactivity investigations. The tests were conducted according to the above mentioned dissolution procedure of wastes under pH controlled conditions. The reactivity of marble waste types were determined with respect to major chemical components and particle size of the wastes, solution temperature and pH.

Materials and methods

Samples and characterization

The study was conducted on nine different marble wastes. The wastes were collected from the major marble quarries in the Aegean Region of Turkey, the leading marble production area of the country. Due to commercial restrictions, names of the marble could not be given and the wastes were coded as Type I to IX (Table 1). The composition characteristics of the wastes were determined using a X-Lab 2000

PED-XRF instrument. For the analysis, representative samples were crushed and ground to a size of $-150\text{ }\mu\text{m}$. Chemical compositions of the marble wastes are presented in Table 1.

Table 1. Chemical compositions of marble wastes

Waste type	Amount (%)					
	CaCO ₃	MgCO ₃	Fe ₂ O ₃	Al ₂ O ₃	SiO ₂	K ₂ O
Type I	97.80	1.20	0.66	0.08	0.12	0.10
Type II	96.04	0.81	0.74	0.66	0.78	0.52
Type III	94.12	3.56	1.02	0.48	0.50	0.24
Type IV	94.00	3.60	1.40	0.52	0.40	0.12
Type V	92.56	5.25	1.10	0.38	0.54	0.12
Type VI	89.28	7.12	1.15	0.86	0.98	0.42
Type VII	89.00	7.36	1.62	0.98	0.88	0.14
Type VIII	87.40	11.22	0.66	0.10	0.10	0.10
Type IX	86.10	9.85	0.96	1.52	0.98	0.42

Determination of dissolution behavior

The study is based on quantification of dissolution behavior of calcareous material in an acidic medium, i.e. measurement of the extent of reaction of the calcareous sorbent with a strong acid such as HCl or H₂SO₄. It is well established that the procedure simulates the SO₂ abatement process in wet flue gas desulphurization (WFGD) systems (Hosten and Gulsun, 2004; Siagi and Mbarawa, 2009; Brown et al., 2010). Hence, this application was used as a standardized procedure to measure the reactivity of calcium based sorbents. Here, reactivity corresponds to the dissolution ability of the sorbent.

For identifying the reactivity of calcareous sorbents, a solution was prepared by dissolving the sorbent. The pH of this solution should be kept constant at a designed level. This was achieved by adding HCl in a controlled way. Consumed acid volume with time, stoichiometrically provided the fractional conversion, i.e. the reactivity of the sorbent and by using the reactivity, dissolution rate of the sorbent was calculated. Details of this procedure and the underlying chemical mechanism are described elsewhere (Shih et al., 2000; Gulsun, 2003; Siagi and Mbarawa, 2009; Altun, 2014).

Tests were conducted using a system that included a pH pump, stirred 5 dm³ reactor for sorbent solution, beaker with acid solution, analytical scale and data-logger (Fig. 1). Finely ground marble waste with mass of 4 g was dissolved in 2.5 dm³ of distilled water in the stirred reactor. pH of this solution was maintained at the desired level by the pH pump with automatic titration. The pH pump were transferring required amount of 0.1 M HCl solution when necessary.

Reactivity of the marble wastes were assessed with respect to the chemical composition and particle size of the sorbent, temperature and pH of the sorbent

solution. First of all, the influence of chemical composition on the reactivity was evaluated. Taking into account industrial scale WFGD requirements, the tests were performed with wastes ground to a size of $-45\text{ }\mu\text{m}$ and at sorbent solution pH equal to 5.0.

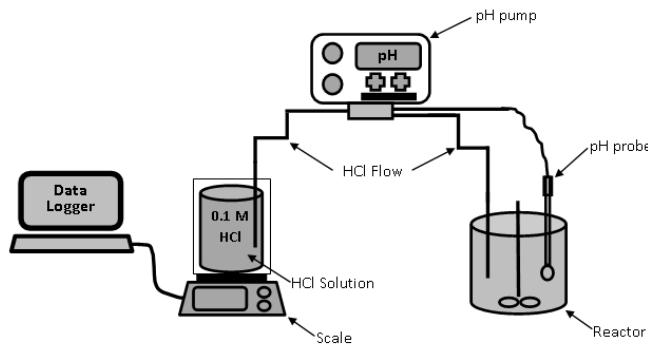


Fig. 1. System for reactivity tests

The tests to determine the effect of sorbent particle size, pH and temperature of the solution were conducted on the marble waste that yielded the highest dissolution ability. For the effect of particle size, reactivity tests on P_{100} sizes of 37, 44, 53, 75 and 100 μm were done. For the effect of temperature, reactivity tests at 25, 35, 45 and 55 $^{\circ}\text{C}$ were performed. For the effect of pH, reactivity tests on solution pH's of 3.0, 4.0, 5.0, 6.0 and 7.0 were conducted.

In the several previous works, dissolution of calcareous materials has been well explained by the shrinking core model, where the rate of dissolution has been anticipated as being controlled by the surface reaction (Gulsun, 2003; Ahlbeck et al., 1995; Siagi and Mbarawa, 2009; Altun, 2014). This yields the following equation for computing the reaction kinetics of marble waste dissolution in aqueous medium:

$$t = \frac{\rho_k R}{k_s C_A} \left[1 - (1 - X)^{\frac{1}{3}} \right], \quad (1)$$

where t is the reaction time (min), R the universal gas constant ($\text{kJ mol}^{-1} \text{ K}^{-1}$), X conversion fraction of dissolving material, ρ_k molar density of sorbent (kg mol m^{-3}), C_A concentration of HCl in solution (mol cm^{-3}), k reaction rate constant (min^{-1}). Further simplification of this equation gives:

$$kt = 1 - (1 - X)^{\frac{1}{3}}. \quad (2)$$

After the computation of $1 - (1 - X)^{\frac{1}{3}}$ values and plotting these as a function of time, the slope of obtained curve corresponds to the k value, i.e. the reaction rate constant. Higher k means higher dissolution rate of the sorbent during reactions in WFGD.

Results and discussion

Effect of chemical composition

Marble wastes considered in this work mainly consisted of CaCO_3 and MgCO_3 with lesser contents of SiO_2 , Fe_2O_3 and other minor components (Table 1). The contents of these components varied significantly with respect to the waste type. Type I and II wastes were distinguished with their superior CaCO_3 content, while types VI to IX involved comparatively higher MgCO_3 (Table 1).

Dissolution behaviors of marble wastes expressed as fractional conversion, X (%) as a function of time (minute) are presented in Fig. 2. The reaction rate constants were calculated by using the plot of $1 - (1 - X)^{\frac{1}{3}}$ vs. time for dissolution reaction of each waste type. The fractional conversion for each waste type at certain time (at 15, 30, 50, 70, 100 and 120 minutes) as well as the calculated reaction rate constants are presented in Table 2 with respect to the major components in the wastes.

Table 2. Dissolution characteristics of marble wastes vs. major components (decreasing order)

Waste type	Fractional conversion, X (%)						Reaction rate const., k (min^{-1})	CaCO_3 (%)	MgCO_3 (%)	Fe_2O_3 (%)
	15 min	30 min	50 min	70 min	100 min	120 min				
Type I	42	56	64	70	77	82	$2.9 \cdot 10^{-4}$	97.80	1.20	0.66
Type II	38	53	62	68	76	80	$2.8 \cdot 10^{-4}$	96.04	0.81	0.74
Type IV	32	47	57	63	71	74	$2.6 \cdot 10^{-4}$	94.00	3.60	1.40
Type III	30	44	54	61	70	72	$2.4 \cdot 10^{-4}$	94.12	3.56	1.02
Type V	26	41	51	58	67	68	$2.3 \cdot 10^{-4}$	92.56	5.25	1.10
Type VII	21	36	46	52	63	64	$2.2 \cdot 10^{-4}$	89.00	7.36	1.62
Type VI	20	33	44	53	63	63	$2.0 \cdot 10^{-4}$	89.28	7.12	1.15
Type IX	17	30	40	48	59	59	$1.8 \cdot 10^{-4}$	86.10	9.85	0.96
Type VIII	13	25	35	44	56	57	$1.5 \cdot 10^{-4}$	87.40	11.22	0.66

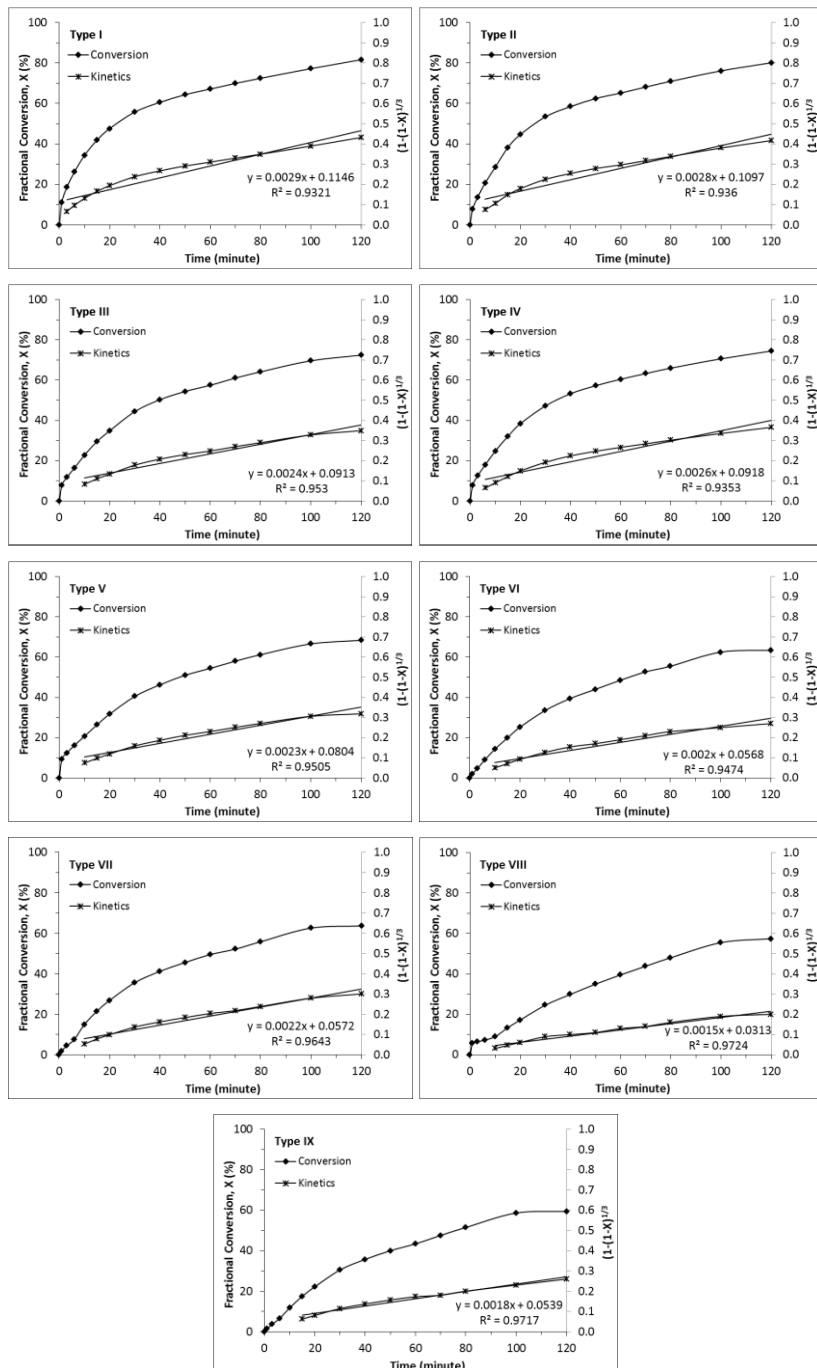


Fig. 2. Dissolution behavior of marble wastes with time

Type I and II wastes provided the highest ability to dissolution after 120 minutes, with fractional conversions of 82 and 80 %, respectively (Table 2). For Types III and IV the best reactivity was equal to 72 and 74%, respectively. For Types V, VI and VII, the ability to dissolution was moderate with the fractional conversions of less than 70% after 120 minutes. For Types VIII and IX the fractional conversions as low as 57 and 59%, respectively were recorded (Fig. 2 and Table 2). The extents of conversion for these two waste types were also low after 15, 30, 50, 70 and 100 minutes (Table 2). In conformity with the dissolution profiles, the waste types with the highest extents of dissolution yielded the highest reaction rate constants (Fig. 2 and Table 2): For Type I and II, k values were $2.9 \cdot 10^{-4}$ and $2.8 \cdot 10^{-4} \text{ min}^{-1}$, respectively, while k was equal to $1.5 \cdot 10^{-4} \text{ min}^{-1}$ for Type VIII waste (Table 2).

The obtained results indicate that despite being calcareous materials, the reactivity of marble wastes may significantly vary. On the basis of the assessment of the changes in the reactivity of wastes and contents of CaCO_3 , MgCO_3 and Fe_2O_3 (Table 2), dissolution behavior of wastes is particularly linked with these three compounds. The abundance of CaCO_3 is a major aspect that favors the dissolution ability of the sorbents. Type I and II wastes, distinguished with the highest fractional conversion had outstanding extent of CaCO_3 among the wastes studied. Also, with decrease of CaCO_3 down to 87.40% (Type VIII waste), the fractional conversion was as low as 57% (Table 2). The favoring effect of CaCO_3 on the reactivity has been reported in several previous studies on the dissolution behavior of calcareous materials (Hosten and Gulsun, 2004; Lianqing and Jingjuan, 2011; Altun 2014). This effect is due to the abundance of carbonate ions that show the ability to dissolution and affinity to reaction with the hydrogen and/or hydronium ions in acidic solutions (Ahlbeck et al., 1995; Carletti et al., 2012).

It would be misleading to attribute the dissolution ability of wastes only to the content of CaCO_3 . The results also revealed an influence of MgCO_3 on the reactivity. Unlike CaCO_3 , MgCO_3 negatively affected dissolution of the wastes. In addition to the reactivity, a low content of CaCO_3 in Types VIII and IX having apparently higher MgCO_3 (11.22 and 9.85%, respectively), should contribute to a low reactivity of these sorbents. Another observation which supports this is the dissolution behavior of marble wastes having similar content of CaCO_3 but varying amounts of MgCO_3 . Type I-II and type VIII- IX illustrate this case. Type II reveals almost an equivalent ability to dissolution to type I waste, despite 2% lower CaCO_3 content. Also, although CaCO_3 content of type VIII waste is higher than that of type IX, type IX, it yields higher fractional conversion and greater reaction rate constant (Fig. 2 and Table 2). It is attributed to the higher MgCO_3 contents of type I and VIII wastes. The inhibiting influence of Mg on reactivity of calcareous sorbents has been reported by other researchers (Ahlbeck et al., 1995; Hosten and Gulsun, 2004; Siagi and Mbarawa, 2009; Lianqing and Jingjuan, 2011; Carletti et al., 2012; Altun, 2014) and is attributed to the lower dissolution rate of dolomite as compared to that of calcite (Lund et al., 1973; Lianqing and Jingjuan, 2011).

The effect of Fe_2O_3 on the dissolution behavior should also be noted. For sorbents with similar CaCO_3 and MgCO_3 contents, as in the cases of type III-IV and type VI-VII couples, the ability to dissolution is influenced by the content of Fe_2O_3 . A higher Fe_2O_3 content favors dissolution and reaction rate: type IV marble waste yields a higher fractional conversion and a greater reaction rate constant as compared to type III. The content of Fe_2O_3 of type IV (1.40 %) is higher than that of type III waste (1.02 % Fe_2O_3). Similar results were attained for the type VI-VII pair. The higher content of Fe_2O_3 in type VII (1.62 %) provided higher dissolution ability and faster dissolution as compared to the type VI waste (1.15 % Fe_2O_3), although these two waste types had similar contents of CaCO_3 and MgCO_3 (Fig. 2 and Table 2). It confirms the previous findings. The presence of iron was reported to increase the dissolution rate of calcareous sorbents as well as their SO_2 capture performance (Davini, 2000; Lianqing and Yin, 2011), and it was associated with the catalytic activity provided by iron over dissolution of sorbent particles.

Type I and II wastes were identified to provide the distinctive dissolution behavior and the highest reactivity as compared to other waste types. Subsequently further research was conducted using the Type I waste.

Effect of particle size

The particle distribution of the sorbent is another major aspect to attain sufficient SO_2 control performance in WFGD units. Limestone, the common sorbent in WFGD units, is used in powder form, and therefore it has to be intensively ground to the required particle size. The commonly applied particle size in WFGD is 100% passing (P_{100}) 45 μm . This is achieved by crushing the limestone in a ball milling. In general, reducing the sorbent to the required fine particle sizes is not a problem, but comminution and particularly grinding is a highly energy-consuming and an expensive process.

The influence of the particle size on the reactivity is investigated to identify the changes in the dissolution behavior of marble wastes with respect to the particle size. The opportunity of using coarser particles for comparable reactivity to the commonly used P_{100} size of 45 μm was also investigated. The dissolution behaviors of type I wastes ground to P_{100} sizes of 37, 44, 53, 75 and 100 μm are shown in Fig. 3. The fractional conversions after 15, 30, 50, 70, 100 and 120 minutes and the reaction rate constants corresponding to different P_{100} sizes are also presented in Table 3.

Table 3. Dissolution characteristics of Type I marble waste as a function of particle size

P_{100} (μm)	Fractional conversion, X (%)						Reaction rate const., k (min^{-1})
	15 min	30 min	50 min	70 min	100 min	120 min	
37	45	59	67	72	79	84	$3.0 \cdot 10^{-4}$
44	42	56	64	70	77	82	$2.9 \cdot 10^{-4}$
53	39	54	63	69	76	80	$2.9 \cdot 10^{-4}$
75	35	49	60	66	73	74	$2.6 \cdot 10^{-4}$
100	31	44	55	62	68	68	$2.4 \cdot 10^{-4}$

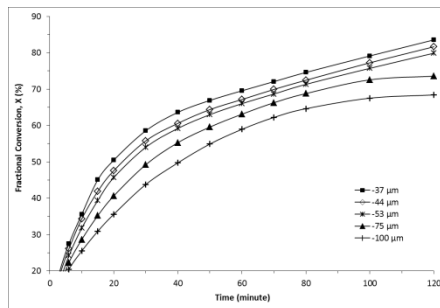


Fig. 3. Dissolution behavior of Type I marble waste with respect to particle size

The results showed that particle size of the sorbent is a critical aspect that remarkably affects the reactivity. Firstly, it should be noted that P_{100} size of 53 μm is a critical point for sorbent fineness and decrease down to -44 μm and further reduction to -37 μm provided slight increases in the fractional conversion values (Fig. 3 and Table 3). At P_{100} size of 53 μm , the fractional conversion after 120 minutes was 80% and gradually increased to 82 and 84% at P_{100} sizes of 44 and 37 μm , respectively. Although 4% difference in the fractional conversion might seem apparent, size reduction to -37 μm rather than -53 μm is a critical trade-off due to the energy-intensive nature of grinding. It should also be noted that the same reaction rate constant value ($2.9 \cdot 10^{-4} \text{ min}^{-1}$) was achieved for dissolution of -53 and -44 μm and it increased only to $3.0 \cdot 10^{-4} \text{ min}^{-1}$ at the extreme fineness of -37 μm (Table 3). This implies that the reactivity of the -53, -44 and -37 μm sizes were slightly different.

Using coarser particles reduced the reactivity of type I marble waste. For particle size of -75 μm , fractional conversions were apparently lower at time as compared to -53 μm and after 120 minutes it was as low as 74% (Fig. 3 and Table 3). For particles -100 μm , the reactivity of the sorbent was quite low, yielding dramatically reduced fractional conversions at all instants. Only 68% fractional conversion was attained after 120 minutes. Relatively lower reactivity of the coarsest particles was also reflected with the lowest reaction rate constant of $2.4 \cdot 10^{-4} \text{ min}^{-1}$ (Table 3).

These results showed that the amount of marble waste converted for the same time periods became higher with increase in fineness. These observations are in agreement with the previous statements on the dissolution-particle size relation of other calcareous sorbents (Hosten and Gulsun, 2004; Siagi and Mbarawa, 2009). The increase in the reactivity of finer particle sizes was attributed to the increase in the surface areas of the sorbent entities, leading to relatively faster dissolution and higher fractional conversions, particularly at the initial phases of reaction.

Effect of temperature

The effect of temperature on the dissolution behavior of marble wastes is shown in Fig. 4. Also, the fractional conversions at time and the reaction rate constants computed at different temperatures are presented in Table 4.

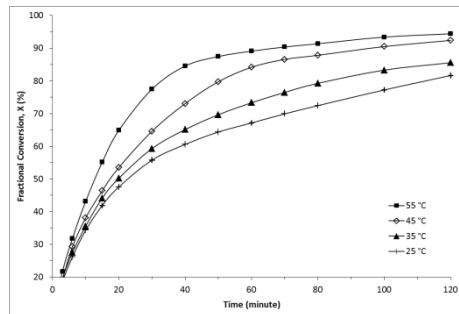


Fig. 4. Dissolution behavior of Type I marble waste with respect to temperature

Table 4. Dissolution characteristics of Type I marble waste as a function of temperature

Temperature (°C)	Fractional conversion, X (%)						Reaction rate constant, k (min ⁻¹)
	15 min	30 min	50 min	70 min	100 min	120 min	
25	42	56	64	70	77	82	$2.9 \cdot 10^{-4}$
35	44	59	70	76	83	86	$3.4 \cdot 10^{-4}$
45	46	65	80	87	90	92	$4.5 \cdot 10^{-4}$
55	55	77	87	90	93	94	$4.6 \cdot 10^{-4}$

At temperatures from 25 to 55 °C the reactivity of marble wastes increased gradually and fractional conversion values became higher with temperature. For instance, the fractional conversion of 70% at 25 °C increased to 90% at 55 °C. After 120 minutes, the fractional conversion of 82% at 25 °C was as high as 94% at 55 °C (Table 4). The effect of temperature on dissolution of wastes was clearly seen in dissolution vs. time profiles (Fig. 4). With increase in temperature, dissolution of wastes occurred much faster (the fractional conversion that approximated to the highest conversion value recorded at the 120th minute was achieved earlier). At temperatures from 45 and 55 °C the fractional conversion equal to 87% was achieved only after 50 and 70 minutes, respectively, and 87% of the fractional conversion was higher than the fractional conversion after 120 minutes at 25 (82%) and at 35 °C (86%) (Table 4). Higher reactivity and increased rates of dissolution with increases in temperature were clearly reflected by the reaction rate constants. As the temperature shifted from 25 to 55 °C, the reaction rate constants increased. The reaction rate constant of $2.9 \cdot 10^{-4}$ min⁻¹ at 25 °C raised to $4.6 \cdot 10^{-4}$ min⁻¹ at 55 °C. The reaction rate

constant increased from $3.4 \cdot 10^{-4}$ to $4.5 \cdot 10^{-4} \text{ min}^{-1}$ when the temperature increased from 35 to 45 °C (Table 4).

The obtained results indicated the favoring influence of temperature on the reactivity of marble wastes. With gradual increments in temperature, dissolution of the wastes occurred more effectively. Not only the ability to dissolution, but also the rate of dissolution was positively affected, with remarkable increases in reaction rates observed particularly at 45 and 55 °C. Here, dissolution temperature of 45 °C would be noted as the optimum level. The increase in fractional conversion values and reaction rate constants from 35 to 45 °C was observed. However the dissolution profiles and reactivity indicators at 45 and 55 °C were slightly different (Fig. 4 and Table 4).

Effect of pH

The effect of pH on dissolution profiles of marble wastes is shown in Fig. 5. Changes in the fractional conversions and reaction rate constants as a function of solution pH are presented in Table 5. The pH was quite influential on the reactivity and the changes in dissolution ability and reaction kinetics were apparent when the pH of the solution was shifted from acidic to neutral. The fractional conversions became gradually less at time as the solution was less acidic. The fractional conversion of 85% at the 120th minute at pH 3.0 dropped by 20% at neutral pH (Table 5). The reaction tended to occur more slowly with pH increase, as revealed by the decrease in the reaction rate constant, particularly above pH 5.0. The reaction rate constant decreased from $3.2 \cdot 10^{-4}$ to $2.2 \cdot 10^{-4} \text{ min}^{-1}$ as the solution pH increased from 3.0 to 7.0 (Table 5). It should be noted that despite the decreasing trend, reductions in the fractional conversion values and reaction rate constants were relatively slight as the pH of the solution increased from 3.0 to 4.0, and then to 5.0. However, above pH 5.0, the negative influence of decreasing acidity on reactivity was apparently observed (Table 5).

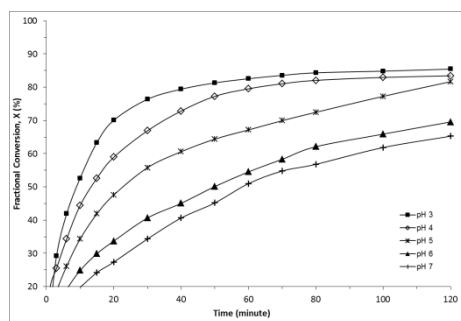


Fig. 5. Dissolution behavior of type I marble waste with respect to pH

Table 5. Dissolution characteristics of Type I marble waste with respect to pH

pH	Fractional conversion, X (%)						Reaction rate constant, k (min $^{-1}$)
	15 min	30 min	50 min	70 min	100 min	120 min	
3.0	63	76	81	84	85	85	$3.2 \cdot 10^{-4}$
4.0	53	67	77	81	83	83	$3.0 \cdot 10^{-4}$
5.0	42	56	64	70	77	82	$2.9 \cdot 10^{-4}$
6.0	30	41	50	58	66	70	$2.4 \cdot 10^{-4}$
7.0	24	34	45	55	62	65	$2.2 \cdot 10^{-4}$

The dissolution ability and reaction rate of marble waste were positively affected by low pH of solution. Considering that the marble waste is a calcareous material, this result was anticipated. As it was suggested by Shih et al. (2000) and confirmed by Siagi and Mbarawa (2009), in dissolution of calcareous sorbents, mass transfer of hydrogen ions is the rate controlling mechanism. As the solution is more acidic, the increase in hydrogen ions causes faster dissolution of calcareous particles. This suggestion also complies with the Ahlbeck et al. (1995) explanation about the interaction of hydronium and carbonate ions during the dissolution of limestone in acidic solution. The findings in this work as well as previous statements imply that, acidic solution pH should be provided in practice, to contribute to the dissolution of marble waste and other potential calcareous sorbents. However, similar to the effect of temperature, a critical level of acidity was observed, which is pH 5.0. Despite the increase in the reactivity and reaction rate of the marble waste below this pH, the changes were not significant. Considering process chemistry and economics, pH 5.0 was proposed as the optimum acidity for a favorable dissolution behavior.

Conclusions

Reactivity, an important aspect for calcareous materials for use as SO_2 sorbent in wet flue gas desulphurization, was assessed for marble wastes. The goal was to identify parameters significantly effecting the dissolution ability of marble wastes. Monitoring fractional conversions with time as a function of chemical compositions of the waste types revealed that CaCO_3 and MgCO_3 mainly determine dissolution characteristics, the latter having a negative factor on reactivity. Fe_2O_3 also influences the reactivity, most probably as a catalyst. Increases in Fe_2O_3 content accelerate dissolution and result in higher dissolution. Fineness was identified as a critical physical sorbent feature. Up to a certain degree of fineness, P_{100} size of 53 μm in this work, dissolution profile and ability were remarkably favored. Temperature and pH were also notably effective and the shifts towards higher dissolution temperatures and lower pH conditions, particularly from 25 to 45 $^{\circ}\text{C}$ and from pH 7.0 to 5.0, increases reactivity and reaction rates and earlier conversion of the sorbent. However, the degree of particles fineness, temperature and solution pH are the

critical parameters to be considered. Optimization is necessary for implementing marble waste utilization in wet flue gas desulphurization because these three parameters are the major economic and environmental factors of SO₂ control.

References

AHLBECK J., ENGMAN T., FALTEN S., VIHMA M., 1995, *Measuring the Reactivity of Limestone for Wet Flue-Gas Desulfurization*, Chem. Eng. Sci. 50 (7), 1081-1089.

ALTUN N.E., 2014, *Assessment of Marble Waste Utilization as an Alternative Sorbent to Limestone for SO₂ Control*, Fuel Process. Technol. 128, 461-470.

BROWN S.R., DEVAULT R.F., WIILIAMS P.J., 2010, *Determination of Wet FGD Limestone Reactivity*, Electric Power, Baltimore, USA, 1-8.

CARLETTI C., BJONDAHL F., DE BLASIO C., AHLBECK J., JARVINEN L., WESTERLUND T., 2012, *Modeling Limestone Reactivity and Sizing the Dissolution Tank in Wet Flue Gas Desulfurization Scrubbers*, Environ. Prog. Sustain. Energ. 32 (3), 663-672.

DAVINI P., 1992, *Behaviour of certain by-products from the manufacture of marble in the desulphurization of flue gases*, Resour. Conserv. Recy. 6 (2), 139-148.

DAVINI P., 2000, *Investigation into the desulphurization properties of by-products of the manufacture of white marbles of Northern Tuscany*, Fuel 79 (11), 1363-1369.

DUZYOL S., 2015, *Evaluation of Flocculation Behavior of Marble Powder Suspensions*, Physicochem. Probl. Miner. Process. 51 (1), 5-14.

GULSUN M. 2003, *Reactivity of limestones of different sources for flue gas desulfurization application*, MSc Thesis, Graduate School of Natural and Applied Sciences, Mining Engineering, Middle East Technical University, Ankara, Turkey.

HOSTEN C., GULSUN M., 2004, *Reactivity of Limestones from Different Sources in Turkey*. Miner. Eng. 17, 97-99.

KAMINSKI J., 2003, *Technologies and costs of SO₂-emissions reduction for the energy sector*, Appl. Energ. 75, 165-172.

KUPICH I., GIRCZYS J., 2008, *Sludge Utilization Obtained from Zn-Pb Mine Water Treatment*, Physicochem. Probl. Miner. Process. 42, 91-106.

LIANQING Y., JINGJUAN G., 2011, *Study on Wet FGD Limestone Quality*, Third International Conference on Measuring Technology and Mechatronics Automation, 605-608.

LUND K., FOGLER S.H., MCCUNE C.C., 1973, *Acidization-I. The Dissolution of Dolomite in Hydrochloric Acid*, Chem. Eng. Sci., 28, 691-700.

SHIH S.-M., LIN J.-P., SHIAU G.-Y., 2000, *Dissolution Rate of Limestones of Different Sources*, J. Hazard. Mater. B79, 159-171.

SIAGI Z.O., MBARAWA M., 2009, *Dissolution rate of South Australian calcium-based materials at constant pH*, J. Hazard. Mater. 163, 678-682.

STUMPF TH., ROEDER A., HENNICKE H.W., 1984, *The reaction behavior of carbonate stone dusts in acid solution, more particularly sulphurous acid. Part II: Important influence parameters, and measurement on various carbonate stone dusts for flue gas desulphurization (in German)*, Zem-Kalk-Gips 37 (9), 454-461.

UKAWA N., TAKASHINA T., SHINODA N., SHIMIZU T., 1993, *Effects of particle size distribution on limestone dissolution in wet FGD process applications*, Environ. Prog. 12 (3), 238-342.

ZHAO J., JIN B., ZHONG Z., 2007, *The degree of desulphurization of limestone/gypsum wet FGD spray tower using response surface methodology*, Chem. Eng. Technol. 30 (4), 517-522.

Professor Janusz Kazimierz Girczys, Ph.D., D.Sc.

a tribute on his 80th birthday



Janusz Kazimierz GIRCZYS obtained his master degree in chemical engineering technology from Chemical Faculty of the Silesian University of Technology in Gliwice in 1958. After graduation he worked for two years as a research assistant at the Department of Physical Chemistry, Faculty of Chemistry of the same University. He supervised students studying corrosion inhibition in the steam phase.

In January 1960 he joined newly established Experimental Research Station of Ores at the Marchlewski Mining Company, later renamed Biały Orzeł Mining and Metallurgy Combine (KGH Biały Orzeł). He participated in research on mineral processing technology for the domestic lead, zinc and copper mining plants. In 1961 he participated in the annual postgraduate course on Radioactive Isotopes Techniques, run by the Department of Physics II of the Mining and Metallurgy University of Technology in Cracow. This allowed him to obtain qualifications to conduct independent projects with the open and closed sources of radiation. While continuing employment at KGH Biały Orzeł, he organized the Isotope Laboratory for Non-Ferrous Metals industry. He designed the laboratory, which after being approved by the Polish Central Laboratory for Radiological Protection, was built in 1965 as a class II Radiometry Laboratory.

Professor Girczys was the leader of the Laboratory for 17 years doing research for the non-ferrous metal industry. During that time he cooperated with the people of the Department of Physics II of the AGH University of Technology and the Commission on Radiometric Analyses. In the framework of this cooperation, he performed studies and implemented methods for rapid radiometric analyses of Zn-Pb ores. Another area

of work that he carried out in his isotopic laboratory was isotopic markers for laboratory and industrial technological processes for mineral processing of ores. In 1969, during a training in the USSR, he acquainted himself with the application of isotopic techniques in mining and metallurgical industry.

In the course of his investigations he created the concept of his doctoral thesis, which main goal was to improve flotation technology of sphalerite ores using radiometric testing of xanthate sorption on sphalerite. He obtained PhD degree from the Silesian University of Technology in 1970. His dissertation was entitled "Flotation of sphalerite in the light of radiometric studies on xanthate adsorption". He supervised master thesis students of the Mineral Processing Department of the Silesian University of Technology working on isotopic tracer methods to study interactions of flotation reagents with minerals. Until 1989 he was a part time employed as contract associate professor at the Mineral Processing Department of the Silesian University of Technology, conducted seminars, and also taught a mineral processing course.

Due to the industry restructuring in 1973, his isotope laboratory was transferred from KGH Biały Orzeł to the CUPRUM Research and Design Establishment in Bytom. While continuing to work in the Laboratory of Radioactive Isotopes, he applied his research results in the non-ferrous metals industry.

In 1975 he participated in the development of the project on utilization of mineral wastes of the non-ferrous metal industry. He directed works on management of wastes and processing of Zn-Pb ores. This program has brought economic effects as a result of a direct implementation of the results of the studies. Most of all, it allowed for putting in order the waste management. Until 1983 he and his team made dozens of documentations and expertise opinions for the non-ferrous metal industry. As a result of the work carried out over this period, Prof. Girczys and his coworkers

- improved health and safety by lowering the concentration of lead in the air at the the Zn-Pb ore mines
- eliminated pollution of silver, designated for export, with isotope ^{110}Ag
- implemented a modern measuring equipment based on isotopic techniques
- reduced consumption of ferro-silicon in industrial streams of heavy liquid leading to a reduction of processing costs.

Until 1983, he published 20 papers, two of them in foreign journals (Transactions of Institution of Mining and Metallurgy and Canadian Metallurgical Quarterly). In addition to that, the results of his investigations on the mechanisms of reagents interactions with sphalerite in the flotation process were industrially implemented.

The results of investigations on sphalerite involving the radioactive markers were presented in the monograph entitled "Studies on conditions of optimal action of activator and collector in flotation of zinc blende" published in the Transaction of the Silesian University of Technology (No. 777, 1983). This paper was a foundation of his Doctor of Science degree (DSc, habilitation), while its results were implemented in practice in the industrial flotation of sphalerite. As a result, there was a significant reduction of CuSO_4 (the most expensive reagent used in the process) consumption at

the increased recovery of zinc. He obtained DSc degree in mineral processing from the Mining Faculty of the Silesian University of Technology in Gliwice on 10 April 1984.

Due to health problems, after 17 years of working with ionizing radiation, he quit using this technique. In 1983 he moved to the Central Mining Institute (Glowny Instytut Gornictwa, GIG) in Katowice. He changed his research interests along with the methodology and he became involved in research on environmental protection, more specifically on utilization of low grade raw materials and waste disposal.

In his flotation research, his main interest was the waste management and fine size materials. He participated in the development of waste management and disposal of waste from desulfurization processes of fine coal preparation plants. Since 1985 he had directed, as a national coordinator, a management program on wastes and landfills impact on the aquatic environment. The research conducted at GIG, from the laboratory to industrial scale, included

- gravity separation of pyrite from coal preparation waste
- flotation of thermal coal under different reagent regimes
- beneficiation of coal grinding wastes
- coal heaps and coal wastes fire prevention.

At that time, he organized the Environmental Protection Research Group in GIG to study ecology in mining areas. He was the leader of the Group for 6 years. From 1989 to 1990 he coordinated research, financed by the Polish Ministry of Industry, conducted by different Polish institutions, dealing with management of salty waters of bituminous coal mines. He published three monographs. The first two contained data of his own research on properties, utilization and impact on the environment and the fine-sized coal waste and wastes of the lead-zinc industry. The third monograph was designed for environmental specialists. It was also appreciated by students as a textbook. The book was based on the premise that the effectiveness of the technology used in the processing of solid wastes requires a close relationship between knowledge on unit operations and changes occurring in the material.

His scientific achievements include

- 65 evaluations and research reports
- development and implementation of two research programs on management of mining and foundry wastes
- obtaining funds and conducting five projects financed by the Polish Research Committee (KBN)
- acquiring financing and implementation of the "Burning of municipal waste including coal fines" financed by the Maria Curie-Sklodowska Fundation (in collaboration with the Argonne National Laboratory-DOE)
- supervising eight PhD thesis
- reviewing fifteen doctoral thesis
- reviewing five books published by the Silesian University of Technology and by the Czestochowa University of Technology Publishing Office
- reviewing several research projects founded by KBN

- obtaining eleven patents and patent claims
- involvement in organizing conferences and seminars, including three international, membership in editorial boards of scientific journals (Physicochemical Problems of Mineral Processing, Natura Silesiae Superioris, Ochrona Powietrza i Problemy Odpadów).

Since 1993 he was employed at the Institute of Environmental Engineering of the Czestochowa University of Technology. Since 1995, this became his primary employment.

At this Institute he organized and chaired the Wastes Utilization and Soil Protection Group. In 1994 he was appointed Professor of GIG and in 1995 Professor of Czestochowa University of Technology.

In 1994–1995 he taught the waste management courses within Postgraduate Studies offered by the Silesian Technical University for teachers. Next to teaching, he continued studies on the storage of hazardous waste on active mineral media. His research was prized by KBN (KBN Service Information, No. 2, 2002). His patented method of disposal of the waste of processing of battery scraps was applied in practice. Among the works utilized industrially is the technology allowing for exploitation of post-coal waste heaps and fire prevention of coal heaps.

He was appointed a full Professor on May 20, 2005. He retired in 2012. His wife Teresa is also retired. They have one daughter, Katarzyna who is a medical doctor with PhD and a granddaughter Karolina.

List of publications

1. J. Girczys: *Oznaczenie podstawowych własności pyłów rafinerii ołowiu*. Rudy i Metale Nieżelazne 1963, vol. 8, 511, p. 447/459.
2. S. Cierpisz, J. Girczys: *Zastosowanie izotopów promieniotwórczych w górnictwie rud i hutnictwie*. Rudy i Metale Nieżelazne 1966, vol. 11, 2, p. 105/108.
3. J. Girczys, Z. Horzela: *Pomiar stężenia roztworów wodnych ksantogenianu znaczonego*. Rudy i Metale Nieżelazne 1967, vol. 12, nr 6, p. 310/312
4. J. Girczys, A. Piątkowski: *Próby przemysłowe izotopowej wagi taśmowej*. Rudy i Metale Nieżelazne 1967, vol. 12, nr 7, p. 359/362.
5. J. Girczys, J. Laskowski: *Zjawiska towarzyszące adsorpcji ksantogenianu amylowego na sfalerycie*. Fizykochemiczne Problemy Przeróbki Mechanicznej Kopalni SITG Politechnika Śląska Gliwice 1967, vol. 2, p. 56/72.
6. J. Girczys, J. Laskowski: *Radiometryczne badania adsorpcji jonów miedzi ksantogenianów na sfalerycie z niecki bytomskiej*. Fizykochemiczne Problemy Przeróbki Kopalni SITG Pol. Śl. Gliwice 1969, vol. 3, p. 162/181.
7. J. Girczys, T. Kusdrzał: *Radiometryczne oznaczenie Zn-Fe analizatorem PIF*. Rudy i Metale Nieżelazne 1970, 1, p.27/30.
8. J. Girczys, *Zastosowanie izotopowego analizatora fluorescencyjnego do analizy koncentratów flotacyjnych*. Rudy i Metale Nieżelazne 1971, 12. p. 595/599.

9. J. Girczys, J. Laskowski: *Badania znacznikowe podstawowych zależności w procesie flotacji sfalerytu dla automatyzowania operacji dozowania odczynników flotacyjnych*. Sympozjum Komitetu Górnictwa PAN Sekcji Utylizacji Kopalń, Katowice 1971.
10. J. Girczys, J. Laskowski: *Badania niektórych podstawowych zależności we flotacji sfalerytu z niecki bytomskiej*. Rudy i Metale Nieżelazne 1972, 3, p.100/103.
11. J. Girczys, J. Laskowski: *Mechanism of flotation of unactivated sphalerite with xanthates* Mineral Processing. Extractive metallurgy Tramp./Section C of the Institution of Mining and Metalurgy, vol. 81, 1972, C 118/119.
12. J. Girczys, J. Laskowski, J. Lekki: *Coper activition studies with sphalerite*. Canadian Metallurgical Quarterly, vol. 11 Oct.-Dec. 1972, 4, p. 553/558.
13. J. Girczys, K. Dąbrowski: *Zależność użycia $CuSO_4$ od pH podczas selektywnej flotacji blendy cynkowej*. Rudy i Metale Nieżelazne 1975, 6, p. 299/304.
14. J. Girczys, J. Laskowski: *Usprawnianie przemysłowego procesu flotacji blendy cynkowej na podstawie laboratoryjnych badań fizykochemicznych*. Zb. Ref. XIV Seminarium Fizykochemiczne Problemy Przeróbki Kopalń, vol. 9, Wrocław 1975, p.81/91.
15. J. Girczys, H. Niezgoda, J. Skowronek: *Badania znacznikowe obiegu cieczy zawiesinowej w procesie wstępnego wzbogacania rud Zn-Pb*. CUPRUM, 6, listopad-grudzień 1975, p. 39/43.
16. J. Girczys, H. Niezgoda: *Wpływ częściowego utlenienia ksantogenianu etylowego na wyniki flotacji blendy*. Rudy i Metale Nieżelazne, 12, 1978, p. 625/630.
17. J. Girczys, D. Kwiecień: *Roztwarzanie elektrochemiczne miedzi w alkalicznej zawiesinie rudy*. Zesz. Nauk. Pol. Śl. Chem., 1979.
18. J. Girczys, D. Kwiecień, H. Niezgoda: *Flotacja blendy cynkowej aktywowanej przez anodowe roztwarzanie miedzi*. CUPRUM 6, 1980.
19. J. Girczys: *Jakość koncentratu i kinetyka flotacji blendy cynkowej*. Rudy i metale, 6, 1980, 25, p. 254/259.
20. J. Girczys, J. Skowronek, H. Niezgoda: *Badania obiegu materiałów w układzie mielenia i klasyfikacji*. CUPRUM, 1, styczeń-luty 1981, p. 7/14.
21. J. Girczys, J. Skowronek, B. Źródłowski: *Badania spektrometryczne gamma rud cynkowo-olowioowych i produktów ich przeróbki*. Zeszyty Nauk. Pol. Śl., 122, Gliwice 1983, p.119/129.
22. J. Girczys: *Możliwości odzysku składników użytecznych z odpadów flotacji blendy cynkowej*. Rudy i metale Nieżelazne 1983, 12, p. 493/495.
23. J. Girczys, *Badania warunków optymalnego działania aktywatora i zbieracza w procesie flotacji blendy cynkowej*, Zeszyty Naukowe Pol. Śl. Seria Górnictwa, 127, Gliwice 1983.
24. J. Girczys, J. Laskowski: *Selectivity in sphalerite – markasite flotation during processing of Pb-Zn-Fe sulphide ores under alkaline conditions with copper sulphate activation*. XV Międzynarodowy Kongres Mineralurgii Cannes 1985, vol. II, Flotation Hydrometallurgy p. 167/179.
25. J. Girczys: *Flotacja blendy o zmiennym składzie mineralogicznym*. Fizykochemiczne Problemy Mineralurgii 17, 1985, p. 43/50.
26. J. Girczys: *Trójproduktowa przeróbka zasiarczonych odpadów węglowych*, Fizykochemiczne Problemy Mineralurgii 18, 1986, p. 107/116.
27. J. Girczys, L. Suchy: *Zastosowanie flotacji i wzbogacania grawitacyjnego w procesie przeróbki odpadów węglowych*. IX naukowo-przemysłowe seminarium Wzbogacanie grawitacyjne węgla, Katowice-Jastrzębie Zdrój 1987.
28. J. Girczys, L. Suchy: *Przygotowanie odpadów po wzbogaceniu zasiarczonych miasłów węglowych do wydzielania pirytów*. Fizykochemiczne Problemy Mieralurgii 20, 1988, p. 27/36.

29. J. Girczys et al., *Problemy bezpiecznego dla wód gruntowych składowania zasiarczonych odpadów powęglowych*. Fizykochemiczne Problemy Mineralurgii, 20, 1988, p. 37/46.
30. J. Girczys et al., *Możliwości produkcji spoiw anhydrytowych z solanek kopalnianych*. Cement Wapno Gips, 10/1991, p.273/275.
31. B. Majka-Myrcha, J. Girczys: *The Effect of Redox Conditions on the Floatability of Coal*. Coal Preparation 1993, vol. 13 p. 21-30.
32. J. Girczys: *Wpływ pH na flotację węgli energetycznych*. Fizykochemiczne Problemy Mineralurgii, 27, 1993, p. 77/88
33. J. Girczys, A. Tabor: *Ochrona środowiska w górnictwie węgla kamiennego*. V Polsko-Niemieckie Forum Ekologiczne, Katowice – marzec 1992. Fridreich-Neuman-Stiffung,. Wyd. DIG Warszawa 1993, p. 65/73.
34. J. Girczys: *Własności zasiarczonych odpadów powęglowych*. Prace Naukowe GIG, 807, Katowice 1996.
35. J. Girczys: *Odpadowe muły węglowe*. Prace naukowe GIG. Nr 815. Katowice 1996.
36. J. Girczys, J. Sobik-SzołysekJ: *Problemy wykorzystania osadników połflotacyjnych rud Zn-Pb rejonu bytomskiego*. Rudy i Metale, R.42, 1997, 7, p. 297/302.
37. J. Girczys, J. Sobik-SzołysekJ: *Wody powierzchniowe w obszarze odpadów flotacyjnych rejonu bytomskiego*. Rudy i Metale, R.43, 1998, 8, p.371/375.
38. J. Girczys, B. Caban-Pabian: *Zanieczyszczenia olejowe i koloidalne wód kopalnianych*. Wiadomości Górnictwa 4, 1999, p. 180/185.
39. J. Girczys, B. Caban-Pabian, W. Pieńkowski: *Substytucja gleby na bazie odpadowych mułów węglowych i osadów ściekowych*. Wiadomości Górnictwa 9, 1999, p. 362/367.
40. J. Girczys, J. Sobik-SzołysekJ: *Uwalnianie i eliminacja metali ciężkich w osadnikach odpadów flotacji blendy*. Fizykochemiczne Problemy Mineralurgii, 33, 1999, p. 33/44.
41. J. Girczys, J. Sobik-SzołysekJ: *Zawartość metali w roślinności osadników połflotacyjnych rud Zn-Pb rejonu bytomskiego*. Rudy i metale, R 44, 1999, 10, p. 500/505.
42. J. Girczys, B. Caban-Pabian: *Oczyszczanie wód kopalnianych z zawiesin*. Wiadomości Górnictwa, 12, 1999, p. 494/499.
43. J. Girczys, B. Caban-Pabian: *Zastosowanie węgla aktywnego do odolejania zasolonych wód kopalnianych*. Wiadomości Górnictwa, 12, 2000, p. 553/556.
44. J. Girczys, J. Sobik-SzołysekJ: *Szlamy po koagulacji wód zrzutowych z kopalni rudnych niecki bytomskiej*. Rudy i metale, R 46, 2001, 4, p. 168/171.
45. J. Girczys, B. Caban-Pabian: *Ocena pracy osadnika zrzutowych wód kopalnianych*. Inżynieria i Ochrona Środowiska, 2001, vol.4., 1, Wyd. P.Cz. p. 95/104.
46. J. Girczys, J. Sobik-SzołysekJ: *Zastosowanie odpadów flotacji blendy jako materiału aktywnie blokującego migrację jonów metali ciężkich*. Wyd. Biblioteka KOMEKO Komdruk-Kaomag Sp. z.o.o. 2001, p. 157/165.
47. J. Girczys, K. Recko: *Możliwość wspólnego zagospodarowania osadów ściekowych z odpadowymi mulami węglowymi*. Inżynieria i Ochrona Środowiska, 2001, vol.4., 1, Wyd. P.Cz. p. 107/116.
48. J. Girczys: *Zagospodarowanie odpadowego gipsu z przerobu złomu akumulatorów. Mikro-zanieczyszczenia w środowisku*. Wyd. P.Cz. Konferencje, 48, 2002, p. 109/115.
49. J. Girczys, J. Szobik- Szoltysek: *Odpady przemysłu cynkowo-ołowiowego*, Wyd. P.Cz., maj 2002, seria Monografie nr 87.

50. J. Girczys: *Warunki zagospodarowania odpadów wtórnego przemysłu cynkowo-ołowiowego*. Ekoprofit, 5, 2002, p. 22/29.
51. J. Girczys, B. Caban-Pabian: *Determination of polycyclic aromatic hydrocarbons in mine water*, Journal of Water Chemistry and Technology, 2003, vol. 25, 4, p. 33/37.
52. J. Girczys, J. Sobik-Szołtysek: *Wpływ na stan wody w Brynicy zrzutu ścieków i wód dołowych*, Inżynieria i Ochrona Środowiska, 2003, vol. 6, 3-4, p. 441/453.
53. J. Girczys, I. Kupich: *Zmiany ładunku zanieczyszczeń w wodach zrzutowych nieczynnych kopalń rud Zn-Pb niecki bytomskiej*. Mikrozanieczyszczenia w środowisku człowieka. Wyd. P.Cz. Konferencje. Częstochowa, 2003, p. 267/272
54. J. Girczys, Z. Trela: *Technical recultivation of coal processing dump*. Tekst polski – materiały Międzynarodowej Konferencji Złów Kopalń Użytecznych, 23-25 listopada 1993, Szczyrk. Tekst angielski, Balkema.
55. J. Girczys, Z. Trela: *Techniczna rekultywacja zwalisk jako podstawowy element ochrony środowiska*. Materiały konferencji nt.: „Wykorzystanie odpadów kopalnianych i pyłów elektrownianych w aspekcie ochrony środowiska”. Instytut Mechaniki Górotworu PAN, Kraków 24 czerwca 1993.
56. J. Girczys: *Wielostronne perspektywy dla gospodarczych zastosowań mulów powęglowych*. IV Konferencja Aktualia i perspektywy Gospodarki Surowcami Mineralnymi. PAN, Centrum Pod. Problemów Gosp. Surowcami Miner. i Energią, Zakopane 5-7 paźdz. 1994, p. – 1/5-18.
57. J. Girczys (współautorstwo): *Applicaton of Coal-Mining Wastes to Diminish Plant Uptake of Heavy Metals from Contaminated Soil*, II Intl. Symposium and Exhibition on Environmental Contamination in Central and Eastern Europe, Budapest, Sept. 1994.
58. J. Girczys, I. Kupich: *Zmiany stężeń zanieczyszczeń w wodach zrzutowych nieczynnych kopalń rud Zn-Pb niecki bytomskiej*, Inżynieria i Ochrona Środowiska 2004, vol. 7, 2, p. 201/208.
59. J. Girczys, I. Kupich: *Zastosowanie glinianu sodu do usuwania siarczanów z wód zrzutowych kopalń Zn-Pb*. Mikrozanieczyszczenia w środowisku człowieka. Wyd. P.Cz. Konferencje 55. Cz-wa 2004, p.49/53.
60. J. Girczys: *Procesy utylizacji odpadów stałych*, Wyd. P.Cz. lipiec 2004, seria Monografie nr 100.
61. J. Girczys: *Sorption of zinc on dolomite from ore deposits* (Polish and English text), Journal of the Polish Mineral Engineering Society, Inż. Mineralna, 1(14), 2005.
62. J. Girczys: *Changes in metal content and grain size inside the body of Pb/Zn flotation dump* (Polish and English text), Journal of the Polish Mineral Engineering Society, Inż. Mineralna, 1(16), 2006.
63. J. Girczys, I. Kupich: *Reduction of sulphate ions concentration in discharge waters from Zn-Pb mines*, Physicochemical Problems of Mineral Processing, 40, 2006, p. 125-134.
64. J. Girczys: *Problemy składowania drobnoziarnistych odpadów mineralnych*, Ochrona powietrza i problemy odpadów, 5, 2006, p.158-164.
65. A. Bajerski, J. Girczys: *Utilization of Waste coal slimes in the aspect of their sorptive prosperites. Workshop on waste management in coal mining and the coal-fired thermal power sector*. 27-29 November 1996, Szczyrk (GIG pod auspicjami Zespołu ds. Węgla Europejskiej Komisji Gospodarczej ONZ).
66. J. Girczys, K. Rećko: *Możliwości termicznej utylizacji osadów ściekowych*. Kraj. Konf. N.B. „Nowe technologie w uzdatnianiu wody, oczyszczaniu ścieków i gospodarce osadowej”. Częstochowa-Ustroń, 25-26 luty 1997, Wyd. Pol. Częstochowska, p. 205/212.

67. J. Girczys: *A sludge granulation as an introductory operation of the thermic utilization.* Invol. Conference on Sludge Menagemenvol. Częstochowa 26-28 June, 1997. The Publishing Office of Technical University of Częstochowa, 1997, p .274/280.
68. J. Girczys: *Muły węglowe jako materiał uszczelniający dla celów prewencji pożarowej i rekultywacji.* Sympozjum N-B. Fundacja Badań Górnictwych i Izba Górnicza. Katowice – 21 listopada 1997.
69. J. Girczys, I. Kupich: *Analiza kierunków utylizacji szlamów z oczyszczania wód zrzutowych górnictwa rud Zn-Pb.* Inżynieria i Ochrona Środowiska.2007, vol. 10, 2, p.153/166.
70. I. Kupich,J., J. Girczys: *Sludge utilization obtained from Zn-Pb mine water treatment* Physicochemical Problems of Mineral Processing, 42, 2008, p. 91-106.
71. V.O.L. Doniecki, J. Girczys, J. Sobik-Szołtysek: *Ocena zastosowania drobnoziarnistych odpadów górnictwa w budowie barier izolacyjnych.* Monografia 149, Wyd. Pol. Koszalińskiej. Koszalin-Kołobrzeg 28-31 maja 2008, p.167/179.
72. J. Girczys, I. Kupich, J. Sobik-Szołtysek: *Usprawnianie procesu oczyszczania wód dolowych kopalń rud rejonu bytomskiego.* Przemysł chemiczny, 5 maja 2008, 87, p.456/459.
73. J. Girczys, I. Kupich: *Skład chemiczny wód zrzutowych górnictwa rud Zn-Pb w aspekcie możliwości ich zagospodarowania.* (Polski and English versions), Journal of the Polish Mineral Engineering Society, Inz. Mineralna, 1(25)-2(26), 2010. p.1/8.

Janusz Laskowski

Jan Drzymala

ISSN 1643-1049

Physicochemical Problems of Mineral Processing, 52(1), January 1, 2016